Control of Single-Molecule Magnetic Properties Using Metallacrowns

by

Thaddeus T. Boron, III

A dissertation submitted in partial fulfillment
of the requirements for the degree of
Doctor of Philosophy
(Chemistry)
in The University of Michigan
2012

Doctoral Committee:

Professor Vincent L. Pecoraro, Co-Chair
Professor Talal Mallah, Co-Chair, Université Paris-Sud 11
Professor Mark M. Banaszak Holl
Professor Rodney C. Ewing
Assistant Professor Bart Bartlett

2012

To my family

Acknowledgements

As anyone who has ever worked on a big project can tell you, it does not come together on its own. I have had the fortunate opportunity to work with a lot of great people during my time at the University of Michigan and I would like to thank them for their help and guidance. First, I would like to thank my advisors Vincent Pecoraro and Talal Mallah. When I came to Michigan, I was not sure if I wanted to study physical or inorganic chemistry. Vince gave me the opportunity to work on a truly physical inorganic project. I think at times it became more physics and less chemistry, which is where Talal came in and really helped, but the project really allowed me to study these two fields. I would like to thank my committee, Profs. Mark Banaszak Holl, Bart Bartlett, and Rodney Ewing for all of their feedback and insightful discussions over the years that have helped frame this work.

I would also like to thank the great crystallographer, Jeff Kampf. I know I have tried Jeff's patience with problematic crystal structures and asking how to solve crystal structures. But I have learned a lot about crystallography from him and I still have a lot to learn. Crystallography played a huge role in my thesis and it certainly would not be what it is without his help.

I had the opportunity to work with some fantastic people in the lab. I could try to thank each individually, but I would surely miss someone. They have given me a lot of feedback and help and made coming into lab a positive experience. I would especially like to thank Curt Zaleski and Curtis Schneider. Curt started the research on this SMM business and really helped me get a handle on the magnetism in my early days. Curtis showed me the ropes my first few years here and taught me how to be a successful researcher.

I would like to thank my friends and family for all their support during the years. I have met a lot of fantastic people along the way and made some truly great friendships. Whether it was road trips or Saturday football or just hanging out, it has been a lot of fun. I would like to thank my family for their support during the years and instilling in me a great love for science, math, and education. My family has really helped me get to this point and have inspired me to do the work that I have done.

Lastly, but certainly not least, I want to thank my wonderful wife Cecily. We have been in different states, time zones, and continents over the past five years. I certainly would not be here today without her support and understanding. She has been my best friend and strongest supporter. I am truly grateful for all that she has done for me.

Table of Contents

Chapter III

Chapter IV

Chapter V

Chapter VI

List of Figures

List of Tables

Abstract

This dissertation studied controlling single-molecule magnetic (SMM) properties by using the metallacrown motif. Large mixed lanthanide-manganese complexes, $\mathbf{Ln^{III}_6Mn^{III}_2Mn^{IV}_2(shi)_6(Hshi)_4(H_2shi)_2(Hsal)_4}$, where H_3shi is salicylhydroxamic acid, H_2sal is salicylic acid, Ln^{III} = Gd^{III}, Tb^{III}, or Dy^{III}, and $\mathbf{Ln^{III}_4Mn^{III}_4(OH)_2(O_2C_2H_3)_2(shi)_4(H_2shi)_4(Hsal)_4}$ Ln^{III} = Dy^{III}, Ho^{III}, or Er^{III}, were produced, with the Dy^{III} analog of each series showing slow magnetic relaxation, a hallmark of SMM behavior.

A new family of $\mathbf{Ln^{III}}$ **14-MC**$_{\mathbf{Mn^{III}Ln^{III}(\mu\text{-}O)(\mu\text{-}OH)N(shi)}}$**-5** complexes ($Ln^{III}$ = Y^{III}, Gd^{III}, Tb^{III}, Dy^{III}, Ho^{III}, or Er^{III}) was prepared which oriented the anisotropy tensors of the Mn^{III} ions in a single direction, perpendicular to the metallacrown plane. The complexes, with the exception of the Y^{III} and Gd^{III} analogs, showed slow magnetic relaxation, with the Dy^{III} analog having a U_{eff} of 16.7 K and $\tau_0 = 4.9 \times 10^{-8}$ s, at the time, the third largest U_{eff} for mixed Mn/Ln complexes, despite using fewer metals than other examples.

Using simpler, planar $\mathbf{Ni^{II}(O_2C_2H_3)_2}$ **12-MC**$_{\mathbf{Mn^{III}N(shi)}}$**-4** complexes revealed that lattice solvents affect whether SMM or single-chain magnetic (SCM) behavior is observed. The $\mathbf{Ni^{II}}$ **12-MC-4** isolated in methanol had a hydrogen-bond network, leading to SCM behavior; the complex isolated in dimethylformamide, lacking the hydrogen-bonding network, shows SMM behavior. To improve SMM properties, the more anisotropic Dy^{III} ion was incorporated, forming $\mathbf{Dy^{III}X_4A}$ **12-MC**$_{\mathbf{Mn^{III}N(shi)}}$**-4** (A = H_3O^+, Na^+, K^+; X = salicylate, benzoate, acetate). SMM behavior occurred only for the salicylate bridged complexes, regardless of counter ion. Slight structural changes due to ligand substitution explain this observation.

Metallacrown single-ion magnet (SIMs) were examined using a series of $\mathbf{Ln^{III}Zn_{16}}$ complexes (Ln^{III} = Gd^{III}, Tb^{III}, Dy^{III}, Ho^{III}, Er^{III}, Yb^{III}), with the $\mathbf{Er^{III}Zn_{16}}$ showing SMM behavior, as revealed by single-crystal SQUID magnetometry measurements. The ligand field around the Ln^{III} ion dramatically affected the magnetic behavior, dependent on the shape of the occupied *f* orbitals.

In conclusion, structures with controlled molecular anisotropy led to well isolated ground states, improving SMM behavior. It was found that for larger Mn/Ln complexes, it is difficult to obtain high U_{eff} without structural control. In addition, Dy^{III} or Er^{III} ions proved to be better Ln^{III} ions due to their intrinsic anisotropy and Kramers doublet ground state.

Chapter I

Metallacrowns and Their Use as Single-Molecule Magnets, Single-Ion Magnets, and Single-Chain Magnets

Pecoraro and Lah first recognized the metallacrown motif in 1989.[1,2] Metallacrowns can be easily thought of as the inorganic analogs to crown ethers[3]. Crown ethers, first recognized in 1967 by Pedersen,[4,5] are supermolecular ionophores capable of selectively binding alkali and alkaline earth cations in their central cavity.[6] Traditional metallacrowns have a simple repeat unit of [M-N-O], and can bind cations in their central cavity. Unlike crown ethers though, metallacrowns can bind a wide range of cations, including alkali,[7] alkali earth,[8,9] *3d*,[2,10] and *4f* cations.[11] Perhaps most interesting in the context of the following work, metallacrowns possess the unique abilities to organize a large number of metals into predictable geometries and to allow for systematic metal substitutions in order to probe their influence on magnetic behavior.

In the late 20th century, there was a great interest in studying the magnetic behavior of molecules. One family of molecular magnets, single-molecule magnets (SMMs), as well as the closely associated group of single-chain magnets (SCMs), became of great interest to chemists and physicists. Two general schemes developed: a top-down approach, where known magnetic materials, such as Prussian blues[12] and magnetite, were shrunk to nanomaterial sizes, and a bottom-up approach, where new magnets were designed from individual molecular building blocks[13]. One of the important advantages of the bottom-up approach was that all molecules would be identical, hopefully leading to relatively easy magnetic experiments.[14] These molecular magnets could possibly be utilized in spintronic devices, high-density information storage, quantum computing, and magnetic refrigeration.[12]

It would be impossible to provide a comprehensive review of all SMMs and SCMs due to the ever-growing collection of new complexes. For those interested in a deeper understanding of SMM theory, please consult one of the numerous reviews.[12,14,15] This chapter will focus on mixed Mn/Ln complexes as well as Ln only complexes that have been studied as single-ion magnets and metallacrowns which have been used as SMMs. A description of metallacrowns will be given first, followed by an in-depth discussion of the theory of molecular magnetism, then a review of the important known mixed Mn/Ln and Ln-only SMMs, SCMs, and single-ion magnets will be given. For the interested reader, in depth reviews of metallacrowns are available.[3,16,17,18]

Metallacrowns

As mentioned above, metallacrowns were first recognized in 1989 by Pecoraro and Lah.[1,2] Since that time, the field has exploded and now extends to labs in the United States, Asia, and Europe. Metallacrowns belong to the family of metallamacrocycles, which fits within the larger classification of metallasupramolecules.[19] Other metallamacrocycles include metallacryptands and metallacryptates, metallahelices and metallahelicates, and metal molecular wheels, rings, squares, cubes, and polygons. Metallacrowns have been used or proposed for varieties of uses, including antibacterial compounds, multi-dimensional solids, molecular recognition agents, and single-molecule magnets.

Metallacrowns borrow the syntax of their crown-ether cousins. For instance, the traditional 12-C-4 is comprised of a twelve-membered ring with a C-C-O base unit that is repeated four times. There is no reason one could not theoretically substitute the C atoms for metals or heteroatoms. An analogous metallacrown would have a M-N-O base unit repeated four times, yielding a 12-MC-4 that appeared analogous to the 12-C-4. Of course, this structure on its own would not be stable; it is important to choose the correct ligand. Thus, the geometry and the size of the metallacrown are often dictated by the ligand choice and overall stoichiometry (Figure 1.1). For a 12-MC-4, in order to form a close loop, the metals must be oriented at 90° angles to each other. To form a 12-MC-4,

four equivalents of metal and ligand are mixed with one equivalent of central metal in solution. The 12-MC-4 geometry and connectivity is promoted by *β*-aminohydroxamic acids or salicylhydroxamic acid. When two metals are bound to a salicylhydroxamic acid ligand, the ligand and metals form a five and a six-membered ring. In order to form the planar 15-MC-5, the metals must be oriented at 108° angles to each other, which are favored by picolinic hydroxamic acid or *α*-aminohydroxamic acids. These hydroxamic acids when bound to metals form two five-membered rings. Again, mixing five equivalents of ligand and ring metal with one equivalent of central metal will yield a 15-MC-5. Both 12-MC-4 and 15-MC-5 clusters have the additional benefit of being planar. Because they are planar, there is an opportunity to orient anisotropy vectors, an important property of SMMs. Without geometric control and planar molecules, anisotropic vectors can accidently coincide and cancel each other.[20] These unique properties are not available to many other complexes used to study SMM phenomena.

The naming of metallacrowns follows the nomenclature of crown ethers. Metallacrowns use the general syntax of crown ethers and substitute MC for C to indicate a metallacrown. As a practical example of this naming scheme, take the complex $Mn^{II}(O_2C_2H_3)_2$ [12-$MC_{Mn^{III}N(shi)}$-4]·$6C_3H_7NO$ (Figure 1.2).[2] This planar structure features a twelve-membered ring The central metal and any coordinated anions are given first; in this case, Mn^{II} is bound with two acetate anions. Next, the ring size, 12 is given. The subscript portion of the name gives the ring metal and its oxidation state, the third heteroatom of the ring (as oxygen makes up the other heteroatom, like a normal crown ether) and an abbreviation for the ligand is given. In the example, the metallacrown ring is comprised of Mn^{III} and a nitrogen from a triply deprotonated salicylhydroximate ligand, commonly abbreviated as shi. The number 4 indicates the number of oxygens binding to the central metal. Lastly, any unbound anions or solvent molecules, in this case, six *N'*-*N'*-dimethylformamide molecules are present. Oftentimes, a shorthand notation of Mn 12-MC-4 or Mn 12MC4 is given, especially when series of complexes are studied where the metallacrown remains constant. Throughout this text, these shorthand notations will be used. For a more rigorous review of naming metallacrowns, please consult one of the many reviews.[3,16,17]

A variety of metallacrown sizes are well-known and present in the literature. For an excellent review, consult Mezei, Zaleski, and Pecoraro.[17] Much work has been dedicated to studying the solid-state and solution properties of 12-MC-4[21] and 15-MC-5[22,23] complexes. For an excellent review on the solution work, consult the review by Tegoni and Remelli.[18] Of the most interest to the current text are the 12-MC-4, 15-MC-5, 28-MC-10, and 22-MC-8 structures, as those have shown slow-magnetic relaxation or have been shown to be single-molecule magnets.

Superparamagnetism

Interest in magnetic phenomena can be traced back to antiquity and the mysterious lodestone. This fascination in magnetic properties has not waned since then. In the late 20th century, a new focus on molecular magnetism began. Molecular magnetism is a multi-disciplinary field, with chemists, physicists, and material scientists working to advance the field.[24] Molecular magnetism has the potential to unlock new spintronic devices (electronics based on the spin of the electron),[25] to provide high-density storage devices, to act as qubits (the quantum equivalent to a bit in computers; it utilizes the superposition principle),[26] to probe physical phenomena at the boarder of the classical and quantum regimes, and to serve as magnetic refrigerants.[12] This potential provides the motivation to probe these molecules.[15]

The phenomenon of most interest in the field of molecular magnetism is superparamagnetism. To understand superparamagnetism, one must first understand how larger magnetic materials work. Magnetism originates from the presence of unpaired electrons (also referred to as spin), which generate a magnetic moment. Within a material, there can be several atoms or molecules that have unpaired electrons, generating a magnetic moment within the complex. To minimize the magnetic energy, regions of space where all the magnetic moments align parallel (or antiparallel) with each other, known as domains, form. The area of the material where the magnetic moments within the domains change directions is known as a Bloch wall. The size of the Bloch wall is

dependent on several factors: the exchange coupling constants within the material that want to align all the moments; the magnetic anisotropy, which wants to minimize high-energy orientations.[14] If one shrinks the magnetic material to the point where the material is on the same order of the magnetic domain, then the energetic drive to form domains is lost, and the particle becomes a single magnetic domain.

If the material is shrunk further, the magnetic anisotropy A becomes a function of the particle's size V and a constant K (Equation 1).[13,27]

$$A = K V \qquad (1)$$

If the anisotropy is Ising in nature, that is, the magnetic moment is parallel to the z-axis, then a double energy well can be drawn (Figure 1.3). The minimum of each energetic well corresponds to when the spin is parallel or antiparallel to the z-axis. The maximum of the well corresponds to when the spin is perpendicular to the z-axis. The spin can flip between the two wells through an applied field or via thermal energy. Over a period of time, the spins of the molecule will reach equilibrium and each well will be equally populated. In this respect, superparamagnets behave just like paramagnets. However, upon application of an applied magnetic field, the two wells are no longer equal in energy; the well parallel to the applied field will lower in energy and the antiparallel well will be higher in energy. Again, this is similar to a simple paramagnet, however, superparamagnets differ from normal paramagnets because the source of this behavior are the individual magnetic centers, not the bulk sample.[14]

If the applied field is maintained for a long enough time, the well parallel to the applied field will be preferentially populated compared to the antiparallel well. Upon removal of the applied field, a simple paramagnet will immediately relax to equilibrium and magnetization is lost. However, for a superparamagnet, the magnetization will be maintained below a critical temperature, T. This temperature corresponds to the energy needed to scale the energy well and can be described by the Arrhenius equation (Equation 2),

$$\tau = \tau_0 e^{\frac{KV}{k_B T}} \qquad (2)$$

Where τ is the relaxation time of the experiment, τ_0 is the pre-exponential factor, and k_B is the Boltzmann constant.[14] What becomes evident from this relationship is that superparamagnets' behavior depends upon the time-scale of the experiment and that it follows statistical mechanics.

Two unique ways of obtaining nanomagnets exist: a "top-down" and a "bottom-up" approach. The "top-down" approach involves taking known bulk magnets and shrinking them to a sufficiently small size such that the domain size is similar to the crystalline size. The other approach, the one that will be discussed in the following sections, attempts to synthesize individual molecules that will display interesting magnetic properties and studying their behavior. This "bottom-up" approach features an interesting class of materials, known as single-molecule magnets. Aromí and co-workers discussed the advantages of the "bottom-up" approach including the fact that since the materials are normally synthesized and isolated from solution, leading to a single, well-defined sized material and that they are normally soluble and, therefore, making them easily processable.[28] Furthermore, they exhibit molecular dimensions and are monodisperse.[29] This makes single-molecule magnets ideal for all of the applications described above, in particular, data storage and quantum computing. Traditional magnetic devices require a single domain comprised of thousands of atoms to store a single bit of data. With a single-molecule magnet device, because each molecule is itself a domain, capacity could potentially be increased a thousand fold.[29] In addition, because of the small size of single-molecule magnets, they can exhibit quantum effects, such as tunneling, that larger, traditional magnets do not exhibit.[30]

Single-Molecule Magnets

Chemists coined the phrase single-molecule magnets (SMMs) to refer to molecules that demonstrate superparamagnetic behavior. Specifically, the properties of SMMs can be

related as the product of the individual molecule's spin and its Ising-type magnetoanisotropy.[31] To understand the source of this magnetic behavior, spin Hamiltonians must be utilized. The full derivation of the spin Hamiltonian is available in a number of places, including Chapter 2 of Gatteschi, Sessoli, and Villain,[14] and Girerd and Journaux.[32] For convenience, the total spin Hamiltonian is:

$$\widehat{H} = g\beta \boldsymbol{H}\widehat{\boldsymbol{S}} + D\hat{S}_z{}^2 + E\left(\hat{S}_x{}^2 - \hat{S}_y{}^2\right) \qquad (3)$$

where β is the Bohr magneton, $\boldsymbol{H}$ is the applied magnetic field, g is the Landé factor, $\hat{\boldsymbol{S}}$ is the spin operator, D is axial anisotropy eigenvalue, $\hat{S}_z$ is the spin operator along the z-axis, E is the equatorial anisotropy eigenvalue, and $\hat{S}_x$ and $\hat{S}_y$ are the spin operators along the x and y-axes, respectively.

This spin Hamiltonian is comprised of two different Hamiltonians. The first term is the Zeeman splitting Hamiltonian, $\hat{H}_Z$ and is given by Equation 4:

$$\widehat{H}_Z = \beta \boldsymbol{H} \cdot g \cdot \widehat{\boldsymbol{S}} \qquad (4)$$

The second term is the zero-field splitting term, $\hat{H}_{ZFS}$, which is given by Equation 5:

$$\widehat{H}_{ZFS} = D\hat{S}_z{}^2 + E\left(\hat{S}_x{}^2 - \hat{S}_y{}^2\right) \qquad (5)$$

In the zero-field splitting Hamiltonian, one can see that in axial symmetric cases, the second term goes to zero. As the name suggests, Equation 5 is present, even in the absence of applied fields. Thus, the root properties of SMMs with Ising-type anisotropy can be given by Equation 6:

$$\widehat{H} = D\hat{S}_z{}^2 \qquad (6)$$

which has an eigenvalue U_{eff} given by Equation 7 for integer spins and Equation 8 for non-integer spins:

$$U_{eff} = -D{M_s}^2 \quad (7)$$

$$U_{eff} = -D\left({M_s}^2 - \frac{1}{4}\right) \quad (8)$$

where M_s is the microspin state values of the $\hat{S}_z$ operator. The sign of D must be negative in order to ensure that the lowest energy states have the largest spin values. This case corresponds to easy-axis type magnetoanisotropy, while positive D corresponds to easy-plane anisotropy (and the smallest spin states being the lowest in energy). Equations 7 and 8 have a negative sign before D to emphasize the importance of axial anisotropy.

Because Equations 7 and 8 do not specify the sign of the microspin states, the M_s and $-M_s$ spin states are degenerate. This will lead to an energy double well, just like the one described above for superparamagnets (Figure 1.4). In this case, the energy well has a barrier described by Equations 7 and 8 for the integer and non-integer cases, respectively. The energy well is comprised of two different wells with quantized spin states, one with M_s spin states and the other with $-M_s$ spin states. Each energy level in the respective wells is separated by varying multiples of D. As was the case for superparamagnets, the anisotropy barrier can be scaled through thermal relaxation. In order to observe this relaxation, all the spins must first populate a single energy well. This is accomplished by applying an external applied field parallel to the z-axis. This applied field will alter the energy levels of the well such that the largest $|M_s|$ state parallel to the applied field ($-M_s$, by convention) is lowest in energy. Upon removal of the applied field, thermal relaxation from the $-M_s$ can occur, proceeding stepwise from $-M_s$ to $(-M_s+1)$ level the $(-M_s+2)$ level and so forth. This relaxation can be given by an Arrhenius equation, similar to Equation 2.

$$\tau = \tau_0 e^{\frac{U_{eff}}{k_B T}} \quad (9)$$

In Equation 9, τ is the relaxation time, τ_0 is the pre-exponential term, U is the energy barrier, k_B is the Boltzmann constant, and T is the temperature.

Equation 9 implies that below a certain temperature T_c, the spin of the material will take a very long time to flip from one spin well to the other. This is important in differentiating SMMs from paramagnets and what gives SMMs their potential utility. Below T_c, the spins of the will only slowly relax to the other energy well through tunneling, discussed below, phonon coupling, spin diffusion, or through modulation of the crystal field[33]. Thus, below T_c after removing an applied field, SMMs maintain magnetization in the direction of the applied field for a long time.

Experimentally, the temperature from Equation 9 that corresponds to the energy barrier is rarely observed. This is due to quantum tunneling of magnetization. Tunneling is a fascinating phenomenon that is only available in the quantum regime. Because of the small size of most SMMs, they can exhibit these quantum effects. Just as in quantum tunneling of particles, spins may tunnel through the energy barrier due to its wave nature. Thus, with the double energy well described in Equations 7 and 8, the possibility for any two M_s states to be degenerate in energy exists. Note that the two tunneling states do not necessarily have to be $+M_s$ and $-M_s$. This is because in the presence of a magnetic field, the energy levels of the double well shift and any spin states may be accidently degenerate. Thus, the probability of tunneling depends on the extent of interactions of the two wavefunctions.[30]

Single-Chain Magnets

An interesting class of molecules similar to SMMs are single-chain magnets (SCMs). Single-chain magnets were first proposed in 1963 by Roy Glauber.[34] Two strict requirements were put forward, first that the material behaves as a 1D Ising-type ferro- or ferromagnet and second that the intrachain/interchain interactions ratio is greater than 10^4. In other terms, the material must have axial anisotropy and each chain must be

isolated from neighboring chains.[35] Despite the fact that the idea of a SCM was first proposed in 1963, it was not until 2001 that the first SCM was reported by Caneschi and co-workers.[36,37] Single-chain magnets share some similar properties with their SMM siblings, but due to their chain structure, SCMs do require some different equations. To treat infinitely long SCMs, the classical-spin Heisenberg chain equation (Equation 10) or the Ising chain model (Equation 11) can be used. The classical-spin Heisenberg chain equation can be used when the spin is large enough (typically greater than 2), and limits the use of quantum mechanics by replacing spin operators with classical vectors:

$$\widehat{H} = -2J \sum_{-\infty}^{+\infty} \hat{S}_i \, \hat{S}_{i+1} = -2JS^2 \sum_{-\infty}^{+\infty} \vec{u}_i \, \vec{u}_{i+1} \qquad (10)$$

where, J is the exchange interaction ($J > 0$ is ferromagnetic), $\hat{S}$ is the spin operator for one magnetic center, S is the total spin, and $\overrightarrow{u_i}$ is a unit vector. The system can also be treated by the Ising chain model, which requires the spins be aligned along the z-axis with an infinite uni-axial magnetoanisotropy also along z. This equation is given as:

$$\widehat{H} = -2J \sum_{+\infty}^{+\infty} \hat{S}_{i,z} \hat{S}_{i+1,z} = -2JS^2 \sum_{-\infty}^{+\infty} \sigma_i \sigma_{i+1} \qquad (11)$$

where, $\hat{S}_i$ is the individual center's spin along the z-axis and σ_i is ± 1.[38] Sometimes, Equation 11 is modified to include interactions in magnetic fields, giving Equation 12

$$\widehat{H} = -2J \sum_{i=1}^{L} \sigma_i \sigma_{i+1} - g\beta H \sum_{i=1}^{L} \sigma_i \qquad (12)$$

where L is the chain length (rather than an infinite chain), g is the Landé factor, β is the Bohr magneton (4.66865374 x 10^{-5} cm^{-1} G^{-1}), and H is the applied field.[39] These equations do not specify the origin of the anisotropy; the source is the anisotropic building blocks described by Equation 6. Although the two cases described above cannot

be reached, they provide a good, fundamental understanding of the magnetic properties. One of the main reasons Equations 10 – 12 fail is due to defects such as non-magnetic or exchange-breaking impurities, lattice defects, etc.;[39] practically, infinite chains cannot be obtained.

Like SMMs, SCMs have a thermal energy barrier given in Equation 9. However, the energy barrier of SCMs is slightly different than that of SMMs. SCMs have three dynamic relaxation routes with different energies, depending on where in the chain the magnetization first reorients (Figure 1.5). If the first relaxation event takes place in the center of the chain, it will require an energy of $8JS^2$ to flip due to exchange interactions with two different spin centers. All subsequent flips are energetically favorable and thus no energetic penalty is paid (Figure 1.5a). However, if the relaxation occurs at the end of the chain, only one energetically unfavorable interaction occurs, and thus only half the energy is required (Figure 1.5b). The third route of relaxation is only valid for very short chains and at very low temperatures. In this route, all spins simultaneously reverse (Figure 1.5c), a process known as collective reversal.[39] Understanding SCM magnets will be important for Chapter 4.

Single-Ion Magnets

Single-molecule magnets and single-chain magnets often have several metal centers present, leading to coupling between magnetic centers. However, if only a single anisotropic metal is used, these interactions can be eliminated. The case where only a single ion is responsible for the magnetic behavior is given by the term single-ion magnet (SIM). Two of the first reported SIMs were lanthanide bis-phthalocyanine complexes[40] and lanthanide polyoxometallates.[41] These two families of molecules utilize the large spin and anisotropic properties of lanthanides. In fact, lanthanides are ideal cations to study as SMMs, SCMs, and SIMs because of these properties.

Lanthanides, however, have very complex spin properties owing to relativistic spin-orbit coupling, often making analysis difficult when part of large complexes. However, the

analysis becomes more straightforward when only a single lanthanide is present. In 2011, Rinehart and Long published a paper describing how to exploit the single-ion anisotropy of lanthanides in SMMs.[42] Of the most importance to the current work, is the conclusion that the properties of lanthanides can be optimized by using the proper coordination environment. The two requirements Rinehart and Long propose for strong single-ion anisotropy are that the ground state must be doubly-degenerate and possess a large $\pm m_j$ quantum number and second, that there be a large energy separation between the ground state and the first excited state.[42]

Based on the *f*-orbitals of the free-ions of the lanthanides, one can hypothesize what shape the ion will take. The observed shapes can be axially elongated (prolate), equatorially elongated (oblate), or spherical (isotropic) and are given in Figure 1.6.[42] This allows one to predict what coordination geometry will best maximize anisotropy. For oblate ions, Rinehart and Long propose that the ligand electron density should be above or below the lanthanide, while for prolate ions are better situated with the ligand field in the plane of the lanthanide.[42] While lanthanides will be encountered in each chapter, single-ion like magnets will be discussed in Chapter 5.

Experimental Techniques

In order to determine if a molecule is an SMM, several experiments need to be performed. Ideally, as the source of SMM behavior is molecular, an x-ray crystal structure of the material should be collected. The molecule needs to demonstrate magnetic behavior. Usually, magnetic susceptibility and magnetization data are collected to try to determine the coupling between magnetic centers and the spin state populations. The molar magnetization and magnetic susceptibility values require Boltzmann averages of individual magnetic moments from the molecules.

In a magnetization experiment, the temperature is held constant and the applied field is varied. The magnetization is related by Equation 13,[32]

$$M = N_A \frac{\sum_n \mu_{n\alpha} e^{-E_n/k_B T}}{\sum_n e^{-E_n/k_B T}} \qquad (13)$$

Where M is the magnetization, N_A is Avogadro's number, $\mu_{n\alpha}$ is the magnetic moment associated with the energy level $|n\rangle$along a direction α, and k_B is the Boltzmann constant (1.380658 x 10^{-23} J K^{-1} = 0.69503877 cm^{-1} K^{-1}). If certain conditions are satisfied, the function can be simplified to terms of spin and applied magnetic field. Equation 13 becomes an expression known as the Brillouin function (Equation 14)

$$M = N_A g \beta S [B_S(x)]$$
$$B_s = \frac{2S+1}{2S} \coth\left(\frac{2S+1}{2S} x\right) - \frac{1}{2S} \coth\left(\frac{x}{2}\right) \qquad (14)$$
$$x = \frac{g\beta SH}{k_B T}$$

where g is the Landé factor, β is the Bohr magneton, S is the spin state, B_s(x) is the Brillouin function proper, and H is the external applied field. If x >>1, which is usually the case at large applied fields or low temperatures, the magnetization can be simplified to

$$M = N_A g \beta S \qquad (15)$$

which corresponds to when the magnetic signal is saturated. The other limiting case is when x << 1, where the magnetization is described as

$$M = \frac{N_A g^2 \beta^2 HS(S+1)}{3k_B T} \qquad (16)$$

which is commonly the situation when the Curie law is observed.[43]

Another important study is the measurement of the magnetic susceptibility, where the field is held constant and the temperature is changed. In 1932, Van Vleck used

perturbation theory to derive an expression for the magnetic susceptibility, χ versus temperature (Equation 17) for the ground spin state energy $E_S^{(0)}$.[43]

$$\chi_m = \frac{N_A g^2 \beta^2}{3k_B T} \frac{\sum_S S(S+1)(2S+1) e^{-E_S^{(0)}/k_B T}}{\sum_S (2S+1)\, e^{-E_S^{(0)}/k_B T}} + N\alpha \qquad (17)$$

Simplifying the equation and including the constants, one can obtain Equation 18.

$$\chi_m T = 0.125 g^2 S(S+1) \qquad (18)$$

The susceptibility, namely $\chi_M T$ versus T, can be very important as it can reveal the nature of the magnetic interactions between different magnetic centers. If the susceptibility increases as the temperature decreases, this can indicate that the magnetic ions are ferromagnetically coupled. If the susceptibility decreases as temperature decreases, one can infer that the magnetic centers are antiferromagnetic coupled and/or one is observing spin-orbit coupling, which is particularly important for complexes that have lanthanides or non-first row transition metals.

In order to determine slow magnetic relaxation a hallmark of SMM behavior, ac magnetic susceptibility data at varying frequencies are collected. If possible, magnetic hysteresis experiments and micro-SQUID measurements should also be taken in order to identify internal barriers to spin relaxation.

An important experimental result that must be present for a molecule to be an SMM is the presence of hysteresis (Figure 1.7). In this experiment, a sample has a magnetic field applied in one direction, *+H*. The field is swept until the magnetization is saturated. After the sample is magnetized in this initial direction, the magnetic field is reversed and swept in the opposite direction (*–H*). As the field decreases from the maximum *+H*, the magnetization values will not coincide with the original values. An SMM will require a coercive field, that is, in order for the magnetization to be zero, the applied field must be in the *–H* direction. This indicates the presence of an energy barrier to spin reversal.

When the sample's magnetization saturates in the direction of *–H*, the field is swept in the direction of *+H*. Again, a coercive field will be required to demagnetize the sample. The field is applied until it reaches the original magnetization values. The temperature and sweep rates can be varied and these will affect the width of the hysteresis plot. On occasion, steps in the hysteresis plot are observed. These steps actually correspond to quantum tunneling of magnetization in the sample.[44]

One of the most useful measurements performed is a single crystal micro-SQUID measurement (SQUID is an acronym for superconducting quantum interference device). There are only a few facilities in the world with micro-SQUID capabilities. Micro-SQUID measurements are extremely sensitive. They also allow for the magnetic properties along the easy axis and hard plane to be measured independently. This is key for determining axial anisotropy and thus true SMM behavior.[14]

In order for a molecule to behave as an SMM, it must show frequency dependence in the out-of-phase, or imaginary component, of the ac magnetic susceptibility measurement. An ac SQUID magnetic susceptibility measurement is actually one experiment that gives two sets of data: in-phase and out-of-phase ac SQUID susceptibility data. The in-phase susceptibility, χ', also called the "real" susceptibility, is given by the equation:

$$\chi' = \chi \cos(\phi) \qquad (19)$$

where ϕ is the phase shift relative to the drive signal and χ is the magnitude of the magnetic susceptibility.[45] From the in-phase molar susceptibility, χ'_M, one can extrapolate the ground spin state of the system using the following equation:

$$\chi'_M = \frac{N_A g^2 \beta^2}{3k_B T} S(S+1) \qquad (20)$$

which is a simplified form of Equation 17. The constants can be grouped together and the equation rearranged to give Equation 18

The other important result from these experiments is the out-of-phase susceptibility χ". The value for χ" is given by:

$$\chi'' = \chi \sin(\varphi) \qquad (21)$$

where φ and χ represent the same terms as given above.[45] The frequency of ac SQUID experiment is on the same time-scale as the slow magnetic relaxation (Equation 9).[14] The presence of frequency dependent out-of-phase ac magnetic susceptibility reveals that the molecule possesses an internal barrier of spin reversal. However, this experiment cannot definitively declare a molecule an SMM as several other materials, most notably spin-glasses,[46] demonstrate similar behavior. One must also take care when conducting ac magnetic susceptibility measurements with an applied dc field. The presence of the dc field, while in some cases increase the temperature where slow magnetic relaxation is observed, it can also artificially give frequency dependent behavior by orienting the equatorial magnetic moments. Thus, varying the ac field leads to a progression of the spins about the easy-plane, returning frequency dependent behavior.

During an out-of-phase ac magnetic susceptibility experiment, a maximum can be observed at a critical temperature, T_c. This temperature shifts according to the frequency. This can be used to differentiate SMMs from spin-glasses. Mydosh presented an equation relating the difference between the highest and lowest critical temperatures, the freezing temperature, T_p, and the frequency f (Equation 22).

$$a = \frac{\Delta T_p(f)/T_p(f)}{\Delta \ln(f)} \qquad (22)$$

Mydosh stated that if a falls between 0.001 and 0.08, it is a spin glass. If a is greater than 0.28, the sample is a paramagnet.[46]

In addition to observing a peak in the out-of-phase ac magnetic susceptibility, ac magnetic susceptibility can be used to create a Cole-Cole plot (Figure 1.8). One plots the ac in-phase magnetic susceptibility data, χ', against the out-of-phase magnetic susceptibility data χ". If the plot results in a semi-circle about the χ" axis, the sample can be said to behave as an SMM.

Electron paramagnetic resonance (EPR) spectroscopy can also be useful, especially for determining the value of *D*. For the simple $S = \pm 1/2$ spin system, a quantum of energy $h\upsilon$ must be provided that corresponds to the energy difference between the spin states. When the system is in resonance, Equation 23 can be used:

$$\Delta E = h\upsilon = g\beta H_R \qquad (23)$$

where ΔE is the energy separation between $S = +1/2$ and $S = -1/2$, υ is the radiation frequency and H_R is the resonance applied field. If magnetic moment is not isotropic, g can be broken down into specific terms along the axes. For anisotropic systems, g can be broken into two cases: for axial cases, $g_x = g_y < g_z$ or $g_x = g_y > g_z$, and for rhombic cases, $g_x \neq g_y \neq g_z$. In the first derivative of the EPR absorption spectrum, these differences in g values are manifested in the number of observed lines: for isotropic values, one line is observed, for axial, two cases, and for rhombic cases, three lines are found. Zero-field splitting (ZFS) complicates the spectrum, but allows for one to determine the *D* value. When the ZFS is smaller than the Zeeman energy, one can use Equation 24 to determine the transition between m_s and m_s+1:

$$H(m_s \rightarrow m_s + 1) = \frac{g_e}{g}\left[H_R - \frac{D(2m_s + 1)}{2g\beta}(3\cos^2\theta - 1)\right] \qquad (24)$$

where g_e is the g value for a free electron (2.0023) and θ is the angle between the unique axis and the external magnetic field. If high field EPR is used, one can determine the sign of *D*, greatly easing determination of SMM behavior.[14] An in depth discussion on EPR spectroscopy is available from Palmer.[47]

A variety of other techniques can be used to characterize SMMs. However, in the interest of brevity and those techniques that are relevant to this thesis, only these techniques will be described. For the interested reader, please consult Chapter 3 of Gatteschi, Sessoli, and Villain for an excellent review of these techniques.[14]

It is also important to note about magnetic units. A variety of terms are often used interchangeably, such as describing a magnetic field in terms of oersted (Oe), gauss (G), or tesla (T), and can make the literature very confusing. In general, all magnetic fields will be given as G and magnetic susceptibility will be given as $\chi_M T$ in the units of cm^3 K mol^{-1}. The magnetic susceptibility $\chi_M T$ is related to the older term μ_{eff} (given in units of Bohr magneton, BM) by Equation 25. Table 1.1 relates $\chi_M T$ to μ_{eff}.

$$\chi_M T = \frac{\mu_{eff}^2}{8} \qquad (25)$$

Table 1.1. The $\chi_M T$ and μ_{eff} values for a given spin *S* if g = 2.00 are summarized.

S	**μ_{eff}**	**$\chi_M T$**
1/2	1.73	0.375
1	2.82	1.00
3/2	3.87	1.875
2	4.9	3.00
5/2	5.92	4.375
3	6.93	6.00
7/2	7.94	7.875

Important Single-Molecule, Single-Chain, and Single-Ion Magnets

Several key molecules and trends in the field of SMMs, SCMs, and SIMs were developed in the 1990s and 2000s. The first, and arguably the most important, and until recently, the SMM with the highest blocking temperature, was **Mn_{12}(OAc)**. Several large Mn clusters were studied, in addition to a variety of Fe clusters. In the early part of the 2000s, mixed *3d*/*4f* complexes, including metallacrowns, began to appear in the literature as SMMs. At

the same time, the concept of using a single paramagnetic ion as a single-ion magnet began to develop. What follows is a brief summary of some of the most important SMMs with a particular focus on mixed Mn/Ln, metallacrown, and single-ion magnets. The importance of lanthanides in new molecular magnets will be discussed as well.

Mn_{12}(OAc)

Perhaps the best studied SMM is $Mn^{III}_8Mn^{IV}_4O_{12}(O_2C_2H_3)_{16}(H_2O)_4$ complex (Figure 1.9), commonly called **Mn_{12}(OAc)**.[14] This molecule was originally synthesized by Lis in 1980[48]. The main structural features of this complex are eight Mn^{III} ions surrounding a Mn^{IV}-oxo cubane core (Figure 1.10). However, it was in 1991 that detailed magnetic experiments were performed, revealing a ground spin state of S = 10 and frequency dependence in the ac susceptibility plot (Figure 1.11).[49] A maximum of χ_M" was found at 7 K at a frequency of 500 Hz. No mention of the term "single-molecule magnet" is made in this paper; rather it refers to similar phenomena found in superparamagnets or spin-glasses. Even in a follow-up paper in *Nature*, Sessoli and co-workers did not define this molecule as a "single-molecule magnet." However, they found that the material displayed a hysteresis in magnetization, like a bulk ferromagnet (Figure 1.12). In ferromagnets, hysteresis originates from moving Bloch walls.[50] However, in the case of **Mn_{12}(OAc)**, because it was on the same order of magnitude of the domain walls, it was obvious that the source of this hysteresis was different than that of bulk ferromagnets. Single crystal electron paramagnetic resonance (EPR) measurements were made in 1998 by Hill and co-workers. They found that the D value was -0.47 cm^{-1}, thus confirming that D was negative and supporting the ground spin state S was ± 10.[51] Using Equation 7, the theoretical energy barrier was determined to be 68 K.

[Co(hfac)$_2$(NITPhOMe)]

Even though the possibility of SCMs was proposed in 1963, it was not until 2001 that the first SCM was reported by Caneschi and co-workers.[36] The complex was comprised of one-dimensional chain made of **[Co(hfac)$_2$(NITPhOMe)]** (Figure 1.13), where hfac is

hexafluoroacetylacetonate and NITPhOMe is 4'-methoxy-phenyl-4,4,5,5-tetramethylimidazoline-1-oxyl-3-oxide. The chain is comprised of alternating $Co(hfac)_2$ and NITPhOMe radicals, which were determined to be antiferromagnetically coupled by observing the magnetic properties of the monomer. [52] The chain showed strong frequency dependence below 17 K (Figure 1.14). The energy barrier was determined to be 154(2) K and the pre-exponential factor was given as 3.0(2) x 10^{-11} s.[36] Hysteresis was observed when the external field was applied parallel to the trigonal axis, while the hysteresis was lost when the field was applied perpendicular to that axis (Figure 1.15).[36]

$[Pc_2Ln^{III}]^-\cdot TBA^+$

In 2003, Ishikawa and co-workers presented a tetrabutylamonium (TBA^+) Tb^{III} bis-phthalocyanine (Pc) salt, $\mathbf{[Pc_2Tb^{III}]^-\cdot TBA^+}$ (Figure 1.16) that showed slow magnetic relaxation.[40], Lanthanide bis-phthalocyanine complexes are well known[53], but their application as SMMs were never studied.[54] Ishikawa and co-workers found that the Tb^{III} and Dy^{III} analogs showed out-of-phase frequency dependence (Figures 1.17 and 1.18). The most exciting result was that these complexes showed frequency dependence at much higher temperatures than previously witnessed. The group found that $\mathbf{[Pc_2Tb^{III}]^-\cdot TBA^+}$ had a maximum in χ_M" at 40 K with a frequency of 997 Hz. The $\mathbf{[Pc_2Tb^{III}]^-\cdot TBA^+}$ sample was doped with $\mathbf{[Pc_2Y^{III}]^-\cdot TBA^+}$ and the slow relaxation was still observed, indicating that the behavior was molecular in origin and not due to intermolecular interactions or long-range order. The barrier height was calculated to 230 cm^{-1} (331.2 K). The $\mathbf{[Pc_2Dy^{III}]^-\cdot TBA^+}$ analog also showed slow magnetic relaxation, but at much lower temperatures. This work opened up the field to study lanthanides as potential SMMs, a field that has become quite popular.

$[Cu^{II}LLn^{III}(Hfac)_2]_2$

While copper-lanthanide complexes have been known for quite a while, no group had successfully studied them as SMMs.[24] In 2004, Osa and co-workers reported the first *3d/4f* SMM, introducing a new avenue to reach potential SMMs.[55] Kido and co-workers

isolated a **[$Cu^{II}LDy^{III}(hfac)_2]_2$** (Figure 1.19), a **[$Cu^{II}LTb^{III}(hfac)_2]_2$**, and the analogous **[$Ni^{II}LTb^{III}(hfac)_2]_2$**, where L is the triply deprotonated 1-(2-hydroxybenzamido)-2-(2-hydroxy-3-methoxy-benzylideneamino)-ethane and hfac is the monodeprotonated hexaflouroacetylacetone. [56] Osa and co-workers studied the magnetic properties of these complexes and saw frequency dependence in the out-of-phase ac magnetic susceptibility signal for the Dy^{III} and Tb^{III} (Figure 1.20) analogs. The Tb^{III} analog had a maximum χ_M" vs. T value of 2.5 K at 1000 Hz. From the out-of-phase data, the calculated energy barrier was determined to be 21 K. While this value was lower than **Mn_{12}(OAc)** or **[$PcTb^{III}]^-$·TBA$^+$**, it revealed the potential of using mixed *3d/4f* systems.

Mn_{19}* and *$Mn_{18}Dy$

In 2006, Ako and co-workers reported a $[Mn^{III}_{12}Mn^{II}_7(\mu_4\text{-}O)_8(\mu_3,\eta^1\text{-}N_3)_8(HL)12\text{-}(CH_3CN)_6]Cl_2\cdot 10CH_3OH\cdot CH_3CN$ (H_3L = 2,6-bis(hydroxymethyl)-4-methylphenol), (Figure 1.21) abbreviated as **Mn_{19}** that displayed a record 83/2 ground spin state.[57] The structure was comprised of two Mn_9 fragments linked via a Mn^{II} center. The halves of the molecule are comprised of cubes, where the center of each face of the cube is comprised of a Mn^{III} ion and the vertices are comprised of either Mn^{II} or the central N of a coordinating μ_3-N_3. Ako and co-workers measured the magnetization using the in-phase component of an ac magnetic susceptibility data to determine the ground spin state. Micro-SQUID measurements showed hysteresis (Figure 1.22), requiring a coercive field of 300 G at 0.04 K. The authors speculated that the source of this hysteresis was due to the anisotropy of the Mn^{III} ions and the anisotropy of dipolar interaction due to the oblong molecular shape. Later, 35 GHz EPR magnetic measurements showed that the anisotropy of the molecule was, in fact, positive, and thus was not a SMM.[20] Two explanations were given for apparent SMM behavior: that the Mn^{III} anisotropy tensors were "tilted away from the cluster anisotropy axis (C_3 axis) with an angle close to but slightly larger than the magic angle"[20] and no anisotropy was contributed from the Mn^{II} ions; or that the anisotropy tensors of Mn^{III} ions accidently aligned (Figure 1.23) and cancelled each other out, leaving only the anisotropy from the Mn^{II} cations.[20] The resultant magnetic hysteresis was concluded to most likely be due to intermolecular

dipolar interactions.[20] This result indicated an important lesson for the field; that larger spin complexes do not necessarily lead to increased energy barriers.[58] This study helped the field start to focus on anisotropy in addition to the spin values.

Another group then performed density functional theory (DFT) calculations and found that the central Mn^{II} ion was in an unusual cubic coordination sphere.[59] This type of coordination environment, together with the unusually long bond lengths for a Mn^{II} ion led the group to speculate that a Ln^{III} ion could be substituted at this position. Because of the previous successes of incorporating lanthanides into manganese clusters and inducing SMM behavior, [60,61,62,63,64,65] Ako and co-workers sought to incorporate a single Dy^{III} ion into the structure at the central Mn^{II} position. They were successful, yielding a $[Mn^{III}_{12}Mn^{II}_{6}Dy^{III}(\mu_4\text{-}O)_8(\mu_3\text{-}Cl)_{6.5}(\mu\text{-}N_3)_{1.5}(HL)_{12}\text{-}(CH_3OH)_6]Cl_3\cdot 25CH_3OH$, where H_3L is the same ligand as before, (Figure 1.24). This **$Mn_{18}Dy$** complex was structurally similar to the **Mn_{19}** complex, only with the central Mn^{II} replaced by Dy^{III}; the other metal positions remained essentially unchanged.[66] The molecule retained a large spin state, but showed the affects of the presence of Dy^{III} in the $\chi_M T$ product; namely, decreases due to the intrinsic anisotropy of the Dy^{III} ion and thermal depopulation of Dy^{III} excited states. Excitingly, the sample did not magnetically saturate even at low temperatures and high fields, indicative of large amounts of anisotropy. The out-of-phase ac magnetic susceptibility of the **$Mn_{18}Dy$** complex revealed frequency dependence below 4 K, a hallmark of SMM behavior. The sample showed magnetic hysteresis, indicating there was an energy barrier to magnetic relaxation (Figure 1.25). This was very exciting, as it was the first time a *3d* metal ion was successfully targeted and replaced by a *4f* ion.[57,66] This could potentially open the doors to modifications of other known *3d*-only SMMs or *3d* complexes with small or positive anisotropy values.

Ln^{III}-Based Polyoxometallates

Based on the exciting results of the **$[Pc_2Ln^{III}]^{-}\cdot TBA^{+}$** clusters, interest in using a single magnetic ion, such as a lanthanide, increased significantly in the field. Polyoxometallates (POMs) possess the ability to bind a lanthanide in a coordination geometry similar to that

found in the phthalocyanine ligand used by Ishikawa and co-workers.[41] AlDamen and co-workers reported that $\mathbf{[Ln(W_5O_{18})_2]^{9-}}$ (Ln = Er^{III} and Ho^{III}) (Figure 1.26) and a family of $\mathbf{[Ln(SiW_{11}O_{39})_2]^{13-}}$ (Ln = Dy^{III}, Ho^{III}, Er^{III}, and Yb^{III}) (Figure 1.27) POMs displayed slow magnetic relaxation.[67] The $\mathbf{[Er(W_5O_{18})_2]^{9-}}$ represented the first SMM-like POM and the energy barrier was determined to be 55.2 K with a pre-exponential factor of 1.6 x 10^{-8} s. Most interesting from these complexes was the impact the skew angle and the axial bond lengths played on the magnetic properties. The skew angle is the offset between the two imaginary squares defined by the mean planes of the coordinating oxygen atoms. The Ln in the $\mathbf{[Ln(W_5O_{18})_2]^{9-}}$ was in an approximate D_{4d} ligand field, which was also observed in the $\mathbf{[Pc_2Ln]^{-}\cdot TBA^{+}}$. The $\mathbf{[Er(W_5O_{18})_2]^{9-}}$ complex had a skew angle of 44.2° while the $\mathbf{[Pc_2Er]^{-}\cdot TBA^{+}}$ structure had a skew angle of 41.4°,[68] deviating significantly from ideal D_{4d} symmetry (45°). The $\mathbf{[Er(W_5O_{18})_2]^{9-}}$ complex also demonstrated an axial compression, where the $\mathbf{[Pc_2Er]^{-}\cdot TBA^{+}}$ complex had an axial elongation. The $\mathbf{[Ln(SiW_{11}O_{39})_2]^{13-}}$ clusters had larger distortions from D_{4d} symmetry and similar compression as found in the $\mathbf{[Ln(W_5O_{18})_2]^{9-}}$ complexes.[67] The extent of the compression and the magnitude of the bond length will affect the ligand field strength, making these important factors to consider in future SMMs.

$Dy_5O(OiPr)_{13}$

In 2011, Blagg and co-workers reported a $\mathbf{Dy_5O(O\textit{i}Pr)_{13}}$ (O*i*Pr = *iso*-propoxide) pyramid (Figure 1.28) that showed a blocking temperature at 41 K.[69] The authors were able to observe blocking temperatures over a large range of temperatures and frequencies (Figure 1.29). The energy barrier was determined to be 528 ± 11 K and the pre-exponential factor was 4.7 x 10^{-10} s. At that time, this was the largest energy barrier reported for any SMM. The molecule also shows a second relaxation pathway at lower temperatures. This pathway was determined to be due to quantum tunneling, which is common for lanthanide complexes. This group also rationalized that this quantum tunneling resulted in the narrow hysteresis.[69]

Structurally similar complexes were also studied. Blagg and co-workers prepared similar Sm^{III}, Gd^{III}, Tb^{III}, Ho^{III}, and Er^{III} pentanuclear structures that were isolated in different unit cells.[70] Regardless, the overall the pentanuclear Ln^{III} core remained intact for the whole series. The Ho^{III} analog also showed slow magnetic relaxation (Figure 1.30). The maximum of χ''_M was observed at 33 K for a 1200 Hz at either 3.5 or 5.5 kG applied dc fields. The Cole-Cole plot had an α value ranging from 0.04 to 0.2. The energy barrier was determined to be 400 ± 5 K and the pre-exponential term was 1.5×10^{-9} s at 3.5 and 5.5 kG applied dc fields.[70] However, hysteresis was not observed.

Metallacrowns as Single-Molecule Magnets

As described earlier, metallacrowns are the inorganic analogs of crown ethers. Metallacrowns organize a large number of metals into a very small volume. As could be imagined, having several metals in a small area could be advantageous for use as SMMs. There have been several reported metallacrown SMMs, including the first mixed manganese/lanthanide SMM. Metallacrowns as SMMs will now be discussed them in depth, beginning with the first reported manganese/lanthanide SMM, the $\mathbf{Dy^{III}_6Mn^{III}_4Mn^{IV}_2}$ complex.

$Ln^{III}_6Mn^{III}_4Mn^{IV}_2$

Shortly after Osa and co-workers reported the first Cu/Ln SMM, Zaleski and co-workers reported the first Mn/Ln SMM, a $\mathbf{Dy^{III}_6Mn^{III}_4Mn^{IV}_2}$ complex. The complex had a formula of $[Dy_6Mn_6(H_2shi)_4(Hshi)_2(shi)_{10}(CH_3OH)_{10}(H_2O)]\cdot 9CH_3OH\cdot 8H_2O$,[60] where H_3shi is salicylhydroxamic acid (Figure 1.31). At the time, it was the largest lanthanide/manganese complex. Although not a traditional metallacrown, this complex could be considered a 28-MC-10 (Figure 1.32). The ring is comprised of both manganese and lanthanide ions and lacks a central cation. The $\mathbf{Dy^{III}_6Mn^{III}_4Mn^{IV}_2}$ complex shows frequency dependence in the ac magnetic susceptibility signal (Figure 1.33), while the Gd^{III} and Tb^{III} analogs do not. Later, Zaleski also found that the $\mathbf{Y^{III}_6Mn^{III}_4Mn^{IV}_2}$ and $\mathbf{Ho^{III}_6Mn^{III}_4Mn^{IV}_2}$ complexes showed slow magnetic relaxation. It was possible to

determine the energy barrier for the Dy^{III} analog. For $\mathbf{Dy^{III}_6Mn^{III}_4Mn^{IV}_2}$, the U_{eff} was found to be 19.0 ± 1.5 K and a pre-exponential term of 1.2 x 10^7 s^{-1} (Figure 1.34). It was not possible to determine the U_{eff} of the Ho^{III} or Y^{III} structures.[71] While it was not surprising that the Dy^{III} and Ho^{III} analogs showed slow magnetic relaxation due to the presence of six highly anisotropic lanthanides, the Y^{III} analog was surprising as the Y^{III} ions provided neither spin nor anisotropy to the system. This seemed to hint that the Mn^{III}/Mn^{IV} ring was sufficient for making the molecule demonstrate slow magnetic relaxation. However, the fact that the Gd^{III}, Tb^{III}, or Er^{III} analogs did not show slow magnetic relaxation makes the Y^{III} analog quite interesting. One might expect that the added spin from the Gd^{III} analog would improve the magnetic behavior or the Tb^{III} and Er^{III} analogs, with their additional spin and anisotropy, would also demonstrate slow magnetic relaxation. Zaleski could not provide an answer for this unusual observation.[71] However, this was an extremely interesting series that, and this opened the field to mixed manganese/lanthanide complexes. Subsequently, this has become a heavily studied and extremely productive field. It also made the possibility of using metallacrowns as SMMs an extremely interesting area of research.

$\boldsymbol{Ln^{III}_4Mn^{III}_6}$

Leaving the solute from the crystallization of $\mathbf{Ln^{III}_6Mn^{III}_4Mn^{IV}_2}$ yielded a new mixed manganese/lanthanide daughter complex, $[Ln^{III}_4Mn^{III}_6(H_2shi)_2(shi)_6(sal)_2(O_2CCH_3)_4(OH)_2(CH_3OH)_8]\cdot 4CH_3OH$, Ln = Gd^{III}, Tb^{III}, Dy^{III}, Ho^{III}, Er^{III}, Y^{III}, Lu^{III}) (Figure 1.35), $\mathbf{Ln^{III}_4Mn^{III}_6}$.[63,71] Only the $\mathbf{Lu^{III}_4Mn^{III}_6}$ complex was not isolated from a parent $\mathbf{Lu^{III}_6Mn^{III}_4Mn^{IV}_2}$ complex. Formally, $\mathbf{Ln^{III}_4Mn^{III}_6}$ can be considered a 22-MC-8, with two symmetry-related Ln^{III} ions contained within the ring of six Mn^{III} ions and two Ln^{III} ions (Figure 1.36). All Ln^{III} ions were 8-coordinate, while all Mn^{III} ions are six-coordinate Jahn-Teller distorted octahedrons.

Examining the ac magnetic susceptibility of the complexes revealed that the $\mathbf{Gd^{III}_4Mn^{III}_6}$, $\mathbf{Er^{III}_4Mn^{III}_6}$, and $\mathbf{Lu^{III}_4Mn^{III}_6}$ complexes did not snow frequency dependence. The $\mathbf{Tb^{III}_4Mn^{III}_6}$, $\mathbf{Dy^{III}_4Mn^{III}_6}$, $\mathbf{Ho^{III}_4Mn^{III}_6}$, and $\mathbf{Y^{III}_4Mn^{III}_6}$ complexes did show frequency

dependence, indicating that they may be possible SMMs. The $\mathbf{Dy^{III}_4Mn^{III}_6}$ and $\mathbf{Ho^{III}_4Mn^{III}_6}$ complexes were dissolved in DMF, frozen, and their ac magnetic susceptibility was then measured. Only the $\mathbf{Dy^{III}_4Mn^{III}_6}$ complex retained slow magnetic relaxation in solution (Figure 1.37), indicating that $\mathbf{Dy^{III}_4Mn^{III}_6}$ and not $\mathbf{Ho^{III}_4Mn^{III}_6}$ was an SMM. The loss of frequency dependence of $\mathbf{Ho^{III}_4Mn^{III}_6}$ was attributed to either glassy behavior or the onset of magnetic ordering. No direct interactions between molecules was observed in the crystal packing diagrams; however there is a hydrogen-bonding network between an axial methanol of Mn1 to a lattice water (2.57 Å) which is hydrogen bonded to an axial methanol of Mn3 (2.88 Å) of a second $\mathbf{Ho^{III}_4Mn^{III}_6}$ molecule. The total separation between Mn1 and Mn3 along the *a* axis is only 7.83 Å. Along the *b* axis, Ho2 of one molecule only 5.52 Å from Ho2 of a second molecule, indicating how closely packed these molecules are in the solid state. It was, therefore, reasonable to expect dipolar and hydrogen-bond pathways to mediate intermolecular exchange and short-order magnetic ordering.[63]

An interesting observation of this system was that the $\mathbf{Y^{III}_4Mn^{III}_6}$ but not the $\mathbf{Lu^{III}_4Mn^{III}_6}$ showed SMM behavior, despite the two being isoelectronic. Both have similar dc magnetic susceptibility behavior, indicating that the six Mn^{III} ions contribution remains relatively constant (3.44 cm^3 K mol^{-1} for $\mathbf{Y^{III}_4Mn^{III}_6}$ and 3.82 cm^3 K mol^{-1} for $\mathbf{Lu^{III}_4Mn^{III}_6}$) in both structures. The two materials crystallize in different unit cells (C2/c or Cc for $\mathbf{Y^{III}_4Mn^{III}_6}$ and $P2_1/c$ for $\mathbf{Lu^{III}_4Mn^{III}_6}$), but as SMM behavior was detected in both unit cells, Zaleski ruled out the possibility of magnetic ordering. Zaleski indicated that because Lu^{III} is a smaller cation than Y^{III}, this could alter bond lengths and bridges within the molecule, perturbing the exchange coupling constants.[71]

Regardless, the series further demonstrated that metallacrowns could provide interesting constructs for SMMs. However, one of the true utilities of metallacrowns, the ability to organize metals into planar, predictable geometries, had not yet been exploited. The next two families of metallacrowns would take advantage of this unique property.

Ln^{III} [15-$MC_{Cu^{II}N((S)\text{-}pheHA)}$-5]$^{3+}$

The **Ln^{III} [15-$MC_{Cu^{II}N((S)\text{-}pheHA)}$-5]$^{3+}$** ((*S*)-pheHA = *S*-phenylalanine) (Figure 1.38) construct is a well known complex, first published in 2001 by Cutland-Van Noord and co-workers.[72] Cutland-Van Noord used an earlier idea of Stemmler to use bulky α-amino-hydroxamic acids to induce chirality in the metallacrown structure.[73] The *S*-phenylalanine ligand differentiates the two faces of the metallacrown (Figure 1.39) by placing the phenyl portion on one side of the metallacrown. If the side-chain portion was flipped, it would break the M-N-O repeat unit, and the metallacrown will not form. Thus, this synthetic protocol easily forms enantiopure, chiral, face-differentiated metallacrowns through incorporating enantiopure chiral ligands.

In an individual 15-MC-5, two of the phenyl rings of the ligands orient underneath the metallacrown and the other three phenyl rings splay outside. However, when synthesized in water, two 15-MC-5 interact, forming a dimer (Figure 1.40). The phenyl rings interact, forming a hydrophobic pocket, which can be used to selectively bind guests.[72,74,75,76] However, when a 5:1 mixture of methanol:water is used, a helical structure is observed (Figure 1.41).[77] The carbonyl oxygen from the hydroxamic acid of one metallacrown binds to a Cu^{II} ion of an adjacent metallacrown. This orients the two metallacrowns perpendicular to one another. This connection repeats to a third metallacrown, propagating the chain. The orientation is also partially stabilized by the hydrophilic faces aligning creating a hydrophilic cavity. The end result is a helix with an S_4 screw axis parallel to the face of the metallacrowns.[77]

The magnetic properties of a similar family of Ln^{III} 15-$MC_{Cu^{II}N(L)}$-5s, the **$Ln^{III}(NO_3)_3$[15-$MC_{Cu^{II}N(picHA)}$-5]** complexes (picHA = picoline hydroxamic acid) (Figure 1.40) had been reported, revealing that the ring from the complexes had a S = ½ ground spin state.[11] Stemmler and co-workers systematically substituted the lanthanides, studying the impact of lanthanide on the magnetism. When the central Ln^{III} was Gd^{III}, there was ferromagnetic coupling with the ring Cu^{II} ions below 15° K. However, the

magnetic properties of either the dimer or the helix of $\mathbf{Ln^{III}\ [15\text{-}MC_{Cu^{II}N((\mathit{S})\text{-}pheHA)}\text{-}5]^{3+}}$ were not reported.[11] Because of the success of the described $\mathbf{Cu^{II}_2Ln^{III}_2}$ SMM described above, it seemed reasonable to test if the dimer would act as an SMM. Also, because a helix could be formed, it seemed reasonable to check if the helix would behave as a SCM.

Studying the ac magnetic susceptibility revealed that the Dy^{III} and Ho^{III} dimers and helices showed slow magnetic relaxation in the solid state. When dissolved in methanol, the Dy^{III} dimer continues to show slow magnetic relaxation (Figure 1.43), while the Ho^{III} dimer does not show slow magnetic relaxation. Thus it was concluded that the Dy^{III} dimer was an SMM, while because the Ho^{III} dimer did not behave as an SMM; the observed ac susceptibility behavior was due to glassy behavior and/or magnetic ordering. The helices fully dissociate in solution, making it impossible to measure the frozen solution ac magnetic susceptibility.[78] It was determined that the Dy^{III} helix was not an SCM, despite the phenyl rings of each chain isolating the magnetic centers. This was based on work by Yoo and co-workers on a chain of tetranuclear Mn complexes and by Ferbinteanu and co-workers on a single chain of Mn^{III}-Fe^{III}-Mn^{III} complexes. Yoo and co-workers found that the magnetic properties of the $\mathbf{[Mn_4(hmp)_6Cl_2]_x}$ polymer (hmp^- = 2-hydroxymethylpyridine) were best described as a chain of individual SMMs, not an individual SCM (Figure 1.44).[79,80] Ferbinteanu and co-workers found that a polymer of $\mathbf{[Mn^{III}(5\text{-}Me\text{-}Osalen)\text{-}Fe^{III}(CN)_6\text{-}Mn^{III}(5\text{-}MeOsalen)]_x}$ complexes behaved as SMMs as monomers, and an SCM when it was a polymer (Figure 1.45). It was noted that the polymer form had a different relaxation time than the monomer, indicative of different magnet behavior when polymerized.[81] Unfortunately for the Dy^{III} helix, there was no difference in out-of-phase behavior between the dimer and the helix, indicating that the same source was responsible for the magnetic behavior. However, it was found that the cation, i.e. Dy^{III} versus Ho^{III} did play a key role in the magnetic properties of the dimer and the helix.

M^+ [12-$MC_{Mn^{III}N(shi)}$-4]

The **M^+ [12-$MC_{Mn^{III}N(shi)}$-4]** family encompasses several interesting central metals in different positions, revealing the versatility of these materials. As described above, the [12-$MC_{Mn^{III}N(shi)}$-4] architecture organizes the four Mn^{III} ions at approximately 90° to each other. More importantly however, is that the shi^{3-} ligand aligns the four Mn^{III} ions such that their Jahn-Teller axes are all parallel to each other, and perpendicular to the plane of the metallacrown (Figure 1.46).[82] As is evidenced in the other described SMMs, little, if any, geometric control is exhibited. Without geometric control, the anisotropy vectors of Mn^{III} can accidently destructively align, as was the case in the **Mn_{19}** complex. It was hoped with the [12-$MC_{Mn^{III}N(shi)}$-4] metallacrowns, it would be possible to align the Jahn-Teller axes, thus improving the anisotropy of the complex.

It was found that metallacrowns can exist as neutral compounds or as positively or negatively charged ions. The smallest central metal bound to a [12-$MC_{Mn^{III}N(shi)}$-4]is Li^+. The Li^+ ion, in fact, is encapsulated in the metallacrown core, sitting near the center of the metallacrown ring (Figure 1.47). The Li^+ ion sits between 0.63(1) Å to 0.66(2) Å above the oxygen plane, depending on the counter anion present (dichloride, trifluoroacetate, unbound triiodide, respectively).[7] The **Li{($LiCl_2$) [12-MC-4]}**, the metallacrown complex carries an overall negative charged due two chloride ions bound to two manganese ions that are related by a pseudo S_2 improper rotation. A Li^+ cation is present in the lattice to provide charge balance. For the trifluoroacetate complex, a single trifluoroacetate ligand bridges the central Li^+ cation to a ring manganese. In the triiodide salt, the triiodide anion does not bind to the metallacrown.[7]

When Na^+ or K^+ is bound, the cation sits both above and below the metallacrown plane (Figure 1.48, 1.49, respectively). The di-cation is accompanied by two anions, such as chloride or bromide, providing charge balance. These anions are related by a pseudo S_2 improper roation. As the Na^+ cation is slightly larger than the Li^+ cation,[7] it cannot fit within the metallacrown ring, and is displaced 1.64 – 1.67 Å from the oxygen mean

plane, depending on whether the anion is chloride or bromide. As one may expect, when a larger cation, such as K^+ is used,[7] the central metal is further displaced. It was observed that the K^+ ion was 2.13 Å above the metallacrown oxygen plane.**Error! Bookmark not defined.**

Magnetic susceptibility measurements of the alkali halide 12-MC-4 structures revealed that at room temperature, the susceptibility roughly corresponded to four, non-interacting Mn^{III} (S = 2) cations.[7] At 2.5 K, the susceptibility trended downwards towards zero at 0 K, indicative of antiferromagnetic coupling between the ring Mn^{III} ions. Later work would determine that the ring Mn^{III} ions were weakly antiferromagnetically coupled to each with a J = -4.0 cm^{-1} and no cross-molecule coupling spin the **Li{($LiCl_2$) [12-MC-4]}** complex (Figure 1.50) using the spin Hamiltonian Equation 26

$$\hat{H} = -J\left(\hat{S}_1 \cdot \hat{S}_2 + \hat{S}_2 \cdot \hat{S}_3 + \hat{S}_3 \cdot \hat{S}_4 + \hat{S}_1 \cdot \hat{S}_4\right) - J'(\hat{S}_1 \cdot \hat{S}_3 + \hat{S}_2 \cdot \hat{S}_4) \qquad (26)$$

where, S_i corresponds to the spins to the spin of Mn_i, J is the coupling between the ring Mn, and J' is the coupling of the diagonal Mn.[82] A **$Ca(O_2CC_6H_5)_4$ [12-$MC_{Mn^{III}N(shi)}$-4]** complex was prepared with the Ca^{2+} cation as the central metal (Figure 1.51). Using a Hamiltonian in the $\hat{H}$ = -2$J(\hat{S}_i\hat{S}_j)$ format, it was found that J = -3.39(7) cm^{-1}, corroborating the presence of a diamagnetic ground state due to antiferromagnetic coupling through the ring.[8,9] As might be expected for a diamagnetic ground state material, none of these complexes showed slow magnetic relaxation. However, it was important for the **$Mn(O_2CCH_3)_2$ [12-$MC_{Mn^{III}N(shi)}$-4]** complex to establish the magnetic properties of the 12-MC-4 ring.

$Mn(O_2CCH_3)_2$ [12-$MC_{Mn^{III}N(shi)}$-4]

The second reported metallacrown was **$Mn(O_2CCH_3)_2$ [12-$MC_{Mn^{III}N(shi)}$-4]** in 1989 (Figure 1.2). The magnetic susceptibility at room temperature was first reported to show slight ferromagnetic interactions between the four Mn^{III} ions and the central Mn^{II} cation.[2]

Further examination revealed that the complex was dominated by antiferromagnetic exchange interactions, just like the alkali and alkaline earth metallacrowns. The best fit for the variable temperature dc magnetic susceptibility revealed between 100 K and 200 K, the magnetic response corresponded to four isolated Mn^{III} cations and one Mn^{II} cations.[82] With MAGPACK software,[83,84] it was determined that neglecting local anisotropy that the *J* and *J'* ratio described by Equation 27

$$\hat{H} = -J\left(\hat{S}_1 \cdot \hat{S}_2 + \hat{S}_2 \cdot \hat{S}_3 + \hat{S}_3 \cdot \hat{S}_4 + \hat{S}_1 \cdot \hat{S}_4\right) - J'\hat{S}_5(\hat{S}_1 + \hat{S}_2 + \hat{S}_3 + \hat{S}_4) \quad (27)$$

where *J'* now is the coupling between the ring Mn^{III} and the central Mn^{II}, corresponded to a 3:2 ratio (J = -6.3 cm^{-1}, J' = -4.2 cm^{-1}) (Figure 1.52). Examining the spin ladder revealed an S = 1/2 ground spin state with a 2 cm^{-1} gap to the first excited spin (S = 3/2). The subsequent excited states were determined to be 1/2 and 3/2.[82]

Modeling the magnetization and taking into account the impact of anisotropy from the Mn^{III} and Mn^{II} cations, it was found that J = -6.0 cm^{-1}, J' = -4.2 cm^{-1}, $D(Mn^{II})$ = 1 cm^{-1}, $g(Mn^{II})$ = 2.0 cm^{-1}, $D(Mn^{III})$ = -3.0 cm^{-1}, $g(Mn^{III})$ = 1.98 cm^{-1}. While the $D(Mn^{III})$ value was close to literature values,[85,86] the $D(Mn^{II})$ values were larger than expected. This observation was explained due to the unusually distorted octahedral geometry of the Mn^{II} ion. This geometry was closer to trigonal prismatic, which could lead to increased D.[82]

Examination of the ac magnetic susceptibility revealed weak frequency dependence in the solid state (Figure 1.53) and stronger frequency dependence when frozen in *N',N'*-dimethylformamide (Figure 1.54). There was a marked improvement in behavior in the frozen solution state that was accounted for by removing lattice effects in the solid state. Examination of the crystal packing diagram did not reveal any H-bonding pathways, thus it was reasoned that only dipolar interactions could be these lattice effects. Fitting the solution state data to the Arrhenius equation (Equation 9) led to a U_{eff} = 14.7 cm^{-1} and a pre-exponential factor τ_0 of 1.4 x 10^{-7} s.[82]

Furthermore, single crystal micro-SQUID magnetometry revealed slow magnetic relaxation (Figure 1.55), indicating that **$Mn(O_2CCH_3)_2$ [12-$MC_{Mn^{III}N(shi)}$-4]** behaves as an SMM. This discovery is extremely interesting in that it seems to violate Equation 8. The fact that there was a very low-lying S = 3/2 excited state helped explain why that, even with an S = 1/2 ground spin state, the complex still showed SMM behavior. It was thus demonstrated that aligning anisotropic barriers, even with low ground spin values, could lead to interesting SMMs. The idea of aligning anisotropic barriers in smaller metallic complexes will be an important theme running throughout this thesis.

Ln^{III} [12-$MC_{Mn^{III}N(shi)}$-4]

In order to improve the magnetic properties observed in **$Mn(O_2CCH_3)_2$ [12-$MC_{Mn^{III}N(shi)}$-4]**, Zaleski attempted to replace the central Mn^{II} cation with various Ln^{III} cations. The logic was that by adding lanthanide ions, with their intrinsic magnetoanisotropy and large spin, would increase the blocking temperature and U_{eff} of the Mn^{II} analog. Zaleski successfully prepared a $\{Mn^{II}(CH_3OH)_2(H_2O)_4\}_{0.5}\{Y^{III}(O_2CCH_3)_4[12\text{-}MC_{Mn^{III}N(shi)}\text{-}4]\cdot 2CH_3OH\}\cdot 2.5H_2O$ (Figure 1.56), **Y^{III} [12-$MC_{Mn^{III}N(shi)}$-4]**, an isostructural $\{Mn^{II}(CH_3OH)_2(H_2O)_4\}_{0.5}\{Gd^{III}(O_2CCH_3)_4[12\text{-}MC_{Mn^{III}N(shi)}\text{-}4]\cdot 2CH_3OH\}\cdot 2.5H_2O$, **$Gd^{III}$ [12-$MC_{Mn^{III}N(shi)}$-4]**, a $Dy^{III}(Hsal)_4(H_3O^+)[12\text{-}MC_{Mn^{III}(N)shi}\text{-}4]\cdot 5DMF\cdot 4H_2O$ (Figure 1.57) **Dy^{III} [12-$MC_{Mn^{III}N(shi)}$-4]**, and an isostructural $Tb^{III}(Hsal)_4(H_3O^+)[12\text{-}MC_{Mn^{III}(N)shi}\text{-}4]\cdot 5DMF\cdot 4H_2O$, **$Tb^{III}$ [12-$MC_{Mn^{III}N(shi)}$-4]**,.[71] As was the case in the **Mn^{II} 12-MC-4**, the lanthanides were all displaced above the oxygen mean plane.

The Y^{III} analog served to confirm the magnetic properties observed in the Li^+ case, the Gd^{III} analog would determine if additional spin in the absence of anisotropy would confer SMM behave, and the Tb^{III} and Dy^{III} analogs would see if additional anisotropy and spin would improve the behavior. This is another theme that will be common in this thesis: studying the impact lanthanides play on the magnetism of metallacrowns. The Y^{III} case, like the Li^+ analog, had a $\chi_M T$ = 2.1 $cm^3K\ mol^{-1}$, which was close to the expected value

of half a Mn^{II} cation. Thus, it appeared that the **Y^{III} 12-MC-4** also was diamagnetic. The **Gd^{III} 12-MC-4** had a magnetic susceptibility that, when the **Y^{III} 12-MC-4** susceptibility was subtracted, was less than the value of a free Gd^{III} $S = 7/2$ ion, indicate possible weak antiferromagnetic coupling with the ring Mn^{III} ions. The same weak antiferromagnetic coupling between the central Ln^{III} and ring Mn^{III} ions was observed in the Dy^{III} and Tb^{III} cases. Examining the out-of-phase ac magnetic susceptibility data revealed that only **Dy^{III} 12-MC-4** showed frequency dependence (Figure 1.58). However, there was not a dramatic increase in behavior; the blocking temperature in the solid state did not increase above 2.0 K. However, the idea of improving magnetic properties through the inclusion of lanthanides and attempting to control geometry showed promise and something worthy of further studies.[71]

Sandwich 12-MC-4 Complexes

Examining the crystal structures of **$(NaBr)_2$ [12-$MC_{Mn^{III}N(shi)}$-4]** and **$(KBr)_2$ [12-$MC_{Mn^{III}N(shi)}$-4]** (Figures 1.48 and 1.49), it seems reasonable that one could create sandwich metallacrowns, much like the known bis-phthalocyanato complexes. If the ring metals were Mn^{III} ions, one could potentially double the anisotropic contributions of the Mn^{III} ions to the magnetic behavior as now eight anisotropic vectors would be aligned parallel to each other and perpendicular to the metallacrown ring. In 1993, Lah reported an **{Na_2(Na[12-$MC_{Ga^{III}N(shi)}$-4]$_2$-(μ-OH)$_4$)}** structure that had two 12-$MC_{Ga^{III}N(shi)}$-4 metallacrowns held together by four μ-OH bridges sandwiching a single Na^+ ion, with two additional Na^+ ions above and below the metallacrown planes (Figure 1.59).[87] The distance between the two metallacrown oxygen mean planes is 3.132 Å and it creates an eight-coordinate D_{4h} binding pocket; one that could easily accommodate an Ln^{III} cation. It does not take a great leap to suppose that analogs with Mn^{III} ions as ring metals and/or replacing the three Na^+ cations with a single Ln^{III} could be isolated and magnetically interesting. The Ln^{III} replacement could be very interesting, as the geometry about the central metal (D_{4h}) would differ significantly from the reported **[Pc_2Ln^{III}]$^-$** and **Ln^{III} POM** complexes (pseudo-D_{4d}). As will be discussed in Chapter V, the ligand field plays a vital role in the magnetic properties of the Ln^{III} ions. Despite diligent efforts, these

metallacrowns have not been isolated. However, as will be seen in Chapter III, a possible stepping stone to these metallacrowns was isolated.

In 2011, Jankolovits and co-workers reported an extremely unique Ln^{III} 12-$MC_{Zn^{II}N(picHA)}$-4 sandwich complex surrounded by a 24-$MC_{Zn^{II}N(picHA)}$-8 metallacrown (Figure 1.60), $\mathbf{Ln^{III}Zn_{16}}$.[88] The 12-MC-4 ring Zn^{II} ions are square pyramidal, while the 24-MC-8 Zn^{II} ions are octahedral. The outer ring is fused with the two inner 12-MC-4 rings, sharing hydroximate oxygen bonds. Perhaps most interesting, there is a very small, contracted cavity located in the center of the sandwich complex with a single Ln^{III} ion. The ligands of the cavity are arranged in nearly ideal D_{4d} symmetry. Jankolovits et al. were able to isolate the La^{III}, Y^{III}, Nd^{III}, Gd^{III}, Tb^{III}, Dy^{III}, Ho^{III}, Er^{III}, and Yb^{III} analogs. While no magnetic properties were reported, it was found that the $\mathbf{Nd^{III}Zn_{16}}$ and $\mathbf{Yb^{III}Zn_{16}}$ were excellent near infrared (NIR)-emitting complexes. The fact that the Ln^{III} ion was well isolated from any C-H bonds greatly enhanced the luminescent properties.[88] In Chapter V of the thesis, the magnetic properties of these complexes will be probed. If SMM behavior was observed, these would be some of the few bi-functional SMMs known.[89,90,91,92]

AIMS OF THIS THESIS

The aims of this thesis are to study the ability to control magnetoanisotropy through geometric constraints further and to synthesize metallacrowns that will lead to well-isolated ground spin states. The idea of optimizing anisotropy is one that has recently gathered increasing interest in the field.[58,20] No attempts to optimize anisotropy through planar geometric controls are reported in the literature. Based on literature precedent, it seemed appropriate to develop metallacrowns' unique abilities to arrange metals in a predictable and controllable manner as SMMs.[78,71,82] Based on the successes of SIM, it appears that the future of SMMs is in creating well isolated ground spin states. One possible route is to use fewer metals in optimized environments, as observed in the $\mathbf{([Pc_2Ln^{III}]^-TBA^+)}$[40] and $\mathbf{Ln_5O(O\mathit{i}Pr)_{13}}$ complexes.[69,70]

The following constructs will be utilized in this work. In Chapter II, the traditional large mixed Mn/Ln complexes will be studied revealing the drawbacks of this design protocol. Chapter III will describe a new family of metallacrowns, the **Ln^{III} [14-$MC_{Mn^{III}Ln^{III}(\mu\text{-}O)(\mu\text{-}OH)N(shi)}$-5]** family. These complexes have two Ln^{III} and four Mn^{III} cations in a relatively planar orientation. The Ln^{III} ions include Y^{III}, Gd^{III}, Tb^{III}, Dy^{III}, Ho^{III}, and Er^{III}, all in similar ligand environments, revealing the impact Ln^{III} cations play on magnetic properties. Chapter IV focuses on **$Ni(O_2CCH_3)_2$ [12-$MC_{Mn^{III}N(shi)}$-4]**, a family of **$Dy^{III}MX_4$[12-$MC_{Mn^{III}N(shi)}$-4]** (M = Na^+ or K^+, X = ($O_2CC_6H_5$), ($O_2CC_6H_4OH$), or (O_2CCH_3), and a family of **$Ho^{III}M(O_2CCH_3)_4$ [12-$MC_{Mn^{III}N(shi)}$-4]**, revealing the impact of solvent choice and bridging ligand choice on magnetic behavior. Lastly, Chapter V will study the new family of mono-lanthanide metallacrowns **$Ln^{III}Zn_{16}$** (Ln^{III} = Y^{III}, Gd^{III}, Tb^{III}, Dy^{III}, Ho^{III}, Er^{III}, Yb^{III}) in an attempt to create a well isolated ground spin state. Chapter VI will summarize the insights gained from this thesis research to provide direction for future work in this exciting research field.

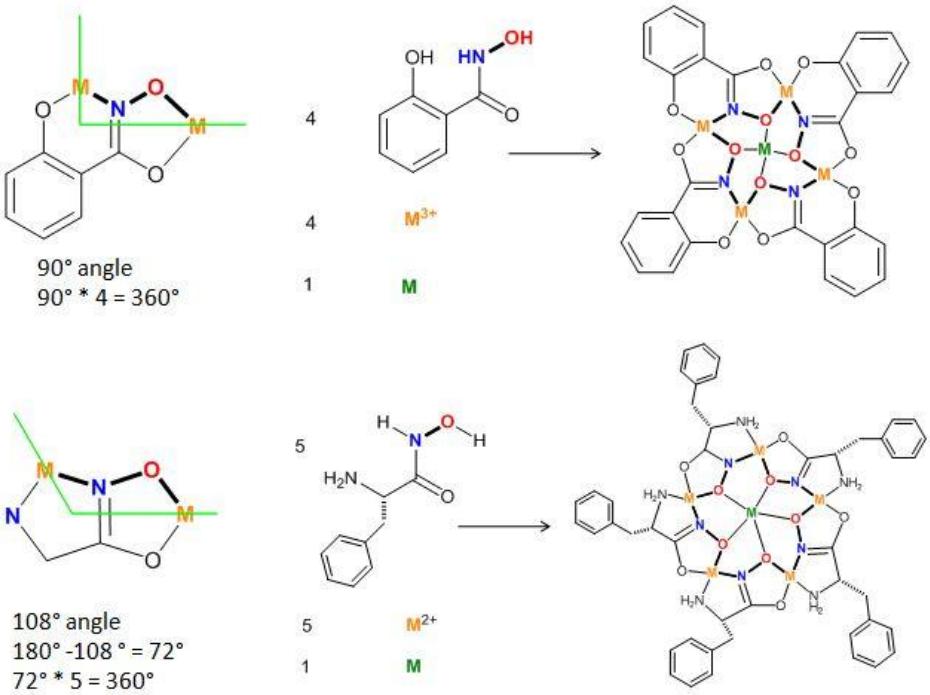

Figure 1.1. Ligand choice dictates what type of metallacrown is isolated. For instance, deprotonated salicylhydroxamic acid has two binding pockets organized 90° apart, favoring 12-MC-4 formation. On the other hand, β-aminohydroxamic acids have two binding pockets 108° degrees apart, giving an external angle of 72°. Repeating five times leads to 15-MC-5 formation.

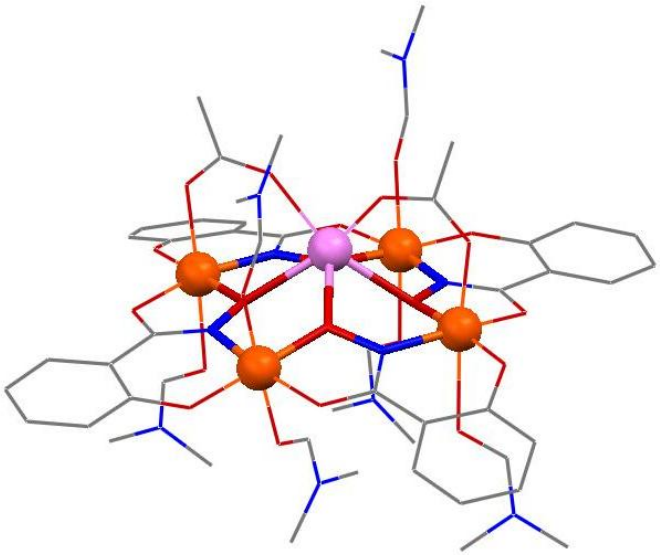

Figure 1.2. The x-ray crystal structure of **$Mn(O_2CCH_3)_2$ [12-$MC_{Mn^{III}N(shi)}$-4]·$6C_3H_7NO$** is shown.[2] The shi^{3-} ligand orients the ring Mn^{III} ions at approximately 90° angles to each other. The central Mn^{II} ion is bridged to the ring Mn^{III} ions by two acetate ions. Color scheme: orange sphere: Mn^{III}; violet sphere: Mn^{II}; red tube: oxygen; blue tube: nitrogen; gray line: carbon. Hydrogen atoms and lattice solvents have been removed for clarity.

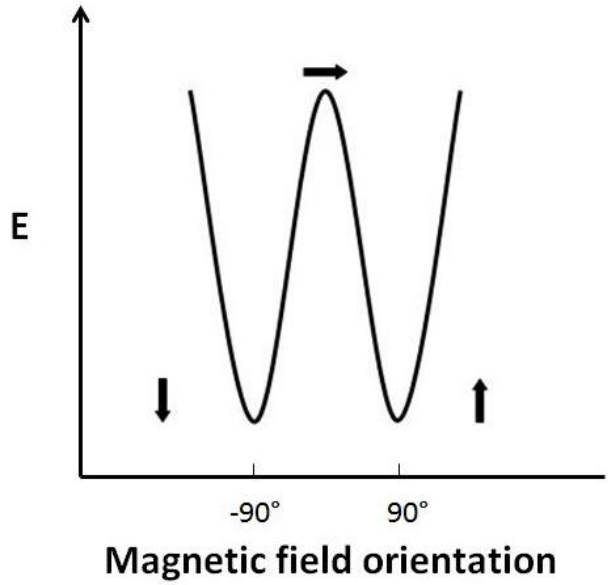

Figure 1.3. A double-energy well showing the energy due to Ising-type anisotropy. When the spin is parallel or anti-parallel to the z-axis, one obtains an energetic minima, while a maximum is reached when the spin is perpendicular to the z-axis.[14]

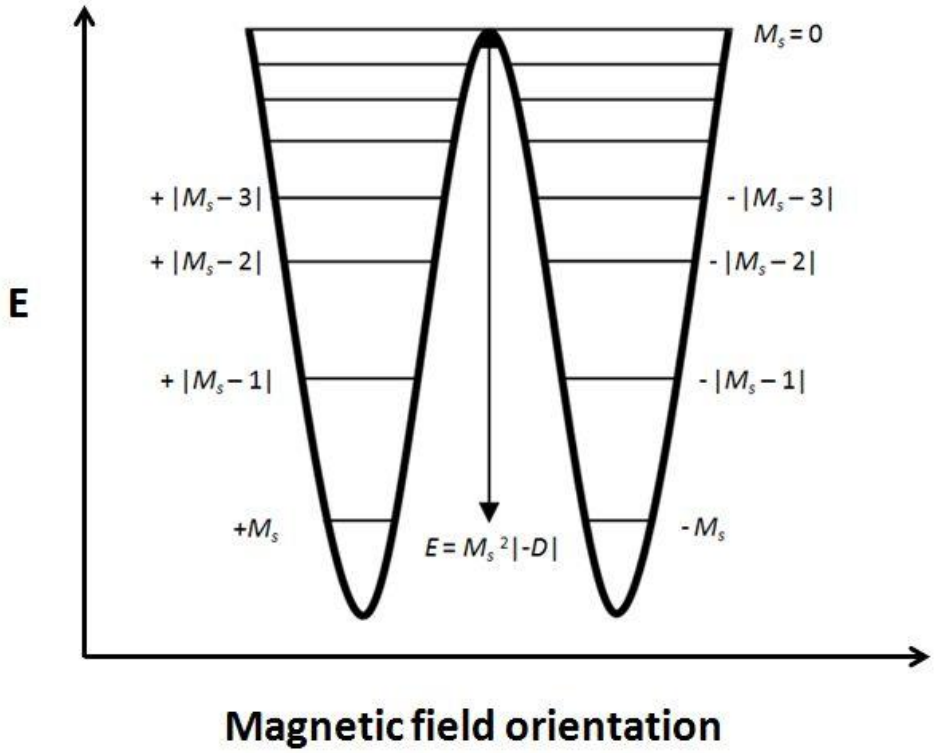

Figure 1.4. For single-molecule magnets, the height of the energy double well is determined by the complex's spin, M_s, and its anisotropy D.[14]

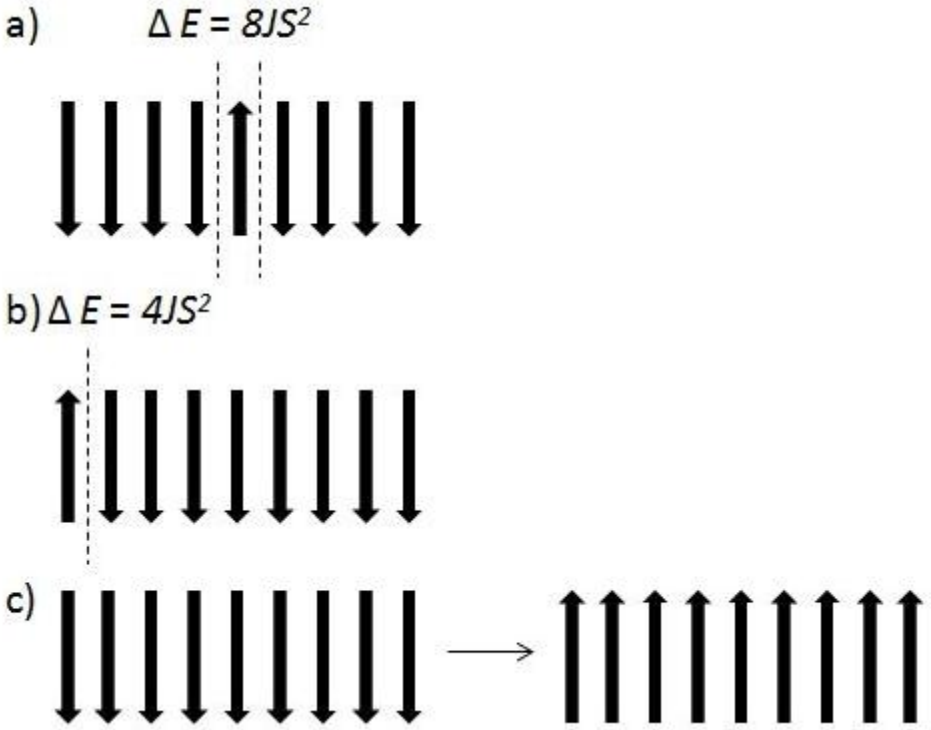

Figure 1.5. Single-chain magnets have three relaxation pathways: a) spin relaxation starting in the center; b) spin relaxation starting at the end of the chain; c) collective reversal of all spins.[39]

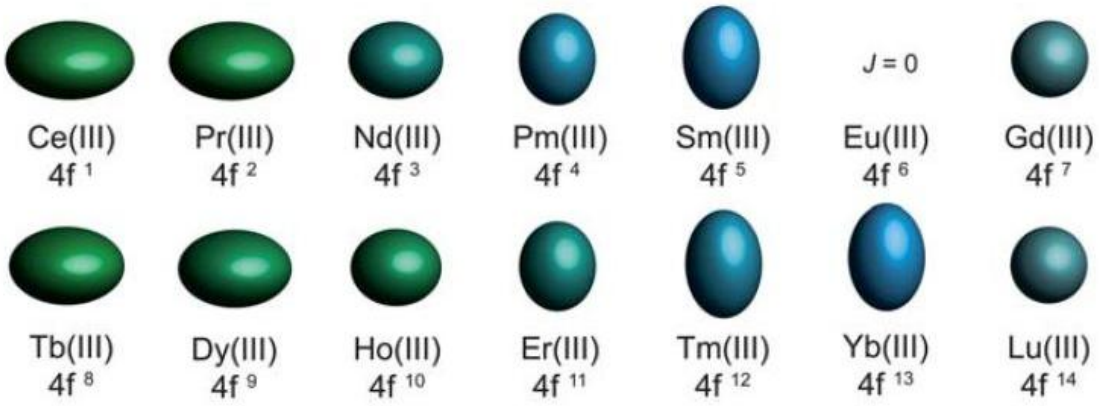

Figure 1.6. The shapes of the lanthanides range from oblate to prolate to spherical based on which *f* orbitals are occupied.[42] The figure is taken directly from Figure 4 in Rinehart, J. D. & Long, J. R. *Chem. Sci*. **2011**, *2*, 2078.

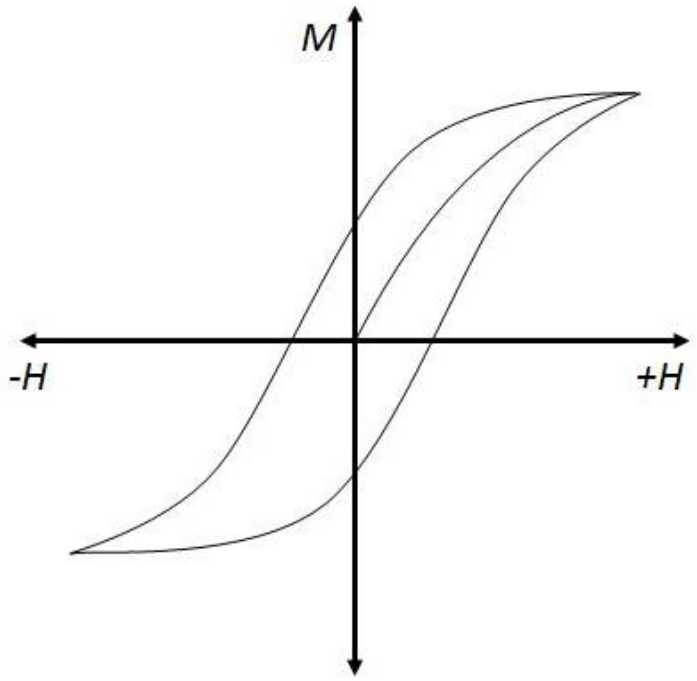

Figure 1.7. An example of a magnetic hysteresis plot is given.

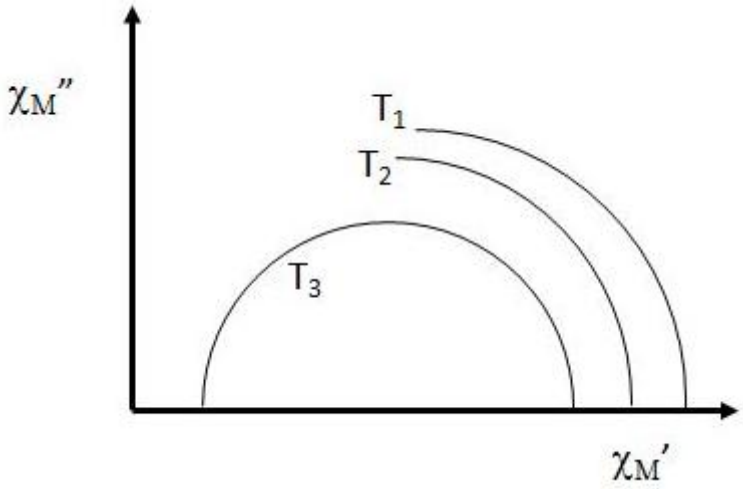

Figure 1.8. An example of a Cole-Cole plot at different temperatures (T_1, T_2, and T_3) is given.

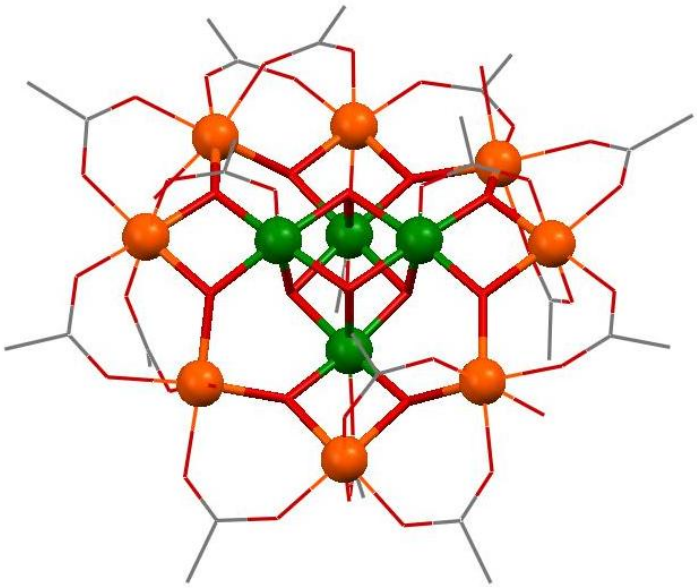

Figure 1.9. The x-ray crystal structure of $\mathbf{Mn^{III}_8Mn^{IV}_4O_{12}(O_2CCH_3)_{16}(H_2O)_4}$ is shown. Lattice solvents and hydrogen atoms have been omitted for clarity. Color scheme: orange spheres: Mn^{III}; green spheres: Mn^{IV}; red tubes: oxygen; gray tubes: carbon.[48]

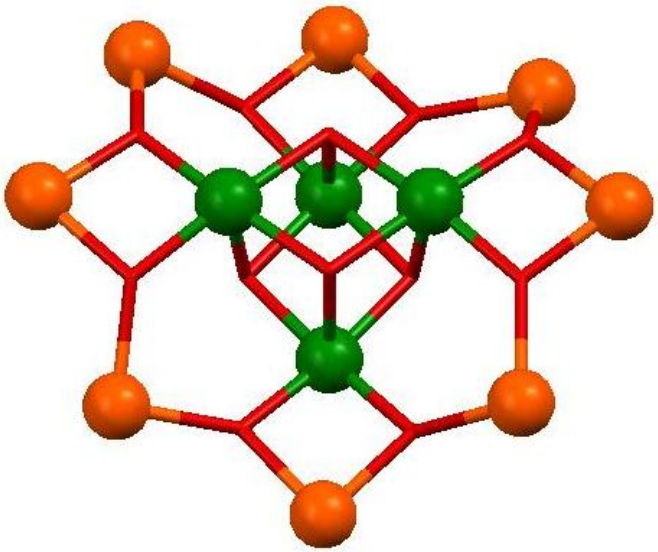

Figure 1.10. The core of **$\mathbf{Mn_{12}(OAc)}$** is shown. The four Mn^{IV} ions occupy the vertices of a cube and are surrounded by the eight Mn^{III}. It was found that the four Mn^{IV} ions are ferromagnetically coupled which are antiferromagnetically coupled to the eight Mn^{III} ions. Color scheme: orange spheres: Mn^{III}; green spheres: Mn^{IV}; red tubes: oxygen.[48]

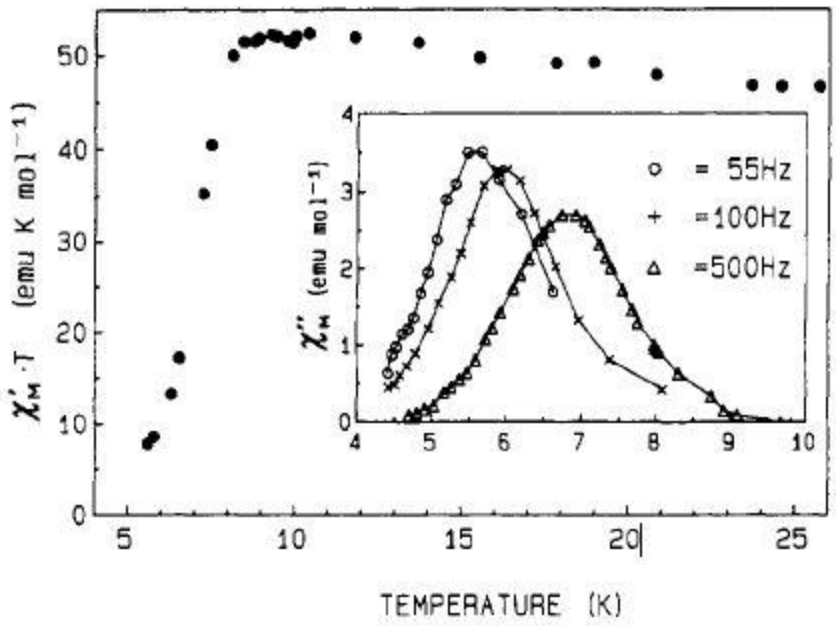

Figure 1.11. The ac magnetic susceptibility data for **Mn_{12}(OAc)** is shown. The inset features the out-of-phase magnetic susceptibility, indicating frequency dependence.[49] This is Figure 1 taken from Caneschi, A.; Gatteschi, D.; Sessoli, R. *J. Am. Chem. Soc*. **1991**, *113*, 5873.

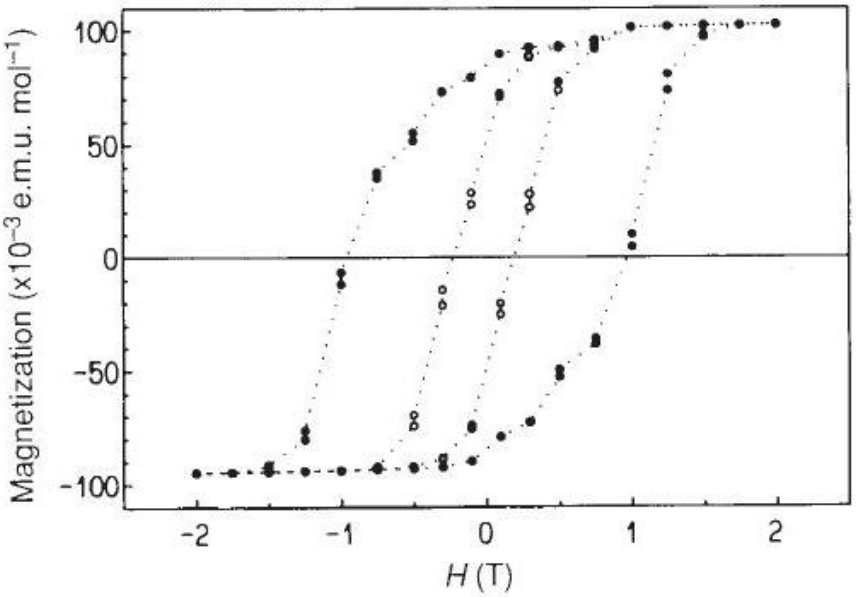

Figure 1.12. The dc magnetic hysteresis of **Mn_{12}(OAc)** is shown. The data was collected along the crystal *c* axis. The closed circles represents data collected at 2.2 K, and the open circles for data collected at 2.8 K.[50] This is Figure 4b taken directly from Sessoli, R.; Gatteschi, D.; Caneschi, A.; Novak, M. A. *Nature*, **1993**, *365*, 141.

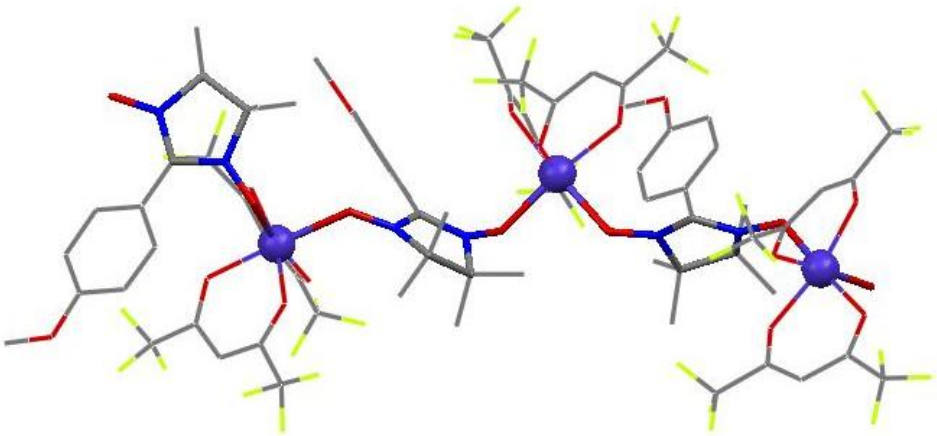

Figure 1.13. The x-ray crystal structure model of **[Co(hfac)$_2$(NITPhOMe)]$_3$** is shown. The mode of chain propagation is highlighted. For clarity, hydrogen atoms have been omitted. Color scheme: purple spheres: Co^{II}; red tubes: oxygen; blue tubes; nitrogen; gray tubes; carbon; lime green tubes: fluorine.[36]

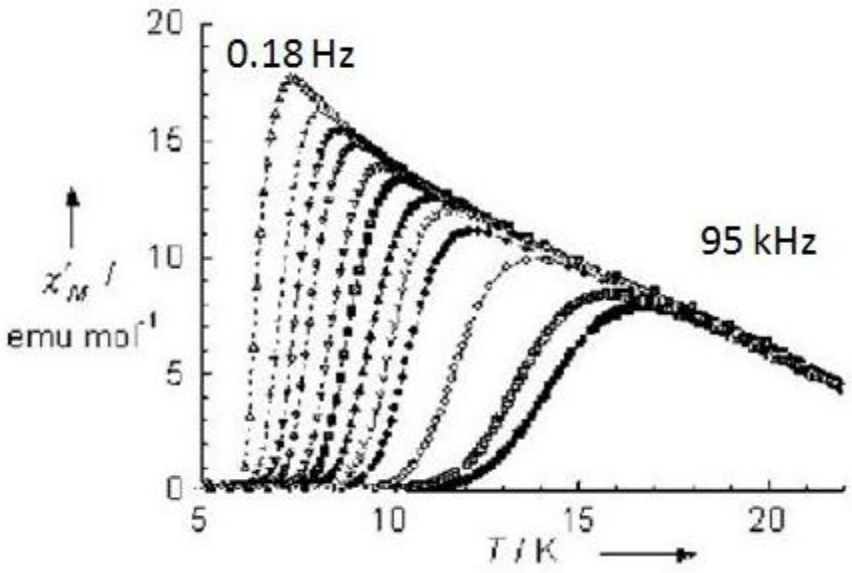

Figure 1.14. The out-of-phase ac magnetic susceptibility frequency data for **[Co(hfac)$_2$(NITPhOMe)]$_x$** are shown. The frequencies range from 0.18 Hz to 95 kHz. The lines were provided as a visual guide.[36] This figure is taken from Figure 3 of Caneschi, A.; Gatteschi, D.; Lalioti, N.; Sangregorio, C.; Sessoli, R.; Venturi, G.; Vindigni, A.; Rettori, A.; Pini, M. G.; Novak, M. A. *Angew. Chem. Int. Ed.* **2001**, *40*, 1760.

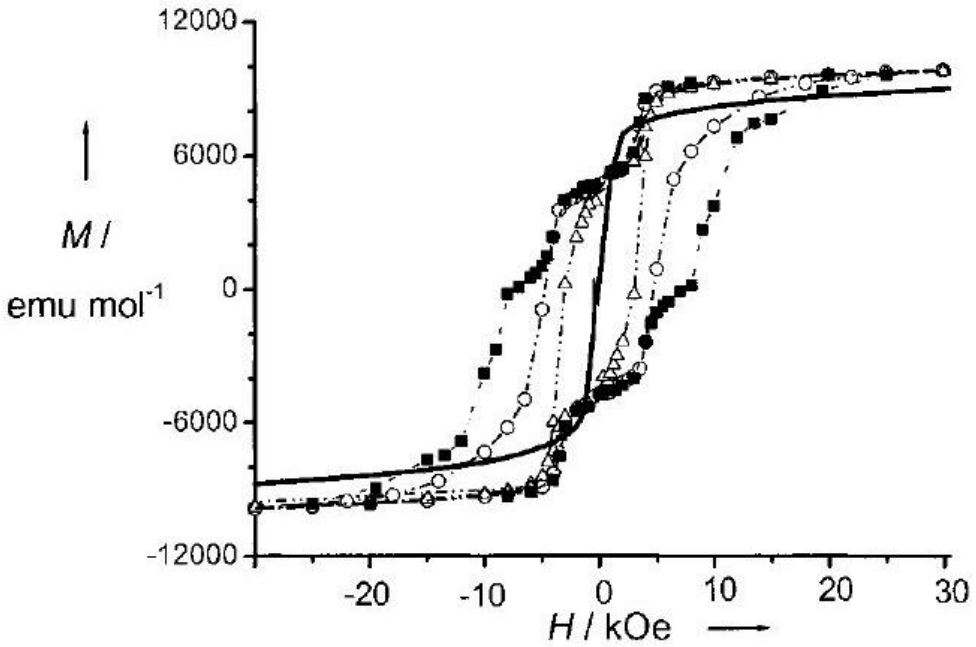

Figure 1.15. The dc magnetic hysteresis of **$[Co(hfac)_2(NITPhOMe)]_x$** is shown. For 2.0 K (■), 3.0 K (○), and 4.5 K (△), the field was applied parallel to the chain axis, while the solid line represents a field applied perpendicular to the chain at 2.0 K.[36] This figure is Figure 4 taken directly from Caneschi, A.; Gatteschi, D.; Lalioti, N.; Sangregorio, C.; Sessoli, R.; Venturi, G.; Vindigni, A.; Rettori, A.; Pini, M. G.; Novak, M. A. *Angew. Chem. Int. Ed*. **2001**, *40*, 1760.

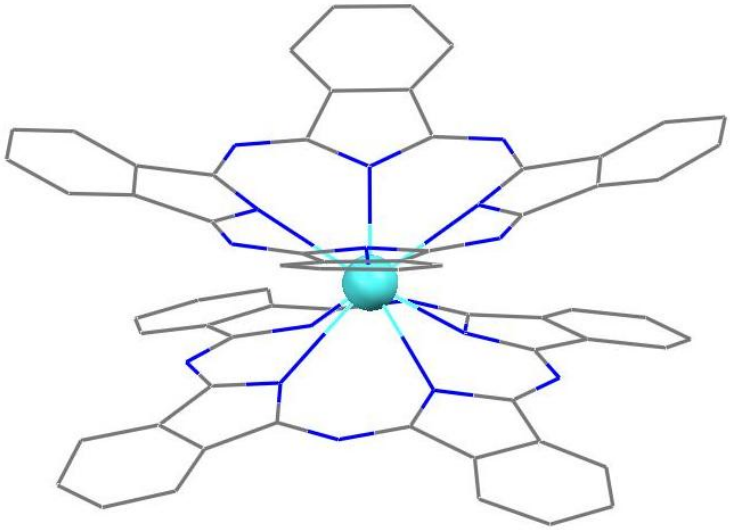

Figure 1.16. The x-ray crystal structure of **$[Pc_2Gd]^-TBA^+$** is given. The TBA cation has been removed for clarity. Color scheme: aqua sphere: Gd^{III}; gray tube: carbon; blue tube: nitrogen.[53]

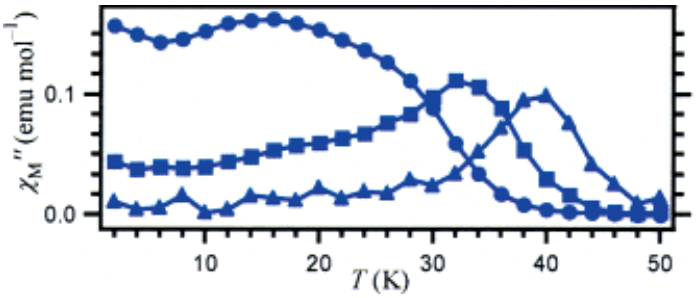

Figure 1.17. The out-of-phase ac magnetic susceptibility of **[Pc_2Tb]$^-$TBA$^+$** diluted in **[Pc_2Y]$^-$TBA$^+$** is shown. The data were collected at 10 Hz (●), 100 Hz (■), and 997 Hz (▲).[40] Figure is taken from Figure 1 of Ishikawa, N.; Sugita, M,; Ishikawa, T.; Koshihara, S. Kaizu, Y. *J. Am. Chem. Soc.* **2003**, *125*, 8694.

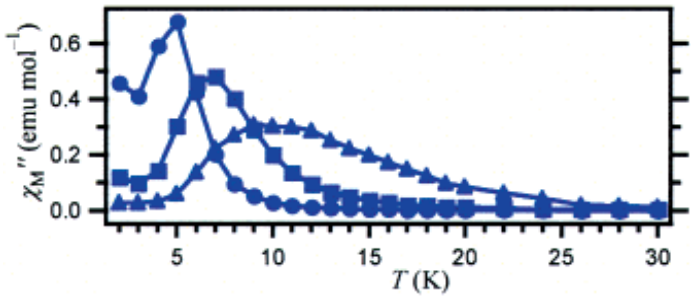

Figure 1.18. The out-of-phase ac magnetic susceptibly of **[Pc_2Dy]$^-$TBA$^+$** diluted in **[Pc_2Y]$^-$TBA$^+$** is shown. The data were collected at 10 Hz (●), 100 Hz (■), and 997 Hz (▲).[40] Figure is taken from Figure 2 of Ishikawa, N.; Sugita, M,; Ishikawa, T.; Koshihara, S. Kaizu, Y. *J. Am. Chem. Soc.* **2003**, *125*, 8694.

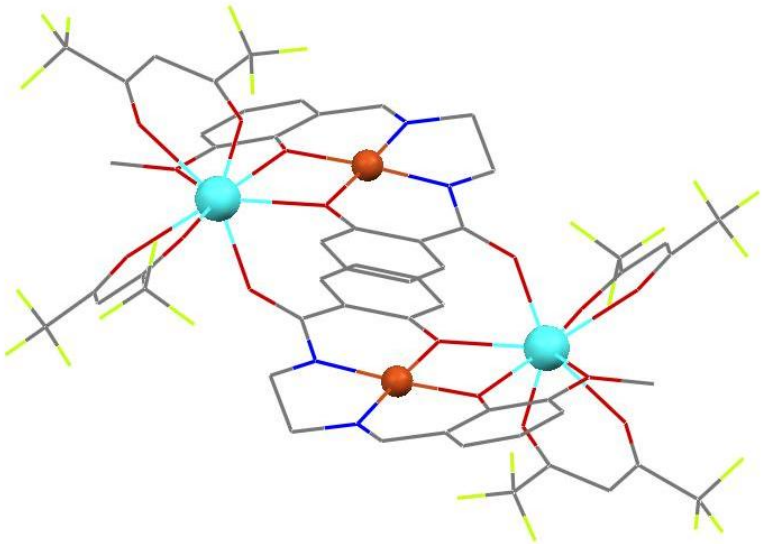

Figure 1.19. The x-ray crystal structure of **[$Cu^{II}LTb^{III}(Hfac)_2]_2$** is shown. Color scheme: aqua sphere: Tb^{III}; orange sphere: Cu^{II}; red tubes: oxygen; blue tubes: nitrogen; gray tubes: carbon; lime green tubes: fluorine. Hydrogen atoms have been omitted for clarity.[56]

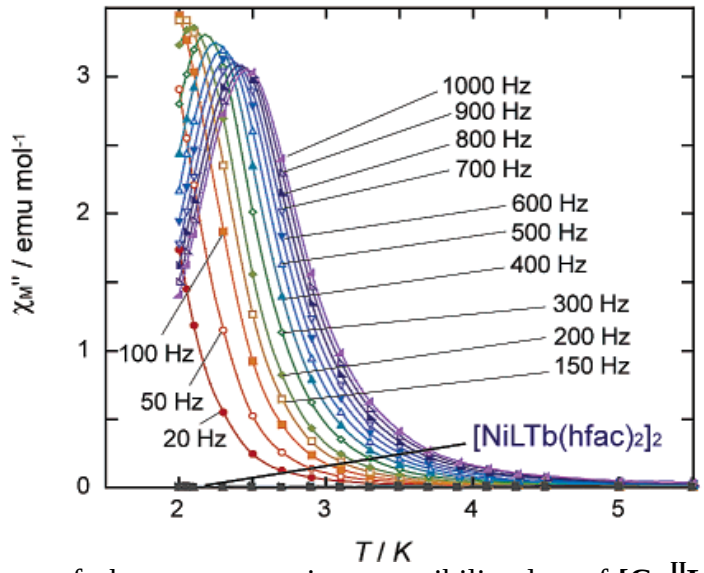

Figure 1.20. The out-of-phase ac magnetic susceptibility data of **$[Cu^{II}LTb^{III}(Hfac)_2]_2$** is shown. The data were collected at the indicated frequencies. An isostructural **$[Ni^{II}LTb^{III}(Hfac)_2]_2$** complex did not show frequency dependence.[55] Figure is taken from Figure 3 of Osa, S.; Kido, T.; Matsumoto, N.; Re, N.; Pochaba, A.; Mrozinski, J. *J. Am. Chem. Soc*. **2003**, *126*, 420.

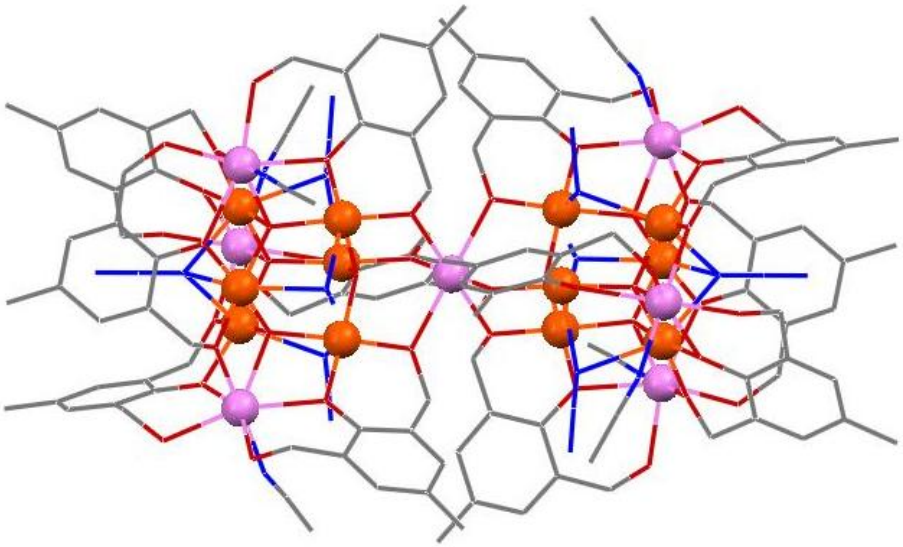

Figure 1.21. The x-ray crystal structure of **Mn_{19}** is shown. Lattice molecules and ions and hydrogen atoms have been omitted for clarity. Color scheme: light purple spheres: Mn^{II}; orange spheres: Mn^{III}; red tubes: oxygen; blue tubes: nitrogen; gray tubes: carbon.[57]

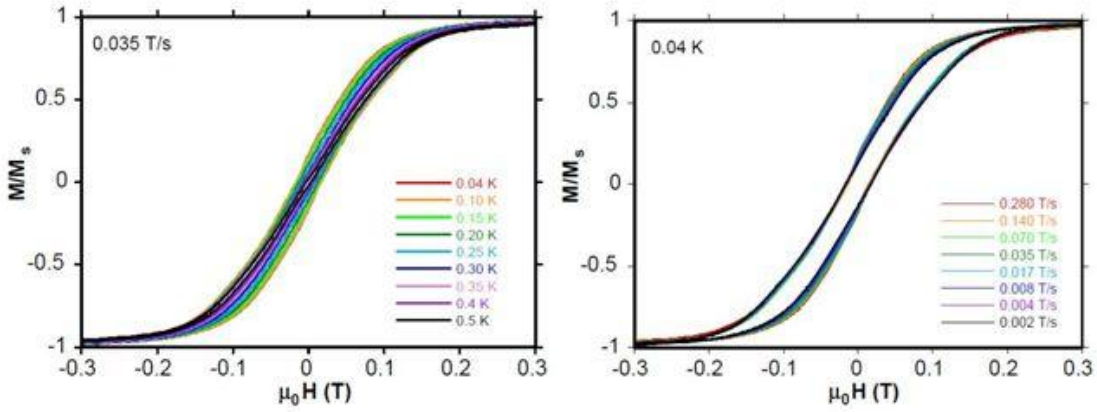

Figure 1.22. The micro SQUID hysteresis of **Mn_{19}** is shown. On the left, the field sweep rate was held constant at 0.035 T/s and the hysteresis was studied at the indicated temperatures. On the right, the temperature was held constant at 0.04 K and the sweep rate was varied.[57] The figures are S3 and S4 of Ako, A. M.; Hewitt, I. J.; Mereacre, V.; Clérac, R.; Wernsdorfer, W.; Anson, C. E.; Powell, A. K. *Angew. Chem.* **2006**, *118*, 5048.

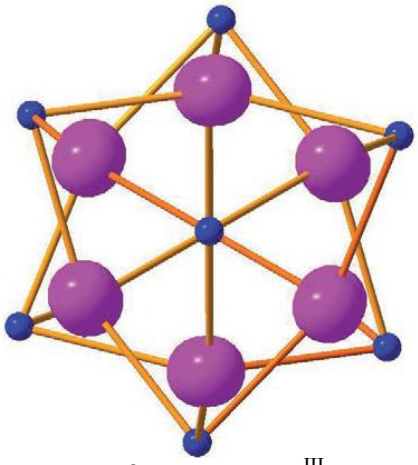

Figure 1.23. The Jahn-Teller axes of the six Mn^{III} ions, highlighted in gold, almost perfectly cancel each other out in each Mn_9 half of the **Mn_{19}** complex.[57] This is Figure 2c of Ako, A. M.; Hewitt, I. J.; Mereacre, V.; Clérac, R.; Wernsdorfer, W.; Anson, C. E.; Powell, A. K. *Angew. Chem.* **2006**, *118*, 5048.

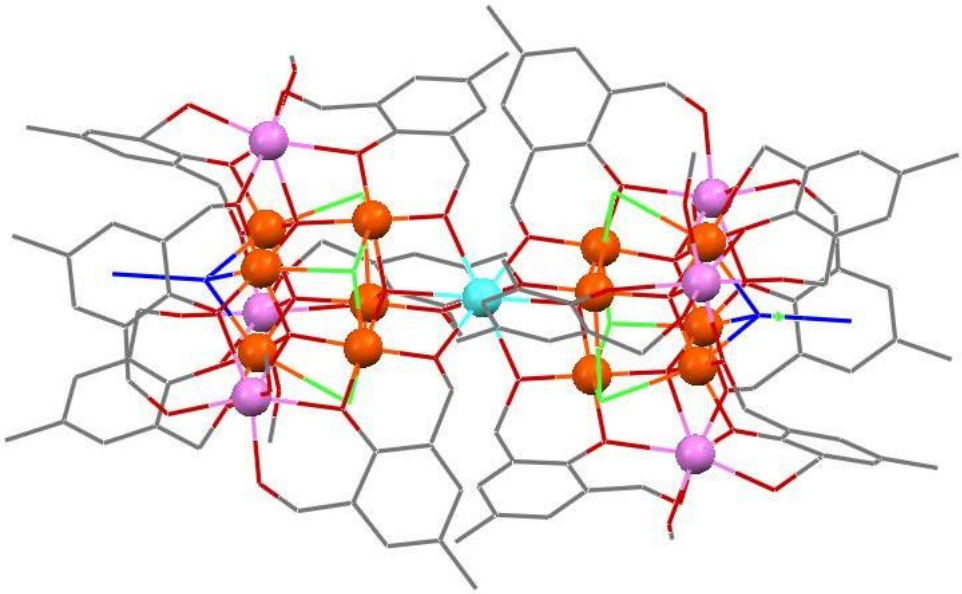

Figure 1.24. The x-ray crystal structure of **$Mn_{18}Dy$** is shown. Interestingly, the unusual coordination environment of the central Mn^{II} in Mn_{19} allowed for site-selective substitution with a Dy^{III} ion. Color scheme: aqua sphere: Dy^{III}; violet sphere: Mn^{II}; orange sphere: Mn^{III}; red tube: oxygen; blue tube: nitrogen; gray tube: carbon; neon green tube: chlorine.[66]

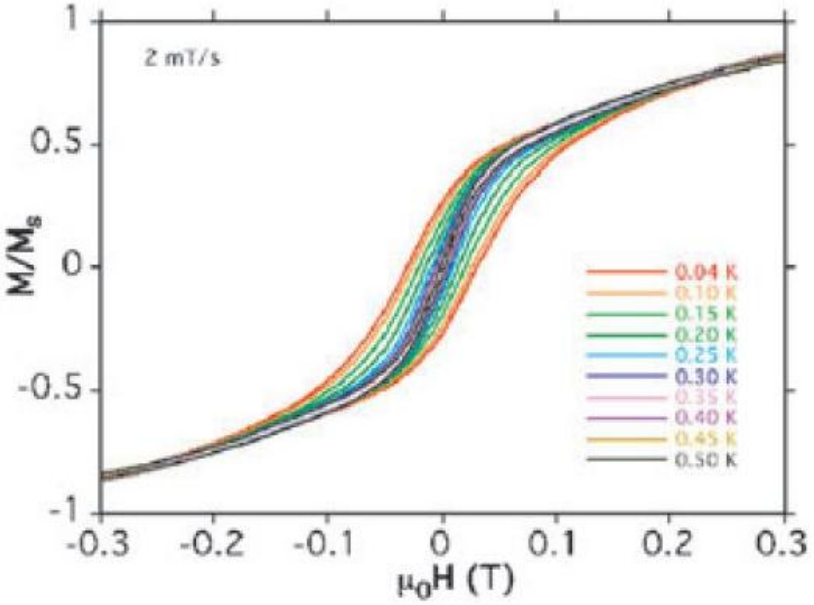

Figure 1.25. The hysteresis of **$Mn_{18}Dy$** is shown. The hysteresis data were collected on a single crystal at a fixed sweep rate of 2 mT/s and at various temperatures.[66] This figure is taken from Figure 3 of Ako, A. M.; Mereacre, V.; Clérac, R.; Wernsdorfer, W.; Hewitt, I. J.; Anson, C. E.; Powell, A. K. *Chem. Commun*. **2009**, 544.

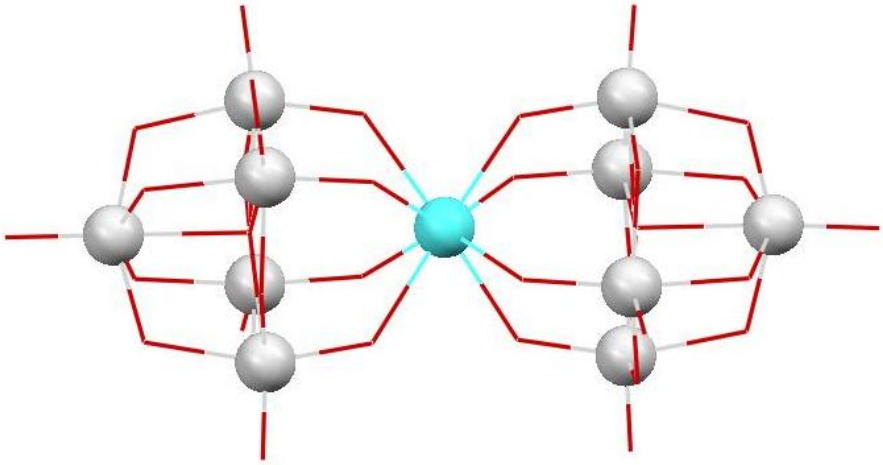

Figure 1.26. The x-ray crystal structure of **$[Er(W_5O_{18})_2]^{9-}$** polyoxometallate is shown. Only the polyoxometallate core is shown for clarity. Color scheme: aqua sphere: Er^{III}; light gray sphere: W^{VI}; red tube: oxygen.[41]

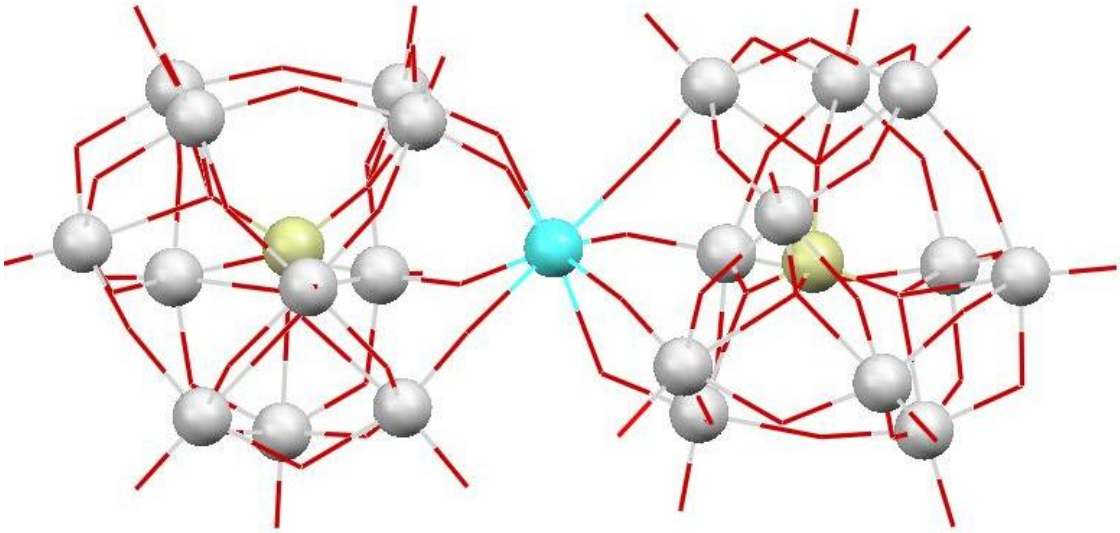

Figure 1.27. The x-ray crystal structure of **$[Er(\beta\text{-}SiW_{11}O_{39})_2]^{13-}$** polyoxometallate is shown. Only the polyoxometallate core is shown for clarity. Color scheme: aqua sphere: Er^{III}; light gray sphere: W^{VI}; gold sphere: Si; red tube: oxygen.[67]

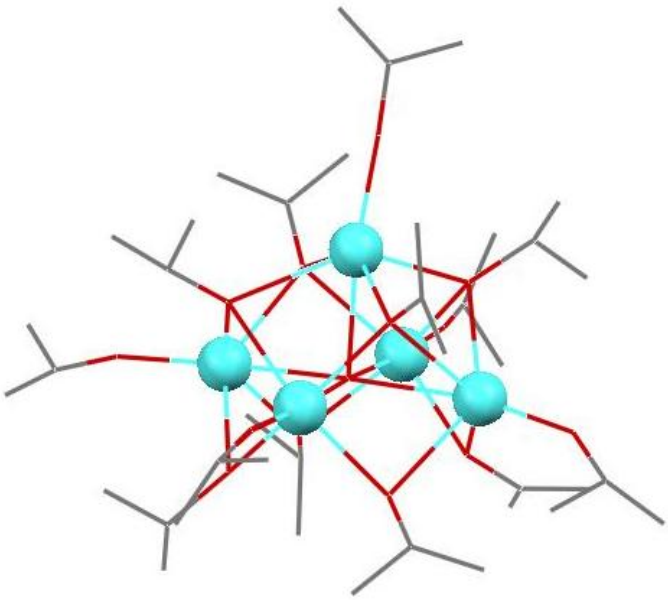

Figure 1.28. The x-ray crystal structure of **$Dy_5O(OiPr)$** is shown. For clarity, disordered *iso*-propoxide molecules were removed. Color scheme: aqua spheres: Dy^{III}; red tubes: oxygen; gray tubes: carbon.[69]

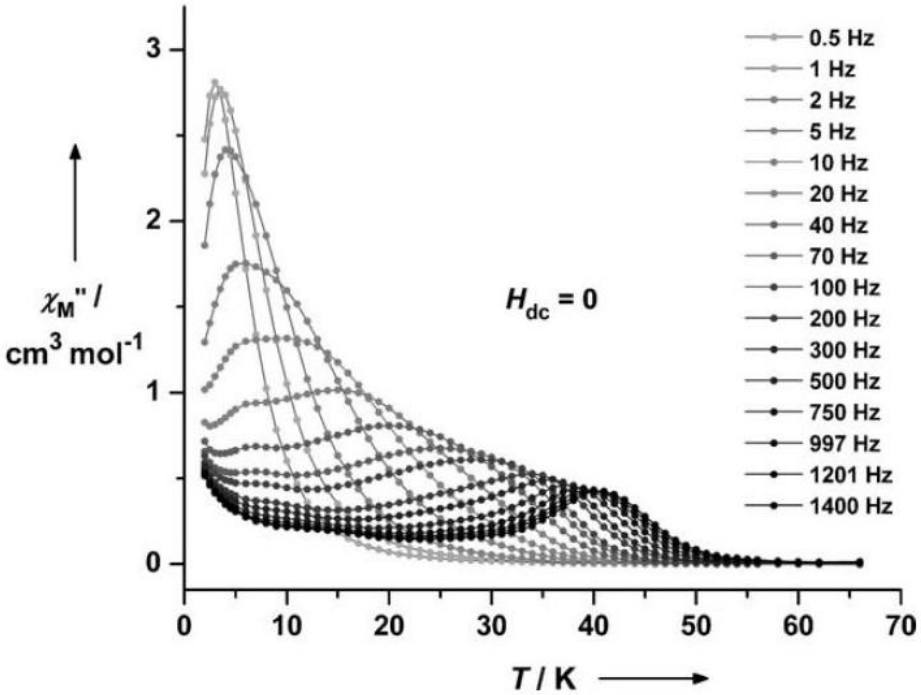

Figure 1.29. The out-of-phase ac magnetic susceptibility of **$Dy_5O(OiPr)$** demonstrated a record blocking temperature of 41 K. The data were collected with 0 G dc applied field and an ac drive field of 1.55 G at the indicated frequencies.[69] This is Figure 2 from Blagg, R. J.; Muryn, C. A.; McInnes, E. J. L.; Tuna, F.; Winpenny, R. E. P. *Angew. Chem. Int. Ed*. **2011**, *50*, 6530.

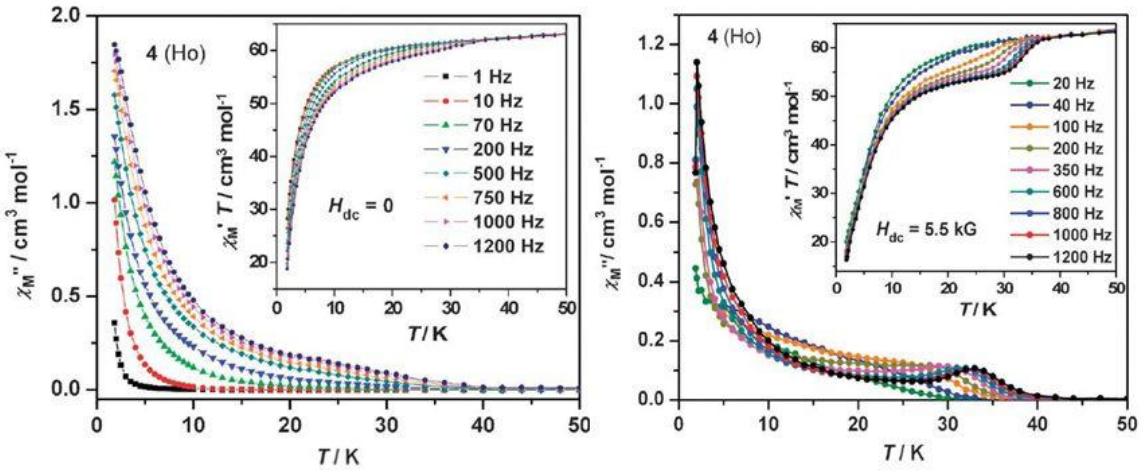

Figure 1.30. The out-of-phase ac magnetic susceptibility of **$Ho_5O(OiPr)$** showed frequency dependence up to 33 K with a 5.5 kG applied dc field. At left, the out-of-phase magnetic susceptibility with 0 G dc applied field is shown At right, the out-of-phase magnetic susceptibility with 5.5 kG dc applied field is shown. Inset of each shows the in-phase magnetic susceptibility data.[68] This is Figure 3 from Blagg, R. J.; Tuna, F.; McInnes, E. J. L.; Winpenny, R. E. P. *Chem. Commun*. **2011**, *47*, 10587.

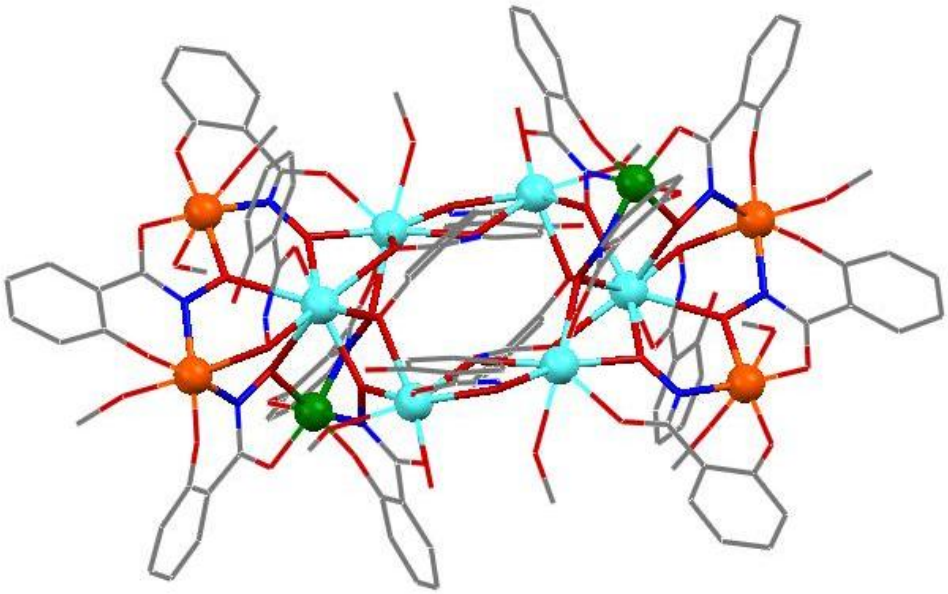

Figure 1.31. The x-ray crystal structure of **$Dy^{III}_6Mn^{III}_4Mn^{IV}_2$** is shown. The six Dy^{III} ions form a hexagon in the center of the molecule, which is surrounded by the Mn^{IV} and Mn^{III} ions. The 28-MC-10 ring is also highlighted. Color scheme: aqua spheres: Dy^{III}; orange spheres: Mn^{III}; green spheres: Mn^{IV}; red tubes: oxygen; blue tubes: nitrogen; gray tubes: carbon.[60]

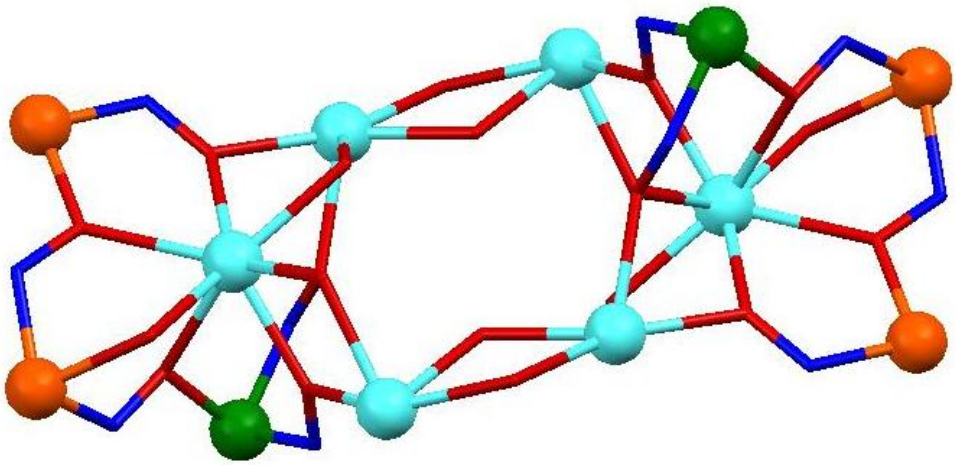

Figure 1.32. The 28-MC-10 ring is highlighted from $\mathbf{Dy^{III}_6Mn^{III}_4Mn^{IV}_2}$. The color scheme is the same as above.[60]

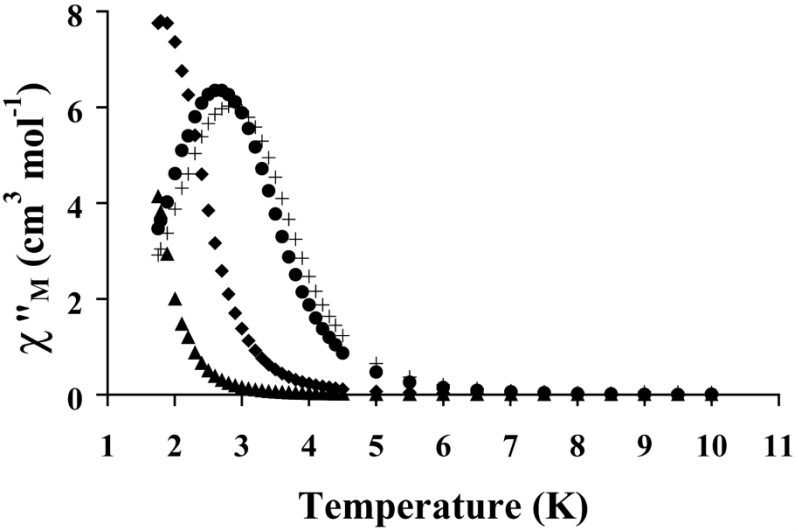

Figure 1.33. The out-of-phase ac magnetic susceptibility data of $\mathbf{Dy^{III}_6Mn^{III}_4Mn^{IV}_2}$ reveals frequency dependence. The frequencies collected were 1500 Hz (+), 1000 Hz (●), 100 Hz (◆), 10 Hz (▲). There was no applied field and a 3.5 G ac drive field was used.[71] This is Figure 3.48 of Zaleski, C. M. Ph.D. Thesis, Utilizing Metallacrowns to Develop New Single-Molecule Magnets, The University of Michigan, 2005.

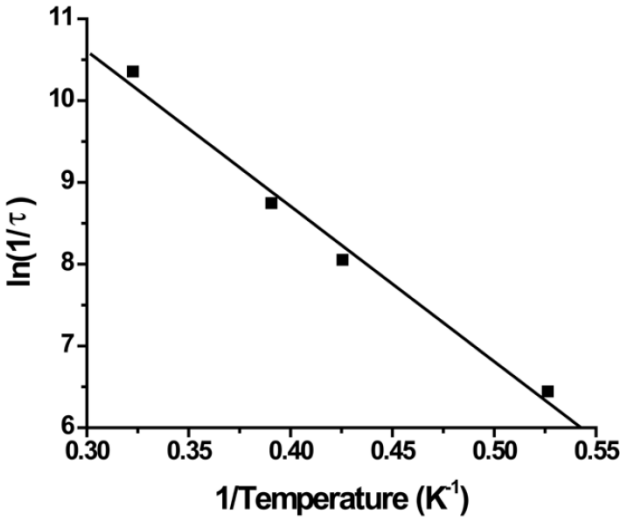

Figure 1.34. The Arrhenius plot of $\mathbf{Dy^{III}_6Mn^{III}_4Mn^{IV}_2}$ and the least-squares fit line revealed a U_{eff} of 19.0 ± 1.5 K (13.2 ± 1.0 cm^{-1}) and an inverse pre-exponential factor of 1.2 x 10^7 s^{-1}.[71] This is Figure 3.49 of Zaleski, C. M. Ph.D. Thesis, Utilizing Metallacrowns to Develop New Single-Molecule Magnets, The University of Michigan, 2005.

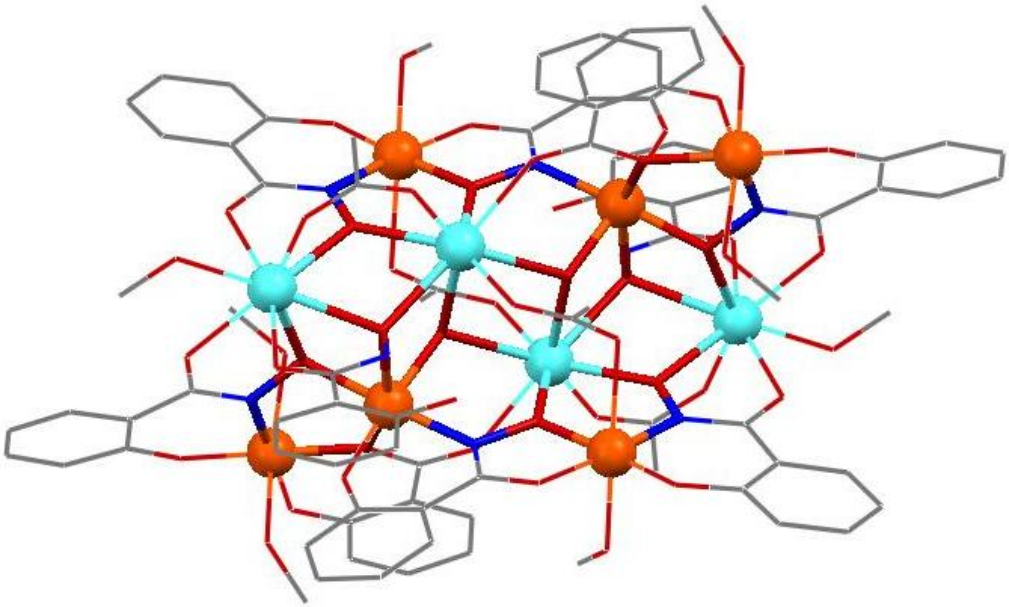

Figure 1.35. The x-ray crystal structure of $\mathbf{Ho^{III}_4Mn^{III}_6}$ is shown. Lattice solvents and hydrogen atoms were removed for clarity. Color scheme: aqua spheres: Ho^{III}; orange spheres: Mn^{III}; red tubes: oxygen; blue tubes: nitrogen; gray tubes: carbon.[63]

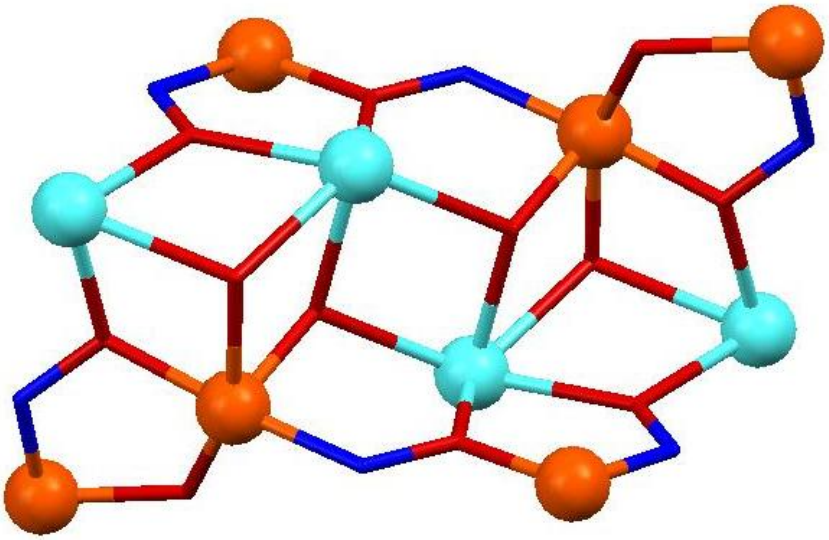

Figure 1.36. The 22-MC-8 core of $\mathbf{Ho^{III}_4Mn^{III}_6}$ is shown. The color scheme is the same as above.[63]

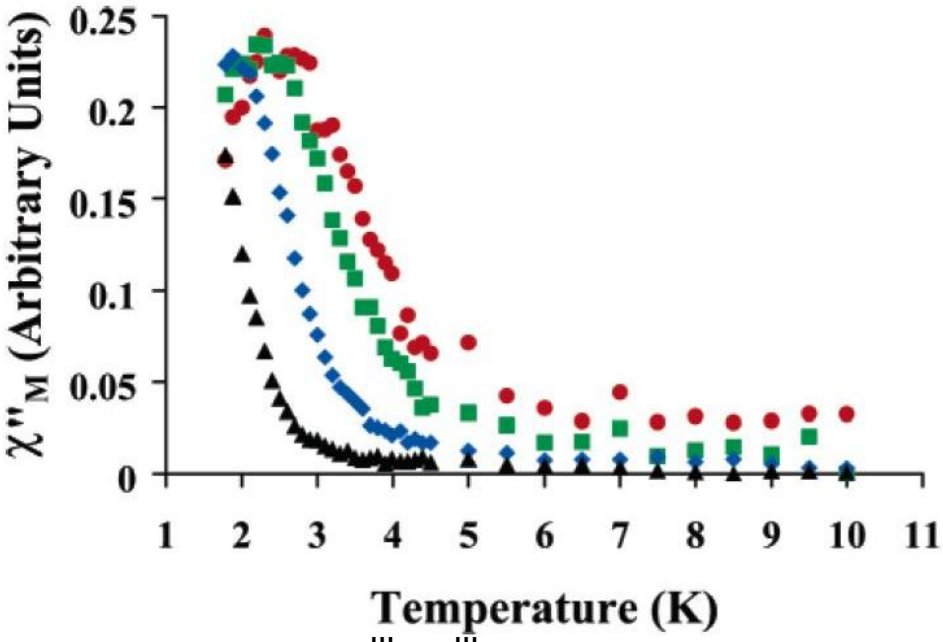

Figure 1.37. The solution state $\mathbf{Dy^{III}_4Mn^{III}_6}$ out-of-phase ac magnetic susceptibility revealed frequency dependence. The frequencies collected were 1000 Hz (●), 500 Hz (■), 100 Hz (◆), and 10 Hz (▲) in no dc applied field and a 3.5 G ac drive field.[63] The figure is taken from Figure 3 of Zaleski, C. M.; Kampf, J. W.; Mallah, T.; Kirk, M. L.; Pecoraro, V. L. *Inorg. Chem*. **2007**, *46*, 1954.

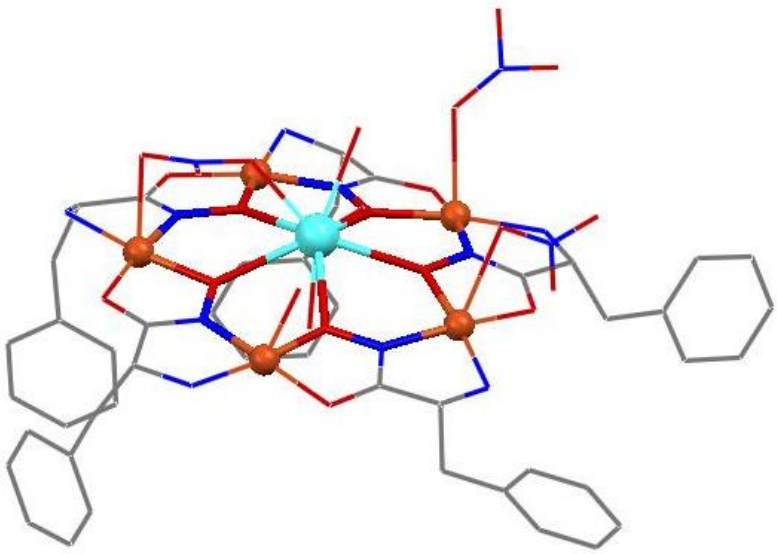

Figure 1.38. The x-ray crystal structure of **La^{III} [15-$MC_{Cu^{II}N((S)\text{-pheHA})}$-5]$(NO_3)_3$** is shown. Lattice solvents and hydrogen atoms were omitted for clarity. Color scheme: aqua sphere: La^{III}; copper spheres: Cu^{II}; red tubes: oxygen; blue tubes: nitrogen; gray tubes: carbon.[72]

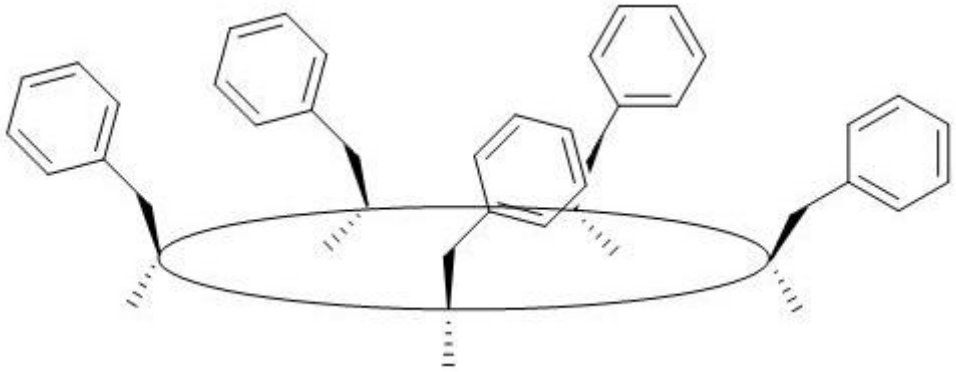

Figure 1.39. The faces of a 15-MC-5 are shown.

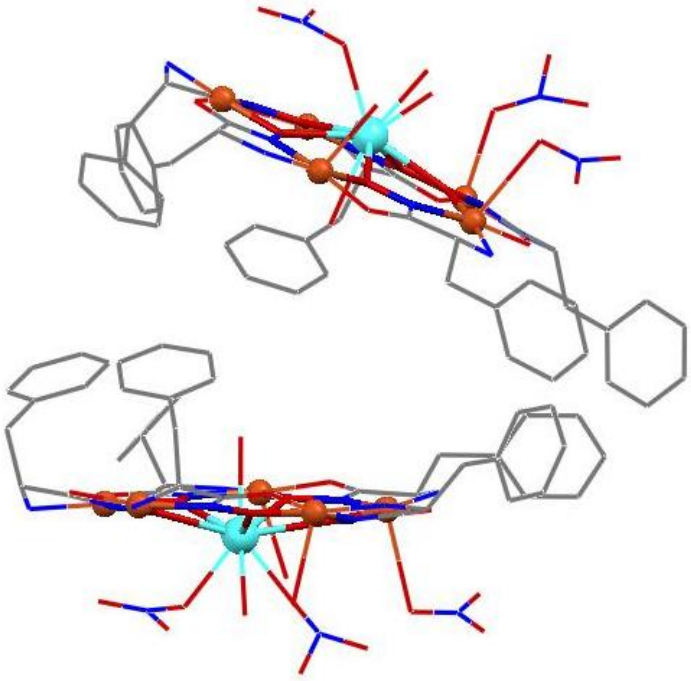

Figure 1.40 The x-ray crystal structure of the **La^{III} [15-$MC_{Cu^{II}N((S)\text{-}pheHA)}$-5]** dimer is shown. Lattice solvent molecules and hydrogen atoms are omitted for clarity. Color scheme: aqua sphere: La^{III}; copper sphere: Cu^{II}; red tube: oxygen; blue tube: nitrogen; gray tube: carbon.[72]

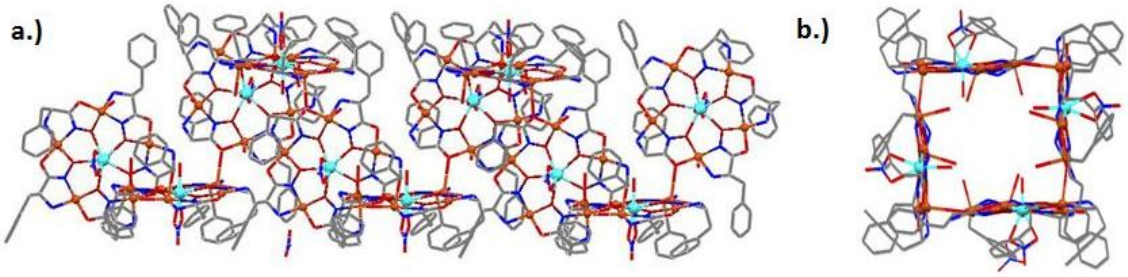

Figure 1.41. The x-ray crystal structure of the helix of **$Sm^{III}(NO_3)$ [15-$MC_{Cu^{II}N((S)\text{-}pheHA)}$-5]$NO_3$** is shown. a.) The image is shown perpendicular to the propagation of the chain, while b.) is parallel to the propagation. Lattice solvents and hydrogen atoms have been omitted for clarity. Color scheme: aqua sphere: Sm^{III}; copper sphere: Cu^{II}; red tube: oxygen; blue tube: nitrogen; gray tube: carbon.[77]

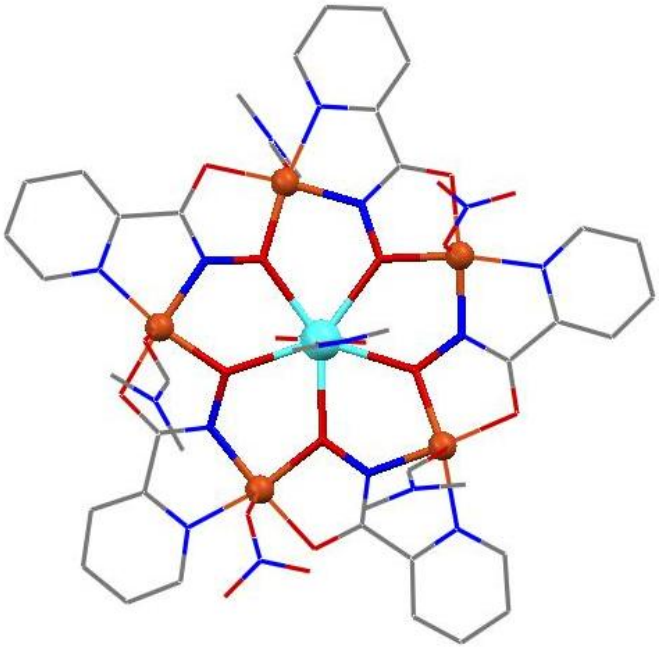

Figure 1.42. The x-ray crystal structure of **$Gd(NO_3)_3$ [15-$MC_{Cu^{II}N(picHA)}$-5]** is shown. The 15-MC-5 ring is highlighted.Lattice solvent molecules and hydrogen atoms have been omitted for clarity. Color scheme: aqua sphere: Gd^{III}; copper sphere: Cu^{II}; red tube: oxygen; blue tube: nitrogen; gray tube: carbon.[11]

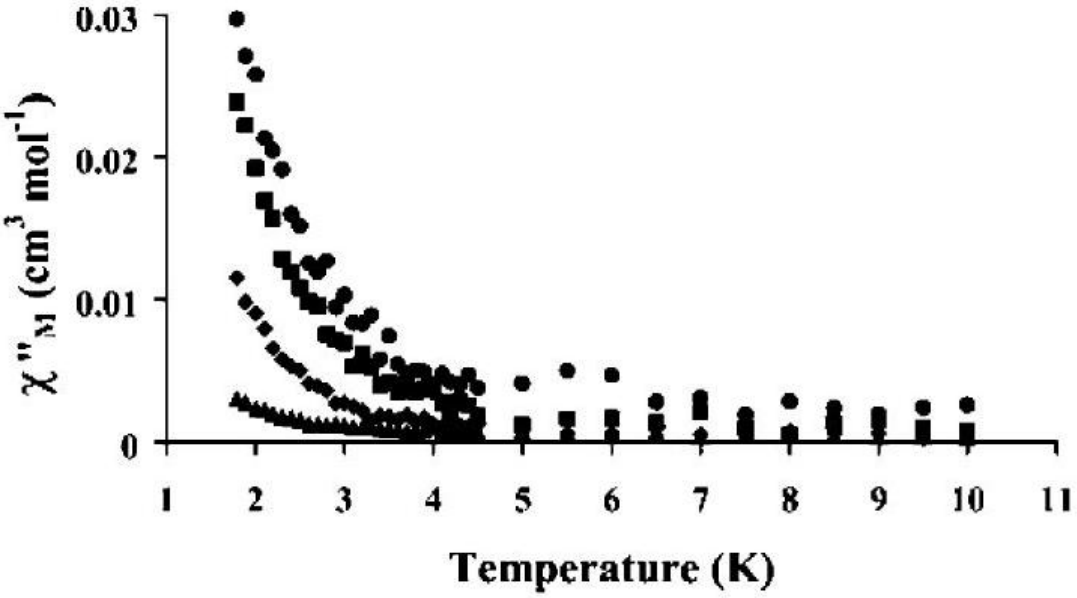

Figure 1.43. The out-of-phase ac magnetic susceptibility of the **Dy^{III}[15-$MC_{Cu^{II}N((S)\text{-}pheHA)}$-5]** dimer shows frequency dependence in a frozen methanol solution. The frequencies examined where 1000 Hz (●), 500 Hz (■), 100 Hz (◆), and 10 Hz (▲). The measurements were taken with no applied dc field and a 3.5 G ac drive field.[77] The figure is Figure 3 from Zaleski, C. M.; Depperman, E. C.; Kampf, J. W.; Kirk, M. L.; Pecoraro, V. L. *Inorg. Chem*. **2006**, *45*, 10022.

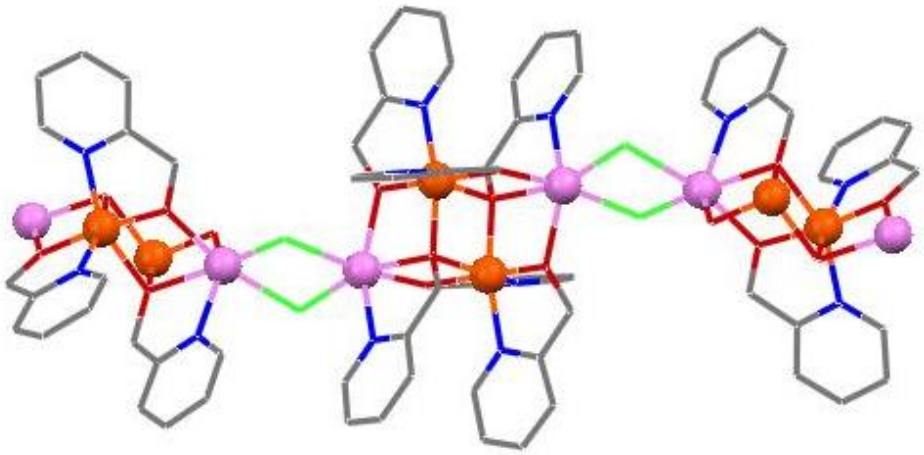

Figure 1.44. The x-ray crystal structure of a **$[Mn_4(hmp)_6Cl_2)]_x$** chain is shown. Unbound perchlorate anions and hydrogen atoms were omitted for clarity. Color scheme: orange spheres: Mn^{III}; violet spheres: Mn^{II}; red tubes: oxygen; blue tubes: nitrogen; gray tubes: carbon; neon green tubes; chlorine.[79]

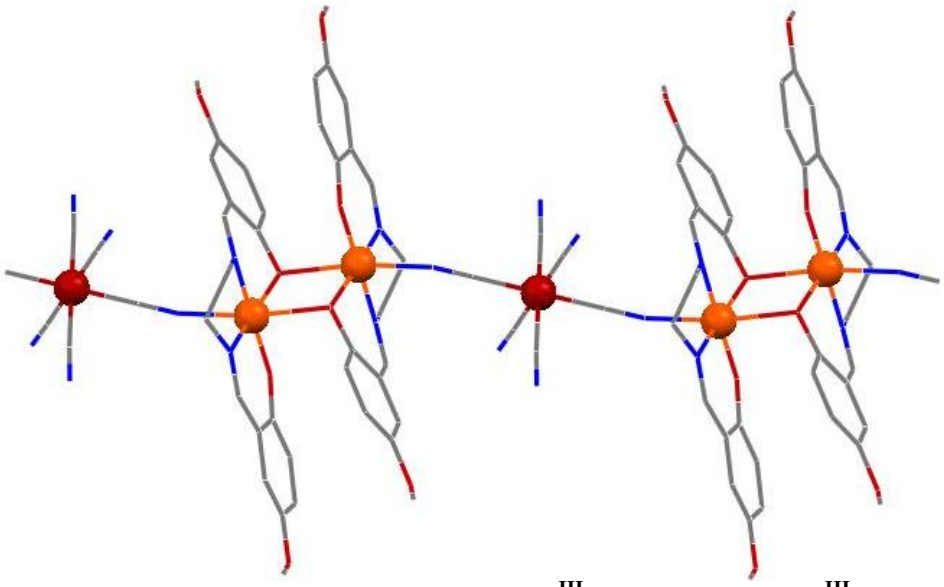

Figure 1.45. The x-ray crystal structure of **$[Mn^{III}$(5-Me-Osalen)-$Fe^{III}(CN)_6$-Mn^{III}(5-MeOsalen)$]_x$** is shown. For clarity, solvent molecules and hydrogen atoms have been removed for clarity. Color scheme: orange spheres: Mn^{III}; ruby spheres: Fe^{III}; red tubes: oxygen; blue tubes: nitrogen; gray tubes: carbon.[81]

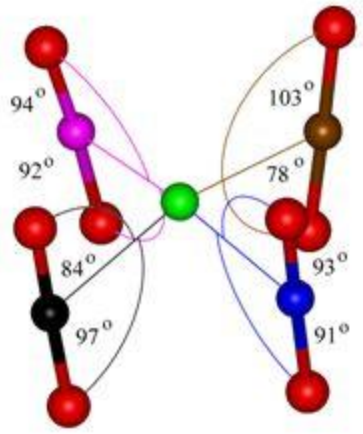

Figure 1.46. The Jahn-Teller axes of **$Mn(O_2CCH_3)_2$ [12-$MC_{Mn^{III}N(shi)}$-4]** are shown. Color scheme: red spheres: oxygen atoms; green sphere: estimated center; black, blue, brown, magenta spheres: Mn^{III} ions.[82] The figure is Figure 2 from Zaleski, C. M.; Tricard, S.; Depperman, E. C.; Wernsdorfer, W.; Mallah, T. Kirk, M. L.; Pecoraro, V. L. *Inorg. Chem*. **2011**, *50*, 11348.

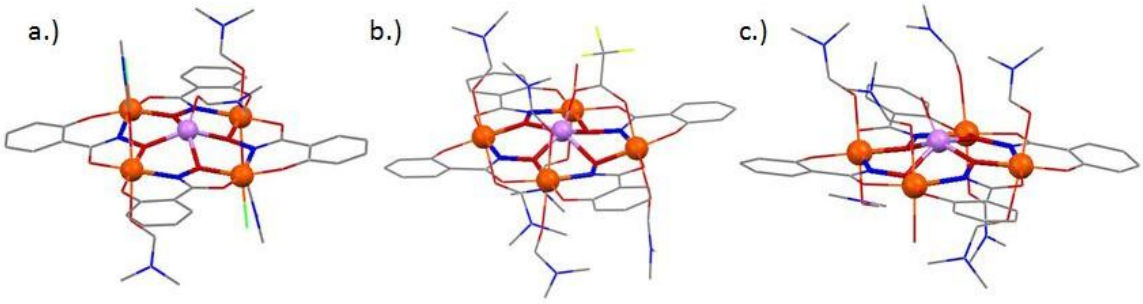

Figure 1.47. The x-ray crystal structures of a.) **$Li^+\{(LiCl_2)^-$ [12-$MC_{Mn^{III}N(shi)}$-4]}**, b.) **LiTFA [12-$MC_{Mn^{III}N(shi)}$-4]**, and c.) **Li^+ [12-$MC_{Mn^{III}N(shi)}$-4] I_3^-** are shown. For clarity, hydrogen atoms, lattice solvents, and non-coordinating ions have been removed. Color scheme: orange spheres: Mn^{III}; lavender sphere: Li^+; red tubes: oxygen; blue tubes: carbon; gray tubes: carbon; lime green tubes: fluorine.[7]

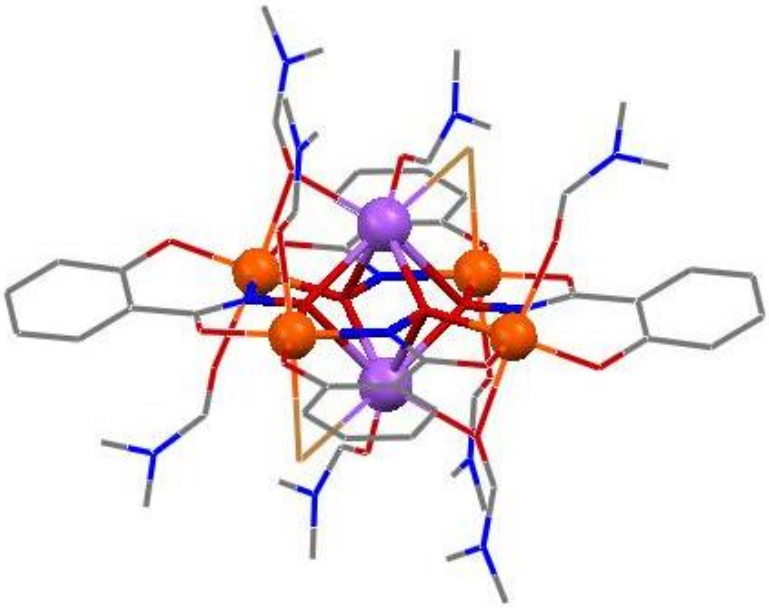

Figure 1.48. The x-ray crystal structure of **$(NaBr)_2$ [12-$MC_{Mn^{III}N(shi)}$-4]** is shown. For clarity, hydrogen atoms have been omitted. Color scheme: orange spheres: Mn^{III}; light purple spheres: Na^+; red tubes: oxygen; blue tubes: nitrogen; gray tubes: carbon; goldenrod tubes: bromine.[7]

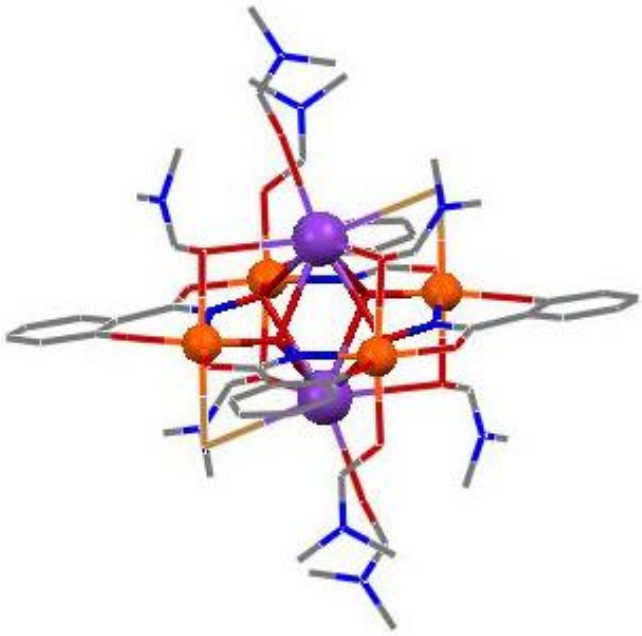

Figure 1.49. The x-ray crystal structure of **$(KBr)_2$ [12-$MC_{Mn^{III}N(shi)}$-4]** is shown. For clarity, hydrogen atoms have been omitted. Color scheme: oranges spheres: Mn^{III}; purple spheres: K^+; red tubes: oxygen; blue tubes: nitrogen; gray tubes: carbon; goldenrod tubes: bromine.[7]

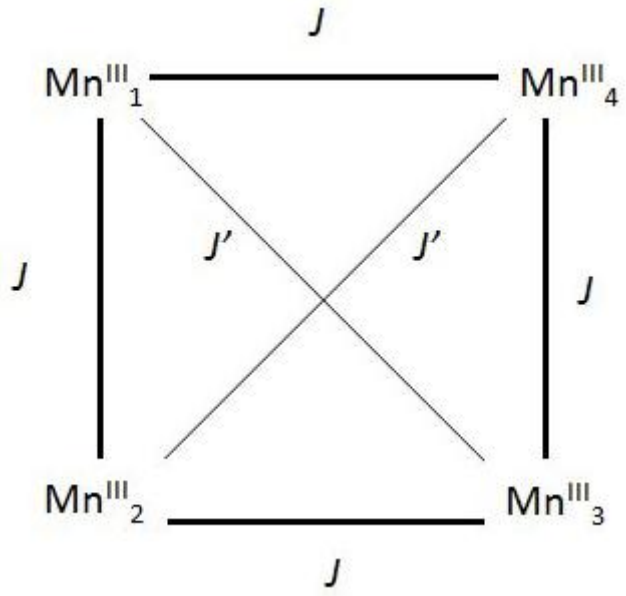

Figure 1.50. The coupling scheme of **Li [12-MC$_{Mn^{III}N(shi)}$-4]** is shown. This scheme was used to generate Equation 26.[82]

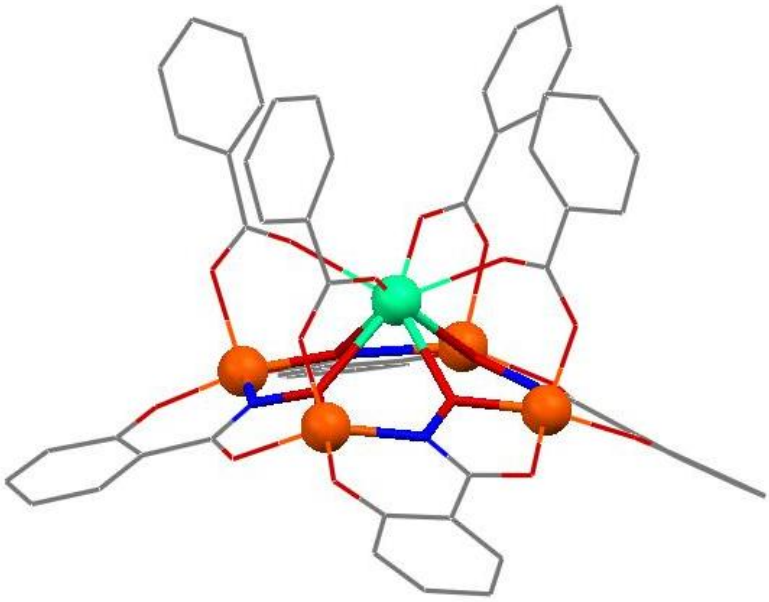

Figure 1.51 The x-ray crystal structure of **Ca(O$_2$CC$_6$H$_5$)$_4$[12-MC$_{Mn^{III}N(shi)}$-4]$^{2-}$** is shown. Uncoordinated triethylammonium cations and hydrogen atoms were omitted for clarity. Color scheme: orange spheres: Mn^{III}; teal sphere; Ca^{2+}; red tube: oxygen; blue tube: nitrogen; gray tube: carbon.[9]

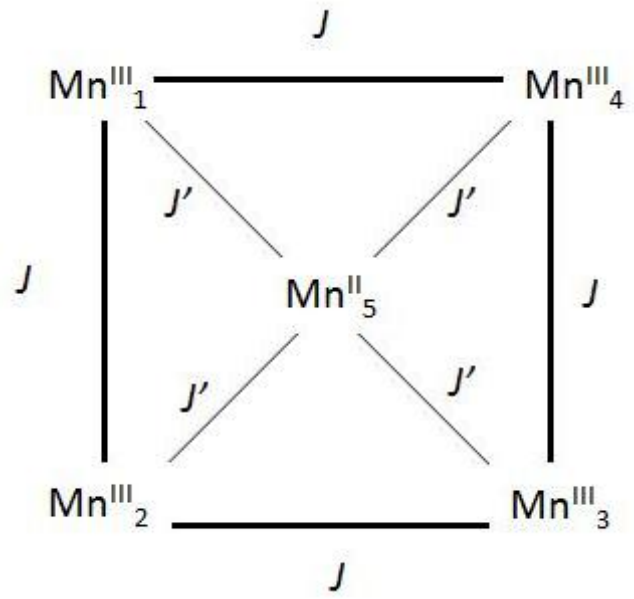

Figure 1.52. The coupling scheme for **$Mn(O_2CCH_3)_2$ [12-$MC_{Mn^{III}N(shi)}$-4]** is shown. This scheme was used to generate Equation 27.[82]

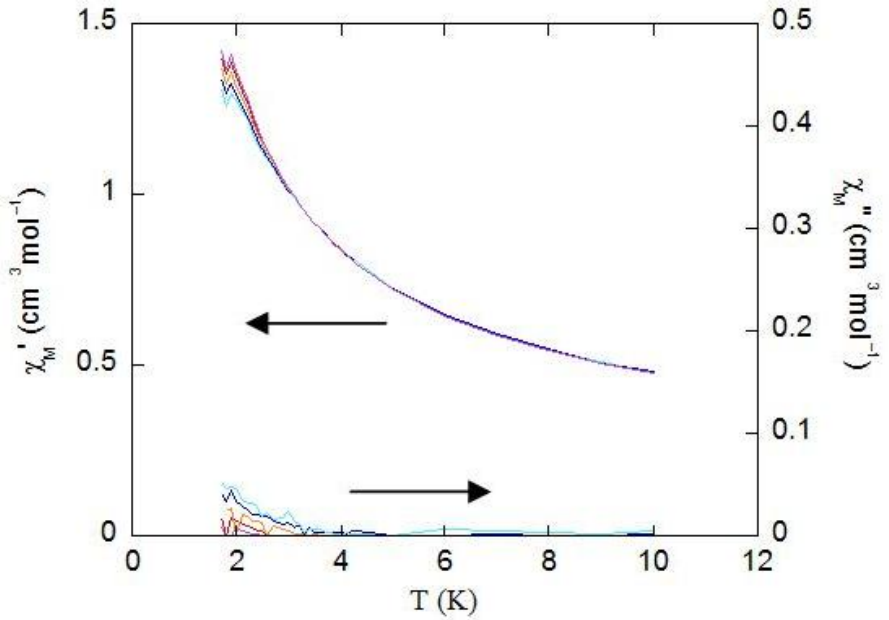

Figure 1.53. The solid state ac magnetic susceptibility of **$Mn(O_2CCH_3)_2$ [12-$MC_{Mn^{III}N(shi)}$-4]** showed weak frequency dependence.[82] The figure is Figure S3 from Zaleski, C. M.; Tricard, S.; Depperman, E. C.; Wernsdorfer, W.; Mallah, T. Kirk, M. L.; Pecoraro, V. L. *Inorg. Chem*. **2011**, *50*, 11348.

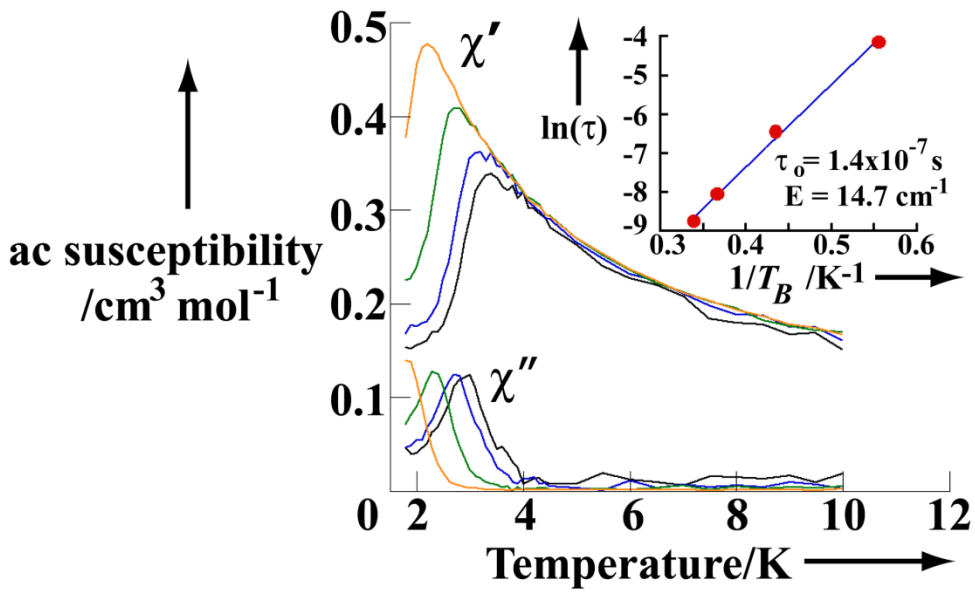

Figure 1.54. The solution state ac magnetic susceptibility of **$Mn(O_2CCH_3)_2$ [12-$MC_{Mn^{III}N(shi)}$-4]** showed weak frequency dependence. Color scheme: black: 1000 Hz, blue: 500 Hz, green: 100 Hz; orange: 10 Hz. The data were collected with zero applied dc field and a 3.5 G ac drive field. Inset: The best fit line for the Arrhenius plot is shown.[81] The figure is Figure 7 from Zaleski, C. M.; Tricard, S.; Depperman, E. C.; Wernsdorfer, W.; Mallah, T. Kirk, M. L.; Pecoraro, V. L. *Inorg. Chem.* **2011**, *50*, 11348.

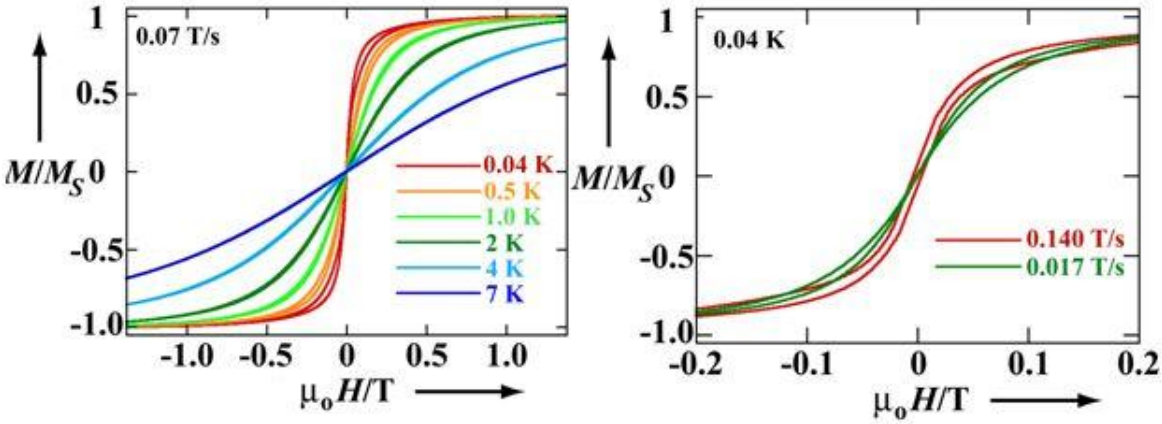

Figure 1.55. The hysteresis data for **$Mn(O_2CCH_3)_2$ [12-$MC_{Mn^{III}N(shi)}$-4]** is shown. On the left, the hysteresis data were collected at 0.07 T/s and at variable temperatures. On the right, the hysteresis data were collected at 0.04 K and measured at different field sweep rates.[82] The figure is Figure 6 from Zaleski, C. M.; Tricard, S.; Depperman, E. C.; Wernsdorfer, W.; Mallah, T. Kirk, M. L.; Pecoraro, V. L. *Inorg. Chem.* **2011**, *50*, 11348.

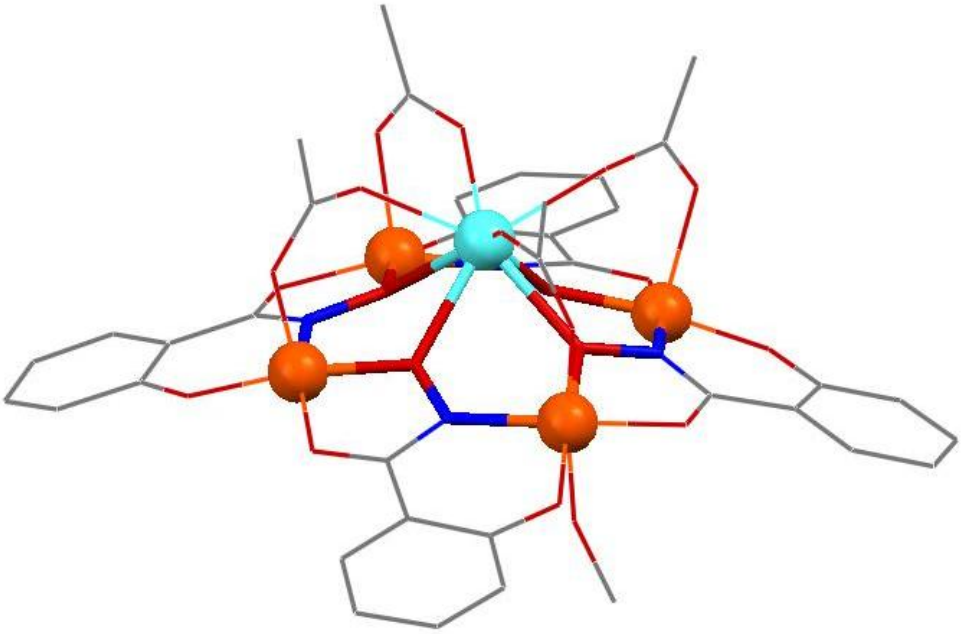

Figure 1.56. The x-ray crystal structure of **{Y(O_2CCH_3)$_4$[12-MC$_{Mn^{III}N(shi)}$-4]}$^-$** is shown. For clarity, hydrogen atoms, lattice solvents, and 0.5 Mn(CH_3OH)$_6$ were omitted. Color scheme: orange spheres: Mn^{III}; aqua sphere: Y^{III}; red tubes: oxygen; blue tubes: nitrogen; gray tubes: carbon.[71]

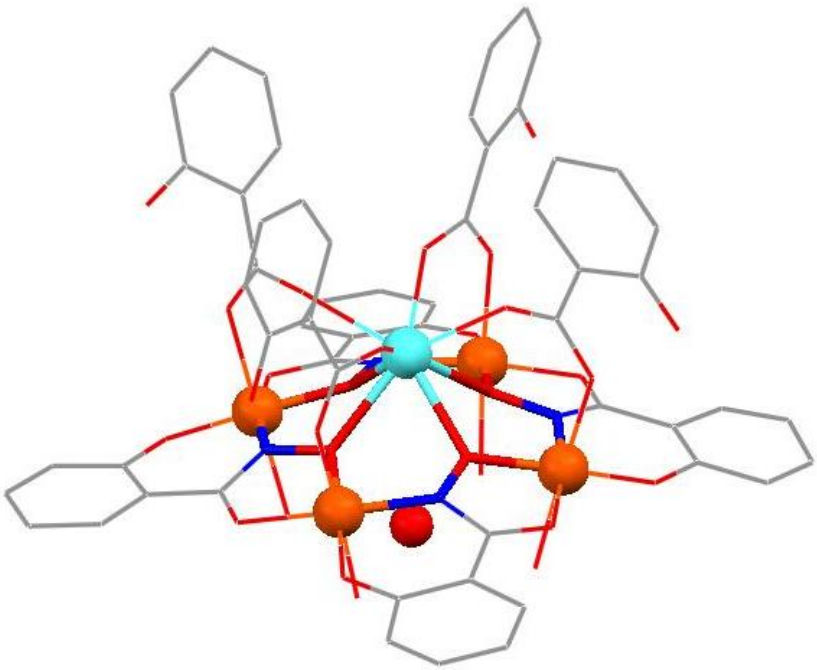

Figure 1.57. The x-ray crystal structure of **Dy($O_2CC_6H_4OH$)$_4$(H_3O)$^+$ [12-MC$_{Mn^{III}N(shi)}$-4]** is shown. For clarity, lattice solvents and hydrogen atoms were removed for clarity. Color scheme: orange spheres: Mn^{III}; aqua sphere: Dy^{III}; red tubes: oxygen; blue tubes: nitrogen; gray tubes: carbon.[71]

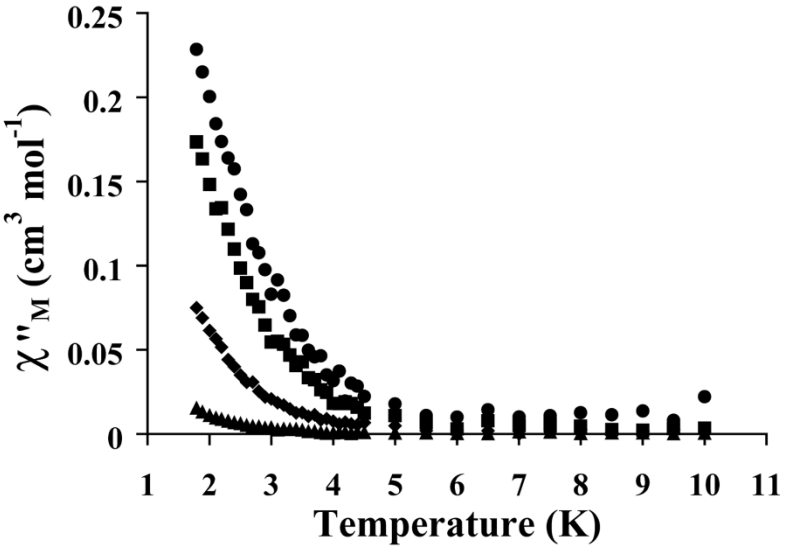

Figure 1.58. The out-of-phase ac magnetic susceptibility for **$Dy(O_2CC_6H_4OH)_4(H_3O)^+$ [12-$MC_{Mn^{III}N(shi)}$-4]** showed frequency dependence. Data were collected with zero applied dc field and a 3.5 G ac drive field. The frequencies used were 1000 Hz (●), 500 Hz (■), 100 Hz (◆) and 10 Hz (▲).[71] The figure is Figure 2.69 from Zaleski, C. M. Ph.D. Thesis, Utilizing Metallacrowns to Develop New Single-Molecule Magnets, The University of Michigan, 2005.

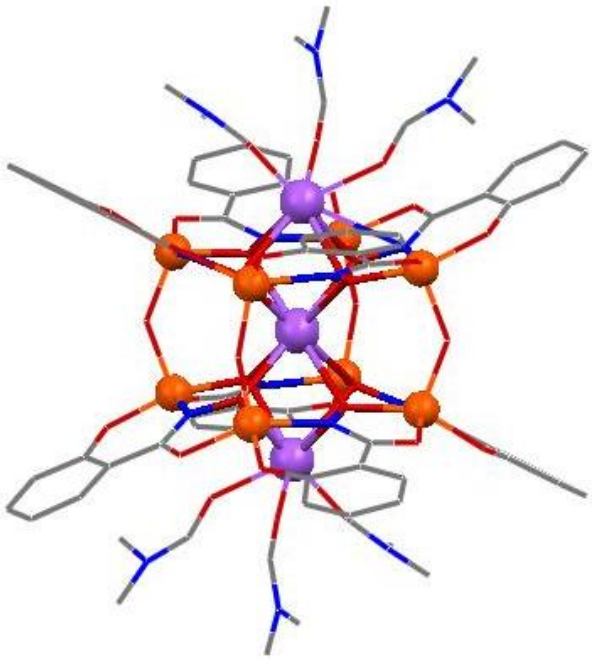

Figure 1.59. The x-ray crystal structure of **{Na_2(Na[12-$MC_{Ga^{III}N(shi)}$-4]$_2$-(μ-OH)$_4$)}** is shown. For clarity, crystal lattice solvents, non-coordinated sodium atoms and hydrogen atoms have been omitted. Color scheme: lavender spheres: Na^+; orange spheres: Ga^{III}; red tubes: oxygen; blue tubes: nitrogen; gray tubes: carbon.[87]

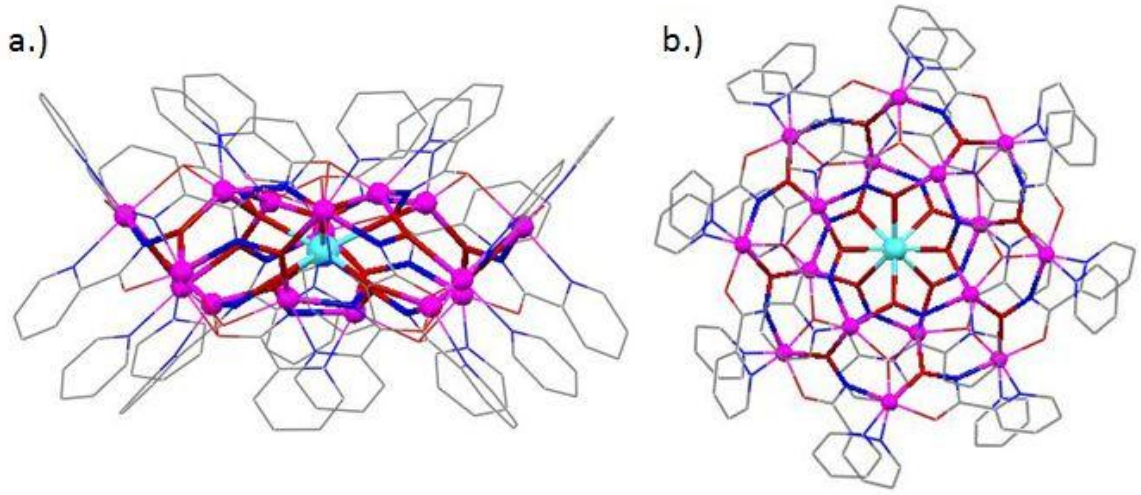

Figure 1.60. The x-ray crystal structure of **$DyZn_{16}$** is shown. The metallacrown rings of the 12-MC-4 and 24-MC-8 are highlighted. a.) The view perpendicular to the C_4 axis is shown. b.) The view along the C_4 axis is shown. Color scheme: aqua sphere: Dy^{III}; pink sphere: Zn^{II}; red tube: oxygen; blue tube: nitrogen; gray tube: carbon.[88]

References

1 Pecoraro, V. L. *Inorg. Chim. Acta*. **1989**, *155*, 171.
2 Lah, M. S.; Pecoraro, V. L. *J. Am. Chem. Soc*. **1989**, *111*, 7258.
3 Lah, M. S.; Pecoraro, V. L. *Comments Inorg. Chem*. **1990**, *11*, 59.
4 Pedersen, C. J. *J. Am. Chem. Soc.* **1967**, *89*, 2495.
5 Pedersen, C. J. *J. Am. Chem. Soc*. **1967**, *89*, 7017.
6 Gokel, G. W.; Goli, D. M.; Minganti, C.; Echegoyen, L.; *J. Am. Chem. Soc*. **1983**, *105*, 6786.
7 Gibney, B. R.; Wang, H.; Kampf, J. W.; Pecoraro, V. L. *Inorg. Chem*. **1996**, *35*, 6184.
8 Meelich, K.; Zaleski, C. M.; Pecoraro, V. L. *Phil. Trans. Soc. B*. **2008**, *363*, 1271.
9 Koumousi, E. S.; Mukherjee, S.; Beavers, C. M.; Teat, S. J.; Christou, G.; Stamatatos, T. C. *Chem. Commun*. **2011**, *47*, 11128.
10 Lah, M. S.; Kirk, M. L.; Hatfield, W.; Pecoraro, V. L. *J. Chem. Soc., Chem. Commun*. **1989**, 1606
11 Stemmler, A. J.; Kampf, J. W.; Kirk, M. L.; Atasi, B. H.; Pecoraro, V. L. *Inorg. Chem*. **1999**, *38*, 2807.
12 Long, J. R. Molecular Cluster Magnets. In *Chemistry of Nanostructured Materials*; Yang, P., Ed.; World Scientific Publishing, Hong Kong, 2003; pp 291 – 315.
13 Gatteschi, D.; Caneschi, A.; Pardi, L.; Sessoli, R. *Science*, **1994**, *265*, 1054.
14 Gatteschi, D.; Sessoli, R.; Villain, J. *Molecular Nanomagnets*; Oxford University Press, New York, 2006.
15 Coronado, E. & Gatteschi, D. *J. Mat. Chem*. **2006**, *16*, 2513.
16 Pecoraro, V. L.; Stemmler, A. J.; Gibney, B. R.; Bodwin, J. J.; Wang, H.; Kampf, J. W.; Barwinski, A. In *Progress in Inorganic Chemistry*; Karlin, K, D., Ed.; Wiley, New York, 1997; Vol. 45, pp 83 – 177.
17 Mezei, G.; Zaleski, C. M.; Pecoraro, V. L. *Chem. Rev*. **2007**, *107*, 4933.
18 Tegoni, M., Remelli, M.; *Coord. Chem. Rev*. **2012**, *256*, 289.
19 Lehn, J. –M. *Supramolecular Chemistry: Concepts and Perspectives*; VCH Verlagsgesellschaft, New York, 1995.
20 Waldmann, O.; Ako, A. M.; Güdel, H. U.; Powell, A. K. *Inorg. Chem*. **2008**, *47*, 3486.
21 Tegoni, M.; Remelli, M.; Bacco, D.; Marchio, L.; Dallavale, F. *Dalton Trans*. **2008**, 2693.
22 Tegoni, M.; Furlotti, M.; Tropiano, M.; Lim, C. S.; Pecoraro, V. L. *Inorg. Chem*. **2010**, *49*, 5190.
23 Bacco, D.; Bertolasi, V.; Dallavale, F.; Galliera, L.; Marchetti, N.; Marchio, L.; Remelli, M.; Tegoni, M. *Dalton Trans*. **2011**, *40*, 2491.
24 Kahn, O. *Molecular Magnetism*; VCH Publishers, New York, 1993.
25 Wolf, S. A.; Awschalom, D. D.; Buhrman, R. A.; Daughton, J. M.; von Molnár, S.; Roukes, M. L.; Chtchelkanova, A. Y.; Treger, D. M. *Science*, **2001**, *294*, 1488.
26 Winpenny, R. E. P. *Angew. Chem. Int. Ed*. **2008**, *47*, 7992.
27 Néel, L.; *Ann. Geophys*. **1949**, *5*, 99.

28 Aromí, G.; Aubin, S. M. J.; Bolcar, M. A.; Christou, G.; Eppley, H. J.; Folting, K.; Hendrickson, D. N.' Huffman, J. C.; Squire, R. C.; Tsai, H. –L.; Wang, S.' Wemple, M. W. *Polyhedron*, **1998**, *17*, 3005.
29 Gómez-Segura, J.; Veciana, J.; Ruiz-Molina, D. *Chem. Commun*. **2007**, 3699.
30 Gatteschi, D.; Sessoli, R. *Angew. Chem. Int. Ed*. **2003**, *42*, 268.
31 Aubin, S. M. J.; Wemple, M. W.; Adams, D. M.; Tsai, H. –L.; Christou, G.; Hendrickson, D. N. *J. Am. Chem. Soc*. **1996**, *118*, 7746.
32 Girerd, J. –J.; Journaux, Y. *Molecular Magnetism in Bioinorganic Chemistry*. In *Physical Methods in Bioinorganic Chemistry: Spectroscopy and Magnetism*; Que, L. Ed. University Science Books, Sausalito, 2000; pp 321-374.
33 Villain, J.; Hartman-Boutron, F.; Sessoli, R.; Rettori, A. *Europhys. Lett*. **1994**, *27*, 159.
34 Glauber, R. J. *J. Mat. Physics*. **1963**, *4*, 294.
35 Brooker, S.; Kitchen, J. A. *Dalton Trans*. **2009**, 7331.
36 Caneschi, A.; Gatteschi, D.; Lalioti, N.; Sangregorio, C.; Sessoli, R.; Venturi, G.; Vindigni, A.; Rettori, A.; Pini, M. G.; Novak, M. A. *Angew. Chem. Int. Ed*. **2001**, *40*, 1760.
37 Caneschi, A.; Gatteschi, D.; Lalioti, N.; Sangregorio, C.; Sessoli, R.; Venturi, G.; Vindigni, A.; Rettori, A.; Pini, M. G.; Novak, M. A. *Europhys. Lett*. **2002**, *58*, 771.
38 Coulon, C.; Miyasaka, H.; Clérac, R.; *Struct. Bond*. **2006**, *122*, 163.
39 Bogani, L.; Vindigni, A.; Sessoli, R.; Gatteschi, D. *J. Mat. Chem*. **2008**, *18*, 4750.
40 Ishikawa, N.; Sugita, M,; Ishikawa, T.; Koshihara, S. Kaizu, Y. *J. Am. Chem. Soc*. **2003**, *125*, 8694.
41 AlDamen, M. A.; Clemente-Juan, J. M.; Coronado, E.; Martí-Gastaldo, C.; Gaita-Ariño, A. *J. Am. Chem. Soc.* **2008**, *130*, 8874.
42 Rinehart, J. D. & Long, J. R. *Chem. Sci*. **2011**, *2*, 2078.
43 Ribas Gispert, J. *Coordination Chemistry*. Wiley-VCH Verlag GmbH & Co. Weinheim, 2008.pp 295-340.
44 Christou, G.; Gatteschi, D.; Hendrickson, D. N.; Sessoli, R. *Mater. Res. Bull*. **2000**, *25*, 66.
45 Martien, D. *Introduction to ac Susceptibility: AC Magnetic Measurements* [online]. Quantum Design. www.qdusa.com/sitedocs/appNotes/ppms/1078-201.pdf (accessed 5 December 2011).
46 Mydosh, J. A. *Spin Glasses: An Experimental Introduction*. Taylor and Francis, Ltd., London, 1993.
47 Palmer, G. *Electron Paramagnetic Resonance of Metalloproteins*. In *Physical Methods in Bioinorganic Chemistry: Spectroscopy and Magnetism*; Que, L. Ed. University Science Books, Sausalito, 2000; pp 121 – 185.
48 Lis, T. *Acta Cryst*. **1980** *B36*, 2042.
49 Caneschi, A.; Gatteschi, D.; Sessoli, R. *J. Am. Chem. Soc.* **1991**, *113*, 5873.
50 Sessoli, R.; Gatteschi, D.; Caneschi, A.; Novak, M. A. *Nature*, **1993**, *365*, 141.
51 Hill, S.; Perenboom, J. A. A. J.' Dalal, N. S.; Hathaway, T.; Stalcup, T.; Brooks, J. S. *Phys. Rev. Lett*. **1998**, *80*, 2453.

52 Caneschi, A.; Gatteschi, D.; Lalioti, N.; Sessoli, R.; Sorace, L.; Tangoulis, V.; Vindigni, A. *Chem. Eur. J*. **2002**, *8*, 286.
53 Koike, N.; Uekusa, H.; Ohashi, Y.; Harnoode, C.; Kitamura, F.; Ohsaka, T.; Tokuda, K. *Inorg. Chem*. **1996**, *35*, 5798.
54 Ishikawa, N. *Polyhedron*, **2007**, *26*, 2147.
55 Osa, S.; Kido, T.' Matsumoto, N.; Re, N.; Pochaba, A.; Mrozinski, J. *J. Am. Chem. Soc*. **2004**, *126*, 420.
56 Kido, T.; Ikuta, Y.; Sunatsuki, Y.; Ogawa, Y.; Matsumoto, N. *Inorg. Chem*. **2003**, *32*, 398.
57 Ako, A. M.; Hewitt, I. J.; Mereacre, V.; Clérac, R.; Wernsdorfer, W.; Anson, C. E.; Powell, A. K. *Angew. Chem*. **2006**, *118*, 5048.
58 Waldmann, O. *Inorg. Chem.* **2007**, *46*, 10035.
59 Ruiz, E.; Cauchy, T.; Cano, J.; Costa, R.; Tercero, J.; Alvarez, S. *J. Am. Chem. Soc*. **2008**, *130*, 7420.
60 Zaleski, C. M. Depperman, E. C.; Kampf, J. W.; Kirk, M. L.; Pecoraro, V. L. *Angew. Chem. Int. Ed.* **2004**, *43*, 3912.
61 Mishra, A.; Wernsdorfer, W.; Abboud, K. A.; Christou, G. *J. Am. Chem. Soc.* **2004**, *126*, 15648.
62 Mishra, A.; Wernsdorfer, W.; Parsons, S.; Christou, G.; Brechin, E. K. *Chem. Commun*. **2005**, 2086.
63 Zaleski, C. M.; Kampf, J. W.; Mallah, T.; Kirk, M. L.; Pecoraro, V. L. *Inorg. Chem*. **2007**, *46*, 1954.
64 Mereacre, V. M.; Ako, A. M.; Clérac, R.; Wernsdorfer, W.; Filoti, G.; Bartolomé, J.; Anson, C. E.; Powell, A. K. *J. Am. Chem. Soc*. **2007**, *129*, 9248.
65 Mereacre, V.; Ako, A. M.; Clérac, R.; Wernsdorfer, W.; Hewitt, I. J.; Anson, C. E.; Powell, A. K. *Chem. Eur. J*. **2008**, *14*, 3577.
66 Ako, A. M.; Mereacre, V.; Clérac, R.; Wernsdorfer, W.; Hewitt, I. J.; Anson, C. E.; Powell, A. K. *Chem. Commun*. **2009**, 544.
67 AlDamen, M. A.; Cardona-Serra, S.; Clemente-Juan, J. M.; Coronado, E.; Gaita-Ariño, A.; Martí-Gastaldo, C.; Luis, F.; Montero, O. *Inorg. Chem*. **2009**, *48*, 3467.
68 Ostendorp, G.; Werner, J.-P.; Homborg, H. *Acta Crystallogr., Sect. C* **1995**, *51*, 1125.
69 Blagg, R. J.; Muryn, C. A.; McInnes, E. J. L.; Tuna, F.; Winpenny, R. E. P. *Angew. Chem. Int. Ed*. **2011**, *50*, 6530.
70 Blagg, R. J.; Tuna, F.; McInnes, E. J. L.; Winpenny, R. E. P. *Chem. Commun*. **2011**, *47*, 10587.
71 Zaleski, C. M. Ph.D. Thesis, Utilizing Metallacrowns to Develop New Single-Molecule Magnets, The University of Michigan, 2005.
72 Cutland, A. D. Halfen, J. A.; Kampf, J. W.; Pecoraro, V. L. *J. Am. Chem. Soc*. **2001**, *123*, 6211.
73 Stemmler, A. J.; Barwinski, A.; Baldwin, M. J.; Young, V. Pecoraro, V. L. *J. Am. Chem. Soc.* **1996**, *118*, 11962.
74 Lim, C.-S. Kampf, J.; Pecoraro, V. L. *Inorg. Chem*. **2009**, *48*, 5224.
75 Lim, C.-S.; Jankolovits, J.; Kampf, J. W.; Pecoraro, V. L. *Chem. Asian. J*. **2010**, *5*, 46.

76 Jankolovits, J.; Kampf, J. W.; Maldonando, S.; Pecoraro, V. L. *Chem. Eur. J.* **2010**, *16*, 6786.
77 Cutland-Van Noord, A. D.; Kampf, J. W.; Pecoraro, V. L. *Angew. Chem. Int. Ed.* **2002**, *41*, 4667.
78 Zaleski, C. M.; Deppermann, E. C.; Kampf, J. W.; Kirk, M. L.; Pecoraro, V. L. *Inorg. Chem*. **2006**, *45*, 10022.
79 Yoo, J.; Yamaguchi, A,; Nakano, M.; Krzystek, J.; Streib, W. E.; Brunel, L.-C.; Ishimoto, H.; Christou, G.; Hendrickson, D. N. *Inorg. Chem*. **2001**, *40*, 4604.
80 Yoo, J.; Wernsdorfer, W.; Yang, E.-C.; Nakano, M.; Rheingold, A. L.; Hendrickson, D. N. *Inorg. Chem*. **2005**, *44*, 3377.
81 Ferbinteanu, M.; Miyasaka, H.; Wernsdorfer, W.; Nakata, K.; Sugiura, K.; Yamashita, M.; Coulon, C.; Clérac, R. *J. Am. Chem. Soc*. **2005**, *127*, 3090.
82 Zaleski, C. M.; Tricard, S.; Depperman, E. C.; Wernsdorfer, W.; Mallah, T.; Kirk, M. L.; Pecoraro, V. L. *Inorg. Chem*. **2011**, *50*, 11348.
83 Borras-Almenar, J. J.; Coronado, E.; Ostrovsky, S. M.; Palii, A. V.; Tsukerblat, B. S. *Chem. Phys*. **1999**, *240*, 149.
84 Borras-Almenar, J. J.; Clemente-Juan, J. M.; Coronado, E.; Tsukerblat, B. S.; *J. Comput. Chem*. **2001**, *22*, 984.
85 Bonadies, J. A.; Kirk, M. L.; Lah, M. S.; Kessissoglou, D. P.; Hatfield, W. E.; Pecoraro, V. L. *Inorg. Chem*. **1989**, *28*, 2037.
86 Barra, A. L.; Gatteschi, D.; Sessoli, R.; Abbati, G. L.; Cornia, A.; Fabretti, A. C.; Uytterhoeven, M. G.; *Angew. Chem. Int. Ed. Engl*. **1998**, *36*, 2329.
87 Lah, M.S.; Gibney, B. R.; Tierney, D. L.; Penner-Hahn, J. E.; Pecoraro, V. L. *J. Am. Chem. Soc*. **1993**, *115*, 5857.
88 Jankolovits, J.; Andolina, C. M.; Kampf, J. W.; Raymond, K. N.; Pecoraro, V. L. *Angew. Chem. Int. Ed*. **2011**, *50*, 9660.
89 Liu, C.-S.; Du, M.; Sañudo, E. C.; Echeverria, J.; Hu, M.; Zhang, Q.; Zhou, L.-M.; Fang, S.-M. *Dalton Trans*. **2011**, *40*, 9366.
90 Car, P.-E.; Perfetti, M.; Mannini, M.; Favre, A.; Caneschi, A.; Sessoli, R. *Chem. Commun*. **2011**, *47*, 3751.
91 Bi, Y.; Wang, X.-T.; Liao, W.; Wang, X.; Deng, R.; Zhang, H.; Gao, S. *Inorg. Chem*. **2009**, *48*, 11743.
92 Kajiwara, T.; Hasegawa, M.; Ishii, A.; Katagiri, K.; Baatar, M.; Takaishi, S.; Iki, N.; Yamashita, M. *Eur. J. Inorg. Chem*. **2008**, 5565.

Chapter II

Studying Large Mixed Mn/Ln Complexes as Single-Molecule Magnets

Introduction

In 2004, Zaleski and co-workers reported a $\mathbf{Ln^{III}_6Mn^{III}_4Mn^{IV}_2}$ complex, the first mixed Mn/Ln complex that behaved as a single-molecule magnet[1]. Prior to this structure, most SMMs consisted of large manganese or iron coordination complexes. The inclusion of lanthanides made it possible to dramatically increase spin and magnetoanisotropy without necessarily increasing the overall number of metals due to the lanthanide series inherently large spin and anisotropy values. Since then, much work has been dedicated to creating new mixed Mn/Ln complexes.

It has also been shown that one can substitute a lanthanide for another metal and bestow SMM properties on a complex that otherwise behaved as a simple paramagnet. The best example of this was reported by Ako and co-workers.[2,3] Ako reported a large Mn_{19} complex with a record 83/2 spin. Unfortunately, the molecule had accidently symmetric components, leading to the almost perfect cancellation of the anisotropy vectors of the Mn^{III} ions.[4] The important lesson from this work became that large clusters, while leading to unprecedentedly large spin values, can also negatively lead to small or even positive anisotropy values. In order to try to add anisotropy to the molecule, Ako reported in 2009 a complex where a single Dy^{III} cation replaced the centrally bridging Mn^{II} ion. The addition of the Dy^{III} ion did in fact add anisotropy to the $\mathbf{Mn_{18}Dy}$ molecule and led to SMM behaviors. Thus the utility of lanthanides to induce SMM behavior in molecules that otherwise would not behave as SMMs was demonstrated.

Our group has also studied the impact of lanthanides on improving the magnetic properties of Mn complexes. As will be discussed in more depth in Chapter IV, Zaleski first showed that the **$Mn^{II}(O_2C_2H_3)_2$ 12-$MC_{Mn^{III}N(shi)}$-4** prepared by Lah in 1989[5] behaved as a SMM in both the solid and the solution phases.[6] In his thesis, Zaleski also demonstrated that Dy^{III} could be incorporated into a 12-$MC_{Mn^{III}N(shi)}$-4 and increase the overall magnetization and susceptibility values when compared to the **Mn^{II} 12-$MC_{Mn^{III}N(shi)}$-4**.[7] Our group has also prepared the third example of a Mn/Ln complex, a **$Ln^{III}_4Mn^{III}_6$** complex that also showed slow magnetic relaxation.[8] This complex was the daughter complex of the **$Ln^{III}_6Mn^{III}_4Mn^{IV}_2$**, which also showed slow magnetic relaxation. With this background, it seemed reasonable to pursue self-assembled mixed Mn/Ln complexes of varying metal ratios with the goal of determining the impact of metal ratio and lanthanide choice. This chapter details the synthesis, structure, and magnetic characteristics of a series of **$Ln^{III}_6Mn^{III}_2Mn^{IV}_2(shi)_6(Hshi)_4(H_2shi)_2(Hsal)_4$** complexes ($Ln^{III}$ = Gd^{III}, Tb^{III}, Dy^{III}), where shi is triply deprotonated salicylhydroximate and sal is doubly deprotonated salicylate, herein referenced as **Ln_6Mn_4**, and a series of **$Ln^{III}_4Mn^{III}_4(OH)_2(O_2C_2H_3)_2(shi)_4(H_2shi)_4(Hsal)_4$** complexes ($Ln^{III}$ = Dy^{III}, Ho^{III}, Er^{III}), herein referred to as **Ln_4Mn_4**. It was found in both series that the Dy^{III} analog showed slow magnetic relaxation. Structural similarities were found between the **$Ln^{III}_6Mn^{III}_4Mn^{IV}_2$** and the **$Ln_6Mn_4$** complexes as well as between the **$Ln^{III}_4Mn^{III}_6$** and **Ln_4Mn_4** complexes. A detailed discussion comparing the structural similarities as well as magnetic properties follows.

Acknowledgement: **Dy_4Mn_4** was first prepared by Katelyn Moore at Shippensburg University working with Prof. Curt Zaleski. Modifying her procedure yielded the **Ln_4Mn_4** complexes described below.

Experimental

Synthetic Methods:

Manganese(II) acetate tetrahydrate ($Mn(OAc)_2 \cdot 4H_2O$), lanthanide chloride hexahydrate salts ($GdCl_3 \cdot 6H_2O$, $TbCl_3 \cdot 6H_2O$, $DyCl_3 \cdot 6H_2O$, $ErCl_3 \cdot 6H_2O$), salicylic acid, and *N*-,*N*-dimethylformamide (DMF) were purchased from Sigma-Aldrich and used as received. Salicylhydroxamic acid and the lanthanide nitrate pentahydrate salts ($Dy(NO_3)_3 \cdot 5H_2O$, $Ho(NO_3)_3 \cdot 5H_2O$)were purchased and used as received from Alfa Aesar.

$[Gd^{III}_6Mn^{III}_2Mn^{IV}_2(shi)_6(Hshi)_4(H_2shi)_2(Hsal)_4(C_3H_7NO)_{10}] \cdot 3H_2O$ (**Gd_6Mn_4**) In a beaker, 2 mmol $Mn(OAc)_2 \cdot 4H_2O$ were dissolved in 12.5 mL DMF. In another beaker, 1 mmol $GdCl_3 \cdot 6H_2O$, 1 mmol H_2sal, and 2 mmol H_3shi were dissolved in 13.0 mL DMF. When the Mn solution was red, it was added to the $GdCl_3$, H_2sal, H_3shi solution and stirred overnight. The next day, the solution was filtered and the solute was allowed to slowly evaporate. Small, 2D plates were isolated in approximately 3 weeks. Yield: 2.1% Elemental analysis for $Gd_6Mn_4C_{142}H_{152}N_{22}O_{61}$ [FW = 4306.132 g/mol] found % (calculated): C = 39.63, 39.80 (39.608); H = 3.46, 3.33 (3.558); N = 7.12, 6.96 (7.156) Unit cell dimensions: a = 16.8643(5) Å, b = 17.3718(5) Å, c = 17.6074(5) Å, α = 63.622(2)°, β = 69.783(2)°, γ = 73.783(2)° V = 4287.76 $Å^3$, space group: $P\bar{1}$.

$[Tb^{III}_6Mn^{III}_2Mn^{IV}_2(shi)_6(Hshi)_4(H_2shi)_2(Hsal)_4(C_3H_7NO)_{10}] \cdot 5C_3H_7NO$ (**Tb_6Mn_4**) In a beaker, 2 mmol $Mn(OAc)_2 \cdot 4H_2O$ were dissolved in 12.5 mL DMF. In another beaker, 1 mmol $TbCl_3 \cdot 6H_2O$, 1 mmol H_2sal, and 2 mmol H_3shi were dissolved in 13.0 mL DMF. When the Mn solution was red, it was added to the $TbCl_3$, H_2sal, H_3shi solution and stirred overnight. The next day, the solution was filtered and the solute was allowed to slowly evaporate. Small, 2D plates were isolated in approximately 3 weeks. Yield: 5.0% Elemental analysis for $Tb_6Mn_4C_{142}H_{146}N_{22}O_{58}$ [FW = 4262.14 g/mol] found % (calculated): C = 39.97; 39.85 (40.017); H = 3.45; 3.45 (3.453); N = 7.40; 7.35 (7.230) Unit cell dimensions: a = 16.8232 Å, b = 17.4496 Å, c = 17.5657 Å, α = 64.011°, β = 69.834°, γ = 73.476° V = 4296.29 $Å^3$, space group: $P\bar{1}$.

$[Dy^{III}_6Mn^{III}_2Mn^{IV}_2(shi)_6(Hshi)4(H_2shi)_2(Hsal)_4(C_3H_7NO)_6(H_2O)_4]\cdot 2C_3H_7NO$ (**Dy_6Mn_4**) In a beaker, 2 mmol $Mn(OAc)_2\cdot 4H_2O$ were dissolved in 12.5 mL DMF. In another beaker, 1 mmol $DyCl_3\cdot 6H_2O$, 1 mmol H_2sal, and 2 mmol H_3shi were dissolved in 13.0 mL DMF. When the Mn solution was red, it was added to the $DyCl_3$, H_2sal, H_3shi solution and stirred overnight. The next day, the solution was filtered and the solute was allowed to slowly evaporate. Small, 2D plates were isolated in approximately 3 weeks. Yield: 7.3% Elemental analysis for $Dy_6Mn_4C_{136}H_{140}N_{20}O_{60}$ [FW = 4209.46 g/mol] found % (calculated): C = 38.81, 38.87 (38.805); H = 3.30, 3.31 (3.352); N = 6.65, 6.69 (6.655) Unit cell dimensions: a = 17.155 Å, b = 17.671 Å, c = 17.788 Å, α = 63.941°, β = 77.170°, γ = 71.449° V = 4570.3 $Å^3$, space group: $P\bar{1}$.

$[Dy^{III}_4Mn^{III}_4(OH)_2(O_2C_2H_3)_2(shi)_4(H_2shi)_4(Hsal)_4(C_3H_7NO)_4]\cdot 3C_3H_7NO$ (**Dy_4Mn_4**) In a beaker, 2 mmol $Mn(OAc)_2\cdot 4H_2O$ were dissolved in 12.0 mL DMF. In another beaker, 1 mmol $Dy(NO_3)_3\cdot 5H_2O$, 1 mmol H_2sal, and 2 mmol H_3shi were dissolved in 12.5 mL DMF. When the Mn solution was orange, it was added to the $Dy(NO_3)_3$, H_2sal, H_3shi solution and stirred overnight. The next day, the solution was filtered and the solute allowed to slowly evaporate. After four months, green needle crystals were obtained. Yield: Elemental analysis for $Dy_4Mn_4C_{103}H_{103}N_{13}O_{47}$ [FW = 3144.76 g/mol] found % (calculated) C = 39.65 (39.339); H = 3.58 (3.301); N = 5.35 (5.790). Unit cell dimensions: a = 13.8909(14) Å, b = 17.0470(17) Å, c = 17.338(2) Å, α = 61.0230 (10)°, β = 71.249(2)°, γ = 89.926(2)°, V = 3341.4(7) $Å^3$, space group $P\bar{1}$.

$[Ho^{III}_4Mn^{III}_4(OH)_2(O_2C_2H_3)_2(shi)_4(H_2shi)_4(Hsal)_4(C_3H_7NO)_4]\cdot 3C_3H_7NO$ (**Ho_4Mn_4**) In a beaker, 2 mmol $Mn(OAc)_2\cdot 4H_2O$ were dissolved in 12.0 mL DMF. In another beaker, 1 mmol $Ho(NO_3)_3\cdot 5H_2O$, 1 mmol H_2sal, and 2 mmol H_3shi were dissolved in 12.5 mL DMF. When the Mn solution was orange, it was added to the $Ho(NO_3)_3$, H_2sal, H_3shi solution and stirred overnight. The next day, the solution was filtered and the solute allowed to evaporate slowly. After four months, green needle crystals were obtained. Yield: 23.3% Elemental analysis for $Ho_4Mn_4C_{106}H_{114}N_{14}O_{50}$ [FW = 3263.61 g/mol] found % (calculated) C = 38.66, 38.70 (39.011); H = 3.40, 3.39 (3.521); N = 6.38, 6.39

(6.008). Unit cell dimensions: a = 13.722 Å, b = 17.554 Å, c = 18.381 Å, α = 106.82°, β = 107.12°, γ = 109.25°, V = 3610.1 $Å^3$, space group $P\bar{1}$.

$[Er^{III}_4Mn^{III}_4(OH)_2(O_2C_2H_3)_2(shi)_4(H_2shi)_4(Hsal)_4(C_3H_7NO)_4]\cdot 3C_3H_7NO$ (**Er_4Mn_4**) In a beaker, dissolve 2 mmol $Mn(OAc)_2\cdot 4H_2O$ in 12.0 mL DMF. In another beaker, dissolve 1 mmol $ErCl_3\cdot 5H_2O$, 1 mmol H_2sal, and 2 mmol H_3shi in 12.5 mL DMF. When the Mn solution was orange, it was added to the $ErCl_3$, H_2sal, H_3shi solution and stirred overnight. The next day, the solution was filtered and the solute allowed to slowly evaporate. After four months, green needle crystals were obtained. Yield: 7.4 % Elemental analysis for $Er_4Mn_4C_{100}H_{106}N_{12}O_{51}$ [FW = 3180.78 g/mol] found % (calculated) C = 37.32, 37.25 (37.761); H = 3.12, 3.10 (3.359); N = 5.58, 5.58 (5.284). Unit cell dimensions: a = 13.7317(3) Å, b = 17.5541(3) Å, c = 18.3104(13) Å, α = 106.895(7)°, β = 106.938(7)°, γ = 109.205(8)°, V = 3604.0(3) $Å^3$, space group $P\bar{1}$.

Physical Methods

X-ray Crystallography. X-ray single crystal diffraction data was collected by Dr. Jeff W. Kampf at the University of Michigan. X-ray single crystal diffraction data of Gd_6Mn_4 and Tb_6Mn_4 were also collected through the SCrALS (Service Crystallography at Advanced Light Source) program at the Small-Crystal Crystallography Beamline 11.3.1 at the Advanced Light Source (ALS), Lawrence Berkeley National Laboratory. Refinements were performed by Dr. Jeff Kampf and myself. For crystal data collected at the University of Michigan, crystals were mounted onto a standard Bruker APEX CCD-based X-ray diffractometer. The diffractometer was equipped with a LT-2 low temperature device and either normal focus Mo-target X-ray tube (λ = 0.71073 Å) and operated at 2000 W power (50 kV, 40 mA) or a sealed tube Cu X-ray tube (λ = 1.5406 Å) operated at the indicated power. For crystal data collected at SCrALS, crystals were mounted on a D8 goniostat equipped with a Bruker APEXII CCD detector at Beamline 11.3.1 at ALS. Synchrotron radiation tuned to λ = 0.7749 Å was used. Data frames were collected using the program APEX2 and data processed using the SAINT routine within

APEX2. Data were corrected for absorption and beam corrections based on the multi-scan technique as implemented in SADABS.

$[Gd^{III}_6Mn^{III}_2Mn^{IV}_2(shi)_6(Hshi)_4(H_2shi)_2(Hsal)_4(C_3H_7NO)_{10}]\cdot 3H_2O$ (**Gd_6Mn_4**) A red-brown plate crystal of dimensions 0.08 mm x 0.05 mm x 0.01 mm was mounted on a D8 goniostat equipped with a Bruker APEXII CCD detector at Beamline 11.3.1 at the Advanced Light Source (Lawrence Berkeley National Laboratory) using synchrotron radiation tuned to $\lambda = 0.7749$ Å. A series of 2 s frames measured at 0.2° increments of ω were collected to calculate a unit cell. For data collection, frames were measured for a duration of 2 s for low angle data and 4 s for high angle data at 0.3° intervals of ω with a maximum 2θ value of ~60°. The data frames were collected using the program APEX2 and processed using the program SAINT routine within APEX2. The data were corrected for absorption and beam corrections based on the multi-scan technique as implemented in SADABS. Of the 67398 reflections collected, 17674 reflections were unique, 1119 parameters and 0 restraints were used Structure solution and refinement were performed with SHELXS-97 and SHELXL-97, respectively. The triclinic space group $P\bar{1}$ and a Z = 1 were assigned. Non-hydrogen atom were refined anisotropically; hydrogen atoms were placed in idealized positions. Full matrix least-squared refinement based on F^2 converged at $R_1 = 0.0488$ and $wR_2 = 0.1235$ for $[I > 2\sigma(I)]$, and $R_1 = 0.0945$ and $wR_2 = 0.1501$ for all data. Experimental parameters and crystallographic data are available in Table 2.1. Important bond distances are provided in Table 2.3

$[Tb^{III}_6Mn^{III}_2Mn^{IV}_2(shi)_6(Hshi)_4(H_2shi)_2(Hsal)_4(C_3H_7NO)_{10}]\cdot 5C_3H_7NO$ (**Tb_6Mn_4**) A dark brown plate crystal of dimensions 0.06 mm x 0.05 mm x 0.005 mm was mounted on a D8 goniostat equipped with a Bruker APEXII CCD detector at Beamline 11.3.1 at the Advanced Light Source (Lawrence Berkeley National Laboratory) using synchrotron radiation tuned to $\lambda = 0.7749$ Å. A series of 7 s frames measured at 0.2° increments of ω were collected to calculate a unit cell. For data collection frames were measured for a duration of 7 s at 0.3° intervals of ω with a maximum 2θ value of ~60°. The data frames were collected using the program APEX2 and processed using the program SAINT routine within APEX2. The data were corrected for absorption and beam corrections

based on the multi-scan technique as implemented in SADABS. Of the 23294 reflections collected, 12405 reflections were unique, 1162 parameters and 6 restraints were used Structure solution and refinement were performed with SHELXS-97 and SHELXL-97, respectively. The triclinic space group $P\bar{1}$ and a Z = 1 were assigned. Non-hydrogen atom were refined anisotropically; hydrogen atoms were placed in idealized positions. Full matrix least-squared refinement based on F^2 converged at $R_1 = 0.1181$ and $wR_2 = 0.2514$ for [$I > 2\sigma(I)$], and $R_1 = 0.2681$ and $wR_2 = 0.3261$ for all data. Experimental parameters and crystallographic data are available in Table 2.1. Important bond distances are provided in Table 2.4

$[Dy^{III}_6Mn^{III}_2Mn^{IV}_2(shi)_6(Hshi)_4(H_2shi)_2(Hsal)_4(C_3H_7NO)_6]\cdot 2C_3H_7NO\cdot 4H_2O$ (**Dy_6Mn_4**) The unit cell data were collected and used to identify **Dy_6Mn_4**. Crystallographic data are available in Table 2.1.

$[Dy^{III}_4Mn^{III}_4(OH)_2(O_2C_2H_3)_2(shi)_4(H_2shi)_4(Hsal)_4(C_3H_7NO)_4]\cdot 3C_3H_7NO$ (**Dy_4Mn_4**) A green needle crystal of dimensions 0.32 mm x 0.04 mm x 0.03 mm was mounted on a standard Bruker SMART APEX CCD-based X-ray diffractometer equipped with a low temperature device and fine focus Mo-target X-ray tube (λ = 0.71073 Å) operated at 1500 W power (50 kV, 30 mA). Data were collected at 85(2) K. The detector was mounted 5.055 cm from the crystal. A total of 4095 frames were collected with a scan width of 0.5° in ω and 0.45° in phi with an exposure time of 60 s/frame. The integration of the data yielded a total of 93898 reflections to a maximum 2θ value of 51.66° of which 12807 were independent and 8774 were greater than $2\sigma(I)$. The final cell constants were based on the xyz centroids of 9983 reflections above $10\sigma(I)$. Analysis of the data showed negligible decay during data collection; the data were processed with SADABS and corrected for absorption. The structure was solved and refined with the Bruker SHELXTL (version 6.12) software package, using the space group $P\bar{1}$ with Z = 1. The complex lies on a crystallographic inversion center. All non-hydrogen atoms were refined anisotropically with the hydrogen atoms placed in idealized positions. Full matrix least-squares refinement based on F^2 converged at $R_1 = 0.0435$ and $wR_2 = 0.1102$ [based on $I > 2\sigma(I)$], $R_1 = 0.0829$ and $wR_2 = 0.1330$ for all data. Experimental parameters and

crystallographic data are provided in Table 2.2. Important bond distances are given in Table 2.5.

$[Ho^{III}_4Mn^{III}_4(OH)_2(O_2C_2H_3)_2(shi)_4(H_2shi)_4(Hsal)_4(C_3H_7NO)_4]\cdot 3C_3H_7NO$ (**Ho_4Mn_4**) The unit cell data were collected and used to identify Ho_4Mn_4. Crystallographic data are available in Table 2.2.

$[Er^{III}_4Mn^{III}_4(OH)_2(O_2C_2H_3)_2(shi)_4(H_2shi)_4(Hsal)_4(C_3H_7NO)_4]\cdot 3C_3H_7NO$ (**Er_4Mn_4**) A green plate crystal with dimensions of 0.16 mm x 0.08 mm x 0.06 mm was mounted on a standard Bruker SMART APEX CCD-based X-ray diffractometer equipped with a low temperature device and fine focus Cu-target X-ray tube (λ = 1.54178 Å) operated at 2000 W power (40 kV, 30 mA). Data were collected at 85(2) K. The detector was mounted 5.055 cm from the crystal. A total of 3109 images were collected with a scan width of 1.0° in ω with an exposure time of 10 s/frame for low angle data and 30 s/frame for high angle data. The integration of the data yielded a total of 77566 reflections to a maximum 2θ value of 68.24° of which 12913 were independent and 11343 were greater than $2\sigma(I)$. Analysis of the data showed negligible decay during data collection; the data were processed with SADABS and corrected for absorption. The structure was solved and refined with the Bruker SHELXTL (version 6.12) software package, using the space group $P\bar{1}$ with Z = 1. The complex lies on a crystallographic inversion center. All non-hydrogen atoms were refined anisotropically with the hydrogen atoms placed in idealized positions. Full matrix least-squares refinement based on F^2 converged at $R_1 = 0.0668$ and $wR_2 = 0.2166$ [based on $I > 2\sigma(I)$], $R_1 = 0.0717$ and $wR_2 = 0.2226$ for all data. Experimental parameters and crystallographic data are provided in Table 2.2. Important bond distances are given in Table 2.6.

Table 2.1 The crystallographic information for **Gd_6Mn_4**, **Tb_6Mn_4**, and **Dy_6Mn_4** is given.

	Gd_6Mn_4	**Tb_6Mn_4**	**Dy_6Mn_4**
Chemical Formula	$Gd_6Mn_4C_{142}H_{146}N_{22}O_{58}$	$Tb_6Mn_4C_{142}H_{146}N_{22}O_{58}$	$Dy_6Mn_4C_{136}H_{140}N_{20}O_{60}$
Formula Weight (g/mol)	4252.09	4262.14	4209.46
Space Group	$P\bar{1}$	$P\bar{1}$	$P\bar{1}$
a (Å)	16.8643(5)	16.823(11)	17.155
b (Å)	17.3718(5)	17.45(3)	17.671
c (Å)	17.6074(5)	17.566(6)	17.788
α (°)	63.622(2)	64.01(7)	63.941
β (°)	69.783(2)	69.83(4)	77.170
γ (°)	73.783(2)	73.48(8)	71.449
V ($Å^3$)	4287.8(2)	4296(8)	4570.3
Temperature (K)	150 K	150 K	85 K
λ (Å)	0.7749	0.7749	1.54178
ρ_{calc}	1.647	1.389	
μ (mm^{-1})	3.33	3.476	
Z	1	1	1
R_1 [I>2σ(I)]	0.0488	0.1131	
R_1 (all)	0.0945	0.2681	
wR_2 [I>2σ(I)]	0.1235	0.2514	
wR_2 (all)	0.1501	0.3261	

Table 2.2. The crystallographic information for **Dy_4Mn_4**, **Ho_4Mn_4**, and **Er_4Mn_4** is given.

	Dy_4Mn_4	**Ho_4Mn_4**	**Er_4Mn_4**
Chemical Formula	$Dy_4Mn_4C_{109}H_{117}N_{15}O_{49}$	$Ho_4Mn_4C_{109}H_{117}N_{15}O_{49}$	$Er_4Mn_4C_{109}H_{117}N_{15}O_{49}$
Formula Weight (g/mol)	3290.95	3300.67	3309.99
Space Group	$P\bar{1}$	$P\bar{1}$	$P\bar{1}$
a (Å)	13.8909(14)	13.948	13.7317(3)
b (Å)	17.0470(17)	17.124	17.5541(3)
c (Å)	17.338(2)	17.443	18.3104(13)
α (°)	61.0230(10)	118.67	106.895(7)
β (°)	71.249(2)	109.14	106.938(7)
γ (°)	89.926(7)	90.09	109.205(8)
V ($Å^3$)	3341.4(7)	3389.5	3604.0(3)
Temperature (K)	85 (2)	85(2)	85(2)
λ (Å)	0.71073	0.71073	1.54178
ρ_{calc}	1.594		1.403
μ (mm^{-1})	2.658		7.469
Z	1	1	1

R_1 [I>2σ(I)]	0.0435	0.0668
R_1 (all)	0.0829	0.07170
wR_2 [I>2σ(I)]	0.1102	.2166
wR_2 (all)	0.1330	0.2226

Table 2.3. Selected bond distances (Å) of **Gd_6Mn_4** are given.

Bond	Length (Å)	Bond	Length (Å)
Gd(1) – O(5)	2.349(5)	Gd(3) – O(6)	2.348(5)
Gd(1) – O(27)	2.353(6)	Gd(3) – O(8)	2.353(5)
Gd(1) – O(23a)	2.362(5)	Gd(3) – O(19)	2.384(5)
Gd(1) – O(11)	2.385(5)	Gd(3) – O(13)	2.397(5)
Gd(1) – O(6)	2.389(5)	Gd(3) – O(16)	2.422(5)
Gd(1) – O(22a)	2.422(5)	Gd(3) – O(11)	2.424(5)
Gd(1) – O(12a)	2.425(5)	Gd(3) – O(28)	2.429(5)
Gd(1) – O(31)	2.439(6)	Gd(3) – O(2)	2.543(4)
		Gd(3) – O(18)	2.550(5)
Gd(2) – O(23)	2.330(5)		
Gd(2) – O(3)	2.349(5)	Mn(1) – O(4)	1.832(6)
Gd(2) – O(19)	2.355(5)	Mn(1) – O(1)	1.877(5)
Gd(2) – O(25)	2.355(6)	Mn(1) – O(16)	1.903(5)
Gd(2) – O(2)	2.382(5)	Mn(1) – N(1)	1.923(6)
Gd(2) – O(12)	2.394(5)	Mn(1) – O(15)	1.951(6)
Gd(2) – O(30)	2.399(7)	Mn(1) – N(2)	1.988(6)
Gd(2) – O(13)	2.422(4)		
		Mn(2) – O(14)	1.868(7)
		Mn(2) – O(17)	1.881(7)
		Mn(2) – O(18)	1.948(6)
		Mn(2) – N(4)	1.970(7)
		Mn(2) – O(9)	2.202(5)
		Mn(2) – O(20)	2.212(6)

Table 2.4. Selected bond distances (Å) of **Tb_6Mn_4** are given.

Bond	Length (Å)	Bond	Length (Å)
Tb(1) – O(6)	2.34(2)	Tb(3) – O(19)	2.16(3)
Tb(1) – O(13)	2.24(3)	Tb(3) – O(23)	2.28(2)
Tb(1) – O(8)	2.39(2)	Tb(3) – O(25)	2.32(3)
Tb(1) – O(16)	2.43(2)	Tb(3) – O(3)	2.33(2)
Tb(1) – O(19)	2.41(2)	Tb(3) – O(12)	2.344(18)
Tb(1) – O(28)	2.42(2)	Tb(3) – O(2)	2.37(2)
Tb(1) – O(11)	2.451(18)	Tb(3) – O(13)	2.410(16)
Tb(1) – O(2)	2.531(18)	Tb(3) – O(30)	2.48(3)
Tb(2) – O(27)	2.09(5)	Mn(1) – O(4)	1.85(2)

Tb(2) – O(11)	2.33(2)	Mn(1) – N(1)	1.84(3)
Tb(2) – O(23a)	2.35(2)	Mn(1) – O(1)	1.89(2)
Tb(2) – O(5)	2.340(19)	Mn(1) – O(15)	1.92(3)
Tb(2) – O(6)	2.373(19)	Mn(1) – O(16)	1.92(2)
Tb(2) – O(12a)	2.39(2)	Mn(1) – N(2)	1.99(3)
Tb(2) – O(22a)	2.419(17)		
Tb(2) – O(31)	2.50(3)	Mn(2) – O(14)	1.74(2)
		Mn(2) – O(17)	1.85(3)
		Mn(2) – O(18)	1.97(2)
		Mn(2) – N(4)	1.96(3)
		Mn(2) – O(20)	2.16(3)
		Mn(2) – O(9)	2.21(2)

Table 2.5. Selected bond distances (Å) of **Dy_4Mn_4** are given

Bond	Length (Å)	Bond	Length (Å)
Dy(1) – O(18)	2.279(4)	Dy(2) – O(2a)	2.251(5)
Dy(1) – O(3a)	2.313(4)	Dy(2) – O(15)	2.322(5)
Dy(1) – O(19)	2.316(4)	Dy(2) – O(8)	2.347(5)
Dy(1) – O(14)	2.344(4)	Dy(2) – O(12)	2.359(4)
Dy(1) – O(6a)	2.369(4)	Dy(2) – O(21)	2.376(4)
Dy(1) – O(9)	2.389(3)	Dy(2) – O(3a)	2.386(3)
Dy(1) – O(23)	2.421(3)	Dy(2) – O(9)	2.387(4)
Dy(1) – O(23a)	2.465(4)	Dy(2) – O(11)	2.415(4)
Mn(1) – O(1)	1.849(5)	Mn(2) – O(4)	1.848(3)
Mn(1) – O(5)	1.928(4)	Mn(2) – O(23a)	1.924(3)
Mn(1) – O(6)	1.935(4)	Mn(2) – N(2)	1.971(5)
Mn(1) – N(1)	1.939(5)	Mn(2) – O(11)	1.988(4)
Mn(1) – O(22)	2.277(6)	Mn(2) – O(20a)	2.318(4)
Mn(1) – O(17)	2.302(5)	Mn(2) – O(9)	2.335(4)

Table 2.6. Selected bond distances (Å) of **Er_4Mn_4** are given.

Bond	Length (Å)	Bond	Length (Å)
Er(1) – O(14)	2.261(4)	Er(2) – O(18)	2.242(5)
Er(1) – O(24)	2.303(4)	Er(2) – O(3)	2.305(5)
Er(1) – O(19)	2.306(5)	Er(2) – O(11)	2.327(5)
Er(1) – O(2)	2.343(4)	Er(2) – O(9)	2.344(5)
Er(1) – O(6a)	2.360(4)	Er(2) – O(21)	2.357(5)
Er(1) – O(12)	2.376(4)	Er(2) – O(19)	2.357(4)
Er(1) – O(23a)	2.412(5)	Er(2) – O(12)	2.362(4)
Er(1) – O(23)	2.442(4)	Er(2) – O(15)	2.392(4)
Mn(1) – O(4)	1.850(5)	Mn(2) – O(17)	1.854(5)
Mn(1) – O(23)	1.925(4)	Mn(2) – O(5a)	1.926(5)

Mn(1) – N(1)	1.983(6)	Mn(2) – O(6a)	1.939(5)
Mn(1) – O(15)	1.992(5)	Mn(2) – N(3)	1.935(6)
Mn(1) – O(28a)	2.4140(5)	Mn(2) – O(20b)	2.270(5)
Mn(1) – O(12)	2.318(4)	Mn(2) – O(13a)	2.369(5)

Preparation of Magnetic Samples. All magnetic measurements were taken on powdered samples that were mulled in eicosane to prevent torqueing of the sample in high applied magnetic fields unless otherwise noted. Samples were ground using a small mortar and pestle, transferred to a gelatin capsule of known mass, and weighed. A small amount of melted eicosane was added and left to solidify. The entire capsule was then weighed and a piece of tape applied to hold the capsule together. The capsule was then inserted into a clear plastic drinking straw.

Magnetic Measurements. All magnetic susceptibility and magnetization values were corrected using Pascal's constants.[9] Corrections were applied for the eicosane, gel capsule, and sample holder by collecting their magnetic susceptibilities and magnetization values and subtracting it from the collected values. Some variable field dc magnetization experiments were performed at 5 K on a Quantum Design (QD) Magnetic Phenomena Measurement System (MPMS) Superconducting Quantum Interference Device (SQUID) magnetometer from 0 to 55000 G at the University of Michigan, Department of Chemistry. Additional variable field dc magnetization experiments were performed at Université Claude Bernard Lyon 1 in Lyon France on an ac QD MPMS SQUID magnetometer at 2 K from 0 to 55000 G. Variable temperature dc susceptibility measurements were conducted on either a QD MPMS SQUID at the University of Michigan, Department of Chemistry at an applied field of 2000 G between 5 and 300 K or at Université Claude Bernard Lyon 1 in Lyon France on an ac QD MPMS XL SQUID magnetometer using the RSO technique with an applied field of 1000 G and temperatures decreasing from 300 K to 2 K. Variable temperature ac magnetic susceptibility measurements were taken on either an ac QD MPMS SQUID magnetometer between 2 and 10 K with zero applied dc magnetic field and a 3.5 G ac alternating field operating at frequencies between 10 and 1500 Hz at the Michigan State University, or at the Department of Physics and Astronomy at Université Claude Bernard Lyon 1 in Lyon

France on an ac QD MPMS XL SQUID magnetometer between 2 and 10 K with variable applied dc field, a 2.7 G ac alternating field operating at frequencies between 10 and 1500 Hz. Measurements collected in Lyon were performed by Ruben Checa.

Results

Synthesis of ***Ln_6Mn_4***

The complexes were synthesized by dissolving 2 mmol $Mn(O_2C_2H_3)_2{\cdot}4H_2O$ in approximately 12.5 mL DMF. In another beaker, dissolve 2 mmol H_3shi, 1 mmol H_2sal, and 1 mmol $LnCl_3{\cdot}6H_2O$ in additional beaker. When the $Mn(OAc)_2$ solution was red or orange, it was added to the Ln/shi/sal solution and the solution was allowed to stir overnight. The following morning, the sample was vacuum filtered. The precipitate was discarded and the dark green solute allowed to slowly evaporate. In approximately 3 weeks, small green crystals were isolated. The first batch of crystals were too small to be measured locally, but with the addition of the Cu-source diffractometer, samples could be measured locally.

Synthesis of ***Ln_4Mn_4***

For **Dy_4Mn_4** and **Ho_4Mn_4**, the complexes were synthesized by dissolving 2 mmol $Mn(O_2C_2H_3)_2{\cdot}4H_2O$ in approximately 12.5 mL DMF. In another beaker, dissolve 2 mmol H_3shi, 1 mmol H_2sal, and 1 mmol $Ln(NO_3)_3{\cdot}5H_2O$ in additional beaker. For **Er_4Mn_4**, the synthesis substituted 1 mmol of $ErCl_3{\cdot}5H_2O$ for the nitrate salt. When the $Mn(OAc)_2$ solution was red or orange, it was added to the Ln/shi/sal solution and the solution was allowed to stir overnight. The following morning, the sample was vacuum filtered. The precipitate was discarded and the dark green solute allowed to slowly evaporate. In approximately 3 weeks, small green crystals were isolated.

Structural Description of ***Ln_6Mn_4***

A general description of **Gd_6Mn_4** will be used to represent the structures of **Dy_6Mn_4** and **Tb_6Mn_4**. The structure of **Gd_6Mn_4** (Figure 2.1) has a central core of six Gd^{III} ions forming a hexagon in a chair conformation (Figure 2.2) surrounded by a $Mn^{III/IV}$ dimer on each side. All the Gd^{III} ions are in an oxygen rich environment. Gd1 and Gd2 are 8-coordinate, while Gd3 is 9-coordinate. Gd1 has a direct interaction with the symmetry generated Gd2 through two μ_2-hydroxamate oxygen (O12, O23) bridges. Gd1 has two bridges with Gd3; a μ_2-phenolate (O11) and a μ_2-hydroximate (O6) bridge, and additionally is bridged through the μ_2-hydroximate (O6-N2) bridge to Mn1. The other coordination sites of Gd1 are occupied by a carbonyl oxygen (O22) and two solvent DMF atoms (O27, O31). In addition to the two μ_2-hydroxamate bridges with Gd1, Gd2 has three bridges with Gd3. One is through a μ_2-carbonyl (O13), one is through a μ_2-hydroxamate (O19), and the last is through a μ_2-hydroximate (O2). This μ_2-hydroximate group (O2-N1) also serves to connect Gd2 to Mn1. The last three coordination sites of Gd2 are occupied by a phenolate (O3), an η_1-carboxylate (O25) from a salicylate ligand, and a solvent DMF (O30). The final Gd^{III} ion, Gd3, has the most connections with other metals. In addition to the bridges described previously, Gd3 has two μ_2-hydroximate bridges to Mn1 (O2-N1, O6-N2) as well as one μ_2-hydroximate bridge (O16) bridge. O16 also serves to bridge Gd3 to Mn2 through a μ_2-hydroximate bridge (O16-N4). A μ_2-carbonyl O18 bridges Gd3 to Mn2 as well. The final Gd3 coordination spot is occupied by the carboxylate oxygen O8 of a salicylate ligand that also bridges Gd3 to Mn2.

Both Mn ions are 6-coordinate octahedral complexes (Figure 2.3). Mn1 has two imine ligands (N1, N2). One bridges Mn1 to Gd1 and Gd3 (N2-O6) and the other bridges Mn1 to Gd2 and Gd3 (N1-O2). Mn1 has two phenolate ligand oxygens (O1, O4). Mn1 also has a carbonyl ligand (O15). The last ligand is made of a μ_2-hydroximate oxygen (O16) that bridges Mn1 to Gd3. This μ_2-hydroximate group (O16-N4) also connects Mn1 to Mn2. Based on charge balance considerations, the Mn to ligand bond distances (Table 2.3), and the average bond distance of 1.913 Å Mn1 was assigned as Mn^{IV}. Mn2 has an equatorial plane comprised of two phenolates (O14, O17) and a μ_2-carbonyl (O18). This μ_2-carbonyl

bridged Mn2 to Gd3. The other equatorial position is occupied by an imine (N4) that is part of the μ_2-hydroximate that bridged Mn2 to Gd3 and Mn1. Along the axis, there is a DMF ligand (O20) on one face and a carboxylate ligand (O9) from a salicylate that bridged Mn2 to Gd3. Mn2 was assigned as a Mn^{III} based on charge balance, bond distances (Table 2.3), and an average bond length of 2.018 Å. From the crystal structure, a Jahn-Teller elongation comprising the DMF and salicylate carboxylate is clearly observed.

In terms of interactions that could have potential magnetic ramifications, all Gd ions are connected by one atom bridges. Mn1 forms a two atom bridge to Gd1 (O6-N2), a two atom bridge to Gd2 (O2-N1), and a one atom bridge (O16) as well as two two-atom bridges (O2-N1, O6-N2) to Gd3. Gd3 is then further bridged to Mn2 through a one atom bridge (O18), a two atom bridge (O16-N4), and three atom carboxylate (O8-C28-O9) bridge. Mn1 and Mn2 have a two atom bridge (O16-N4) between them. Thus, all the metal atoms are highly connected and one could expect complicated magnetic interactions (Figure 2.3).

Structural Description of ***Ln_4Mn_4***

A general description of **Dy_4Mn_4** (Figure 2.4) will serve to describe the structures of **Ho_4Mn_4** and **Er_4Mn_4**. **Dy_4Mn_4** consists of two crystallographically unique Dy^{III} ions, Dy1 and Dy2, and two unique Mn^{III} ions, Mn1 and Mn2. The main structural feature of **Dy_4Mn_4** is the plane of four Dy^{III} ions that runs down the center of the molecule(Dy2 Dy1 Dy1a Dy2a). To either side of the Dy^{III} ions sits a Mn^{III} dimer. If the molecule is rotated 90° to this Dy^{III} plane, one can see that each Mn^{III} dimer is planar and run parallel to each other. It is also observed that the Mn^{III} dimer (Mn1, Mn2) is also roughly co-planar to a Dy^{III} dimer (Dy1, Dy2). This Mn^{III}/Dy^{III} plane is in turn parallel to the other Mn^{III} Dy^{III} dimer pair and can be thought of as two Mn^{III}/Dy^{III} tetranuclear planes (Figure 2.5).

The Dy^{III} ions are all in oxygen-rich 8-coordinate environments (Figure 2.5). Dy1 is bridged by two μ_3-hydroxo atoms (O23 and its symmetry generated partner O23a) to its symmetry generated Dy1a partner. Dy1 is bridged to Dy2 through a μ_2-hydroximate oxygen (O3), a μ_3-hydroxamate oxygen (O9) and a carboxylate group from a salicylate. Dy1 is bridged to the coplanar Mn1 through a μ_2-hydroximate oxygen (O6) which also couples Dy1 to the coplanar Mn2 as well. Dy1 is also bridged to the coplanar Mn2 by the μ_3-hydroxo O23 as well as by an acetate. Dy1 is bridged to the Mn1a and Mn2a ions in the lower plane as well. The carboxylate portion of a salicylate ligand bridges Dy1 to Mn1a. Dy1 is bridged to the parallel plane Mn2a through a μ_3-hydroxo (O23a) as well as by a μ_3-hydroxamate (O9). Dy2 is connected to Dy1 through the paths described above and is also bridged to Mn2a through the μ_3-hydroxmate O9 and the μ_2-hydroxamate O11. Through the μ_2-hydroximate pair O3-N1 group, Dy2 is bridged to Mn1. The remainder of Dy2 coordination sphere is comprised of a solvent DMF (O21), a carbonyl oxygen (O2) of an shi^{3-} ligand and the carbonyl group of two different H_2shi^- ligands (O8 and O12).

The Mn connectivity is simpler than the Dy^{III}. Mn1 and Mn2 are connected through the familiar M-N-O connectivity seen in other Mn-shi metallacrowns.[10,11,12,13] Mn1 is connected to Dy1 and Dy2 as described above and to Mn2 through the μ_2-hydroximate oxygen-nitrogen (O6 and N2). The remaining equatorial ligand positions of Mn1 are comprised of the carbonyl oxygen (O5) of one shi ligand and the iminophenolate six-membered ring of another shi^{3-} ring (O1 and N1). The axial positions include the bridging carboxylate group of a salicylate and a solvent DMF. Mn2's remaining equatorial position contains the phenolate O4 of the iminophenolate ring. The other axial position of Mn2 is occupied by the acetate that helps bridge it to Dy1. Based on charge balance, bond distances (Table 2.5), and the average bond lengths of 2.038 Å and 2.034 Å for Mn1 and Mn2, respectively, a +3 oxidation state was assigned to both Mn ions.

There are numerous bridges that could provide significant exchange pathways for magnetic coupling. Until recently, it has been felt that Ln^{III} ions did not exhibit significant magnetic exchange with either transition or other lanthanide ions; however, it now appears that this belief may be too simplistic.[14] Considering all the possible

exchange pathways, we see that Dy1 may be coupled to the symmetry related Dy1a through the symmetry related O23/O23a pair. Dy1 could then be coupled to Dy2 through O3, O9 and a salicylate (O14 and O15), to Mn1 through O6 and the O3-N1 bridge, and to Mn1a through another salicylate (O17 and O18). Dy1 could also be exchange coupled with Mn2 through the O6-N2 bridge, through O23 and an acetate (O19 and O20). Dy2 has the potential to couple with Mn1 through the O3-N1 bridge and with Mn2 through O9 and O11. Mn1 and Mn2 could exchange couple through the O6-N2 bridge. Thus, all the metals have a high degree of connectivity and one could expect significant magnetic interactions (Figure 2.5). Unfortunately, due to the multiple possible exchange pathways and the high single ion anisotropy for both Dy^{III} and Mn^{III}, detailed interpretation of the exchange coupling from experimental data is precluded.

Variable Field dc Magnetization Measurements

The **Dy_6Mn_4**, **Dy_4Mn_4**, **Ho_4Mn_4**, and **Er_4Mn_4** data were collected at the University of Michigan, Department of Chemistry on a dc QD MPMS SQUID magnetometer. The experiments were conducted at 5 K with a varying field from 0 to 55000 G. The **Gd_6Mn_4** and **Tb_6Mn_4** complexes were measured at the Université Claude Bernard Lyon 1 on an ac QD MPMS SQUID magnetometer at 2 K with a varying field from 0 to 50000 G. The magnetization values for the samples did not saturate, which prevented the determination of a ground spin state.

The **Gd_6Mn_4** magnetization values at 2 K increased steadily with applied field until about 7000 G, at which point the magnetization began to increase more slowly until it reached a maximum of 71130 cm^3 G mol^{-1} (Figure 2.6). **Tb_6Mn_4** increased linearly with applied field until 5000 G, at which point the magnetization curved from linearity and increased more slowly until a maximum of 172600 cm^3 G mol^{-1} (Figure 2.7). **Dy_6Mn_4** magnetization at 5 K increased linearly until 7500 G, where it began to slowly increase, reaching a maximum of 185300 cm^3 G mol^{-1} (Figure 2.8).

The **Dy_4Mn_4** magnetization values at 5 K increased linearly with applied field until 10000 G, then slowly increased until it reaches a maximum of 137900 cm^3 G mol^{-1}

(Figure 2.9). For **Ho_4Mn_4**, the magnetization at 5 K increased linearly until 9000 G, at which point it slowly increased until it reaches a maximum of 139200 cm^3 G mol^{-1} (Figure 2.10). The **Er_4Mn_4** values at 5 K increased linearly until 15000 G, where the values slightly deviated and increased slower than before, but quicker than **Dy_4Mn_4** and **Ho_4Mn_4**. The maximum magnetization value observed was 130600 cm^3 G mol^{-1} (Figure 2.11).

Variable Temperature dc SQUID Magnetometer Magnetic Susceptibility Measurements

Variable temperature dc SQUID magnetometer magnetic susceptibility measurements were taken on the samples prepared as described above. **Dy_6Mn_4**, **Dy_4Mn_4**, **Ho_4Mn_4**, and **Er_4Mn_4** was measured at the University of Michigan, Department of Chemistry on a QD MPMS dc SQUID magnetometer. There was an applied field of 2000 G and the temperature was raised slowly from 5 K to 300 K. All samples except **Dy_4Mn_4** were also measured on a QD MPMS ac SQUID magnetometer with the RSO setting at Université Claude Bernard Lyon 1 with an applied field of 1000 G and the temperature decreased from 300 K to 2 K. For simplicity, only the $\chi_M T$ versus T values will be discussed.

Gd_6Mn_4 (Figure 2.12) had a susceptibility $\chi_M T$ at 300 K of 6.96 cm^3 K mol^{-1}. As the temperature decreased, the susceptibility product increased until it reach a plateau of approximately 13.5 cm^3 K mol^{-1} from 45 K to 25 K, before rapidly increasing a maximum of 14.14 cm^3 K mol^{-1} before decreasing to 12.60 cm^3 K mol^{-1} at 2 K. The $\chi_M T$ value at 300 K was less than expected for six Gd^{III}, two Mn^{III}, and two Mn^{IV} non-interacting ions ($\chi_M T$ = 57.03 cm^3 K mol^{-1}). **Tb_6Mn_4** (Figure 2.13) had a susceptibility at 300 K of 63.18 cm^3 K mol^{-1}. In this case, the susceptibility product increased slightly with lowered temperatures, reaching a maximum of 68.73 cm^3 K mol^{-1} at 110 K before decreasing to a minimum of 48.81 cm^3 K mol^{-1} at 2 K. The susceptibility at 300 K was less than expected if all the ions were non-interacting ($\chi_M T$ = 80.67 cm^3 K mol^{-1}). **Dy_6Mn_4** (Figure 2.14), collected at the University of Michigan, had a $\chi_M T$ value of 81.13 cm^3 K mol^{-1} at 300 K. It slightly increased, reaching a plateau of 84.6 cm^3 K mol^{-1} from 160 K to 120 K, at which point it continuously decreased until a minimum value of 68.78

cm^3 K mol^{-1} was reached at 5 K. The $\chi_M T$ value at 300 K was less than expected for non-interacting ions ($\chi_M T$ = 94.77 cm^3 K mol^{-1}).

Dy_4Mn_4 (Figure 2.15) was measured only on the dc SQUID magnetometer at the University of Michigan. The susceptibility product $\chi_M T$ at 300 K was 60.19 cm^3 K mol^{-1}, which is slightly less than four non-interacting Dy^{III} and four non-interacting Mn^{III} ions ($\chi_M T$ = 68.68 cm^3 K mol^{-1}). The susceptibility product slightly increased, reaching a maximum of 62 cm^3 K mol^{-1} from 160 K to 110 K. The $\chi_M T$ value then slowly decreased, reaching a minimum of 46.95 cm^3 K mol^{-1} at 5 K. **Ho_4Mn_4** and **Er_4Mn_4** were measured at both locations. In Michigan, **Ho_4Mn_4** (Figure 2.16) had a $\chi_M T$ of 66.73 cm^3 K mol^{-1} at 300 K, which is close to the expected susceptibility if all the metals were non-interacting ($\chi_M T$ = 68.28 cm^3 K mol^{-1}). The susceptibility product remained fairly constant with decreasing temperatures, reaching a minimum at 5 K of 39.48 cm^3 K mol^{-1}. **Er_4Mn_4** (Figure 2.17) had a susceptibility product of 55.58 cm^3 K mol^{-1} at 300 K, coming close to the expected value for non-interacting metals ($\chi_M T$ = 57.92 cm^3 K mol^{-1}). The susceptibility remained fairly constant until around 40 K, where it dropped dramatically until it reached a minimum of 28.05 cm^3 K mol^{-1} at 5 K.

Variable Temperature ac SQUID Magnetometer Magnetic Susceptibility

All samples were prepared as described above. **Dy_4Mn_4** was collected at Michigan State University, Department of Physics and Astronomy on a QD MPMS ac SQUID magnetometer. The sample was measured with an ac drive field of 3.5 G, 0 G dc applied field, temperatures ranging from 10 K to 2 K, and at frequencies ranging from 0 to 1000 Hz. All other samples were collected at Université Claude Bernard Lyon 1 on a QD MPMS ac SQUID magnetometer. For these samples, an initial scan was performed at an ac drive field of 2.7 G, a frequency of 700 Hz, between temperatures of 10 K and 2 K and varying applied dc fields (between 0 G and 1000 G). Based on the best performance of the sample, the measurements were then conducted at that applied dc field, with an ac drive field of 2.7 G, frequencies ranging from 10 Hz to 1400 Hz, and between temperatures of 10 K and 2 K. If no frequency dependence in the out-of-phase was

observed under any applied dc field, then the variable frequency experiment was not conducted.

For the **Gd_6Mn_4** in-phase data (Figure 2.18) were collected at 0 G and 500 G applied dc field, the data was relatively linear, although it was noisy. For 0 G applied dc field, at 10 K, the $\chi'_M T$ value was 10.84 cm^3 K mol^{-1}. For **Tb_6Mn_4** (Figure 2.19), the in-phase data were collected at 700 Hz applied field with an applied dc field of 0 G and 500 G between 2 K and 3.5 K. At 0 G, at 3.5 K, the $\chi'_M T$ value was 58.02 cm^3 K mol^{-1} and at 2 K, the $\chi'_M T$ value was 52.06 cm^3 K mol^{-1}. For **Dy_6Mn_4** (Figure 2.20), the in-phase data were collected from 8 K to 2 K with 0 dc applied field for frequencies between 1400 Hz and 10 Hz. For all frequencies, the $\chi'_M T$ vs. T plot was nearly constant until 3.5 K, at which point there was a slight increase. After this slight increase, each frequency curve diverged from each other and decreased. Extrapolating the data from 8 K to 3.5 gave a $\chi'_M T$ value of about 70.5 cm^3 K mol^{-1}.

The **Dy_4Mn_4** (Figure 2.21) in-phase data were collected from 10 K to 2 K with 0 dc applied field, 3.5 G drive field, and frequencies of 1000 Hz to 10 Hz. The data was linear for all frequencies until 4 K, where it began to diverge for each frequency. Extrapolating the data from 10 K to 4 K to 0 K gave a $\chi'_M T$ value of 40 cm^3 K mol^{-1}. The **Ho_4Mn_4** (Figure 2.22) in-phase data were collected from 10 K to 2 K with 0 dc applied field between frequencies of 1200 Hz and 100 Hz. The data were linear from 10 K to 4.5 K for all frequencies, where it began to diverge. Extrapolating data from 10 K to 4.5 K to 0 K, the $\chi'_M T$ value was 32.23 cm^3 K mol^{-1}. The **Er_4Mn_4** (Figure 2.23) in-phase data were collected from 10 K to 2 K with 0 G or 500 G dc applied field and a frequency of 700 Hz. For the 0 G data, the curve of $\chi'_M T$ vs. *T* was linear until 3 K, where it began to curve. Extrapolating the data from 10 K to 3 K to 0 K led to a $\chi'_M T$ value of 21.69 cm^3 K mol^{-1}.

The out-of-phase data of **Gd_6Mn_4** (Figure 2.24) showed no frequency dependence both in the presence and absence of applied dc fields. The out-of-phase data of **Tb_6Mn_4** (Figure 2.25) also lacked frequency dependence, whether an applied dc field was present or not. For **Dy_6Mn_4** (Figure 2.26) out-of-phase data, there was frequency dependence with zero

applied dc field. However, even for the highest frequency, the χ''_M versus *T* plot did not reach a maximum, meaning a blocking temperature could not be determined.

The out-of-phase data of **Dy_4Mn_4** (Figure 2.27) showed frequency dependence with no applied field. As seen with **Dy_6Mn_4**, the χ''_M versus *T* plot did not reach a maximum, making it impossible to determine a blocking temperature. The **Ho_4Mn_4** (Figure 2.28) out-of-phase plot did not show frequency dependence. Even with a 500 G applied field, there was no frequency dependence. The **Er_4Mn_4** (Figure 2.29) out-of-phase plot did not show frequency dependence at 700 Hz with 0 G or 500 G applied dc field.

Discussion

The preparations of **Ln_6Mn_4** and **Ln_4Mn_4** are important in a purely synthetic aspect. It is still difficult to prepare mixed Mn/Ln complexes where the Ln^{III} ions are systematically substituted, leaving the same metal stoichiometry.[15,16,17,18,19,20,21,22,23,32] Most reported structures feature only one or two Mn/Ln complexes.[24,25,26,27,28,29] The fact that these two series (**Ln_6Mn_4** and **Ln_4Mn_4**) can be synthesized with multiple lanthanides allows one to determine the role of the lanthanide on the magnetic properties. For instance, by introducing La^{III} or Y^{III}, one can determine the magnetic properties that originate from the Mn ions, such as spin and even anisotropy. If Gd^{III} is used, one can test to see if adding a $S = 7/2$ to the system, but no anisotropy, bestows SMM properties. This allows one to determine if the anisotropy from the Mn ions in addition to the Gd^{III} spin results in SMM behavior. Introduction of Tb^{III} through Yb^{III} allow for one to study the introduction of both spin and anisotropy to the system. Making series that are so closely structurally related (**Ln_6Mn_6** vs. **Ln_6Mn_4** and **Ln_4Mn_6** vs. **Ln_4Mn_4**) also allows one to examine the role of Mn to Ln ratio. In the following discussion, the **Ln_6Mn_4** series of complexes will be compared to the **Ln_6Mn_6** series[1] and the **Ln_4Mn_4** series will be compared to the **Ln_4Mn_6** series.[8] There are remarkable structural similarities allowing one to study the impact of Mn to Ln ratio on magnetic properties.

The **Ln_6Mn_4** series provided a very interesting general structure type. There were three different protonation states of the shi^{3-} ligand (shi^{3-}, $Hshi^{2-}$, H_2shi^-) as well as four singly deprotonated salicylic acid ($Hsal^-$) ligands. In order to identify the charges on the Mn ions in the **Ln_6Mn_4** series, bond lengths, average bond lengths, and charge balance considerations needed to be satisfied. There were six shi^{3-} ligands, four $Hshi^{2-}$ ligands, two H_2shi^- ligands, and four $Hsal^-$ ligands, giving the complex thirty two negative charges. The six lanthanides were 3+, leaving fourteen unaccounted negative charges, and an average charge of 3.5 for each Mn ion. The most likely distribution would be an equal number of 3+ and 4+ Mn ions. To determine the identity of the individual Mn ions, bond lengths and average bond lengths were used. Mn2 had two bonds trans to each other that were much longer (average for **Gd_6Mn_4**: 2.207 Å; for **Tb_6Mn_4**: 2.18 Å) than the other four bonds (average for **Gd_6Mn_4**: 1.917 Å; for **Tb_6Mn_4**: 1.88 Å) (Table 2.3 and Table 2.4). The average bond length for Mn2 for **Gd_6Mn_4** was 2.018 Å, which is ideal for a Mn^{III} ion. Examining Mn1, there were no bonds significantly longer than the other. The average bond length was 1.913 Å for Mn1 for the **Gd_6Mn_4** structure. This bond length was ideal for Mn^{IV} ions.[30] This also conveniently balances the charge of the structure.

Examining the structure of **Gd_6Mn_4,** reveals remarkable structural similarity to the previously published **Dy_6Mn_6** (Figure 1.31), only with two of Mn^{III} ions removed. Both structures feature a similar Ln_6-O core (Figure 2.30) as well as having the lanthanide ions in a chair-like orientation (Figure 2.31). The Mn^{IV} ions also have similar environments in both structures. Both Mn^{IV} ions have one direct and two indirect (two atom) interactions with the Ln^{III} ions.

The key difference between the **Ln_6Mn_6** and **Ln_6Mn_4** structure types is the lack of two Mn^{III} ions. The missing Mn^{III} ions lead to slightly different coordination environments of the remaining Mn^{III} and Mn^{IV} ions in the **Ln_6Mn_4** structures compared to the **Ln_6Mn_6** class. In the **Gd_6Mn_4** complex, Mn2 has a single nitrogen ligand (N4) in the equatorial position that is part of a bridge to the Mn1 ion and Gd3. Two of the other equatorial positions are occupied by an oxygen atom that bridges Mn2 to Gd3 ion. This leads to Mn2 having two direct and one indirect interactions with the Gd3 ion and one indirect

interaction with Mn1. In the **Dy_6Mn_6** example, one Mn^{III} ion has two nitrogen ligands in the equatorial plane; this Mn^{III} ion has one direct and two indirect interactions with the Dy^{III} ion, one indirect interaction with the Mn^{IV} ion, and one indirect interaction with the other Mn^{III} ion. The other Mn^{III} ion has one direct and two indirect interactions with the Dy^{III} ion and no interactions with the Mn^{IV} ion. This difference in bridging could affect the magnetic properties of **Ln_6Mn_4** in comparison to **Ln_6Mn_6** by changing the couplings, in addition to the obvious decrease in spin due to the missing Mn^{III} ions, which indeed manifested in the magnetic susceptibilities of the **Ln_6Mn_4** complexes.

Examining the magnetic properties of **Ln_6Mn_4** reveals some very interesting properties. The magnetization plot of **Gd_6Mn_4** and **Tb_6Mn_4** (Figures 2.6 and 2.7) did not saturate, thus ground spin states could not be determined. The magnetic susceptibilities at 300 K (Figures 2.12 and 2.13) are much lower than one would expect for six Gd^{III} ions (S = 7/2, L = 0, $^8S_{7/2}$) or six Tb^{III} ions ($S = 3, L = 1, {}^7F_6$), two Mn^{III} ions (S = 2), and two Mn^{IV} (S = 3/2) ions if the metals were all non-interacting ($\chi_M T$ = 57.03 cm^3 K mol^{-1} and 80.67 cm^3 K mol^{-1}, respectively). For **Gd_6Mn_4**, the reason is most likely due to an experimental error in the mass. However looking at the overall shape of the curve, one observes significant magnetic interactions. The exchange coupling between the Gd^{III} ions themselves and the Gd^{III} ions and the Mn ions above 100 K is negligible, thus any interactions are likely between the manganese ions in the $Mn^{III/IV}$ dimers Because the susceptibility increases as the temperature decreases, the $Mn^{III/IV}$ ions most likely are ferromagnetically coupled and the Gd^{III} ions are non-interacting. Below 10 K, the susceptibility again increases, indicating small amounts of ferromagnetic coupling between Gd^{III} ions or between Gd^{III} and the $Mn^{III/IV}$ dimers. It is not possible to say which interaction has the largest magnitude, but it does indicate that the high degree of connectivity of the metals revealed in the crystal structure is manifested magnetically. At temperatures below 3 K, zero-field splitting is observed, leading to a decrease in overall magnetic susceptibility.

The curves reflect the nature of the free Ln^{III} ion incorporated in the complex. The $\chi_M T$ product for both increase as the temperature decreases and ordinarily, one could say that

as temperature decreased and susceptibility increased, the metals were ferromagnetically interacting. However, due to the close similarity of the observed curve with the curve of a free Ln^{III} ion and the large number of Ln^{III} ions, this conclusion is not valid. What can be said is that the decrease at low temperatures is indicative of large amounts of spin-orbit coupling originating from the Mn^{III} ions and a large number of spins from the Gd^{III} ions in the Gd^{III} case and spin-orbit coupling from both the Mn^{III} and Tb^{III} ions in the **Tb_6Mn_4** case. This would help explain the very low observed susceptibilities; that there are so many spin states that there is very little energy between the states, making it possible to access these states even at very low temperature. Examining the in-phase data (Figures 2.18 and 2.19) demonstrate that there are multiple spin levels available, even at low temperatures. The out-of-phase data (Figures 2.24 and 2.25) showed no frequency dependence, indicating that **Gd_6Mn_4** and **Tb_6Mn_4** are not SMMs. From the **Gd_6Mn_4** complex, it was clear that any observed SMM properties for this series would not originating from the $Mn^{III}/^{IV}$ ions, but from the Ln^{III} ions. The **Tb_6Mn_4** series demonstrated that most likely, a bistable ground state was not maintained. Because non-Kramers' doublets do not necessarily have bistable ground states, axial symmetry or exchanged induced biases were not present.[31] In order to bestow SMM properties, the Kramers' doublet Dy^{III} would be used.

The **Dy_6Mn_4** complex shows similar magnetic behavior in the magnetization (Figure 2.8) and magnetic susceptibility (Figure 2.14) as observed in the **Tb_6Mn_4** example. The explanation for the complex susceptibility behavior is the presence of so many lanthanide ions and the associated spin-orbit coupling. The various magnetic exchange coupling pathways and large amounts of spin-orbit coupling furthermore make it difficult to determine the ground spin state as well as magnetic exchange pathways. Examining the in-phase data, there is a divergence in the frequency plots at 3.5 K, indicative of frequency dependence as well as quantum effects; something not observed in the **Gd_6Mn_4** and the **Tb_6Mn_4** examples. The out-of-phase (Figure 2.26) data, revealed frequency dependence in zero applied dc field, a hallmark of SMM behavior. This indicated that the Kramers' doublet Dy^{III} bestowed a stable ground state as well as sufficient anisotropy, something that the non-Kramers Tb^{III} ion nor the isotropic Gd^{III} ion

could.[31] Another way, for Kramers' doublets, the spin is always a non-integer, ensuring that a $J = 0$, something available in non-Kramers' doublet systems, cannot occur. This means that Kramers' doublets always have a bistable ground state, regardless of the ligand environment or magnetic exchange coupling. Due to the limitations of the SQUID instrument, a blocking temperature could not be calculated, a common problem among SMMs, especially complexes with large mixed Mn/Ln complexes.[3,7,8,16,17,18,20,22,23,25]

Because of the structural similarities between the previously published **Ln_6Mn_6** complexes[7] and the **Ln_6Mn_4** complexes, it seemed reasonable to compare their magnetic properties. Plotting the susceptibilities of **Dy_6Mn_6** and **Dy_6Mn_4** on the same graphs, it was found that the susceptibilities differed significantly (Figure 2.32). This is not surprising, given that **Dy_6Mn_4** lacks two Mn^{III} ions. To account for this difference, a spin-only approximation of the contribution of two Mn^{III} ($S = 2$, $\chi_M T = 3.0$ cm^3 K mol^{-1}) ions to the magnetic susceptibility was added to the observed susceptibility. The addition of two Mn^{III}, however, did not make up the difference in susceptibility, indicating that something else was affecting the magnetism. This trend was observed for **Tb_6Mn_6** versus **Tb_6Mn_4** (Figure 2.33) case as well. Because of the similar connectivity of the Ln^{III} ions, one can assume that the magnetic contributions from the Ln^{III} ions would remain the same in the two complexes. As discussed above, there is a different coupling scheme between the Mn ions because two Mn^{III} ions were lost in the **Ln_6Mn_4** complexes compared to the **Ln_6Mn_6** series, which could affect the magnetism. However, it would be rather odd that the observed differences in susceptibilities would be only due to the spin-only contribution of two Mn^{III} ions or slight changes in exchange coupling constants due to structural changes. Another possible source of the difference in susceptibility is due in fact to the anisotropic contributions from the Mn^{III} ions. The additional magnetoanisotropy from the Mn^{III} ions could also explain why the **Dy_6Mn_6** had an observable blocking temperature in the out-of-phase susceptibility, where the **Dy_6Mn_4** complex did not. As the other systems **Ln_6Mn_6** or **Ln_6Mn_4** did not show SMM behavior, it is hard to further support this claim. What would have been particularly interesting is if one of the **Ln_6Mn_6** complexes did show SMM behavior and the analogous **Ln_6Mn_4** did

not. This would indicate the importance of the spin and anisotropy from the two Mn^{III} ions that are missing from the **Ln_6Mn_6** complexes.

Examining the structure of the **Ln_4Mn_4** complexes revealed some interesting structural characteristics. The **Dy_4Mn_4** complex (Figures 2.4 and 2.5) will be described as an example of the entire series. To assign the oxidation states of the Mn ions, bond lengths, average bond lengths, and charge balance considerations were made. There were two hydroxo, two acetate, four shi^{3-}, four H_2shi^-, and four salicylate ligands, giving the complex an overall charge of -24. The four Dy^{III} ions balance twelve of the negative charges, leaving twelve negative charges unaccounted for and four Mn ions to account for the charge. Logically, four Mn^{III} ions would balance this charge. However, to ensure the charges were correct, the bond lengths were used to check the oxidation states. Mn1 had an average bond length of 2.038 Å and Mn2 had an average bond length of 2.034 Å, both ideal average distances for Mn^{III}.[30] In addition, both Mn ions had a clear bond length elongation along one axis and a bond length contraction along a plane perpendicular to the elongation axis, a hallmark of a Jahn-Teller distortion and Mn^{III} ions.

This structure is remarkably similar to the previously published **Ln_4Mn_6** complex Zaleski and co-workers (Figure 1.35).[8] The **Ho_4Mn_6** structure is reported, but the entire series is isostructural to this example. Like the **Ln_4Mn_4**, the **Ho_4Mn_6** molecule also had a line of Ho^{III} ions running down the center. Comparing the metal core (Figure 2.34) of the **Ho_4Mn_6** complex to the **Ln_4Mn_4** series, it appears that two Mn^{III} ions that are above the Mn1, Mn2, Ho1, Ho2 plane are removed from the **Ln_4Mn_6** series, leaving the remaining metals intact. Based on this structural observation and knowledge that the **Dy_4Mn_6** structure showed slow magnetic relaxation,[8] the magnetic properties of **Ln_4Mn_4** were studied.

For all the **Ln_4Mn_4** complexes, none showed saturation of magnetization (Figures 2.9 – 2.11). The susceptibilities of the **Ln_4Mn_4** series differed from the larger **Ln_6Mn_4** complexes in that the susceptibilities did not as closely match the shape of the curves of free lanthanides. The susceptibilities at 300 K were often close to that of the

susceptibilities if all the metals acted independently. Upon lower the temperatures, the susceptibility values decreased to values much less than if the metals behaved independently. However, without an isotropic metal example, it is not possible to fully discuss the type of coupling amongst the metals beyond saying that there appears to be antiferromagnetic coupling among the metals.

Studying the out-of-phase behavior, only the **Dy_4Mn_4** (Figure 2.27) showed frequency dependent out-of-phase behavior; the **Ho_4Mn_4** (Figure 2.28) and **Er_4Mn_4** (Figure 2.29) structures did not show frequency dependence. As was the case with **Dy_6Mn_4**, the SQUID magnetometer could not reach low enough temperatures to determine the blocking temperature of **Dy_4Mn_4**. The onset of slow magnetic relaxation of both the **Dy_6Mn_4** and the **Dy_4Mn_4** were at very similar temperatures. The main difference between the two was the magnitude of χ''_M value, which was about three times larger for the **Dy_6Mn_4** complex. This reflects the larger susceptibility of **Dy_6Mn_4** compared to **Dy_4Mn_4.**

Comparing **Dy_4Mn_4** and **Dy_4Mn_6**, it was found that in this case the spin-only addition of two Mn^{III} ions almost made up the difference in susceptibility between the two structures perfectly (Figure 2.35). Examining the **Ho_4Mn_4** versus **Ho_4Mn_6** (Figure 2.36) and **Er_4Mn_4** versus **Er_4Mn_6** (Figure 2.37) on the other hand, it can be seen that the two missing Mn^{III} ions have almost no impact on the susceptibility properties of the larger complexes. In fact, in these cases, the magnetic data for the **Ln_4Mn_6** is almost exactly the same as the **Ln_4Mn_4** data., which is rather surprising. It may be that the identity of the Ln^{III} (e.g., Dy^{III}) dominate the magnetic properties of the whole complex.

Using all of these observations it can be seen how important the lanthanides are on the magnetic properties. When there are more lanthanides than Mn ions in these systems, the spin-only approximation for additional Mn^{III} ions does not seem to be as accurate as when there are an equal number of lanthanides and Mn ions. This seems to indicate that the lanthanides accentuate the spin-orbit coupling properties of the Mn ions; the more lanthanides present, the more important the spin-obit coupling properties become. It also

appears that some Ln^{III} ions, such as Dy^{III} have a more pronounced affect on the magnetic properties than other Ln^{III} ions, such as Ho^{III} or Er^{III}. There are two competing changes that in spin and anisotropy that occur upon comparing **Dy_6Mn_4** and **Dy_4Mn_4**. On the one hand, there is a significant decrease in both anisotropy and spin substituting two Mn^{IV} ions for two Mn^{III} ions. However, **Dy_6Mn_4** contains two additional Dy^{III} ions **Dy_4Mn_4,** that provide spin and anisotropy to the complex. A simple comparison of these effects might lead to the conclusion that the **Dy_6Mn_4** would be a superior SMM, yet experimental data indicate that there was not a significant increase in blocking temperature for the larger cluster. One might conclude that predicting SMM performance solely on total spin or perceived single ion anisotropy is a dangerous game as other factors (such as multiple energy levels that are closely spaced) may dominate relaxation rates. Clearly, this demonstrates that predicting the magnetic behavior of *d-f* complexes is still in its infancy and that the interactions which govern the relaxation rates is poorly understood.

In summary, examination of the **Gd_6Mn_4** complex seemed to indicate that in general, the anisotropy available from the Mn^{III} ions was not sufficient to bestow SMM properties on these large mixed Ln/Mn complexes. Oftentimes, it is the anisotropic Kramers' doublet Dy^{III} ion that behaves as an SMM,[16] or at least shows the best SMM behavior.[15, 26,32,] As discussed above, non-Kramers' doublets, such as Tb^{III} and Ho^{III} do not necessarily have bistable ground states. Thus it is synthetically more difficult to produce Tb^{III}-based SMMs.[31]

These observations led to the realization that large, mixed Mn/Ln complexes may not be the best path forward for SMM research. Yes, Mn^{III} and Ln^{III} ions have large spin and anisotropy values, but it seems that it is difficult to control their properties. As was seen in the **Mn_{19}/$DyMn_{18}$** complex, with large spin complexes, the likelihood of accidental symmetry increases.[2,3,4] This can decrease overall anisotropy, despite the presence of many anisotropic ions. It appeared that introduction of Dy^{III} is best for inducing SMM properties. This is because Dy^{III} has a Kramers ground state and sufficient anisotropy.[31,32] In these large systems, magnetic exchange coupling between the metal sites leads to

complicated spin systems. With so many spin states available, there is a distinct possibility that some of the states lie closely in energy, lowering the blocking temperature. At the very least, it leads to complicated magnetic properties, as seen in the $\mathbf{Ln_xMn_y}$ structures given here. It appeared that the best path forward would be to utilize fewer metals that are arranged in a predesigned order. This would prevent accidental symmetry and allow one to control both magnetic coupling as well as magnetoanisotropy, One way to accomplish this is through geometric design, an idea that will be explored in Chapters III and IV.

Conclusion

Examining the mixed Mn/Ln series as a whole give some important conclusions about the state of large mixed Mn/Ln complexes. First, this work shows that it is possible to synthesize a series of series of mixed Mn/Ln complexes, something that has rarely done in the literature.[15,16,17,18,19,20,21,22,23,30,32] Second, mixed Mn/Ln complexes yield complex magnetic interactions and properties that are dominated by the magnetic properties of the lanthanides contained within them. It is difficult to determine spin state interactions at both high and low temperatures. Because the susceptibilities at high temperatures are far less than what one would expect for non-interacting ions, it seems that multiple spin states are populated at higher temperatures. At lower temperatures, the susceptibilities also differ from what one would expect for interacting metals. The values seem to indicate weak antiferromagnetic coupling, but the spin values are not what one would obtain for fully antiferromagnetically coupled systems. This indicates that it is likely that multiple spin states are populated. Third, only a few of the known mixed Mn/Ln complexes show relaxation blocking temperature above 2 K.[1,15,21,24,27,28,32] The $\mathbf{Dy_6Mn_4}$ and $\mathbf{Dy_4Mn_4}$ show slow magnetic relaxation. The $\mathbf{Dy_6Mn_4}$ has a blocking temperature lower than that of the $\mathbf{Dy_6Mn_6}$ system. It is difficult to compare the blocking temperatures of $\mathbf{Dy_4Mn_4}$ to $\mathbf{Dy_4Mn_6}$, as both fall below 2 K. Importantly, though, even with fewer metals, comparable SMM behaviors can be obtained. The source of the low blocking temperature could reflect the fact that the ground spin states at low temperatures are not well isolated. As was shown with the $\mathbf{Ln_6Mn_4}$ and $\mathbf{Ln_4Mn_4}$ series, there are

complex interactions between the metals. These complex interactions are manifested in the unusual calculated magnetic spin states. It seems that these large mixed Mn/Ln complexes make it difficult to obtain well-isolated ground spin states, something that appears to be important to obtaining well behaved SMMs. The results are summarized in Table 2.7.

Planar metallacrowns will be used in the following chapters to better isolate the ground spin state and increase the anisotropy of the system through geometric control. The metallacrown motif could allow for controllable and predictable coupling between magnetic centers. Additionally, by using planar molecules, the anisotropy vectors could be aligned and thus maximizing the molecular anisotropy. In Chapter III, a new family of Mn/Ln metallacrowns, the **Ln^{III} 14-MC-5** family will be introduced. This was the first series of planar mixed Mn/Ln metallacrowns that showed slow magnetic relaxation. Importantly, a blocking temperature above 2 K was observed despite the presence of only two Ln^{III} ions and four Mn^{III} ions. Chapter IV will continue the use of planar metallacrowns, using only a central anisotropic metal and four planar Mn^{III} ions in the 12-MC-4 structural motif.

Table 2.7. The magnetic results from the **Ln_6Mn_4** and **Ln_4Mn_4** are summarized.

Complex	Low Temperature $\chi_M T$ (cm^3 K mol^{-1})	High Temperature $\chi_M T$ (cm^3 K mol^{-1})	Slow magnetic relaxation
Gd_6Mn_4	12.60 (2 K)*	6.96 (300 K)*	NO
Tb_6Mn_4	48.81 (2 K)	63.18 (300 K)	NO
Dy_6Mn_4	68.78 (5 K)	81.13 (300 K)	YES
Dy_4Mn_4	46.95 (5 K)	60.19 (300 K)	YES
Ho_4Mn_4	39.48 (5 K)	66.73 (300 K)	NO
Er_4Mn_4	28.05 (5 K)	55.58 (300 K)	NO

* The mass for this sample was incorrect, hence the extremely low values measured.

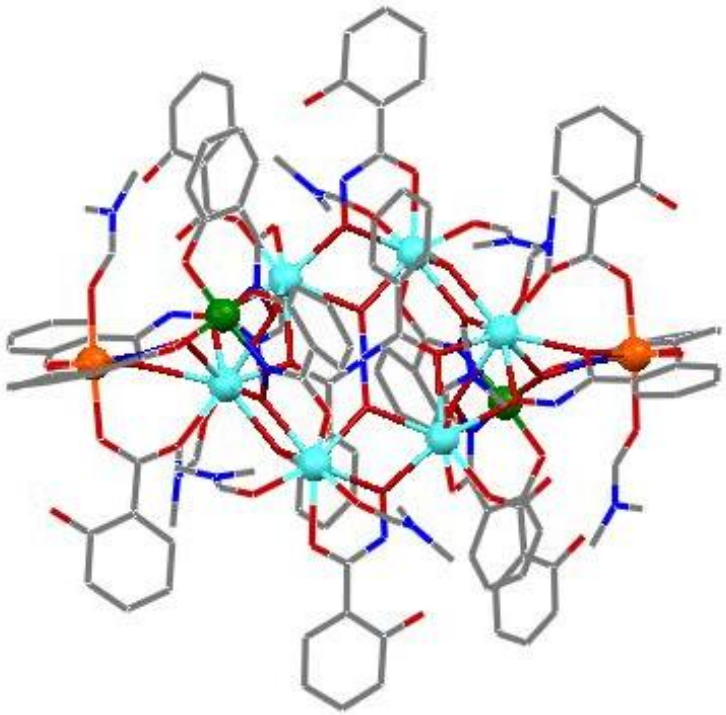

Figure 2.1. The x-ray crystal structure of **Gd_6Mn_4** is shown with hydrogen atoms and lattice solvent molecules removed for clarity. Color scheme: aqua spheres: Gd^{III}; orange spheres: Mn^{III}; green spheres: Mn^{IV}; gray tubes: carbon, red tubes: oxygen, blue tubes: nitrogen.

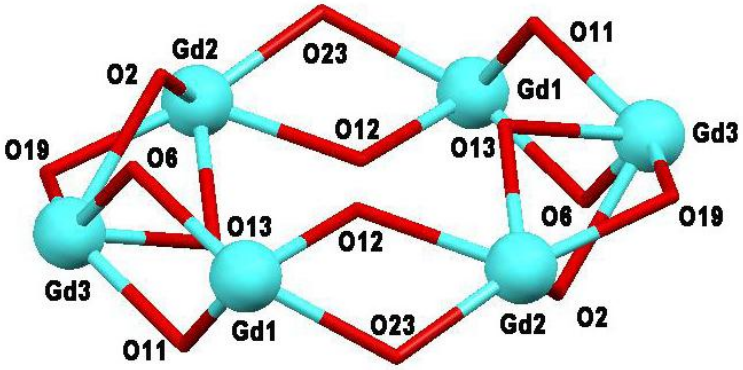

Figure 2.2. The hexagon Gd^{III} core of **Gd_6Mn_4** is highlighted. Color scheme: aqua spheres: Gd^{III}; red tubes: oxygen.

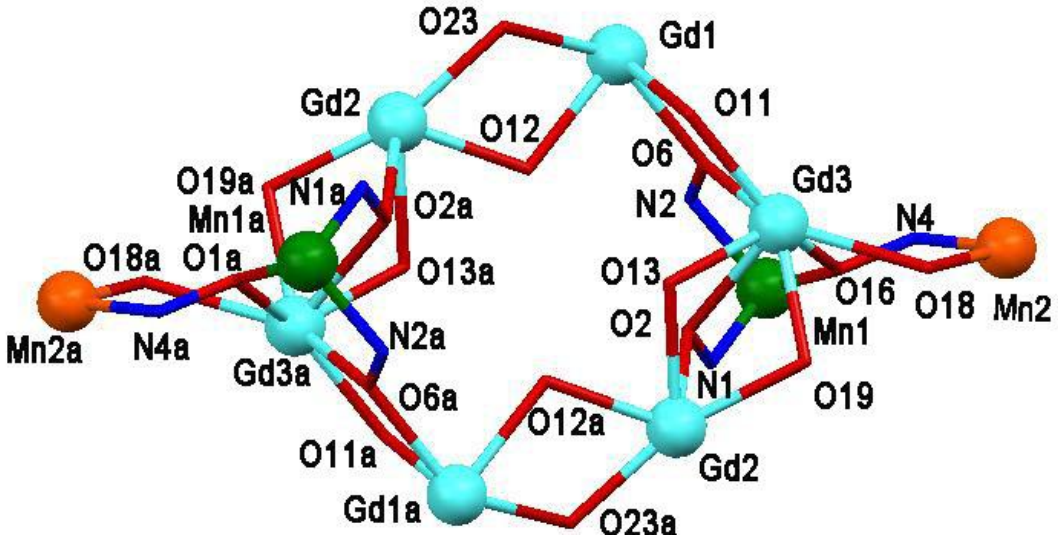

Figure 2.3. The metal connectivity of **Gd_6Mn_4** is highlighted. Color scheme: aqua spheres: Gd^{III}; orange spheres: Mn^{III}; green spheres: Mn^{IV}; gray tubes: carbon, red tubes: oxygen, blue tubes: nitrogen.

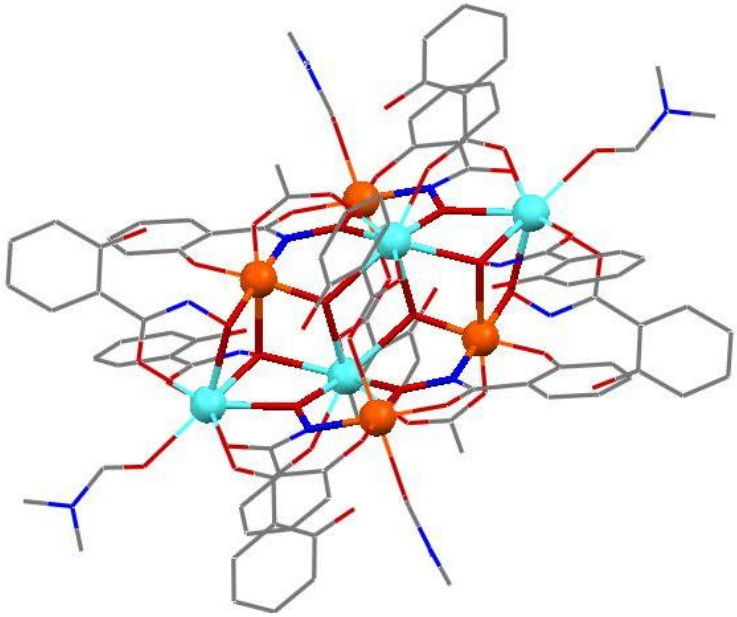

Figure 2.4. The x-ray crystal structure of **Dy_4Mn_4** is shown with hydrogen atoms and lattice solvent molecules removed for clarity. Color scheme: aqua sphere: Dy^{III}; orange sphere: Mn^{III}; gray tubes: carbon; red tubes: oxygen; blue tubes: nitrogen.

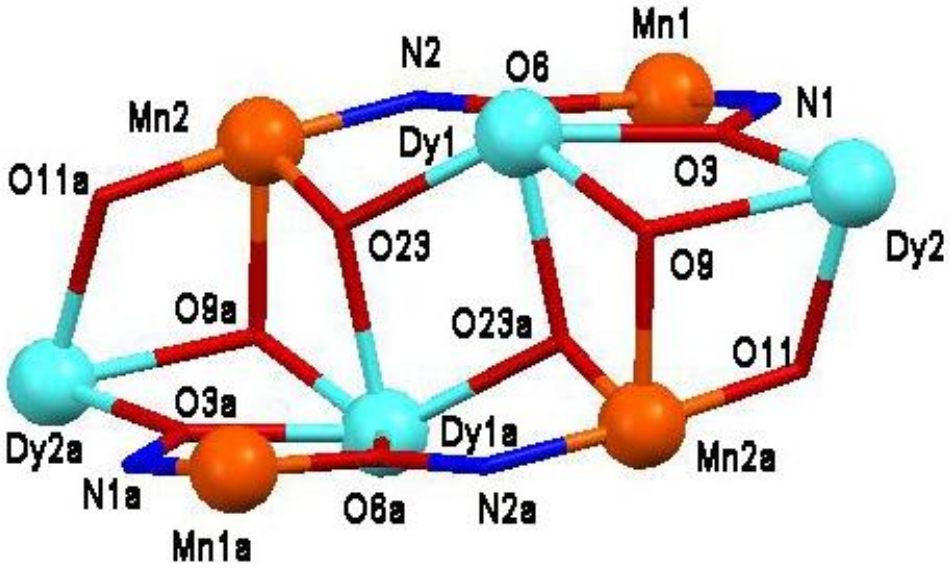

Figure 2.5. The metal connectivity of **Dy_4Mn_4** is highlighted. Color scheme: aqua sphere: Dy^{III}; orange sphere: Mn^{III}; gray tubes: carbon; red tubes: oxygen; blue tubes: nitrogen.

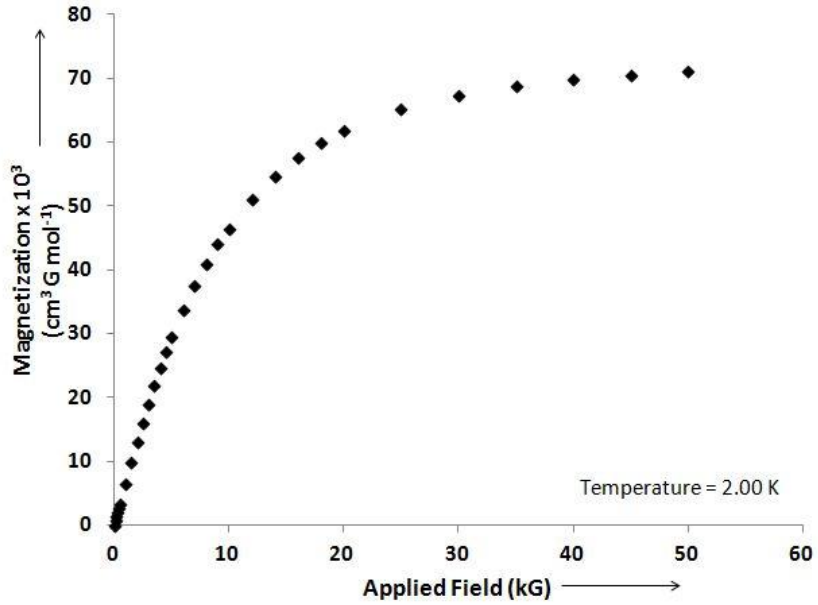

Figure 2.6. The variable field magnetization plot of **Gd_6Mn_4** is shown. The magnetization data were collected at 2.00 K.

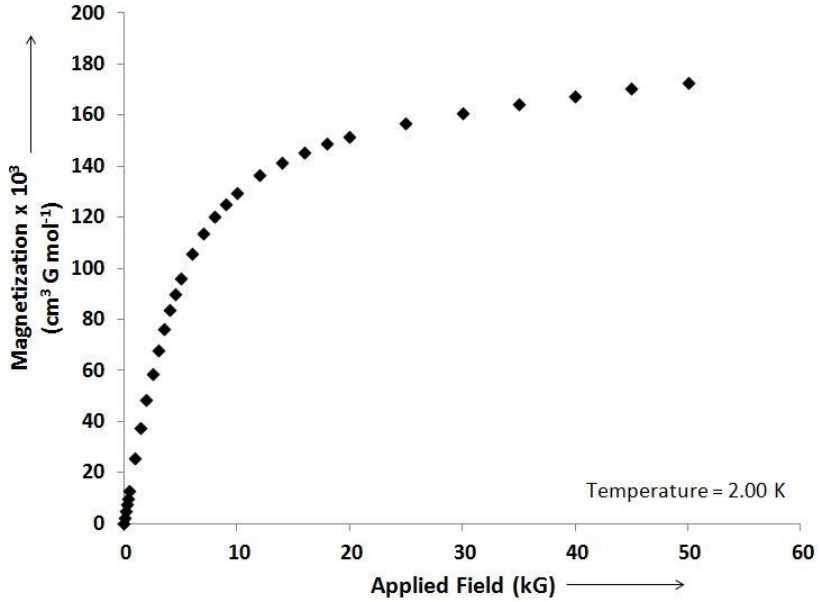

Figure 2.7. The variable field magnetization plot of **Tb_6Mn_4** is shown. The magnetization data were collected at 2.00 K.

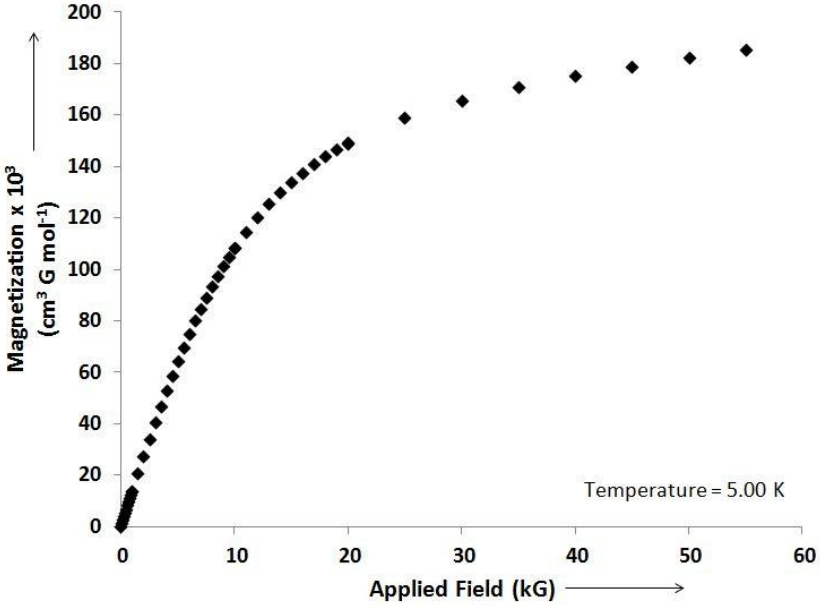

Figure 2.8. The variable field magnetization plot of **Dy_6Mn_4** is shown. The magnetization data were collected at 5.00 K.

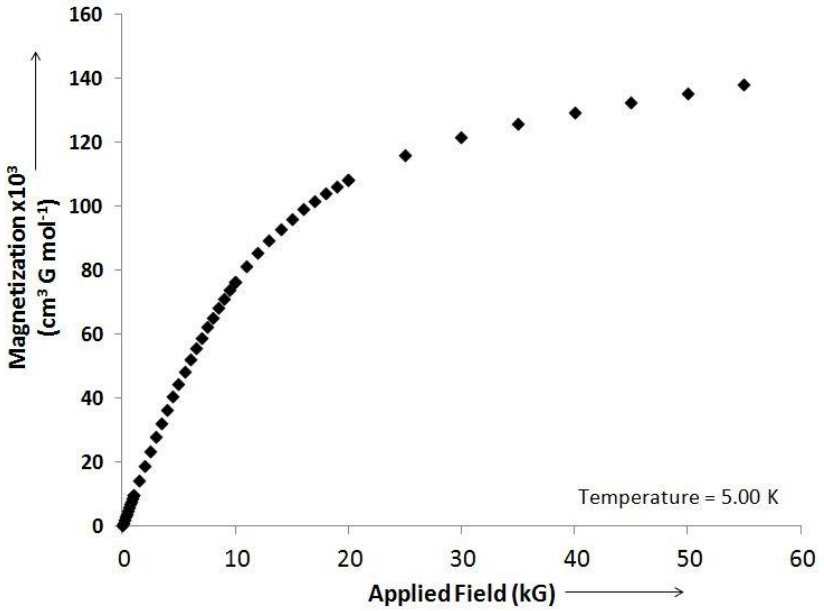

Figure 2.9. The variable field magnetization plot of **Dy_4Mn_4** is shown. The magnetization data were collected at 5.00 K.

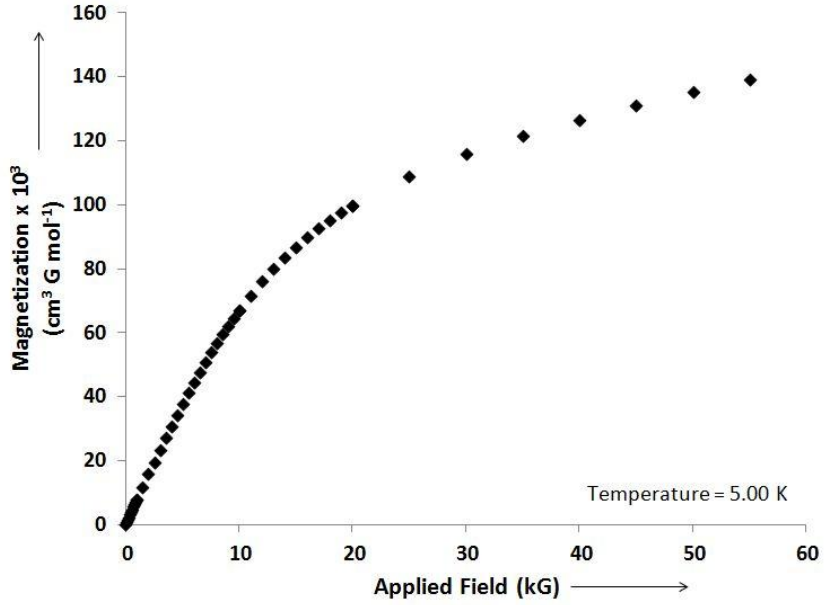

Figure 2.10. The variable field magnetization plot of **Ho_4Mn_4** is shown. The magnetization data were collected at 5.00 K.

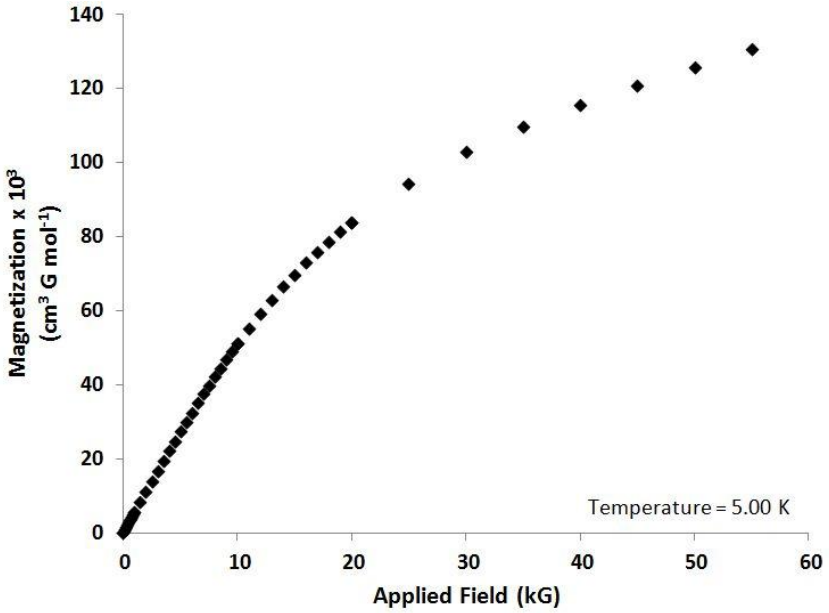

Figure 2.11. The variable field magnetization plot of **Er_4Mn_4** is shown. The magnetization data were collected at 5.00 K.

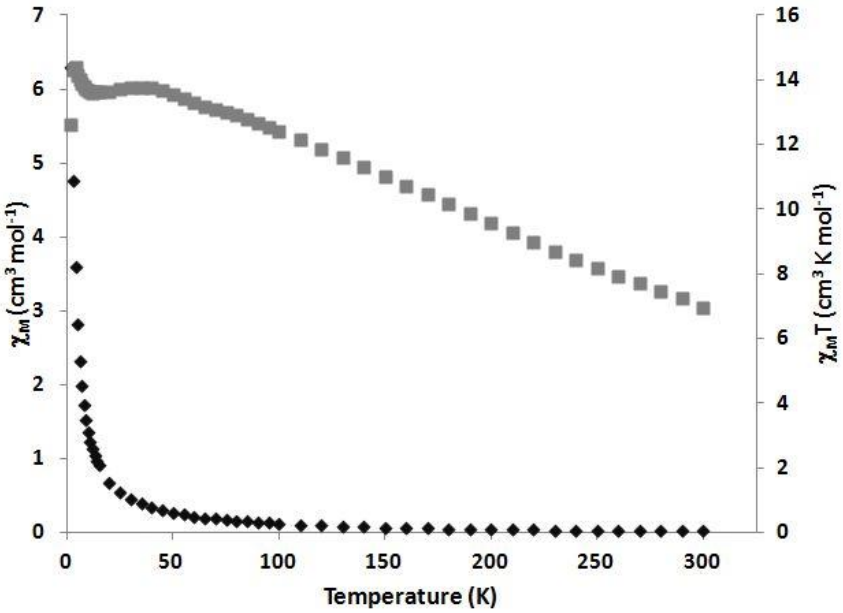

Figure 2.12. The variable temperature susceptibility plot of **Gd_6Mn_4** is shown. The susceptibility was collected with a 1000 G applied field. χ_M: ◆ $\chi_M T$: ■

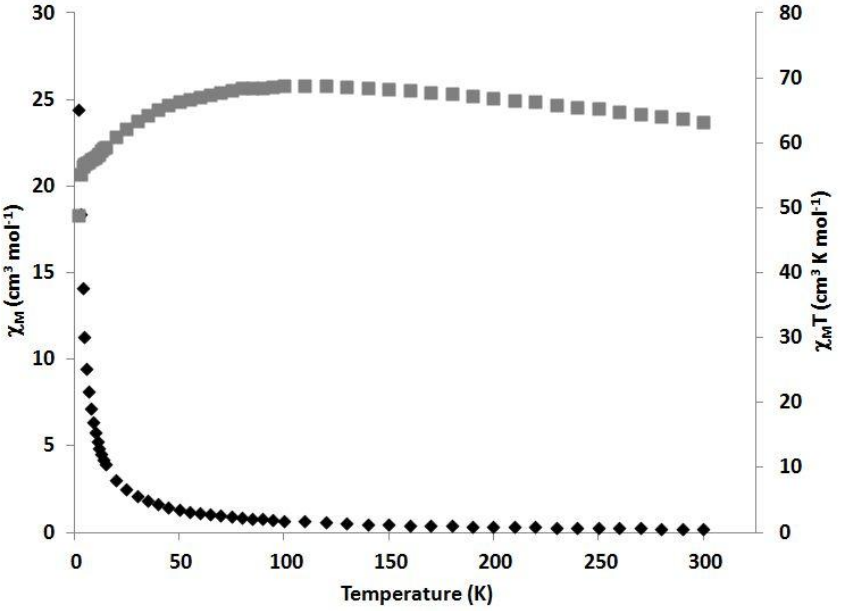

Figure 2.13. The variable temperature susceptibility plot of **Tb_6Mn_4** is shown. The susceptibility was collected with a 1000 G applied field. χ_M: ◆ $\chi_M T$: ■

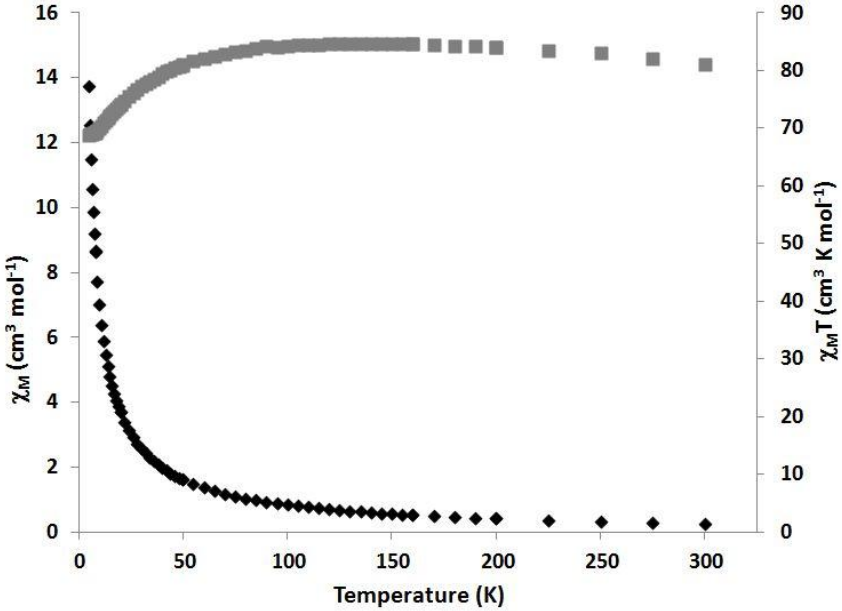

Figure 2.14. The variable temperature susceptibility plot of **Dy_6Mn_4** is shown. The susceptibility was collected with a 2000 G applied field. χ_M: ◆ $\chi_M T$: ■

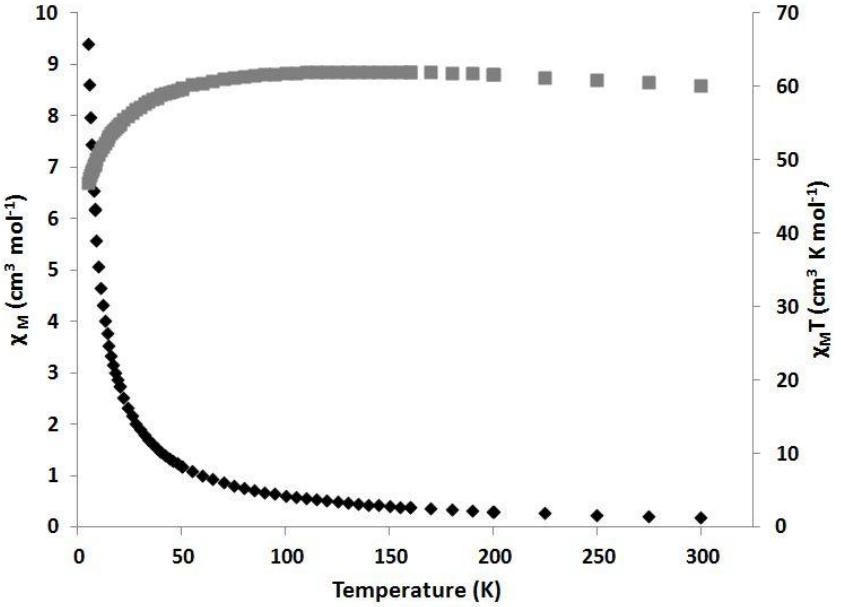

Figure 2.15. The variable temperature susceptibility plot of **Dy_4Mn_4** is shown. The susceptibility was collected with a 2000 G applied field. χ_M: ◆ $\chi_M T$: ■

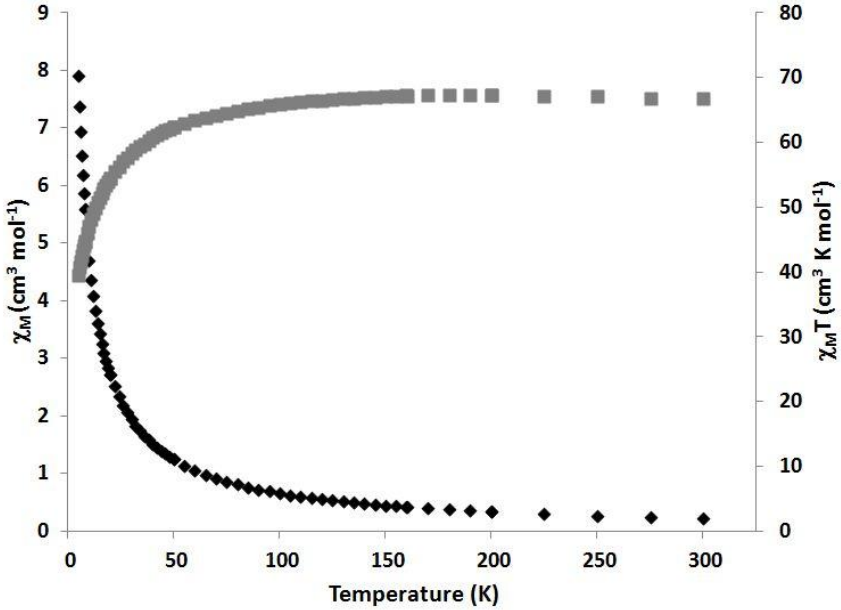

Figure 2.16. The variable temperature susceptibility plot of **Ho_4Mn_4** is shown. The susceptibility was collected with a 2000 G applied field. χ_M: ◆ $\chi_M T$: ■

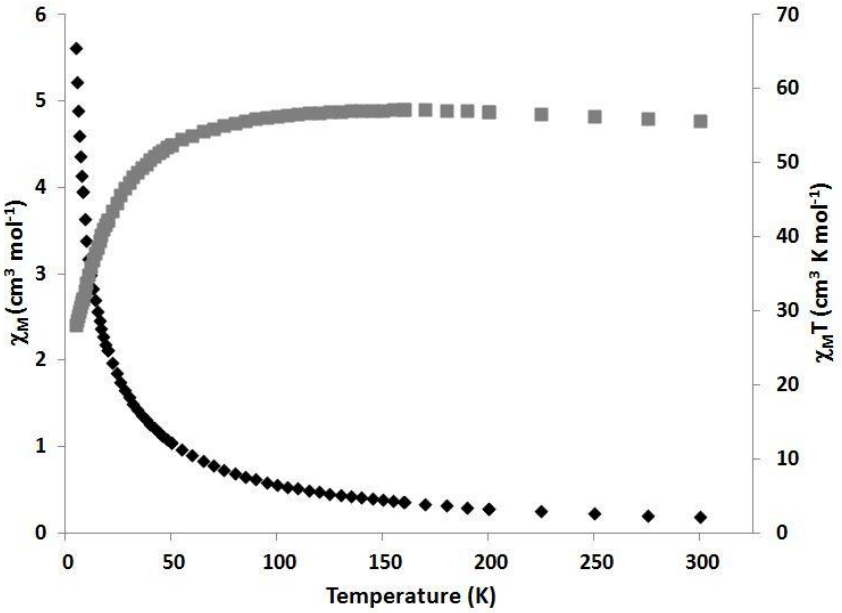

Figure 2.17. The variable temperature susceptibility plot of **Er_4Mn_4** is shown. The susceptibility was collected with a 2000 G applied field. χ_M: ◆ $\chi_M T$: ■

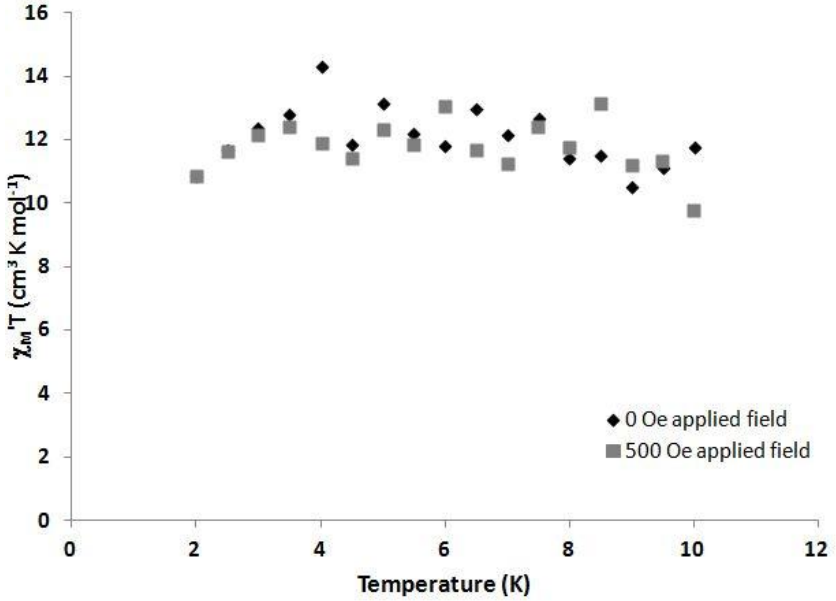

Figure 2.18. The in-phase variable temperature susceptibility plot of **Gd_6Mn_4** is shown. The susceptibility was collected with a 2.7 G drive field, 700 Hz frequency, and at the given dc applied fields.

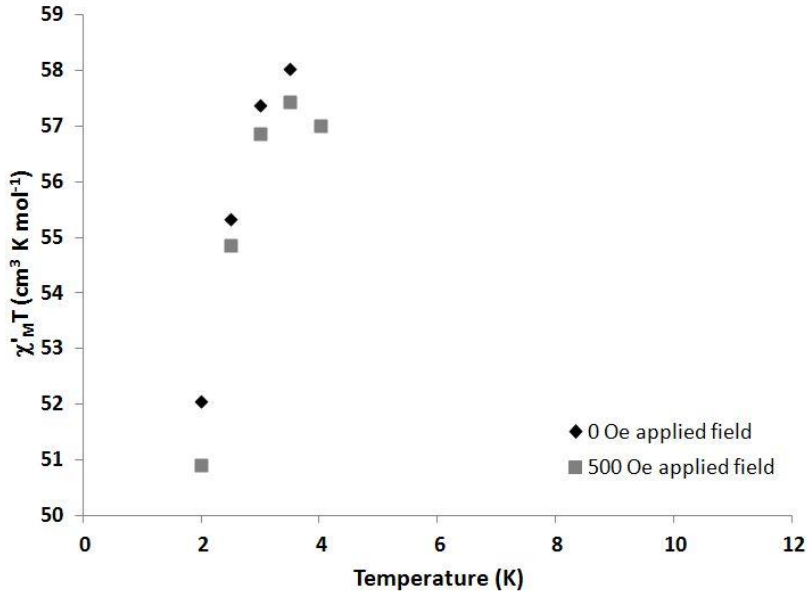

Figure 2.19. The in-phase variable temperature susceptibility plot of **Tb_6Mn_4** is shown. The susceptibility was collected with a 2.7 G drive field, 700 Hz frequency, and at the given dc applied fields.

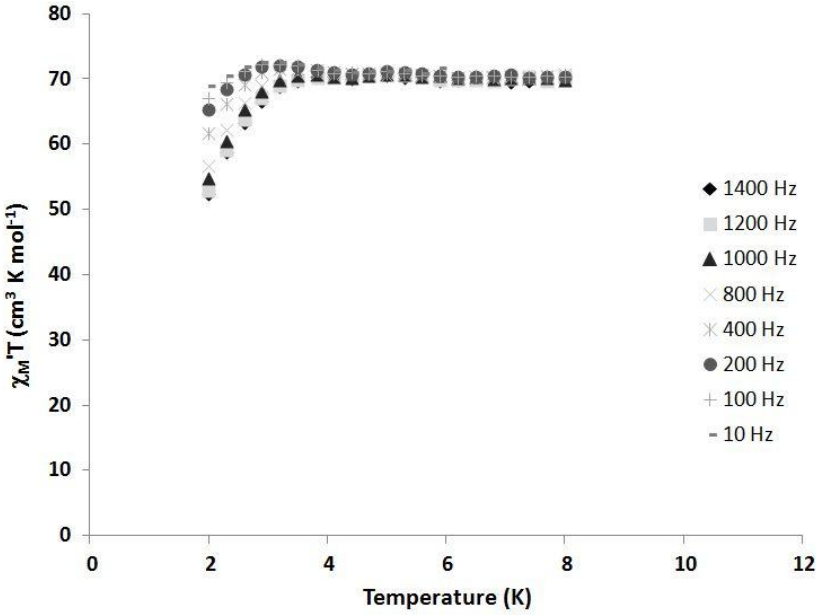

Figure 2.20. The in-phase variable temperature susceptibility plot of **Dy_6Mn_4** is shown. The susceptibility was collected with a 2.7 G drive field, 0 G dc applied field, and at the indicated frequencies.

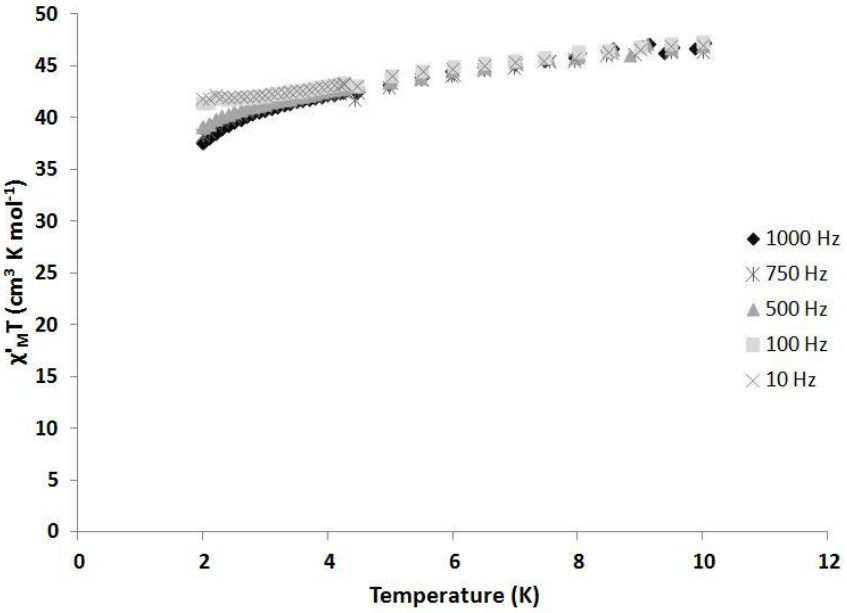

Figure 2.21. The in-phase variable temperature susceptibility plot of **Dy_4Mn_4** is shown. The susceptibility was collected with a 3.5 G drive field, 0 G dc applied field, and at the indicated frequencies.

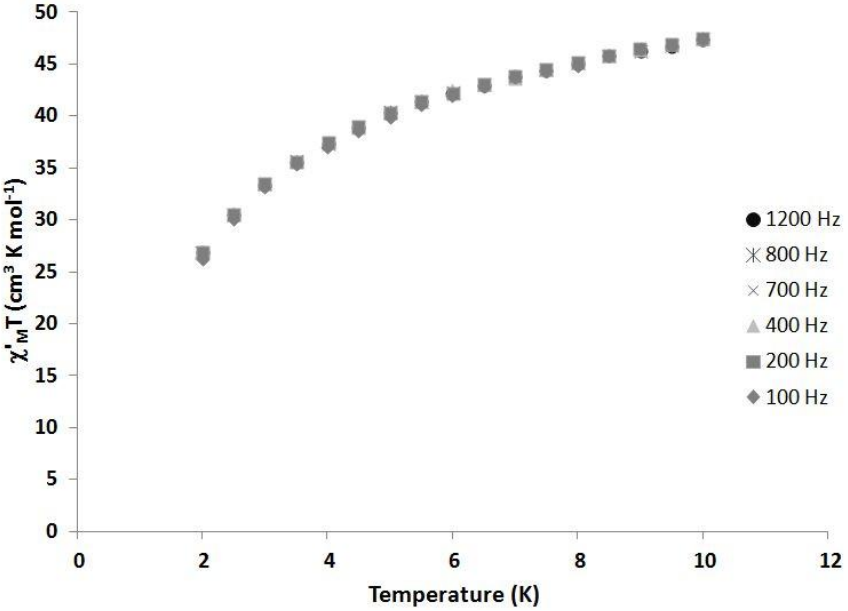

Figure 2.22. The in-phase variable temperature susceptibility plot of **Ho_4Mn_4** is shown. The susceptibility was collected with a 2.7 G drive field, 0 G dc applied field, and at the indicated frequencies.

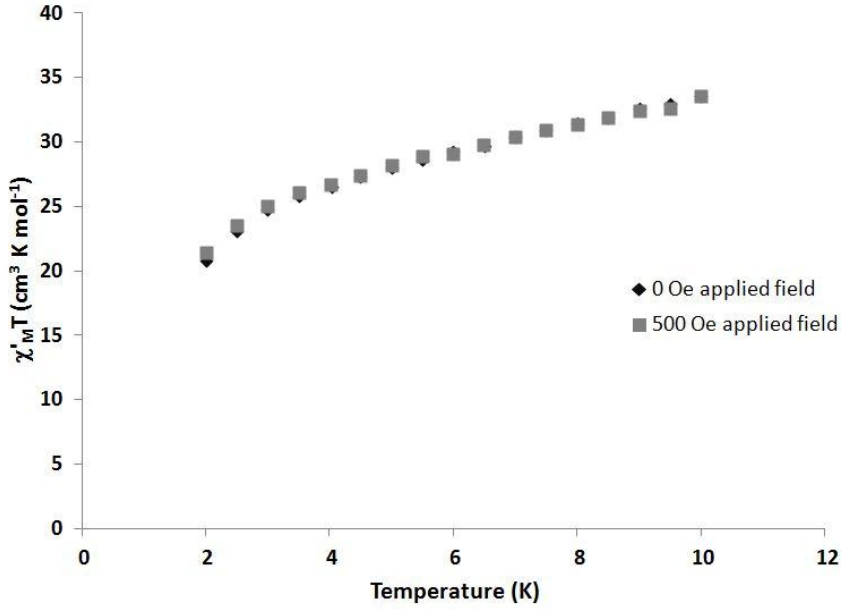

Figure 2.23. The in-phase variable temperature susceptibility plot of **Er_4Mn_4** is shown. The susceptibility was collected with a 2.7 G drive field, 700 Hz frequency, and at the indicated applied field.

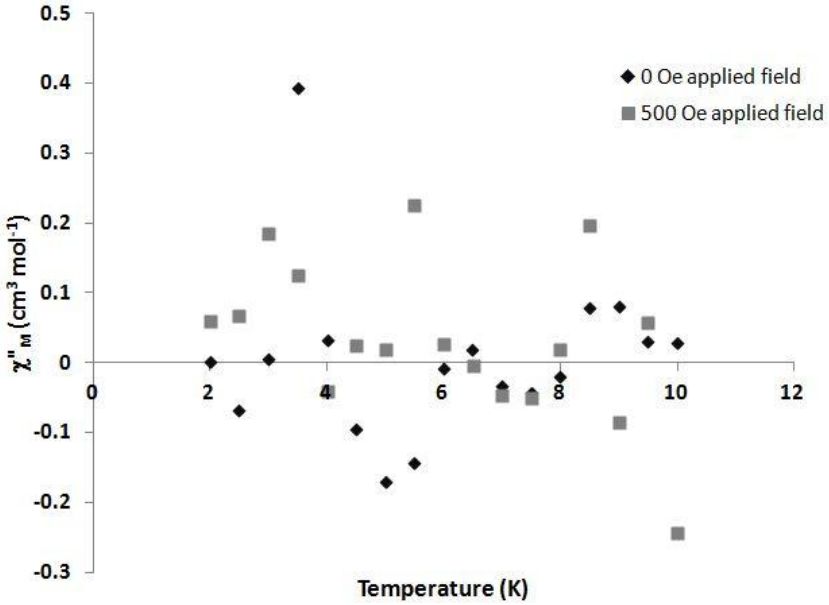

Figure 2.24. The out-of-phase variable temperature susceptibility plot of **Gd_6Mn_4** is shown. The susceptibility was collected with a 2.7 G drive field, 700 Hz frequency, and at the indicated applied fields.

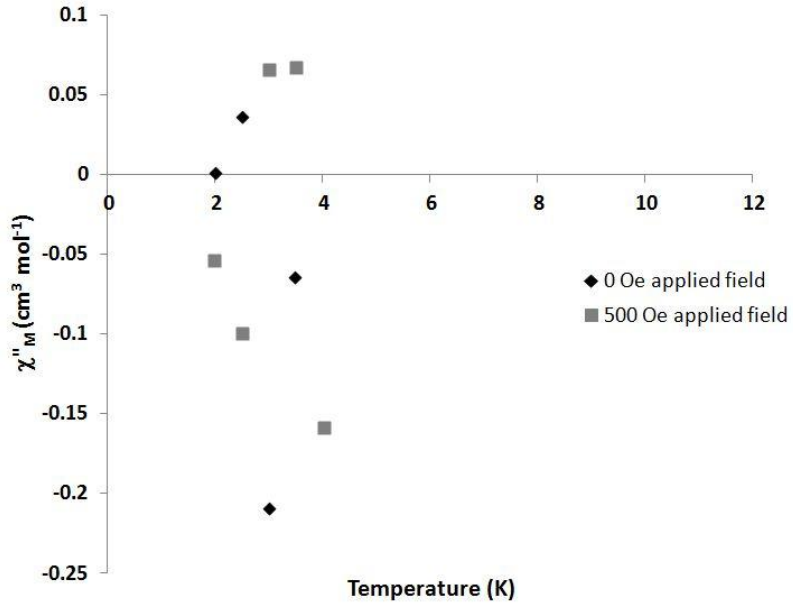

Figure 2.25. The out-of-phase variable temperature susceptibility plot of **Tb_6Mn_4** is shown. The susceptibility was collected with a 2.7 G drive field, 700 Hz frequency, and at the indicated applied fields.

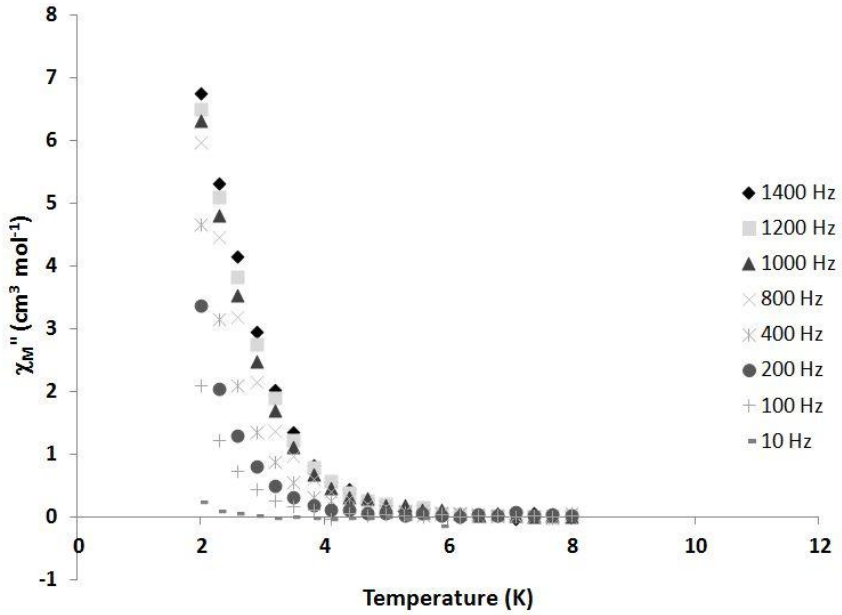

Figure 2.26. The out-of-phase variable temperature susceptibility plot of **Dy_6Mn_4** is shown. The susceptibility was collected with a 3.5 G drive field, 0 G dc applied field, and at the indicated frequencies.

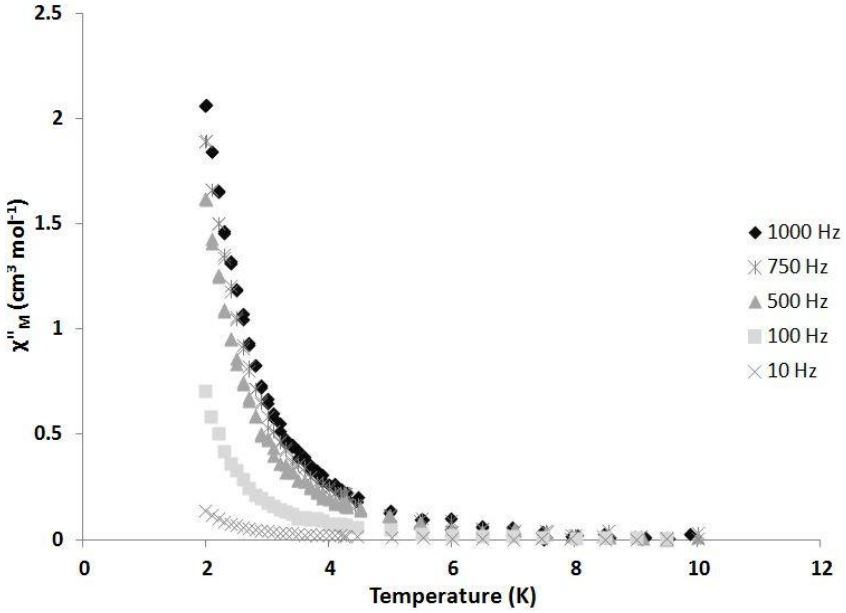

Figure 2.27. The out-of-phase variable temperature susceptibility plot of **Dy_4Mn_4** is shown. The susceptibility was collected with a 3.5 G drive field, 0 G dc applied field, and at the indicated frequencies.

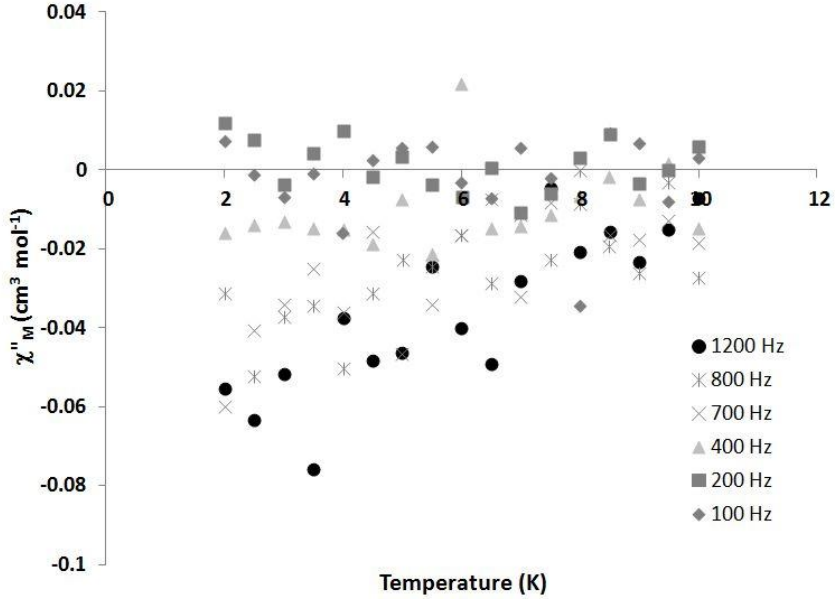

Figure 2.28. The out-of-phase variable temperature susceptibility plot of **Ho_4Mn_4** is shown. The susceptibility was collected with 2.7 G drive field, 0 G dc applied field, and at the indicated frequencies.

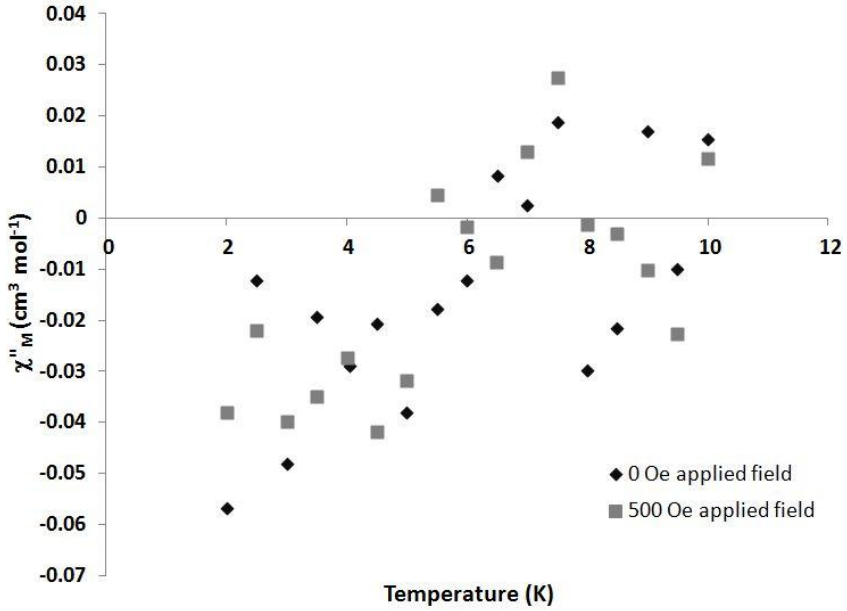

Figure 2.29. The out-of-phase variable temperature susceptibility plot of **Er_4Mn_4** is shown. The susceptibility was collected with 2.7 G drive field, 700 Hz frequency, and at the indicated applied dc fields.

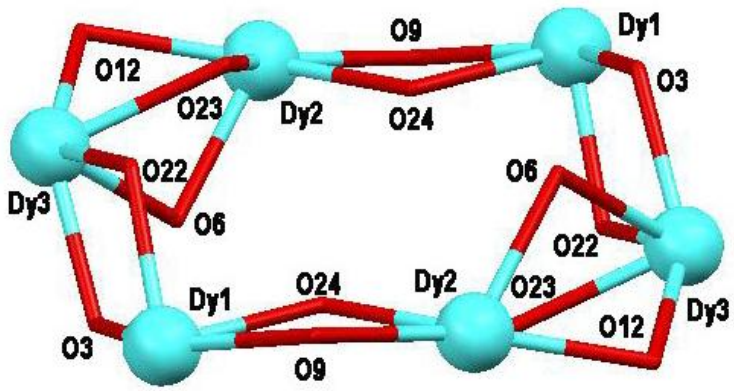

Figure 2.30. The Dy-oxo core of **Dy_6Mn_6** is highlighted. Color scheme: aqua sphere: Dy^{III}; red tube: oxygen.[1]

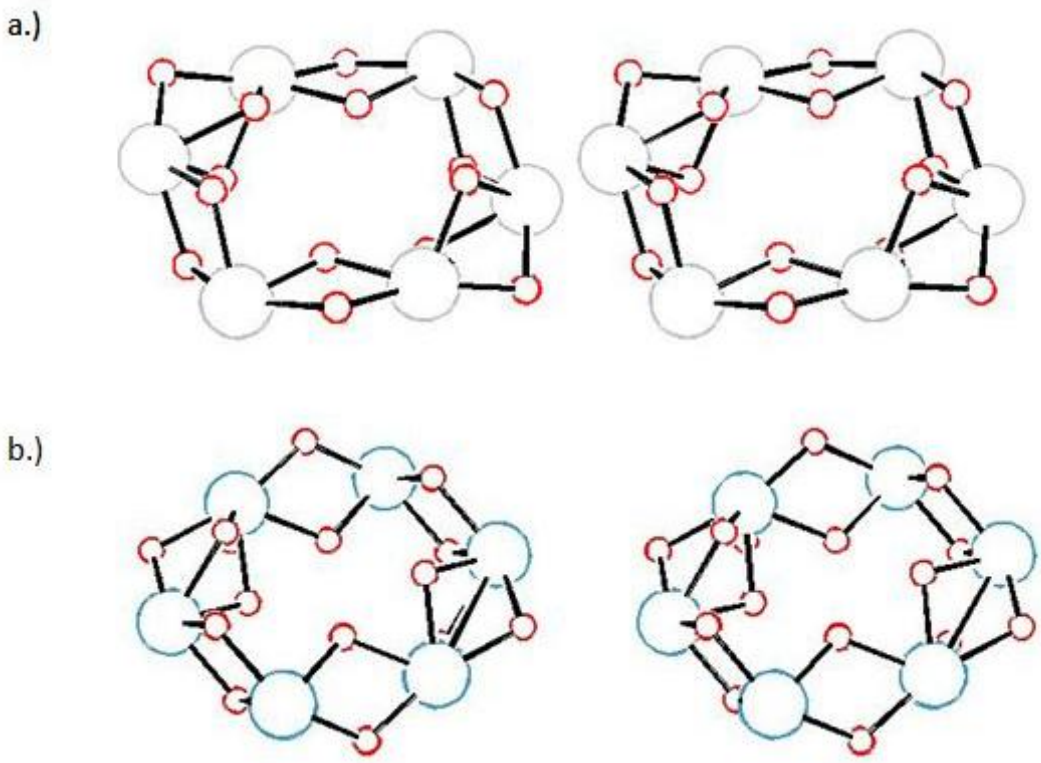

Figure 2.31. The stereo-view of the Ln_6-oxo core for a) **Ln_6Mn_6** and b) **Ln_6Mn_4** are shown.[1]

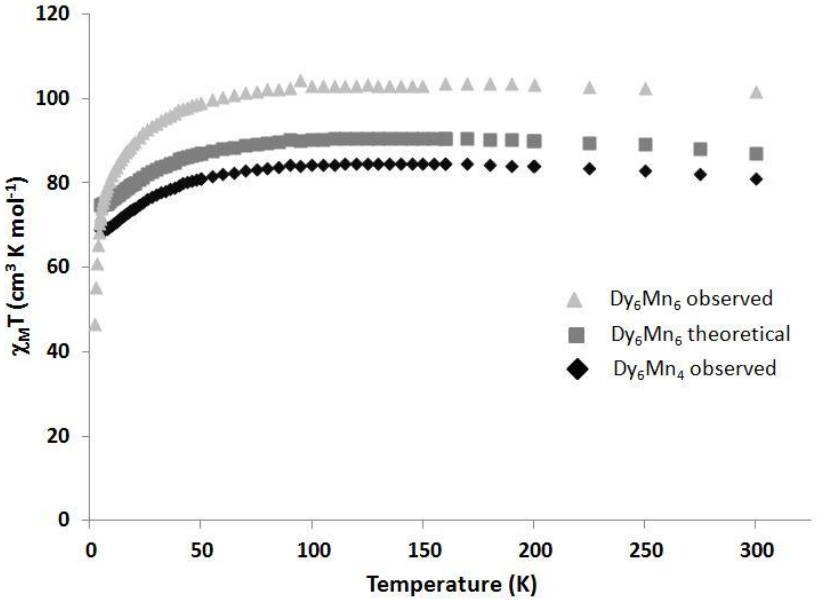

Figure 2.32. Comparing the variable temperature susceptibility plots of **Dy_6Mn_6** with **Dy_6Mn_4** reveals that the simple addition of the spin values from two Mn^{III} ions does not make up the difference. **Dy_6Mn_6** data from Zaleski, C. M. Ph.D. Thesis, Utilizing Metallacrowns to Develop New Single-Molecule Magnets, The University of Michigan, 2005.[7]

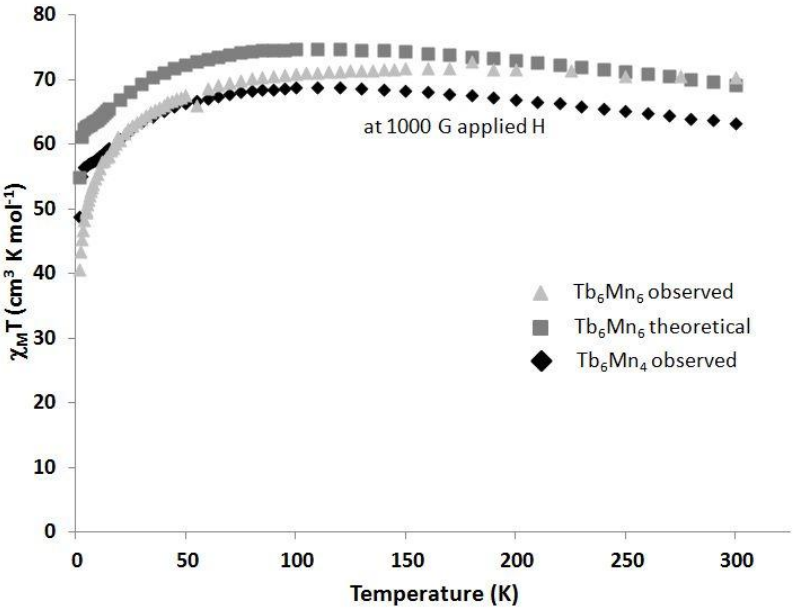

Figure 2.33. Comparing the variable temperature susceptibility plots of **Tb_6Mn_6** with **Tb_6Mn_4** reveals that the simple addition of the spin values from two Mn^{III} ions does not make up the difference. **Tb_6Mn_6** data from Zaleski, C. M. Ph.D. Thesis, Utilizing Metallacrowns to Develop New Single-Molecule Magnets, The University of Michigan, 2005.[7]

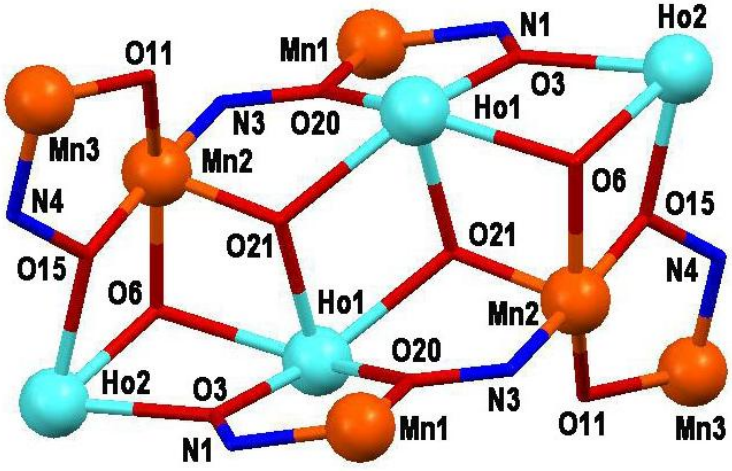

Figure 2.34. The metal core of **Ho_4Mn_6** is highlighted. Color scheme: aqua sphere: Ho^{III}; orange sphere: Mn^{III}; red tube: oxygen; blue tube: nitrogen.[8]

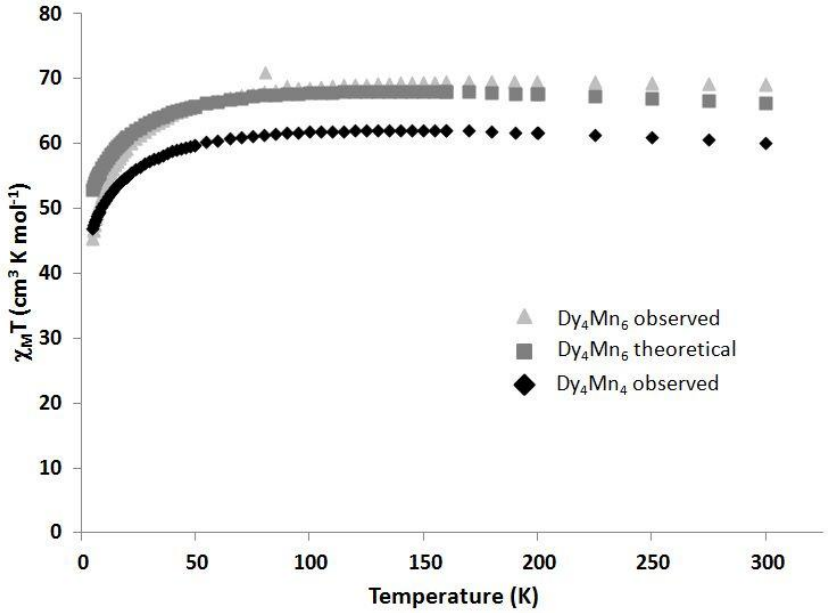

Figure 2.35. Comparing the variable temperature susceptibility data of **Dy_4Mn_6** and **Dy_4Mn_4** reveal that adding the spin-only contribution of two Mn^{III} ions is sufficient to make up the difference between the susceptibilities.[8]

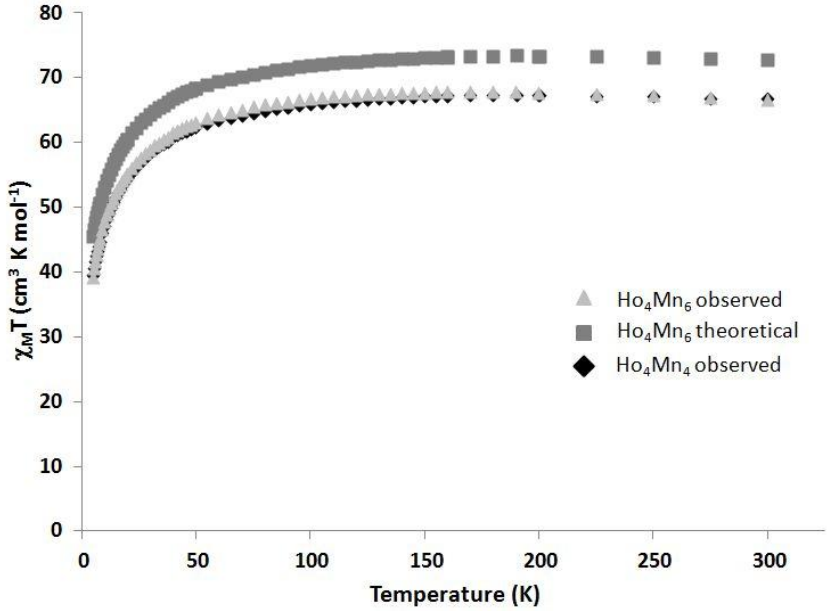

Figure 2.36. Comparing the variable temperature susceptibility data of **Ho_4Mn_6** and **Ho_4Mn_4** reveal that removing two MnIII ions does not dramatically impact the values.[8]

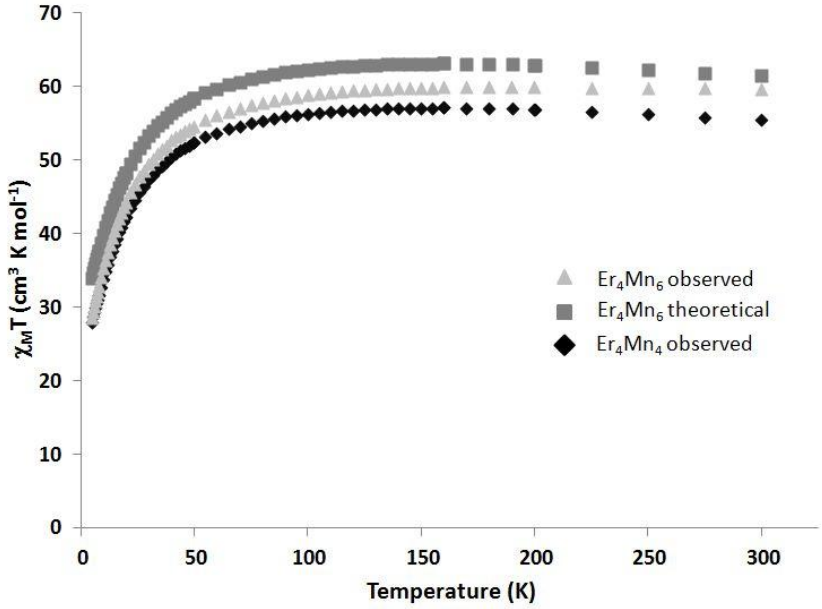

Figure 2.37. Comparing the variable temperature susceptibility data of **Er_4Mn_6** and **Er_4Mn_4** reveal that removing two Mn^{III} ions does not dramatically impact the values. **Er_6Mn_6** data from Zaleski, C. M. Ph.D. Thesis, Utilizing Metallacrowns to Develop New Single-Molecule Magnets, The University of Michigan, 2005.[7]

References

1 Zaleski, C. M.; Depperman, E. C.; Kampf, J. W.; Kirk, M. L.; Pecoraro, V. L. *Angew. Chem. Int. Ed*. **2004**, *43*, 3912.

2 Ako, A. M.; Hewitt, I. J.; Mereacre, V.; Clérac, R.; Wernsdorfer, W.; Anson, C. E. Powell, A. K. *Angew. Chem. Int. Ed*. **2006**, *118*, 5048.

3 Ako, A. M.; Mereacre, V.; Clérac, R.; Wernsdorfer, W.; Hewitt, I. J.; Anson, C. E.; Powell, A. K. *Chem. Commun*. **2009**, 544.

4 Waldmann, O.; Ako, A. M.; Güdel, H. U.; Powell, A. K. *Inorg. Chem*. **2008**, *47*, 3486.

5 Lah, M. S., Pecoraro, V. L. *J. Am. Chem. Soc*. **1989**, *111*, 7258.

6 Zaleski, C. M.; Tricard, S.; Depperman, E. C.; Wernsdorfer, W.; Mallah, T.; Kirk, M. L.; Pecoraro, V. L. *Inorg. Chem*. **2011**, *50*, 11348.

7 Zaleski, C. M. Ph.D. Thesis, Utilizing Metallacrowns to Develop New Single-Molecule Magnets, The University of Michigan, 2005.

8 Zaleski, C. M.; Kampf, J. W.; Mallah, T.; Kirk, M. L.; Pecoraro, V. L. *Inorg. Chem*. **2007**, *46*, 1954.

9 Kahn, O. *Molecular Magnetism*; VCH Publishers, New York, 1993.

10 Lah, M. S.; Pecoraro, V. L. *J. Am. Chem. Soc*. **1989**, *111*, 7258.

11 Gibney, B. R.; Wang, H.; Kampf, J. W.; Pecoraro, V. L. *Inorg. Chem*. **1996**, *35*, 6184.

12 Mezei, G.; Zaleski, C. M.; Pecoraro, V. L. *Chem. Rev*. **2007**, *107*, 4933.

13 Koumousi, E. S.; Mukherjee, S.; Beavers, C. M.; Teat, S. J.; Christou, G.; Stamatatos, T. C. *Chem. Commun*. **2011**, *47*, 11128.

14 Sessoli, R. & Powell, A. K. *Coord. Chem. Rev*. **2009**, *253*, 2328.

15 Mereacre, V.; Ako, A. M.; Clérac, R.; Wernsdorfer, W.; Hewitt, I. J.; Anson, C. E.; Powell, A. K. *Chem. Eur. J*. **2008**, *14*, 3577.

16 Mereacre, V.; Akhtar, M. N.; Lan, Y.; Ako, A. M.; Clérac, R.; Anson, C. E.; Powell, A. K. *Dalton Trans*., **2010**, *39*, 4918.

17 Mereacre, V.; Lan, Y.; Clérac, R.; Ako, A. M.; Hewitt, I. J.; Wernsdorfer, W.; Buth, G.; Anson, C. E.; Powell, A. K. *Inorg. Chem*. **2010**, *49*, 5293.

18 Mereacre, V.; Lan, Y.; Clérac, R.; Ako, A. M.; Wernsdorfer, W.; Buth, G.; Anson, C. E.; Powell, A. K. *Inorg. Chem*. **2011**, *50*, 12001.

19 Akhtar, M. N.; Lan, Y.; Mereacre, V.; Clérac, R.; Anson, C. E.; Powell, A. K. *Polyhdron*, **2009**, *28*, 1698.

20 Li, M.; Lan, Y.; Ako, A. M.; Wernsdorfer, W.; Anson, C. E.; Buth, G.; Powell, A. K.; Wang, Z.; Gao, S. *Inorg. Chem*. **2010**, *49*, 11587.

21 Mishra, A.; Wernsdorfer, W.; Abboud, K. A.; Christou, G. *J. Am. Chem. Soc*. **2004**, *126*, 15648.

22 Papatriantafyllopoulou, C.; Abboud, K. A.; Christou, G. *Inorg. Chem*. **2011**, *50*, 8959.

23 Yang, P.-P.; Wang, X.-L.; Li, L.C.; Liao, D.-Z. *Dalton Trans*. **2011**, *40*, 4155.

24 Holyńska, M.; Premuźić, D.; Jeon, I.-R.; Wernsdorfer, W.; Clérac, R.; Dehnen, S. *Chem. Eur. J*. **2011**, *17*, 9605.

25 Ke, H.; Zhao, L.; Guo, Y.; Tang, J. *Dalton Trans*. **2012**, *41*, 2314.

26 Mishra, A.; Wernsdorfer, W.; Parsons, S.; Christou, G.; Brechin, E. K. *Chem. Commun*. **2005**, 2086.
27 Papatriantafyllopoulou, C.; Wernsdorfer, W.; Abboud, K. A.; Christou, G. *Inorg. Chem*. **2011**, *50*, 421.
28 Rigaux, G.; Inglis, R.; Morrison, S.; Precimone, A.; Cadiou, C.; Evangelisti, M.; Brechin, E. K. *Dalton Trans*. **2011**, *40*, 4797.
29 Saha, A.; Thompson, M.; Abboud, K. A.; Wernsdorfer, W.; Christou, G. *Inorg. Chem*. **2011**, *50*, 10476.
30 Pecoraro, V. L.; Baldwin, M. J.; Gelasco, A. *Chem. Rev*. **1994**, *94*, 807.
31 Rinehart, J. D.; Long, J. R. *Chem. Sci*. **2011**, *2*, 2078.
32 Boron, III, T. T.; Kampf, J. W.; Pecoraro, V. L. *Inorg. Chem*. **2010**, *49*, 9104.

Chapter III

Utilizing Ln^{III} 14-$MC_{Mn^{III}Ln^{III}(\mu\text{-}O)(\mu\text{-}OH)N(shi)}$-5 as Single-Molecule Magnets

Introduction

As shown in Chapter I, metallacrowns present a unique opportunity to organize metals in a predictable geometry.[1,2,3] Metallacrowns that are organized in a planar geometry show interesting magnetic behaviors and can function as single-molecule magnets (SMMs).[4] In order to improve the magnetic properties of metallacrowns, one can attempt to perturb the system through the introduction of lanthanides. Lanthanides, intrinsically anisotropic and with large spins, present interesting, if not complicated, modifications to the magnetic properties. Vast amounts of literature are available describing the impact of lanthanides on mixed 3*d*/4*f* complexes. However, as shown in Chapter II, few complexes exist where the lanthanide can be systematically altered within a given geometry.

In metallacrown research, there are no previous reports of lanthanide metals incorporated into the metallacrown ring. A new metallacrown family, [Ln^{III} $(O_2CCH_3)_x(NO_3)_y$ 14-$MC_{Mn^{III}Ln^{III}(\mu\text{-}O)(\mu\text{-}OH)N(shi)}$-5] (herein referred to as **Ln14MC5**), where shi = triply deprotonated salicylhydroxamic acid, Ln^{III} = Y^{III}, Gd^{III}, Tb^{III}, Dy^{III}, Ho^{III}, and Er^{III}, x = 2, y = 1 for Y^{III}, Gd^{III}, Tb^{III}, Dy^{III}, and Ho^{III} , x = 0, y = 3 for Ho^{III} and Er^{III}, demonstrates a new class of planar metallacrown that behave as SMMs. It is also interesting to see how the addition of a second lanthanide into the metallacrown ring affects the magnetic properties in comparison to the previously studied **Ln 12-MC-4**.[5] This chapter will discuss the synthesis, structure, and magnetic properties of this unique MC family and the role of the lanthanide on the magnetic properties

This text relies heavily on Boron, III, T. T.; Kampf, J. W.; Pecoraro, V. L. *Inorg. Chem.* **2010**, *49*, 9104.

Experimental

Synthetic Methods

All lanthanide nitrate hydrate salts [$Gd(NO_3)_3 \cdot 6H_2O$, $Tb(NO_3)_3 \cdot 5H_2O$, $Dy(NO_3)_3 \cdot 5H_2O$, $Ho(NO_3)_3 \cdot 5H_2O$, $Er(NO_3)_3 \cdot 5H_2O$], yttrium nitrate pentahydrate [$Y(NO_3)_3 \cdot 5H_2O$], manganese acetate tetrahydrate [$Mn(O_2CCH_3)_2 \cdot 4H_2O$] were used as received from Sigma Aldrich and Alfa Aesar. Eicosane was obtained from Sigma-Aldrich and used as received. Salicylhydroxamic acid [H_3shi] was obtained from Alfa Aesar and used as received. *N,N'*-dimethylformamide [DMF] was received from Sigma Aldrich and pyridine was received from Fisher Scientific and used without any further purification.

*Synthesis of **Ln14MC5***

$[Y^{III}(O_2CCH_3)(NO_3)_2$ 14-$MC_{Mn^{III}Y^{III}(\mu\text{-}O)(\mu\text{-}OH)N(shi)}$-5]$\cdot 3C_3H_7NO \cdot 7C_5H_5N \cdot H_2O$ (**Y14MC5**). Dissolve 4 mmol $Mn(O_2CCH_3)_2 \bullet 4H_2O$ in 8.5 mL dimethylformamide. In another beaker, dissolve 4 mmol H_3shi and 0.5 mmol $Y(NO_3)_3 \bullet 5H_2O$ in 7.0 mL DMF. When $Mn(O_2CCH_3)_2 \bullet 4H_2O$ solution becomes red/orange in color, add to the $Y(NO_3)/H_3$shi solution. Stir overnight, then filter the solution, discarding the precipitate. To the filtrated, add 23.25 mL pyridine, and allow to slowly evaporate. X-ray quality crystals were obtained in 6 weeks. Yield: 68.5% Elemental analysis for $C_{79}H_{83}N_{17}O_{26}Mn_4Y_2$ [FW = 2084.19 g/mol] found % (calculated): C = 45.57, 45.42 (45.53) H = 3.96, 3.94 (4.01) N = 11.39, 11.49 (11.42). Space group: Pnnm. Unit cell dimensions: a = 28.996(3) Å, b = 16.7033(17) Å, c = 18.4340(19) Å, $\alpha = \beta = \gamma = 90.00$, V = 8928.0(16) $Å^3$.

$[Gd^{III}(O_2CCH_3)(NO_3)_2$ 14-$MC_{Mn^{III}Gd^{III}(\mu\text{-}O)(\mu\text{-}OH)N(shi)}$-5]$\cdot 3C_3H_7NO \cdot 8C_5H_5N \cdot H_2O$ (**Gd14MC5**). Dissolve 4 mmol $Mn(O_2CCH_3)_2 \bullet 4H_2O$ in 7.4 mL dimethylformamide. In another beaker, dissolve 4 mmol H_3shi and 0.5 mmol $Gd(NO_3)_3 \bullet 6H_2O$ in 6.6 mL DMF.

When $Mn(O_2CCH_3)_2 \cdot 4H_2O$ solution becomes red/orange in color, add it to the $Gd(NO_3)/H_3$shi solution. Stir overnight, then filter the solution, discarding the precipitate. To the filtrated, add 21.0 mL pyridine, and allow to slowly evaporate. X-ray quality crystals were obtained in 6 weeks. Yield 72.8%. Elemental analysis for **2**: $C_{79}H_{83}N_{17}O_{26}Mn_4Gd_2$ (FW = 2220.83 g/mol) found % (calculated): C = 42.14, 42.28 (43.74) H = 3.44, 3.50 (3.77) N = 10.70, 10.64 (10.72) Space group: Pnnm. Unit cell dimensions: a = 28.951(6) Å, b = 16.707(3) Å, c = 18.486(6) Å, $\alpha = \beta = \gamma = 90.00°$, V = 8942(4) $Å^3$.

$[Tb^{III}(O_2CCH_3)(NO_3)_2$ 14-$MC_{Mn^{III}Tb^{III}(\mu\text{-}O)(\mu\text{-}OH)N(shi)}$-5]$\cdot 3C_3H_7NO \cdot 8C_5H_5N \cdot H_2O$ (**Tb14MC5**). Dissolve 4 mmol $Mn(O_2CCH_3)_2 \cdot 4H_2O$ in 8.0 mL dimethylformamide. In another beaker, dissolve 4 mmol H_3shi and 0.5 mmol $Tb(NO_3)_3 \cdot 5H_2O$ in 7.5 mL DMF. When $Mn(O_2CCH_3)_2 \cdot 4H_2O$ solution becomes red/orange in color, add to the $Tb(NO_3)/H_3$shi solution. Stir overnight, then filter the solution, discarding the precipitate. To the filtrated, add 21.75 mL pyridine, and allow to slowly evaporate. X-ray quality crystals were obtained in 6 weeks. Yield 31.6%. Elemental analysis for $C_{79}H_{83}N_{17}O_{26}Mn_4Tb_2$ (FW = 2224.23 g/mol) found % (calculated): C = 41.76, 41.65 (42.66) H = 3.70, 3.80 (3.76) N = 10.72, 10.89 (10.71) Space group: Pnnm. Unit cell dimensions: a = 29.179(2) Å, b = 16.7785(14) Å, c = 18.5163(15) Å, $\alpha = \beta = \gamma = 90.00°$, V = 9065.1(13) $Å^3$.

$[Dy^{III}(O_2CCH_3)(NO_3)_2$ 14-$MC_{Mn^{III}Dy^{III}(\mu\text{-}O)(\mu\text{-}OH)N(shi)}$-5]$\cdot 3C_3H_7NO \cdot 8C_5H_5N \cdot H_2O$ (**Dy14MC5**). Dissolve 4 mmol $Mn(O_2CCH_3)_2 \cdot 4H_2O$ in 7.0 mL dimethylformamide. In another beaker, dissolve 4 mmol H_3shi and 0.5 mmol $Dy(NO_3)_3 \cdot 5H_2O$ in 7.0 mL DMF. When $Mn(O_2CCH_3)_2 \cdot 4H_2O$ solution becomes red/orange in color, add to the $Dy(NO_3)/H_3$shi solution. Stir overnight, then filter the solution, discarding the precipitate. To the filtrated, add 21.0 mL pyridine, and allow to slowly evaporate. X-ray quality crystals were obtained in 6 weeks. Yield 36.9%. Elemental analysis for $C_{79}H_{83}N_{17}O_{26}Mn_4Dy_2$ (FW = 2231.38 g/mol) found % (calculated): C = 42.35, 42.46 (42.52) H = 3.60, 3.60 (3.75) N = 10.69, 10.63 (10.67). Space group: Pnnm. Unit cell

dimensions: a = 29.125(4) Å, b = 16.760(3) Å, c = 18.514(3) Å, $\alpha = \beta = \gamma$ = 90.00°, V = 9037(2) Å^3.

[$Ho^{III}(O_2CCH_3)(NO_3)_2$ 14-$MC_{Mn^{III}Ho^{III}(\mu\text{-}O)(\mu\text{-}OH)N(shi)}$-5]·$2C_3H_7NO$·$7C_5H_5N$ (**Ho14MC5-1**). Dissolve 4 mmol $Mn(O_2CCH_3)_2$•$4H_2O$ in 13.0 mL dimethylformamide. In another beaker, dissolve 4 mmol H_3shi and 0.5 mmol $Ho(NO_3)_3$•$5H_2O$ in 12.0 mL DMF. When $Mn(O_2CCH_3)_2$•$4H_2O$ solution becomes red/orange in color, add to the $Ho(NO_3)$/H_3shi solution. Stir overnight, then filter the solution, discarding the precipitate. To the filtrated, add 37.5 mL pyridine, and allow to slowly evaporate. X-ray quality crystals were obtained in 4 weeks. Yield: % Elemental analysis for $C_{71}H_{69}N_{15}O_{24}Mn_4Ho_2$ (FW = 2066.028 g/mol) found % (calculated) C = 41.61, 41.71 (41.276) H = 3.57, 3.54 (3.366) N = 10.23, 10.09 (10.169) Space group: Pnnm. Unit cell dimensions: a = 29.0010(19) Å, b = 16.7165(11) Å, c = 18.4233(12) Å, $\alpha = \beta = \gamma$ = 90.00°, V = 8931.5(10) Å^3.

[$Ho^{III}(O_2CCH_3)_3$ 14-$MC_{Mn^{III}Ho^{III}(\mu\text{-}O)(\mu\text{-}OH)(N)shi}$-5]·$2C_3H_7NO$·$7C_5H_5N$·$2H_2O$ (**Ho14MC5-2**). Dissolve 4 mmol $Mn(O_2CCH_3)_2$•$4H_2O$ in 12.5 mL dimethylformamide. In another beaker, dissolve 4 mmol H_3shi and 0.5 mmol $Ho(NO_3)_3$•$5H_2O$ in 12.0 mL DMF. When $Mn(O_2CCH_3)_2$•$4H_2O$ solution becomes red/orange in color, add to the $Ho(NO_3)$/H_3shi solution. Stir overnight, then filter the solution, discarding the precipitate. To the filtrated, add 37.5 mL pyridine, and allow to slowly evaporate. X-ray quality crystals were obtained in 6 weeks. Yield 8.4 %. Elemental analysis for $C_{75}H_{79}N_{13}O_{24}Mn_4Ho_2$ (FW = 2096.14 g/mol) found % (calculated): C = 42.20, 42.20 (42.97) H = 3.64, 3.64 (3.79) N = 8.66, 8.60 (8.69). Space group: P2(1)/n. Unit cell dimensions: a = 20.450(1) Å, b = 16.428(1) Å, c = 22.926(2) Å, α = 90.000 β = 95.042(6) γ = 90.000°, V = 7672(1) Å^3.

[$Er^{III}(O_2CCH_3)_3$ 14-$MC_{Mn^{III}Er^{III}(\mu\text{-}O)(\mu\text{-}OH)(N)shi}$-5]·$2C_3H_7NO$·$6C_5H_5N$·$2H_2O$ (**Er14MC5**). Dissolve 4 mmol $Mn(O_2CCH_3)_2$•$4H_2O$ in 12.0 mL dimethylformamide. In another beaker, dissolve 4 mmol H_3shi and 0.5 mmol $Er(NO_3)_3$•$5H_2O$ in 11.0 mL DMF. When $Mn(O_2CCH_3)_2$•$4H_2O$ solution becomes red/orange in color, add to the $Er(NO_3)$/H_3shi solution. Stir overnight, then filter the solution, discarding the precipitate. To the

filtrated, add 23.0 mL pyridine, and allow to slowly evaporate. X-ray quality crystals were obtained in 6 weeks. Yield 4.4 %. Elemental analysis for $C_{70}H_{74}N_{12}O_{24}Mn_4Er_2$ (FW = 2021.7 g/mol) found % (calculated): C = 41.84, 41.84 (41.59) H = 3.42, 3.50 (3.69) N = 8.34, 8.40 (8.34). Space group: P2(1)/n. Unit cell dimensions: a = 20.4526 Å, b = 16.4126 Å, c = 22.8776 Å, α = 90.000 β = 95.101 γ = 90.000°, V = 7649.15 Å^3.

Physical Methods

X-ray Crystallography. X-ray single crystal diffraction data was collected by Dr. Jeff W. Kampf at the University of Michigan. X-ray single crystal diffraction data of **Tb14MC5** and **Dy14MC5** were also collected through the SCrALS (Service Crystallography at Advanced Light Source) program at the Small-Crystal Crystallography Beamline 11.3.1 at the Advanced Light Source (ALS), Lawrence Berkeley National Laboratory. Refinements were performed by Dr. Jeff Kampf and myself. For crystal data collected at the University of Michigan, crystals were mounted onto a standard Bruker APEX CCD-based X-ray diffractometer. The diffractometer was equipped with a LT-2 low temperature device and normal focus Mo-target X-ray tube (λ = 0.71073 Å) and operated at 2000 W power (50 kV, 40 mA). For crystal data collected at SCrALS, crystals were mounted on a D8 goniostat equipped with a Bruker APEXII CCD detector at Beamline 11.3.1 at ALS. Synchrotron radiation tuned to λ = 0.7749 Å was used. Data frames were collected using the program APEX2 and data processed using the SAINT routine within APEX2. Data were corrected for absorption and beam corrections based on the multi-scan technique as implemented in SADABS.

$[Y_2Mn_4(O_2CCH_3)(NO_3)_2(shi^{3-})_4(\mu\text{-}O)(\mu\text{-}OH)](C_5H_5N)_8(C_3H_7NO)_3H_2O$ **Y14MC5**. A green plate crystal of dimensions 0.26 x 0.15 x 0.05 mm was mounted on a standard Bruker APEX CCD-based X-ray diffractometer. Data were collected at 85(2) K. The detector was mounted 5.055 cm from the crystal. A total of 2470 frames with an exposure time of 30 s/frame was collected with 0.5° steps in ω and 0.45° steps in φ. Bruker SAINT software was used to integrate the frames using a narrow frame algorithm. A total of 169371 reflections were collected to a 2θ = 52.235°, of which 9469 reflections were unique. For the full matrix least squares refinement of F^2, 9469 reflections, 735

parameters, and 316 restraints were used. Data were processed with SADAABS and corrected for absorption. Structure solution and refinement used SHELXS-97 and SHELXL-97, respectively. The orthorhombic space group pnnm and a Z = 4 were used. Non-hydrogen atoms were refined anisotropically; hydrogen atoms were placed in idealized positions. Full matrix least-squared refinement based on F^2 converged at R_1 = 0.0633 and wR_2 = 0.1957 for [I > 2σ(I)], and R_1 = 0.0813 and wR_2 = 0.2118 for all data. Experimental parameters and crystallographic data are available in Table 3.1. Important bond distances are provided in Table 3.2.

$[Gd_2Mn_4(O_2CCH_3)(NO_3)_2(shi^{3-})_4(\mu\text{-}O)(\mu\text{-}OH)](C_5H_5N)_8(C_3H_7NO)_3H_2O$ **Gd14MC5**. The unit cell data were collected and used to characterize **Gd14MC5**.

$[Tb_2Mn_4(O_2CCH_3)(NO_3)_2(shi^{3-})_4(\mu\text{-}O)(\mu\text{-}OH)](C_5H_5N)_8(C_3H_7NO)_3H_2O$ **Tb14MC5**. A green plate crystal with dimensions 0.12 x 0.10 x 0.02 mm was mounted on a D8 goniostat with a Bruker APEXII CCD detector at Beamline 11.3.1 at ALS. Data were collected at 150(2) K. A series of 2 s data frames were measured at 0.3° intervals in ω with a maximum 2θ value of 58.26°. The data frames were collected using the program APEX2 and processed using the SAINT routine within APEX2. The data were corrected for absorption and beam corrections based on the multi-scan technique as implemented in SADABS. Of 97123 reflections collected, 9679 were unique. A total of 9679 reflections, 729 parameters and 303 restraints were used. Structure solution and refinement used SHELXS-97 and SHELXL-97, respectively. The orthorhombic space group pnnm and a Z = 4 were used. Non-hydrogen atoms were refined anisotropically; hydrogen atoms were placed in idealized positions. Full matrix least-squared refinement based on F^2 converged at R_1 = 0.0624 and wR_2 = 0.1666 for [I > 2σ(I)], and R_1 = 0.0824 and wR_2 = 0.1803 for all data. Experimental parameters and crystallographic data are available in Table 3.1. Important bond distances are provided in Table 3.3.

$[Dy_2Mn_4(O_2CCH_3)(NO_3)_2(shi^{3-})_4(\mu\text{-}O)(\mu\text{-}OH)]$ $(C_5H_5N)_8(C_3H_7NO)_3H_2O$ **Dy14MC5**. A green plate crystal with dimensions 0.06 x 0.04 x 0.01 mm was mounted on a D8 goniostat with a Bruker APEXII CCD detector at Beamline 11.3.1 at ALS. Data were

collected at 150(2) K. A series of 2 s data frames were measured at 0.3° intervals in ω with a maximum 2θ value of 49.348°. The data frames were collected using the program APEX2 and processed using the SAINT routine within APEX2. The data were corrected for absorption and beam corrections based on the multi-scan technique as implemented in SADABS. Of 98380 reflections collected, 9569 were unique. A total of 9569 reflections, 729 parameters and 303 restraints were used. Structure solution and refinement used SHELXS-97 and SHELXL-97, respectively. The orthorhombic space group pnnm and a Z = 4 were used. Non-hydrogen atoms were refined anisotropically; hydrogen atoms were placed in idealized positions. Full matrix least-squared refinement based on F^2 converged at R_1 = 0.0519 and wR_2 = 0.1332 for [I > 2σ(I)], and R_1 = 0.0904 and wR_2 = 0.1538 for all data. Experimental parameters and crystallographic data are available in Table 3.1. Important bond distances are provided in Table 3.4.

$[Ho_2Mn_4(O_2CCH_3)(NO_3)_2(shi^{3-})_4(\mu\text{-}O)(\mu\text{-}OH)](C_5H_5N)_8(C_3H_7NO)_3H_2O$ **Ho14MC5-1**. A green plate crystal with dimensions of 0.17 x 0.17 x 0.04 mm was mounted on a standard Bruker APEX-II CCD detector. Data were collected at 85(2) K. A total 2340 frames were collected for 30 s/frame at a distance 5.055 cm with 0.5° steps in ω and 0.45° steps in φ. Bruker SAINT software was used to integrate the frames using a narrow frame algorithm. A total of 162509 reflections were collected to a 2θ = 52.206°, of which 9443 reflections were unique. For the full matrix least squares refinement of F^2, 9443 reflections, 735 parameters, and 316 restraints were used. Data were processed with SADABS and corrected for absorption. Structure solution and refinement used SHELXS-97 and SHELXL-97, respectively. The orthorhombic space group pnnm and a Z = 4 were used. Non-hydrogen atoms were refined anisotropically; hydrogen atoms were placed in idealized positions. Full matrix least-squared refinement based on F^2 converged at R_1 = 0.0526 and wR*2* = 0.1578 for [I > 2σ(I)], and R_1 = 0.0649 and wR*2* = 0.1674 for all data. Experimental parameters and crystallographic data are available in Table 3.1. Important bond distances are provided in Table 3.5.

$[Ho_2Mn_4(O_2CCH_3)_3(shi^{3-})_4(\mu\text{-}O)(\mu\text{-}OH)](C_5H_5N)_7(C_3H_7N)_2(H_2O)_2$ **Ho14MC5-2**. The unit cell data were collected and used to characterize **Ho14MC5-2**.

$[Er_2Mn_4(O_2CCH_3)_3(shi^{3-})_4(\mu\text{-}O)(\mu\text{-}OH)](C_5H_5N)_6(C_3H_7N)_2(H_2O)_2$ **Er14MC5.** A green block crystal of dimensions 0.20 x 0.12 x 0.12 mm was mounted on a standard Bruker APEX-II CCD detector. Data were collected at 85(2) K. A total of 2740 frames were collected for 30 s/frame at a distance of 5.055 cm with 0.5° steps in ω and 0.45° steps in φ. Bruker SAINT software was used to integrate frames using a narrow frame algorithm. A total of 179786 reflections were collected to a 2θ = 56.64°, of which 19029 reflections were unique. For the full matrix least squares refinement of F^2, 19029 reflections and 1139 parameters were used. Data were processed with SADABS and corrected for absorption. Structure solution and refinement used SHELXS-97 and SHELXL-97, respectively. The monoclinic space group P2(1)/n and a Z = 4 were used. Non-hydrogen atoms were refined anisotropically; hydrogen atoms were placed in idealized positions. Full matrix least-squared refinement based on F^2 converged at R_1 = 0.0319 and wR_2 = 0.0825 for [I > 2σ(I)], and R_1 = 0.0409 and wR_2 = 0.0927 for all data. Experimental parameters and crystallographic data are available in Table 3.1. Important bond distances are provided in Table 3.6.

Table 3.1 The crystallographic information for **Y14MC5**, **Gd14MC5**, **Tb14MC5**, **Dy14MC5**, **Ho14MC5-1**, **Ho14MC5-2**, and **Er14MC5**.

	Y14MC5	**Gd14MC5**	**Tb14MC5**	**Dy14MC5**
Chemical Formula	$Y_2Mn_4C_{79}H_{83}N_{17}O_{26}$	$Gd_2Mn_4C_{79}H_{83}N_{17}O_{26}$	$Tb_2Mn_4C_{79}H_{83}N_{17}O_{26}$	$Dy_2Mn_4C_{79}H_{83}N_{17}O_{26}$
Formula Weight (g/mol)	2084.13	2220.83	2224.23	2231.38
Space Group	Pnnm	Pnnm	Pnnm	Pnnm
a (Å)	28.996(3)	28.951(6)	29.179(2)	29.125(2)
b (Å)	16.7033(17)	16.707(3)	16.7785(14)	16.760(3)
c (Å)	18.4340(19)	18.486(3)	18.5163(15)	18.514(3)
α (°)	90.00	90.00	90.00	90.00
β (°)	90.00	90.00	90.00	90.00
γ (°)	90.00	90.00	90.00	90.00
V (Å^3)	8928.0(16)	8942(4)	9065.1(13)	9037(2)
Temperature (K)	85(2)	85(2)	150(2)	150(2)
λ (Å)	0.71073	0.71073	0.7749	0.7749
ρ_{calc}	1.551		1.630	1.640
μ (mm^{-1})	1.92		2.70	2.93

Z	4	4	4	4
R_1 [I>2σ(I)]	0.0633		0.0624	0.0519
R_1 (all)	0.0813		0.0824	0.0904
wR_2 [I>2σ(I)]	0.1957		0.1666	0.1332
wR_2 (all)	0.2118		0.1803	0.1538

	Ho14MC5-1	**Ho14MC5-2**	**Er14MC5**
Chemical Formula	$Ho_2Mn_4C_{79}H_{83}N_{17}O_{26}$	$Ho_2Mn_4C_{75}H_{79}N_{13}O_{24}$	$Er_2Mn_4C_{70}H_{74}N_{12}O_{24}$
Formula Weight (g/mol)	2236.24	2096.14	2021.70
Space Group	Pnnm	P2(1)/n	P2(1)/n
a (Å)	29.0010(19)	20.450(1)	20.4526
b (Å)	16.7165(11)	16.428(1)	16.4126
c (Å)	18.4233(12)	22.926(2)	22.8776
α (°)	90.00	90.00	90.00
β (°)	90.00	95.042	95.101
γ (°)	90.00	90.00	90.00
V ($Å^3$)	8931.5	7672(1)	7649.15
Temperature (K)	85(2)	85(2)	85(2)
λ (Å)	0.71073	0.71073	0.71073
ρ_{calc}	1.663		1.684
μ (mm^{-1})	2.38		2.89
Z	4	4	4
R_1 [I>2σ(I)]	0.0526		0.0319
R_1 (all)	0.0649		0.0409
wR_2 [I>2σ(I)]	0.1578		0.0825
wR_2 (all)	0.1674		0.0927

Table 3.2. Selected distances (Å) of **Y14MC5** are given.

Bond	**Length (Å)**	**Bond**	**Length (Å)**
Y(1) – O(2)a	2.269(5)	Mn(1) – O(1)	1.862(4)
Y(1) – O(2)	2.269(5)	Mn(1) – O(6)	1.930(3)
Y(1) – O(12)	2.292(6)	Mn(1) – O(5)	1.935(4)
Y(1) – O(3)	2.326(3)	Mn(1) – N(1)	1.942(5)
Y(1) – O(3)a	2.326(3)	Mn(1) – N(5)	2.358(4)
Y(1) – O(13)	2.338(5)	Mn(1) – N(7)	2.300(4)
Y(1) – O(9)	2.427(18)		
Y(1) – O(11)	2.428(16)	Mn(2) – O(7)	1.862(3)
		Mn(2) – O(4)	1.885(4)
Y(2) – O(7)	2.238(4)	Mn(2) – O(8)	1.926(3)
Y(2) – O(15)	2.239(4)	Mn(2) – N(2)	1.983(4)

Y(2) – O(14)	2.280(4)	Mn(2) – N(6)	2.272(5)
Y(2) – O(3)	2.319(3)	Mn(2) – O(16)	2.352(3)
Y(2) – O(3)a	2.319(3)		
Y(2) – O(6)	2.399(3)	**Dimer Pair**	**Separation (Å)**
Y(2) – O(6)a	2.399(3)	Mn(2) – Mn(2)a	2.8025(15)

Table 3.3. Selected distances (Å) of **Tb14MC5** are given.

Bond	**Length (Å)**	**Bond**	**Length (Å)**
Tb(1) – O(2a)	2.277(7)	Mn(1) – O(1)	1.861(6)
Tb(1) – O(2)	2.277(7)	Mn(1) – O(5)	1.929(5)
Tb(1) – O(12)	2.315(9)	Mn(1) – O(6)	1.934(5)
Tb(1) – O(3)	2.343(5)	Mn(1) – N(1)	1.940(6)
Tb(1) – O(3a)	2.343(5)	Mn(1) – N(7)	2.312(6)
Tb(1) – O(13)	2.362(8)	Mn(1) – N(5)	2.368(6)
Tb(1) – O(11)	2.41(2)		
Tb(1) – O(9)	2.44(2)	Mn(2) – O(7)	1.881(5)
		Mn(2) – O(4)	1.892(6)
Tb(2) – O(7)	2.227(7)	Mn(2) – O(8)	1.924(5)
Tb(2) – O(15)	2.267(6)	Mn(2) – N(2)	1.998(6)
Tb(2) – O(14)	2.304(7)	Mn(2) – N(6)	2.274(7)
Tb(2) – O(3a)	2.329(5)	Mn(2) – O(16)	2.367(5)
Tb(2) – O(3)	2.329(5)		
Tb(2) – O(6)	2.416(5)	**Dimer Pair**	**Separation (Å)**
Tb(2) – O(6a)	2.416(5)	Mn(2) – Mn(2)a	2.815(2)

Table 3.4. Selected distances (Å) of **Dy14MC5** are given.

Bond	**Length (Å)**	**Bond**	**Length (Å)**
Dy(1) – O(2)	2.277(5)	Mn(1) – O(1)	1.860(4)
Dy(1) – O(2a)	2.277(5)	Mn(1) – O(5)	1.927(4)
Dy(1) – O(12)	2.321(7)	Mn(1) – O(6)	1.936(4)
Dy(1) – O(3a)	2.343(4)	Mn(1) – N(1)	1.938(5)
Dy(1) – O(3)	2.343(4)	Mn(1) – N(7)	2.306(4)
Dy(1) – O(13)	2.361(6)	Mn(1) – N(5)	2.367(5)
Dy(1) – O(9)	2.444(16)		
Dy(1) – O(11)	2.467(14)	Mn(2) – O(7)	1.878(4)
		Mn(2) – O(4)	1.884(4)
Dy(2) – O(7)	2.223(5)	Mn(2) – O(8)	1.925(4)
Dy(2) – O(15)	2.266(5)	Mn(2) – N(2)	1.998(5)
Dy(2) – O(14)	2.297(5)	Mn(2) – N(6)	2.279(5)
Dy(2) – O(3)	2.335(4)	Mn(2) – O(16)	2.368(4)
Dy(2) – O(3a)	2.335(4)		
Dy(2) – O(6a)	2.415(4)	**Dimer Pair**	**Separation (Å)**
Dy(2) – O(6)	2.415(4)	Mn(2) – Mn(2)a	2.8130(18)

Table 3.5. Selected distances (Å) of **Ho14MC5-1** are given.

Bond	Length (Å)	Bond	Length (Å)
Ho(1) – O(2)	2.268(6)	Mn(1) – O(1)	1.864(5)
Ho(1) – O(2a)	2.268(6)	Mn(1) – O(6)	1.922(4)
Ho(1) – O(12)	2.296(7)	Mn(1) – O(5)	1.925(4)
Ho(1) – O(3a)	2.333(4)	Mn(1) – N(1)	1.938(5)
Ho(1) – O(3)	2.333(4)	Mn(1) – N(7)	2.300(5)
Ho(1) – O(13)	2.340(6)	Mn(1) – N(5)	2.360(5)
Ho(1) – O(11)	2.424(18)		
Ho(1) – O(9)	2.43(2)	Mn(2) – O(7)	1.868(4)
		Mn(2) – O(4)	1.885(5)
Ho(2) – O(7)	2.231(6)	Mn(2) – O(8)	1.925(4)
Ho(2) – O(15)	2.251(5)	Mn(2) – N(2)	1.983(5)
Ho(2) – O(14)	2.272(5)	Mn(2) – N(6)	2.278(6)
Ho(2) – O(3)	2.321(4)	Mn(2) – O(16)	2.355(4)
Ho(2) – O(3a)	2.321(4)		
Ho(2) – O(6)	2.403(4)	**Dimer Pair**	**Separation (Å)**
Ho(2) – O(6a)	2.403(4)	Mn(2) – Mn(2)a	2.8021(19)

Table 3.6. Selected bond distances (Å) of **Er14MC5** are given.

Bond	Length (Å)	Bond	Length (Å)
Er(1) – O(20)	2.227(3)	Er(2) – O(7)	2.206(2)
Er(1) – O(13)	2.255(2)	Er(2) – O(18)	2.258(2)
Er(1) – O(23)	2.258(3)	Er(2) – O(17)	2.294(2)
Er(1) – O(3)	2.286(2)	Er(2) – O(14)	2.315(2)
Er(1) – O(2)	2.295(2)	Er(2) – O(3)	2.354(2)
Er(1) – O(14)	2.307(2)	Er(2) – O(6)	2.370(2)
Er(1) – O(19)	2.315(2)	Er(2) – O(11)	2.380(2)
Mn(1) – O(1)	1.850(2)	Mn(3) – O(7)	1.875(2)
Mn(1) – O(5)	1.916(2)	Mn(3) – O(9)	1.888(2)
Mn(1) – O(6)	1.931(2)	Mn(3) – O(8)	1.932(2)
Mn(1) – N(1)	1.939(3)	Mn(3) – N(3)	1.994(3)
Mn(1) – N(5)	2.342(3)	Mn(3) – O(16)	2.240(3)
Mn(1) – N(6)	2.423(3)	Mn(3) – N(8)	2.331(3)
Mn(2) –O(4)	1.881(2)	Mn(4) – O(12)	1.865(2)
Mn(2) – O(7)	1.924(2)	Mn(4) – O(10)	1.926(2)
Mn(2) – O(8)	1.924(2)	Mn(4) – O(11)	1.936(2)
Mn(2) – N(2)	1.996(3)	Mn(4) – N(4)	1.937(3)
Mn(2) – O(15)	2.198(2)	Mn(4) – N(9)	2.301(3)
Mn(2) – N(7)	2.342(3)	Mn(4) – N(10)	2.377(3)

Preparation of Magnetic Samples. All magnetic measurements were taken on powdered samples that were mulled in eicosane to prevent torqueing of the sample in high applied magnetic fields unless otherwise noted. Samples were ground using a small mortar and pestle, transferred to a gelatin capsule of known mass, and weighed. A small amount of melted eicosane was added and left to harden. The entire capsule was then weighed and a piece of tape applied to hold the capsule together. The capsule was then inserted into a clear plastic drinking straw.

Magnetic Measurements. All magnetic susceptibility and magnetization values were corrected using Pascal's constants.[6] Corrections were applied for the eicosane, gel capsule, and sample holder. Variable field dc magnetization experiments were performed at 5 K on a Quantum Design (QD) Magnetic Phenomena Measurement System (MPMS) Superconducting Quantum Interference Device (SQUID) magnetometer from 0 to 55000 G at the University of Michigan Department of Chemistry. Variable temperature dc susceptibility measurements were also conducted on a QD MPMS SQUID at the University of Michigan Department of Chemistry at an applied field of 2000 G between 5 and 300 K. Variable temperature ac magnetic susceptibility measurements were taken on a QD MPMS SQUID magnetometer between 2 and 10 K with zero applied dc magnetic field and a 3.5 G ac alternating field operating at frequencies between 10 and 1500 Hz at the Michigan State University Department of Physics and Astronomy.

Results

Synthesis.

All complexes are synthesized by dissolving 4 mmol $Mn(O_2CCH_3)_2 \cdot 4H_2O$ in approximately 12.5 mL DMF in one beaker. In another beaker, 4 mmol of H3shi and 0.5 mmol $Ln(NO_3)_3 \cdot 5H_2O$ are dissolved in an additional 12.5 mL DMF. Once the $Mn(O_2CCH_3)_2$ solution is reddish-orange, add to the Ln/shi solution, stirring overnight. Vacuum filter the solution in the morning, discarding and solid dark green precipitate.

One may take two routes to obtain the crystals: 1) Pour the filtrate into a large beaker and add 1.5x by volume pyridine; or 2) Pour the filtrate into small scintillation vials, adding an equal volume of pyridine to each vial. Cover the recrystallization vials or beakers with parafilm and make a single needle hole. The beakers or vials were left in the hood. In six weeks, x-ray quality crystals can be isolated.

Structural Description

A general description of **Dy14MC5** will represent **Y14MC5**, **Gd14MC5**, **Tb14MC5**, and **Ho14MC5-1**. A general description of **Er14MC5** will also represent the structure of **Ho14MC5-2**. The general metallacrown ring and connectivity is remarkably similar for these two structures. First, the orthorhombic structures will be discussed.

The structure of **Dy14MC5** (Figure 3.1) has many unique features not previously observed in manganese-lanthanide metallacrowns. The most obvious is the lack of a pseudo-rotation axis found in other metallacrowns.. There is not a standard M-N-O repeat unit as observed in a 12-MC-4 or 15-MC-5. Rather the 14-MC-5 structure has a mirror plane running down the center of the molecule, leading to a M-N-O-M-N-O-Ln-O-N-M-O-N-M connectivity. This is also the first M-N-O metallacrowns to incorporate a μ-O and μ-OH into the MC ring. The μ-O and μ-OH bridge two Mn^{III} ions. While many mixed metal[3,7,8,9] and mixed ligand metallacrowns[7] are known, **Ln14MC5** represents the first metallacrown where one ring metal differs from the other ring metals. In this case, one ring metal is a lanthanide and the other four ring metals are Mn^{III} ions.

The **Dy14MC5** has a plane of symmetry running down the Dy^{III}, Dy^{III}, oxo, hydroxo plane. Examining the metallacrown ring (Figure 3.2), two Mn^{III} ions on each half of the molecule (Mn1 and Mn2, Mn1a and Mn2a) are connected through this M-N-O connectivity found in other metallacrowns. The equatorial plane Mn1 is comprised of a six membered iminophenolate ring from one shi^{3-} ligand (O1 and N1) and a five-membered hydroximate ring from another shi^{3-} ligand (O5 and O6). The average equatorial bond length is 1.91(3) Å. The axial positions are occupied by pyridines with an

average bond length of 2.33(2) Å. The short planar bond lengths and elongated axial distances are tell-tale signs of a Jahn-Teller distortion, supporting the conclusion that Mn1 is in the 3+ oxidation state. The equatorial plane of Mn2 is also comprised of a six-membered ring iminophenolate ring provided by one shi^{3-} ligand (O4 and N2), but the other two equatorial positions are occupied by an oxo (O7) and a hydroxo ligand (O8). The bond lengths make it evident, as the bound hydroxo has a Mn2 – O8 bond length of 1.925 Å while the oxo has a Mn2 – O7 bond length of 1.878 Å. One can also deduce that O8 is a hydroxo by the close proximity of a pyridine, 2.780 Å away from the oxygen, and 1.949 Å away from the hydrogen atom. The average equatorial bond length for Mn2 is 1.92(5) Å. The axial positions are occupied by a pyridine (N6) and an oxygen (O16) from a nitrate bridging its symmetry related partner Mn2a, with an average bond length of 2.32(4) Å. Mn2 also has the signature contracted planar bond lengths and longer axial bond length of a Jahn-Teller elongated molecule. Thus, we can assign that Mn2 to also be in a 3+ oxidation state. The four manganese form the corners of a trapezoid. Mn1 and Mn1a form the base of the trapezoid and are separated by 7.555 Å. The cap of the trapezoid is formed by Mn2 and Mn2a, which are separated by 2.813 Å. The sides of the trapezoid are comprised of Mn1 to Mn2 and Mn1a to Mn2a, which have a separation of 4.701 Å. Table 4.4 provides all the bond lengths.

The last metal in the metallacrown ring is Dy1. Dy1 is in an oxygen rich, eight coordinate environment. Dy1 is bound by two five-membered hyroximate ring oxygens (O2, O2a, O3, O3a), an oxygen (O12) from a disordered dimethylformamide, two oxygens (O9 and O11) in a disordered η_2-nitrate, and an acetate oxygen (O13) which bridges it to Dy2. Dy1 and Dy2 are separated by 3.831 Å. Dy2 is seven coordinate and is also in an oxygen rich environment. It forms a pentagonal bipyramid, with four equatorial sites occupied by oxygens from the hydroximate of the shi^{3-} ligand (O3, O3a, O6, O6a) and the fifth equatorial spot occupied by an μ_3-oxo (O7) that bridges the symmetry related Mn2 ions. The axial positions are occupied by the oxygen (O14) from the acetate bridge shared with Dy1 and by an oxygen (O15) from a coordinated DMF. If a plane through the four Mn^{III} cations is drawn, Dy1 lies above the plane by 1.734 Å. Dy2 is only 0.300 Å above the manganese plane. Thus, essentially at the fifth metal of the MC ring, Dy1, the

metallacrown ring is not planar. The four Mn^{III} ions exist in a single plane and Dy2 is slightly above the plane. The planarity of the molecule is important because the likelihood of anisotropy vectors accidentally canceling decreases significantly with this topology. Table 3.4 provides the details of the bond lengths.

Across the series, there is not a significant change in topology. Looking at the bond lengths reported in Tables 3.2 – 3.5 there is not a significant change across the series. For **Y14MC5**, the Y1 ion sits 1.743 Å above the Mn plane and Y2 sits 0.306 Å above the plane. In the **Tb14MC5** structure, Tb1 is 1.738 Å above the Mn mean plane and Tb2 is 0.301Å above the plane. For **Ho14MC5-1**, Ho1 sits 1.742 Å above the Mn mean plane and Ho2 sits 0.307 Å above the plane.

The structure of **Er14MC5** (Figure 3.3) and **Ho14MC5-2** has many of the same unique features as **Dy14MC5**. **Er14MC5** lacks the pseudo rotation symmetry element found in standard 12-MC-4 and 15-MC-5 complexes. Like **Dy14MC5**, there is the same M-N-O-M-N-O-Ln-O-N-M-O-N-M connectivity as well as a molecular mirror plane down the center of the molecule. Two Mn^{III} ions are connected by a μ-O and μ-OH. One ring metal is different than the other four and is again a Ln^{III} ion (Figure 3.4). These similarities should not be surprising, given that the syntheses of **Er14MC5** and **Dy14MC5** are so similar.

As the metallacrown connectivity is so similar, it is best to simply compare the major similarities and differences between **Er14MC5** (Figure 3.3) and **Dy14MC5** (Figure 3.1). The oxidation states were found to be the same as above, only substituting acetate ions for nitrates. Like before, the four manganese ions form an imaginary trapezoid, with Mn1 and Mn4 creating the long base and Mn2 and Mn3 forming the short cap. Mn1 and Mn4 are separated by 7.515 Å. Mn2 and Mn3 are separated by a distance of 2.785 Å. Mn1 and Mn2 are separated by 4.679 Å while Mn3 and Mn4 are separated by 4.705 Å. Er1 and Er2 are separated by 3.800 Å. These distances are remarkably similar to those found in **Dy14MC5** (Mn1 – Mn1a = 7.555 Å; Mn2 – Mn2a = 2.813 Å; Mn1 – Mn2 = 4.701 Å; Dy1 – Dy2 = 3.831 Å). These slight differences can be attributed to the so-called

lanthanide contraction.[10] Similarities were also found in the bond lengths; the bond lengths for **Er14MC5** are summarized in Table 3.6.

One difference between **Er14MC5** and **Dy14MC5** is the fact that Er1 and Er2 are both seven coordinate. However, this should not be surprising; Er, because of its smaller ionic radius (0.945 Å), can only accommodate seven ligands.[10] The difference in coordination environment is only observed by the fact that the one acetate can only bind monodentate to Er1 in **Er14MC5** where a bidentate nitrate was possible in **Dy14MC5**. Another difference is the distance Er1 is out of the Mn plane. There is a plane that can be defined by the four Mn ions, as was the case in **Dy14MC5**. However, in the **Er14MC5** structure, Er1 is 1.447 Å above the plane, which is much less than that of the other Ln^{III} ions. Er2 matches closely to the out of plane distances (0.306 Å) of the other **Ln14MC5** structures. Another key difference is the change of the hydrogen bonding partner to O8; a water (2.800 Å) in **Er14MC5** and a pyridine (2.780 Å) in **Dy14MC5**. Crystallographically, **Dy14MC5** has a mirror plane running through the center of the molecule whereas the **Er14MC5** structure does not have this crystallographic mirror. The last key difference is in the packing diagrams of the two structures. **Dy14MC5** is packed much closer to its neighbors: the smallest separation between magnetic centers is 7.442 Å between Dy1 of one molecule and Dy1 of its neighbor. For **Er14MC5**, the closest interaction between magnetic centers is 9.099 Å between Mn1 of one structure and Mn4 of its neighbor.By comparing the magnetic properties of **Ho14MC5-1** and **Ho14MC5-2**, one can directly detect if these structural parameters affect the magnetism.

Variable Field dc SQUID Magnetometer Magnetization Measurements

Variable field dc magnetization measurements for all compounds were taken on samples prepared as described above using a QD MPMS SQUID magnetometer operating at a temperature of 5 K and varying an external applied field from 0 G to 55000 G. For **Ho14MC5-1**, the measurements were taken on a QD MPMS7 SQUID magnetometer at 2 K and varying an external applied field from 0 G to 55000 G. At the largest applied field,

none of the samples showed a saturated signal, thus the ground spin state of the complexes could not be determined using the Brillion function.

The magnetization values of **Y14MC5** continuously increases from 0 G applied field to a maximum of 27650 cm^3 G mol^{-1} at 55000 G (Figure 3.5). This increase is almost linear and very different from any other complex studied. For **Gd14MC5**, magnetization values reach a maximum of 118900 cm^3 G mol^{-1} at an applied field of 55000 G (Figure 3.6). This plot also seems to be quite linear, but there is an inflection point near 25000 G where the magnetization values begin to slope. For **Tb14MC5**, the magnetization increases to a maximum of 75900 cm^3 G mol^{-1} at an applied field of 55000 G (Figure 3.7). For **Dy14MC5**, the magnetization increases to a maximum of 87420 cm^3 G mol^{-1} at an applied field of 55000 G (Figure 3.8). For both **Tb14MC5** and **Dy14MC5**, the deviation from linear magnetization values begins near 10000 G applied field. For **Ho14MC5-1**, the magnetization increases linearly until 5000 G, before slowly increasing and reaching a maximum of 84040 cm^3 G mol^{-1} (Figure 3.9). **Ho14MC5-2** shows a deviation point at 10000 G applied field and reaches a maximum of 97950 cm^3 G mol^{-1} at 55000 G (Figure 3.10). Lastly, **Er14MC5** reaches a maximum of 86520 cm^3 G mol^{-1} at an applied field of 55000 G (Figure 3.11). **Er14MC5** seems to deviate from linear behavior closer to 15000 G applied field.

Variable Temperature dc SQUID Magnetometer Magnetic Susceptibility Measurements

Variable temperature dc SQUID magnetometer magnetic susceptibility measurements were taken on powdered samples that were prepared as described above. They were measured on a QD MPMS dc SQUID magnetometer. There was an applied field of 2000 G and the temperature was raised slowly from 5 K to 300 K. For Ho14MC5-1, the measurements were conducted on a QD MPMS7 dc SQUID magnetometer with an applied field of 1000 G and decreasing the temperature from 300 K to 2 K. For simplicity, only the $\chi_M T$ values will be discussed.

For **Y14MC5** (Figure 3.12), the complex had a maximum $\chi_M T$ at 300 K of 7.1 cm^3 K mol^{-1}, which is less for four non-interacting Mn^{III} ions ($\chi_M T$ = 12.00 cm^3 K mol^{-1}). From 300 K to 5 K, the susceptibility curve slowly decreased. A sharp decrease is observed near 16 K, which continued until 5 K (2.5 cm^3 K mol^{-1}). If the data from 8.00 K to 5.00 K is extrapolated to 0 K, the $\chi_M T$ value reaches 0.55 $\chi_M T$ $cm^3 K mol^{-1}$, which is close to 0. For **Gd14MC5** (Figure 3.13), from 300 K (24.8 cm^3 K mol^{-1}) until 50 K, the $\chi_M T$ value actually slightly increases, before decreasing slowly before decreasing quicker near 19 K until it reaches a minimum of 19.6 cm^3 K mol^{-1} at 5 K. Extrapolating the data from 8 K to 5 K to 0 K gives a $\chi_M T$ value of 15.3 cm^3 K mol^{-1}. In the case of **Tb14MC5** (Figure 3.14), from 300 K (27.1 cm^3 K mol^{-1}), there is a very small increase until approximately 150 K, at which point the susceptibility slowly decreases. Near 100 K, there is a significant decrease in the $\chi_M T$ vs. T plot, which led to a more precipitous decline near 20 K before reaching a value of 21.4 cm^3 K mol^{-1} at 5 K. Extrapolating the data from 8 K to 5 K to 0 K gave a $\chi_M T$ value of 19.0 cm^3 K mol^{-1}. For **Dy14MC5** (Figure 3.15), from 300 K (36.1 cm^3 K mol^{-1}) until approximately 28 K, there is a steady decrease. Near 15 K, there is a dramatic decrease until the minimum at 5 K (26.2 cm^3 K mol^{-1}) is obtained. Extrapolating the $\chi_M T$ value from 8 K to 5 K leads to a $\chi_M T$ value of 23.2 cm^3 K mol^{-1}. The susceptibility of **Ho14MC5-1** (Figure 3.16) remained fairly constant from 300 K to 45 K before dramatically decreasing. At 300 K, the susceptibility was 31.08 cm^3 K mol^{-1}. At 2 K, the susceptibility was 18.77 cm^3 K mol^{-1}. Extrapolating from 8 K to 2 K, a susceptibility at 0 K was found to be 17.51 cm^3 K mol^{-1}. For **Ho14MC5-2**, (Figure 3.17), there is a constant and significant decrease from 300 K (57.0 cm^3 K mol^{-1}) until near 14 K, where this is the dramatic decrease until 5 K (27.4 cm^3 K mol^{-1}). Extrapolating the $\chi_M T$ value from 8 K to 5 K, the $\chi_M T$ value reaches a minimum of 23.3 cm^3 K mol^{-1}. For **Er14MC5** (Figure 3.18), from 300 K (27.9 cm^3 K mol^{-1}) until 50 K, the $\chi_M T$ value remains relatively constant. It then decreases until it reaches a minimum of 16.8 cm^3 K mol^{-1} at 5 K. Extrapolating the $\chi_M T$ value from 8 K to 5 K leads to a value of 13.0 cm^3 K mol^{-1}.

Variable Temperature ac SQUID Magnetometer Magnetic Susceptibility.

Variable temperature ac SQUID magnetic susceptibility measurements were conducted on the prepared powdered samples. Measurements were made in 0 G dc applied field, a 3.5 G ac drive field, with temperatures ranging from 2 K to 10 K, and frequencies ranging from 10 Hz to 1000 Hz. In addition to these measurements, **Dy14MC5** was also measured to a temperature of 100 K and an additional high frequency data (1500 Hz) was conducted. Measurements were conducted at the Michigan State University Department of Physics and Astronomy on a QD MPMS ac SQUID magnetometer or at the Unviersity of Michigan Department of Chemistry on a QD MPMS7 SQUID magnetometer. The help of Dr. Reza Loloee is acknowledged for his help with setting up the SQUID at Michigan State and assisting in the measurements.

The experiments were conducted as follows: The sample was loaded and centered at a small dc field of 1000 G at 125 K. The dc field was removed and the sample was cooled to 10 K. A drive field of 3.5 G and a frequency of 1000 Hz was set, and the temperature was then lowered from 10 K to 4.5 K in 0.5 K increments. From 4.3 K to 2 K, the temperature was decreased in 0.1 K increments. The temperature was then set to 10 K, the frequency changed to 100 K and repeated. This process continued for 500 K, 10 K and 750 K (when applicable). From these experiments, in-phase and out-of-phase ac SQUID susceptibility data were collected.

If a complex shows slow magnetic relaxation, one can estimate the magnitude of the energy barrier of spin relaxation U_{eff} by fitting the maximum of χ''_M vs. T to the Arrhenius plot,

$$\frac{1}{\tau} = \frac{1}{\tau_0} e^{-\frac{U_{eff}}{k_B T}} \qquad (1)$$

which can be rearranged to solve for U_{eff},

$$\ln\frac{1}{\tau} = -\frac{U_{eff}}{k_B T} + \ln\frac{1}{\tau_0} \quad (2)$$

where k_B is the Boltzmann constant, T is the temperature at the maximum χ''_M, τ_0 is the pre-exponential factor, and τ is related to the frequency f through the equation.

$$\frac{1}{\tau} = 2\pi f \quad (3)$$

The in-phase susceptibility of **Y14MC5** showed that for all frequencies, nearly the same $\chi'_M T$ vs. T values were obtained (Figure 3.19). At 10 K and 1000 Hz frequency, the $\chi'_M T$ value was 4.25 cm^3 K mol^{-1}, and at 2 K and 1000 Hz, the $\chi'_M T$ value was 0.83 cm^3 K mol^{-1}. Below 8 K, the data was linear. Using the data between 10 K and 4.5 K, the ground spin state was calculated to be 0.22; practically 0. For **Gd14MC5**, nearly the same $\chi'_M T$ vs. T values were obtained for all studied frequencies (Figure 3.20). At 10 K and 1000 Hz, the $\chi'_M T$ value was 23.88 cm^3 K mol^{-1}, and at 2 K and 1000 Hz, the $\chi'_M T$ value was 14.78 cm^3 K mol^{-1}. For **Tb14MC5**, nearly the same $\chi'_M T$ vs. T values were obtained for all studied frequencies (Figure 3.21). At 10 K and 1000 Hz, the $\chi'_M T$ value was 21.88 cm^3 K mol^{-1}, and at 2 K and 1000 Hz, the $\chi'_M T$ value was 16.36 cm^3 K mol^{-1}. For **Dy14MC5**, nearly the same $\chi'_M T$ vs. T values were obtained for all studied frequencies until approximately 3 K, where there was significant divergence for all frequencies (Figure 3.22). At 10 K and 1500 Hz, the $\chi'_M T$ value was 27.23 cm^3 K mol^{-1}, which was very close to the value of $\chi'_M T$ for all the other studied frequencies. At 2 K and 1500 Hz, the $\chi'_M T$ value was 14.89 cm^3 K mol^{-1}, at 1000 Hz, the $\chi'_M T$ value was 16.09 cm^3 K mol^{-1}, at 750 Hz, the $\chi'_M T$ value was 16.49 cm^3 K mol^{-1}, at 500 Hz, the $\chi'_M T$ value was 17.97 cm^3 K mol^{-1}, at 100 Hz, the $\chi'_M T$ value was 21.19 cm^3 K mol^{-1}, and at 10 Hz, the $\chi'_M T$ value was 21.97 cm^3 K mol^{-1}. For **Ho14MC5-1** (Figure 3.23), the $\chi'_M T$ vs. T values were the same until near 2.5 K, where they begin to diverge slightly. At 10 K and 1000 Hz, the $\chi'_M T$ value was 27.74 cm^3 K mol^{-1}. At 2 K for 1000 Hz, the $\chi'_M T$ value was 18.8 cm^3 K mol^{-1}, for 500 Hz, the $\chi'_M T$ value was 19.08 cm^3 K mol^{-1}, for 100 Hz, $\chi'_M T$ value was 19.51 cm^3 K mol^{-1}, and for 10 Hz, the $\chi'_M T$ value was 19.77 cm^3 K mol^{-1}. For

Ho14MC5-2, the $\chi'_M T$ vs. T values were the same until near 2.5 K, at which point they began to diverge (Figure 3.24). At 10 K and 1000 Hz, the $\chi'_M T$ value was 28.58 cm^3 K mol^{-1}. At 2 K, for a frequency of 1000 Hz, the $\chi'_M T$ value was 19.39 cm^3 K mol^{-1}; at a frequency of 750 Hz the $\chi'_M T$ value was 19.55 cm^3 K mol^{-1}; when the frequency was 500, the $\chi'_M T$ value was 19.79 cm^3 K mol^{-1}; at 100 Hz, the $\chi'_M T$ value was 20.48 cm^3 K mol^{-1}; and at 10 Hz, the $\chi'_M T$ value was 20.79 cm^3 K mol^{-1}. For **Er14MC5**, the $\chi'_M T$ vs. T values were fairly similar for all frequencies in the studied temperature regime (Figure 3.25). At 10 K, the 1000 Hz frequency $\chi'_M T$ value was 18.8 cm^3 K mol^{-1}. At 2 K, the 1000 Hz frequency $\chi'_M T$ value was 12.16 cm^3 K mol^{-1}.

Studying the out-of-phase behavior of the complexes, **Y14MC5** (Figure 3.26) and **Gd14MC5** (Figure 3.27) did not show frequency dependence. On the other hand, the **Tb14MC5** (Figure 3.28), **Dy14MC5** (Figure 3.29) (showing the area near the blocking temperature (Figure 3.30)), **Ho14MC5-1** (Figure 3.31), **Ho14MC5-2** (Figure 3.32), and **Er14MC5** (Figure 3.33) complexes all demonstrated frequency dependent behavior. The **Tb14MC5**, **Ho14MC5-1**, **Ho14MC5-2**, and **Er14MC5** complexes all showed weak frequency dependence behavior, with the onset of slow relaxation beginning near 2.5 K for **Ho14MC5-1** and **Ho14MC5-2**, and near 2 K for **Tb14MC5** and **Er14MC5**. The **Dy14MC5** analog, on the other hand, showed very strong frequency dependence and even had turnover values for χ''_M vs. *T*, allowing for the calculation of an effective barrier of spin relaxation as described in Equation 4. Maxima were found at 1500 Hz, 1000 Hz (this was measured twice), and 750 Hz at temperatures of 2.17 K, 2.07, and 1.99 K, respectively. Plotting the values $1/T$ vs. $\ln(1/(2\pi * f))$ (Figure 3.34) led to a linear equation $\ln(\tau) = 16.687*(1/T) + 16.824$. From this, a U_{eff} of 16.7 K (11.6 cm^{-1}) and a pre-exponential value $\tau_0 = 4.9 \times 10^{-8}$ s was determined.

Trying to better understand the magnetic coupling of the complexes, a spin Hamiltonian was written for **Y14MC5**. The proposed spin Hamiltonian is based on Figure 3.35. Because Y is diamagnetic, it will not contribute to the spin Hamiltonian. The derived equation was

$$\mathbf{H} = -2J_1(\mathbf{S}^1\cdot\mathbf{S}^2+\mathbf{S}^3\cdot\mathbf{S}^4) - 2J_2(\mathbf{S}^2\cdot\mathbf{S}^3) - 2J_3(\mathbf{S}^1\cdot\mathbf{S}^4) - 2J_4(\mathbf{S}_1\cdot\mathbf{S}_3+\mathbf{S}_2\cdot\mathbf{S}_4) \qquad (4)$$

where, $\mathbf{S}_1$ is the spin operator of Mn1, $\mathbf{S}_2$ is the spin operator of Mn2, $\mathbf{S}_3$ is the spin operator of Mn2a, and $\mathbf{S}_4$ is the spin operator of Mn1a, J_1 is the coupling constant between Mn1 and Mn2 and between Mn1a and Mn2a, J_2 is the coupling constant between Mn2 and Mn2a, J_3 is the coupling constant between Mn1 and Mn1a, and J_4 is the coupling constant across the molecule between Mn1 and Mn2a and between M1a and Mn2. Due to the complex nature of this Hamiltonian, Kambe vector coupling could not be used and a solution could not be determined.[11] In addition, due to the complicated nature of lanthanides, other spin Hamiltonians could not be derived or solved.

Discussion

The **Ln14MC5** series provides a good opportunity to study the impact of Ln on magnetic properties. Because the connectivity of the series is fairly similar, very little change is expected in the overall magnetic coupling between the magnetic centers. Thus, one can probe whether any SMM behavior is due solely to the manganese ions by examining **Y14MC5**, through the introduction of additional spin by examining **Gd14MC5**, or through some combination of spin and anisotropy through the other complexes. The ability to systematically alter specific metals is a unique property of metallacrowns and one not commonly found in the literature.[12,13,14,15,16]

The **Y14MC5** provides a good starting point to discuss the properties of **Ln14MC5**. Because of the inclusion of diamagnetic Y^{III} ions, one can determine the coupling between the Mn^{III} ions based on what the ground spin state was at low temperatures. The susceptibility was approximately 0 cm^3 K mol^{-1} at 0 K, indicating that the Mn^{III} ions must be antiferromagnetically coupled. This is supported by the $\chi_M T$ vs. T plot (Figure 3.12); from 300 K to 5 K, there is a continual decrease in the plot, indicative of antiferromagnetic coupling. Another source of this decrease could be zero-field splitting (ZFS), as Mn^{III} ions have large amounts of ZFS. This also allows the rationalization of the non-zero ground spin state. The value at 300 K is 7.09 cm^3 K mol^{-1}, which is less than

four non-interacting Mn^{III} ions (S = 2, g = 2.00, $\chi_M T$ = 36 cm^3 K mol^{-1}). Thus, one can predict this series of metallacrowns will demonstrate strong antiferromagnetic behavior and the ring will contribute no spin to the system. The μ-O, μ-OH bridge of **Ln14MC5** could lead to very strong antiferromagnetic coupling between Mn2 and Mn2a. Hodgson and co-workers demonstrated that in a bis (μ-O) Mn^{III} dimer, where the Mn^{III} ions are 2.693(2) Å apart, their spin values are strongly antiferromagnetically coupled (J = -201 cm^{-1}).[17] As the Mn2 – Mn2a distance in **Ln14MC5** is similar to the length in Hodgson's complexes, this interaction in **Ln14MC5** could be potentially strong, overwhelming the other interactions. This could explain why at even large temperatures, the calculated spin values are less than that of four non-interacting Mn^{III} ions. Unfortunately, because of the geometry of **Y14MC5**, the Kambe method could not be used to solve Equation 4. Attempts to solve with MAGPACK also were not successful.[18,19] Thus, the exchange parameters between the Mn ions in the system cannot be definitively given.

Examination of the out-of-phase susceptibility plot (Figure 3.26) reveals no frequency behavior and thus **Y14MC5** is not an SMM. This is very important as it indicates that the spin and anisotropy from the Mn^{III} ions alone will not be sufficient for showing SMM behavior. It also indicates that the central Ln^{III} will need to contribute spin, as the Mn^{III} ions are strongly antiferromagnetically coupled. In order to test if simply adding spin to the system and if the anisotropy from the Mn^{III} ions would yield SMM behavior, the Gd^{III} analog was studied.

Studying **Gd14MC5** can indicate whether adding spin to the system will lead to SMM properties. Gd^{III} (S = 7/2, L = 0, $^8S_{7/2}$) has no anisotropy. Mn^{III}, on the other hand, has a large amount of anisotropy. Thus, it is interesting to see if adding spin to an anisotropic system of four antiferromagnetically coupled Mn^{III} ions would lead to SMM behavior. The low temperature dc susceptibility and in-phase susceptibility values for **Gd14MC5** were less than two independent Gd^{III} ions. This indicates that the Mn^{III} ions remain strongly antiferromagnetically coupled and that at low temperature, there may be weak antiferromagnetic coupling between the ring Mn^{III} ions and the Gd^{III} ions, antiferromagnetic coupling between the two Gd^{III} ions, or there are low lying excited

states. Examining the dc susceptibility plot of **Gd14MC5** (Figure 3.13), one sees a sharp decrease from approximately 50 K to low temperature. This is indicative of antiferromagnetic coupling as well as ZFS from the Mn^{III} ions. The value at 300 K for the dc susceptibility plot was close to the expected value for four independent Mn^{III} ions and two Gd^{III} ions (27.76 cm^3 K mol^{-1}), indicating that the decrease in susceptibility is partially due to antiferromagnetic coupling between the metal ions.

In order to see if there is coupling between the two Gd^{III} ions, the magnetic susceptibility of **Y14MC5** was subtracted from **Gd14MC5** (Figure 3.36). This would remove all magnetic contributions from the Mn^{III} ions. At high temperature, the susceptibility was slightly less than that of two non-interacting Gd^{III} ions ($\chi_M T$ = 15.76 cm^3 K mol^{-1}). At low temperature, the $\chi_M T$ was 17.06 cm^3 K mol^{-1}. This value is approximately the value expected for two non-interacting Gd^{III} ions ($\chi_M T$ = 16.15 cm^3 K mol^{-1}).* This indicates that at 5 K, the Gd^{III} ions are fairly independent of the surrounding, or perhaps even slightly ferromagnetically coupled to the Mn^{III} ions. This is not surprising because it is known that Cu^{II} and Gd^{III} can ferromagnetically couple.[6,20] The possibility of low lying excited states was ruled out as examining the energy level diagram of GdF_3 indicates that there is a large energy separation between the ground state and the first excited state.[21]

As **Gd14MC5** has the prerequisite non-zero ground spin state, it was hoped that it may show slow magnetic relaxation. Studying the out-of-phase magnetic susceptibility (Figure 3.27) indicated that no frequency dependence was detected. Therefore, it was concluded that **Gd14MC5** is not an SMM. This indicated that the anisotropy from the ring Mn^{III} ions and the spin value from the central lanthanide was not sufficient for SMM behavior. The central lanthanide would need to contribute both spin and anisotropy to the system in order to show SMM behavior.

It was hoped that with the introduction of Ln^{III} ions with both spin and anisotropy, slow magnetic relaxation would be observed. Examining the magnetic susceptibility values of **Tb14MC5** (Figure 3.14), **Dy14MC5** (Figure 3.15), **Ho14MC5-1** (Figure 3.16),

* The low temperature value was taken from the magnetic data of **$LnZn_{16}$** presented in Chapter V.

Ho14MC5-2 (Figure 3.17), and **Er14MC5** (Figure 3.18) at 300 K, it was found that the values were less than those expected for four non-interacting Mn^{III} ions and two non-interacting Ln^{III} ions for all except **Ho14MC5-2** ($\chi_M T$ = 35.64 cm^3 K mol^{-1}, 40.34 cm^3 K mol^{-1}, 40.14 cm^3 K mol^{-1}, and 34.96 cm^3 K mol^{-1} for Tb_2Mn_4, Dy_2Mn_4, Ho_2Mn_4, and Er_2Mn_4, respectively). Subtracting out the Mn^{III} contribution for **Tb14MC5** (Figure 3.37), **Dy14MC5** (Figure 3.38), and **Ho14MC5-1** gave susceptibility values that varied across the series. For **Tb14MC5** and **Ho14MC5-1**, the contribution from the two lanthanides ($\chi_M T$ = 20.05 cm^3 K mol^{-1} and 23.99 cm^3 K mol^{-1} for Tb^{III} and Ho^{III}, respectively) were smaller than expected for two non-interacting Tb^{III} or Ho^{III} ions ($\chi_M T$ = 23.64 cm^3 K mol^{-1} and 28.14 cm^3 K mol^{-1}, respectively). For **Dy14MC5**, the contribution from the Dy^{III} ions (28.99 cm^3 K mol^{-1}) almost matches the theoretical susceptibility of two non-interacting Dy^{III} ions (28.34 cm^3 K mol^{-1}). Presumably, because of the structural similarities, all interactions would be the same across the series. Thus the differences observed most likely originate from the population of a variety of spin states at higher temperatures.

At 5 K, the susceptibility became more difficult to describe, as the susceptibility of the two Tb^{III} ions of **Tb14MC5** (18.86 cm^3 K mol^{-1}) was slightly higher than for two Tb^{III} ions (16.61 cm^3 K mol^{-1}).* For **Dy14MC5**, the susceptibility contribution at 5 K from the Dy^{III} ions was 23.71 cm^3 K mol^{-1}, which closely matches that expected from two non-interacting Dy^{III} ions (22.16 cm^3 K mol^{-1}).* For **Ho14MC5-1**, the susceptibility contribution from the Ho^{III} ions was 22.19 cm^3 K mol^{-1}, which is significantly larger than expected for two non-interacting Ho^{III} ions (13.91 cm^3 K mol^{-1}).* Clearly, there is unusual magnetic behavior for these systems that does not have an obvious answer. As stated above, as the metal ions have the same connectivity, all magnetic interactions should remain similar across the series. If the convention that *4f* orbitals are highly contracted and do not interact with the ligand environment or other metals is true, the observed magnetic behavior upon removal of the Mn^{III} contributions should closely match that of two non-interacting Ln^{III} ions. As this is not the case, the magnetic behavior can be contributed to either population of a variety of spin states or there are weak interactions between the Ln^{III} ions and the ring Mn^{III} ions or between the Ln^{III} ions themselves.

Studying the **Ho14MC5-2** (Figure 3.17), the susceptibility at 300 K was much larger (57.0 cm^3 K mol^{-1}) than expected for four non-interacting Mn^{III} and two non-interacting Ho^{III} ions (40.14 cm^3 K mol^{-1}). For **Er14MC5** (Figure 3.18), the susceptibility at 300 K (27.9 cm^3 K mol^{-1}) was less than four non-interacting Mn^{III} and two non-interacting Er^{III} ions (34.96 cm^3 K mol^{-1}). If the large susceptibility of **Ho14MC5-2** was due to ferromagnetic coupling, one could expect the same feature to be present in **Er14MC5**, as they both have the same structures. However, this is not the case; in fact, the opposite is observed. This indicates there are complicated and multiple spin states populated at high temperatures. Because an Y^{III} analog was not observed, the same type of analysis provided above, i.e. subtraction of the Mn^{III} ions to determine the Ln^{III} contributions, cannot be performed. Thus the interactions in the complex cannot be clearly described.

Looking at the **Ho14MC5** structures allows one to see if there is any difference between the two 14-MC-5 types. The magnetization values (Figures 3.9 and 3.10) reach different maxima, but that is most likely due to the measurements being taken at two different temperatures (2 K for **Ho14MC5-1** and 5 K **for Ho14MC5-2**). The most obvious difference between the two structures is the magnetic susceptibility measurements. At 300 K, the magnetic susceptibility of **Ho14MC5-2** is significantly higher than that of **Ho14MC5-1**. At 300 K, the magnetic susceptibility of **Ho14MC5-2** was 57.00 cm^3 K mol^{-1}, while for **Ho14MC5-1**, it was 31.08 cm^3 K mol^{-1}. At 5 K, the susceptibility of **Ho14MC5-2** is still slightly larger than **Ho14MC5-1** (27.36 cm^3 K mol^{-1} and 23.71 cm^3 K mol^{-1}, respectively). The in-phase magnetic susceptibility (Figures 3.23 and 3.24 for **Ho14MC5-1** and **Ho14MC-2**, respectively), however, had similar values, indicating that both complexes likely have the same ground spin state. Without a crystal structure of **Ho14MC5-2**, it is very difficult to explain the high temperature magnetic phenomena because the exact coordination environment around the Ho^{III} ions in **Ho14MC5-2** is unknown. If the crystal structure of **Er14MC5** is representative of **Ho14MC5-2**, it could be that Ho1 in **Ho14MC5-2** does not extend as far out of the Mn plane as the analogous Ho1 in **Ho14MC5-1**. This could affect the exchange interactions. If Ho1 in **Ho14MC5-2** is seven coordinate, as was the case for Er1 in **Er14MC5**, this could change the ligand

field environment around the Ln, modifying the order of the magnetic states and thus the magnetic properties. Perhaps changing the hydrogen bonded partner on O8 from pyridine for **Ho14MC5-1** to H_2O for **Ho14MC5-2** modified the coupling constants in the ring. The pyridine is closer to O8 (2.760 Å) in **Ho14MC5-1** than the water is to O8 in **Er14MC5** (2.800 Å). With the small structural changes and the fact that no crystal structure exists of **Ho14MC5-2**, it is very difficult to definitively answer this question.

What did become apparent, however, is that at lower temperatures, the metallacrown type did not seem to affect the magnetic properties. Looking at the low temperature dc susceptibilities and the out-of-phase magnetic susceptibilities, almost identical behavior was observed. This indicates that at high temperatures, there is unusual interactions between the Ho^{III} ions and the ring Mn^{III} ions that is lost at lower temperatures. It would be interesting to see if these properties are exclusive to the Ho^{III} ion or a common trait among the two **Ln14MC5** structure types. Crystals of other **Ln14MC5-2** types were obtained and their unit cell parameters measured, but it proved difficult to reproduce the synthesis and to obtain enough crystalline material to measure.

Examining the out-of-phase ac magnetic susceptibility of **Tb14MC5** (Figure 3.28), **Ho14MC5-1** (Figure 3.31), **Ho14MC5-2** (Figure 3.32), and **Er14MC5** (Figure 3.33), all the complexes show slow magnetic relaxation, a hallmark of SMM behavior. Because no external dc field was applied, the odds of observing easy-plane magnetism are decreased. Unfortunately, none of the χ''_M vs. T curves reached a maximum at the temperatures studied, so it is difficult to define the blocking temperature and ultimately the height of the energy barrier. It is not possible to definitively declare **Tb14MC5, Ho14MC5-1**, **Ho14MC5-2**, or **Er14MC5** SMMs without observing either a hysteresis (Figure 1.7) in a dc magnetization experiment or calculating a Cole-Cole plot (Figure 1.8). Neither experiment could be performed with the available instrumentation due to temperature limitations.

In Chapter II, it was found that only the Kramers' doublet Dy^{III} systems showed slow magnetic relaxation. However, in the **Ln14MC5** case, Tb^{III} and Ho^{III}, two non-Kramers'

doublets, showed slow magnetic relaxation. As mentioned before, a bistable ground spin state is not guaranteed in non-Kramers' systems.[22] The ligand environment must maintain a strong axial symmetry[23] or magnetic coupling must create an exchange bias.[24,25] It appears that both conditions are met in the **Ln14MC5** system, as the metallacrown ring created a central binding pocket that enforced strict axial symmetry (pseudo C_5) and the low temperature susceptibility of Tb^{III} and Ho^{III} was larger than expected for two isolated Tb^{III} and Ho^{III} ions, respectively.

Dy14MC5 shows the most interesting magnetic behavior. The in-phase susceptibility data (Figure 3.22) shows unique properties, namely frequency dependence. This frequency dependence begins near 3 K. Frequency dependence is also observed in the out-of-phase susceptibility plot (Figure 3.29). The onset of slow magnetic relaxation starts near 4 K (Figure 3.30). For 1500 Hz, there is a maximum in the out-of-phase at 2.17 K, at which point the χ''_M value begins to decrease. At 1000 Hz, there is also a maximum, this time at 2.07 K and there is also turnover. The experiment at 1000 Hz was repeated and the same value was obtained. For 750 Hz, there is a maximum at 1.97 K. From these values, Equations 1 and 2 where used to plot 1/T vs. ln(τ) (Figure 3.34) and to calculate a energy barrier height. Taking the slope of the best-fit line affords the blocking temperature in K, which may be converted to cm^{-1} by multiplying by Boltzmann's constant. The relaxation time τ_0 is given by the exponential of the y-intercept. For **Dy14MC5**, the blocking temperature was calculated to be 16.68 K and τ_0 was determined to be 4.93×10^{-8} s. The R^2 value of the best fit line was 0.9949, indicating a very good fit. At the time of publication, this was the third largest U_{eff} calculated for a mixed Mn/Ln SMM. What was exciting was that the molecule with the largest U_{eff} needed five manganese and four lanthanide ions,[26] whereas, the second largest U_{eff} was obtained using a structure with eleven manganese ions and two gadolinium ions.[27] **Dy14MC5,** using fewer metals to achieve this blocking temperature, indicates the utility of controlling geometry: orienting anisotropy vectors can lead to improved magnetic properties. In order to rule out spin glass behavior, Equation 5 was used:

$$\frac{\Delta T_p / T_p}{\Delta(\log f)} = a \qquad (5)$$

where T_p is the χ''_M peak temperature and f is the frequency. Mydosh found that spin glass complexes tend to have an a less than 0.08.[28] An ideal SMM tends to have a around 0.24.[29]

Using Equation 5, a was determined to be approximately 0.34, well within the domain of SMM and out of the domain of spin glasses. Thus, it could be argued, even without a hysteresis plot, that **Dy14MC5** is a SMM.

This series of complexes demonstrate the power of controlling magnetoanisotropy through geometrical constraints. Comparing the **Ln14MC5** family to the mixed $\mathbf{Ln_6Mn_4}$ and $\mathbf{Ln_4Mn_4}$ complexes in Chapter II and other large mixed Mn/Ln complexes (see Chapter II for references), one can see dramatically improved slow magnetic relaxation properties with fewer metals. In the large mixed Ln/Mn complexes, it is possible that the magnetoanisotropy of the complexes decreased due to the molecule's symmetry accidentally, and destructively, aligning the anisotropy vectors of the individual ions. By using planar metallacrowns, it was possible to align the individual Mn^{III} ions' anisotropy vectors parallel to each other. This prevented accidental alignment in a destructive manner. This could prove to be a very important methodological advance as the SMM with one of the largest U_{eff} is a square pyramid of Dy^{III} ions (Figure 1.28). Essentially, this Dy_5 complex is using the idea of a planar base geometry except with all Ln^{III} ions.[30]

The fact that so many Ln^{III} ions could be studied in **Ln14MC5** allows for a thorough study of the magnetic properties. **Y14MC5** revealed that the Mn^{III} ions were antiferromagnetically coupled. Knowing the magnetic properties of **Y14MC5** also allowed for a thorough study of the exchange coupling between the Ln^{III} ions and the ring Mn^{III} ions. It revealed that there is very complicated magnetic exchange occurring in these complexes. **Gd14MC5** indicated that adding a large isotropic spin ion to the complex with the hope that the Mn^{III} ions would provide the needed anisotropy would not

work. The large spin and anisotropic lanthanides showed slow magnetic relaxation, indicating the Ln^{III} ion would need to provide both spin and anisotropy in order to behave as an SMM.

Although all the large spin and anisotropic lanthanides showed slow magnetic relaxation, the Dy analog again showed the best magnetic properties, i.e. the largest blocking temperature. This most likely reflects that Dy^{III}, a Kramers' doublet, has a bistable ground state. This ground state is slightly more isolated from the first excited state than for Tb^{III}, Ho^{III}, or Er^{III}.[21] Because it is difficult to calculate *D* or the exact spin states, it is not possible to discuss the order of the states in these complexes and build a spin ladder.

Comparing **Ln14MC5** with the **Ln 12-MC-4** and **Mn 12-MC-4** structures studied by Zaleski, it was found that the **Dy14MC5** had the highest blocking temperature for the metallacrowns studied.[5] This could be because there is a second lanthanide present in **Ln14MC5**, where there is only one Ln^{III} ion in **Ln 12-MC-4**[5] and an unusually oriented Mn^{II} ion in **Mn 12-MC-4**.[4] It could also be the fact that the geometry around the Ln^{III} ions in **Ln14MC5** is better suited for the magnetic properties of the Ln^{III} ions compared to **Ln 12-MC-4**. As will be shown in Chapter IV, the ligand environment around **Dy 12-MC-4** is best characterized as compressed D_{4d}, while for **Ln14MC5**, it is pseudo C_5. It could be that this compressed D_{4d} environment perturbed the ligand field, leading to energetically unfavorable interactions between the ligands and the Ln^{III} ions' electronic orbitals. It was also hoped that by studying **Ln 12-MC-4**, which has fewer paramagnetic metals, the magnetic ground states would not be so complicated. With less complicated spin states, the possibility of having a well-isolated spin state seemed likely to increase.

Because there are two Ln^{III} binding sites in **Ln14MC5**, it would be extremely interesting, although synthetically challenging, to see if two different Ln^{III} ions could be introduced. By leaving an Y^{III} ion as the non-planar ring metal and then introducing a different Ln^{III} at the center position, would the magnetic properties match those of the analogous **Ln 12-MC-4**? Does one site perturb the SMM properties more than the other. i.e. is it the planar central pocket, the tilted ring position, or both that are required for SMM behavior? These

could be potentially interesting avenues of future study because it allows for a deeper understanding of the influences the ligand environment has on the magnetic properties of Ln^{III} ions.

Conclusion

Most reported SMMs have tended to have randomly oriented metals that sometimes result in anisotropy values close to zero or positive (Chapter II for references). This random orientation is due to the nature of self-assembly. Using metallacrowns, one can predictably control geometry and form rational clusters while still using self-assembled molecules. **Ln14MC5** demonstrates the power of using geometry to control magnetoanisotropy. **Dy14MC5**, with only six metals was capable of showing the third largest U_{eff} for a Mn/*4f* SMM; the two with larger thermal barriers utilized 9 and 13 metals.

Because **Ln14MC5** had preformed binding pockets, it was possible to easily study the affect of different lanthanides on the magnetic properties of the whole complex (Table 3.7). Using **Y14MC5,** it was found that the Mn^{III} ions from the **Ln14MC5** do not have the necessary spin or anisotropy to induce SMM behavior. In fact, the **Y14MC5** complex revealed that the Mn^{III} ions are antiferromagnetically coupled. Introducing Gd^{III} added spin to the system, but no anisotropy. The hoped for goal was that the anisotropy from the Mn^{III} ions, together with the large spin of Gd^{III} would lead to slow magnetic relaxation. Unfortunately, that was not the case, indicating that it is absolutely necessary to have Ln^{III} ions that have both spin and anisotropy.

It was found that **Tb14MC5**, **Dy14MC5**, **Ho14MC5-1**, **Ho14MC5-2**, and **Er14MC5** all showed slow magnetic relaxation, with **Dy14MC5** having a blocking temperature above 2 K. This demonstrated that introducing anisotropic Ln^{III} ions into the 14MC5 framework, regardless of structure type, would lead to SMM behavior. Because the non-Kramers' doublet ions Tb^{III} and Ho^{III} showed slow magnetic relaxation, it could be

argued that the metallacrown geometry induced a bistable ground state by forcing axial symmetry as well as altering the magnetic interactions through exchange coupling.[22]

When compared to the **Ln 12-MC-4** family reported by C. M. Zaleski in his thesis,[5] **Ln14MC5** demonstrated a larger U_{eff} than the analogous **Ln 12-MC-4** complexes. This may be because there are two Ln^{III} ions present in **Ln14MC5** versus one in **Ln 12-MC-4**, and thus, **Ln14MC5** has a larger spin value and more overall anisotropy. Perhaps the coordination environment around the Ln ion perturbs the ligand field. These ideas will be studied more in more depth in Chapter IV.

Table 3.7. The magnetic properties of **Ln14MC5** are summarized.

Complex	Low Temperature $\chi_M T$ (cm^3 K mol^{-1})	High Temperature $\chi_M T$ (cm^3 K mol^{-1})	Slow Magnetic Relaxation
Y14MC5	2.5 (5 K)	7.1 (300 K)	NO
Gd14MC5	19.6 (5 K)	24.8 (300 K)	NO
Tb14MC5	21.4 (5 K)	27.1 (300 K)	YES
Dy14MC5	26.2 (5 K)	36.1 (300 K)	YES
Ho14MC5-1	18.8 (2 K)	31.1 (300 K)	YES
Ho14MC5-2	27.4 (5 K)	57.0 (300 K)	YES
Er14MC5	16.8 (5 K)	27.9 (300 K)	YES

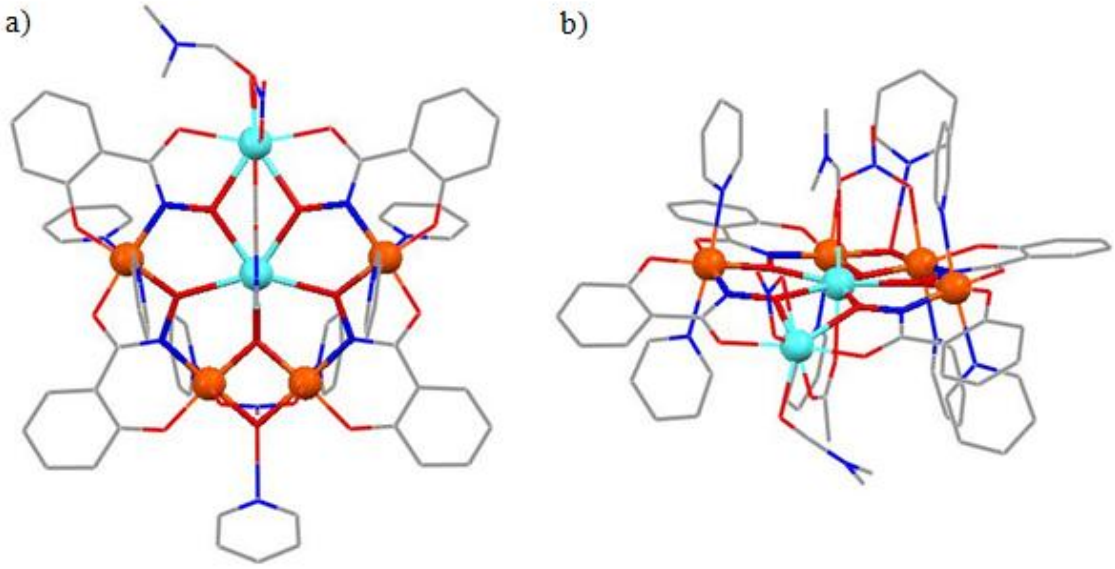

Figure 3.1. The x-ray crystal structure of **Dy14MC5** is shown with the metallacrown ring highlighted. Solvent molecules and hydrogen atoms have been removed for clarity. Color scheme: aqua spheres: Dy^{III}; orange spheres: Mn^{III}; gray tubes: carbon; blue tubes: nitrogen; red tubes: oxygen.

Figure 3.2. An isolation of the metallacrown ring highlights the unique features of **Dy14MC5**.

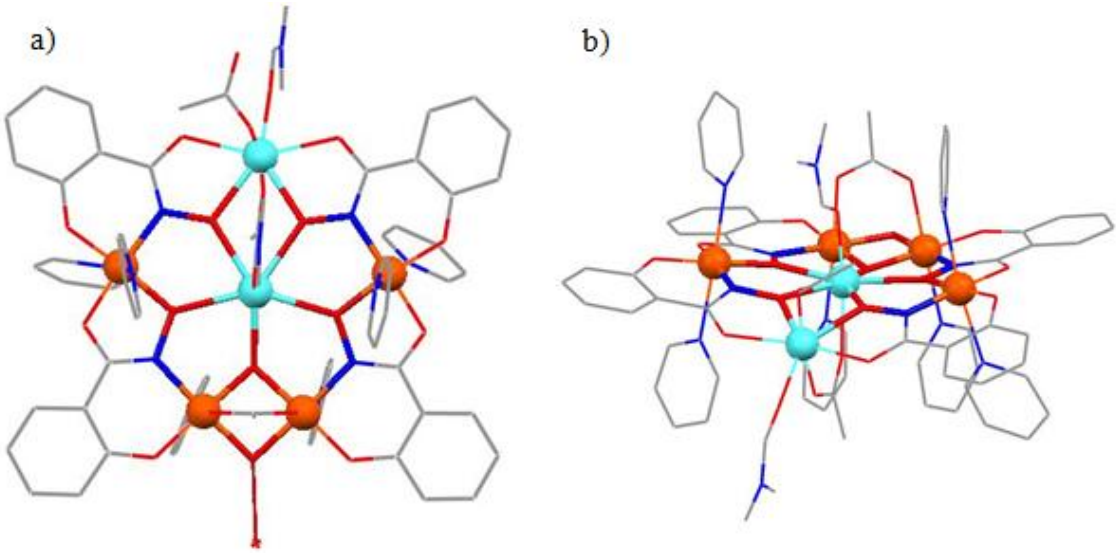

Figure 3.3. The x-ray crystal structure of **Er14MC5** is shown with the metallacrown ring highlighted. Solvent molecules and hydrogen atoms have been removed for clarity. Color scheme: aqua sphere: Er^{III}; orange sphere: Mn^{III}; gray tubes: carbon; blue tubes: nitrogen; red tubes: oxygen.

Figure 3.4. An isolated view of the core shows the unique features of **Er14MC5**.

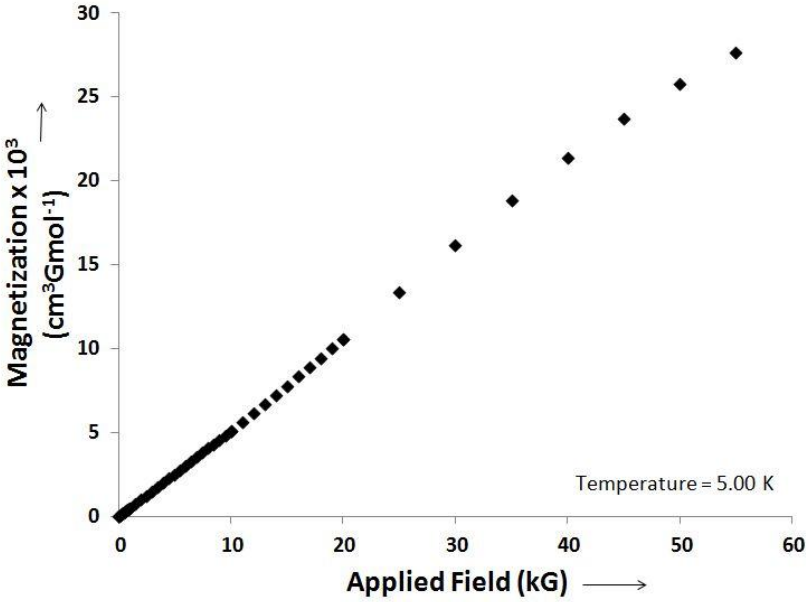

Figure 3.5. The dc variable field magnetization of **Y14MC5** is shown. The measurement was collected at 5.00 K.

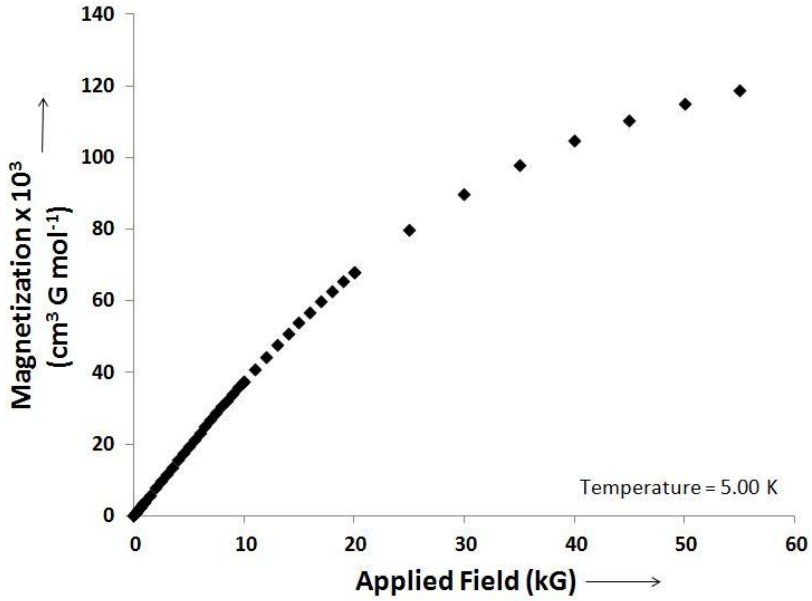

Figure 3.6. The dc variable field magnetization of **Gd14MC5** is shown. The measurement was collected at 5.00 K.

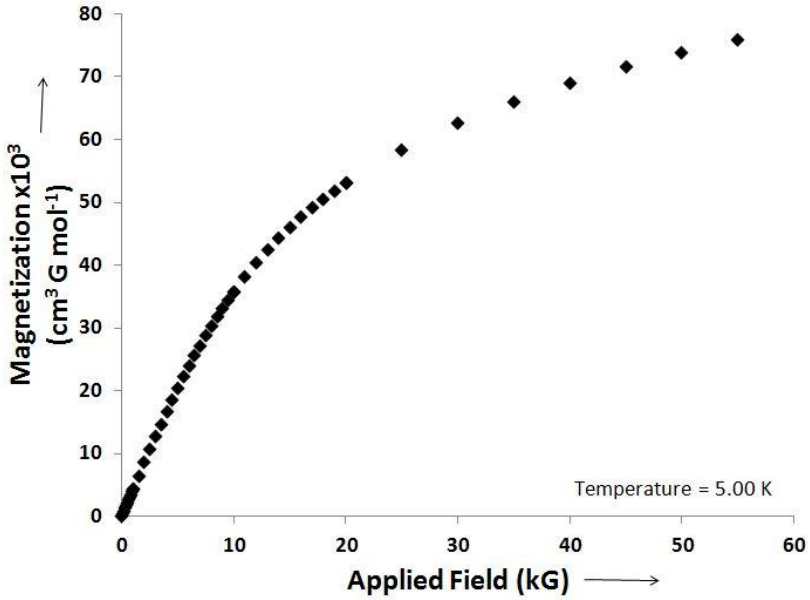

Figure 3.7. The dc variable field magnetization of **Tb14MC5** is shown. The measurement was collected at 5.00 K.

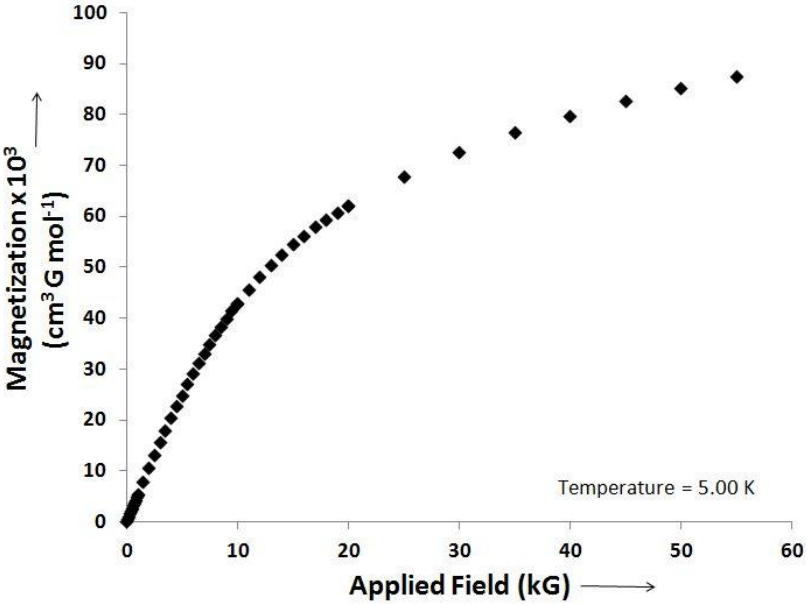

Figure 3.8. The dc variable field magnetization of **Dy14MC5** is shown. The measurement was collected at 5.00 K.

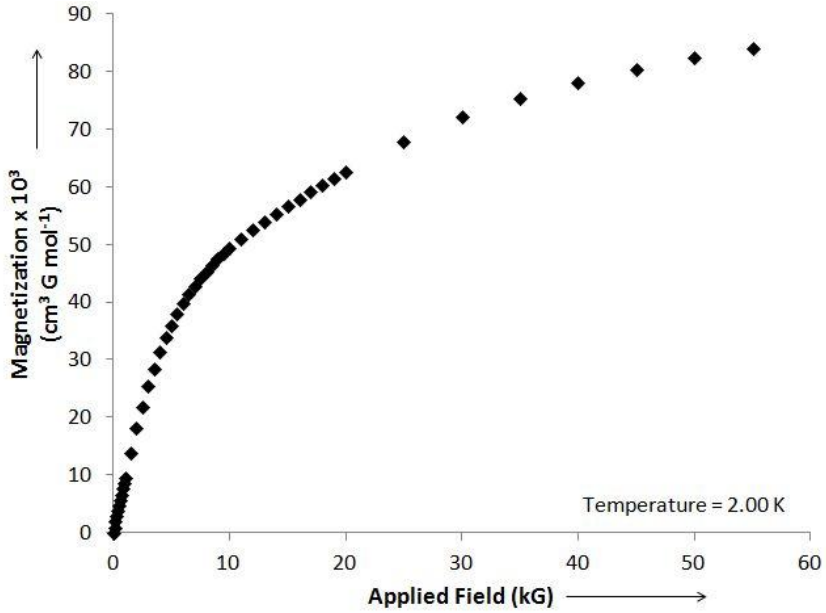

Figure 3.9. The dc variable field magnetization of **Ho14MC5-1** is shown. The measurement was collected at 2.00 K.

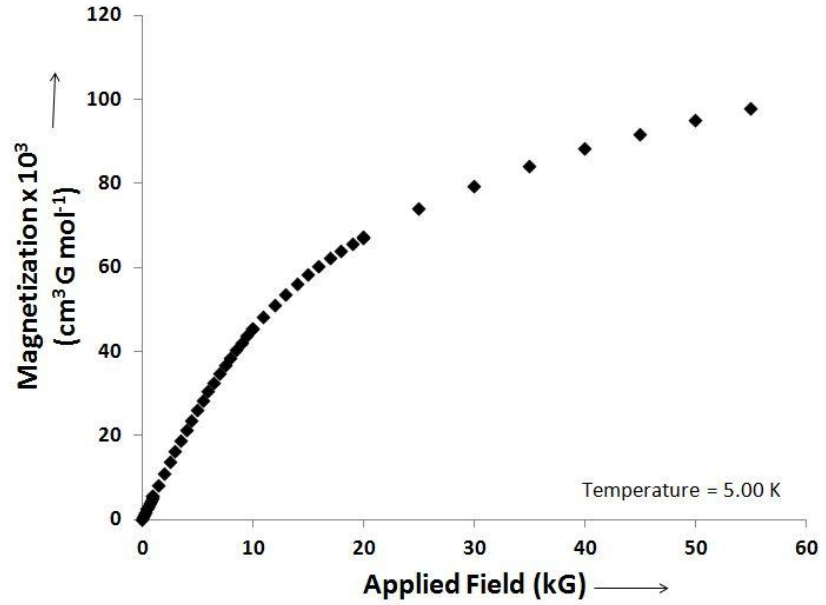

Figure 3.10. The dc variable field magnetization of **Ho14MC5-2** is shown. The measurement was collected at 5.00 K.

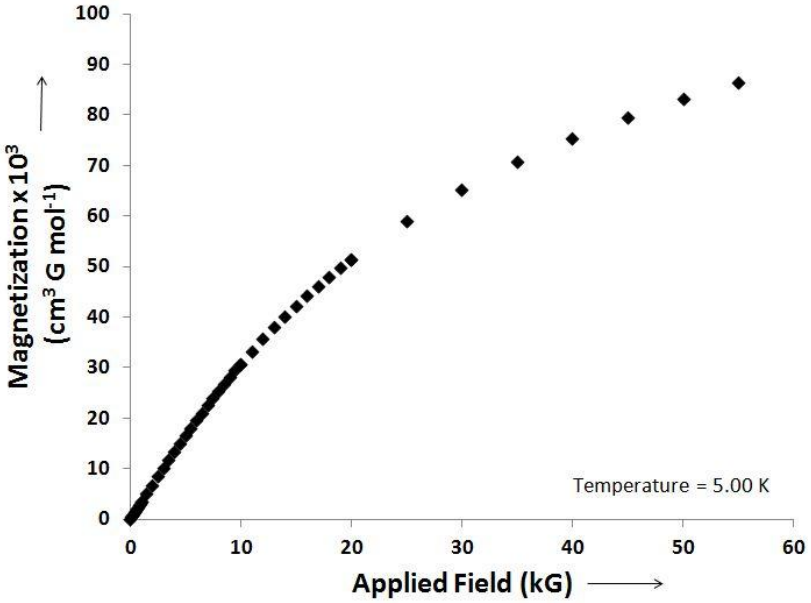

Figure 3.11. The dc variable field magnetization of **Er14MC5** is shown. The measurement was collected at 5.00 K.

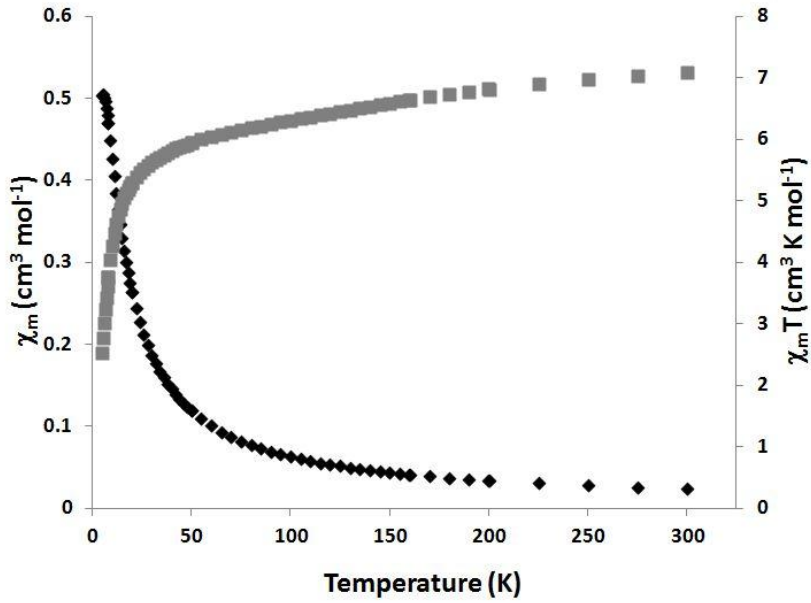

Figure 3.12. The dc variable temperature susceptibility of **Y14MC5** is shown. The measurement was collected with an applied field of 2000 G. χ_M: ◆ $\chi_M T$: ■

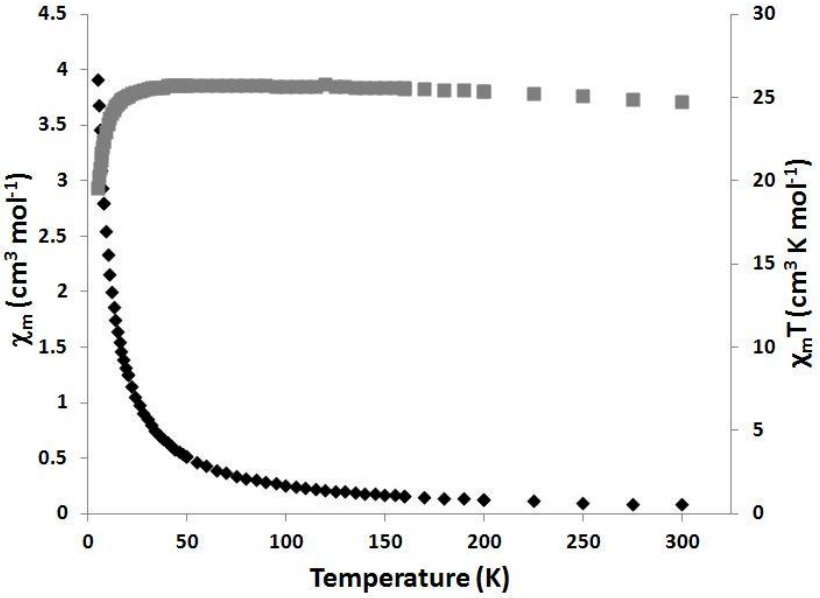

Figure 3.13. The dc variable temperature susceptibility of **Gd14MC5** is shown. The measurement was collected with an applied field of 2000 G. χ_M: ◆ $\chi_M T$: ■

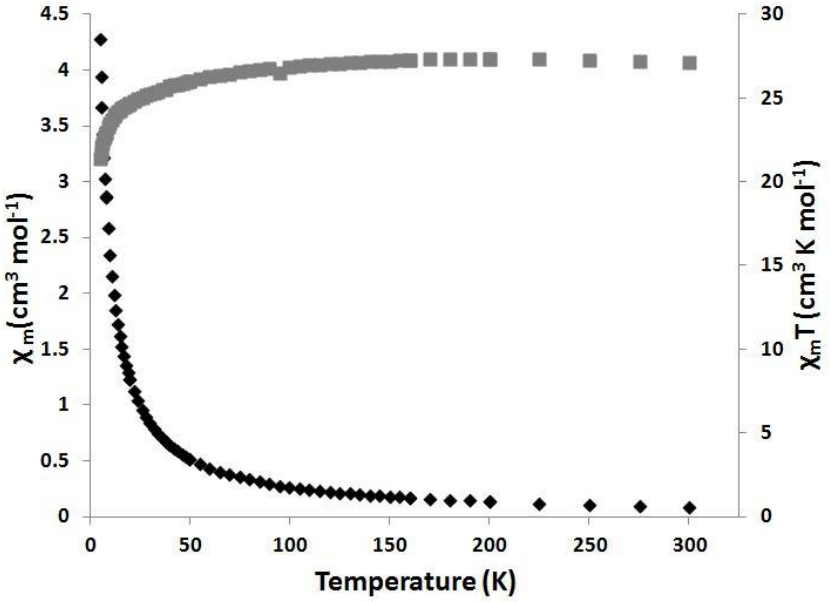

Figure 3.14. The dc variable temperature susceptibility of **Tb14MC5** is shown. The measurement was collected with an applied field of 2000 G. χ_M: ◆ $\chi_M T$: ■

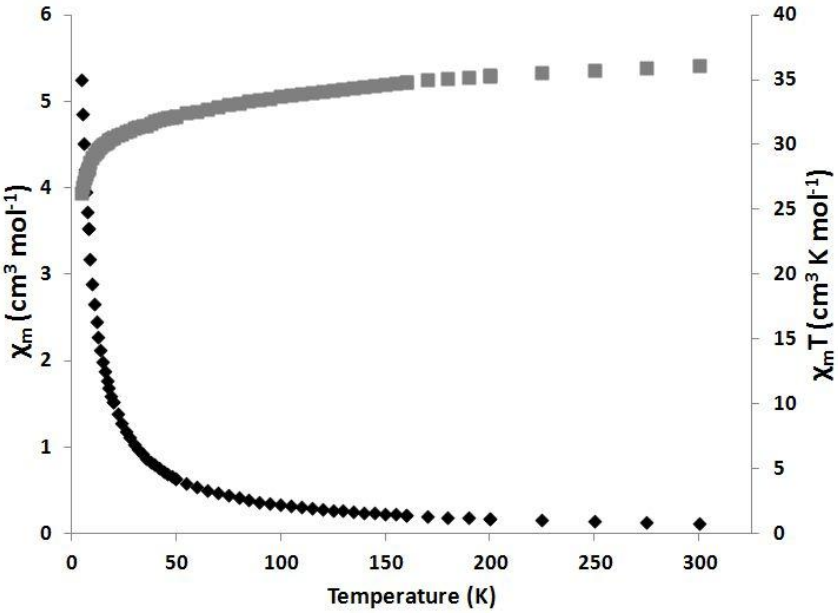

Figure 3.15. The dc variable temperature susceptibility of **Dy14MC5** is shown. The measurement was collected with an applied field of 2000 G. χ_M: ◆ $\chi_M T$: ■

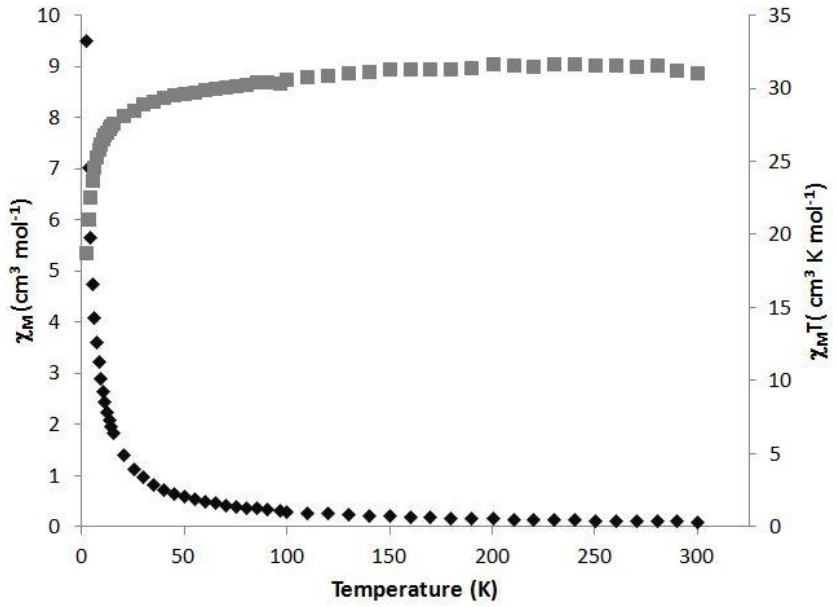

Figure 3.16. The dc variable temperature susceptibility of **Ho14MC5-1** is shown. The measurement was collected with an applied field of 1000 G. χ_M: ◆ $\chi_M T$: ■

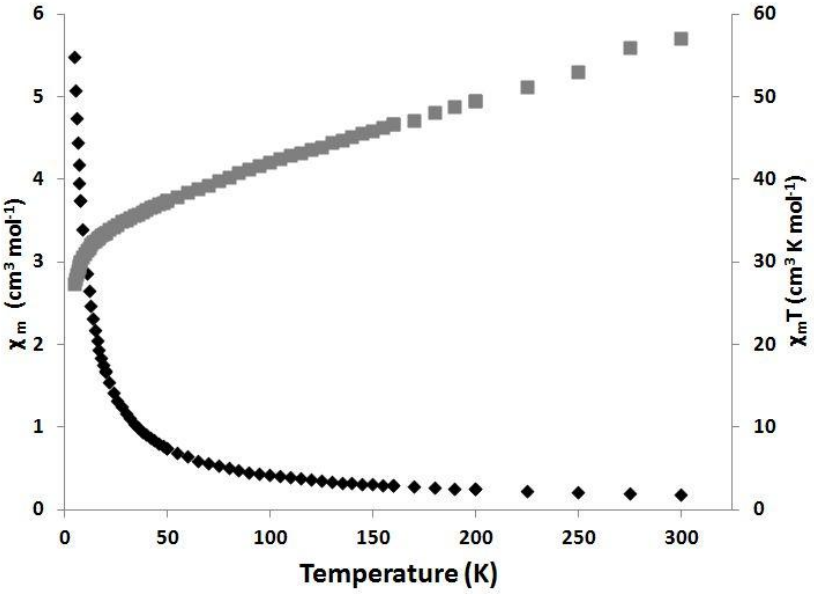

Figure 3.17. The dc variable temperature susceptibility of **Ho14MC5-2** is shown. The measurement was collected with an applied field of 2000 G. χ_M: ◆ $\chi_M T$: ■

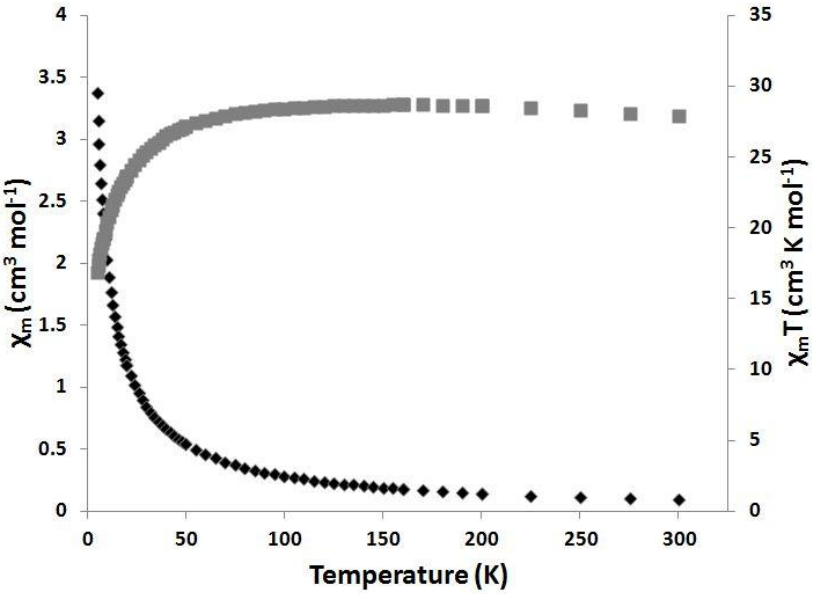

Figure 3.18. The dc variable temperature susceptibility of **Er14MC5** is shown. The measurement was collected with an applied field of 2000 G. χ_M: ◆ $\chi_M T$: ■

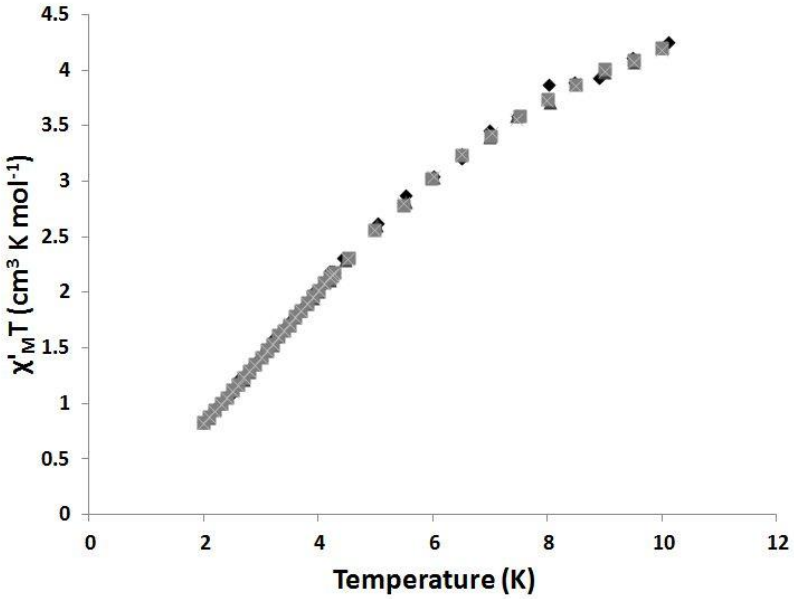

Figure 3.19. The variable temperature in-phase ac magnetic susceptibility component of **Y14MC5** is shown. The measurement was collected with no applied dc field and 3.5 G drive field. 1000 Hz: ◆ 500 Hz: ▲ 100 Hz: ■ 10 Hz: ×

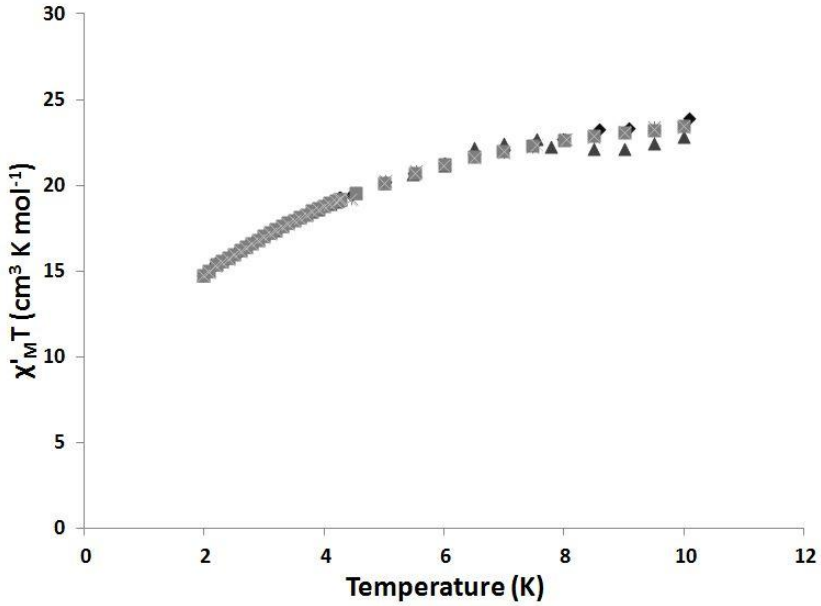

Figure 3.20. The variable temperature in-phase ac magnetic susceptibility component of **Gd14MC5** is shown. The measurement was collected with no applied dc field and 3.5 G drive field. 1000 Hz: ◆ 750 Hz: ✳ 500 Hz: ▲ 100 Hz: ■ 10 Hz: ×

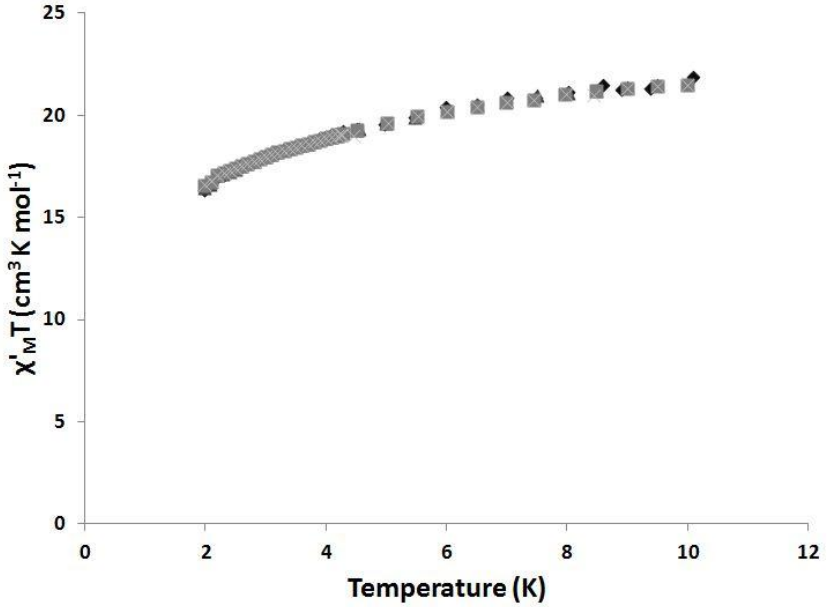

Figure 3.21. The variable temperature in-phase ac magnetic susceptibility component of **Tb14MC5** is shown. The measurement was collected with no applied dc field and 3.5 G drive field. 1000 Hz: ◆ 500 Hz: ▲ 100 Hz: ■ 10 Hz: ×

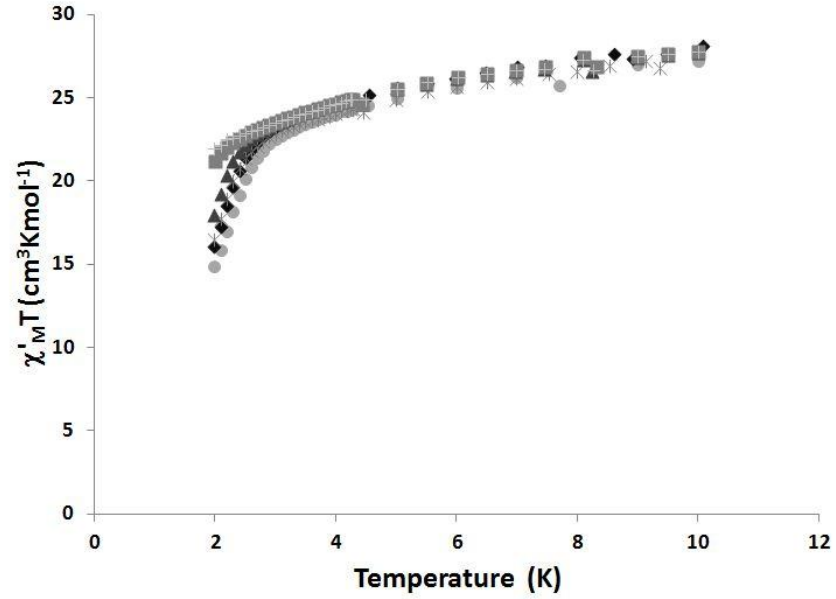

Figure 3.22. The variable temperature in-phase ac magnetic susceptibility component of **Dy14MC5** is shown. The measurement was collected with no applied dc field and 3.5 G drive field. 1500 Hz: ● 1000 Hz: ◆ 750 Hz: ✳ 500 Hz: ▲ 100 Hz: ■ 10 Hz: ×

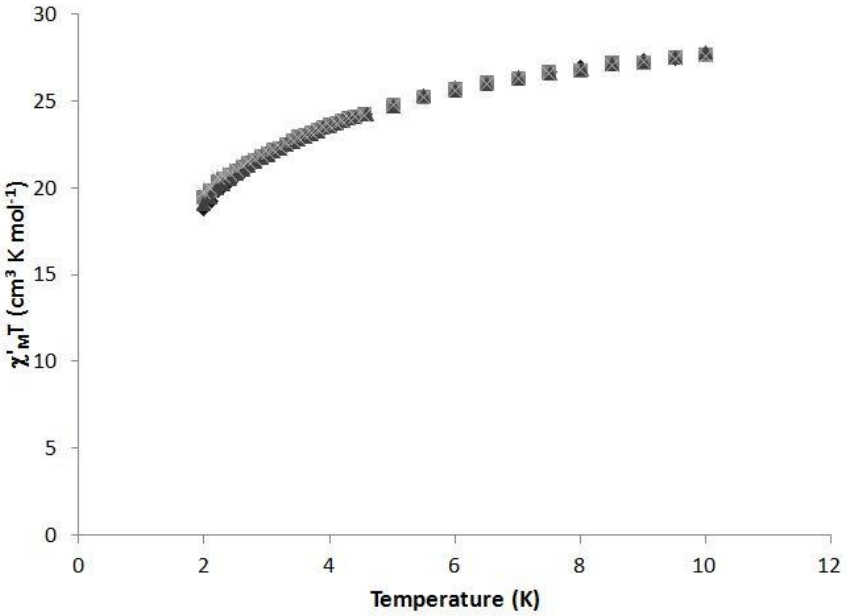

Figure 3.23. The variable temperature in-phase ac magnetic susceptibility component of **Ho14MC5-1** is shown. The measurement was collected with no applied dc field and 3.5 G drive field. 1000 Hz: ◆ 500 Hz: ▲ 100 Hz: ■ 10 Hz: ×

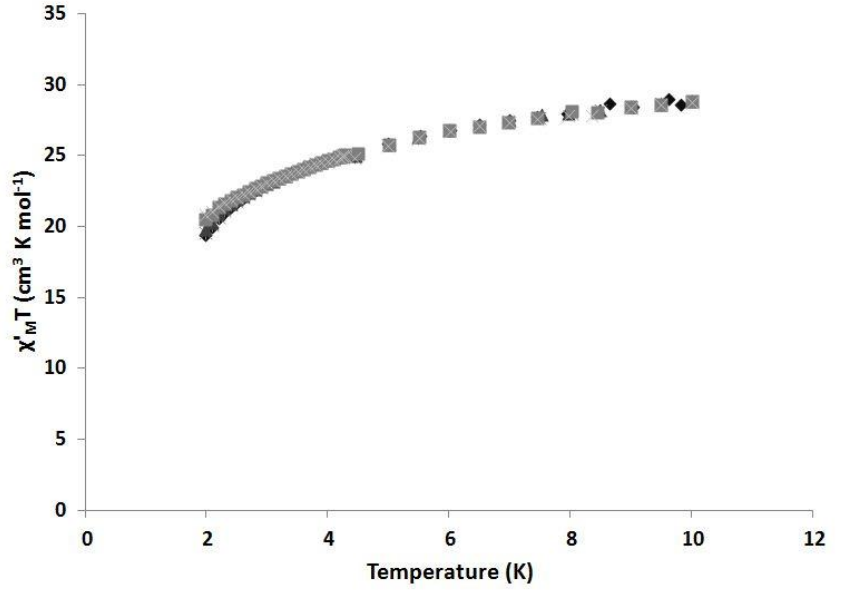

Figure 3.24. The variable temperature in-phase ac magnetic susceptibility component of **Ho14MC5-2** is shown. The measurement was collected with no applied dc field and 3.5 G drive field. 1000 Hz: ◆ 750 Hz: ✳ 500 Hz: ▲ 100 Hz: ■ 10 Hz: ×

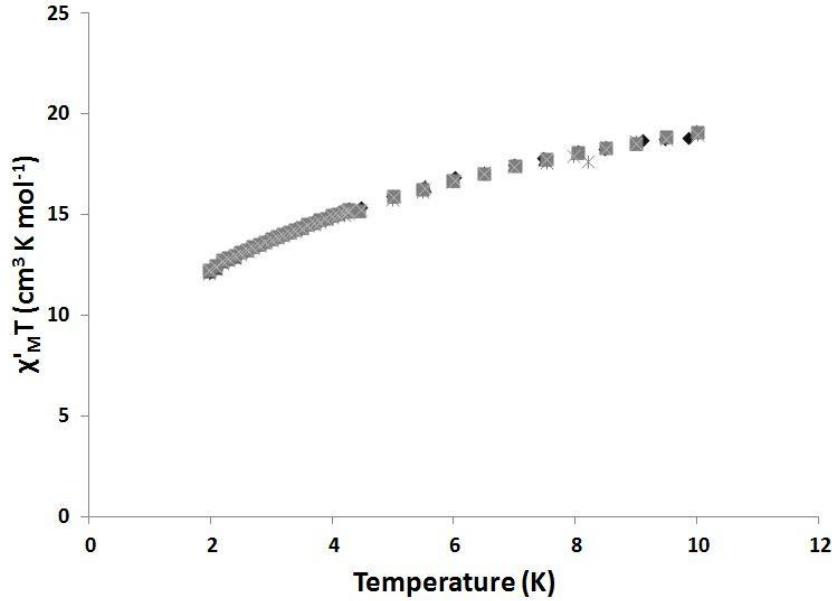

Figure 3.25. The variable temperature in-phase ac magnetic susceptibility component of **Er14MC5** is shown. The measurement was collected with no applied dc field and 3.5 G drive field. 1000 Hz: ◆ 750 Hz: ✳ 500 Hz: ▲ 100 Hz: ■ 10 Hz: ×

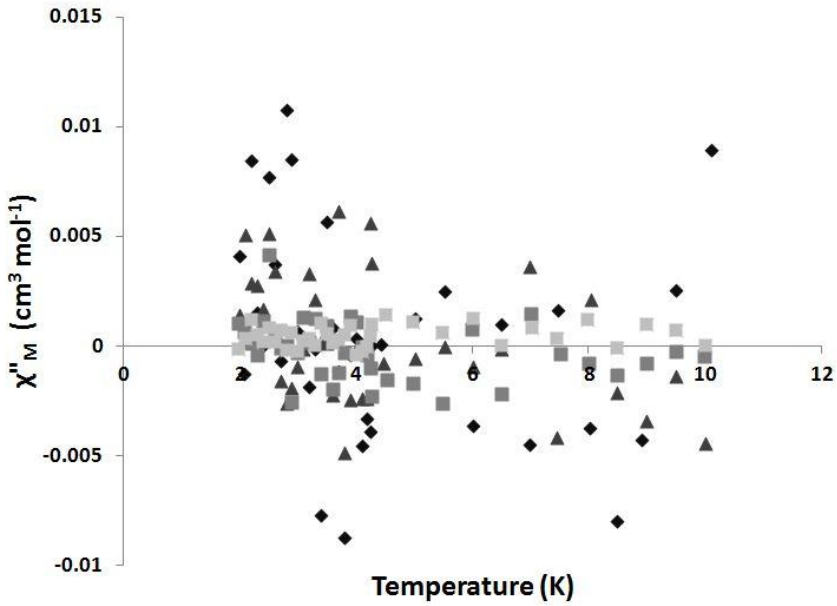

Figure 3.26. The variable temperature out-of-phase ac magnetic susceptibility component of **Y14MC5** is shown. The measurement was collected with no applied dc field and 3.5 G drive field. 1000 Hz: ◆ 500 Hz: ▲ 100 Hz: ■ 10 Hz: ×

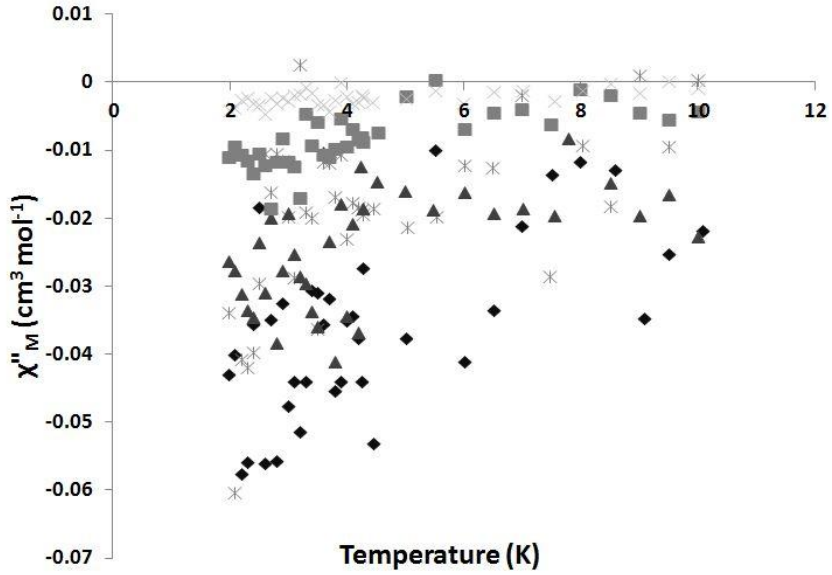

Figure 3.27. The variable temperature in-phase ac magnetic susceptibility component of **Gd14MC5** is shown. The measurement was collected with no applied dc field and 3.5 G drive field. 1000 Hz: ◆ 750 Hz: ✳ 500 Hz: ▲ 100 Hz: ■ 10 Hz: ×

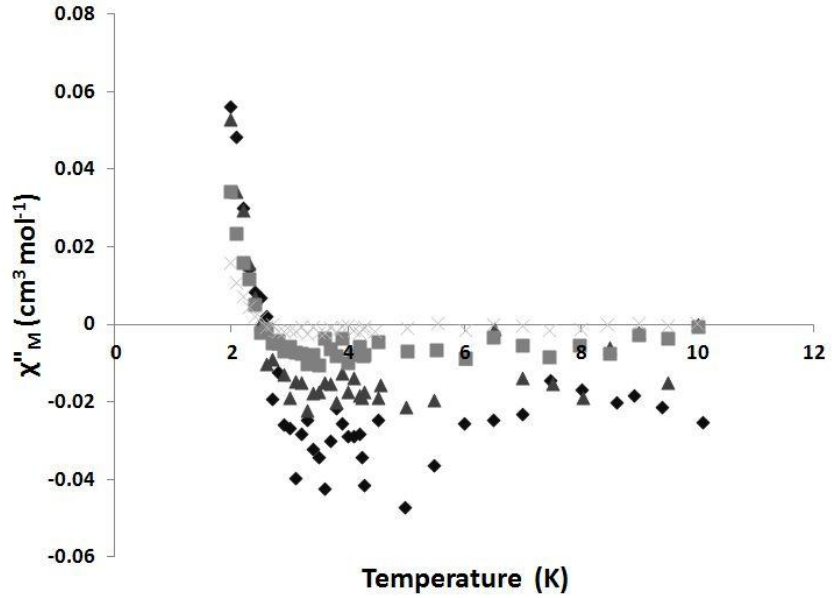

Figure 3.28. The variable temperature out-of-phase ac magnetic susceptibility component of **Tb14MC5** is shown. The measurement was collected with no applied dc field and 3.5 G drive field. 1000 Hz: ◆ 500 Hz: ▲ 100 Hz: ■ 10 Hz: ×

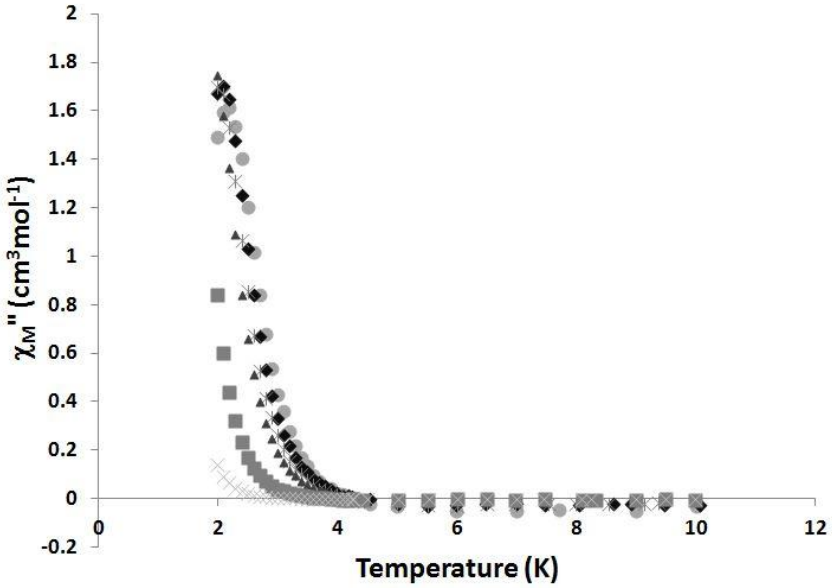

Figure 3.29. The variable temperature out-of-phase ac magnetic susceptibility component of **Dy14MC5** is shown. The measurement was collected with no applied dc field and 3.5 G drive field. 1500 Hz: ● 1000 Hz: ◆ 750 Hz: ✳ 500 Hz: ▲ 100 Hz: ■ 10 Hz: ×

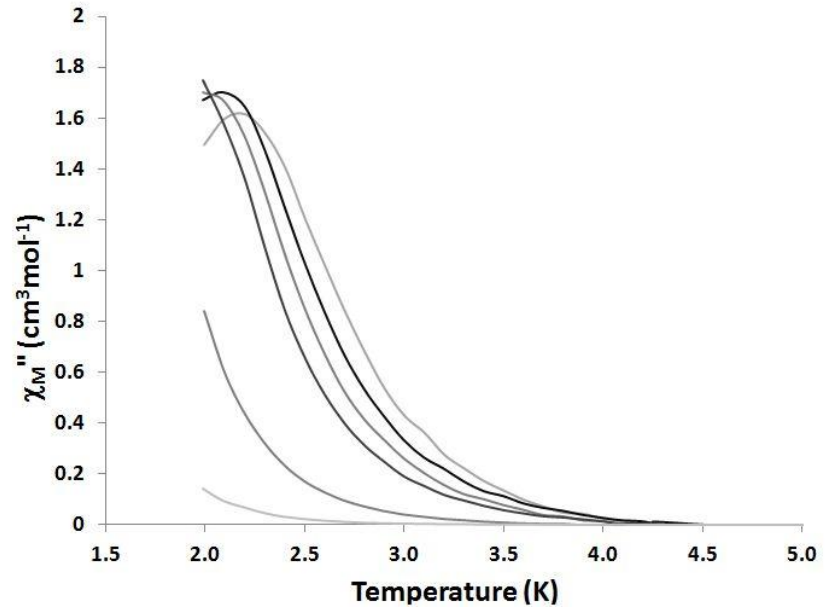

Figure 3.30. The variable temperature out-of-phase ac magnetic susceptibility component of **Dy14MC5** near the blocking temperature is shown. The measurement was collected with no applied dc field and 3.5 G drive field. 1500 Hz: ● 1000 Hz: ◆ 750 Hz: ✳ 500 Hz: ▲ 100 Hz: ■ 10 Hz: ×

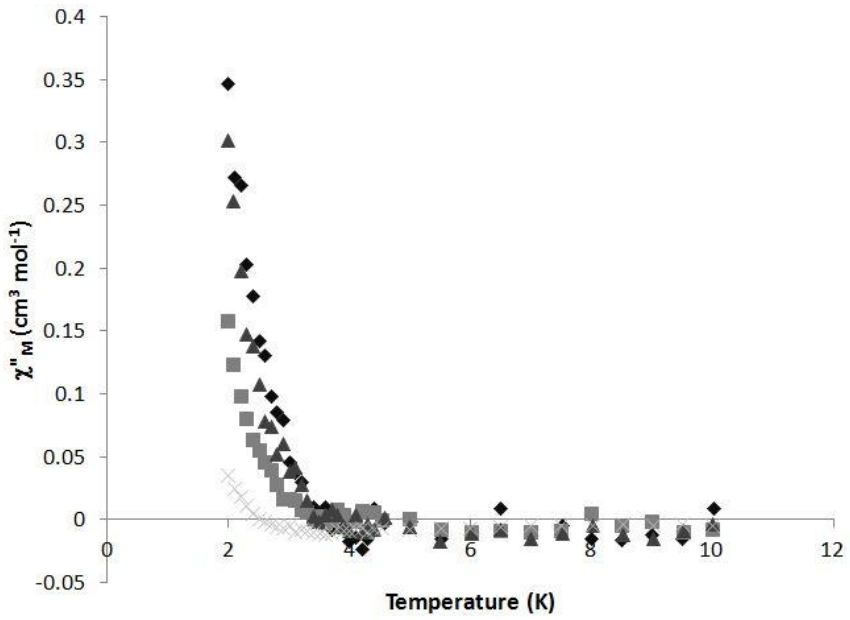

Figure 3.31. The variable temperature out-of-phase ac magnetic susceptibility component of **Ho14MC5-1** is shown. The measurement was collected with no applied dc field and 3.5 G drive field. 1000 Hz: ◆ 500 Hz: ▲ 100 Hz: ■ 10 Hz: ×

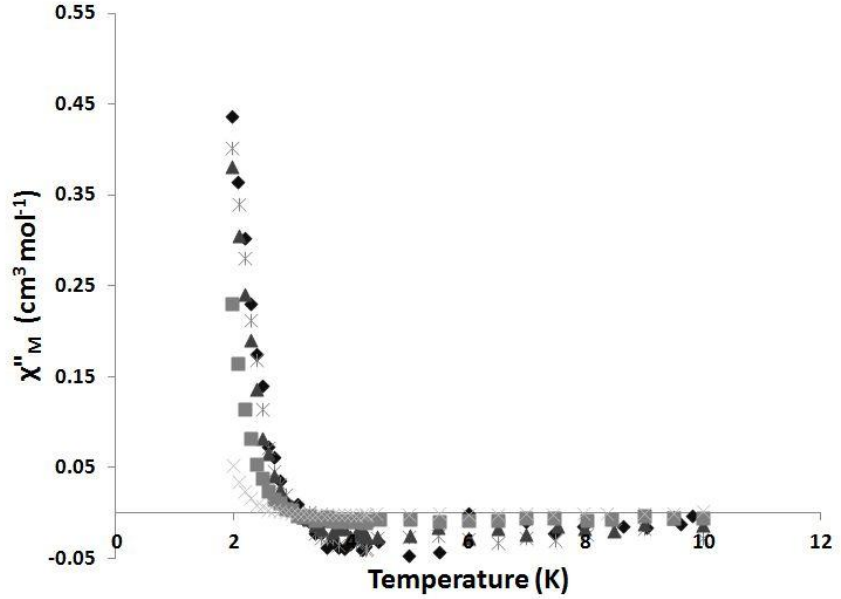

Figure 3.32. The variable temperature out-of-phase ac magnetic susceptibility component of **Ho14MC5-2** is shown. The measurement was collected with no applied dc field and 3.5 G drive field. 1000 Hz: ◆ 750 Hz: ✳ 500 Hz: ▲ 100 Hz: ■ 10 Hz: ×

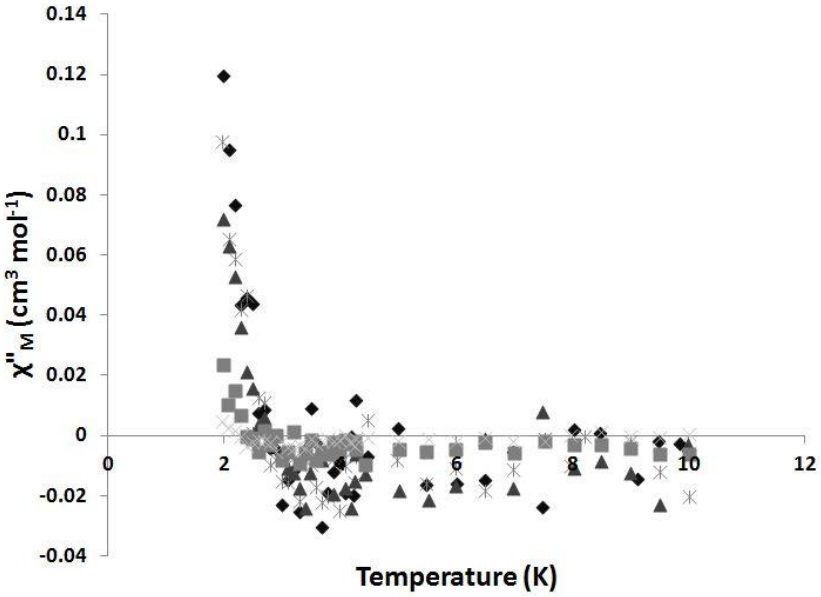

Figure 3.33. The variable temperature out-of-phase ac magnetic susceptibility component of **Er14MC5** is shown. The measurement was collected with no applied dc field and 3.5 G drive field. 1000 Hz: ◆ 750 Hz: ✳ 500 Hz: ▲ 100 Hz: ■ 10 Hz: ×

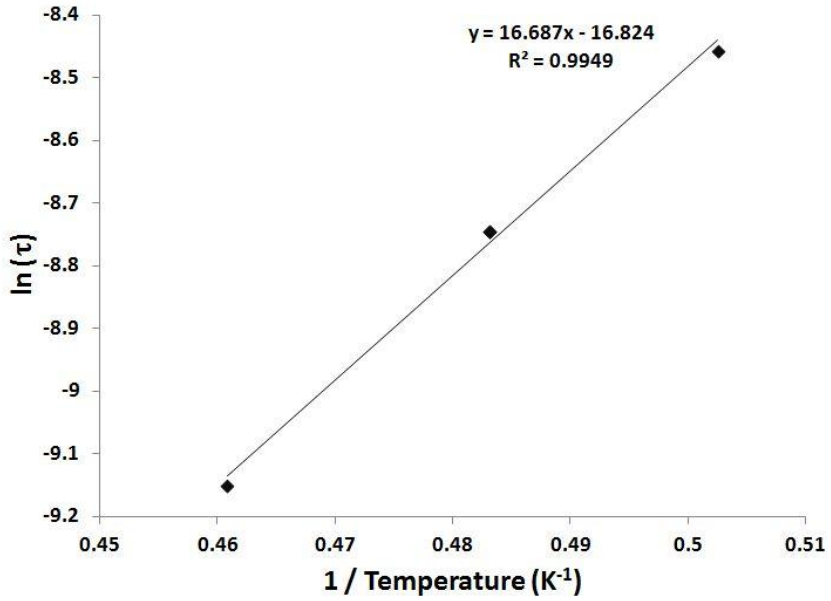

Figure 3.34. The Arrhenius plot showing the natural log of the magnetization relaxation (ln(τ)) versus the inverse of the blocking temperature (1/T) for **Dy14MC5**. The solid line is the best-fit line for the linear equation shown.

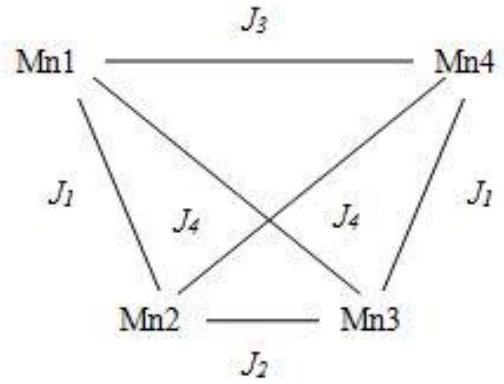

Figure 3.35. The coupling scheme for **Y14MC5** was used to derive a spin Hamiltonian given in Equation 4.

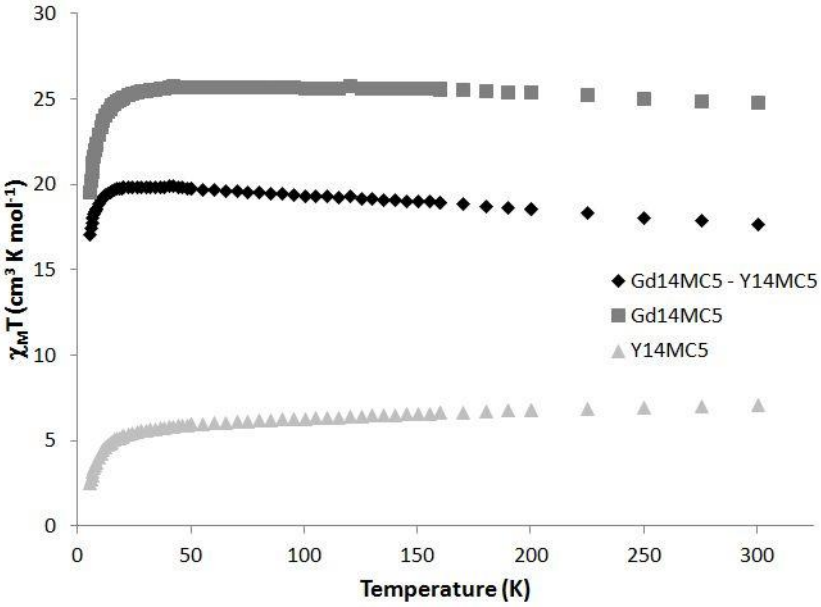

Figure 3.36. The difference between **Gd14MC5** and **Y14MC5** is shown.

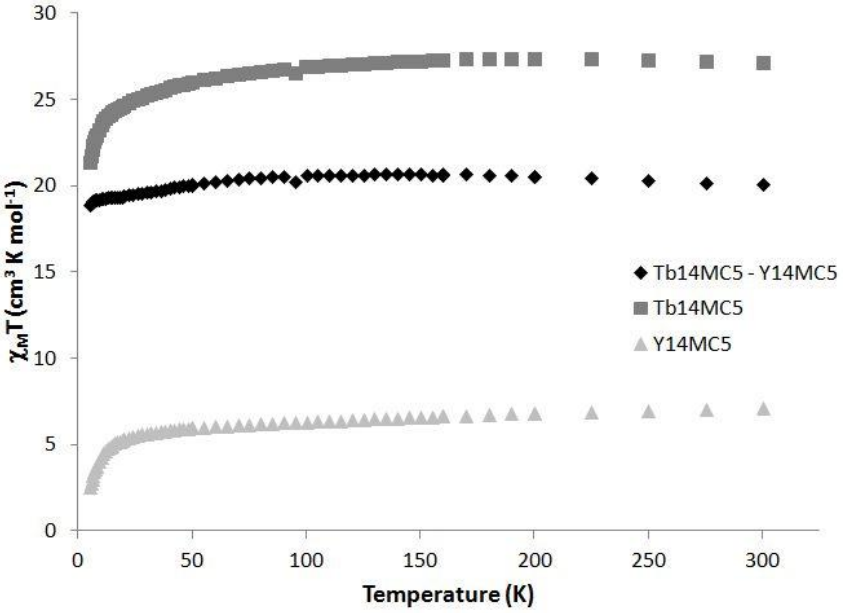

Figure 3.37. The difference between **Tb14MC5** and **Y14MC5** is shown.

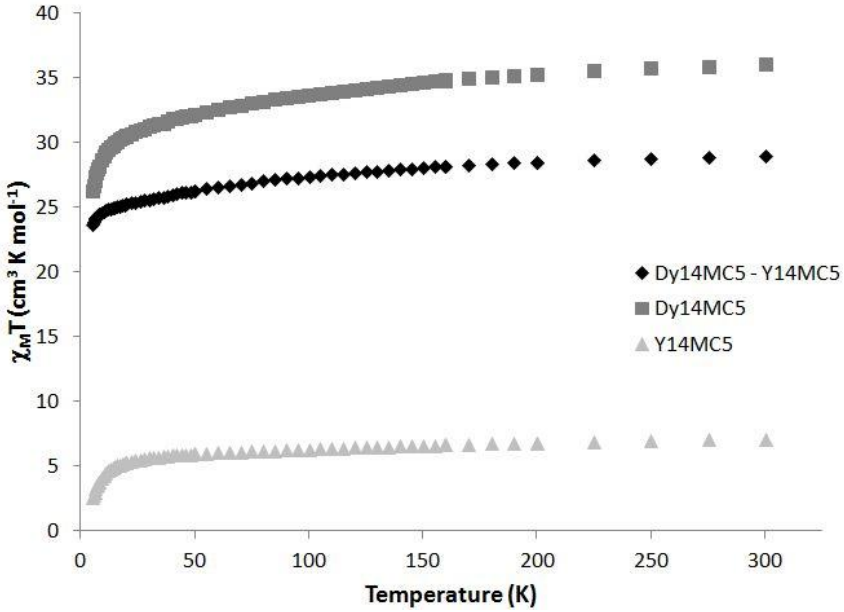

Figure 3.38. The difference between **Dy14MC5** and **Y14MC5** is shown.

References

1 Gibney, B. R.; Wang, H.; Kampf, J. W.; Pecoraro, V. L. *Inorg. Chem*. **1996**, *35*, 6184.

2 Pecoraro, V. L.; Stemmler, A. J.; Gibney, B. R.; Wang, H.; Kampf, J. W.; Barwinski, A. *Prog. Inorg. Chem*. **1997**, *45*, 83.

3 Mezei, G.; Zaleski, C. M.; Pecoraro, V. L. *Chem. Rev*. **2007**, *107*, 4933.

4 Zaleski, C. M.; Tricard, S.; Depperman, E. C.; Wernsdorfer, W.; Mallah, T.; Kirk, M. L.; Pecoraro, V. L. *Inorg. Chem*. **2011**, *50*, 11348.

5 Zaleski, C. M. Utilizing Metallacrowns to Develop New Single-Molecule Magnets. Ph.D Thesis. The University of Michigan. 2005.

6 Kahn, O. *Molecular Magnetism*, VCH Publishers, New York, 1993.

7 Psomas, G.; Dendrinou-Samara, C.; Alexiou, M; Tsohos, A.; Raptopoulou, C. P.; Terzis, A.; Kessissoglou, D. P. *Inorg. Chem.* **1998**, *37*, 6556.

8 Choo, I. Y.; Yeo, H. J.; Jeong, J. H. *Bull. Korean Chem. Soc.* **1995**, *15*, 1244.

9 Psomas, G.; Stemmler, A. J.; Dendrinou-Samara, C.; Bodwin, J. J.; Schneider, M. W.; Alexiou, M.; Kampf, J. W.; Kessissoglou, D. P.; Pecoraro, V. L. *Inorg. Chem.* **2001**, *40*, 1562.

10 Shannon, R. D. *Acta Cryst.* **1976**. *A32*, 751.

11 Yoo, J.; Yamaguchi, A.; Nakano, M.; Krzystek, J.; Streib, W. E.; Brunel, L.-C.; Ishimoto, H.; Christou, G.; Hendrickson, D. N. *Inorg. Chem*. **2001**, *40*, 4604.

12 Ako, A. M.; Mereacre, V.; Clérac, R.; Hewitt, I. J.; Lan, Y.; Buth, G.; Anson, C. E.; Powell, A. K. *Inorg. Chem*. **2009**, *48*, 6713.

13 Mereacre, V.; Ako, A. M.; Clérac, R.; Wernsdorfer, W.; Hewitt, I. J.; Anson, C. E.; Powell, A. K. *Chem. Eur. J*. **2008**, *14*, 3577.

14 Akhtar, M. N.; Lan, Y. Mereacre, V.; Clérac, R.; Anson, C. E.; Powell, A. K. *Polyhedron*, **2009**, *28*, 1698.

15 Zaleski, C. M.; Kampf, J. W.; Mallah, T.; Kirk, M. L.; Pecoraro, V. L.; *Inorg. Chem.* **2007**, *46*, 1954.

16 Akhtar, M. N.; Zheng, Y. Z.; Lan, Y. H.; Mereacre, V.; Anson, C. E.; Powell, A. K.; *Inorg. Chem.* **2009**, *48*, 3502.

17 Glerup, J.; Goodson, P. A.; Hazell, A.; Hazell, R.; Hodson, D. J.; McKenzie, C. J.; Michelsen, K.; Rychlewska, U.; Toftlund, H. *Inorg. Chem*. **1994**, *33*, 4105.

18 Borras-Almenar, J. J.; Coronado, E.; Ostrovsky, S. M.; Palii, A. V.; Tsukerblat, B. S. *Chem. Phys*. **1999**, *240*, 149.

19 Borras-Almenar, J. J.; Clemente-Juan, J. M.; Coronado, E.; Tsukerblat, B. S.; *J. Comput. Chem*. **2001**, *22*, 984.

20 Stemmler, A. J. Kampf, J. W.; Kirk, M. L.; Atasi, B. H.; Pecoraro, V. L. *Inorg. Chem*. **1999**, *38*, 2807.

21 Carnall, W. T.; Goodman, G. L.; Rajnak, K.; Rana, R. S. *J. Chem. Phys*. **90**, *1989*, 3443.

22 Rinehart, J. D. & Long, J. R. *Chem. Sci*. **2011**, *2*, 2078.

23 Ishikawa, N.; Sugita, M,; Ishikawa, T.; Koshihara, S. Kaizu, Y. *J. Am. Chem. Soc*. **2003**, *125*, 8694.

24 Rinehart, J. D.; Fang, M.; Evans, W. J.; Long, J. R. *J. Am. Chem. Soc*. **2011**, *133*, 14236.

25 Gonidec, M.; Biagi, R.; Corradini, V.; Moro, F.; De Renzi, V.; del Pennino, U.; Muccioli, L.; Zannoni, C.; Amabilino, D. B.; Veciana, J. *J. Am. Chem. Soc*. **2011**, *133*, 6603.
26 Mereacre, V.; Ako, A. M.; Clérac, R.; Wernsdorfer, W.; Hewitt, I. J.; Anson, C. E.; Powell, A. K. *Chem. Eur. J*. **2008**, *14*, 3577.
27 Mereacre, V. M.; Ako, A. M.; Clérac, R.; Wernsdorfer, W.; Filoti, G.; Bartolomé, J.; Anson, C. E.; Powell, A. K. *J. Am. Chem. Soc*. **2007**, *129*, 9248.
28 Mydosh, J. A. Spin Glasses: An Experimental Introduction; Taylor and Francis: London, 1993.
29 Gatteschi, D.; Sessoli, R.; Villain, J.; *Molecular Nanomagnets*; Oxford University Press: New York, 2006.
30 Blagg, R. J.; Muryn, C. A.; McInnes, E. J. L.; Tuna, F.; Winpenny, R. E. P. *Angew. Chem. Int. Ed*. **2011**, *50*, 6530.

Chapter IV

Studying Planar M^{n+} 12-$MC_{Mn^{III}N(shi)}$-4 Complexes for Single-Molecule Magnetic Properties

Introduction

Curt Zaleski laid the ground work to study **M^{n+} 12-$MC_{Mn^{III}N(shi)}$-4** complexes in 2005, when he reported in his thesis that **Mn^{II} 12-MC-4** (Figure 1.2) and **Dy^{III} 12-MC-4** (Figure 1.57) showed frequency-dependent out-of-phase ac magnetic susceptibility, a hallmark of single-molecule magnets (SMMs).[1] He expounded on this work in a manuscript published in 2011.[2] Based on the interesting magnetic properties of the **Mn^{II} 12-MC-4** complex, it was hoped that introducing a more anisotropic central metal, such as octahedral Ni^{II}, would increase the anisotropy leading to an enhancement of the overall magnetic behavior. It also seemed interesting to further understand the magnetic properties of the **Dy^{III} 12-MC-4** complex, as it was observed that though Dy^{III} is more anisotropic than Mn^{II}, there was not a significant improvement in the observed blocking temperatures.

Zaleski and co-workers studied the magnetism of the **Li{$(LiCl)_2$ [12-MC-4]}** (Figure 1.47a) in order to determine the coupling constants in the ring as well as to determine if the four ring Mn^{III} ions were the origin of the observed slow magnetic relaxation in the series. Studying the crystallographic data, it was observed that Jahn-Teller axes of the four Mn^{III} ions aligned roughly parallel to each other and perpendicular to the metallacrown plane (Figure 1.46). This could potentially maximize the anisotropy of the complex, as the anisotropy tensor of Mn^{III} falls along the Jahn-Teller axis. It was found that the four Mn^{III} metals weakly antiferromagnetically coupled through the ring (J = -4.0

cm^{-1}, using the $\hat{H} = -2J(\hat{S}_i\hat{S}_j)$ convention) (Figure 1.50) and there was no cross-molecule coupling. The **Li 12-MC-4** showed no slow magnetic relaxation, as may be expected.[2]

Turning to the **Mn^{II} 12-MC-4**, it was found that the four Mn^{III} ions remained antiferromagnetically coupled (J = -6.3 cm^{-1}). The central Mn^{II} was antiferromagnetically coupled to the four Mn^{III} ions (J = -4.2 cm^{-1}) (Figure 1.52). The Jahn-Teller axes of the four Mn^{III} ions remained parallel to each other and perpendicular to the metallacrown plane. The central Mn^{II} ion was in an usual trigonal prismatic orientation. This complex showed slow-magnetic relaxation as well as magnetic hysteresis at 0.04 K. Using simulations, it was found that anisotropic contributions were -3.0 cm^{-1} from the Mn^{III} ions and +1 cm^{-1} from the central Mn^{II} ion. The anisotropic value for Mn^{II} was unusually large for $^6A_1$ ion. This large value, however, was attributed to the distorted trigonal prismatic geometry of the ion. Fitting the Arrhenius equation to the solution data revealed a U_{eff} of 14.7 cm^{-1} and a τ_0 of 1.4 x 10^{-7} s.[2]

Using the magnetic program MAGPACK,[3,4] the magnetization and susceptibility plots were fitted, revealing an unusual S = ½ ground spin state for the **Mn^{II} 12-MC-4** complex. This seemingly does not make sense because one of the fundamental equations for SMM behavior is

$$U_{eff} = -(S^2 - 1/4)|D| \qquad (1)$$

where S is the total spin and D is the molecular magnetoanisotropy. If the ground spin state is, in fact, 1/2, then the energy barrier should become zero. What was observed was that there was a low-lying S = 3/2 excited state, only 2 cm^{-1} above the ground state. The next excited states were S = 1/2 and S = 3/2, 6.6 cm^{-1} above the ground spin state.2 It was determined that if the coupling constants were slightly altered, it would be possible to access higher ground spin states, which could increase the observed blocking temperature.

It was hoped that by substituting Ln^{III} ions for Mn^{II} or the Li^{+} ions in the 12-MC-4 architecture, the blocking temperatures would increase above 2 K. Four **Ln^{III} 12-MC-4** (Ln^{III} = Y^{III}, Gd^{III}, Tb^{III}, and Dy^{III}) complexes were prepared. The Y^{III} complex (Figure 1.56) corroborated the coupling found from the **Li^{+} 12-MC-4** example. Introduction of Gd^{III} would provide a large spin (S = 7/2, L = 0, $^{8}S_{7/2}$, g_J = 2) and little or no anisotropy, allowing one to determine if only the metallacrown ring could provide sufficient anisotropy for the system. Lastly, the Tb^{III} (S = 3, L = 3, $^{7}F_{6}$, g_J = 3/2) and Dy^{III} (S = 5/2, L = 5, $^{6}H_{15/2}$, g_J = 4/3) complexes would provide both anisotropy and spin to the system. The Y^{III} and Gd^{III} examples did not show slow-magnetic relaxation. This indicated that the central lanthanide needed to not only have some spin component, but also needed to provide anisotropy to the system, as was seen in the **Mn^{II} 12-MC-4** complex. The **$Tb^{III}(Hsal)_4H_3O^{+}$12-MC-4** complex, where $Hsal^{-}$ is monodeprotonated salicylic acid, also did not show slow magnetic relaxation [NOTE: Zaleski did not assign the hydronium cation in this structure. Based on the crystal structure of the **Dy^{III}12-MC-4** analog, there was an unassigned *q* peak on the face trans to the Dy^{III} ion. It was realized that the original **$Dy^{III}(Hsal)_3(H_2sal)$12-MC-4** assignment was not accurate, as it was not possible to differentiate the four salicylate ligands. The unassigned *q* peak was close enough to the oxygen atoms of the metallacrown to be a hydrogen bonded hydronium ion (2.749 Å and 2.781 Å). The series were then assigned as **$Ln^{III}(Hsal)_4H_3O^{+}$ 12-MC-4** (Figure 1.57).] Because Tb^{III} is a non-Kramer's system, it may not have a bistable ground state.[5] The Kramer's doublet system, **$Dy^{III}(Hsal)_4H_3O^{+}$ 12-MC-4** did, on the other hand, show slow magnetic relaxation (Figure 1.58), a hallmark of SMM behavior. However, the blocking temperature fell below 2 K, so it was not possible to determine an actual blocking temperature and overall SMM performance.

The MAGPACK calculations indicated that for the **Mn^{II} 12-MC-4** complex, if the coupling constants between the ring metals or the exchange coupling between the central metal and the ring metals changed, different spin states could be accessed (Figure 4.1). It was hoped that similar phenomena would be observed for the **Dy^{III}M 12-MC-4** complexes. It is known in other complexes, such as the Mn_{12} or Mn_4 systems, that changing the bridging carboxylate ligand affects the magnetization as well as the

magnetic susceptibility.[6,7,8] With the presumably contracted *f* orbitals of the Dy^{III} ion, would a similar impact be observed? Answering this question, as well as identifying the influence of diamagnetic monovalent cations on the magnetic properties on these 12-**MC-4** based *3d*/*4f* structures will be the focus of the studies in this chapter.

Experimental

Synthetic Methods

Manganese(II) acetate tetrahydrate ($Mn(OAc)_2{\cdot}4H_2O$), manganese(II) chloride tetrahydrate ($MnCl_2{\cdot}4H_2O$), nickel(II) acetate tetrahydrate ($Ni(OAc)_2{\cdot}4H_2O$), salicylic acid (H_2sal), sodium benzoate ($Na(O_2C_7H_5)$), sodium trichloroacetate ($Na(O_2C_2Cl_3)$), potassium trichloroacetate ($K(O_2C_2Cl_3)$), and *N*-,*N*- dimethylformamide (DMF) were purchased from Sigma-Aldrich and used as received. Methanol (MeOH), diethyl ether, sodium hydroxide (NaOH), and potassium hydroxide (KOH) were obtained from Fischer Scientific and used as received. Salicylhydroxamic acid (H_3shi) and the lanthanide nitrate pentahydrate salts ($Dy(NO_3)_3{\cdot}5H_2O$, $Ho(NO_3)_3{\cdot}5H_2O$) were purchased and used as received from Alfa Aesar.

$[Ni^{II}Mn^{III}_4(shi)_4(OAc)_2]{\cdot}12H_2O$ (**$Ni(OAc)_2$ [12-$MC_{Mn^{III}N(shi)}$-4]·12H_2O**). In 20.0 mL MeOH, 4 mmol of $Mn(OAc)_2{\cdot}4H_2O$ were dissolved. In a different beaker, 4 mmol H_3shi and 2 mmol NaOH were dissolved in 200 mL MeOH. The $Mn(OAc)_2$ solution was added to the H_3shi and NaOH solution. To this solution, 1 mmol $Ni(OAc)_2{\cdot}4H_2O$ was added and stirred overnight. The following morning, the solution was vacuum filtered and slowly evaporated. Approximately three weeks later, brown block crystals of X-ray quality were isolated. Yield: 46.9%. Elemental analysis for $NiMn_4C_{32}H_{46}N_4O_{28}$ [FW = 1213.173 g/mol] found % (calculated) C = 31.96, 31.86 (31.682); H = 3.62, 3.71 (3.822); N = 4.50, 4.60 (4.618). Unit cell dimensions: a = 10.3280(8) Å, b = 10.7455(8) Å, c = 11.7777(9) Å, α = 85.236(1)°, β = 86.154(1)°, γ = 77.343(1)°, V = 1269.31(17) $Å^3$, space group: $P\bar{1}$.

$[Ni^{II}Mn^{III}_4(shi)_4(OAc)_2(DMF)_5]\cdot 2H_2O$ (**$Ni(OAc)_2$[12-$MC_{Mn^{III}N(shi)}$-4]·5DMF**). In 12.5 mL DMF, 4 mmol of $Mn(OAc)_2\cdot 4H_2O$ were dissolved. In another beaker, 4 mmol H_3shi and 0.5 mmol $Ni(OAc)_2\cdot 4H_2O$ were dissolved in 13.0 mL DMF. The $Mn(OAc)_2$ solution was stirred until it turned red, at which point it was added to the H_3shi and $Ni(OAc)_2$ solution. The solution was stirred three hours, gravity filtered, and allowed to slowly evaporate. In five weeks, green plate crystals of X-ray quality were isolated. Yield: 94.98%. Elemental analysis for $NiMn_4C_{47}H_{61}N_9O_{23}$ [FW = 1398.493 g/mol] found % (calculated) C = 40.51, 40.45 (40.366); H = 4.38, 4.31 (4.396); N = 9.05, 8.92 (9.014). Unit cell dimensions: a = 10.713(2) Å, b = 12.200(2) Å, c = 13.085(3) Å, α = 98.95(3)°, β = 108.66(3)°, γ = 106.03(3)°, V = 1500.4(5) $Å^3$, space group $P\bar{1}$.

$DyKMn_4(shi)_4(Hsal)_4(DMF)_6(H_2O)_5$ (**$Dy(Hsal)_4K$ [12-$MC_{Mn^{III}N(shi)}$-4]·6DMF·5H_2O**). Four mmol of $Mn(OAc)_2\cdot 4H_2O$, 2.7 mmol KOH, and 4 mmol H_2sal were dissolved in 15.0 mL DMF. In another beaker, 4 mmol H_3shi and 0.5 mmol $Dy(NO_3)_3\cdot 5H_2O$ were dissolved in 16.0 mL DMF. When the $Mn(OAc)_2$, KOH, and H_2sal solution turned red, it was added to the $Dy(NO_3)$ and H_3shi solution, and stirred overnight. The following day, the solution was vacuum filtered and the solute left to slowly evaporate. After 6 months, green prism crystals of X-ray quality were isolated. Yield: 71.9%. Elemental analysis for $DyKMn_4C_{74}H_{88}N_{10}O_{35}$ [FW = 2098.909 g/mol] found % (calculated) C = 42.27, 42.18 (42.346); H = 4.15, 4.11 (4.226); N = 6.99, 6.88 (6.673). Unit cell dimensions: a = 23.2718(16) Å, b = 24.3346(4) Å, c = 14.6609(3) Å, α = 90.00°, β = 90.907(6)°, γ = 90.00°, V = 8301.6(6)$Å^3$, space group: Cc.

$DyNaMn_4(shi)_4(Hsal)_4(DMF)_4(H_2O)_4$ (**$Dy(Hsal)_4Na$ [12-$MC_{Mn^{III}N(shi)}$-4]·4DMF·4H_2O**). Four mmol of $Mn(OAc)_2\cdot 4H_2O$, 4 mmol H_2sal, and 2.7 mmol NaOH were dissolved in 15.0 mL DMF. In another beaker, 4 mmol H_3shi, 4 mmol $Na(O_2C_2Cl_3)$, and 0.5 mmol $Dy(NO_3)_3\cdot 5H_2O$ were dissolved in 16.0 mL DMF. When the $Mn(OAc)_2$, H_2sal, and NaOH solution turned red, it was added to the $Na(O_2C_2Cl_3)_2$, $Dy(NO_3)_3$, and H_3shi solution and stirred overnight. The next day, the solution was vacuum filtered and the solute allowed to slowly evaporate. After 6 months, X-ray quality crystals were isolated. Yield: 46.8%. Elemental analysis for $DyNaMn_4C_{68}H_{72}N_8O_{32}$ [FW = 1918.596 g/mol]

found % (calculated) C = 42.35, 42.35 (42.570); H = 3.70, 3.63 (3.783); N = 5.83, 5.81 (5.840). Unit cell dimensions: a = 24.218 Å, b = 23.799 Å, c = 14.361 Å, α = 90.00°, β = 90.097°, γ = 90.00° V = 8276.68 $Å^3$, space group: Cc.

$DyKMn_4(shi)_4(OAc)_4(DMF)_5 \cdot 2(K(Hsal))$ (**$Dy(OAc)_4K$ [12-$MC_{Mn^{III}N(shi)}$-4]·5DMF**). Four mmol of $Mn(OAc)_2 \cdot 4H_2O$ and 2.7 mmol KOH were dissolved in 15.0 mL DMF. In another beaker, 4 mmol H_3shi and 0.05 mmol $Dy(NO_3)_3 \cdot 5H_2O$ were dissolved in 16.0 mL DMF. When the $Mn(OAc)_2$ and KOH solution was red, it was added to the $Dy(NO_3)_3$ and H_3shi solution and stirred overnight. The next day, the solution was filtered, and the solute was divided into multiple small 20 mL scintillation vials to slowly evaporate. After 5 months, green block crystals of X-ray quality were isolated. Yield: 5.9 %. Elemental analysis for $DyK_3Mn_4C_{65}H_{73}N_9O_{31}$ [FW = 1975.883 g/mol] found % (calculated) C = 39.84, 39.90 (39.512); H = 3.90, 3.93 (3.724); N = 6.70, 6.78 (6.38). Unit cell dimensions a = 16.1208(13) Å, b = 16.3127(13) Å, c = 23.4413(18) Å, α = 90.00°, β = 95.3460(10)°, γ = 90.00°, V = 6137.6(8) $Å^3$, space group: C2/c.

$DyNaMn_4(shi)_4(benzoate)_4(DMF)_5(H_2O)_4$ (**$Dy(benzoate)_4Na$ [12-$MC_{Mn^{III}N(shi)}$-4]·5DMF·$4H_2O$**) Four mmol of $MnCl_2 \cdot 4H_2O$ and 8 mmol sodium benzoate were dissolved in 16.0 mL DMF. In another beaker, 4 mmol H_3shi and 0.5 mmol $Dy(NO_3)_3 \cdot 5H_2O$ were dissolved in 15.0 mL DMF. When the $MnCl_2$ and $Na(O_2C_7H_5)$ solution was red, it was added to the $Dy(NO_3)_3$ and H_3shi solution. The solution was stirred overnight and vacuum filtered the next day. The solute was allowed to slowly evaporate and X-ray quality crystals were isolated 10 months later. Yield: 60.8 %. Elemental analysis for $DyNaMn_4C_{71}H_{79}N_9O_{29}$ [FW = 1927.693 g/mol] % found (calculated) C = 44.21, 44.04 (44.238); H = 4.04, 4.10 (4.131); N = 6.39, 6.28 (6.539). Unit cell dimensions: a = 14.1639(3) Å, b = 16.5724(3) Å, c = 16.7075(12) Å, α = 90.00°, β = 95.927(7)°, γ = 90.00°, V = 3900.8(3) $Å^3$, space group: Cc.

$HoKMn_4(shi)_4(OAc)_4(DMF)_5$ (**$Ho(OAc)_4K$ [12-$MC_{Mn^{III}N(shi)}$-4]·5DMF**). Four mmol $Mn(OAc)_2 \cdot 4H_2O$ and 2.7 mmol KOH were dissolved in 15.0 mL DMF. In another beaker, 4 mmol H_3shi and 0.5 mmol $Ho(NO_3)_3 \cdot 5H_2O$ were dissolved in 15.0 mL DMF.

The $Mn(OAc)_2$ and KOH solution was stirred until it was red and was then added to the $Ho(NO_3)_3$ and H_3shi solution. The solution was stirred overnight and then filtered. The solute was slowly evaporated in the fume hood. X-ray quality crystals were isolated in 3 months. Yield: 36.1 %. Elemental analysis for $HoKMn_4C_{51}H_{63}N_9O_{25}$ [FW = 1625.887 g/mol] % found (calculated) C = 37.84, 38.01 (37.675); H = 3.88, 3.86 (3.906); N = 7.77, 7.94 (7.753). Unit cell dimensions: a = 16.114(3) Å, b = 16.336(3) Å, c = 23.428(5) Å, α = 90.00°, β = 95.38(3)°, γ = 90.00°, V = 6140(2) $Å^3$, space group: C2/c.

$HoNaMn_4(shi)_4(OAc)_4(DMF)_7(H_2O)_5$ (**$Ho(OAc)_4Na$ [12-$MC_{Mn^{III}N(shi)}$-4]·7DMF·5H_2O**). Four mmol $Mn(OAc)_2·4H_2O$ and 2.7 mmol NaOH were dissolved in 16.0 mL DMF. In another beaker, 4 mmol H_3shi and 0.05 $Ho(NO_3)_3·5H_2O$ in 16.0 mL DMF. When the $Mn(OAc)_2$ and NaOH solution was red, it was added to the H_3shi and $Ho(NO_3)_3$ solution, and stirred overnight. The next day, the solution was filtered and the solute was slowly evaporated in a fume hood. After 3 months, X-ray quality crystals were isolated. Yield: 104.3 %. Elemental analysis for $HoNaMn_4C_{57}H_{87}N_{11}O_{32}$ [FW = 1846.044 g/mol] % found (calculated) C = 37.28, 37.44 (37.086); H = 4.63, 4.51 (4.750); N = 8.26, 8.11 (8.346). Unit cell dimensions: a = 13.0281(11) Å, b = 16.0866(14) Å, c = 17.3161(15) Å, α = 89.248(2)°, β = 88.795(2)°, γ = 72.992(2)°, V = 3469.5(5) $Å^3$, space group: $P\bar{1}$.

Physical Methods

X-ray Crystallography. X-ray single crystal diffraction data was collected by Dr. Jeff W. Kampf at the University of Michigan. Crystals were mounted onto a standard Bruker APEX CCD-based X-ray diffractometer. For the **$Ni(OAc)_2$ 12-MC-4** structures, **HoX_4M 12-MC-4**, and **$Dy(OAc)_4K$ 12-MC-4** complexes, the diffractometer was equipped with a LT-2 low temperature device and normal focus Mo-target X-ray tube (λ = 0.71073 Å) and operated at the indicated power. For all other crystals, the diffractometer was equipped with a LT-2 low temperature device and Cu X-ray tube (λ = 1.54178 Å) at the indicated power. For both instruments, data frames were collected using the program APEX2 and the data processed using the SAINT routine.

$[Ni^{II}Mn^{III}_4(shi)_4(OAc)_2]\cdot 12H_2O$ (**$Ni(OAc)_2$ [12-$MC_{Mn^{III}N(shi)}$-4]·$12H_2O$**). A brown block crystal of dimensions 0.18 x 0.11 x 0.10 mm was mounted on a Bruker SMART APEX CCD-based X-ray diffractometer equipped with a low temperature device and fine focus Mo-target X-ray tube (λ = 0.71073 A) operated at 1500 W power (50 kV, 30 mA). The X-ray intensities were measured at 85(1) K; the detector was placed at a distance 5.055 cm from the crystal. A total of 3730 frames were collected with a scan width of 0.5° in ω and phi with an exposure time of 30 s/frame. The integration of the data yielded a total of 41415 reflections to a maximum 2θ value of 56.72° of which 6356 were independent and 5724 were greater than $2\sigma(I)$. The final cell constants were based on the xyz centroids of 9955 reflections above $10\sigma(I)$. Analysis of the data showed negligible decay during data collection; the data were processed with SADABS and corrected for absorption. The structure was solved and refined with the Bruker SHELXTL (version 6.12) software package, using the space group $P\bar{1}$ with Z = 1 for the formula $C_{40}H_{40}N_4O_{24}Mn_4Ni$. All non-hydrogen atoms were refined anisotropically with the hydrogen atoms placed in idealized positions except for those involved in hydrogen bonding which were allowed to refine isotropically. Full matrix least-squares refinement based on F^2 converged at $R_1 = 0.0379$ and $wR_2 = 0.0869$[based on $I > 2\sigma(I)$], $R_1 = 0.0435$ and $wR_2 = 0.0897$ for all data. Experimental parameters and crystallographic data are given in Table 4.1. Important bond distances are given in Table 4.4.

$[Ni^{II}Mn^{III}_4(shi)_4(OAc)_2(DMF)_5]\cdot 2H_2O$ (**$Ni(OAc)_2$[12-$MC_{Mn^{III}N(shi)}$-4]·5DMF**). A green plate crystal of dimensions 0.14 x 0.14 x 0.05 mm was mounted on a Bruker SMART APEX CCD-based X-ray diffractometer equipped with a low temperature device and fine focus Mo-target X-ray tube (λ = 0.71073 A) operated at 2000 W power (50 kV, 30 mA). The X-ray intensities were measured at 85(1) K; the detector was placed at a distance 5.055 cm from the crystal. A total of 3440 frames were collected with a scan width of 0.5° in ω and 0.45° in phi with an exposure time of 45 s/frame. The integration of the data yielded a total of 44027 reflections to a maximum 2θ value of 56.7° of which 7476 were independent and 6187 were greater than $2\sigma(I)$. The final cell constants were based on the xyz centroids of 9341 reflections above $10\sigma(I)$. Analysis of the data showed

negligible decay during data collection; the data were processed with SADABS and corrected for absorption. The structure was solved and refined with the Bruker SHELXTL (version 6.12) software package, using the space group $P\bar{1}$ with Z = 1 for the formula $C_{50}H_{43}N_{10}O_{23}Mn_4Ni$. All non-hydrogen atoms were refined anisotropically with the hydrogen atoms placed in idealized positions. Full matrix least-squares refinement based on F^2 converged at $R_1 = 0.0522$ and $wR_2 = 0.1682$ [based on $I > 2\sigma(I)$], $R_1 = 0.0635$ and $wR_2 = 0.1759$ for all data. Experimental parameters and crystallographic data are given in Table 4.1. Important bond distances are given in Table 4.5.

$DyKMn_4(shi)_4(Hsal)_4(DMF)_6(H_2O)_5$ (**$Dy(Hsal)_4K$ [12-$MC_{Mn^{III}N(shi)}$-4]·6DMF·5H_2O**). A green prism crystal of dimensions 0.15 x 0.12 x 0.11 mm was mounted on a Bruker SMART APEX CCD-based X-ray diffractometer equipped with a low temperature device and Cu-target X-ray tube (λ = 1.54178 Å) operated at 2000 W power (20 kV, 10 mA). The X-ray intensities were measured at 85(1) K; the detector was placed at a distance 42.00 mm from the crystal. A total of 3095 images were collected with a scan width of 1.0° in ω with an exposure time of 10 s/frame for low angle data and 30 s/frame for high angle data. The integration of the data yielded a total of 87160 reflections to a maximum 2θ value of 50.7° of which 14273 were independent and 13158 were greater than $2\sigma(I)$. Analysis of the data showed negligible decay during data collection; the data were processed with SADABS and corrected for absorption. The structure was solved and refined with the Bruker SHELXTL (version 6.12) software package, using the space group Cc with Z = 4 for the formula $C_{74}H_{88}N_{10}O_{35}Mn_4DyK$. All non-hydrogen atoms were refined anisotropically with the hydrogen atoms placed in idealized positions. Full matrix least-squares refinement based on F^2 converged at $R_1 = 0.0748$ and $wR_2 = 0.2068$ [based on $I > 2\sigma(I)$], $R_1 = 0.0789$ and $wR_2 = 0.2115$ for all data. Experimental parameters and crystallographic data are given in Table 4.2. Important bond distances are given in Table 4.6.

$DyNaMn_4(shi)_4(Hsal)_4(DMF)_4(H_2O)_4$ (**$Dy(Hsal)_4Na$ [12-$MC_{Mn^{III}N(shi)}$-4]·4DMF·$4H_2O$**). Unit cell parameters were collected for identification. The unit cell matched that of **$Dy(Hsal)_4K$ 12-MC-4**, given above.

$DyKMn_4(shi)_4(OAc)_4(DMF)_5$·2(K(Hsal)) (**$Dy(OAc)_4K$ [12-$MC_{Mn^{III}N(shi)}$-4]·5DMF**). A green block crystal of 0.28 x 0.10 x 0.09 mm was mounted on a Bruker SMART APEX CCD-based X-ray diffractometer equipped with a low temperature device and fine focus Mo-target X-ray tube (λ = 0.71073 A) operated at 2000 W power (50 kV, 30 mA). The X-ray intensities were measured at 85(2) K; the detector was placed at a distance 5.055 cm from the crystal. A total of 3328 frames were collected with a scan width of 0.5° in ω and 0.45° in phi with an exposure time of 45 s/frame. The integration of the data yielded a total of 85907 reflections to a maximum 2θ value of 56.68° of which 7662 were independent and 6938 were greater than 2σ(I). The final cell constants were based on the xyz centroids of 9643 reflections above 10σ(I). Analysis of the data showed negligible decay during data collection; the data were processed with SADABS and corrected for absorption. The structure was solved and refined with the Bruker SHELXTL (version 6.12) software package, using the space group C_2/c with Z = 4 for the formula $C_{51}H_{63}N_9O_{25}Mn_4DyK$. All non-hydrogen atoms were refined anisotropically with the hydrogen atoms placed in idealized positions. Full matrix least-squares refinement based on F^2 converged at R_1 = 0.328 and wR_2 = 0.852 [based on I > 2σ(I)], R_1 = 0.0372 and wR_2 = 0.0880 for all data. Experimental parameters and crystallographic data are given in Table 4.2. Important bond distances are given in Table 4.7.

$DyNaMn_4(shi)_4(benzoate)_4(DMF)_5(H_2O)_4$ (**$Dy(benzoate)_4Na$ [12-$MC_{Mn^{III}N(shi)}$-4]·5DMF·$4H_2O$**). A green block crystal of 0.12 x 0.09 x 0.07 mm was mounted on a Bruker SMART APEX CCD-based X-ray diffractometer equipped with a low temperature device and fine focus Cu-target X-ray tube (λ = 1.54178 A) operated at 2000 W power (20 kV, 10 mA). The X-ray intensities were measured at 85(2) K; the detector was placed at a distance 42.00 mm from the crystal. A total of 3162 images were collected with a scan width of 1.0° in ω with an exposure time of 10 s/frame for low

angle data and 30 s/frame for high angle data. The integration of the data yielded a total of 82097 reflections to a maximum 2θ value of 50.70° of which 14068 were independent and 12326 were greater than 2σ(I). Analysis of the data showed negligible decay during data collection; the data were processed with SADABS and corrected for absorption. The structure was solved and refined with the Bruker SHELXTL (version 6.12) software package, using the space group Cc with Z = 1 for the formula $C_{71}H_{79}N_9O_{29}Mn_4DyNa$. All non-hydrogen atoms were refined anisotropically with the hydrogen atoms placed in idealized positions. Full matrix least-squares refinement based on F^2 converged at R_1 = 0.0774 and wR_2 = 0.2006 [based on I > 2σ(I)], R_1 = 0.0984 and wR_2 = 0.2235 for all data. Experimental parameters and crystallographic data are given in Table 4.2. Important bond distances are given in Table 4.8.

$HoKMn_4(shi)_4(OAc)_4(DMF)_5$ (**$Ho(OAc)_4K$ [12-$MC_{Mn^{III}N(shi)}$-4]·5DMF**). A green block crystal of 0.46 x 0.23 x 0.07 mm was mounted on a Bruker SMART APEX CCD-based X-ray diffractometer equipped with a low temperature device and fine focus Mo-target X-ray tube (λ = 0.71073 A) operated at 2000 W power (50 kV, 30 mA). The X-ray intensities were measured at 85(1) K; the detector was placed at a distance 5.055 cm from the crystal. A total of 4095 frames were collected with a scan width of 0.5° in ω and 0.45° in phi with an exposure time of 45 s/frame. The integration of the data yielded a total of 14443 reflections to a maximum 2θ value of 42.98° of which 3279 were independent and 3055 were greater than 2σ(I). Analysis of the data showed negligible decay during data collection; the data were processed with SADABS and corrected for absorption. The structure was solved and refined with the Bruker SHELXTL (version 6.12) software package, using the space group C_2/c with Z = 4 for the formula $C_{51}H_{63}N_9O_{25}Mn_4HoNa$. All non-hydrogen atoms were refined anisotropically with the hydrogen atoms placed in idealized positions. Full matrix least-squares refinement based on F^2 converged at R_1 = 0.0451 and wR_2 = 0.1480 [based on I > 2σ(I)], R_1 = 0.0484 and wR_2 = 0.1509 for all data. Experimental parameters are given in Table 4.3. Important bond distances are given in Table 4.9.

$HoNaMn_4(shi)_4(OAc)_4(DMF)_7(H_2O)_5$ (**$Ho(OAc)_4Na$ [12-$MC_{Mn^{III}N(shi)}$-4]·7DMF·$5H_2O$**). A green block crystal of 0.33 x 0.32 x 0.03 mm was mounted on a Bruker SMART APEX CCD-based X-ray diffractometer equipped with a low temperature device and fine focus Mo-target X-ray tube (λ = 0.71073 A) operated at 2000 W power (50 kV, 30 mA). The X-ray intensities were measured at 85(2) K; the detector was placed at a distance 5.055 cm from the crystal. A total of 3646 frames were collected with a scan width of 0.5° in ω and 0.45° in phi with an exposure time of 45 s/frame. The integration of the data yielded a total of 17309 reflections to a maximum 2θ value of 56.76° of which 17309 were independent and 14310 were greater than 2σ(I). Analysis of the data showed negligible decay during data collection; the data were processed with SADABS and corrected for absorption. The structure was solved and refined with the Bruker SHELXTL (version 6.12) software package, using the space group $P\bar{1}$ with Z = 2 for the formula $C_{57}H_{87}N_{11}O_{32}Mn_4HoNa$. All non-hydrogen atoms were refined anisotropically with the hydrogen atoms placed in idealized positions. Full matrix least-squares refinement based on F^2 converged at $R_1 = 0.0832$ and $wR_2 = 0.2137$ [based on $I > 2\sigma(I)$], $R_1 = 0.1105$ and $wR_2 = 0.2333$ for all data. Experimental parameters and crystallographic data re given in Table 4.3. Important bond distances are given in Table 4.10.

Table 4.1. The crystallographic data for **$Ni(OAc)_2$ 12-MC-4** in methanol and **$Ni(OAc)_2$ 12-MC-4** in DMF are given.

	Ni(OAc)2 12-MC-4 (MeOH)	**Ni(OAc)2 12-MC-4 (DMF)**
Chemical Formula	$NiMn_4C_{32}H_{46}N_4O_{28}$	$NiMn_4C_{47}H_{61}N_9O_{23}$
Formula Weight (g/mol)	1213.173	1398.493
Space Group	$P\bar{1}$	$P\bar{1}$
a (Å)	10.3280(8)	10.713(2)
b (Å)	10.7455(8)	12.200(2)
c (Å)	11.7777(9)	13.085(3)
α (°)	85.236(1)	98.95(3)
β (°)	86.154(1)	108.66(3)
γ (°)	77.343(1)	106.03(3)
V ($Å^3$)	1269.31(17)	1500.4(5)
Temperature (K)	85 (2)	153(2)
λ (Å)	0.71073	0.71073
ρ_{calc}	1.621	1.610

μ (mm^{-1})	1.418	1.22
Z	1	1
R_1 [I>2σ(I)]	0.0379	0.0522
R_1 (all)	0.0435	0.0635
wR_2 [I>2σ(I)]	0.0869	0.1682
wR_2 (all)	0.0897	0.1759

Table 4.2. The crystallographic data for **Dy(Hsal)$_4$K 12-MC-4**, **Dy(OAc)$_4$K 12-MC-4** and **Dy(benzoate)$_4$Na 12-MC-4** are given.

	Dy(Hsal)$_4$K 12-MC-4	**Dy(Hsal)$_4$Na 12-MC-4**	**Dy(OAc)$_4$K 12-MC-4**	**Dy(benzoate)$_4$Na 12-MC-4**
Chemical Formula	$DyKMn_4$ $C_{74}H_{88}N_{10}O_{35}$	$DyNaMn_4$ $C_{68}H_{72}N_8O_{32}$	$DyKMn_4$ $C_{51}H_{63}N_9O_{25}$	$DyNaMn_4$ $C_{71}H_{79}N_9O_{29}$
Formula Weight (g/mol)	2098.909	1918.596	1623.457	1927.693
Space Group	Cc	Cc	C2/c	Cc
a (Å)	23.2718(16)	24.218	16.1208(13)	14.1639(3)
b (Å)	24.3346(4)	23.799	16.3127(13)	16.5724(3)
c (Å)	14.6609(3)	14.361	23.4413(18)	16.7075(12)
α (°)	90.00	90.00	90.00	90.00
β (°)	90.907(6)	90.097	95.3460(10)	95.927(7)
γ (°)	90.00	90.00	90.00	90.00
V ($Å^3$)	8301.6(6)	8276.68	6137.63(8)	3900.8(3)
Temperature (K)	85(1)	85(1)	85(2)	85(2)
λ (Å)	1.54178	1.54178	0.71073	1.54178
ρ_{calc}	1.231		1.900	1.387
μ (mm^{-1})	1.579		2.169	10.816
Z	4		4	1
R_1 [I>2σ(I)]	0.0748		0.0328	0.0774
R_1 (all)	0.0789		0.0372	0.0984
wR_2 [I>2σ(I)]	0.2068		0.0852	0.2006
wR_2 (all)	0.2115		0.0880	0.2235

Table 4.3. The crystallographic data for **$Ho(OAc)_4K$ 12-MC-4** and **$Ho(OAc)_4Na$ 12-MC-4** are given.

	$Ho(OAc)_4K$ 12-MC-4	**$Ho(OAc)_4Na$ 12-MC-4**
Chemical Formula	$HoKMn_4C_{51}H_{63}N_9O_{25}$	$HoNaMn_4C_{57}H_{87}N_{11}O_{32}$
Formula Weight (g/mol)	1625.887	1846.044
Space Group	C2/c	$P\bar{1}$
a (Å)	16.114(3)	13.0281(11)
b (Å)	16.336(3)	16.0866(14)
c (Å)	23.428(5)	17.3161(15)
α (°)	90.00	89.248(2)
β (°)	95.38(3)	88.795(2)
γ (°)	90.00	72.992(2)
V ($Å^3$)	6140(2)	3469.5(5)
Temperature (K)	85(1)	85(2)
λ (Å)	0.71073	0.71073
ρ_{calc}	1.907	1.471
μ (mm^{-1})	2.25	1.915
Z	4	2
R_1 [I>2σ(I)]	0.0451	0.0832
R_1 (all)	0.0484	0.1105
wR_2 [I>2σ(I)]	0.1480	0.2137
wR_2 (all)	0.1509	0.2333

Table 4.4. Important bond distances for **$Ni(OAc)_2$ 12-MC-4 (MeOH)** are given.

Bond	**Distance (Å)**	**Bond**	**Distance (Å)**
Ni(1) – O(3)	1.9649(14)	Mn(1) – O(5a)	1.9846(15)
Ni(1) – O(3a)	1.9649(14)	Mn(1) – O(8)	2.1967(16)
Ni(1) – O(6a)	2.0064(14)	Mn(1) – O(9)	2.1998(17)
Ni(1) – O(6)	2.0064(14)		
Ni(1) – O(7)	2.0808(15)	Mn(2) – O(4)	1.8544(16)
Ni(1) – O(7a)	2.0808(15)	Mn(2) – O(3)	1.8770(15)
		Mn(2) – O(2)	1.9936(15)
Mn(1) – O(1)	1.8760(16)	Mn(2) – N(2)	1.9964(17)
Mn(1) – O(6a)	1.9240(15)	Mn(2) – O(10)	2.1788(18)
Mn(1) – N(1)	1.9743(18)	Mn(2) – O(11)	2.2679(17)

Table 4.5. Important bond distances for **$Ni(OAc)_2$ 12-MC-4 (DMF)** are given.

Bond	**Distance (Å)**	**Bond**	**Distance (Å)**
Ni(1) – O(8)	1.881(9)	Mn(1) – N(1)	1.992(5)
Ni(1) – O(8a)	1.881(9)	Mn(1) – O(7)	2.178(5)
Ni(1) – O(5)	1.954(4)	Mn(1) – O(9)	2.241(4)
Ni(1) – O(5a)	1.954(4)		
Ni(1) – O(3)	1.972(3)	Mn(2) – O(4)	1.856(4)

Ni(1) – O(3a)	1.972(3)	Mn(2) – O(3a)	1.909(4)
		Mn(2) – N(2)	1.967(4)
Mn(1) – O(1)	1.846(4)	Mn(2) – O(2a)	1.980(4)
Mn(1) – O(5)	1.903(4)	Mn(2) – O(12)	2.163(4)
Mn(1) – O(6)	1.985(4)	Mn(2) – O(10)	2.289(5)

Table 4.6. Important bond distances for **Dy(Hsal)$_4$K 12-MC-4** are given.

Bond	Distance (Å)	Bond	Distance (Å)
K(1) – O(27)	2.704(8)	Mn(2) – O(4)	1.866(7)
K(1) – O(28)	2.739(8)	Mn(2) – O(3)	1.883(7)
K(1) – O(26)	2.743(7)	Mn(2) – O(2)	1.926(7)
K(1) – O(29)	2.755(12)	Mn(2) – N(2)	1.988(9)
K(1) – O(25)	2.809(8)	Mn(2) – O(16)	2.234(7)
K(1) – O(6)	2.935(8)	Mn(2) – O(26)	2.306(8)
K(1) – O(9)	2.974(6)		
K(1) – O(3)	3.073(7)	Mn(3) – O(7)	1.833(7)
K(1) – (12)	3.136(8)	Mn(3) – O(6)	1.918(6)
		Mn(3) – N(3)	1.947(8)
Dy(1) – O(14)	2.253(6)	Mn(3) – O(5)	1.958(8)
Dy(1) – O(23)	2.277(6)	Mn(3) – O(19)	2.188(7)
Dy(1) – O(17)	2.291(6)	Mn(3) – O(27)	2.328(7)
Dy(1) – O(20)	2.306(6)		
Dy(1) – O(12)	2.376(7)	Mn(4) – O(10)	1.823(8)
Dy(1) – O(9)	2.407(6)	Mn(4) – O(9)	1.941(7)
Dy(1) – O(3)	2.412(6)	Mn(4) – N(4)	1.956(8)
Dy(1) – O(6)	2.415(6)	Mn(4) – O(8)	1.973(7)
		Mn(4) – O(22)	2.215(7)
Mn(1) – O(1)	1.846(6)	Mn(4) – O(28)	2.316(7)
Mn(1) – O(12)	1.927(6)		
Mn(1) – O(11)	1.952(7)		
Mn(1) – N(1)	1.973(8)		
Mn(1) – O(13)	2.185(7)		
Mn(1) – O (25)	2.363(7)		

Table 4.7. Important bond distances for **Dy(OAc)$_4$K 12-MC-4** are given.

Bond	Distance (Å)	Bond	Distance (Å)
K(1) – O(10a)	2.679(2)	Mn(1) – O(4)	1.846(2)
K(1) – O(10)	2.679(2)	Mn(1) – O(2)	1.904(2)
K(1) – O(7a)	2.758(2)	Mn(1) – O(3)	1.954(2)
K(1) – O(7)	2.758(2)	Mn(1) – N(2)	1.961(2)
K(1) – O(6)	2.866(2)	Mn(1) – O(11)	2.139(2)
K(1) – O(6a)	2.866(2)		
K(1) – O(2)	2.904(2)	Mn(2) – O(1)	1.849(2)
K(1) – O(2a)	2.904(2)	Mn(2) – O(6a)	1.912(2)

K(1) – N(2a)	3.441(2)	Mn(2) – O(5a)	1.950(2)
K(1) – N(2)	3.441(2)	Mn(2) – N(1)	1.965(3)
		Mn(2) – O(8)	2.151(3)
Dy(1) – O(9)	2.254(3)	Mn(2) – O(7)	2.421(2)
Dy(1) – O(9a)	2.254(3)		
Dy(1) – O(12a)	2.289(2)		
Dy(1) – O(12)	2.289		
Dy(1) – O(6a)	2.436(2)		
Dy(1) – O(6)	2.436(2)		
Dy(1) – O(2)	2.456(2)		
Dy(1) – O(2a)	2.456(2)		

Table 4.8. Important bond distances for **Dy(benzoate)$_4$Na 12-MC-4** are given.

Bond	Distance (Å)	Bond	Distance (Å)
Na(1) – O(23)	2.396(10)	Mn(2) – O(4)	1.853(8)
Na(1) – O(21)	2.437(10)	Mn(2) – O(3)	1.922(7)
Na(1) – O(22)	2.444(8)	Mn(2) – O(2)	1.943(6)
Na(1) – O(24)	2.470(10)	Mn(2) – N(2)	1.985(9)
Na(1) – O(9)	2.663(8)	Mn(2) – O(15)	2.190(8)
Na(1) – O(6)	2.674(10)	Mn(2) – O(22)	2.480(7)
Na(1) – O(12)	2.689(8)		
Na(1) – O(3)	2.738(7)	Mn(3) – O(7)	1.857(11)
		Mn(3) – O(6)	1.932(7)
Dy(1) – O(14)	2.265(7)	Mn(3) – O(5)	1.962(8)
Dy(1) – O(20)	2.271(7)	Mn(3) – N(3)	1.972(9)
Dy(1) – O(16)	2.270(7)	Mn(3) – O(17)	2.128(17)
Dy(1) – O(18)	2.282(11)	Mn(3) – O(23)	2.402(17)
Dy(1) – O(6)	2.396(8)		
Dy(1) – O(9)	2.410(7)	Mn(4) – O(10)	1.845(7)
Dy(1) – O(3)	2.421(6)	Mn(4) – O(9)	1.920(7)
Dy(1) – O(12)	2.435(7)	Mn(4) – O(8)	1.937(7)
		Mn(4) – N(4)	1.968(8)
Mn(1) – O(1)	1.853(7)	Mn(4) – O(19)	2.179(8)
Mn(1) – O(12)	1.917(7)	Mn(4) – O(24)	2.485(10)
Mn(1) – O(11)	1.946(7)		
Mn(1) – N(1)	1.952(9)		
Mn(1) – O(13)	2.182		

Table 4.9. Important bond distances for **Ho(OAc)$_4$K 12-MC-4** are given.

Bond	Distance (Å)	Bond	Distance (Å)
K(1) – O(11)	2.669(5)	Mn(1) – O(1)	1.853(5)
K(1) – O(11a)	2.669(5)	Mn(1) – O(6)	1.902(4)
K(1) – O(12)	2.757(5)	Mn(1) – O(5)	1.953(5)
K(1) – O(12a)	2.757(5)	Mn(1) – N(1)	1.970(6)

K(1) – O(3a)	2.876(5)	Mn(1) – O(7)	2.142(5)
K(1) – O(3)	2.876(5)		
K(1) – O(6a)	2.913(5)	Mn(2) – O(4a)	1.856(5)
K(1) – O(6)	2.913(5)	Mn(2) – O(3)	1.907(4)
K(1) – N(1)	3.439(6)	Mn(2) – O(2)	1.948(4)
K(1) – N(1a)	3.439(6)	Mn(2) – N(2a)	1.969(6)
		Mn(2) – O(9)	2.144(5)
Ho(1) – O(10)	2.238(5)	Mn(2) – O(12)	2.424(5)
Ho(1) – O(10a)	2.238(5)		
Ho(1) – O(8a)	2.284(5)		
Ho (1) – O(8)	2.284(4)		
Ho(1) – O(3a)	2.421(5)		
Ho(1) – O(3)	2.421(5)		
Ho(1) – O(6)	2.446(4)		
Ho(1) – O(6a)	2.446(4)		

Table 4.10. Important bond distances of **$Ho(OAc)_4Na$ 12-MC-4** are given.

Bond	**Distance (Å)**	**Bond**	**Distance (Å)**
Na(1) – O(21)	2.380(6)	Mn(2) – O(4)	1.843(5)
Na(1) – O(23)	2.398(6)	Mn(2) – O(3)	1.916(5)
Na(1) – O(24)	2.461(6)	Mn(2) – O(2)	1.941(5)
Na(1) – O(22)	2.475(6)	Mn(2) – N(2)	1.956(6)
Na(1) – O(6)	2.616(6)	Mn(2) – O(15)	2.132(6)
Na(1) – O(9)	2.640(5)	Mn(2) – O(22)	2.505(5)
Na(1) – O(12)	2.658(6)		
Na(1) – O(3)	2.707(6)	Mn(3) – O(7)	1.853(5)
		Mn(3) – O(6)	1.917(5)
Ho(1) – O(16)	2.259(5)	Mn(3) – O(5)	1.926(5)
Ho(1) – O(20)	2.261(6)	Mn(3) – N(3)	1.958(6)
Ho(1) – O(18)	2.269(5)	Mn(3) – O(17)	2.117(6)
Ho(1) – O(14)	2.305(6)		
Ho(1) – O(3)	2.401(4)	Mn(4) – O(10)	1.852(5)
Ho(1) – O(12)	2.443(5)	Mn(4) – O(9)	1.907(5)
Ho(1) – O(9)	2.445(5)	Mn(4) – O(8)	1.945(5)
Ho(1) – O(6)	2.450(5)	Mn(4) – N(4)	1.947(6)
		Mn(4) – O(19)	2.131(5)
Mn(1) – O(1)	1.837(5)		
Mn(1) – O(12)	1.916(5)		
Mn(1) – O(11)	1.934(5)		
Mn(1) – N(1)	1.950(6)		
Mn(1) – O(13)	2.126(6)		

Preparation of Magnetic Samples. Magnetic measurements were taken on powdered samples that were mulled in eicosane to prevent torqueing of the sample in high applied

magnetic fields. Samples were ground using a small mortar and pestle, transferred to a gelatin capsule of known mass, and weighed. A small amount of melted eicosane was added and left to solidify. The entire capsule was then weighed and a piece of tape applied to hold the capsule together. The capsule was then inserted into a clear plastic drinking straw. Holes were punched into the straw to allow air to escape.

Single crystal micro-SQUID measurements of the **$Ni(OAc)_2$ 12-MC-4** samples were performed by Wolfgang Wernsdorfer at the Néel Institut in Grenoble, France. Crystals were removed from the mother liquor and mounted onto the micro-SQUID array.[9] The applied dc field was swept from + 1.4 T to -1.4 T at various temperatures and sweep rates.

Magnetic Measurements. All magnetic susceptibility and magnetization values taken above 2 K at the University of Michigan or Michigan State University were corrected using Pascal's constants.[10] Corrections were applied for the eicosane, gelatin capsule, and sample holder by collecting their magnetic susceptibilities and magnetization values and subtracting them from the collected values. Variable field dc magnetization experiments were performed at 5 K on a Quantum Design Magnetic Phenomena Measurement System (QD MPMS) Superconducting Quantum Interference Device (SQUID) magnetometer from 0 to 55000 G at the University of Michigan, Department of Chemistry. Variable temperature dc magnetic susceptibility measurements were performed at an applied field of 2000 G with temperatures increasing from 5 K to 300 K at the University of Michigan. Variable temperature ac magnetic susceptibility measurements were taken at the Michigan State University, Department of Physics and Astronomy on a QD MPMS SQUID magnetometer at frequencies of 1000 Hz, 500 Hz, 100 Hz, and 10 Hz, temperatures decreasing from 10 K to 2 K, a 3.5 G ac drive field, and no applied dc field. Variable temperature ac magnetic susceptibility measurements were also taken at the University of Michigan on a QD MPMS7 SQUID magnetometer under the same conditions. Magnetic measurements were taken at the Néel Institut as well, and the procedures for those measurements were given above.

Results

Synthesis of ***Ni(OAc)$_2$ 12-MC-4***

The original synthesis was of **Ni(OAc)$_2$ 12-MC-4 (MeOH)** performed by Xiaowen Fang by dissolving 0.5 mmol $Ni(OAc)_2 \cdot 4H_2O$, 0.5 mmol $Mn(OAc)_2 \cdot 4H_2O$, and 1 mmol H_3shi in 20 mL MeOH. Unfortunately, this synthesis was not reproducible. A new synthesic method was devised that was reproducible and yielded the different isomers depending on the solvent used. The difference between Fang's method and the one used below was that the ligand and central metal were isolated from the $Mn(OAc)_2$ until the Mn was air oxidized slightly. In the new protocol, synthetically, the only difference was the solvent used. It was also found that it was possible to dissolve the precipitate isolated from the MeOH preparation in DMF and obtain the DMF crystals, indicating the importance of the crystallization solvent.

Synthesis of ***LnX$_4$A 12-MC-4***

It was found that the preparation of the desired **LnX$_4$A 12-MC-4** depended on the type of anions used. If the potassium salicylate analog was desired, it was found that dissolving KOH (or $KO_2C_2Cl_3$) and salicylic acid in DMF was necessary. On the other hand, if the sodium benzoate was desired, it was necessary to dissolve sodium benzoate in DMF was required. In order to avoid complicated mixed ligand sets, $Mn(OAc)_2$ was only employed as a starting material for the acetate bridged complexes or, if absolutely necessary. When $MnCl_2$ was used as a starting material, the solution did not turn dark red. However, upon addition to the ligand solution, it would become green.

Structural Description of ***Ni(OAc)$_2$ 12-MC-4***

A general description of the X-ray crystal structure of **Ni(OAc)$_2$ 12-MC-4** will be given. Please refer back to Tables 4.4 and 4.5 for important bond lengths and Figures 4.2 and 4.3 for the numbering scheme. The Ni^{II} ion is six-coordinate, and located in the central

cavity of the 12-MC-4. It is octahedral, with the axial positions occupied by two acetates in a trans-anti fashion. This trans-anti coordination environment was observed for **$Fe(SO_4)_2$ [12-$MC_{FeN(shi)}$-4]**[11] as well as a **$Ni(OAc)_2$ 12-$MC_{Ni^{II}N(shi)_2(pko)_2}$-4** structure,[12] however, this orientation was never observed for the **12-$MC_{Mn^{III}N(L)}$-4** family before.[13,14,15] In order to accommodate the Ni^{II} ion (radius = 0.690 Å),[16] the metallacrown must deform from planarity slightly. It should be noted that this is the only metallacrown where the central cation is in the center of the metallacrown. For the **Li 12-MC-4** structure (Figure 1.47), the Li^+ cation sits between 0.63 Å to 0.66 Å above the metallacrown oxygen plane. For the Na^+ and K^+ 12-MC-4 analogs (Figures 1.48 and 1.49), the central cation is displaced 1.64 Å – 1.67 Å and 2.13 Å respectively.[14] The methanol analog (Figure 4.2) adopts a ruffled geometry. The central cavity is characterized by an O3 – O3a distance of 3.930 Å and an O6 – O6a distance of 4.013 Å. The DMF analog (Figure 4.3) adopts a more chair-like geometry. The central cavity has an O3 – O3a distance of 3.907 Å and the O5 – O5a distance is 3.942 Å. The metallacrown ring retains the familiar structure seen in previous 12-$MC_{Mn^{III}N(shi)}$-4 metallacrowns.[11,13,14,15] Each Mn^{III} ion is bound equatorially by a six-membered ring comprised of a hydroxyl and an imine nitrogen from one shi^{3-} ligand and by a five-membered ring comprised of two hydroximate oxygens from a different shi^{3-} ligand. The axial positions are slightly elongated (Table 4.4 and 4.5) due to a Jahn-Teller elongation. In both structures, one axial position of Mn1 is occupied by an acetate oxygen. The other position is occupied by a solvent molecule. Both axial positions of Mn2 are occupied by solvent molecules.

The nature of the solvent molecule plays an important role in intermolecular interactions. In **$Ni(OAc)_2$ 12-MC-4 (MeOH)**, the acetate group on Mn1 is hydrogen bonded to a solvent MeOH that is 2.722 Å away (Figure 4.4). This MeOH is then hydrogen bonded to Mn2 of a different **$Ni(OAc)_2$ 12-MC-4 (MeOH)** molecule (2.640 Å). This is a rather strong hydrogen bond. This places the two Mn^{III} ions 7.314 Å apart. In addition, the MeOH coordinated to Mn1 is hydrogen bonded to a hydroximate oxygen of another **$Ni(OAc)_2$ 12-MC-4 (MeOH)** molecule that is 2.762 Å away (Figure 4.5). This places the two Mn1 ions of different metallacrowns 5.053 Å apart. The **$Ni(OAc)_2$ 12-MC-4 (DMF)**

lacks these hydrogen bond networks. Examining the packing diagram (Figure 4.6) only reveals close contacts due to simple packing. In this system, Mn1 is separated from Mn2 by 8.651 Å and Mn1 is separated from and adjacent Mn1 by 7.336 Å.

Structural description of ***LnX_4A 12-MC-4***

In the following sections, the structural properties of the **LnX_4A 12-MC-4** will be given. The idea of a skew angle, introduced by Coronado and co-workers[17,18] for Ln polyoxometallates (POM), is important. Imagining that the two parallel planes of ligands form squares with the atoms at the vertices of the squares, one can draw an angle between the neighboring vertices (Figure 4.7). For D_{4d}, symmetry, which is the type observed in these complexes, the skew angle should equal 45°. Also the ratio between the length of the edge (O_{edge}) of one of these squares and the height of the binding site ($O_{mp} - O_{mp}$)is important. If $O_{mp} - O_{mp}/O_{edge}$ is less than 1, then a certain axial compression is expected.

The structures show familiar **12-$MC_{Mn^{III}N(shi)}$-4** shapes. For reference, a brief review of other known **12-$MC_{Mn^{III}N(shi)}$-4** are given. The metallacrown cross-cavity distances remained fairly constant, regardless of central metal(s) present. When Li^+ was present, the cross-cavity distances ranged from 3.688 Å to 3.816 Å; for $(NaBr)_2$, the distance was 3.671 Å and 3.848 Å; for $(KBr)_2$, the distance was 3.674 Å and 3.734 Å;[14] for $Mn(OAc)_2$, the distance was 3.710 Å and 3.826 Å.[13] The out-of-plane distance for the Na^+ analog was 1.647 Å and for the K^+ analog, the distance was 2.132 Å[14] As the two cations are symmetry related, they're separation distances are 3.294 Å and 4.264 Å for the Na^+ and K^+ structures, respectively. In general, the metallacrown plane of the alkali series could be described as planar or slightly ruffled.[14] For the $Mn(OAc)_2$ complex, the metallacrown is quite planar.[13]

In order to determine the angles of the Jahn-Teller axes of the Mn^{III} ions, it is useful to calculate the angle between the coordinated ligand, Mn, and the hydroximate centroid (Figure 1.46). For the Na^+ structure, the angles were 83.16° and 98.41° for one Mn and

74.39° and 107.82° for the other Mn. For the K^+ structure, the angles were 88.09° and 92.10° for one Mn and 102.80° ad 82.71° for the other Mn.[14]

For all the **DyX_4M 12-MC-4** structures, two faces were formed. The one face was composed of the bridging ligand and Dy^{III} ion, while the other face included the counter ion and any coordinated solvent molecules. This was also observed in the **Mn 12-MC-4** complex.[13]

The cross-cavity diameter is 3.722 Å and 3.716 Å for **$Dy(Hsal)_4K$ 12-MC-4** (Figure 4.8) and 3.751 Å and 3.676 Å for **$Dy(OAc)_4K$ 12-MC-4**(Figure 4.9). Unlike many of the known 12-$MC_{Mn^{III}N(shi)}$-4 structures, it is important to note is that in **$Dy(Hsal)_4K$ 12-MC-4** and **$Dy(OAc)_4K$ 12-MC-4,** the metallacrown ring takes a bowled shape, with the phenyl rings from the shi^{3-} ligands pointing down towards the K^+ ion, forcing the hydroximate oxygens upwards towards the Dy^{III} ion. The impact of the bowl shape can be seen in the bond angles of the Mn^{III} Jahn-Teller axes and the centroid comprised by the hydroximate oxygens. The bond angles of the ligand oxygen atoms O_{Mnx} to the centroid in the O mean plane, with the vertex of the angle at the Mnx ion are given in Tables 4.11 and 4.12.

Table 4.11. The bond angle between the salicylate oxygen, the Mn^{III} ion, and the centroid of the hydroximate oxygen plane for **$Dy(Hsal)_4K$ 12-MC-4**are given.

Bond	Angle (°)
O_{Mn1} – Mn1 – Centroid	100.55
O_{Mn2} – Mn2 – Centroid	98.89
O_{Mn3} – Mn3 – Centroid	101.71
O_{Mn4} – Mn4 – Centroid	100.71

Table 4.12. The bond angle between the acetate oxygen, the Mn^{III} ion, and the centroid of the hydroximate oxygen plane for **$Dy(OAc)_4K$ 12-MC-4** are given.

Bond	Angle (°)
O_{Mn1} – Mn1 - Centroid	101.16
O_{Mn2} – Mn2 – Centroid	101.59

The Dy^{III} ion, due to its size (radius = 1.207 Å),[16] sits 1.521 Å and 1.593 Å above the mean plane comprised of the four hydroximate oxygens for **$Dy(Hsal)_4K$ 12-MC-4** and **$Dy(OAc)_4K$ 12-MC-4**, respectively. For **$Dy(Hsal)_4K$ 12-MC-4,** the Dy^{III} ion sits 1.136 Å below a mean comprised of four carboxyl oxygens from the bridging salicylates, while the Dy^{III} ion sits 1,068 Å below the acetate oxygen plane for **$Dy(OAc)_4K$ 12-MC-4**. This forces the Dy^{III} ion to take on pseudo D_{4d} symmetry. Table 4.13 gives the skew angles between the salicylate carboxylate oxygens and the adjacent hydroximate oxygens. Table 4.14 gives the skew angles between the acetate oxygens and the adjacent hydroximate oxygens for **$Dy(OAc)_4K$ 12-MC-4**.

Table 4.13. The skew angle between the salicylate carboxylate oxygens, Dy1, and the hydroximate ring oxygens for **$Dy(Hsal)_4K$ 12-MC-4** are given.

Bond	Skew Angle (°)
O14 – Dy1 – O3	46.27
O17 – Dy1 – O3	43.22
O17 – Dy1 – O6	46.22
O20 – Dy1 – O6	44.08
O20 – Dy1 – O9	45.75
O23 – Dy1 – O9	43.91
O23 – Dy1 – O12	46.40
O14 – Dy1 – O12	44.14

Table 4.14. The skew angle between the acetate carboxylate oxygens, Dy1, and the hydroximate ring oxygens for **$Dy(OAc)_4K$ 12-MC-4** are given.

Bond	Skew Angle (°)
O9 – Dy1 – O2	43.48
O12 – Dy1 – O2	44.32
O12 – Dy1 – O6	45.93
O9 – Dy1 – O6	46.27

For **$Dy(Hsal)_4K$ 12-MC-4** the K^+ ion sits 2.387 Å below the hydroximate oxygen mean plane and is nine-coordinate; for **$Dy(OAc)_4K$ 12-MC-4**, the K^+ ion sits 2.209 Å below the hydroximate oxygen mean plane and is eight-coordinate Examining charge balance, there are four $Hsal^-$ or OAc^- ligands and four shi^{3-} ligands, giving a total of sixteen negative charges. With four Mn^{III} ions and one Dy^{III} ion, fifteen of these negative charges

are accounted for. The last change is neutralized by the K^+ ion. Thus, the K^+ ion is electrostatically bonded to the metallacrown, providing charge balance.

Because **Dy(Hsal)$_4$Na 12-MC-4** crystallizes in the same unit cell, it presumably has the same structure. The main difference could be that because Na^+ is smaller than K^+ (1.24 Å vs. 1.55 Å for 9-coordinate),[16] the Na^+ ion could sit closer to the metallacrown plane.

Unlike the other **DyX$_4$M 12-MC-4** complexes, though, **Dy(benzoate)$_4$Na 12-MC-4** is not nearly as bowled; it is more ruffled than the other structures (Figure 4.10). This manifests in several areas. First, the central cavity is smaller than the other **DyX$_4$M 12-MC-4** complexes; the diameter is 3.681 Å and 3.676 Å. Second, the O – Dy – centroid angles are more obtuse than in the other structures (Table 4.15).

Table 4.15. The bond angle between the benzoate oxygen, the Mn^{III} ion, and the centroid of the hydroximate oxygen plane for **Dy(benzoate)$_4$Na 12-MC-4** are given.

Bond	Angle (°)
O_{Mn1} – Mn1 – Centroid	101.33
O_{Mn2} – Mn2 – Centroid	102.28
O_{Mn3} – Mn3 – Centroid	102.63
O_{Mn4} – Mn4 – Centroid	102.34

Lastly, Dy^{III} and Na^+ ions are closer to the hydroximate oxygen mean; the Dy^{III} ion is only 1.565 Å from the plane and the Na^+ ion is 1.953 Å from the plane. The Dy^{III} ion sits 1.036 Å below the benzoate oxygen mean plane. The skew angles are given in Table 4.16.

Table 4.16. The skew angle between the benzoate carboxylate oxygens, Dy1, and the hydroximate ring oxygens for **Dy(benzoate)$_4$Na 12-MC-4** are given.

Bond	Skew Angle (°)
O14 – Dy1 – O3	46.44
O16 – Dy1 – O3	43.00
O16 – Dy1 – O6	47.26
O18 – Dy1 – O6	42.66
O18 – Dy1 – O9	47.41
O20 – Dy1 – O9	43.65
O20 – Dy1 – O12	45.87
O14 – Dy1 – O12	43.71

Both the **Ho(OAc)$_4$Na 12-MC-4** (Figure 4.11) and **Ho(OAc)$_4$K 12-MC-4** (Figure 4.12) retain the structural features (two different faces and connectivity) described above. For **Ho(OAc)$_4$K 12-MC-4**, Mn2 and Mn2a are six coordinate, with the other axial position occupied by a DMF molecule, while Mn1 and Mn1a are five coordinate square pyramidal polyhedra. The K^+ ion is eight coordinate; four coordination sites from the hydroximate ring and four from DMF molecules, two bridging it to Mn2 and Mn2a and two additional DMF molecules. The K^+ ion is 2.217 Å from the hydroximate mean plane. For **Ho(OAc)$_4$Na 12-MC-4**, all four Mn^{III} ions are five coordinate square pyramidal geometries. The Na^+ ion is coordinated by the four metallacrown plane hydroximates and four waters. The Na^+ ion is 1.904 Å below the hydroximate oxygen mean plane.

Both **Ho(OAc)$_4$K 12-MC-4** and **Ho(OAc)$_4$Na 12-MC-4** are bowl-shaped. The central cavity of **Ho(OAc)$_4$K 12-MC-4** is characterized by a distance of 3.678 Å and 3.764 Å. The central cavity of **Ho(OAc)$_4$Na 12-MC-4** is comprised of a distance of 3.707 Å and a distance of 3.693 Å. The Ho^{III} ion in **Ho(OAc)$_4$K 12-MC-4** sits 1.569 Å above the hydroximate oxygen mean plane, while it sits 1.583 Å above the hydroximate mean plane in the **Ho(OAc)$_4$Na 12-MC-4**. The bond angles of the acetate oxygen to Mn to hydroximate plane centroid are summarized in Table 4.17 and 4.18 for the **Ho(OAc)$_4$K 12-MC-4** and **Ho(OAc)$_4$Na 12-MC-4**, respectively.

Table 4.17. The bond angle between the acetate oxygen, the Mn^{III} ion, and the centroid of the hydroximate oxygen plane for **$Ho(OAc)_4K$ 12-MC-4** are given.

Bond	Angle (°)
O_{Mn1} – Mn1 - Centroid	100.90
O_{Mn2} – Mn2 – Centroid	101.46

Table 4.18. The bond angle between the acetate oxygen, the Mn^{III} ion, and the centroid of the hydroximate oxygen plane for **$Ho(OAc)_4Na$ 12-MC-4** are given.

Bond	Angle (°)
O_{Mn1} – Mn1 – Centroid	101.92
O_{Mn2} – Mn2 – Centroid	101.99
O_{Mn3} – Mn3 – Centroid	101.80
O_{Mn4} – Mn4 – Centroid	102.16

The environment around the Ho^{III} ion for both structures is pseudo D_{4d}. In **$Ho(OAc)_4K$ 12-MC-4**, the Ho^{III} ion is 1.076 Å below the acetate mean plane. For **$Ho(OAc)_4Na$ 12-MC-4**, the Ho^{III} ion is 1.039 Å below the acetate mean plane. The skew angles for **$Ho(OAc)_4K$ 12-MC-4** and **$Ho(OAc)_4Na$ 12-MC-4** are given in Tables 4.19 and 4.20, respectively.

Table 4.19. The skew angle between the acetate carboxylate oxygens, Ho1, and the hydroximate ring oxygens are given for **$Ho(OAc)_4K$ 12-MC-4**.

Bond	Skew Angle (°)
O8 – Ho1 – O3	46.00
O10 – Ho1 – O3	46.06
O10 – Ho1 – O6	43.56
O8 – Ho1 – O6	44.37

Table 4.20. The skew angle between the acetate carboxylate oxygens, Ho1, and the hydroximate ring oxygens are given for **$Ho(OAc)_4Na$ 12-MC-4**.

Bond	Skew Angle (°)
O14 – Ho1 – O3	47.08
O16 – Ho1 – O3	44.50
O16 – Ho1 – O6	44.78
O18 – Ho1 – O6	44.69
O18 – Ho1 – O9	45.92
O20 – Ho1 – O9	45.09
O20 – Ho1 – O12	43.91
O14 – Ho1 – O12	44.03

Variable Field dc Magnetization Measurements

The variable field dc magnetization measurements of the samples were collected at the University of Michigan on powdered samples mulled in eicosane. All lanthanide-containing samples were measured at 5.0 K with field increasing from 0 G to 55000 G. The Ni^{II} samples were collected at 2.0 K with fields increasing from 0 G to 55000 G. No sample gave a saturated signal, thus the ground spin state could not be calculated.

For **$Ni(OAc)_2$ 12-MC-4 (MeOH)**, the magnetization value increased linearly until approximately 6500 G, reaching a slight inflection point. It then continually increased, reaching a maximum of 23130 cm^3 G mol^{-1} at 55000 G (Figure 4.13). For **$Ni(OAc)_2$ 12-MC-4 (DMF)**, the magnetization increased linearly to 10000 G before reaching an inflection point. The magnetization then continuously increased, reaching a maximum of 32350 cm^3 G mol^{-1} at 55000 G (Figure 4.14).

For **$Dy(Hsal)_4K$ 12-MC-4**, the magnetization value increased linearly until 10000 G, reached an inflection point, then continued to increase. At 55000 G, it reached a value of 43690 cm^3 G mol^{-1} (Figure 4.15). For **$Dy(Hsal)_4Na$ 12-MC-4**, similar behavior was observed: the magnetization increased linearly until 10000 G, then increased at a slower rate. The maximum magnetization observed was 39510 cm^3 G mol^{-1} at 55000 G (Figure 4.16). For **$Dy(OAc)_4K$ 12-MC-4**, the magnetization increased linearly to 11000 G before increasing at a slower rate. The magnetization reached a maximum of 40630 cm^3 G mol^{-1} at 55000 G (Figure 4.17). For **$Dy(benzoate)_4Na$ 12-MC-4**, the magnetization increased linearly to 11000 G and then slowly increased until 55000 G, reaching a maximum of 39960 cm^3 G mol^{-1} (Figure 4.18).

For **$Ho(OAc)_4K$ 12-MC-4**, the magnetization values increased linearly until 10000G, at which point the magnetization increased at a slower rate. The maximum magnetization at 55000 G was 43880 cm^3 G mol^{-1} (Figure 4.19). For **$Ho(OAc)_4Na$ 12-MC-4**, the

magnetization increased linearly until 11000 G. It then increased more slowly until it reached a maximum of 39990 cm^3 G mol^{-1} (Figure 4.20).

Variable Temperature Magnetic Susceptibility Measurement

The variable temperature dc magnetic susceptibility of the **$Ni(OAc)_2$ 12-MC-4** samples were measured by decreasing the temperature from 300 K to 2 K with an applied field of 1000 G. These measurements were performed at the University of Michigan on a QD MPMS7 SQUID magnetometer. For the **LnX_4A 12-MC-4** samples, the susceptibility was measured by increasing the temperature from 5 K to 300 K with an applied field of 2000 G. These measurements were conducted at the University of Michigan on a QD MPMS SQUID magnetometer. Due to the complicated spin values, the value g = 2.00 was used for the calculations of the susceptibilities of Ni^{II} and Mn^{III}, the susceptibilities of Dy^{III} and Ho^{III} were calculated using the corresponding g_J values.

For **$Ni(OAc)_2$ 12-MC-4 (MeOH)**, the sample had a susceptibility of 10.89 cm^3 K mol^{-1} at 300, which is slightly less than non-interacting Mn^{III} and Ni^{II} ($\chi_M T$ = 12 cm^3 K mol^{-1}). The susceptibility remained constant until 240 K, at which point it began to steadily decrease until about 85 K. At 85 K, the susceptibility began to sharply decrease, reaching a minimum of 2.37 cm^3 K mol^{-1} at 2.00 K (Figure 4.21). For **$Ni(OAc)_2$ 12-MC-4 (DMF)**, the sample had a susceptibility of 10.98 cm^3 K mol^{-1} at 300 K, which is again slightly less than if all the ions were not interacting. It remained relatively constant until 230 K, at which point the susceptibility slowly decreased. At 55 K, the susceptibility sharply decreased, reaching a minimum of 3.82 cm^3 K mol^{-1} at 2.00 K (Figure 4.22).

For **$Dy(Hsal)_4K$ 12-MC-4**, the susceptibility at 300 K was 25.33 cm^3 K mol^{-1}, which is less than four non-interacting Mn^{III} and one Dy^{III} ions ($\chi_M T$ = 26.17 cm^3 K mol^{-1}). It remained at this value until 145 K, at which point the susceptibility linearly decreased to 105 K. At 50 K, the susceptibility decreased dramatically, reaching a value of 11.55 cm^3 K mol^{-1} at 5.00 K (Figure 4.23). Similar behavior was observed for **$Dy(Hsal)_4Na$ 12-MC-4**, the susceptibility at 300 K was 23.13 cm^3 K mol^{-1}, which is smaller than

expected, and remained fairly constant to 110 K. Again at 50 K, the susceptibility then dramatically decreased, reaching a minimum of 12.20 cm^3 K mol^{-1} at 5.00 K (Figure 4.24). For **$Dy(OAc)_4K$ 12-MC-4**, the susceptibility at 300 K was 23.60 cm^3 K mol^{-1}, which is less than the sum of non-interacting ions . The susceptibility linearly decreased until about 115 K. At 60 K, the susceptibility decreased markedly, reaching a minimum of 11.14 cm^3 K mol^{-1} at 5.00 K (Figure 4.25). For **$Dy(benzoate)_4Na$ 12-MC-4**, the susceptibility at 300 K was 23.74 cm^3 K mol^{-1}, which was less than expected for non-interacting ions. This remained relatively constant until 95 K. A dramatic decrease started at 55 K, reaching a minimum of 12.56 cm^3 K mol^{-1} at 5.00 K (Figure 4.26).

For **$Ho(OAc)_4K$ 12-MC-4**, the susceptibility at 300 K was 23.67 cm^3 K mol^{-1} which is less than four non-interacting Mn^{III} and one Ho^{III} ion ($\chi_M T$ = 26.07 cm^3 K mol^{-1}). It remained relatively constant until 120 K. At 50 K, the susceptibility dramatically decreased, reaching a minimum of 9.42 cm^3 K mol^{-1} at 5.00 K (Figure 4.27). For **$Ho(OAc)_4Na$ 12-MC-4**, the susceptibility at 300 K was 23.84 cm^3 K mol^{-1} which is less than non-interacting ions. The susceptibility steadily decreased until 130 K. At 55 K, the susceptibility sharply decreased, reaching a minimum at 5.00 K of 9.10 cm^3 K mol^{-1} (Figure 4.28).

Variable Temperature ac SQUID Magnetometer Magnetic Susceptibility

The variable temperature ac magnetic susceptibility data of **$Dy(OAc)_4K$ 12-MC-4** and the **$Ho(OAc)_4M$ 12-MC-4** complexes were measured at the Michigan State University Department of Physics and Astronomy on a QD MPMS ac SQUID magnetometer. All the other samples were measured at the University of Michigan, Department of Chemistry on a QD MPMS7 SQUID magnetometer. The same conditions were used for all measurements, which were given above. For clarity, the in-phase susceptibility will be discussed first.

The in-phase magnetic susceptibility of **$Ni(OAc)_2$ 12-MC-4 (MeOH)** decreased linearly from 10 K to 5 K for all frequencies (Figure 4.29). Extrapolating the in-phase

susceptibility from 5.00 K to 0 K gave a value of 2.51 cm^3 K mol^{-1}. For **$Ni(OAc)_2$ 12-MC-4 (DMF)**, the in-phase magnetic susceptibility decreased linearly from 10 K to 3.20 K for all studied frequencies (Figure 4.30). Extrapolating the in-phase susceptibility from 3.20 K led to a value of 3.97 cm^3 K mol^{-1}.

For the **$Dy(Hsal)_4K$ 12-MC-4**, the in-phase susceptibility decreased linearly from 10 K to 2.00 K for all frequencies (Figure 4.31). Extrapolating the in-phase susceptibility to 0 K led to a value of 10.48 cm^3 K mol^{-1}. For **$Dy(Hsal)_4Na$ 12-MC-4**, the in-phase susceptibility linearly decreased from 10 K to 2.00 K for all frequencies (Figure 4.32). Extrapolating the in-phase susceptibility to 0 K gave a value of 11.96 cm^3 K mol^{-1}. For **$Dy(OAc)_4K$ 12-MC-4**, the in-phase susceptibility again decreased linearly from 10 K to 2.00 K for all measured frequencies (Figure 4.33). Extrapolating the in-phase susceptibility from 4.5 K to 0 K led to a value of 9.41 cm^3 K mol^{-1}. For **$Dy(benzoate)_4K$ 12-MC-4**, the in-phase susceptibility decreased linearly from 10 K to 2.00 K for all frequencies (Figure 4.34). Extrapolating the in-phase susceptibility to 0 K from 2.00 K lead to an in-phase susceptibility of 12.55 cm^3 K mol^{-1}.

The in-phase susceptibility of **$Ho(OAc)_4K$ 12-MC-4** decreased linearly from 10 K to 4.5 K, then curved down slightly to a 2.0 K for all the frequencies (Figure 4.35). Extrapolating the in-phase susceptibility from 4.5 K to 0 K, the in-phase susceptibility was found to be 6.74 cm^3 K mol^{-1}. For **$Ho(OAc)_4Na$ 12-MC-4**, the in-phase susceptibility linearly decreased from 10 K to 4.5 K for all frequencies, then slightly curved downward (Figure 4.36). Extrapolating the in-phase susceptibility from 4.5 K to 0 K, the in-phase susceptibility was found to be 6.99 cm^3 K mol^{-1}.

Studying the out-of-phase magnetic susceptibility, both **$Ni(OAc)_2$ 12-MC-4 (MeOH)** (Figure 4.37) and **$Ni(OAc)_2$ 12-MC-4 (DMF)** (Figure 4.38) show frequency dependence, although no turn-over was observed. Thus, no blocking temperature could be determined.

Looking at the **LnX_4A 12-MC-4** complexes, it was found that the **$Dy(Hsal)_4K$ 12-MC-4** (Figure 4.39) and **$Dy(Hsal)_4Na$ 12-MC-4** (Figure 4.40) showed frequency dependence.

However, no maxima were observed, so a blocking temperature could not be calculated. The **$Dy(OAc)_4K$ 12-MC-4** (Figure 4.41) and the **$Dy(benzoate)_4Na$ 12-MC-4** (Figure 4.42) did not show frequency dependence in the out-of-phase. For the **$Ho(OAc)_4K$ 12-MC-4** (Figure 4.43) and **$Ho(OAc)_4Na$ 12-MC-4** (Figure 4.44), neither showed frequency dependence in the out-of-phase.

Single-Crystal micro-SQUID Magnetometer Measurements

The single-crystal micro-SQUID magnetometer measurements were performed by Wolfgang Wernsdorfer. The hysteresis of **$Ni(OAc)_2$ 12-MC-4 (MeOH)** was studied from + 1.4 T to -1.4 T at a sweep rate of 0.14 T/s (Figure 4.45). It should be noted that at the large applied fields, the magnetization does not saturate, but slowly increases. Looking closer at the **$Ni(OAc)_2$ 12-MC-4 (MeOH)** hysteresis plot with a sweep rate of 0.14 T/s, a small hysteresis can be observed below 0.8 K. The hysteresis gap increases as the temperature decreases (Figure 4.46). At 40 mK, a hysteresis can also be seen for various sweep rates (Figure 4.47).

Turning next to the **$Ni(OAc)_2$ 12-MC-4 (DMF)**, the magnetic hysteresis from + 1.4 T to -1.4 T was measured at a sweep rate of 0.14 T/s at various temperatures (Figure 4.48). At 30 mK, a small hysteresis can be observed. Looking at the large applied fields, it was observed that the magnetization saturated. Studying the affect of sweep rate at 30 mK, a hysteresis was observed at various sweep rates (Figure 4.49).

Discussion

Zaleski's **$Mn(OAc)_2$ 12-$MC_{Mn^{III}N(shi)}$-4** and **$Dy(Hsal)_4H_3O^+$ 12-$MC_{Mn^{III}N(shi)}$-4** created great interest in further developing planar **12-$MC_{Mn^{III}N(shi)}$-4** complexes as SMMs.[1,2] Zaleski found that the **$Mn(OAc)_2$ 12-MC-4** showed slow magnetic relaxation and a blocking temperature above 2 K when it was measured in a frozen DMF solution. He also found that the **$Dy(Hsal)_4H_3O^+$ 12-MC-4** complex showed the onset of slow magnetic relaxation near 2 K in the solid state. It was hoped that the introduction of different

anisotropic metals, such as octahedral Ni^{II} (high spin, d^8, $S = 1$) or further study of the Ln^{III} ions, would lead to larger blocking temperatures.

$Ni(OAc)_2$ 12-MC-4

Zaleski and co-workers reported that due to the unusual coordination environment of Mn^{II} in the **$Mn(OAc)_2$ 12-MC-4**, a large amount of anisotropy originated from the normally isotropic Mn^{II} central ion. In order to fit the low temperature (0.6 K), high field (0 – 30 T) magnetization data, Mn^{II} was assigned a $D = +1$ cm^{-1}, a value larger than anticipated for a $^6A_1$ ion.[19] However, most Mn^{II} ions adopt an octahedral geometry. In this case, the Mn^{II} ion adopted a trigonal prismatic geometry, which would explain the large observed anisotropy.[2] It was hoped that by introducing naturally anisotropic metals the blocking temperatures would increase.

Octahedral Ni^{II} is a high spin d^8 ion with $S = 1$. It is an anisotropic metal with an ionic radius (0.690 Å) that is smaller than high spin six-coordinate Mn^{II} (0.830 Å) and larger than four-coordinate Li^+ (0.590 Å).[16] Thus, it seemed like an ideal ion to introduce to the 12-MC-4. A visiting Chinese undergraduate student, Xiaowen Fang, first isolated the **$Ni(OAc)_2$ 12-MC-4 (MeOH)** complex. However, the described procedure did not reproduce the complex, and a new synthesis was prepared, which did deliver the desired structure (Figure 4.2). It was also found that the complex could be prepared in DMF, which yielded a molecule with the same connectivity (Figure 4.3), but different packing patterns and space groups due to the presence of hydrogen bonds in the methanol derivative (Figures 4.4 & 4.5). For both structures, it was found that the Ni^{II} ion was six-coordinate, the four equatorial positions occupied by the shi^{3-} ligands forming the metallacrown plane and the two axial positions occupied by the oxygen atoms from the acetate. The acetates arrange in a trans-anti fashion,[20] bridging the central Ni^{II} to two of the ring Mn^{III} ions. This trans-anti orientation had been observed in the **$Fe^{III}(SO_4)_2$ 12-$MC_{Fe^{III}N(shi)}$-4** metallacrown,[11] where the bridging sulfate groups oriented trans-anti, and the Fe^{III} ion (radius = 0.645 Å)[16] was coordinated at the center of the metallacrown. In order to accommodate the Ni^{II} ion, the metallacrown had to ruffle slightly. In other Mn

metallacrowns, the ring bows slightly. However, because of the trans-anti acetates, the metallacrown cannot bow. This could slightly change the coupling between the ring Mn^{III} ions as it would perturb bond angles, both within the metallacrown ring Mn ions and between the Mn ring metals and the central Ni^{II} ion.

It was quite interesting to examine the packing pattern of these **$Ni(OAc)_2$ 12-MC-4** complexes. In methanol, a hydrogen bond network exists between the proton on the alcohol group of one methanol molecule coordinated to Mn1 and the hydroximate carbonyl oxygen of another metallacrown (2.762 Å). This interaction is enforced by the symmetry related equivalent hydrogen bond from the second metallacrown Mn1 to the carbonyl oxygen of the first metallacrown (Figure 4.5). This separates the two different Mn1 ions by 5.053 Å away. There is a second, longer hydrogen bonding network, this time between the acetate bonded to Mn1 and the proton on a solvent methanol (2.722 Å) and then to a methanol coordinated to Mn2 of a different metallacrown (2.640 Å) (Figure 4.4). As a result, Mn1 is 7.314 Å away from Mn2. In **$Ni(OAc)_2$ 12-MC-4 (DMF)**, there are no hydrogen bond networks available, with the molecules simply close packed (Figure 4.6). The Mn1 – Mn1 distance was 8.651 Å and the Mn1 – Mn2 distance was 7.336 Å.

As both species have the same magnetic components and the same intramolecular interactions, it would be expected that any differences in magnetic properties should be the result of intermolecular interactions. Using **$Ni(OAc)_2$ 12-MC-4 (DMF)** (Figures 4.14 and 4.22) as demonstrating the type of magnetic behavior one expects for an isolated **$Ni(OAc)_2$ 12-MC-4**, there appears to be slight antiferromagnetic coupling. If all the Mn^{III} ions and the Ni^{II} ion ferromagnetically interacted, the observed susceptibility should be 13.00 cm^3 K mol^{-1}. If the ring Mn^{III} ions antiferromagnetically coupled, the susceptibility of the system would be that of the Ni^{II} ion, $\chi_M T$ = 1 cm^3 K mol^{-1}. The last possibility is if the ring Mn^{III} ions ferromagnetically coupled and the Ni^{II} ion was antiferromagnetically coupled, which would give $\chi_M T$ = 11.00 cm^3 K mol^{-1}. The sample did not saturate in the magnetization experiment (Figure 4.14), so the magnetic interaction cannot be determined that way. Looking at the magnetic susceptibility (Figure 4.22), at 300 K, the

susceptibility was found to be 10.98 cm^3 K mol^{-1}. This would seem to indicate the third coupling scheme is being employed. At low temperatures, the susceptibility was 3.82 cm^3 K mol^{-1}. This indicates that Mn^{III} ions are weakly ferromagnetically coupled to the Ni^{II} ions. This value was corroborated by the in-phase susceptibility data (Figure 4.30).

The **$Ni(OAc)_2$ 12-MC-4 (MeOH)** complex, due to the packing extensive and hydrogen bonding network, could be subject to intermolecular interactions which would cause it to diverge from the DMF analog's magnetic properties. It was hoped that the packing interactions would manifest themselves in the observed magnetization properties. The magnetization values at large applied fields (Figure 4.13,) for the **$Ni(OAc)_2$ 12-MC-4 (MeOH)** was smaller than the **$Ni(OAc)_2$ 12-MC-4 (DMF)**, suggesting intermolecular antiferromagnetic coupling in the methanol case. Both complexes have similar $\chi_M T$ values at 300 K, 10.89 cm^3 K mol^{-1} (Figure 4.20) as may be expected from **$Ni(OAc)_2$ 12-MC-4 (DMF)** example. At low temperature, however, the susceptibilities diverge and **$Ni(OAc)_2$ 12-MC-4 (MeOH)** reaches a minimum of 2.37 cm^3 K mol^{-1}.This indicates that at low temperature, there is probably weak antiferromagnetic coupling between the **$Ni(OAc)_2$ 12-MC-4 (MeOH)** complexes as the susceptibility and the magnetization values were smaller than those observed from the **$Ni(OAc)_2$ 12-MC-4 (DMF)** case. The most likely source of this coupling is the hydrogen bond network.

Examining the out-of-phase magnetic susceptibility for **$Ni(OAc)_2$ 12-MC-4 (MeOH)** (Figure 4.37) and **$Ni(OAc)_2$ 12-MC-4 (DMF)** (Figure 4.38), one can again see slight differences in the magnitude of their behavior and the onset of slow magnetic relaxation. The magnitude of the frequency dependence of **$Ni(OAc)_2$ 12-MC-4 (DMF)** is approximately double that of the **$Ni(OAc)_2$ 12-MC-4 (MeOH)**. Using Equations 19 and 21 from Chapter I, the magnitude of the out-of-phase susceptibility relates back to the magnitude of the susceptibility. As the susceptibility of **$Ni(OAc)_2$ 12-MC-4 (DMF)** is roughly twice that of **$Ni(OAc)_2$ 12-MC-4 (MeOH)**, the difference in magnitude is not surprising. The onset of slow magnetic relaxation for **$Ni(OAc)_2$ 12-MC-4 (MeOH)** occurs around 5 K, while for **$Ni(OAc)_2$ 12-MC-4 (DMF)**, it begins around 4 K.

Lastly, the difference in magnetic behavior can also be seen in the micro-SQUID hysteresis plots. For **$Ni(OAc)_2$ 12-MC-4 (MeOH)** (Figure 4.45), the magnetization above ± 0.25 T begins to curve and does not saturate. The curve is very serpentine and does not have strong, abrupt changes. This can indicate single-chain magnetization as well as large amounts of anisotropy. The **$Ni(OAc)_2$ 12-MC-4 (DMF)** does saturate at 1.4 T (Figure 4.48) and in general is comprised of more definitive transitions. At the very low temperatures, the **$Ni(OAc)_2$ 12-MC-4 (MeOH)** has a wider hysteresis than the DMF analog (Figures 4.47 and 4.49). While they are at two different temperatures, presumably the DMF hysteresis would be smaller at 40 mK and the MeOH hysteresis would be wider at 30 mK. This seems to indicate that the **$Ni(OAc)_2$ 12-MC-4 (MeOH)** has a slightly larger energy barrier than the DMF construct, which could be due to its chain-like behavior. This has been observed in the literature: it was found that the a chain of SMMs are perturbed by hydrogen bonding, inducing SCM behavior. The energy barrier changed upon switching from SMM form to SCM type.[21]**Error! Bookmark not defined.** The shape of the curves from the variable sweep rate experiments also differ (Figures 4.47 and 4.49). The hysteresis for the MeOH system is very smooth, while for DMF (Figure 4.49), there appears to be more dramatic transitions which could be indicative of quantum tunneling of spin.[22] As demonstrated above, structurally, the metallacrown cores of both complexes are nearly identical, thus the non-saturation properties of **$Ni(OAc)_2$ 12-MC-4 (MeOH)** can be attributed to its hydrogen bonded chains. It is rare to observe single-chain magnetic properties with hydrogen bonded complexes.[21,23, 24]

This could prove a very interesting route forward; linking SMM metallacrowns through hydrogen bonds to form longer chains. Because metallacrowns can be prepared in a variety of solvents, such as methanol and water, and often possess carboxylate bridging groups as well as carboxyl groups in the hydroximate rings, this could be a relatively easy way to link metallacrowns together to change the magnetic properties. The onset of slow magnetic relaxation for the MeOH structure was slightly higher than the DMF case. This could mean that the chain has a higher blocking temperature due to the different relaxation pathways for SCMs described in Chapter I. It would also be interesting to see if blocking one of the exchange pathways described above in the MeOH case perturbed

the magnetic properties. As there were two hydrogen bond networks, one may induce SCM behavior while the other does not. It would be interesting to see which pathways gives SCM behavior, or if both are needed for the observed behavior.

LnX_4A 12-MC-4

Zaleski and co-workers had stated that in **$Mn(OAc)_2$ 12-MC-4**, a slight change in the coupling constants could perturb the observed magnetic ground spin state (Figure 4.1).2 Ideally, one could perturb the interactions by altering the exchange pathways. This could be done two ways: changing the ring metals by modifying the shi^{3-} ligand, or second, by changing the coupling between the central metal and the ring metals. Chemically speaking, it would be very difficult to modify the shi^{3-} ligand because its geometry and binding sites induce the 12-MC-4 shape. The most straightforward way would be to modify the bridging ligands by introducing carboxylates with different electron-withdrawing or electron donating-properties. In addition to perturbing the exchange pathways, substituting the ligand could also perturb the anisotropy of the Mn^{II} ion. Precedent for studying the magnetic behavior by changing bridging ligands existed in the literature,[6,7,8] so this seemed a worthy route of exploration.

This idea of modifying the bridging ligand was extended to the **DyX_4A 12-MC-4** series. Presumably, this modification idea would work in the Mn 12-MC-4 case, and was, in fact, attempted. However, the systems proved difficult for isolating crystalline material. So the idea was tested with **$Dy(Hsal)_4H_3O^+$ 12-MC-4**, which had larger magnetization and magnetic susceptibility values compared to the **Mn 12-MC-4** structure, as could be expected by substituting the central Mn^{II} for Dy^{III}.[1] Furthermore, Dy^{III} would provide additional spin and anisotropy, which could improve the SMM properties. Combined with the known $Y(OAc)_4$ 12-MC-4 structure (Figure 1.56) it seemed likely that it would be possible to build a 12-$MC_{Mn^{III}N(shi)}$-4 with different bridging ligands.

During the synthesis of these metallacrowns, it was noted that different counter ions occurred on the face opposite the central Ln^{III} ion, begging the question of what role, if

any, do these diamagnetic counter ions have on the magnetic properties. It was clear that structurally, the diamagnetic ion provided charge balance. The four Mn^{III} ions and Dy^{III} provided a 15+ charge. The four shi^{3-} ligands and four X^- ligands provided a 16- charge. Thus, the bound cation balanced the remnant negative charge. It should be noted that the corresponding cation was not needed to balance the charge in the **$Mn(OAc)_2$ 12-MC-4** structure. To study what, if any, role the diamagnetic counter ion played on the magnetic properties, the **$Dy(Hsal)_4A$ 12-MC-4** series, with A = K^+ and Na^+ (H_3O^+ was previously made),1 was prepared. To study the role of the bridging ligand, **$Dy(OAc)_4K$ 12-MC-4** and **$Dy(benzoate)_4Na$ 12-MC-4** were prepared. The syntheses of the corresponding Na^+ and K^+ metallacrowns were attempted, but were not isolated.

The **$Dy(Hsal)_4K$ 12-MC-4** (Figure 4.8), **$Dy(OAc)_4K$ 12-MC-4** (Figure 4.9), **$Ho(OAc)_4Na$ 12-MC-4** (Figure 4.11) and **$Ho(OAc)_4K$ 12-MC-4** (Figure 4.12) adopted bowled shapes, with the hydroximate oxygens pointing towards the Ln^{III} ion and the counter ion on the opposite face. Presumably the **$Dy(Hsal)_4Na$ 12-MC-4** has a closely related structure to the **$Dy(Hsal)_4K$ 12-MC-4** structure, although the **$Dy(benzoate)_4Na$ 12-MC-4** (Figure 4.10) adopted a more ruffled geometry. Because of its smaller ionic radius, the Na^+ ion was able to get closer to the hydroximate plane than the K^+ ion.[16] This slight difference could perturb the electronics of the metallacrown ring, as more electron density would be directed towards the Na^+ than the K^+ ion. This should however, manifest itself in different Dy-hydroximate mean plane distances. However, the Dy – hydroximate mean plane distances for all the structures remained fairly constant (1.521 Å for **$Dy(Hsal)_4K$**, 1.593 Å for **$Dy(OAc)_4K$**, 1.565 Å for **$Dy(benzoate)_4Na$**, 1.569 Å for **$Ho(OAc)_4K$ 12-MC-4** and 1.583 Å for **$Ho(OAc)_4Na$ 12-MC-4**), regardless of counter ion.

Further information can be gathered by comparing the structural parameters of **LnX_4A 12-MC-4** to their respective **$(MBr)_2$ 12-MC-4** analogs. As described above, the cavity radii for the **DyX_4K 12-MC-4** complexes was 3.716 Å and 3.722 Å for the $Hsal^-$ analog and 3.676 and 3.751 Å for the OAc^- analog, which are within the range of the **$(KBr)_2$** structure (3.679 Å and 3.734 Å). Similar values were observed in the **$Ho(OAc)_4K$ 12-**

MC-4 example (3.678 Å and 3.764 Å). This indicates that although the metallacrowns overall have different shapes, the hydroximate plane does not change significantly. When **Dy(benzoate)$_4$Na 12-MC-4** and **Ho(OAc)$_4$Na 12-MC-4** are compared to **(NaBr)$_2$ 12-MC-4**, the cross-cavity distances for the Dy^{III} structure (3.681 Å and 3.676 Å) and the the Ho^{III} structure (3.693 Å and 3.707 Å) do differ slightly compared to the $(NaBr)_2$ structure (3.670 Å and 3.848 Å), indicating some structural deviation. Looking at the distances between the Ln and the counter ion compared to the di-monovalent cation reveal that the Ln and cation are closer together in the **LnX$_4$K 12-MC-4** structures: 3.908 Å for **Dy(Hsal)$_4$K 12-MC-4**; 3.802 Å for **Dy(OAc)$_4$K 12-MC-4**; and 3.786 Å for **Ho(OAc)$_4$K 12-MC-4** versus 4.264 Å for **(KBr)$_2$ 12-MC-4**). These shorter distances reflect the fact that in the KBr structure, the K^+ ion is present to counter balance the Br- bound to the Jahn-Teller axes of the Mn^{III} ions, which also results in the monovalent cations slight displacement from the center of the cavity In the present structures, the K^+ ion must balance a negative charge present on the opposite metallacrown face. In the **LnX$_4$Na 12-MC-4** structures, the Ln – M distance is longer than the Na – Na distance (3.548 Å for **Dy(benzoate)$_4$Na 12-MC-4** and 3.487 Å for **Ho(OAc)$_4$Na 12-MC-4** versus 3.294 Å for $(NaBr)_2$ 12-MC-4).[14] The role of the Na^+ ion is the same as before, but this result indicates that there is a minimum distance the counter ion must have from the Ln^{III} ion due to electrostatic repulsion affects.

Work by Coronado and co-workers on polyoxometallates (POMs) indicated that the skew angles and the extent of distortion from idealized D_{4d} symmetry could affect the ligand field properties and thus the magnetic properties of single Ln^{III} magnets,[17,18] a topic studied in more depth in Chapter V. A similar analysis for these complexes seems warranted. Thinking of the two ligand planes above and below the Ln^{III} as squares, the ratio of the distance between the two planes (O_{mp} – O_{mp} length) and the sides of the squares (O_{edge} length) gives some indication of the degree of elongation (ratio greater than 1) or contraction (ratio less than 1) of the prism. Measuring the angle between the corners of the squares and the central lanthanide, known as the skew angle, also indicates the type of prism. If the skew angle is 45°, it is a square antirprism and had D_{4d} symmetry (Figure 4.7), where as if the skew angle is 0°, it is a square prism and can have D_{4h}

symmetry. If the angle varies between these two extremes, the degree of deformation from the ideal can be observed. Lastly, the extent that the two ligand fields run parallel can provide information on deformations.

Looking at **Dy(Hsal)$_4$K 12-MC-4** (Figure 4.8), the skew angles are given in Table 4.13. In general, the ligands were oriented close to 45° (the average skew angle was 45(1)°). The distance between the two ligand oxygen planes was 2.658 Å. The edges of the squares composed of the ligands varied slightly. On average, the edge of the Hsal$^-$ oxygen mean plane was 2.799(13) Å and the lengths ranged from 2.784 Å – 2.814 Å and the hydroximate oxygen mean plane edge was 2.63(2) Å with a range of 2.607 Å – 2.647 Å. Taking the ratio of the interplane distance and the edge length of the Hsal$^-$ ligand, the ratio is less than one, indicating a compressed D_{4d} environment.

Looking at **Dy(OAc)$_4$K 12-MC-4** (Figure 4.9), the skew angles (Table 4.14) averaged 45(1)°. The distance between the two ligand planes was 2.662 Å. The edge of the square formed by the acetate oxygens had an average of 2.83(8) Å and a range of 2.781 Å – 2.890 Å. The average edge of the square from the metallacrown hydroximate oxygens was 2.624(8) Å and a range of 2.619 Å – 2.630 Å. The ratio of interplane distance to the edge length of the acetate plane indicated that the degree of compression was roughly the same for **Dy(OAc)$_4$K 12-MC-4** as for **Dy(Hsal)$_4$K 12-MC-4**.

For **Dy(benzoate)$_4$Na 12-MC-4** (Figure 4.9), the skew angles (Table 4.16) averaged 45(2)°. The distance between the two ligand planes was 2.601 Å. The edge lengths for the benzoate plane had an average of 2.86(3) Å and a range of 2.827 Å – 2.907 Å. The hydroximate plane had an average edge length was 2.60(1) Å and a range of 2.582 Å – 2.615 Å. This molecule shows the largest compression of the series. It should be noted, however, that compared to Coronado's POMs,[18] none of the reported metallacrowns are as compressed as the POMs.

What role would these structural parameters play on the magnetic properties? Examining the magnetization values for all the **DyX$_4$A 12-MC-4**, the **Dy(Hsal)$_4$K 12-MC-4** has a

slightly higher value (43690 cm^3 G mol^{-1}) than the rest of the complexes, which, in decreasing magnetization values are **Dy(OAc)$_4$K 12-MC-4** (40630 cm^3 G mol^{-1}), **Dy(benzoate)$_4$Na 12-MC-4** (39960 cm^3 G mol^{-1}), and **Dy(Hsal)$_4$Na 12-MC-4** (39510 cm^3 G mol^{-1}) (Figure 4.145 – 4.18). These values compared nicely to **Dy(Hsal)$_4$H$_3$O$^+$ 12-MC-4** (40400 cm^3 G mol^{-1}).[1] If the bridging ligand alone was affecting the magnetic properties, then it would be expected that the **Dy(Hsal)$_4$A 12-MC-4** complexes would all have the same values and they would differ from the other examples studied. Since that is not the case, it appears that the bridging ligand alone does not affecting magnetic properties. If the counter ion alone affected magnetic properties, the values would be different for the **Dy(Hsal)$_4$A 12-MC-4**. This appears to be the case, potentially meaning that the counter ion can perturb the magnetic properties.

For the dc variable temperature magnetic susceptibility, it again appeared that the identity of the diamagnetic cation or the bridging ligand played no role on the magnetic properties. The susceptibility at 300 K for **DyX$_4$A 12-MC-4** ranged from 23.13 cm^3 K mol^{-1} for **Dy(Hsal)$_4$Na 12-MC-4** to 25.33 cm^3 K mol^{-1} for **Dy(Hsal)$_4$K 12-MC-4** (Figures 4.23 – 4.26). The susceptibility values were slightly smaller than expected for four non-interacting Mn^{III} and one Dy^{III} ion at high temperatures. This indicates that at higher temperatures, there may be multiple spin states in the Dy^{III} ion at higher temperatures. At low temperature, the susceptibilities remained remarkably similar: **Dy(benzoate)$_4$Na 12-MC-4** was the largest at 23.74 cm^3 K mol^{-1} and **Dy(OAc)$_4$K 12-MC-4** was the smallest at 11.14 cm^3 K mol^{-1}. For **Dy(Hsal)$_4$H$_3$O$^+$ 12-MC-4**, the observed susceptibility was slightly smaller at 11.00 cm^3 K mol^{-1}.[1] This seems to indicate that at low temperatures with a small dc magnetic field, the counter ion and the bridging ligand play no role in the magnetic properties. Additionally, the susceptibilities were smaller than expected for the ions present. The observed susceptibilities could correspond to a Dy^{III} ion in an excited spin state and the four Mn^{III} ions antiferromagnetically coupled. It is also possible that the Dy^{III} ion was antiferromagnetically coupled to the Mn^{III} ions, which were antiferromagnetically coupled to each other. Both hypotheses are reasonable based on the exchange coupling shown in the **Mn(OAc)$_2$ 12-MC-4** complex

or the **Li 12-MC-4** complex, where the Mn^{III} ring ions were antiferromagnetically coupled.[2]

The susceptibility values from the in-phase ac magnetic susceptibility values observed for the structures (Figures 4.31 – 4.34) corroborated the dc magnetic data. Again, **$Dy(OAc)_4K$ 12-MC-4** had the smallest susceptibility (9.41 cm^3 K mol^{-1}), while **$Dy(benzoate)_4Na$ 12-MC-4** again had the largest susceptibility (12.55 cm^3 K mol^{-1}). Again, the observed susceptibility values were smaller than expected for the present cations if they were non-interacting. The values also do not lead to a clear antiferromagnetic coupling scheme between the ions. For the **$Dy(Hsal)_4H_3O^+$** complex, the extrapolate susceptibility was found to be 9.19 cm^3 K mol^{-1}, which was again the smallest observed.[1] Again, it did not appear that the bridging ligand or the counter ion dramatically affected the magnetic properties.

However, upon examining the out-of-phase magnetic susceptibility, it became clear that the bridging ligand played a larger role on the magnetic behaviors. Only the **$Dy(Hsal)_4A$ 12-MC-4** complexes (Figure 4.38 and 4.39, K and Na, respectively) as well as the **$Dy(Hsal)_4H_3O^+$ 12-MC-4** complex showed slow magnetic relaxation. The **$Dy(OAc)_4K$ 12-MC-4** (Figure 4.40) and **$Dy(benzoate)_4Na$ 12-MC-4** (Figure 4.41) did not show onset of slow magnetic relaxation. What can explain this observation, especially considering that all the other magnetic parameters seemed to be invariant across the species?

Two explanations exist in the literature. The first is that the small changes in the compression ratio affected the magnetic properties (0.95 for **$Dy(Hsal)_4K$ 12-MC-4**, 0.94 for **$Dy(OAc)_4K$ 12-MC-4**, and 0.91 for **$Dy(benzoate)_4Na$ 12-MC-4**). Dy^{III} is an oblate ion, and is favored in axially elongated coordination environments.[5] The more compressed **$Dy(benzoate)_4Na$ 12-MC-4** placed the Dy^{III} ion in an unfavorable ligand field, thus perturbing the anisotropic and spin parameters. However, if this explanation were true, then one may expect that **$Dy(Hsal)_4A$ 12-MC-4** and **$Dy(OAc)_4K$ 12-MC-4** would also show SMM properties, which is not the case.

The second explanation relies on perturbations of the electronic properties of the bridging ligands. One way presented in the literature to account for these perturbations is to use something called the accumulated electronegativity (AEN) of the ligands, proposed by Boukhvalov and co-workers.[7] They found that to characterize the ligands in their system, the "bond dissociation energy for R – H analogs of the R – COO^- carboxylate groups" would "characterize the strength of the covalent bonds between hydrogen and R and is valid for the description of bonds between R and COO groups in {Mn12}."[7] However, because bond dissociate energies for all their investigate ligands did not exist, they used the AEN values, which are easily calculated using the sum of Pauling's electronegativity values for each atom in the R portion of the ligand. For example, the AEN of acetate was the sum of the electronegativity of C and three H atoms, or 8.8.[25] Table 4.21 provides all the calculated AEN values.

Table 4.21. The accumulated electronegativity (AEN) of the ligands used in **DyX_4A 12-MC-4** are given using the values from reference 25 (X = $^-$OOC-R).

R =	**AEN**
$-CH_3$	8.8
$-C_6H_5$	25.5
$-C_6H_4OH$	29.0

Boukhvalov and co-workers found that as the AEN increased in Mn_{12} species, the density of states for the Mn *3d* and O *2p* moved closer together, enhancing ferromagnetic exchange.[7] This observation and the calculated values could help provide some sense to the observed out-of-phase properties observed in the **DyX_4A 12-MC-4** complexes. The more electronegative salicylate ligands perturbed the ligand field around the Dy^{III} ion more than the acetate or benzoate ligands.

This observation is further supported by looking at the pK_a values of the ligands studied, which report on the basicity, and hence the donor capacity, of the ligands. The pK_a of salicylic acid (2.93)[26] is smaller than that of benzoic (4.20) or acetic acid (4.77).[27] This indicates that salicylate is the most electron withdrawing of the group, with benzoate and acetate having similar electron withdrawing properties. This could affect the strength of the exchange coupling between the ring metals and the central Dy^{III} ion. Or, this could

again perturb the electronic states of the Dy^{III} ion, changing the order of the *J* states, something that could be easily missed in the experiments above because of the temperatures at which the properties were measured. The pK_a correlates nicely with the observed out-of-phase behavior: **$Dy(Hsal)_4A$ 12-MC-4** showed dramatically different out-of-phase properties compared to **$Dy(OAc)_4K$ 12-MC-4** or **$Dy(benzoate)_4Na$ 12-MC-4**. As the out-of-phase properties of **$Dy(Hsal)_4K$ 12-MC-4** and **$Dy(Hsal)_4Na$ 12-MC-4** differed slightly (Figures 4.39 and 4.40), it could be that the counter ion "fine tunes" the magnetic properties based on its interactions with the hydroximate ring.

Examining the **$Ho(OAc)_4K$ 12-MC-4** structures, it was found that the **$Ho(OAc)_4K$ 12-MC-4** complex had the same susceptibility value ($\chi_M T$ = 23.67 cm^3 K mol^{-1}) (Figure 4.27) than the **$Ho(OAc)_4Na$ 12-MC-4** complex ($\chi_M T$ = 23.84 cm^3 K mol^{-1}) (Figure 4.28). Again, these values were less than expected for four non-interacting Mn^{III} ions and a single Ho^{III} ion ($\chi_M T$ = 26.07 cm^3 K mol^{-1}). At low temperature, the susceptibilities were quite similar, 9.42 cm^3 K mol^{-1} for the **$Ho(OAc)_4K$ 12-MC-4** derivative and 9.10 cm^3 K mol^{-1} for the **$Ho(OAc)_4Na$ 12-MC-4** complex. These values are lower than expected for a single Ho^{III} ion and four antiferromagnetically coupled Mn^{III} ions. Again, it indicates that even at low temperatures, multiple spin states are populated. In the **$Ho(OAc)_4M$ 12-MC-4** structures, no out-of-phase frequency dependence was observed (Figures 4.43 and 4.44) for either metallacrown. As both metallacrowns had similar magnetic behavior, it is difficult to determine if the bridging ligand or the counter ion is affecting the SMM properties. One would have hoped that if the counter ion was affecting the SMM properties due to its proximity to the Ho^{III}, one metallacrown and not the other would show slow magnetic relaxation. However, there is another phenomenon that could be at play here: Ho^{III} is a non-Kramers' doublet and there is not a bistable ground state available.[5] Zaleski found that the **$Tb(Hsal)_4H_3O^+$ 12-MC-4** metallacrown did not show SMM properties.[1] Even with different bridging ligands, neither displayed slow magnetic relaxation. Because Tb^{III} and Ho^{III} are both non-Kramers' doublets, this could be the reason that neither shows SMM properties.

The fact that the diamagnetic counter ion does dramatically not affect the slow magnetic relaxation properties is not a trivial one. In the future, if one hopes to place metallacrowns on surfaces, one potential route is to tether the metallacrown to the surface with a diamagnetic ion, such as a gold atom. If the counter ion had caused the slow magnetic relaxation behavior to disappear, it would force alternative binding routes to be studied. In addition, because it appears that the counter ion does not affect the magnetic properties, it could be possible to use large di-cations, such as Ba^{2+} to electrostatically bring two metallacrowns together. This would prove to be an interesting future direction of research as it could perturb the electronics of the metallacrown ring by introducing a cation of similar charge to the Ln^{III} ions.

Based on the studies conducted in this chapter, it became apparent that controlling the ligand field parameters around the Ln^{III} would be paramount to understanding the observed magnetic properties. Using a structure first identified by Joseph Jankolovits, the **$Ln^{III}Zn_{16}$**, it would be possible to study a wide range of Ln^{III} in a similar coordination environment. This allowed for a detailed study of ligand field effects on the magnetic properties. This work will be discussed in the next chapter.

Conclusions

Inspired by the work on **$Mn(OAc)_2$ 12-MC-4** and **$Dy(Hsal)_4H_3O^+$ 12-MC-4**, two different **$Ni(OAc)_2$ 12-MC-4** complexes, a series of **DyX_4M 12-MC-4** complexes, and two **$Ho(OAc)_4M$ 12-MC-4** complexes were studied with the goal of increasing the anisotropy by incorporating anisotropic central metals. It was shown in the **$Mn(OAc)_2$ 12-MC-4** complex that the 12-MC-4 ring oriented the anisotropy vectors of the Mn^{III} ions perpendicular to the metallacrown plane and parallel to each other. It was hoped that utilizing this optimized geometry with different central metals would increase the blocking temperature. While that was not observed, fascinating magnetic properties were found (Table 4.22).

Studying the **$Ni(OAc)_2$ 12-MC-4** complexes revealed the importance of lattice solvent on the magnetic properties. When the metallacrowns are non-interacting, as in the **$Ni(OAc)_2$ 12-MC-4 (DMF)** complex, it showed single-molecule magnetic behavior. Upon introduction of a hydrogen bonding network, found in **$Ni(OAc)_2$ 12-MC-4 (MeOH)** the material behaved as a single-chain magnet. The source of this magnetic behavior was due to hydrogen bonds between the molecules. There are only a few examples of hydrogen bonded SCMs in the literature. The idea that is possible to use hydrogen bonds to create SCMs is something that could be of great use to the field, as it can be difficult to physically link clusters together using conventional ligands

Attempting to perturb the magnetic properties further, Ln^{III} ions were introduced. This idea, one that is established in the literature,[1,28] showed that the magnetic properties changed upon introduction of *4f* Ln^{III} ions. Next, the impact of altering the bridging ligand as well as the counter ion in a series of **DyX_4A 12-MC-4** and **$Ho(OAc)_4M$ 12-MC-4** complexes were studied. It was found that changing the bridging ligand in the **DyX_4A 12-MC-4** complex possibly altered the exchange interactions, the electron withdrawing properties of the ligand field around the Dy^{III} ion and possibly the ordering of the *J* states . This was most manifested in the out-of-phase magnetic susceptibility plots. It was found for the **LnX_4A 12-MC-4** series that the range of counter ions investigated ($A = H_3O^+$, K^+, Na^+) had little impact on the magnetic properties. This is not a trivial observation, as if the diamagnetic cation dramatically altered the magnetic properties, it could make grafting future metallacrowns on surfaces a difficult endeavor. It could also prevent the possibility of electrostatically bringing two metallacrowns together around a large di-cation.

Because of the complicated magnetic phenomena observed in this chapter, it was hoped that another series of metallacrowns, the **$Ln^{III}Zn_{16}$** series, would allow for a clearer understanding of the factors that perturb Ln SMM properties. By removing all other paramagnetic ions, all exchange pathways were lost. The large ligand environment around the Ln^{III} would also "protect" it from intermolecular interactions. All magnetic properties would owe solely to the Ln^{III} ion. Thus, one could better study the ligand field

parameters without worrying about different electron withdrawing groups or exchange coupling. These factors will be studied in Chapter V.

Table 4.22. The magnetic properties of the planar 12-MC-4 complexes studied in the chapter are summarized.

Complex	Low Temperature $\chi_M T$ (cm^3 K mol^{-1})	High Temperature $\chi_M T$ (cm^3 K mol^{-1})	Slow Magnetic Relaxation?
$Ni(OAc)_2$ 12-MC-4 (DMF)	3.82 (2 K)	10.98 (300 K)	YES
$Ni(OAc)_2$ 12-MC-4 (MeOH)	2.37 (2 K)	10.89 (300 K)	YES
$Dy(Hsal)_4K$ 12-MC-4	11.55 (5 K)	25.33 (300 K)	YES
$Dy(Hsal)_4Na$ 12-MC-4	12.20 (5 K)	23.13 (300 K)	YES
$Dy(OAc)_4K$ 12-MC-4	11.14 (5 K)	23.60 (300 K)	NO
$Dy(benzoate)_4Na$ 12-MC-4	12.56 (5 K)	23.74 (300 K)	NO
$Ho(OAc)_4K$ 12-MC-4	9.42 (5 K)	23.67 (300 K)	NO
$Ho(OAc)_4Na$ 12-MC-4	9.10 (5 K)	23.84 (300 K)	NO

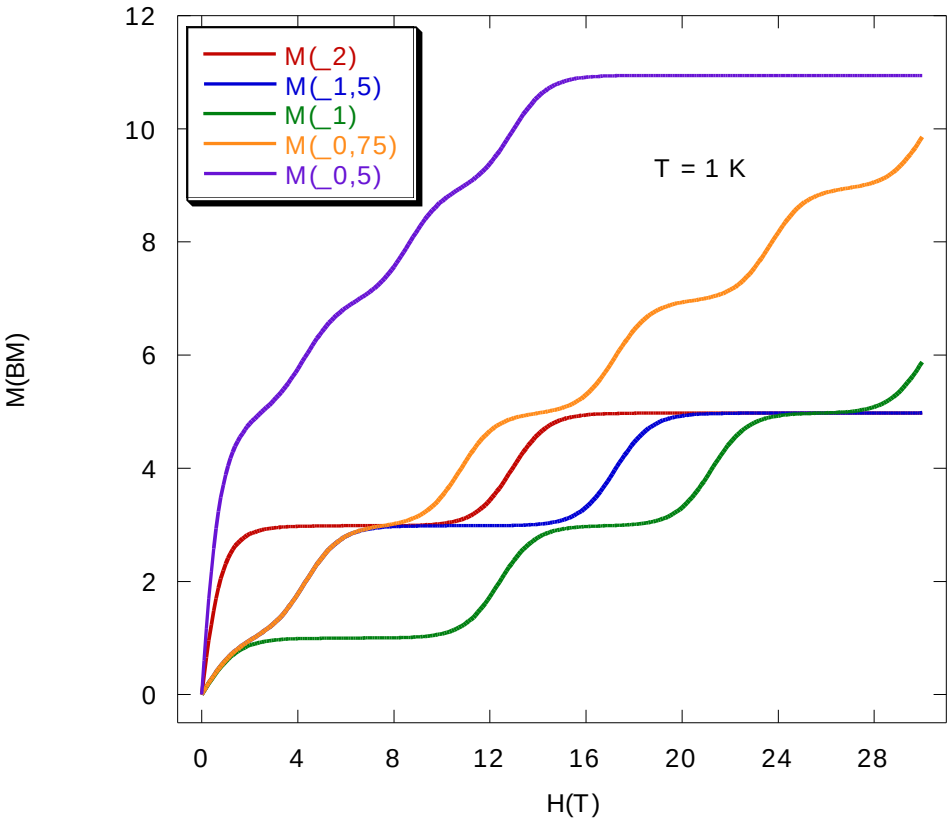

Figure 4.1. The magnetic coupling could dramatically impact the ground spin state of the **Mn(OAc)$_2$ 12-MC-4** complex. The ratio between *J* and *J'* (given as M) afforded different spin states. The coupling scheme is given in Figure 1.52.

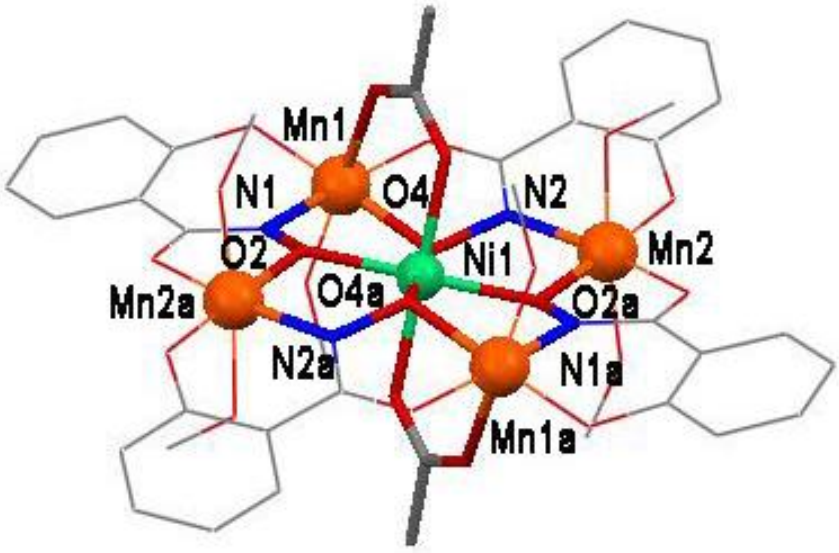

Figure 4.2. The X-ray crystal structure of **Ni(OAc)$_2$ 12-MC-4 (MeOH)** is shown. Color scheme: orange spheres: Mn^{III}; teal sphere: Ni^{II}; red tubes: oxygen; blue tubes: nitrogen; gray tubes: carbon. Hydrogen atoms and lattice solvents have been omitted for clarity.

Figure 4.3. The X-ray crystal structure of **$Ni(OAc)_2$ 12-MC-4 (DMF)** is shown. Color scheme: orange spheres: Mn^{III}; teal sphere: Ni^{II}; red tubes: oxygen; blue tubes: nitrogen; gray tubes: carbon. Hydrogen atoms and non-coordinated solvents have been omitted for clarity

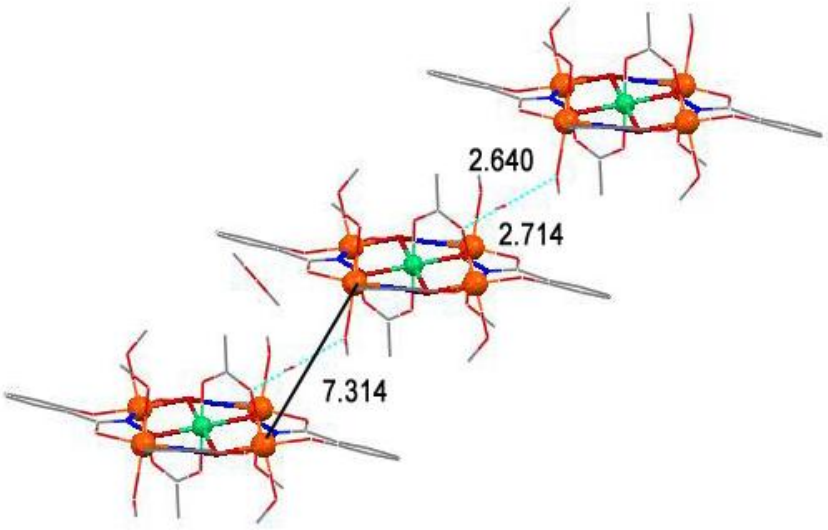

Figure 4.4. The crystal packing diagram of **$Ni(OAc)_2$ 12-MC-4 (MeOH)** shows a hydrogen bonding network (light blue dashed line) between the coordinated acetate on Mn1 of one metallacrown, a solvent methanol, and then a methanol coordinated to Mn2 of a second metallacrown. From the acetate on Mn1 to the solvent MeOH, the distance is 2.722 Å. From that MeOH to the MeOH coordinated on Mn2, the distance is 2.640 Å. The Mn1 – Mn2 distance is 7.314 Å (black line). Color scheme: orange spheres: Mn^{III}; teal sphere: Ni^{II}; red tubes: oxygen; blue tubes: nitrogen; gray tubes: carbon. Hydrogen atoms have been omitted for clarity.

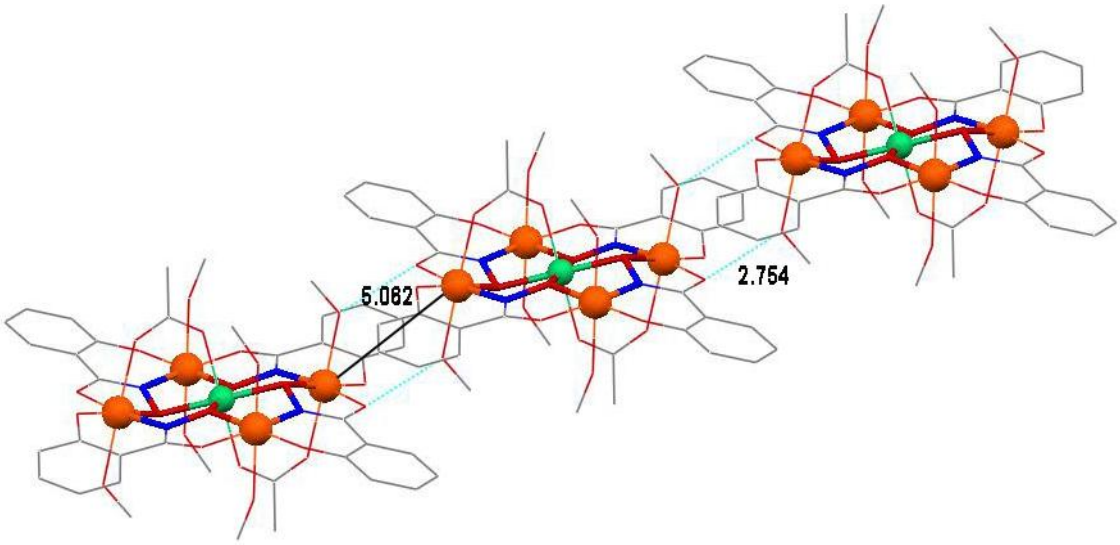

Figure 4.5. The crystal packing diagram of **$Ni(OAc)_2$ 12-MC-4 (MeOH)** shows a hydrogen bonding network (light blue dashed line) between the coordinated methanol on Mn1 of one metallacrown and the methanol coordinated to Mn1 of a second metallacrown. The hydrogen bond length is 2.754 Å. The Mn1 – Mn1 distance is 5.062 Å (black line). Color scheme: orange spheres: Mn^{III}; teal sphere: Ni^{II}; red tubes: oxygen; blue tubes: nitrogen; gray tubes: carbon. Hydrogen atoms have been omitted for clarity.

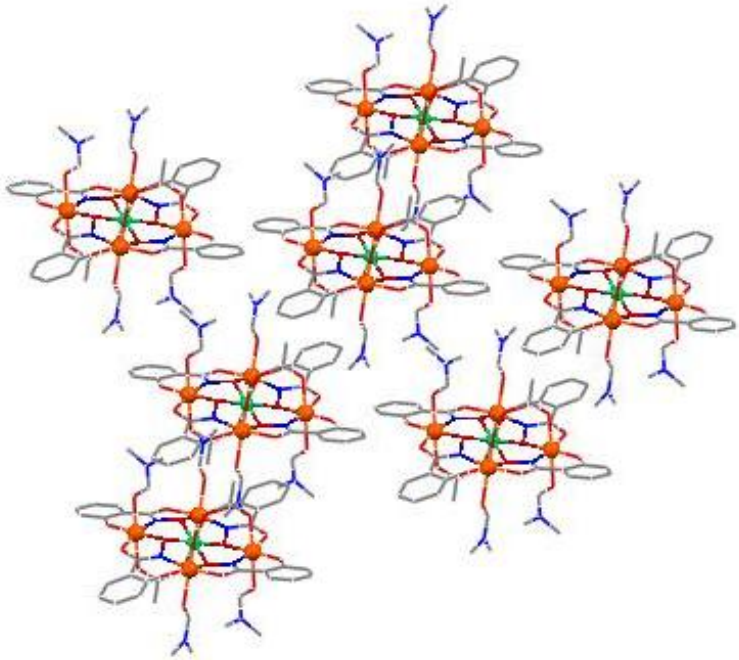

Figure 4.6. The crystal packing diagram of **$Ni(OAc)_2$ 12-MC-4 (DMF)** shows that the metallacrowns simply close pack. Color scheme: orange spheres: Mn^{III}; teal sphere: Ni^{II}; red tubes: oxygen; blue tubes: nitrogen; gray tubes: carbon. Hydrogen atoms and lattice solvents have been omitted for clarity.

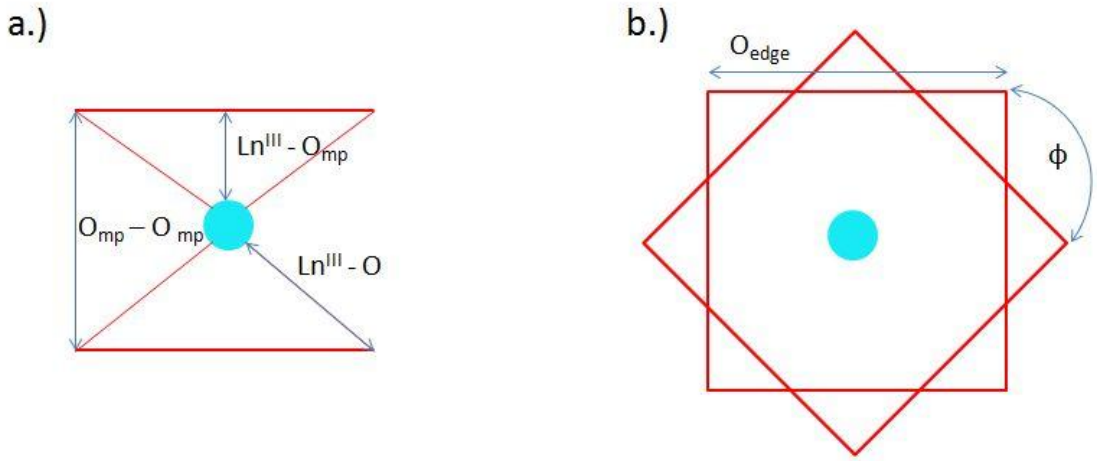

Figure 4.7. The important structural parameters of **LnX_4A 12-MC-4** are shown. a.) Looking perpendicular to the C_4 axis, the oxygen mean-plane distances (O_{mp} – O_{mp}), the distance between the metallacrown oxygen mean-plane and central Ln^{III} (Ln^{III} – O_{mp}), and the distance between the Ln^{III} atom and the oxygen of the metallacrown ring (Ln^{III} – O) are shown. b.) Along the C_4 axis, the O – O length of the metallacrown (O_{edge}) and skew angle (φ) are shown. Color scheme: red line: oxygen mean plane; aqua sphere: Ln^{III}.

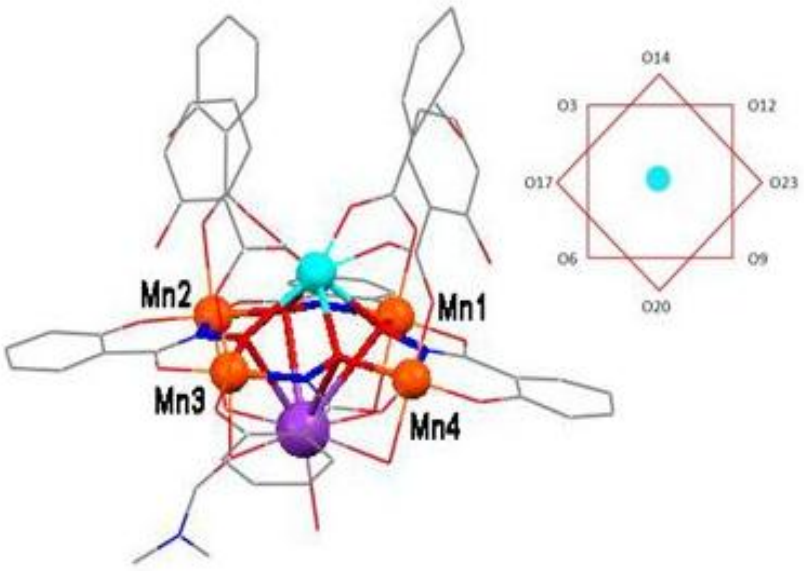

Figure 4.8. The X-ray crystal structure of **$Dy(Hsal)_4K$ 12-MC-4** is shown. Color scheme: orange sphere: Mn^{III}; aqua sphere: Dy^{III}; purple sphere: K^+; red tubes: oxygen; blue tubes: nitrogen; gray tubes; carbon. For clarity, hydrogen atoms and lattice solvents have been omitted.

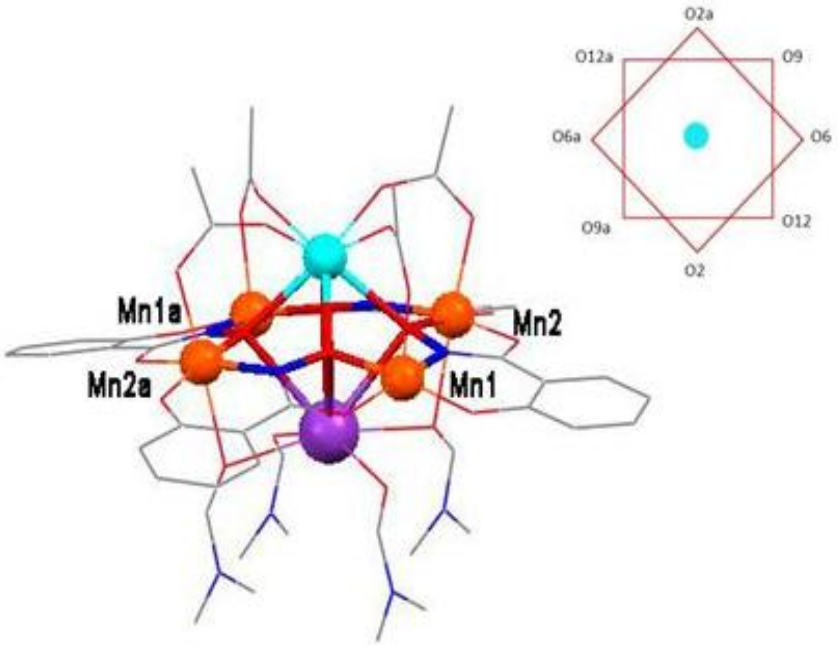

Figure 4.9. The X-ray crystal structure of **Dy(OAc)$_4$K 12-MC-4** is shown. Color scheme: Mn^{III}; aqua sphere: Dy^{III}; purple sphere: K^+; red tubes: oxygen; blue tubes: nitrogen; gray tubes; carbon. For clarity, hydrogen atoms and lattice solvents have been omitted.

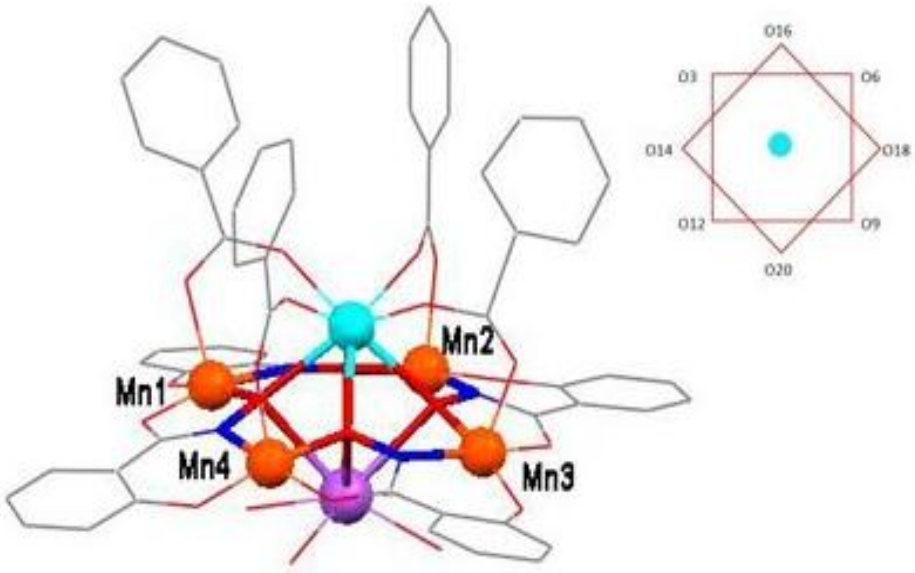

Figure 4.10. The X-ray crystal structure of **Dy(benzoate)$_4$Na 12-MC-4** is shown. Color scheme: Mn^{III}; aqua sphere: Dy^{III}; light purple sphere: Na^+; red tubes: oxygen; blue tubes: nitrogen; gray tubes; carbon. For clarity, hydrogen atoms and lattice solvents have been omitted.

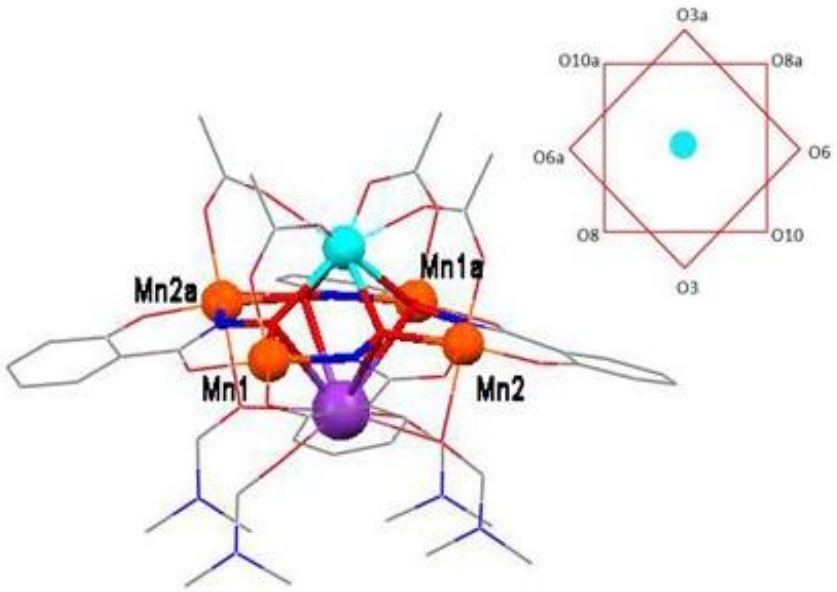

Figure 4.11. The X-ray crystal structure of **$Ho(OAc)_4K$ 12-MC-4** is shown. Color scheme: Mn^{III}; aqua sphere: Ho^{III}; purple sphere: K^+; red tubes: oxygen; blue tubes: nitrogen; gray tubes; carbon. For clarity, hydrogen atoms and lattice solvents have been omitted.

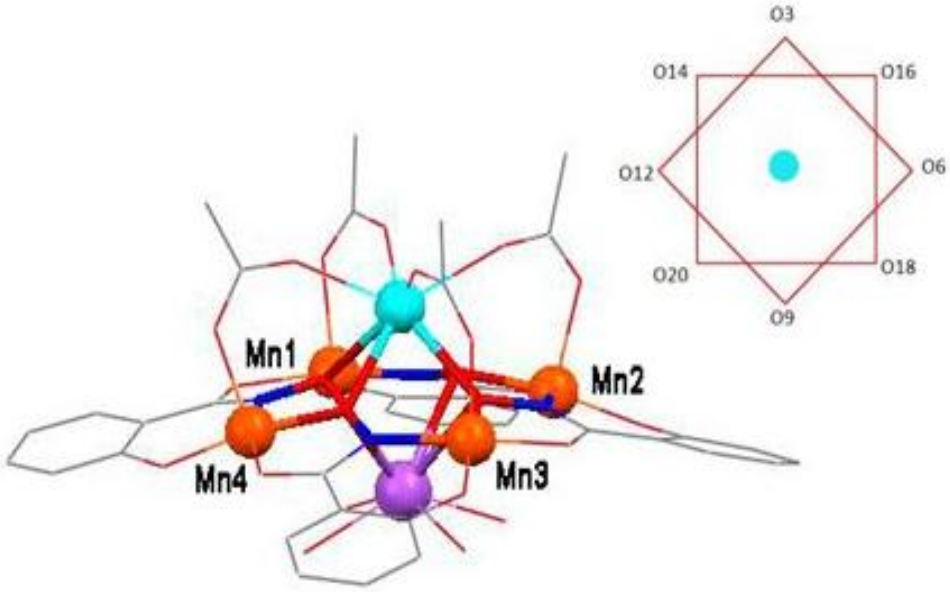

Figure 4.12. The X-ray crystal structure of **$Ho(OAc)_4Na$ 12-MC-4** is shown. Color scheme: Mn^{III}; aqua sphere: Ho^{III}; light purple sphere: Na^+; red tubes: oxygen; blue tubes: nitrogen; gray tubes; carbon. For clarity, hydrogen atoms and lattice solvents have been omitted.

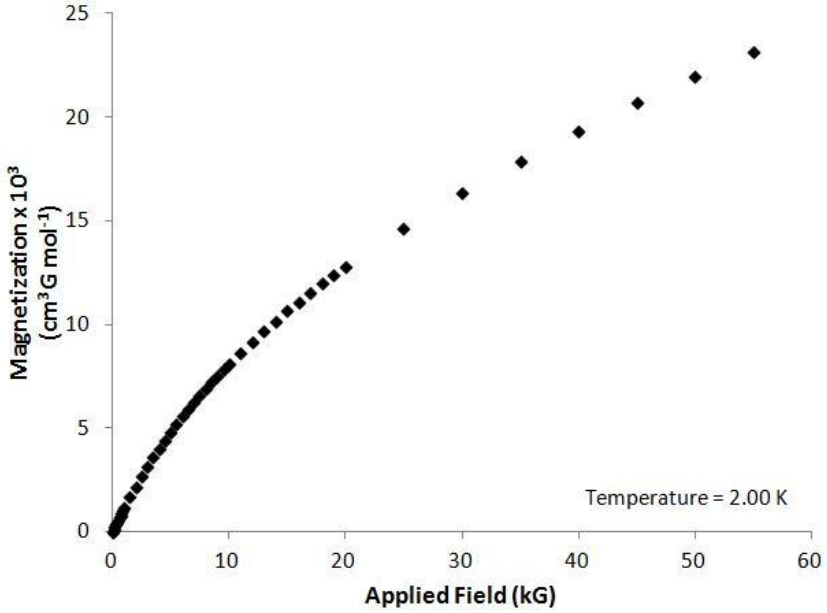

Figure 4.13. The dc variable field magnetization data for **$Ni(OAc)_2$ 12-MC-4 (MeOH)** are shown. The magnetization data were collected at 2.00 K and with an applied field ranging from 0 G to 55000 G.

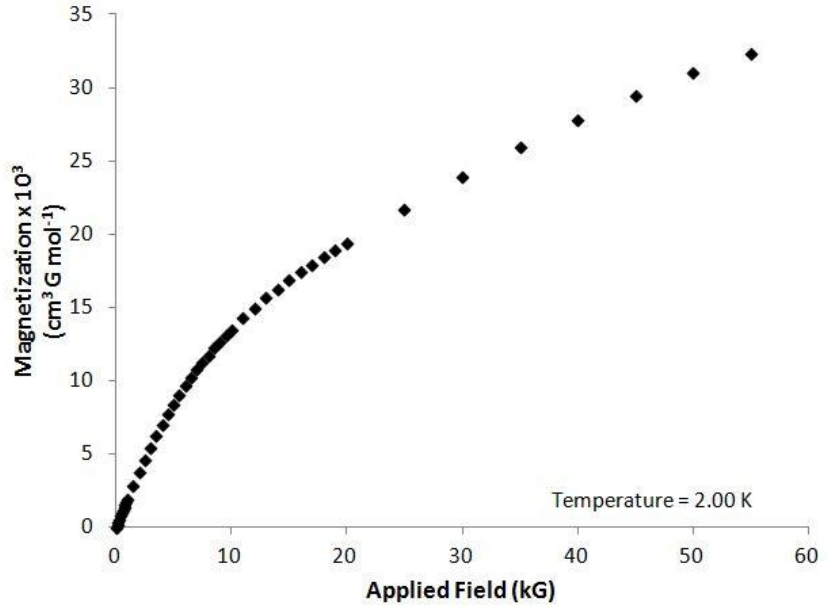

Figure 4.14. The dc variable field magnetization data for **$Ni(OAc)_2$ 12-MC-4 (DMF)** are shown. The magnetization data were collected at 2.00 K and with an applied field ranging from 0 G to 55000 G.

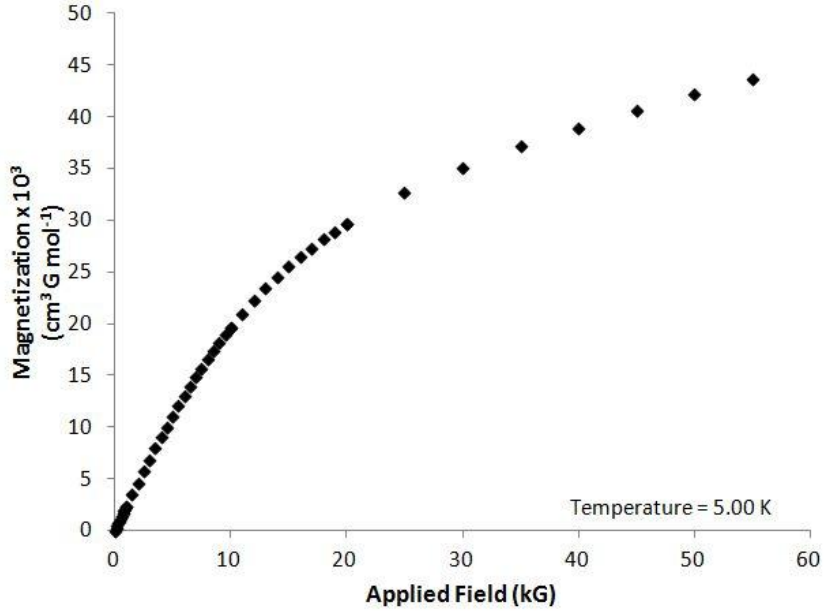

Figure 4.15. The dc variable field magnetization data for **Dy(Hsal)$_4$K 12-MC-4** are shown. The magnetization data were collected at 5.00 K with an applied field ranging from 0 G to 55000 G.

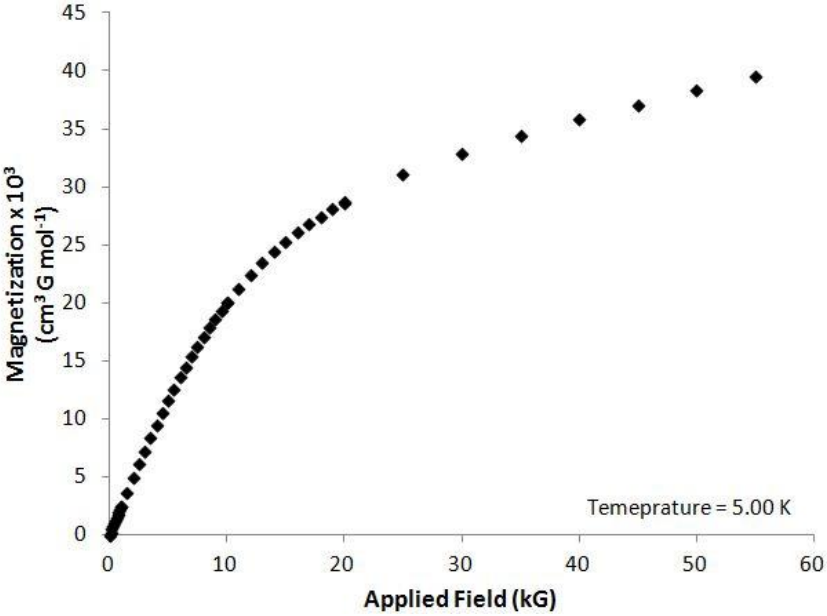

Figure 4.16. The dc variable field magnetization data for **Dy(Hsal)$_4$Na 12-MC-4** are shown. The magnetization data were collected at 5.00 K with an applied field ranging from 0 G to 55000 G.

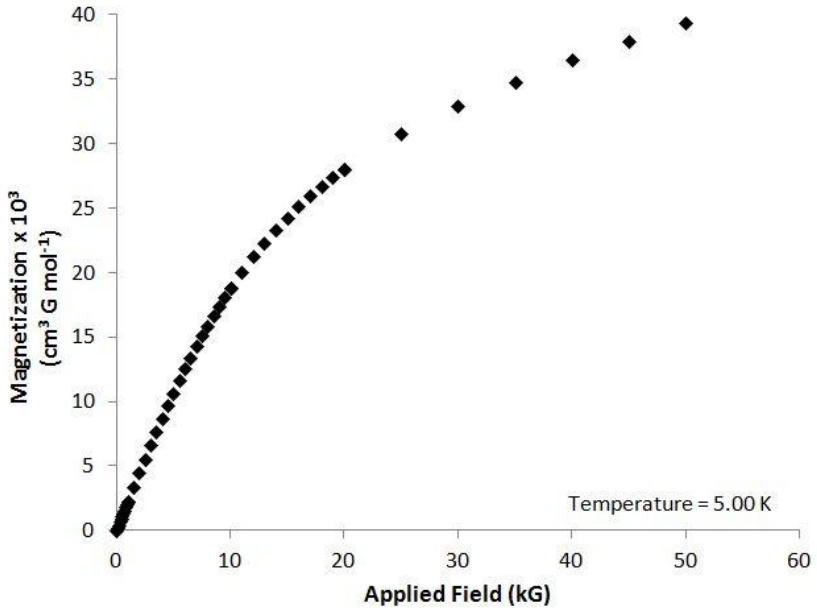

Figure 4.17. The dc variable field magnetization data for **$Dy(OAc)_4K$ 12-MC-4** are shown. The magnetization data were collected at 5.00 K with an applied field ranging from 0 G to 55000 G.

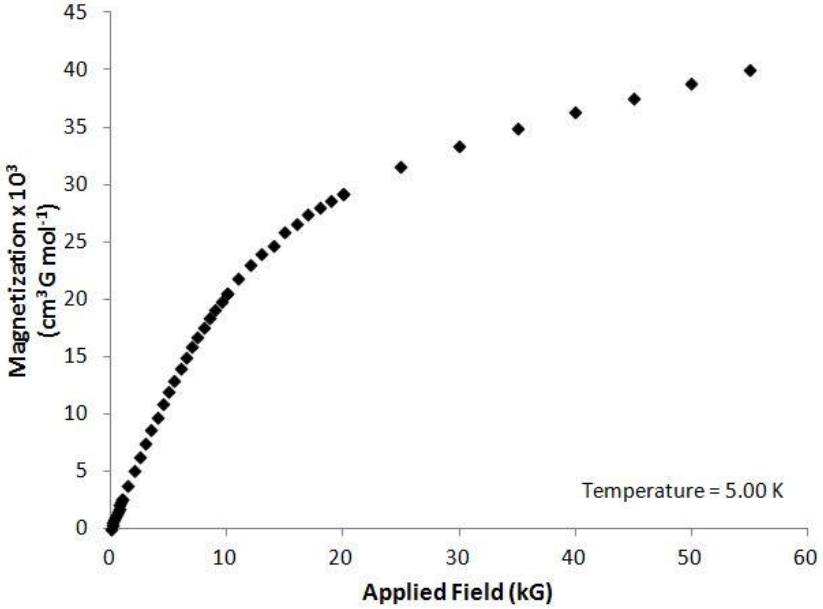

Figure 4.18. The dc variable field magnetization data for **$Dy(benzoate)_4Na$ 12-MC-4** are shown. The magnetization data were collected at 5.00 K with an applied field ranging from 0 G to 55000 G.

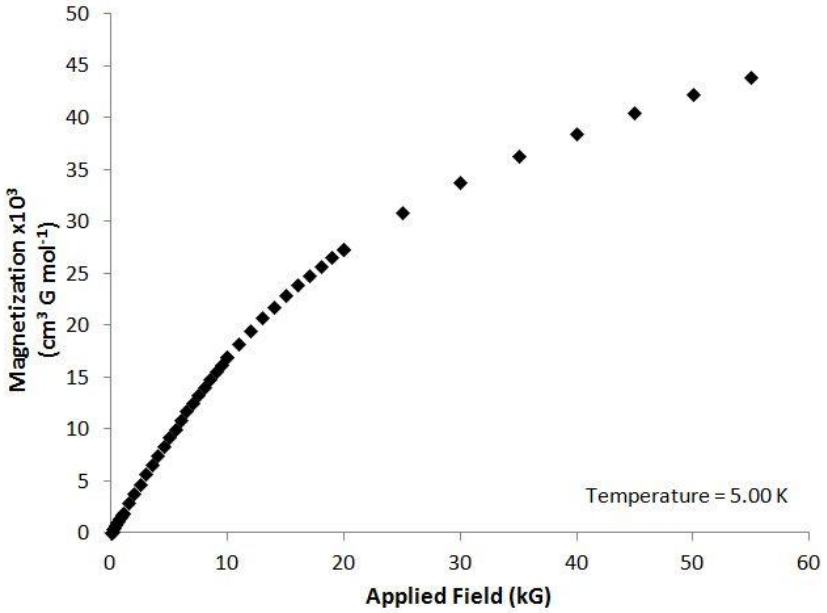

Figure 4.19. The dc variable field magnetization data for **Ho(OAc)$_4$K 12-MC-4** are shown. The magnetization data were collected at 5.00 K with an applied field ranging from 0 G to 55000 G.

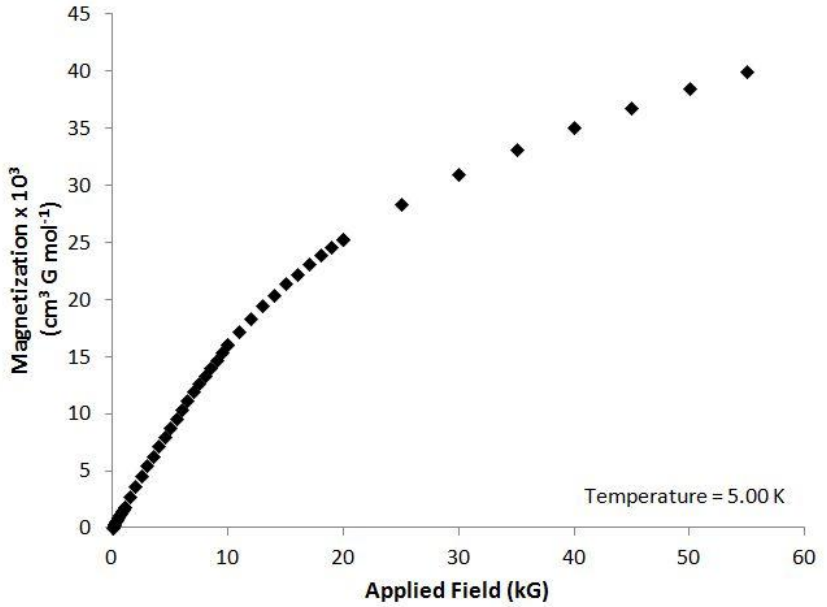

Figure 4.20. The dc variable field magnetization data for **Ho(OAc)$_4$Na 12-MC-4** are shown. The magnetization data were collected at 5.00 K with an applied field ranging from 0 G to 55000 G.

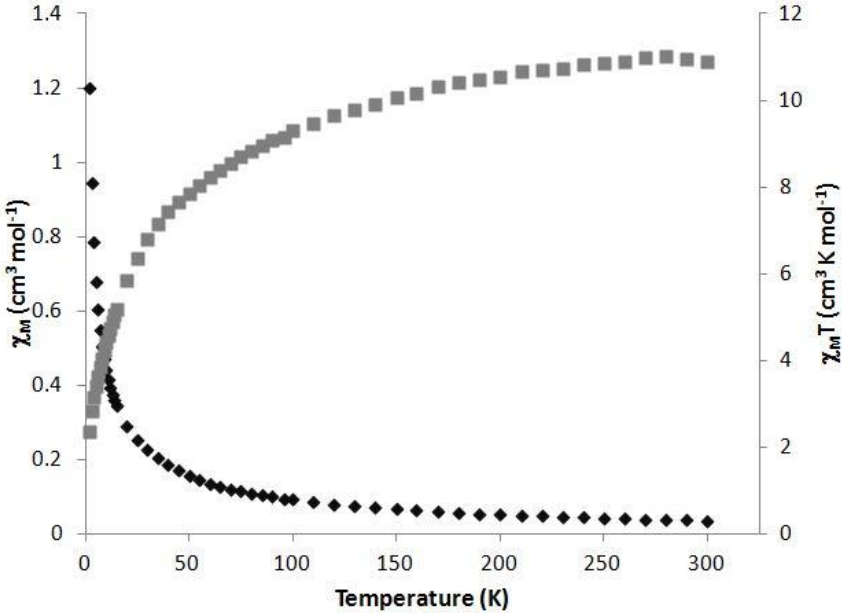

Figure 4.21. The dc variable temperature magnetic susceptibility of **$Ni(OAc)_2$ 12-MC-4 (MeOH)** is shown. The magnetic susceptibility data was collected with an applied dc field of 1000 G and lowering the temperature from 300 K to 2.00 K. χ_M = ◆ $\chi_M T$ = ■

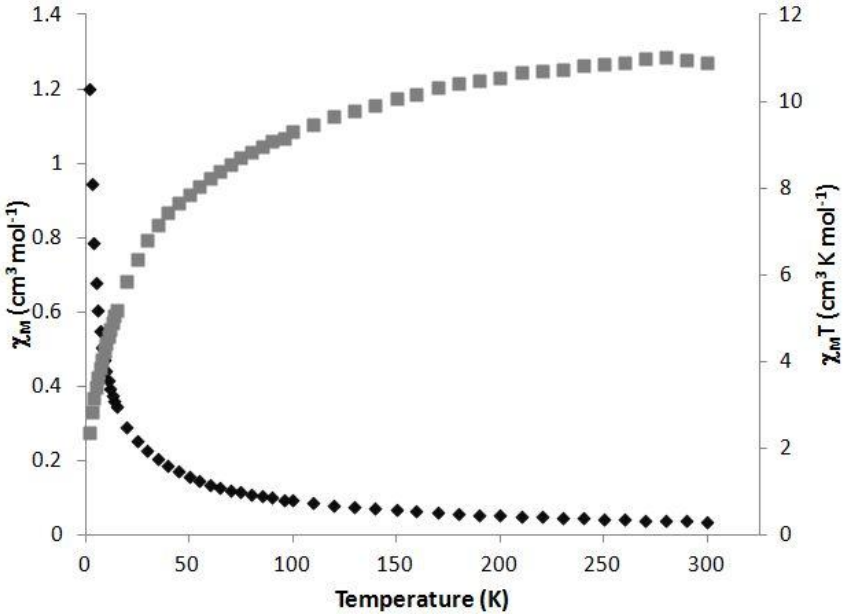

Figure 4.22. The dc variable temperature magnetic susceptibility of **$Ni(OAc)_2$ 12-MC-4 (DMF)** is shown. The magnetic susceptibility data were collected with an applied dc field of 1000 G and lowering the temperature from 300 K to 2.00 K. χ_M = ◆ $\chi_M T$ = ■

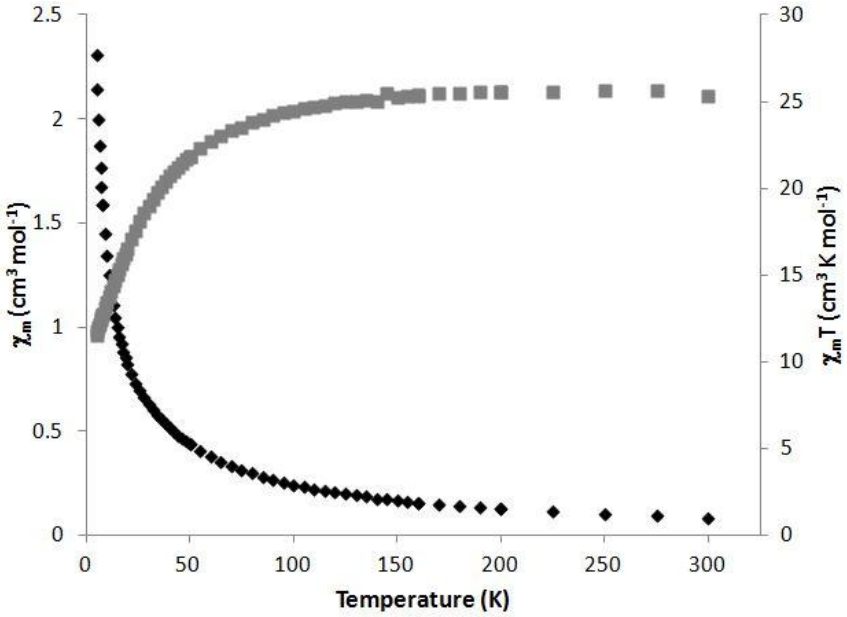

Figure 4.23. The dc variable temperature magnetic susceptibility of **Dy(Hsal)$_4$K 12-MC-4** is shown. The magnetic susceptibility was collected with an applied dc field of 2000 G and raising the temperature from 5.00 K to 300 K. χ_M = ◆ χ_MT = ■

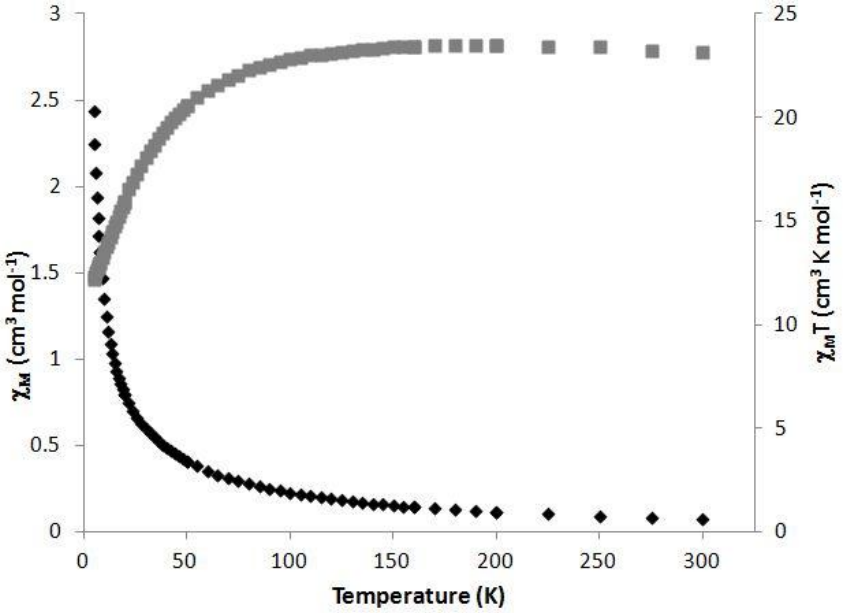

Figure 4.24. The dc variable temperature magnetic susceptibility of **Dy(Hsal)$_4$Na 12-MC-4** is shown. The magnetic susceptibility was collected with an applied dc field of 2000 G and raising the temperature from 5.00 K to 300 K. χ_M = ◆ χ_MT = ■

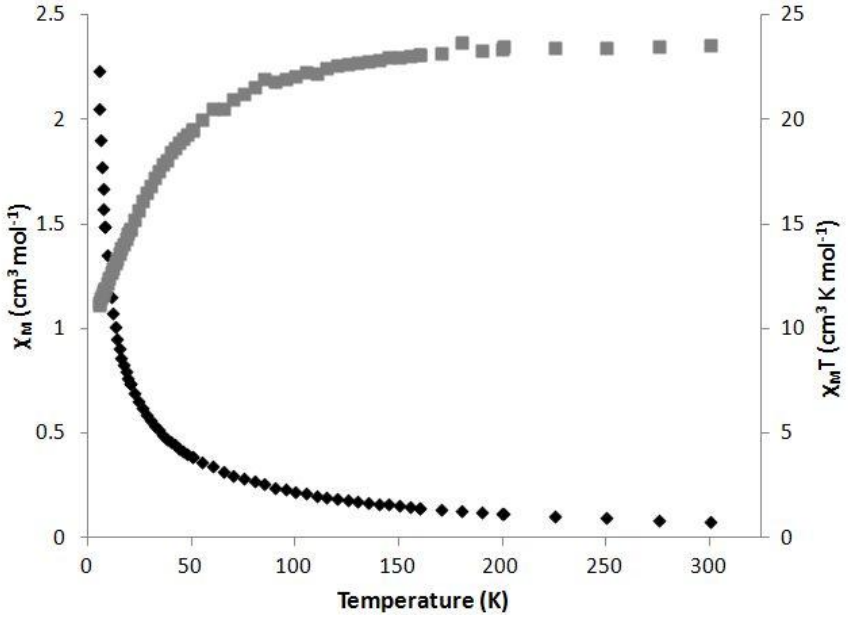

Figure 4.25. The dc variable temperature magnetic susceptibility of **Dy(OAc)$_4$K 12-MC-4** is shown. The magnetic susceptibility was collected with an applied dc field of 2000 G and raising the temperature from 5.00 K to 300 K. χ_M = ◆ χ_MT = ■

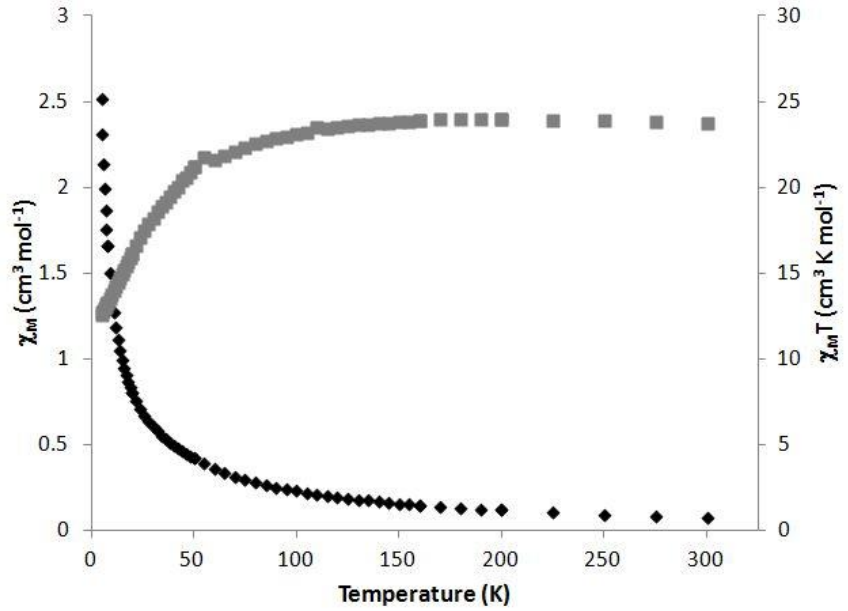

Figure 4.26. The dc variable temperature magnetic susceptibility of **Dy(benzoate)$_4$Na 12-MC-4** is shown. The magnetic susceptibility was collected with an applied dc field of 2000 G and raising the temperature from 5.00 K to 300 K. χ_M = ◆ χ_MT = ■

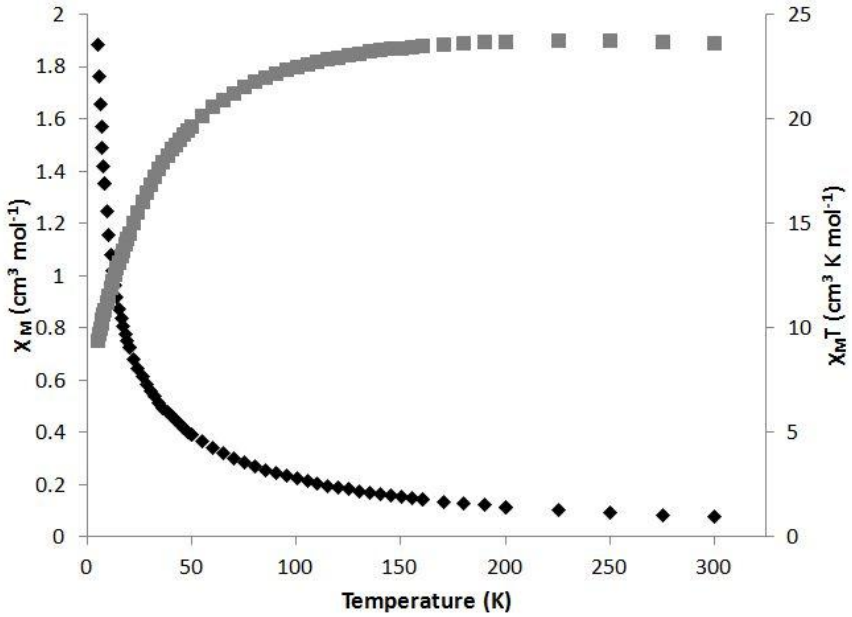

Figure 4.27. The dc variable temperature magnetic susceptibility of **Ho(OAc)$_4$K 12-MC-4** is shown. The magnetic susceptibility was collected with an applied dc field of 2000 G and raising the temperature from 5.00 K to 300 K. χ_M = ◆ χ_MT = ■

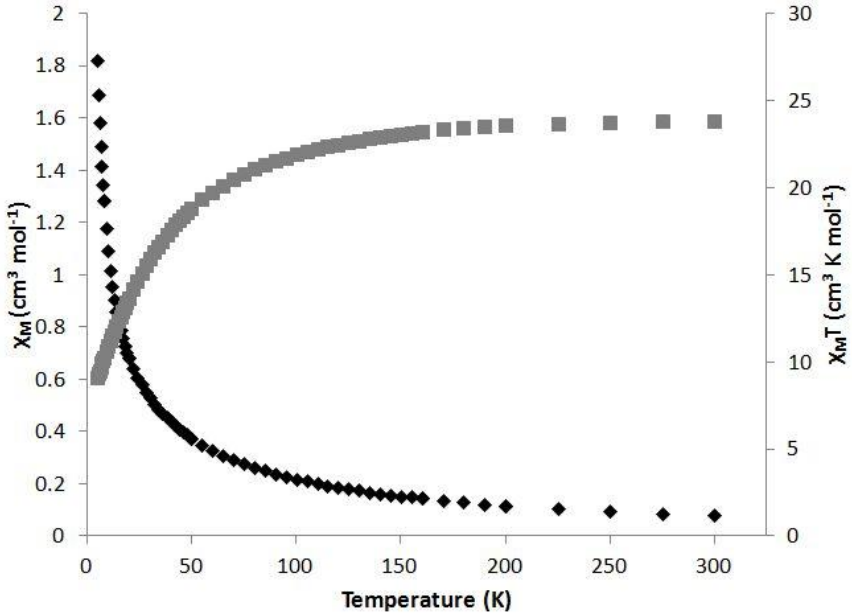

Figure 4.28. The dc variable temperature magnetic susceptibility of **Ho(OAc)$_4$Na 12-MC-4** is shown. The magnetic susceptibility was collected with an applied dc field of 2000 G and raising the temperature from 5.00 K to 300 K. χ_M = ◆ χ_MT = ■

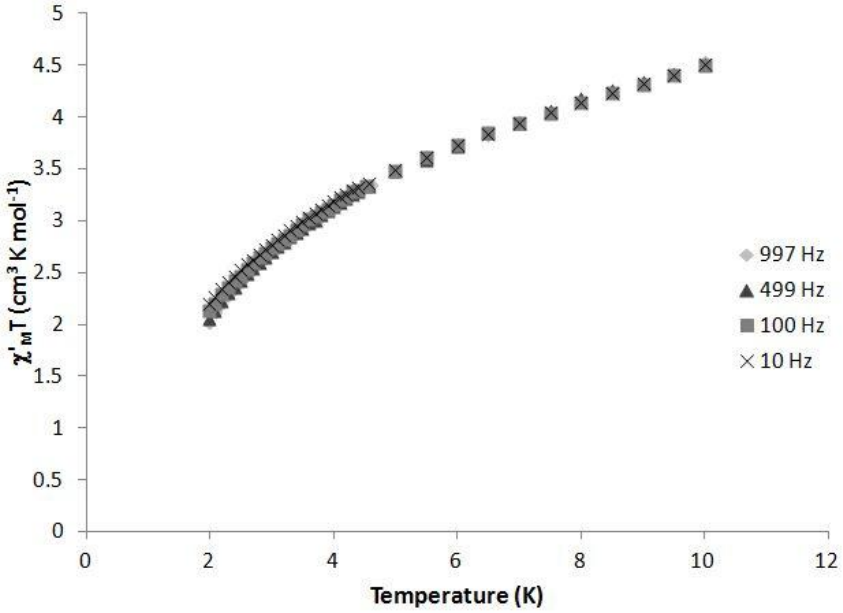

Figure 4.29. The in-phase ac variable temperature magnetic susceptibility of **Ni(OAc)$_2$ 12-MC-4 (MeOH)** is shown. The susceptibility was collected between 10 K and 2.00 K with a 3.5 G drive field, no dc applied field, and at the indicated frequencies.

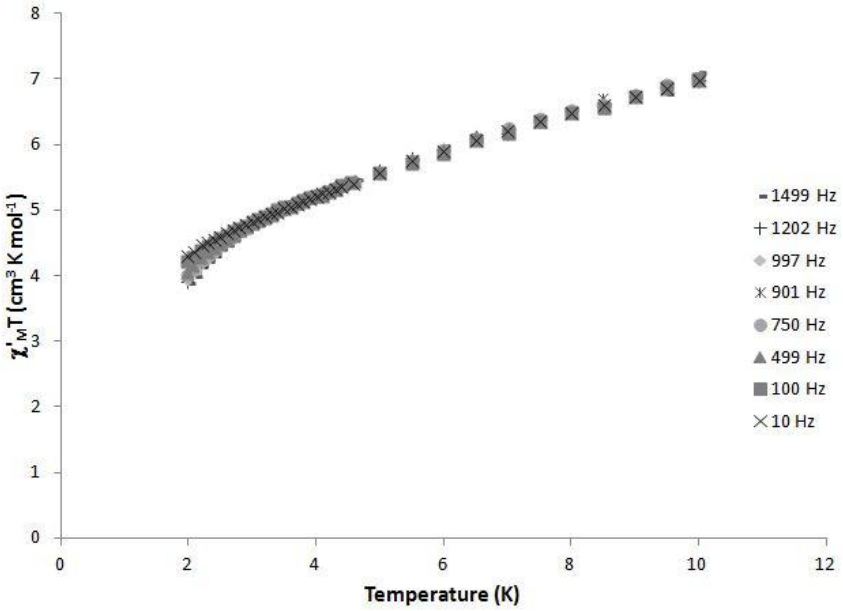

Figure 4.30. The in-phase ac variable temperature magnetic susceptibility of **Ni(OAc)$_2$ 12-MC-4 (DMF)** is shown. The susceptibility was collected between 10 K and 2.00 K with a 3.5 G drive field, no dc applied field, and at the indicated frequencies.

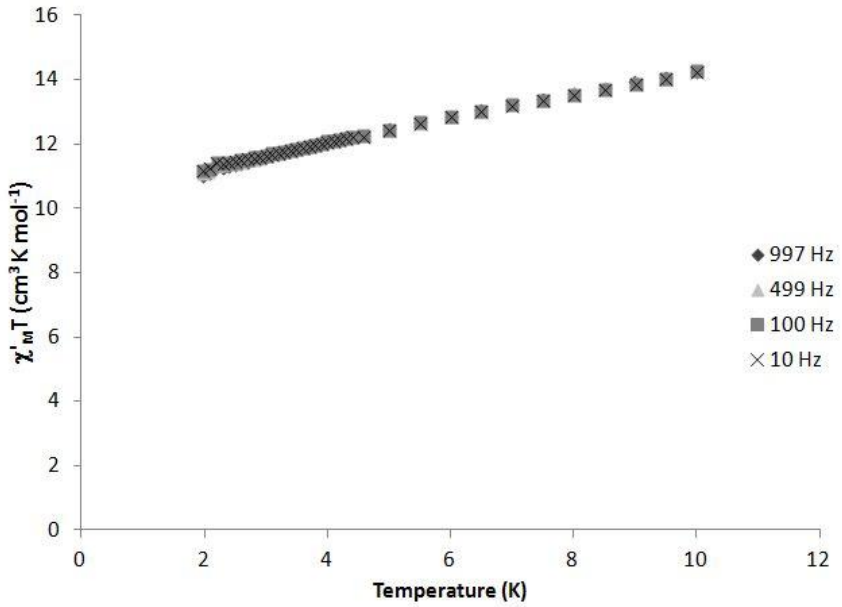

Figure 4.31. The in-phase ac variable temperature magnetic susceptibility of **Dy(Hsal)$_4$K 12-MC-4** is shown. The susceptibility was collected between 10 K and 2.00 K with a 3.5 G drive field, no dc applied field, and at the indicated frequencies.

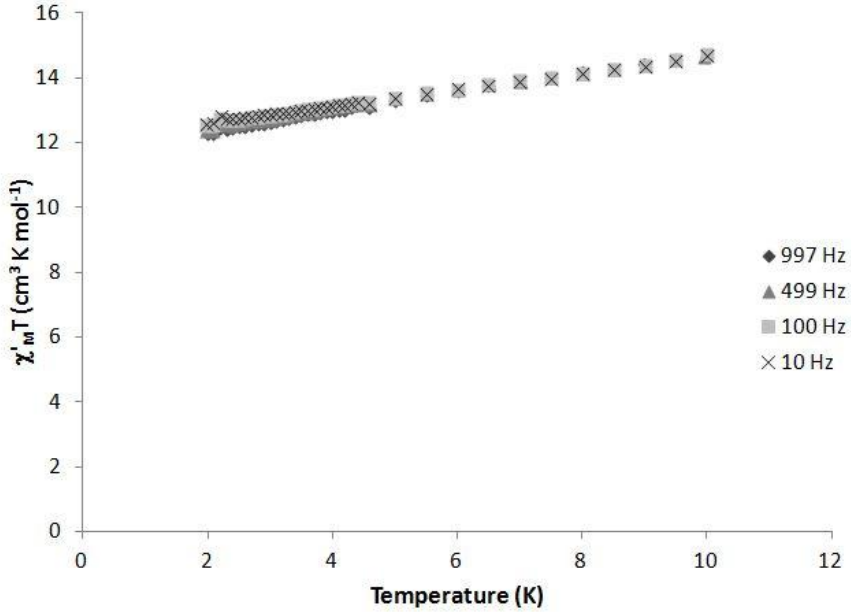

Figure 4.32. The in-phase ac variable temperature magnetic susceptibility of **Dy(Hsal)$_4$Na 12-MC-4** is shown. The susceptibility was collected between 10 K and 2.00 K with a 3.5 G drive field, no dc applied field, and at the indicated frequencies.

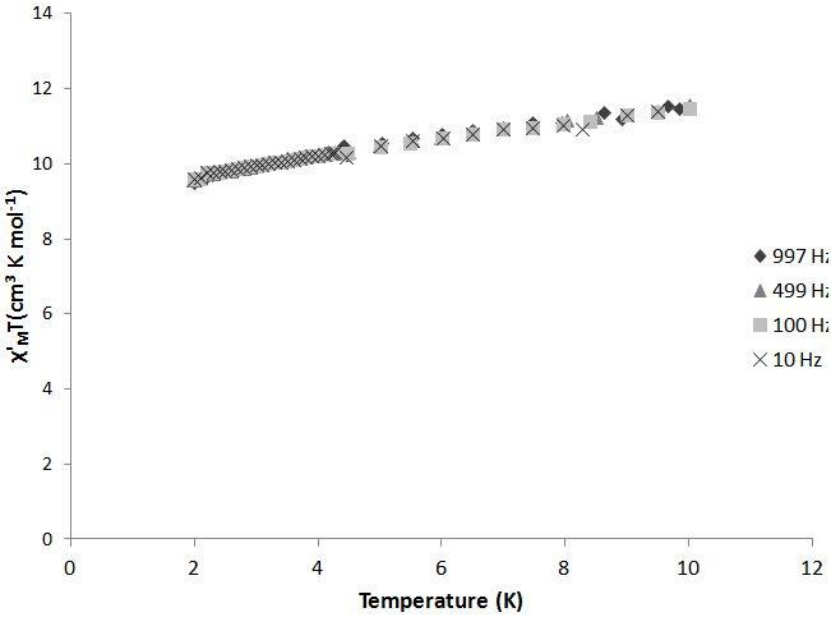

Figure 4.33. The in-phase ac variable temperature magnetic susceptibility of **Dy(OAc)$_4$K 12-MC-4** is shown. The susceptibility was collected between 10 K and 2.00 K with a 3.5 G drive field, no dc applied field, and at the indicated frequencies.

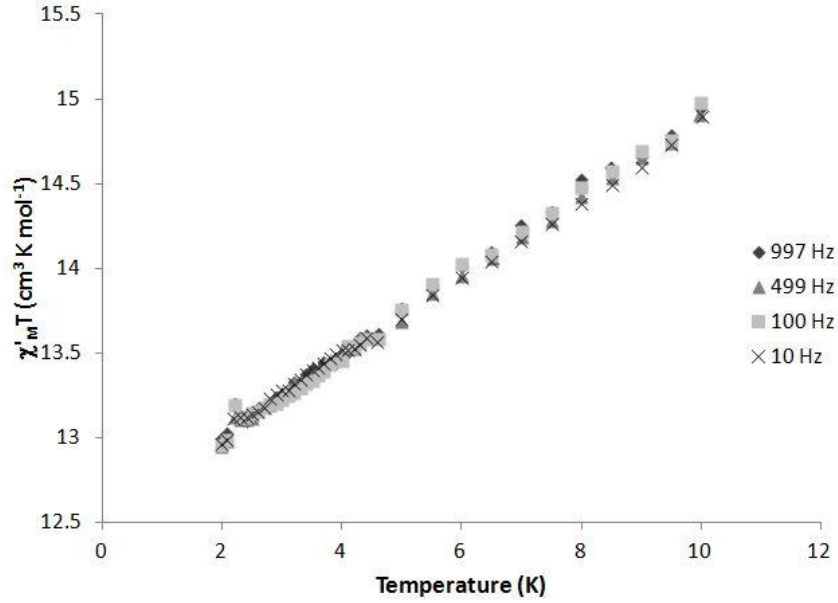

Figure 4.34. The in-phase ac variable temperature magnetic susceptibility of **Dy(benzoate)$_4$Na 12-MC-4** is shown. The susceptibility was collected between 10 K and 2.00 K with a 3.5 G drive field, no dc applied field, and at the indicated frequencies.

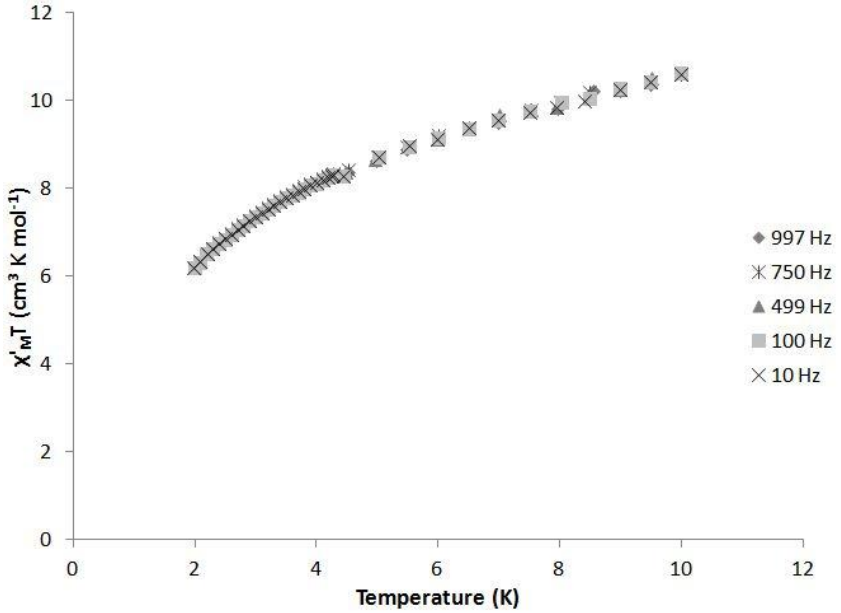

Figure 4.35. The in-phase ac variable temperature magnetic susceptibility of **Ho(OAc)$_4$K 12-MC-4** is shown. The susceptibility was collected between 10 K and 2.00 K with a 3.5 G drive field, no dc applied field, and at the indicated frequencies.

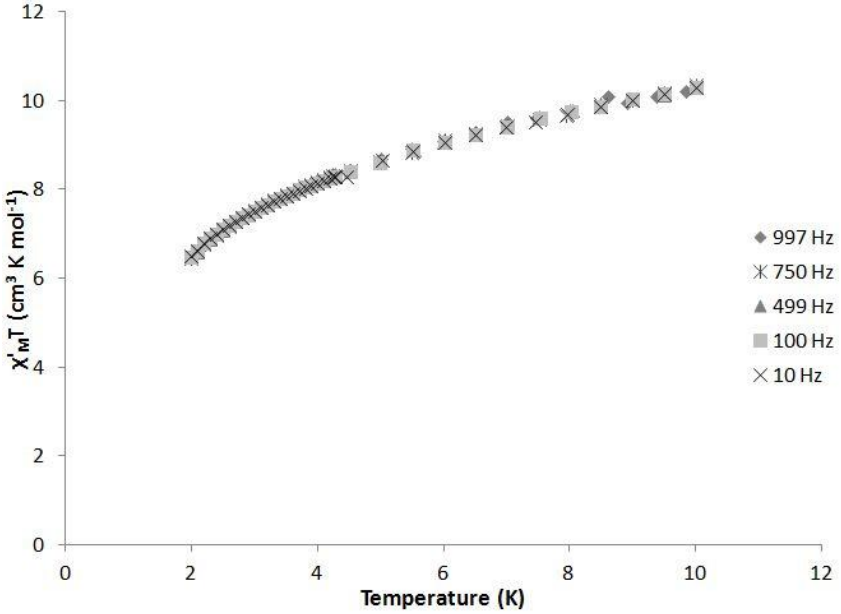

Figure 4.36. The in-phase ac variable temperature magnetic susceptibility of **Ho(OAc)$_4$Na 12-MC-4** is shown. The susceptibility was collected between 10 K and 2.00 K with a 3.5 G drive field, no dc applied field, and at the indicated frequencies.

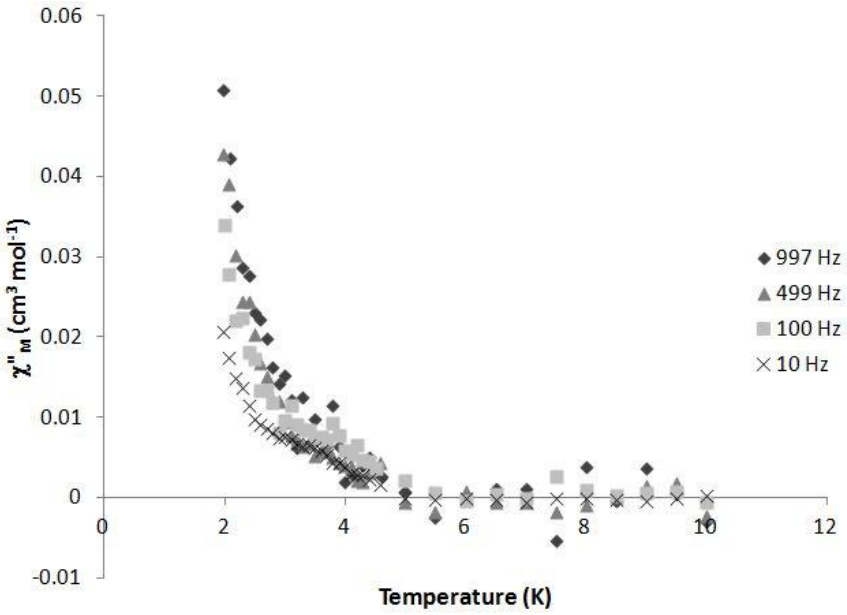

Figure 4.37. The out-of-phase ac variable temperature magnetic susceptibility of **$Ni(OAc)_2$ 12-MC-4 (MeOH)** is shown. The susceptibility was collected between 10 K and 2.00 K with a 3.5 G drive field, no dc applied field, and at the indicated frequencies.

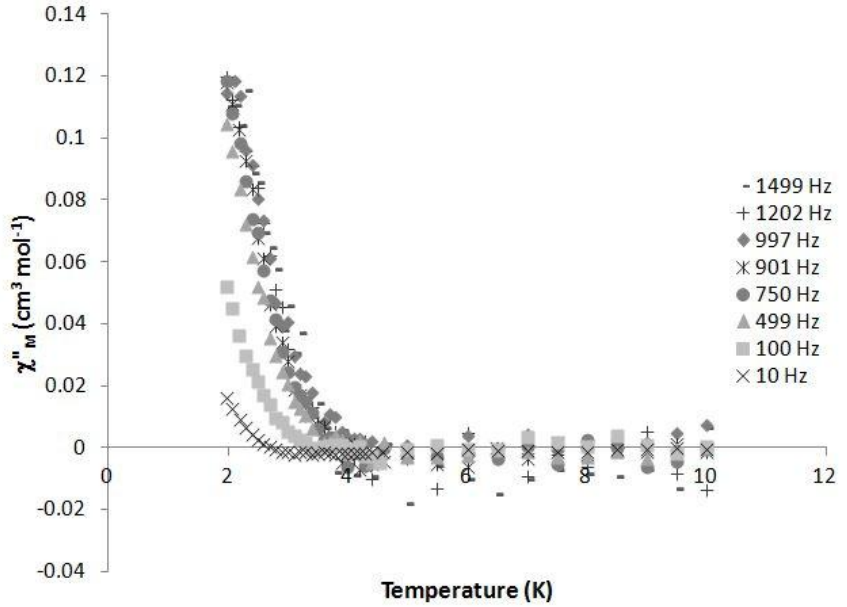

Figure 4.38. The out-of-phase ac variable temperature magnetic susceptibility of **$Ni(OAc)_2$ 12-MC-4 (DMF)** is shown. The susceptibility was collected between 10 K and 2.00 K with a 3.5 G drive field, no dc applied field, and at the indicated frequencies.

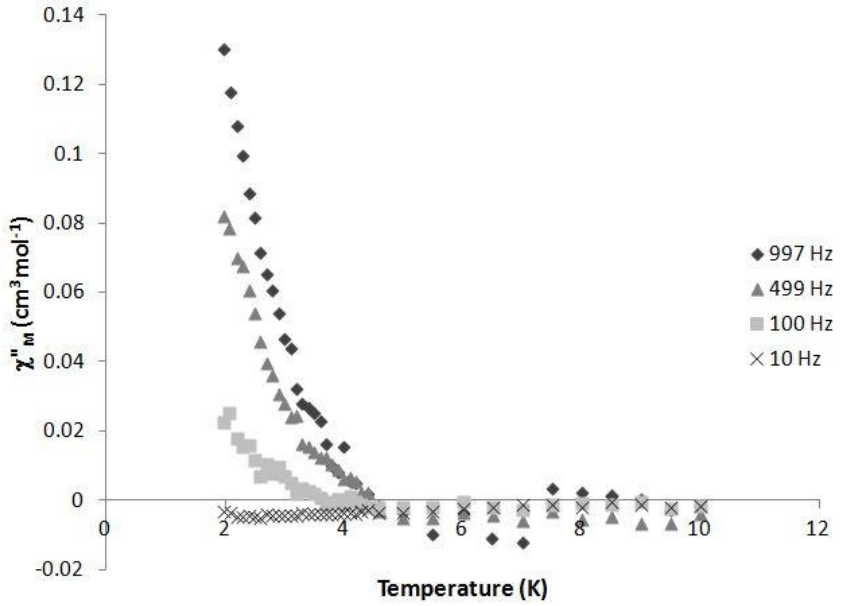

Figure 4.39. The out-of-phase ac variable temperature magnetic susceptibility of **Dy(Hsal)$_4$K 12-MC-4** is shown. The susceptibility was collected between 10 K and 2.00 K with a 3.5 G drive field, no dc applied field, and at the indicated frequencies.

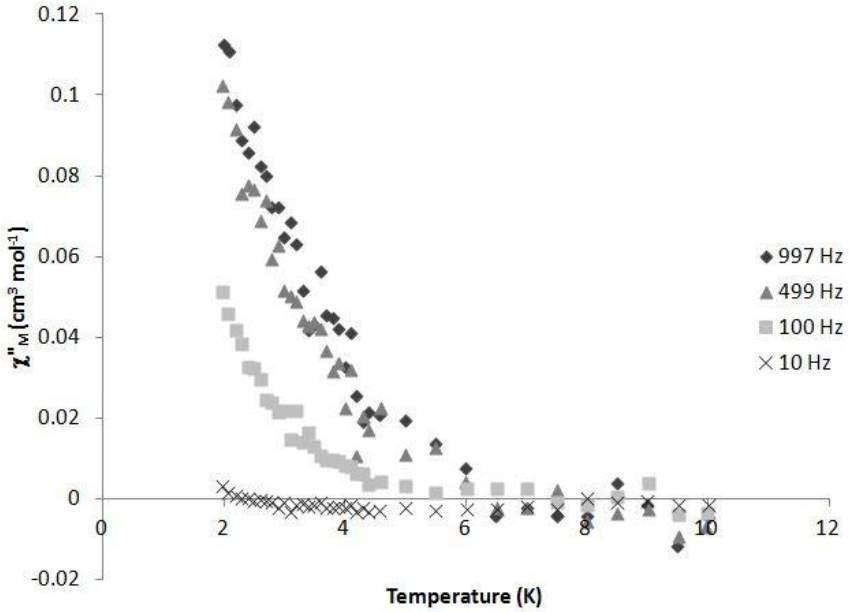

Figure 4.40. The out-of-phase ac variable temperature magnetic susceptibility of **Dy(Hsal)$_4$Na 12-MC-4** is shown. The susceptibility was collected between 10 K and 2.00 K with a 3.5 G drive field, no dc applied field, and at the indicated frequencies.

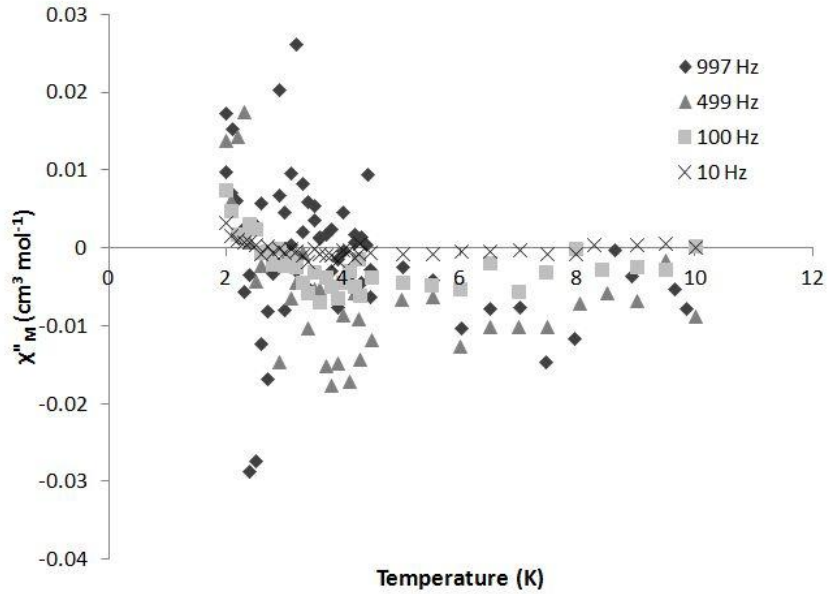

Figure 4.41 The out-of-phase ac variable temperature magnetic susceptibility of **$Dy(OAc)_4K$ 12-MC-4** is shown. The susceptibility was collected between 10 K and 2.00 K with a 3.5 G drive field, no dc applied field, and at the indicated frequencies.

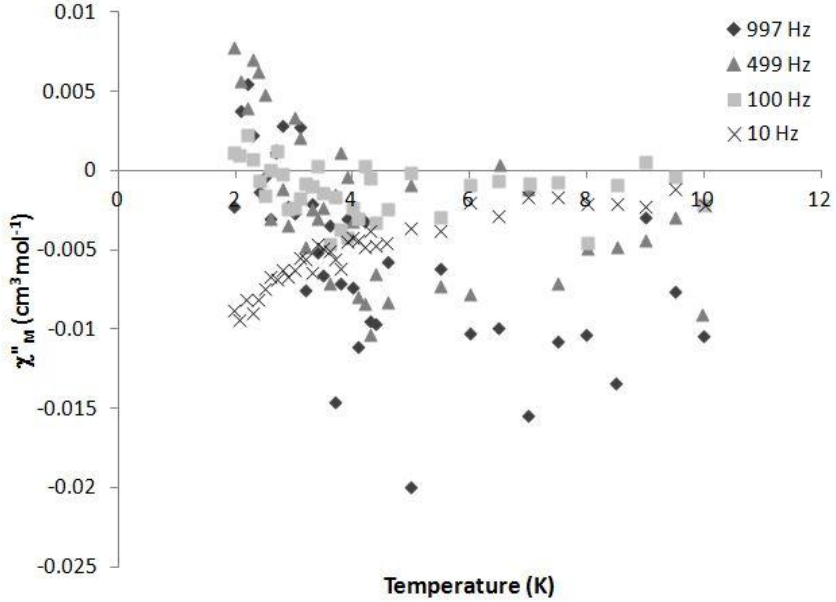

Figure 4.42. The out-of-phase ac variable temperature magnetic susceptibility of **$Dy(benzoate)_4Na$ 12-MC-4** is shown. The susceptibility was collected between 10 K and 2.00 K with a 3.5 G drive field, no dc applied field, and at the indicated frequencies.

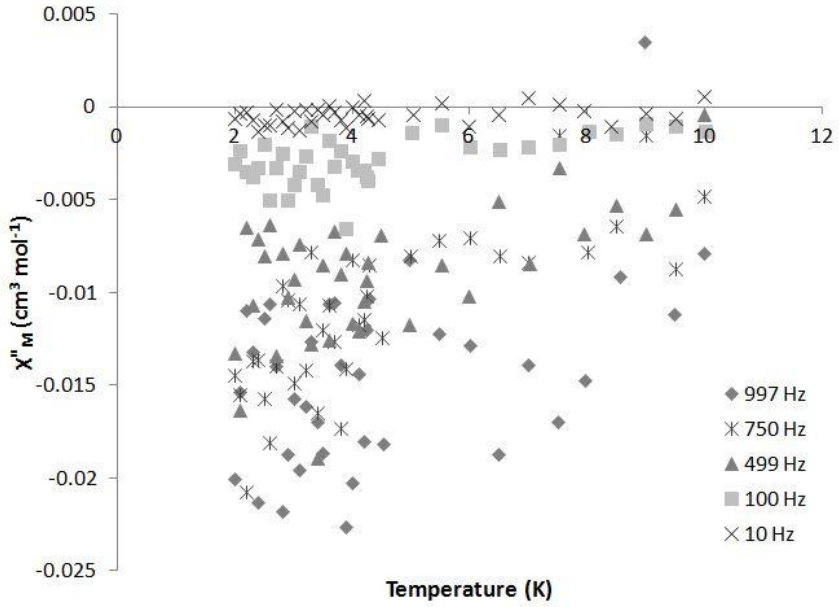

Figure 4.43. The out-of-phase ac variable temperature magnetic susceptibility of **$Ho(OAc)_4K$ 12-MC-4** is shown. The susceptibility was collected between 10 K and 2.00 K with a 3.5 G drive field, no dc applied field, and at the indicated frequencies.

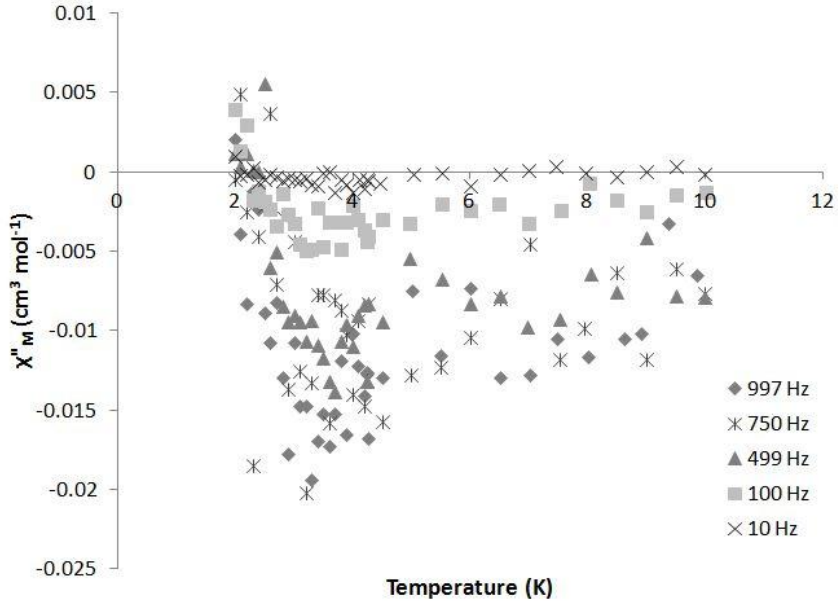

Figure 4.44. The out-of-phase ac variable temperature magnetic susceptibility of **$Ho(OAc)_4Na$ 12-MC-4** is shown. The susceptibility was collected between 10 K and 2.00 K with a 3.5 G drive field, no dc applied field, and at the indicated frequencies.

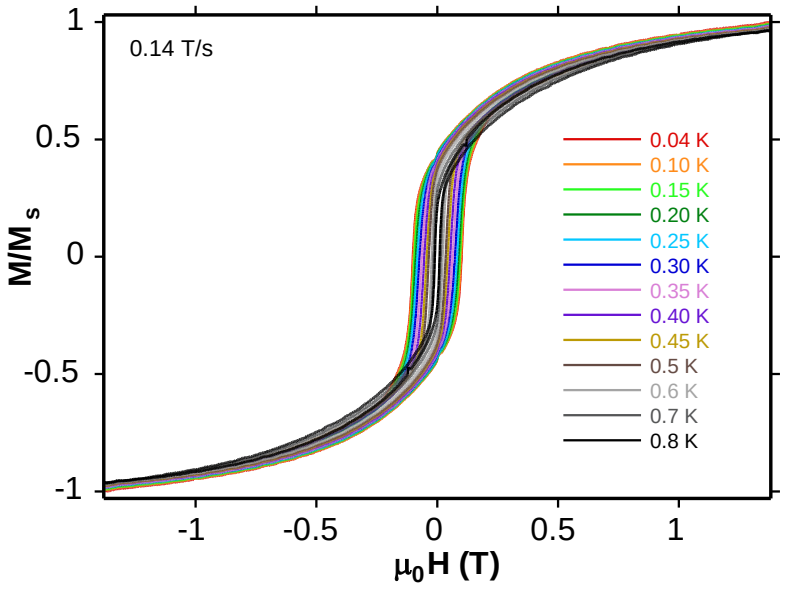

Figure 4.45. Single crystal micro-SQUID hysteresis experiments of **$Ni(OAc)_2$ 12-MC-4 (MeOH)** showed non-saturating magnetization as well as hysteresis at a constant sweep rate of 0.14 T/s and at the indicated temperatures.

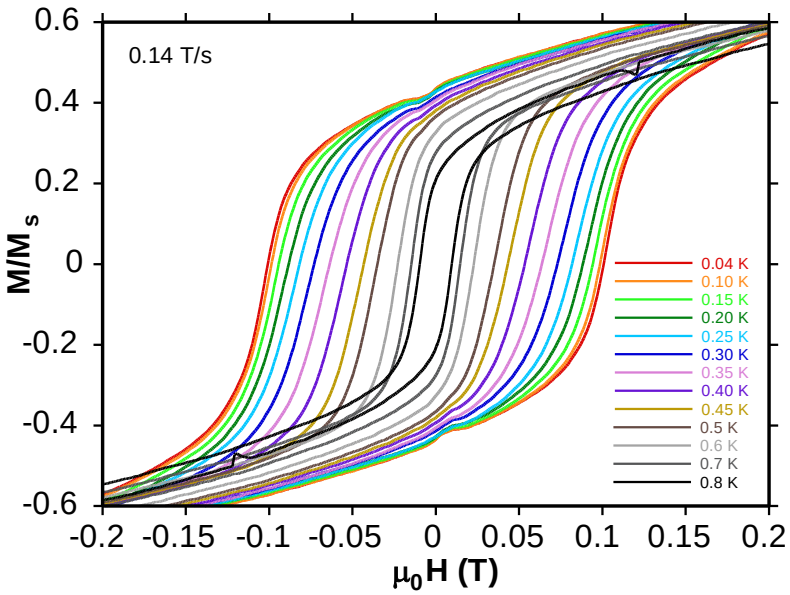

Figure 4.46. An expansion of the single crystal micro-SQUID hysteresis experiment of **$Ni(OAc)_2$ 12-MC-4 (MeOH)** at a constant sweep rate shows the hysteresis gap.

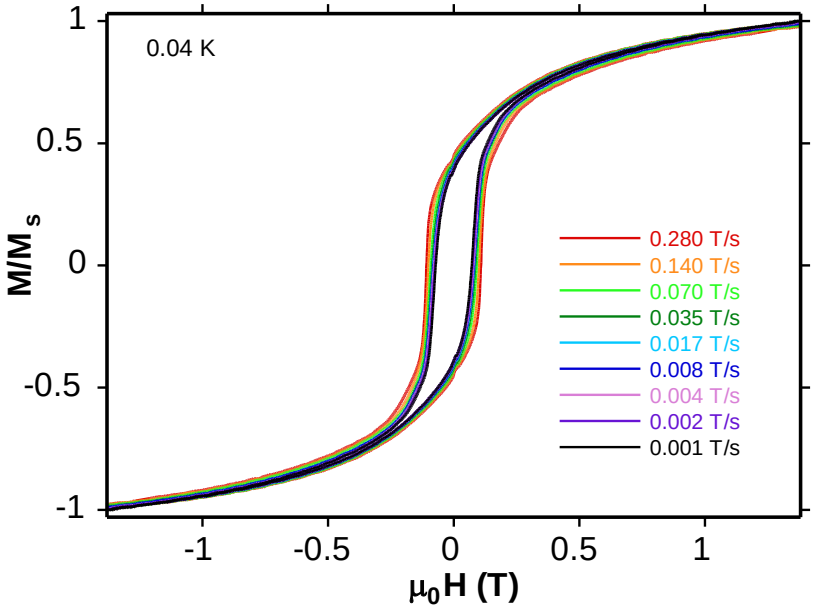

Figure 4.47. The single crystal micro-SQUID magnetization measurement of **$Ni(OAc)_2$ 12-MC-4 (MeOH)** at a set temperature of 40 mK showed hysteresis at different sweep rates.

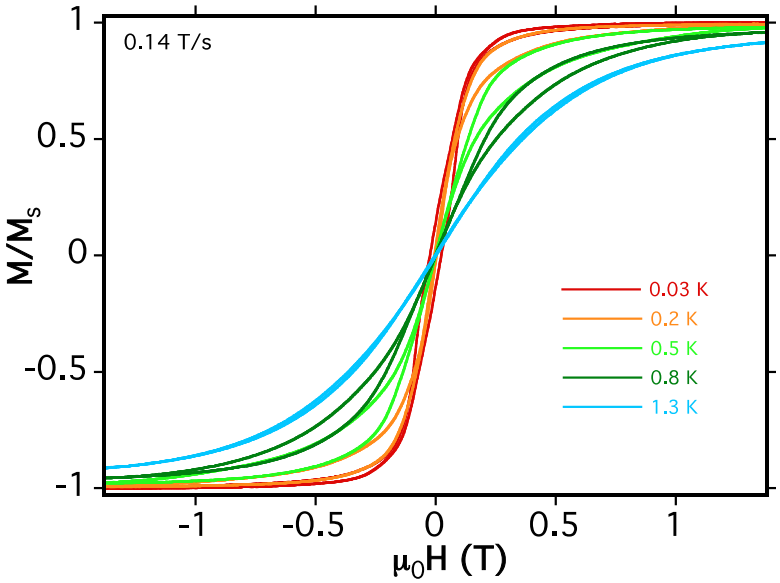

Figure 4.48. The single crystal micro-SQUID magnetization measurements of **$Ni(OAc)_2$ 12-MC-4 (DMF)** at a constant sweep rate of 0.14 T/s and at varying temperatures showed hysteresis.

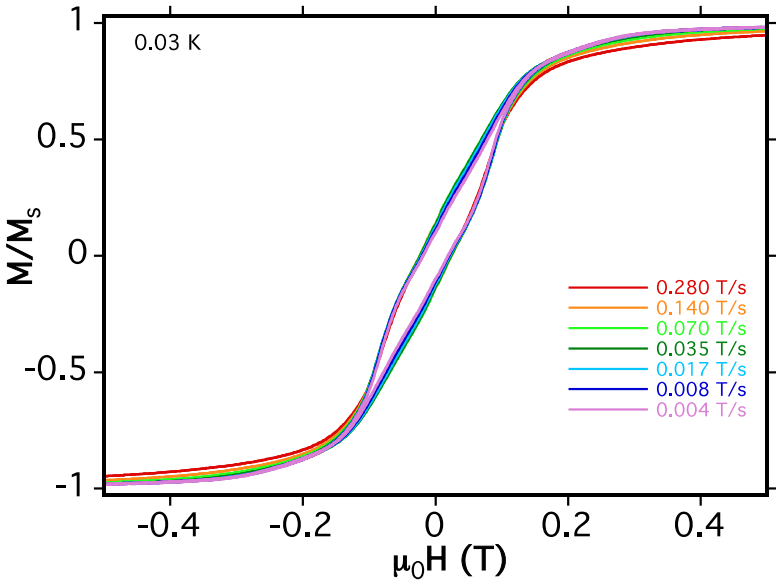

Figure 4.49. The single crystal micro-SQUID magnetization measurements of **Ni(OAc)$_2$ 12-MC-4 (DMF)** at a set temperature of 30 mK and varying sweep rates showed hysteresis.

References

1 Zaleski, C. M. Ph.D. Thesis, Utilizing Metallacrowns to Develop New Single-Molecule Magnets, The University of Michigan, 2005.

2 Zaleski, C. M.; Tricard, S.; Depperman, E. C.; Wernsdorfer, W.; Mallah, T.; Kirk, M. L.; Pecoraro, V. L. *Inorg. Chem*. **2011**, *50*, 11348.

3 Borras-Almenar, J. J.; Coronado, E.; Ostrovsky, S. M.; Palii, A. V.; Tsukerblat, B. S. *Chem. Phys*, **1999**, *240*, 149.

4 Borras-Almenar, J. J.; Clemente-Juan, J. M.; Coronado, E.; Tsukerblat, B. S. *J. Comput. Chem*. **2001**, *22*, 985.

5 Rinehart, J. D. & Long, J. R. *Chem. Sci*. **2011**, *2*, 2078.

6 Sessoli, R.; Tsai, H.-L.; Schake, A. R.; Wang, S.; Vincent, J. B.; Folting, K.; Gatteschi, D.; Christou, G.; Hendrickson, D. N. *J. Am. Chem. Soc*. **1993**, *115*, 1804.

7 Boukhvalov, D. W.; Dobrowitski, V. V.; Kögerler, P.; Al-Saqer, M.; Katsnelson, M. I.; Lichtenstein, A. I.; Harmon, B. N. *Inorg. Chem*. **2010**, *49*, 10902.

8 Kampert, E.; Janssen, F. F. B. J.; Boukhvalov, D. W.; Russcher, J. C.; Smits, J. M. M.; de Gelder, R.; de Bruin, B.; Christianen, P. C. M.; Zeitler, U.; Katsnelson, M. I.; Maan, J. C.; Rowan, A. E. *Inorg. Chem*. **2009**, *48*, 11903.

9 Wernsdorfer, W. Classical and Quantum Magnetization Reversal Studied in Nanometer Sized Particles and Clusters, In *Advances in Chemical Physics*, Volume 118; I. Prigogine & S. A. Rice, Eds.; John Wiley & Sons, Inc. Hoboken, 2007; pp 99-190.

10 Kahn, O. *Molecular Magnetism*; VCH Publishers, New York, 1993.

11 Lah, M. S. & Pecoraro, V. L. *Comments. Inorg. Chem*. **1990**, *11*, 59.

12 Psomas, G.; Stemmler, A. J.; Dendrinou-Samara, C.; Bodwin, J. J.; Scheider, M.; Alexiou, M.; Kampf, J. W.; Kessissoglou, D. P.; Pecoraro, V. L. *Inorg. Chem*. **2001**, *40*, 1562.

13 Lah, M. S.; Pecoraro, V. L. *J. Am. Chem. Soc*. **1989**, *111*, 7258.

14 Gibney, B. R.; Wang, H.; Kampf, J. W.; Pecoraro, V. L. *Inorg. Chem*. **1996**, *35*, 6184.

15 Mezei, G.; Zaleski, C. M.; Pecoraro, V. L. *Chem. Rev*. **2007**, *107*, 4933.

16 Shannon, R. D. *Acta Cryst*. **1976**, *A32*, 751.

17 AlDamen, M. A.; Clemente-Juan, J. M.; Coronado, E.; Martí-Gastaldo, C.; Gaita-Ariño, A. *J. Am. Chem. Soc*. **2008**, *130*, 8874.

18 AlDamen, M. A.; Cardona-Serra, S.; Clemente-Juan, J. M.; Coronado, E.; Gaita-Ariño, A.; Martí-Gastaldo, C.; Luis, F.; Montero, O. *Inorg. Chem*. **2009**, *48*, 3467.

19 Krzystek, J.; Ozarowski, A.; Telser, J. Coord. *Chem. Rev*. **2006**, *250*, 2308.

20 Lah, M. S. Ph.D. Thesis. Development of Metallacrowns and Structural Characterization of Manganese Chain Structures. The University of Michigan, 1991.

21 Lecren, L.; Wernsdorfer, W.; Li, Y. G.; Vindigni, A.; Miyasaka, H.; Clérac, R. *J. Am. Chem. Soc*. **2007**, *129*, 5045.

22 Gatteschi, D. & Sessoli, R. *Angew. Chem. Int. Ed*. **2003**, *42*, 268.

23 Shaikh, N.; Panja, A.; Goswami, S.; Banerjee, P.; Vojtisek, P.; Zhang, Y. Z.; Su, G.; Gao, S. *Inorg. Chem*. **2004**, *43*, 849.

24 Chen, Q.; Zeng, M.-H.; Zhou, Y.-L.; Zou, H.-H.; Kurmoo, M. *Chem. Mater*. **2010**, *22*, 2114.
25 Pauling, L. *General Chemistry*; Dover Publishing, Inc., New York, 1970.
26 Geiser, L.; Henchoz, Y.; Galland, A.; Carrupt, P.-A.; Veuthey, J.-L. *J. Separation Sci*. **2005**, *28*, 2374.
27 Ebbing, D. D. & Gammon, S. D. *General Chemistry* 7th Ed. Houghton-Mifflin Co. Boston, 2002.
28 Ako, A. M.; Mereacre, V.; Clérac, R.; Wernsdorfer, W.; Hewitt, I. J.; Anson, C. E.; Powell, A. K. *Chem. Commun*. **2009**, 544.

Chapter V

Utilizing $Ln^{III}Zn^{II}_{16}$ Metallacrowns as Single-Molecule Magnets

Introduction

In the early 21st century, interest in the field of single-molecule magnets (SMMs) moved from using solely transition metals to utilizing lanthanide ions. Lanthanide ions appear ideally suited for use as SMMs as, outside of La^{III} and Lu^{III}, they possess large spin values (ranging from 1/2 for Ce^{III} and Yb^{III} to 7/2 for Gd^{III}), and outside of La^{III}, Gd^{III}, and Lu^{III}, large amounts of anisotropy. Unlike first-row transition metals, lanthanides require the use of spin-orbit coupling, resulting in *J* terms rather than well-defined *S* and *L* quantum numbers. Nonetheless, lanthanides can still provide the pre-requisite spin and anisotropy needed for SMMs.[1]

Early attempts to use lanthanides in SMMs focused on inclusion of these ions in large *3d* clusters, leading to several interesting *3d*/*4f* clusters. The first reported mixed *3d*/*4f* cluster was a $\mathbf{[Cu^{II}LLn^{III}(Hfac)_2]_2}$ complex (L is the triply deprotonated 1-(2-hydroxybenzamido)-2-(2-hydroxy-3-methoxy-benzylideneamino)-ethane and hfac is the monodeprotonated hexaflouroacetylacetone, Ln^{III} is Tb^{III} or Dy^{III}) by Osa and co-workers in 2004[2]. A short time later, Zaleski and co-workers reported a large mixed Mn/Ln complex, the $\mathbf{Ln^{III}_6Mn^{III}_4Mn^{IV}_2(H_2shi)_4(Hshi)_2(shi)_{10}(CH_3OH)_{10}(H_2O)_2}$ complex (Ln^{III} is Dy^{III}, Tb^{III}, or Gd^{III}; H_3shi is salicylhydroxamic acid).[3] This complex launched an incredibly popular field of mixed Mn/Ln complexes, including a mixed $\mathbf{Ln^{III}_4Mn^{III}_6}$ series,[4] a family of $\mathbf{Mn_{11}Ln_2}$ bell-shaped complexes,[5,6] a series of $\mathbf{Mn_5Ln_4}$ complexes,[7] a large $\mathbf{Mn_{18}Dy}$ complex,[8] and two $\mathbf{Mn^{III}_4Ln^{III}_4}$ series,[9,10] to name a few.

Concurrent with the mixed *3d*/*4f* work, efforts began on utilizing only Ln^{III} cations as SMMs. This design protocol utilized the large spin and anisotropy values inherent in the

Ln^{III}. If only a single lanthanide was used, it also removed the possibility of coupling between the magnetic centers. In the proper ligand environment, a single, well isolated spin state could most easily be obtained for a mononuclear SMM.

The first reported mono-lanthanide SMM used the familiar phthalocyanato (Pc^{2-}) ligand to create a family of mono-lanthanide bis-phthalocyanato sandwich complexes.[11,12] Ishikawa and co-workers studied the series and found that the **$[Pc_2Tb^{III}]^-$·TBA$^+$**, where TBA^+ is tetrabutylammonium (Figure 1.14), showed a blocking temperature near 40 K for a frequency of 997 Hz, a record at that time. It was found that the spin in these complexes relaxes through energy exchange between the *f* orbitals and phonon-assisted radiation.[13]

Another important family of mono-lanthanide SMMs is the polyoxometallate (POM) family studied by Coronado and co-workers. AlDamen and co-workers found that the **$[Er(W_5O_{18})_2]^{9-}$** (Figure 1.24) showed frequency dependence in the out-of-phase ac magnetic susceptibility.[14] Both the POM and Pc^{2-} ligands formed a pseudo D_{4d} coordination environment around the lanthanide. The POM differed from the bis-phthalocyaninato complexes in that only the Er^{III} and Ho^{III} POMs showed frequency dependence, while the Tb^{III}, Dy^{III}, and Ho^{III} bis-phthalocyanato complexes showed frequency dependence. Furthering the study to **$[Ln(\beta_2\text{-}SiW_{11}O_{39})_2]^{13-}$** ($Ln^{III}$ was Tb, Dy, Ho, Er, Tm, and Yb) (Figure 1.25), found that Dy, Ho, Er, and Yb analogs showed frequency dependence in the out-of-phase ac magnetic susceptibility data. For all of these POMs, only the **$[Er(W_5O_{18})_2]^{9-}$**, showed a blocking temperature above 2 K.[15]

A key lesson from studying these complexes is that the ligand field plays a vital role on the magnetic properties of the complexes. Because lanthanides are normally found in a 3+ oxidation state in mono-lanthanide complexes, the only way to modify the magnetic properties is through changing the ligand field around the ligand. In the **$[Pc_2Tb^{III}]^-$·TBA$^+$**, the ligand field separated the ground ± 6 state from the first excited ± 5 state by more than 400 cm^{-1}. The **$[Pc_2Dy^{III}]^-$·TBA$^+$** complex, on the other hand, has an energy gap between the ± 13/2 ground state and the ± 11/2 excited state less than 100 cm^{-1}.[12]

Demonstration of this theory was provided by Takamatsu and co-workers in 2007 through oxidation of the phthalocyaninato ligand. It was found that the highest occupied molecular orbital (HOMO) of the $\mathbf{[Pc_2Tb^{III}]^-}$ complex had anti-bonding character. Thus, oxidation of the ligand led to increased bonding strength and thus a shorter inter-planar distance. This led to an increase in the blocking temperature.[16]

Coronado found that changing the skew angle, the angle between the two squares defined by the coordinating oxygen mean planes as well as the interplane distance affected magnetic properties. Comparing the $\mathbf{[Pc_2Er^{III}]^-}$ to the $\mathbf{[Er(W_5O_{18})_2]^{9-}}$, the Er POM had a skew angle (44.2°) close to ideal D_{4d} symmetry (45°), while the $\mathbf{[Pc_2Er^{III}]^-}$ had a skew angle of 41.4°. It was also found that the Er POM was more axially compressed that the $\mathbf{[Pc_2Er^{III}]^-}$ complex. Coronado stated that these differences could properly account for the magnetic differences between the two structures.[15] Examination of the $\mathbf{[Ln(\beta_2\text{-}SiW_{11}O_{39})_2]^{13-}}$ complexes revealed skew angles larger than the ideal D_{4d} (47.5° for Er^{III} and 48.0° for Tm^{III}) as well as non-parallel oxygen ligand planes. These deviations could affect the ligand field, and thus the magnetism.[15]

Rinehart and Long nicely summarized the magnetic properties of the lanthanides and the impact the ligand field has on those properties in a 2011 Chemical Science paper.[17] Because the shape of the lanthanides' *f* orbitals are strongly angular dependent, one can predict their shapes relatively easily based on Aufbau principle, Pauli's exclusion principle, and Hund's rule. These shapes can be classified as oblate (i.e. short and wide), isotropic (spherical), and prolate (tall and narrow). The shapes progress along the Periodic Table according to the occupied orbitals: Ce^{III} being oblate and the ions becoming more prolate until the isotropic Gd^{III} ion, the same trend is repeated from oblate Tb^{III} to isotropic Lu^{III} (Figure 1.6).[17] This trend predicts that in order to optimize the anisotropic contribution of oblate ions, electron density from the ligand should fit above and below the xy plane. For prolate ions, the optimal geometry will feature the electron density along the equator of the ion.[17]

In 2011, Joseph Jankolovits isolated a new $\mathbf{Ln^{III}Zn^{II}_{16}}$ metallacrown (Figure 5.1).[18] This unique metallacrown featured two 12-$MC_{Zn^{II}N(picHA)}$-4 sandwiching a Ln^{III} ion (Figure 5.2). Around this sandwich was a 24-$MC_{Zn^{II}N(picHA)}$-8 ring (Figure 5.3). Jankolovits and co-workers reported the luminescent properties of the $\mathbf{Ln^{III}Zn^{II}_{16}}$ series, finding that the $\mathbf{Nd^{III}Zn^{II}_{16}}$ and $\mathbf{Yb^{III}Zn^{II}_{16}}$ complexes had excellent luminescent properties in the near infrared (NIR). In addition to these NIR properties, the metallacrowns seemed to align the lanthanides in a fashion described by Ishikawa, Coronado, and Long. Thus these systems became excellent candidates for detailed magnetic characterization. This chapter will describe the magnetic properties of this family of structures and attempts to assess the basis for the observed behavior.

Experimental

Synthetic and Physical Methods. The syntheses of these structures were performed by Joseph Jankolovits. Details are available in Reference 18 as well as his thesis.[19] All structural characterization was also performed by Joseph Jankolovits and Jeff W. Kampf and are available in the references given above.

Preparation of Magnetic Samples. All magnetic measurements were taken on powdered samples that were mulled in eicosane to prevent torqueing of the sample in high applied magnetic fields unless otherwise noted. Samples were ground using a small mortar and pestle, transferred to a gelatin capsule of known mass, and weighed. A small amount of melted eicosane was added and left to solidify. The entire capsule was then weighed and a piece of clear tape applied to hold the capsule together. The capsule was then inserted into a clear plastic drinking straw.

Magnetic Measurements: All magnetic susceptibility and magnetization values were corrected using Pascal's constants.[20] Corrections were applied for the eicosane, gel capsule, and sample holder by collecting their magnetic susceptibilities and magnetization values and subtracting them from the collected values.

Variable field dc magnetization experiments were performed on two different magnetometers at the University of Michigan: on a Quantum Design Magnetic Phenomena Measurement System (QD MPMS) Superconducting Quantum Interference Device (SQUID) magnetometer at 5 K from 0 to 55000 G or on a QD MPMS XL SQUID magnetometer at 2 K from 0 to 50000 G. Variable temperature dc magnetic susceptibility measurements were performed at two locations on three different magnetometers. At the University of Michigan, measurements were performed either on a QD MPMS SQUID magnetometer with an applied field of 2000 G from 5 K to 300 K or on a QD MPMS XL SQUID magnetometer with an applied field of 1000 G from 300 K to 2 K. At the Université Claude Bernard Lyon 1 in Lyon, France, measurements were performed on a QD MPMS XL SQUID magnetometer fitted with an RSO sample holder and with an applied field of 1000 G from 300 K to 2 K.

Alternating current (ac) magnetic susceptibility measurements were collected at either the University of Michigan or at the Université Claude Bernard Lyon 1 in Lyon, France on a QD MPMS XL SQUID magnetometer from 30 K to 2 K with a drive field of 2.7 G, at frequencies ranging from 1488 Hz to 100 Hz and with dc fields ranging from 0 G to 1000 G.

Results

Synthesis and Structural Descriptions: These discussions are available in Reference 19. A brief summary of important structural details will is given in order to understand the presented magnetostructural correlation.

Because the series of $\mathbf{Ln^{III}Zn^{II}_{16}}$ is isostructural, the ligand environment for each structure will remain constant. What will change, however, is the bond distances and skew angles due to lanthanide size. Lanthanides are commonly said to undergo the "lanthanide contraction," that is that lanthanides shrink as one progresses along the Periodic Table.[21] Due to these changes in bond distances and skew angles, the ligand field will change slightly, altering the magnetic properties.

Table 5.1 summarizes and Figure 5.4 demonstrates the important structural parameters. A mean plane for each oxygen metallacrown plane was calculated. The distance between the two mean planes of each structure are reported ($O_{mp} - O_{mp}$). In addition, the distances between Ln and the mean plane ($Ln^{III} - O_{mp}$), the distance between the Ln^{III} and the ring oxygen atoms of the metallacrown, ($Ln^{III} - O$), and the cis-distances from oxygen to oxygen of the metallacrown ring are reported (O – O). Lastly, the skew angle (φ) are also determined. This was calculated by measuring the torsion angle between the oxygen of one metallacrown plane to the centroid of that oxygen plane, through the lanthanide to the centroid generated by the other oxygen plane, and then to the neighboring oxygen.

Table 5.1. Important structural data for three **$Ln^{III}Zn^{II}_{16}$** metallacrowns are given.

Metallacrown	**$Tb^{III}Zn^{II}_{16}$**	**$Er^{III}Zn^{II}_{16}$**		**$Dy^{III}Zn^{II}_{16}$**
	Distance (Å)	**Distance (Å)**		**Distance (Å)**
O_{mp} - O_{mp}	2.150	2.145	**O_{mp} - O_{mp}**	2.130
Ln – $O2_{mp}$	1.088	1.072	**Ln – $O8_{mp}$**	1.055
Ln – O2	2.349	2.312	**Ln – O8**	2.340
O2 – O2 edge	2.944	2.897	**O8 – O8 edge**	2.954
Ln – $O4_{mp}$	1.062	1.073	**Ln – $O4_{mp}$**	1.074
Ln – O4	2.356	2.322	**Ln – O4**	2.339
O4 – O4 edge	2.974	2.913	**O4 – O4 edge**	2.939
Skew angle (°)	43.93	44.98	**Skew angle (°)**	44.89

Variable Field dc Magnetization Measurements

The variable field dc measurements of **$GdZn_{16}$**, **$TbZn_{16}$**, and **$DyZn_{16}$** were collected at the University of Michigan on the QD MPMS SQUID magnetometer at 5 K with fields varying from 0 to 55000 G. The variable field dc measurements of **$HoZn_{16}$**, **$ErZn_{16}$**, and **$YbZn_{16}$** were collected at the University of Michigan on the QD MPMS XL SQUID magnetometer at 2 K with fields varying from 0 to 50000 G. None of the data saturated, making it difficult to fit with the Brillouin function.

The magnetization data for **$GdZn_{16}$** (Figure 5.5) increased linearly until the field reached 10000 G. The data began to curve before reaching a maximum of 37450 cm^3 G mol^{-1} at 55000 G. The **$TbZn_{16}$** complex behaved similarly (Figure 5.6); the magnetization increased linearly until the field was approximately 9000 G. After this field, the magnetization curved, reaching a maximum of 24800 cm^3 G mol^{-1} at 55000 G. For the **$DyZn_{16}$** complex (Figure 54.7), the magnetization increased linearly until 8500 G, then curved, reaching a maximum of 32030 cm^3 G mol^{-1} at 55000 G. The **$HoZn_{16}$** complex (Figure 5.8) is fairly linear to 16000 G, then slowly sloping, reaching 30100 cm^3 G mol^{-1} at 50000 G. The **$ErZn_{16}$** complex (Figure 5.9) increased linearly to 4500 G, then quickly curved to 20000 G, then linearly increased until 50000 G, reaching a maximum of 26630 cm^3 G mol^{-1}. The **$YbZn_{16}$** complex (Figure 5.10) appeared to increase linearly to 8000 G, then sloped slightly, then increased linearly from 10000 G to 35000 G, reaching a maximum of 10520 cm^3 G mol^{-1} at 55000 G.

Variable Temperature dc Magnetic Susceptibility

The variable temperature dc magnetic susceptibility data of **$GdZn_{16}$**, **$TbZn_{16}$**, and **$DyZn_{16}$** were collected at both the University of Michigan on a QD MPMS SQUID magnetometer and on a QD MPMS XL SQUID magnetometer at the Université Claude Bernard Lyon 1 in Lyon, France. The susceptibility data at the University of Michigan were collected with an applied field of 2000 G, with the temperature increasing from 5 K to 300 K. The variable temperature dc magnetic susceptibility of **$HoZn_{16}$**, **$ErZn_{16}$**, and **$YbZn_{16}$** were collected on the QD MPMS XL SQUID magnetometer at the University of Michigan. For the data collected at the University of Michigan and at the Université Claude Bernard Lyon 1 in Lyon, France, the data were collected with an applied field of 1000 G from 300 K to 2 K. The *J* values can be calculated using Equation 1:

$$\chi_M T = \frac{N_A \beta^2}{3k_B} g_J{}^2 J(J+1) \qquad (1)$$

where $\chi_M T$ is the susceptibility in cm^3 K mol^{-1}, g_J is the Lande factor for each lanthanide from Table 5.2 calculated by Equation 2, N_A is Avogadro's number, β is the Bohr magneton, k_B is the Boltzmann constant, and J is the angular momentum quantum number defined by Equation 3:

$$g_J = \frac{3}{2} + \frac{S(S+1)-L(L+1)}{2J(J+1)} \qquad (2)$$

$$J = L + S, \text{ such that } |L - S| \leq J \leq L + S \qquad (3)$$

where L is the orbital angular momentum quantum number and S is the spin number. For lanthanides with less than seven electrons, the smallest J is the ground state, while for lanthanides with seven or more electrons, the largest J is the ground state.[1]

Table 5.2. The g_J values for the lanthanides of interest are summarized.

Lanthanide(III)	g_J
Gd	2
Tb	3/2
Dy	4/3
Ho	5/4
Er	6/5
Yb	8/7

At the University of Michigan, the **$GdZn_{16}$** complex (Figure 5.11) increased linearly from 4.41 cm^3 K mol^{-1} at 300 K to 7 K, then leveling off at 8.08 cm^3 K mol^{-1} at 5 K, which is approximately the expected susceptibility for a Gd^{III} ion (7.88 cm^3 K mol^{-1}). At the Université Claude Bernard Lyon 1 in Lyon, France, the **$GdZn_{16}$** complex (Figure 5.12) increased linearly of 3.29 cm^3 K mol^{-1} at 300 K to 7 K, finally reaching 7.19 cm^3 K mol^{-1} at 2 K. For **$TbZn_{16}$** at the University of Michigan, the susceptibility (Figure 5.13) slightly increased from 9.39 cm^3 K mol^{-1} at 300 K until approximately 90 K (10.21 cm^3 K mol^{-1}), then decreasing to 8.31 cm^3 K mol^{-1} at 5 K, which is a smaller susceptibility value than expected for a Tb^{III} ion (11.82 cm^3 K mol^{-1}). At the Université Claude Bernard Lyon 1, the **$TbZn_{16}$** data (Figure 5.14) increased slightly from 9.14 cm^3 K mol^{-1} at 300 K to 10.26 cm^3 K mol^{-1} at 100 K, then reaching a minimum of 6.89 cm^3 K mol^{-1} at 2 K. For **$DyZn_{16}$**, at the University of Michigan, the susceptibility (Figure 5.15) increased from

9.97 cm^3 K mol^{-1} at 300 K to a maximum of 13.12 cm^3 K mol^{-1} at 42 K, before decreasing to 11.08 cm^3 K mol^{-1} at 5 K, which is less than expected for a single Dy^{III} ion (14.17 cm^3 K mol^{-1}). At the Université Claude Bernard Lyon 1, **$DyZn_{16}$** (Figure 5.16), the susceptibility started at 9.09 cm^3 K mol^{-1} at 300 K, increasing until 45 K, reaching a maximum of 12.85 cm^3 K mol^{-1}, before decreasing to 9.72 cm^3 K mol^{-1} at 2 K.

Examining the susceptibility of **$HoZn_{16}$** complex (Figure 5.17), at 300 K, the susceptibility was 12.71 cm^3 K mol^{-1}. The susceptibility remained relatively constant until the temperature reached 14 K, at which point it decreased, reaching a minimum of 3.81 cm^3 K mol^{-1} at 2 K, which is significantly smaller than for a Ho^{III} ion (14.07 cm^3 K mol^{-1}). For the **$ErZn_{16}$** complex (Figure 5.18), the susceptibility remained constant from 300 K to 40 K at a value of 10.13 cm^3 K mol^{-1}. From 40 K to 2 K, the susceptibility decreased steadily, reaching a minimum of 7.99 cm^3 K mol^{-1} at 2 K, which is smaller than the susceptibility of a Er^{III} ion (11.48 cm^3 K mol^{-1}). The **$YbZn_{16}$** complex (Figure 5.19) increased linearly to 130 K, then broke continuity, increased linearly again until 85 K, and then at 80 K until 2 K, it remained relatively linear, reaching a value of 1.50 cm^3 K mol^{-1} at 2 K , which is again smaller than susceptibility of Yb^{III} (2.57 cm^3 K mol^{-1}).[*]

Variable Temperature ac SQUID Magnetometer Magnetic Susceptibility

All samples were prepared as described above. The **$GdZn_{16}$**, **$TbZn_{16}$**, and **$DyZn_{16}$** complexes were measured at the Université Claude Bernard Lyon 1 in Lyon, France. Measurements were taken with an ac drive field of 2.7 G, an applied dc field ranging from 0 G to 1000 G, and at frequencies ranging from 1200 Hz to 10 Hz from 30 K to 2 K. The **$HoZn_{16}$**, **$ErZn_{16}$**, and **$YbZn_{16}$** complexes were measured at the University of Michigan. The data were collected with an ac drive field of 2.7 G, with an applied dc field ranging from 0 G to 1000 H, and at frequencies ranging from 1400 Hz to 10 Hz, from 80 K to 2 K.

[*] The susceptibility was found to be negative at 300 K, which is unusual. The sample was measured multiple times, with similar results observed each time.

The in-phase ac magnetic susceptibility data will be discussed first. The **$GdZn_{16}$** data were collected at a frequency of 700 Hz, with an applied dc field of either 0 G or 500 G and from 10 K to 2 K (Figure 5.20). The data could not be described by any particular shape. At 2 K, both the susceptibility measured with and without an applied dc field were 6.80 cm^3 K mol^{-1} and 6.76 cm^3 K mol^{-1}. The **$TbZn_{16}$** data were collected at a frequency of 700 Hz and with an applied dc field of either 0 G or 500 G from 10 K to 2 K (Figure 5.21). The susceptibility curves overlay very well for both dc field strengths and linearly decreased from 10 K to 4 K, at which point the susceptibilities began to curve, reaching a minimum of 3.52 cm^3 K mol^{-1} at 2 K.

The **$DyZn_{16}$** susceptibility data were collected over a wide range of applied fields and frequencies. First, the data were collected at a constant frequency of 700 Hz and the applied dc field ranged from 0 G to 1000 G from 10 K to 2 K (Figure 5.22). From 10 K to 7 K, regardless of the applied dc field, the susceptibilities remained linear with a value near 11.43 cm^3 K mol^{-1}. At 7 K, the susceptibility values diverged, decreasing at varying rates depending on the strength of the applied dc field. With an applied dc field of 1000 G, at 2 K, the susceptibility reached a minimum of 4.84 cm^3 K mol^{-1}. For an applied field of 750 G, the susceptibility reached a minimum of 5.43 cm^3 K mol^{-1} at 2 K. When the applied field was 500 G, the susceptibility reached a value of 6.30 cm^3 K mol^{-1} at 2 K. With a 250 G dc applied field, the susceptibility at 2 K was 8.52 cm^3 K mol^{-1}. When no dc applied field was present, the susceptibility was 9.41 cm^3 K mol^{-1} at 2 K. Based on the out-of-phase behavior, it was decided to measure the frequency dependence with an applied field of 500 G (Figure 5.23). The data for 800 Hz were collected from 30 K to 2 K. It linearly decreased until approximately 7 K, at which point it dramatically decreased. All of the susceptibility curves showed frequency dependence, diverging around 8 K from each other. The final values at 2 K are given in Table 5.3 for convenience.

Table 5.3. The susceptibility values at 500 G dc applied field and 2 K for the different frequencies measured are given for **$DyZn_{16}$**.

Frequency (Hz)	χ_M'T (cm^3 K mol^{-1})
1399	5.47
1202	5.61
997	5.89
801	6.17
400	6.96
200	7.66
100	8.23
50	8.75
10	9.40

The susceptibility of **$HoZn_{16}$** was collected with an applied dc field of 500 G (Figure 5.24). The susceptibility linearly decreased until 4.7 K, where the susceptibility began to curve. The susceptibility for 1488 Hz diverged from the other curves at 2.7 K, reaching a minimum of 2.75 cm^3 K mol^{-1}. For the other susceptibility plots, the curves reached similar minima at 2 K: about 3.72 cm^3 K mol^{-1}.

For **$ErZn_{16}$**, multiple applied fields ranging from 1000 G to 0 G were studied at a frequency of 997 Hz (Figure 5.25). Regardless of the applied field, the susceptibility linear declined from 10 K to 4.5 K. At 4.5 K, the susceptibilities diverged until the minima for each curve were reached. For an applied dc field of 1000 G, the minimum susceptibility at 2 K was 4.13 cm^3 K mol^{-1}. For an applied dc field of 750 G, the minimum susceptibility at 2 K was 4.53 cm^3 K mol^{-1}. For an applied dc field of 500 G, the susceptibility at 2 K was 5.08 cm^3 K mol^{-1}. For an applied dc field of 250 G, the susceptibility reached a minimum of 6.12 cm^3 K mol^{-1} at 2 K. When no dc applied field was present, the susceptibility was 4.81 cm^3 K mol^{-1}.

For **$ErZn_{16}$**, multiple frequencies ranging from 1399 Hz to 10 Hz with an applied dc field of 750 G (Figure 5.26). The susceptibility linear decreased from 10 K to 4.96 K, at which point, the susceptibilities diverged for each frequency. The data are summarized in Table 5.4.

Table 5.4. The susceptibility values at 750 G applied dc field for each frequency for **$ErZn_{16}$** are summarized.

Frequency (Hz)	χ_M'T (cm^3 K mol^{-1})
1399	4.15
1202	4.34
997	4.53
801	4.76
401	5.48
200	6.11
50	7.03
25	7.29
10	7.64

For **$YbZn_{16}$**, various dc applied fields were studied at a frequency of 997 Hz (Figure 5.27). The susceptibility plots remained linear from 10 K to 3.50 K, where it then deviated depending on the strength of the dc applied field. For 1000 G applied dc field, the minimum at 2 K was 0.81 cm^3 K mol^{-1}. For an applied dc field of 750 G, the minimum at 2 K was 0.98 cm^3 K mol^{-1}. For an applied dc field of 500 G, the minimum at 2 K was 1.14 cm^3 K mol^{-1}. For an applied dc field of 250 G, the minimum at 2 K was 1.32 cm^3 K mol^{-1}. For no dc applied field, the minimum at 2 K was 1.45 cm^3 K mol^{-1}

The variable frequency data for **$YbZn_{16}$** were collected with an applied dc field of 1000 G and with frequencies ranging from 1399 Hz to 10 Hz (Figure 5.28). The data were noisy, but was relatively linear until 3.48 K, at which point the larger frequencies diverged from the other frequencies. The data are summarized in Table 5.5. The data were also collected with no applied dc field and at frequencies of 997 Hz, 500 Hz, 100 Hz, and 10 Hz (Figure 5.29). All were relatively linear and below 4 K, all had similar values, reaching a minimum at 2 K of 1.48 cm^3 K mol^{-1}, which agreed with the variable field experiment.

Table 5.5. The susceptibility values at 1000 G applied dc field for each frequency for **$YbZn_{16}$** are summarized.

Frequency (Hz)	χ_M'T (cm^3 K mol^{-1})
1399	0.71
1202	0.76
997	0.88
801	0.97
401	1.23
200	1.38
50	1.44
25	1.44
10	1.45

The out-of-phase ac magnetic susceptibility of **$GdZn_{16}$** data were collected at 700 Hz with either 0 G or 500 G dc applied field (Figure 5.30). No frequency dependence was observed, regardless of the strength of the dc applied field. The out-of-phase ac magnetic susceptibility of **$TbZn_{16}$** was collected at 700 Hz with either a 0 G or 500 G dc applied field (Figure 5.31). No frequency dependence was observed, regardless of the strength of the dc applied field. The out-of-phase ac magnetic susceptibility data of **$HoZn_{16}$** were collected at 700 Hz with either a 0 G or 700 G dc applied field (Figure 5.32). No frequency dependence was observed, regardless of the strength of the dc applied field. This was corroborated by examining the susceptibility at varying frequencies and a 500 G dc field (Figure 5.33).

The out-of-phase ac magnetic susceptibility of **$DyZn_{16}$** data showed frequency dependence at 700 Hz, which was intensified upon application of a dc applied field (Figure 5.34). Using an applied dc field of 500 G, various frequencies were probed, indicating frequency dependence (Figure 5.35). However, even at 1399 Hz, no maximum was observed in the χ_M" vs. T plot.

The out-of-phase ac magnetic susceptibility of **$ErZn_{16}$** data were collected at 1000 Hz and at varying fields (Figure 5.36). There was frequency dependence for the different applied fields. An applied dc field was set to 750 G, and different frequencies were

studied (Figure 5.37). Frequency dependence was observed, but no maximum was observed.

Looking at the out-of-phase ac magnetic susceptibility of **$YbZn_{16}$** at a frequency of 997 Hz and various applied fields (Figure 5.38) revealed that with no applied field, there is very little, if any, frequency dependence. Adding the slightest applied field resulted in frequency dependence; the dependence becoming stronger as the field strength increased from 250 G to 500 G to 750 G to 1000 G. It was decided to probe the out-of-phase behavior with a 1000 G applied dc field and without a field at various frequencies. With no dc applied field, there appears to be no frequency dependence (Figure 5.39). Applying a 1000 G applied dc field, however, reveals frequency dependence in the out-of-phase ac magnetic susceptibility (Figure 5.40). At higher frequencies, there is a larger signal, but no maximum in the χ_M" vs. T plot was observed.

Discussion

As the structure was synthesized and crystallographically characterized by Joseph Jankolovits, it will not be discussed in depth here. The interested reader is directed to References 18 and 19 for an in depth discussion. The important structural characteristics and their impact on the magnetism, however, will be discussed here. Examining the crystal structure of **$TbZn_{16}$**, **$DyZn_{16}$**, and **$ErZn_{16}$** reveals that these complexes are isostructural. Only slight perturbations were observed. However, as indicated by Coronado[15], small structural changes can affect the magnetic behavior. Thus, it seemed worthwhile to provide analysis on the major parameters given in Table 5.1 and how they compare to Ishikawa's **$[Pc_2Ln^{III}]^-$** and Coronado's **$[Ln(W_5O_{18})_2]^{9-}$** complexes.

First, examining the overall ligand environment of the metallacrown cluster seems to indicate this is an ideal construct for oblate lanthanides, such as Tb^{III} and Dy^{III}. The eight oxygens coordinating the lanthanide fall above and below the lanthanide.17 The ligands are oriented in a distorted D_{4d} symmetry: the skew angle for the oxygens in the mean planes is nearly 45° for each complex. The ideal skew angle in D_{4d} symmetry should be

45°. Ishikawa's sandwich complexes and Coronado's complexes show similar distorted D_{4d} square anti-prisms, although the skew angle often deviates from the ideal depending on the lanthanide present.[11,15,22]

Examining the oxygen mean plane to oxygen mean plane distance of the metallacrowns shows a very small pocket; the two planes are separated by 2.150 Å for the Tb^{III} analog, 2.130 Å for the Dy^{III} analog, and 2.145 Å for the Er^{III} analog. Using Shannon's effective ionic radii can help as a guide to show how cramped each 8-coordinate lanthanide is in this binding site. The 8-coordinate ionic and crystal radii, respectively, for Tb^{III}, Dy^{III}, and Er^{III}, are 1.180 Å and of 1.040 Å (Tb^{III}), 1.167 Å and 1.027 Å (Dy^{III}), and 1.144 Å and 1.004 Å (Er^{III}).[21] This "lanthanide contraction" can help explain the shrinking in the mean plane separation distance, as well as the changes in Ln – O bond lengths seen across the series. The lanthanide contraction also indicates that it is quite likely that the Er^{III} ion and other, smaller Ln^{III} ions are in an energetically better environment than the larger ions, such as Gd^{III}, Tb^{III} and Dy^{III}, which are "cramped" and are packed in an energetically unfavorable way. Taking the ratio of $O_{mp} – O_{mp}$ and O – O edge lengths indicates that there is a certain axial compression.

Compared to Ishikawa's and Coronado's complexes, the metallacrowns are the most axially compressed. For the Er^{III} series, the distance between the two Pc^- ligand planes in the $\mathbf{[Pc_2Er^{III}]^-}$ complex is 2.740 Å[23] and the oxygen mean plane distance between the two POMs in $\mathbf{[Er(W_5O_{18})2]^{9-}}$ is reported as 2.47(1) Å.[15] Then, comparing the in-plane distance of two coordinating ligands that comprise two vertices of the square, it was found that for $\mathbf{[Pc_2Er^{III}]^-}$ structure, the distance was 2.804 Å,[23] while for $\mathbf{[Er(W_5O_{18})2]^{9-}}$ POM, the distance was reported as 2.86(5) Å.[23] Thus, it can be seen that for the $\mathbf{[Pc_2Er^{III}]^-}$ structure, there is little or no compression, while for the $\mathbf{Er(W_5O_{18})2]^{9-}}$ POM, there is more compression, but not as much as the $\mathbf{ErZn_{16}}$ complex. This could dramatically affect the ligand field, which would be observable in the magnetism of the complexes. As will be seen, the severely axially compressed square-antiprismatic orientation does affect the magnetism of these structures.

Examining the magnetization of each complex did not reveal much about the occupation of *J* states as none of the curves saturated. It was not possible to use the Brillouin function to calculate a ground *J* state. In order to calculate a *J* state, the variable temperature dc susceptibilities were measured. As Zn^{II} will not contribute any magnetism to the structure and there are no organic radicals or other paramagnetic source, the magnetism of each **$LnZn_{16}$** complex should reflect the properties of the present lanthanide. The expected $\chi_M T$ values for each lanthanide are given in Table 5.6.

Table 5.6. The susceptibility associated for each trivalent lanthanide studied is given.

Lanthanide(III)	**Ground State**	**$\chi_M T$ (cm^3 K mol^{-1})**
Gd	$^8S_{7/2}$	7.88
Tb	$^7F_6$	11.82
Dy	$^6H_{15/2}$	14.14
Ho	$^5I_8$	14.06
Er	$^4I_{15/2}$	11.46
Yb	$^2F_{7/2}$	2.53

The **$GdZn_{16}$** metallacrown had a magnetic susceptibility at low temperature that closely matched the ideal Gd^{III} ion, with a $\chi_M T$ of 8.08 cm^3 K mol^{-1} at 5 K and 7.19 cm^3 K mol^{-1} at 2 K. The measured susceptibility closely matched the theoretical susceptibility of a Gd^{III} ion. The **$TbZn_{16}$** metallacrown had a $\chi_M T$ of 8.31 cm^3 K mol^{-1} at 5 K and 6.89 cm^3 K mol^{-1} at 2 K. The susceptibility deviates significantly from the value given in Table 5.6 indicating the population of higher energy states, as there is no possibility for magnetic coupling. For **$DyZn_{16}$**, the susceptibility at 5 K was found to be 11.08 cm^3 K mol^{-1} and at 2 K, was 9.72 cm^3 K mol^{-1}. Again, both of these values deviate from the expected value given in Table 5.6. The susceptibility of **$HoZn_{16}$** was found to be 3.81 cm^3 K mol^{-1} at 2 K. For **$ErZn_{16}$,** the susceptibility at 2 K was 7.99 cm^3 K mol^{-1}, which is again less than expected for an Er^{III} ion. For **$YbZn_{16}$**, the susceptibility was 1.51 cm^3 K mol^{-1} at 2 K. As before, all of these values deviated from the expected $\chi_M T$ values given in Table 5.6 indicating that excited states are most likely populated.

However, the observed susceptibilities can be explained if one looks at the energy diagram of the lanthanides and imagines populating excited energy states. Using

Carnall's LnF_3 energy level diagram (Figure 5.41)[24] one can see that except for **$GdZn_{16}$**, an excited *J* state of the Ln^{III} could be populated, even at very low temperatures. It appears that the first excited state for **$TbZn_{16}$** (*J* = 5), **$DyZn_{16}$** (*J* = 13/2) **$ErZn_{16}$** (*J* = 13/2) and **$YbZn_{16}$** (*J* = 5/2) is occupied, while for **$HoZn_{16}$**, the fifth excited state (*J* = 4) is occupied for the studied complexes.

Looking at the in-phase data of **$GdZn_{16}$**, at both 0 G and 500 G, the magnetic susceptibility at 2 K was approximately 6.80 cm^3 K mol^{-1}. This value was close to the value found from the dc variable temperature susceptibility. The in-phase magnetic susceptibility of **$TbZn_{16}$** at both 0 G and 500 G at 2 K was 3.52 cm^3 K mol^{-1}. This value was significantly lower than that observed for the dc variable temperature susceptibility.

The in-phase magnetic susceptibility of **$DyZn_{16}$** ranged from 8.52 cm^3 K mol^{-1} at 0 G dc applied field to 4.84 cm^3 K mol^{-1} at 1000 G dc applied field. These susceptibility values reveal that there are numerous spin states populated at low temperatures and with a strong applied field and that the population of the spin states are frequency dependent. It is difficult to determine the distribution of the excited states as the energy diagram of Dy^{III} is not straightforward. The same problem is observed when a 500 G dc field is applied and various frequencies were measured.

For the in-phase magnetic susceptibility of **$HoZn_{16}$** with an applied dc field of 500 G was 2.75 cm^3 K mol^{-1} for 1488 Hz and 3.72 cm^3 K mol^{-1}, which matched the variable temperature data nicely. Examining the in-phase magnetic susceptibility of **$ErZn_{16}$** depending on the applied field ranged from 4.81 cm^3 K mol^{-1} for 0 G dc applied field to 4.13 cm^3 K mol^{-1} for 1000 G dc applied field. When the applied dc field was set to 750 G, and the frequencies varied from 1399 Hz to 10 Hz, the magnetic susceptibility varied from 4.15 cm^3 K mol^{-1} to 7.64 cm^3 K mol^{-1}. These susceptibility values could corresponded to the first few excited states of Er^{III}. Finally, for **$YbZn_{16}$**, the in-phase magnetic susceptibility for various applied fields and a set frequency led to magnetic susceptibilities ranging from 1.48 cm^3 K mol^{-1} for 0 G to 0.81 cm^3 K mol^{-1}. These values correspond to the excited states.

Based on the susceptibility data, it was concluded that even at 2 K, the ground state values for most of the metallacrowns could not be isolated. If lower temperatures could be obtained, it's possible that the ground state could be isolated. In comparison to the other complexes in this work, this is the first series, however, where well-isolated states are observed. One reason for this is that the only source of magnetism in these complexes was the lanthanide present. The other complexes studied had multiple metals which could couple, leading to multiple spin states.

The out-of-phase magnetic susceptibility of **GdZn$_{16}$**, **TbZn$_{16}$**, and **HoZn$_{16}$** did not demonstrate frequency dependence, indicating that they were not single-molecule magnets. On the other hand, **DyZn$_{16}$**, **ErZn$_{16}$**, and **YbZn$_{16}$** did show frequency dependence, albeit when an applied dc field was present. None of these complexes had a maximum in the χ''_M vs. T plot, thus the energy barriers for each complex could not be calculated. One must be careful, however, declaring **DyZn$_{16}$**, **ErZn$_{16}$**, or **YbZn$_{16}$** SMMs. This is because when dc field is applied, it can increase the blocking temperature and the onset of slow magnetic relaxation of SMMs. However, the field can also orient the spins of the molecule, thus giving the appearance of frequency dependence. For instance, if the molecule has easy plane anisotropy, the applied field can orient the spins in the xy plane. Thus, when performing the ac out-of-phase magnetic susceptibility, the spins process along the axis, giving the appearance of frequency dependence. However, because the anisotropy is not axial, the molecule could not be an SMM.

To check if **DyZn$_{16}$**, **ErZn$_{16}$**, or **YbZn$_{16}$** were SMMs, the complexes were sent to Wolfgang Wernsdorfer for single-crystal micro SQUID measurements. In addition, the **GdZn$_{16}$**, **TbZn$_{16}$**, and **HoZn$_{16}$** complexes were sent as well. These measurements were performed, which revealed as expected, the **GdZn$_{16}$**, **TbZn$_{16}$**, and **HoZn$_{16}$** were not SMMs. Surprisingly, the **DyZn$_{16}$** did not behave as an SMM. It was determined that **DyZn$_{16}$** had easy plane magnetoanisotropy. Thus, the observed out-of-phase magnetic susceptibility was due to the presence of the applied dc field. The **ErZn$_{16}$** complex, on the other hand, did show easy axis magnetoanisotropy, thus **ErZn$_{16}$** is an SMM.

These magnetic observations for **$TbZn_{16}$**, **$DyZn_{16}$**, and **$ErZn_{16}$** were supported by theoretical calculations performed by Hélène Bolvin of Laboratoire de Chimie et Physique Quantiques, Système Èntendu et Magnétisme at Université Paul Sabatier, Toulouse, France. Using SO-CASSCF calculations with ANO-RCC basis sets, DZP on Ln and DZ on the other atoms, with only N and O having basis sets, the rest of the environment was modeled by ECPs. These calculations indicating that **$TbZn_{16}$** and **$DyZn_{16}$** had positive anisotropy and thus the smallest *J* state would be the ground state. The **$ErZn_{16}$** metallacrown, on the other hand, had negative anisotropy and thus the largest *J* state was the ground state.

Based on the structures, one can explain why the oblate Tb^{III} and Dy^{III} ions did not behave as SMMs and the **$ErZn_{16}$** metallacrown is an SMM. The compressed nature of the ligand field of the metallacrown favored the smaller, prolate Er^{III} ion. This result nicely matches the result found by Ishikawa and Coronado. The axially distorted **$[Pc_2Ln]^-$** environment favored the Tb^{III} and Dy^{III} ions, resulting in these complexes showing the onset of slow magnetic relaxation at higher temperatures.[12] However, the Er^{III} complex did not show slow magnetic relaxation. Coronado's **$[Ln(W_5O_{18})_2]^{9-}$** complex had a more compressed axial environment. In this case, the Er^{III} complex showed slow magnetic relaxation, but the Tb^{III} or Dy^{III} complexes did not show SMM behavior.[14,15] As the metallacrowns had an even more compressed binding site, one would expect the smaller Er^{III} ion would show SMM behavior, while the larger Tb^{III} and Dy^{III} complexes would not show SMM behavior. In addition, the fact that the coordination environment is even more compressed than the POM, one may expect changes in magnetic behavior. Unfortunately, the **$ErZn_{16}$** metallacrown had a blocking temperature below 2 K, which was smaller than that of the **$[Er(W_5O_{18})_2]^{9-}$**.[15]

For the **$[Pc_2Ln^{III}]^-$**, **$[Er(W_5O_{18})_2]^{9-}$**, and **$Ln^{III}Zn_{16}$** complexes, the two coordination planes run parallel to each other, prohibiting the introduction of transverse anisotropy. Transverse anisotropy results in the spin states no longer being orthogonal. If the states are not orthogonal, the states can be mixed and the likelihood tunneling increases.[25] To

understand what would happen if the skew angles deviate from ideal D_{4d} symmetry, one needs to look at the ligand field parameters and the source Hamiltonian. With an applied external field, the Hamiltonian is given by Equation 4,

$$\widehat{H} = \beta\left(\widehat{\boldsymbol{L}} + 2\widehat{\boldsymbol{S}}\right) \cdot \boldsymbol{H} + \mathbf{F} \qquad (4)$$

The first term is simply the Zeeman effect, the second term is the ligand field interaction.[26] Simplifying to C_4 symmetry coinciding with the z-axis and using the notation given by Abragam and Bleaney,[27] the ligand field term $\boldsymbol{F}$ can be written as Equation 5.

$$\mathbf{F} = A_2{}^0\langle r^2\rangle\alpha\mathbf{O}_2{}^0 + A_4{}^0\langle r^4\rangle\beta\mathbf{O}_4{}^0 + A_4{}^4\langle r^4\rangle\beta\mathbf{O}_4{}^4 + A_6{}^0\langle r^6\rangle\gamma\mathbf{O}_6{}^0 + A_6{}^4\langle r^6\rangle\gamma\mathbf{O}_6{}^4 \quad (5)$$

The coefficients $A_k{}^q\langle r^k\rangle$ are the experimentally determined values, while $\mathbf{O}_k{}^q$ matrices are polynomials of the total angular momentum.[27] Stevens was able to calculate the coefficients α, β, and γ.[28] When the ligand rings are parallel and oriented at 45°, the $A_4{}^4\langle r^4\rangle$ and $A_6{}^4\langle r^6\rangle$ terms go to zero, and the ligand field value obviously decreases.[26] Thus for the presented **$Ln^{III}Zn_{16}$** complexes, one would expect very small ligand field parameters for each complex studied.

Compared with other systems reported in this thesis, these complexes are not significantly better than the mixed Mn/Ln complexes. The blocking temperature was less than the **Dy^{III} 14-MC-5** complex. However, the **$Ln^{III}Zn_{16}$** complexes allowed for a clearer and more fundamental probe of the source of SMM behavior. As only the Ln^{III} contributes to the magnetic behavior, there is no possibility of changes in magnetic coupling due changing the size of the central Ln^{III}, as could be the case in the other systems presented previously.

Conclusion

The **$LnZn_{16}$** metallacrown is a new family of metallacrowns that place Ln^{III} ions in an environment previously unobtainable for metallacrowns. Without any other paramagnetic

metals or radicals present allows for an in depth, detailed study of the magnetic properties of the Ln^{III} ion. This also allows for the opportunity to isolate a single *J* state. It was found that the **$ErZn_{16}$** metallacrown showed slow magnetic relaxation as well as directional dependent magnetic hysteresis data, consistent with being an SMM. The magnetic data was supported by computational studies. The **$TbZn_{16}$** and **$DyZn_{16}$** metallacrowns did not show directional dependent magnetic hysteresis data (Table 5.7), which was supported by computational studies. The **$DyZn_{16}$** complex showed slow magnetic relaxation in the out-of-phase ac magnetic susceptibility with an applied field. This demonstrates the drawbacks of studying out-of-phase ac magnetic susceptibility with an applied field; it can sometimes lead to planar magnetization.

The **$LnZn_{16}$** complex demonstrates the importance of the ligand field on the magnetic properties. The highly axially compressed ligand environment favors smaller, prolate Ln^{III} ions. This conclusion can be further probed by other **$LnZn_x$** complexes prepared by Joseph Jankolovits. Joe created a **Ln(12-$MC_{Zn^{II}_L}$-4)$_2$** sandwich complex which removes the larger 24-MC-8 ring. He also prepared a **Ln(12-$MC_{Zn^{II}_L}$-4)(12-C-4)** complex that removes a single part of the sandwich and replaced it with a 12-C-4. Lastly, there is a **Ln(12-$MC_{Zn^{II}_L}$-4)** without any "topper". These complexes would allow one to study the impact of ligand field. It is difficult to predict *a priori* the magnetic behavior of these complexes as numerous effects begin to manifest for each complex. In the **Dy^{III}(12-$MC_{Zn^{II}_L}$-4)$_2$** sandwich complex, the two metallacrown planes are not parallel, thus opening up the possibility of transverse anisotropy. The **Ln(12-$MC_{Zn^{II}_L}$-4)$_2$** sandwich complex is still axially contracted, although less than the **$Ln^{III}Zn_{16}$** complexes, thus it would be expected that the Er^{III} analog would perform better than the Dy^{III} analog. The **Ln(12-$MC_{Zn^{II}_L}$-4)(12-C-4)** complex is axially contracted, but less than the **Ln(12-$MC_{Zn^{II}_L}$-4)$_2$** sandwich complex or the **$Ln^{III}Zn_{16}$** complex. Thus, the Dy^{III} analog could show slow magnetic relaxation. The **Ln(12-$MC_{Zn^{II}_L}$-4)** complex is also axially contracted and falls between the **Ln(12-$MC_{Zn^{II}_L}$-4)(12-C-4)** complex and the **Ln(12-$MC_{Zn^{II}_L}$-4)$_2$** sandwich complex. Again, the Dy^{III} analog could show slow magnetic relaxation. There are few examples in the literature were so many structural changes are

possible for a family of complexes, allowing for a deeper understanding of ligand field effects on SIM behavior.

Table 5.7. The magnetic properties of $\mathbf{Ln^{III}Zn^{II}_{16}}$ are summarized below.

Complex	Low Temperature $\chi_M T$ (cm^3 K mol^{-1})	High Temperature $\chi_M T$ (cm^3 K mol^{-1})	Single-ion magnetic behavior?
$GdZn_{16}$	8.08 (5 K)	4.41 (300 K)	NO
	7.19 (2 K)*	3.29 (300 K)*	NO*
$TbZn_{16}$	8.31 (5 K)	9.39 (300 K)	NO
	6.89 (2 K)*	9.14 (300 K)*	NO
$DyZn_{16}$	11.08 (5 K)	9.97 (300 K)	NO
	9.72 (2 K)	9.09 (300 K)*	NO
$HoZn_{16}$	3.81 (2 K)	12.71 (300 K)	NO
$ErZn_{16}$	7.99 (2 K)	10.13 (300 K)	YES
$YbZn_{16}$	1.50 (2 K)**	-5.58 (300 K)**	NO

* Data collected at Université Claude Bernard Lyon 1 in Lyon, France.
** Data was collected multiple times, but still had a negative susceptibility at 300 K.

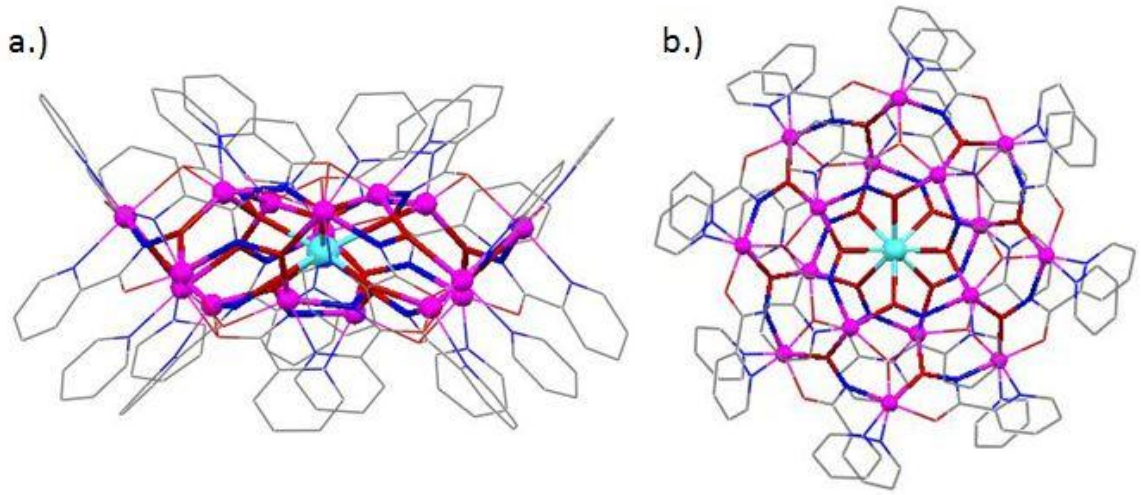

Figure 5.1. The x-ray crystal structure of **$DyZn_{16}$** is shown. The metallacrown rings of the 12-MC-4 and 24-MC-8 are highlighted. a.) The view perpendicular to the C_4 axis is shown. b.) The view along the C_4 axis is shown. Color scheme: aqua sphere: Dy^{III}; pink sphere: Zn^{II}; red tube: oxygen; blue tube: nitrogen; gray tube: carbon.[18]

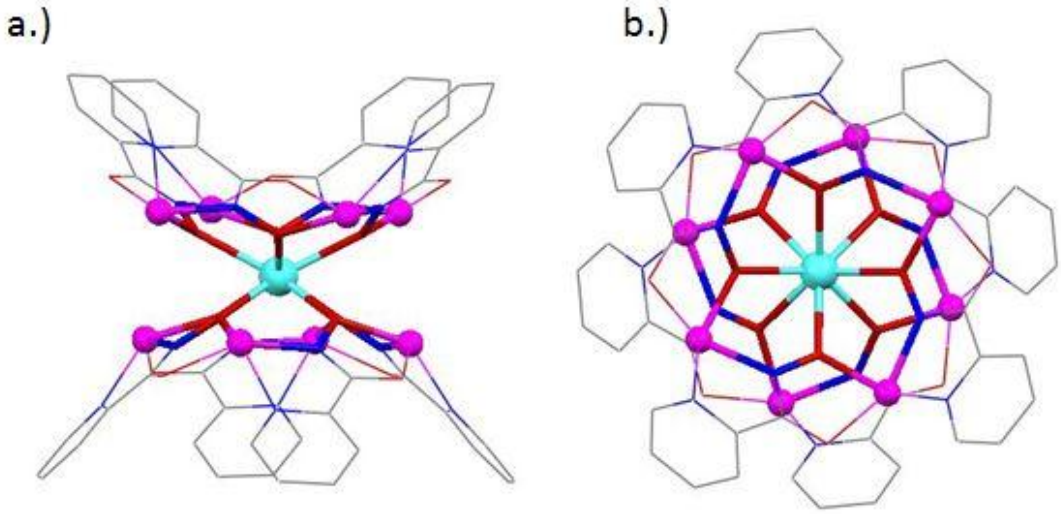

Figure 5.2. The unique 12-$MC_{Zn^{II}N(picHA)}$-4 sandwich structure of **$DyZn_{16}$** is shown. a.) The view perpendicular to the C_4 axis is shown. b.) The view along the C_4 axis is shown. Color scheme: aqua sphere: Dy^{III}; pink sphere: Zn^{II}; red tube: oxygen; blue tube: nitrogen; gray tube: carbon.[18]

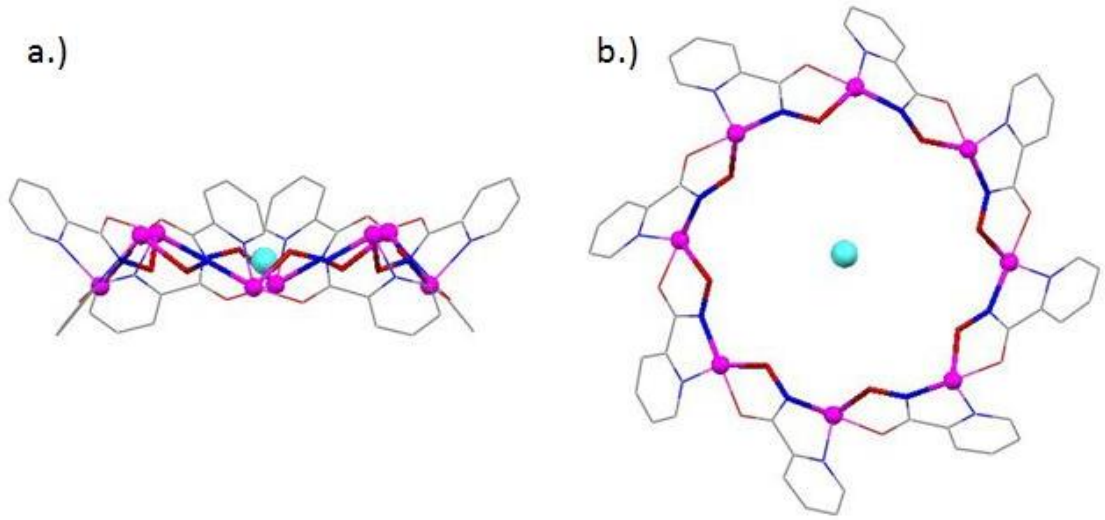

Figure 5.3. The 24-$MC_{Zn^{II}N(picHA)}$-8 ring which encloses **$DyZn_{16}$** is shown. a.) The view perpendicular to the C_4 axis is shown. b.) The view along the C_4 axis is shown. Color scheme: aqua sphere: Dy^{III}; pink sphere: Zn^{II}; red tube: oxygen; blue tube: nitrogen; gray tube: carbon.[18]

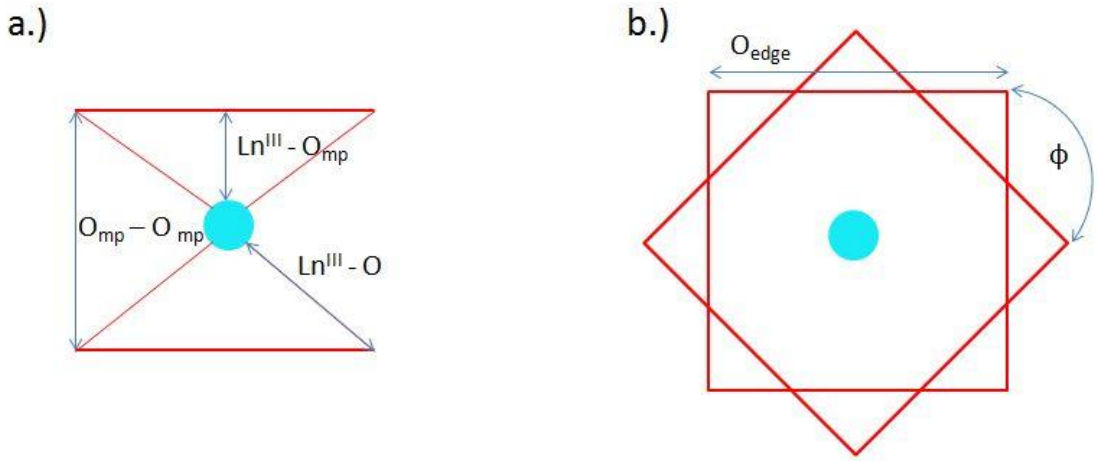

Figure 5.4. The important structural parameters of **$LnZn_{16}$** are shown. a.) Looking perpendicular to the C_4 axis, the oxygen mean-plane distances ($O_{mp} – O_{mp}$), the distance between the metallacrown oxygen mean-plane and central Ln^{III} ($Ln^{III} – O_{mp}$), and the distance between the Ln^{III} atom and the oxygen of the metallacrown ring ($Ln^{III} – O$) are shown. b.) Along the C_4 axis, the O – O length of the metallacrown (O_{edge}) and skew angle (φ) are shown. Color scheme: red line: oxygen mean plane; aqua sphere: Ln^{III}.

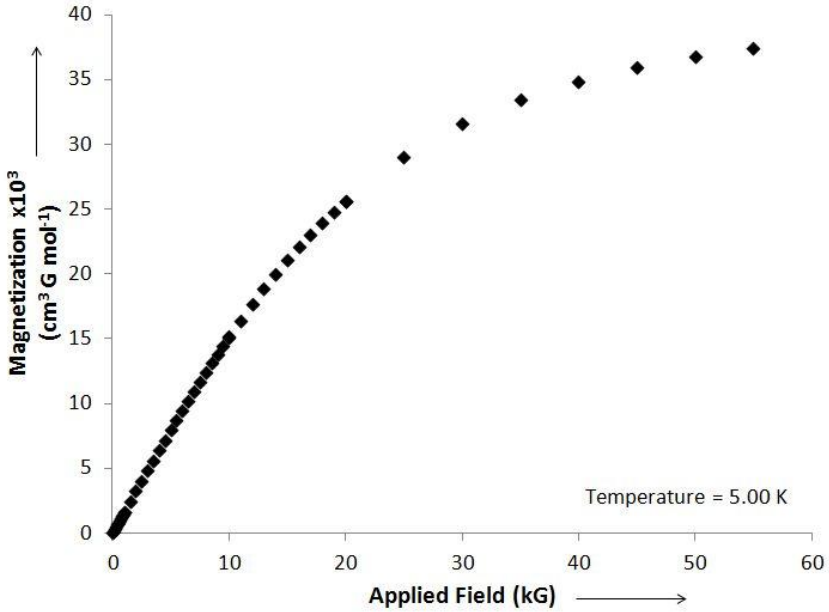

Figure 5.5. The dc magnetization of **$GdZn_{16}$** is shown. The magnetization was collected at 5 K and the applied field was varied from 0 G to 55000 G.

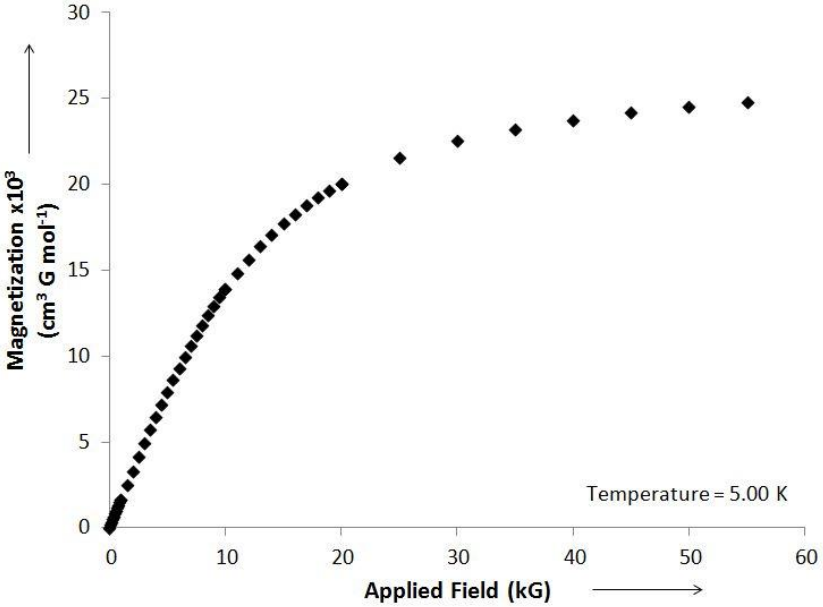

Figure 5.6. The dc magnetization of **$TbZn_{16}$** is shown. The magnetization was collected at 5 K and the applied field was varied from 0 G to 55000 G.

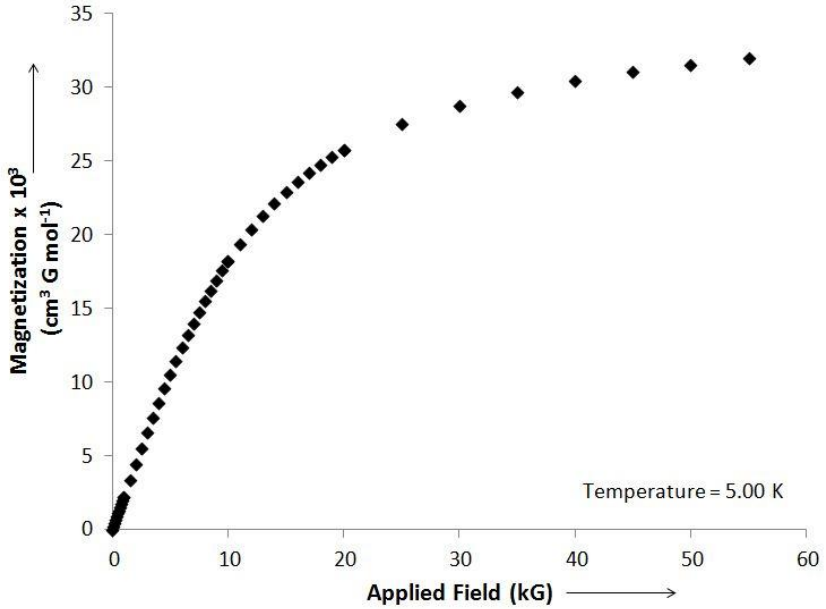

Figure 5.7. The dc magnetization of **$DyZn_{16}$** is shown. The magnetization was collected at 5 K and the applied field was varied from 0 G to 55000 G.

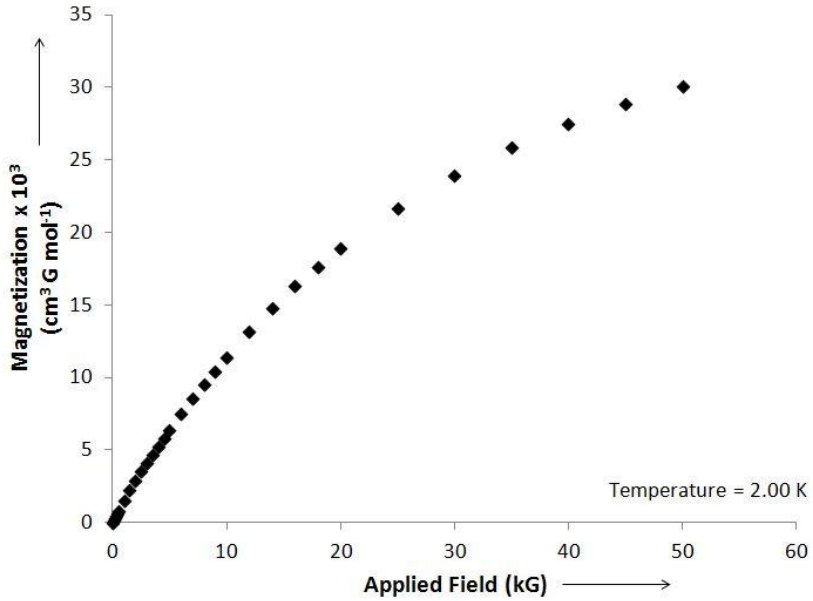

Figure 5.8. The dc magnetization of **$HoZn_{16}$** is shown. The magnetization was collected at 2 K and the applied field was varied from 0 G to 50000 G.

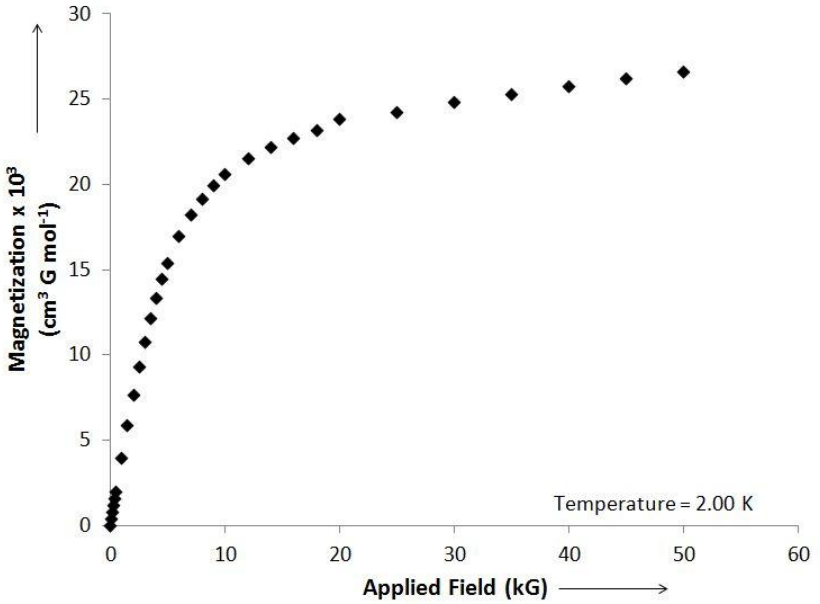

Figure 5.9. The dc magnetization of **$ErZn_{16}$** is shown. The magnetization was collected at 2 K and the applied field was varied from 0 G to 50000 G.

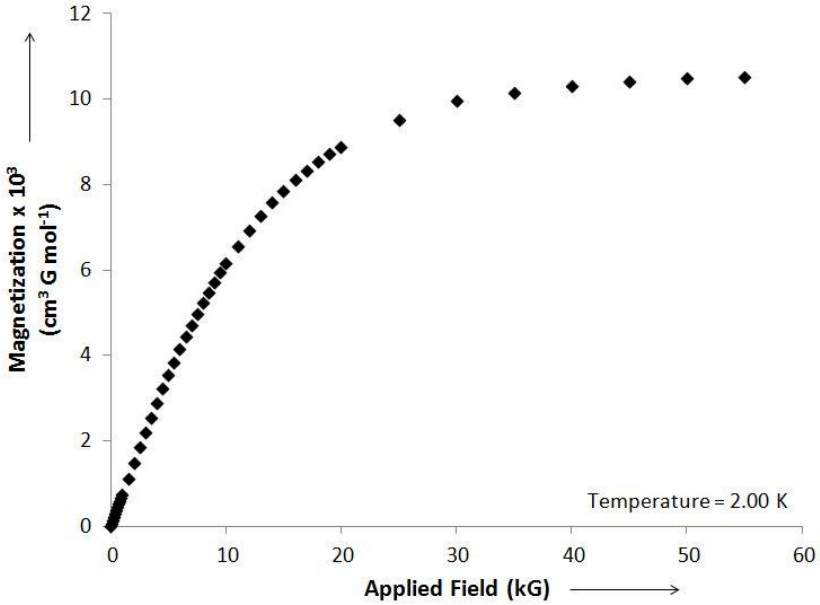

Figure 5.10. The dc magnetization of **$YbZn_{16}$** is shown. The magnetization was collected at 2 K and the applied field was varied from 0 G to 55000 G.

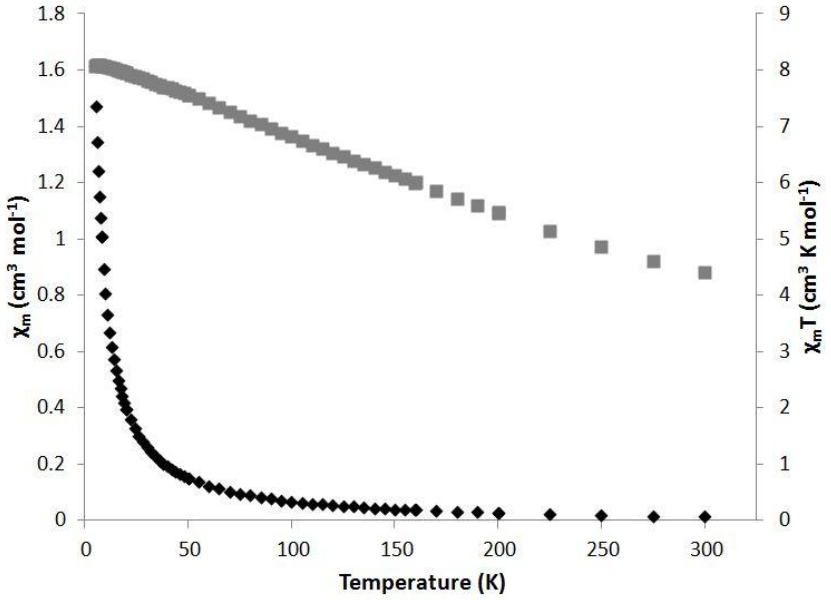

Figure 5.11. The variable temperature magnetic susceptibility of **$GdZn_{16}$** collected at an applied field of 2000 G from 5 K to 300 K is shown. χ_M: ◆ $\chi_M T$: ■

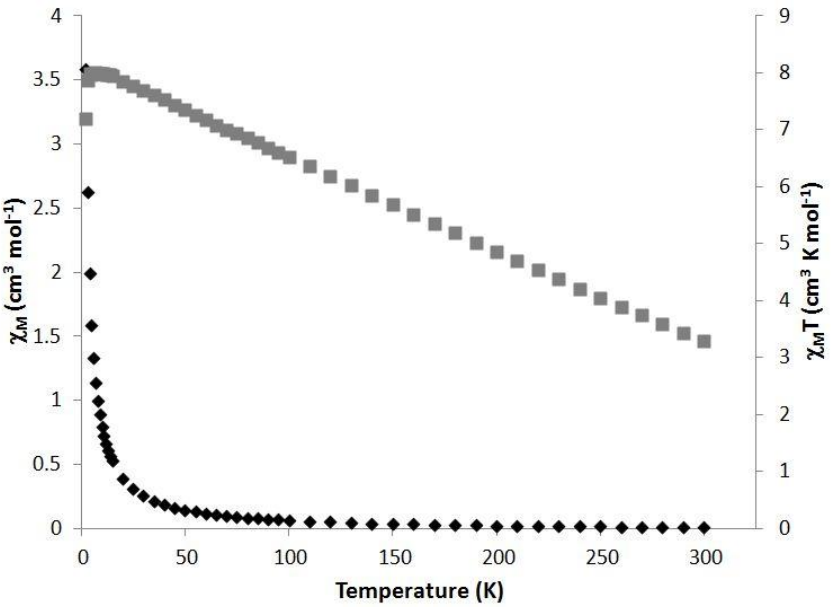

Figure 5.12 The variable temperature susceptibility of **$GdZn_{16}$** collected with an applied field of 1000 G from 300 K to 2 K using the RSO setting is shown. χ_M: ◆ $\chi_M T$: ■

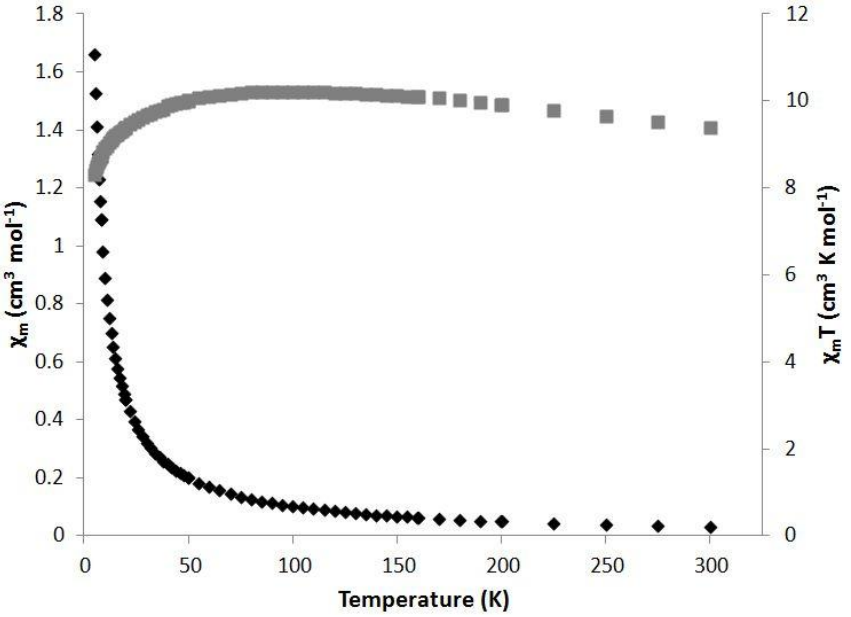

Figure 5.13. The variable temperature magnetic susceptibility of **$TbZn_{16}$** collected at an applied field of 2000 G from 5 K to 300 K is shown. χ_M: ◆ $\chi_M T$: ■

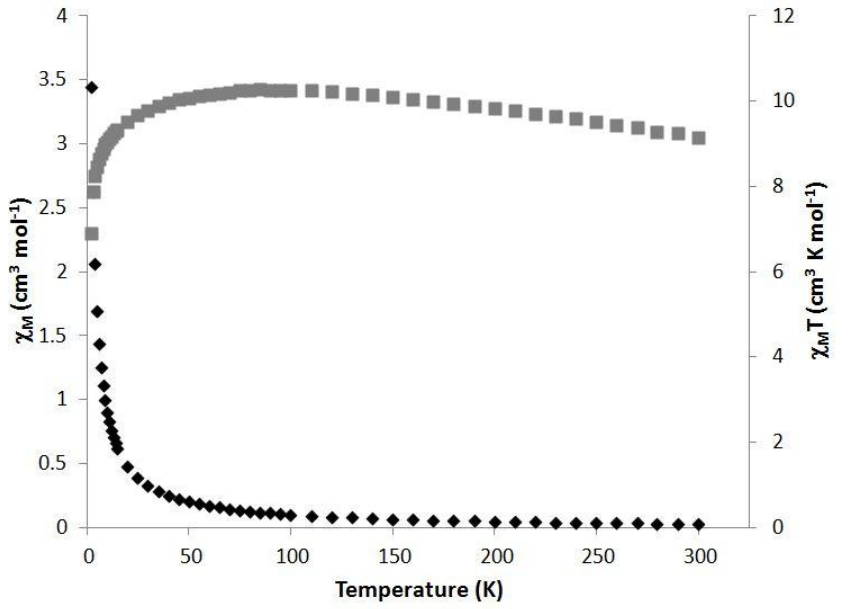

Figure 5.14 The variable temperature susceptibility of **$TbZn_{16}$** collected with an applied field of 1000 G from 300 K to 2 K using the RSO setting is shown. χ_M: ◆ $\chi_M T$: ■

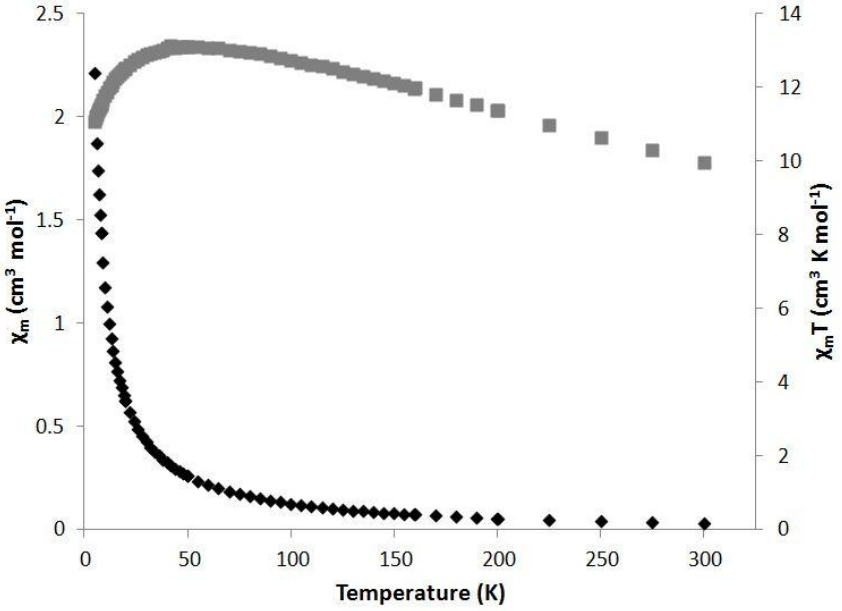

Figure 5.15. The variable temperature magnetic susceptibility of **$DyZn_{16}$** collected at an applied field of 2000 G from 5 K to 300 K is shown. χ_M: ◆ $\chi_M T$: ■

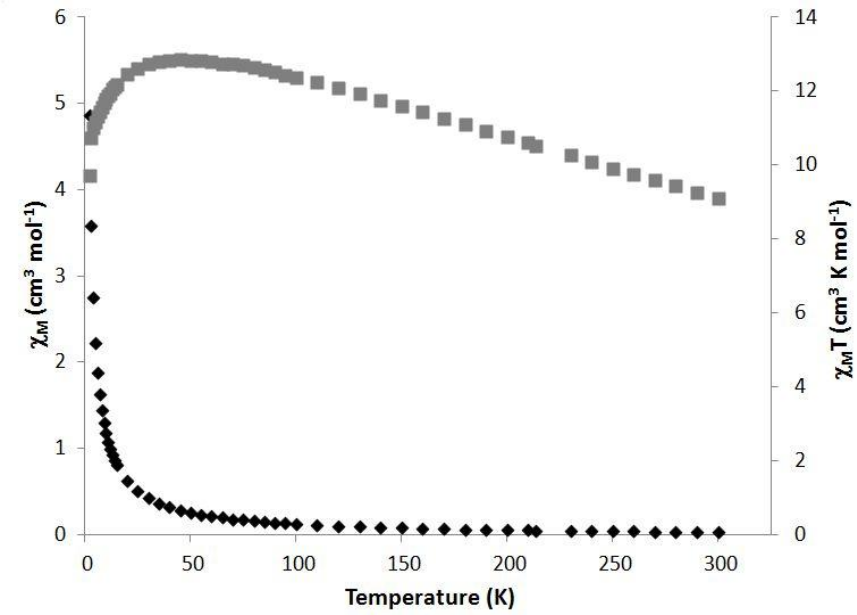

Figure 5.16 The variable temperature susceptibility of **$DyZn_{16}$** collected with an applied field of 1000 G from 300 K to 2 K using the RSO setting is shown. χ_M: ◆ $\chi_M T$: ■

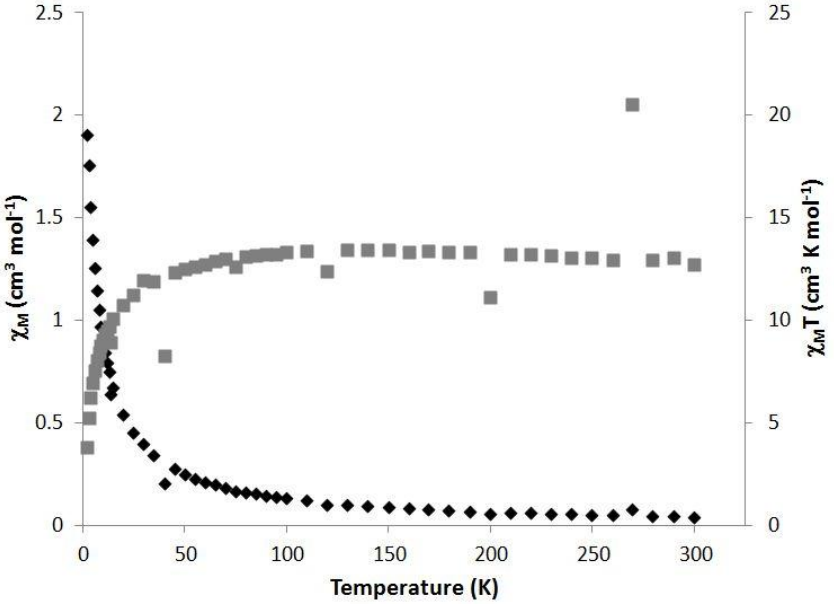

Figure 5.17. The variable temperature susceptibility of **$HoZn_{16}$** collected with an applied field of 1000 G from 300 K to 2 K is shown. Discontinuities were most likely due to the cold head starting. χ_M: ◆ $\chi_M T$: ■

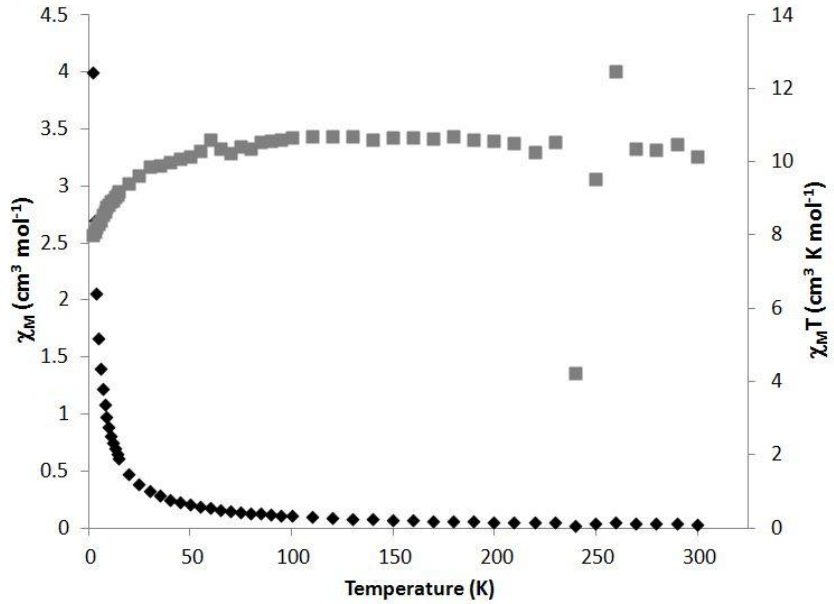

Figure 5.18. The variable temperature susceptibility of **$ErZn_{16}$** collected with an applied field of 1000 G from 300 K to 2 K is shown. Discontinuities were most likely due to the cold head starting. χ_M: ◆ $\chi_M T$: ■

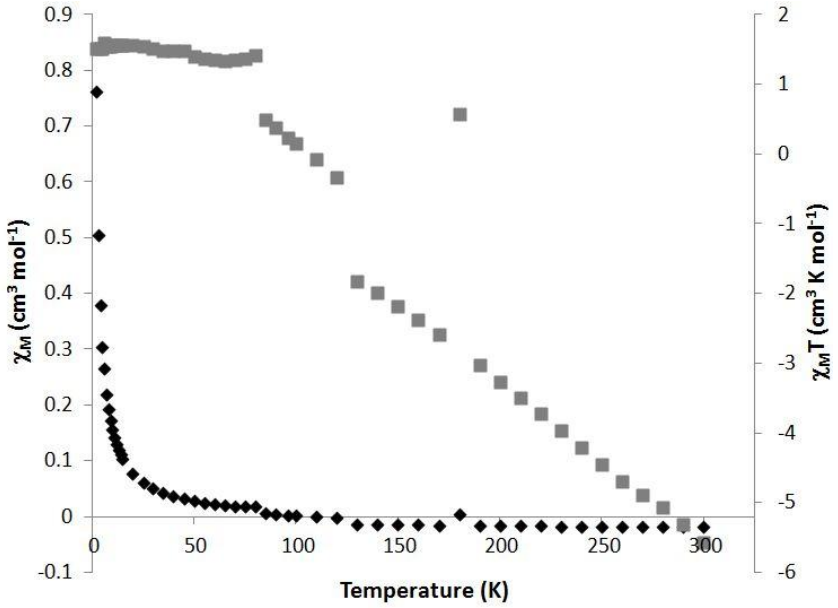

Figure 5.19. The variable temperature susceptibility of **$YbZn_{16}$** collected with an applied field of 1000 G from 300 K to 2 K is shown. χ_M: ◆ $\chi_M T$: ■

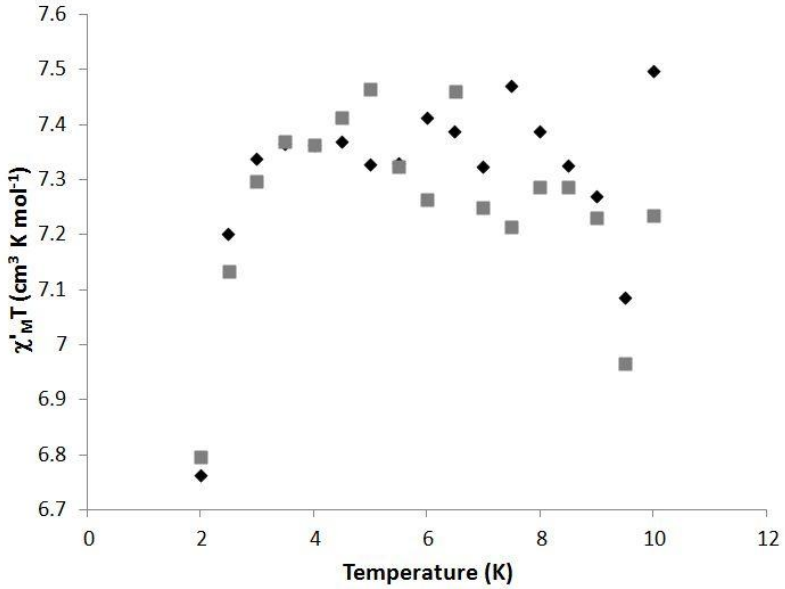

Figure 5.20. The in-phase variable temperature susceptibility of **$GdZn_{16}$** was collected at a frequency of 700 Hz, an ac drive field of 2.7 G, and applied dc fields of either 0 G or 500 G from 10 K to 2 K. 0 G dc applied field: ◆ 500 G dc applied field: ■

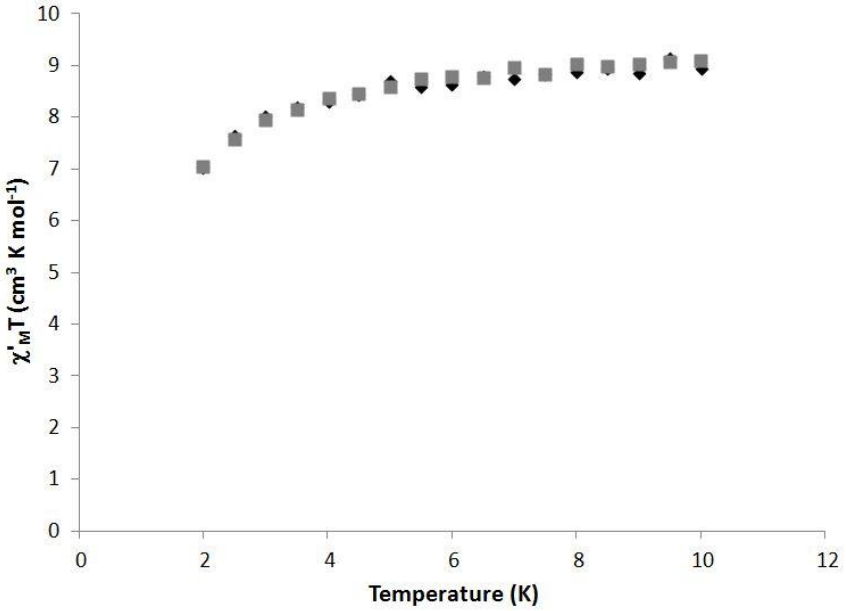

Figure 5.21. The in-phase variable temperature susceptibility of **$TbZn_{16}$** was collected at a frequency of 700 Hz, an ac drive field of 2.7 G, and applied dc fields of either 0 G or 500 G from 10 K to 2 K. 0 G dc applied field: ◆ 500 G dc applied field: ■

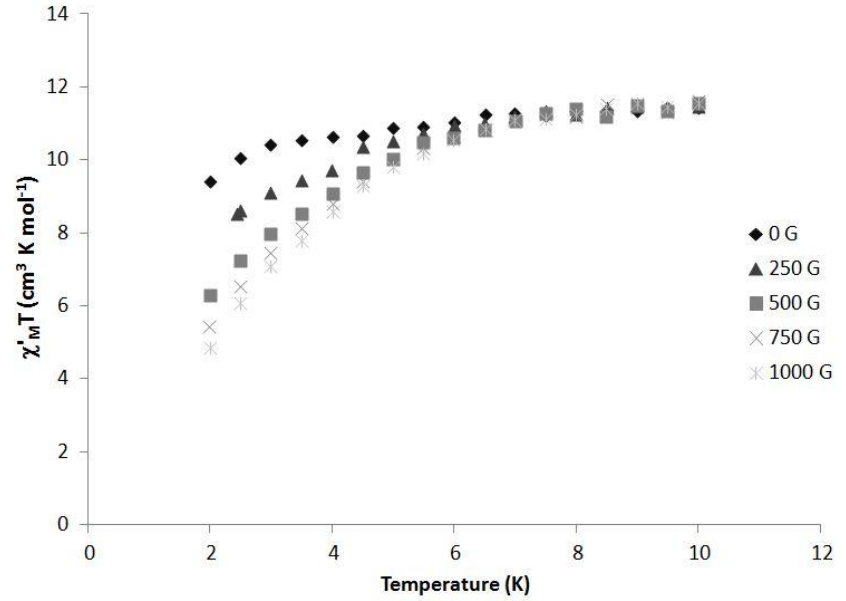

Figure 5.22. The in-phase variable temperature susceptibility of **$DyZn_{16}$** was collected at a frequency of 700 Hz, an ac drive field of 2.7 G, and applied dc fields ranging from 0 G to 1000 G from 10 K to 2 K. The applied dc fields are indicated in the legend.

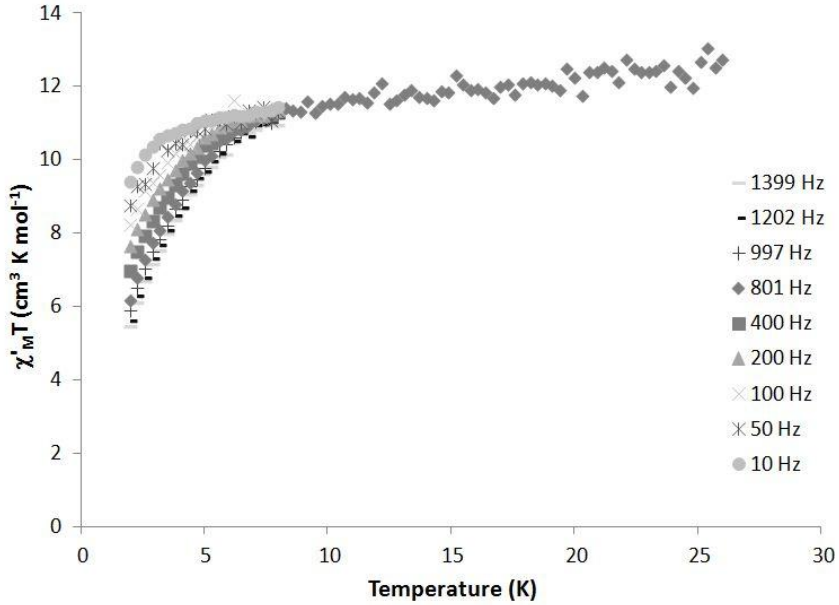

Figure 5.23. The in-phase variable temperature susceptibility of **$DyZn_{16}$** was collected with an applied dc field of 500 G and an ac drive field of 2.7 G from 30 K to 2 K at the indicated frequencies.

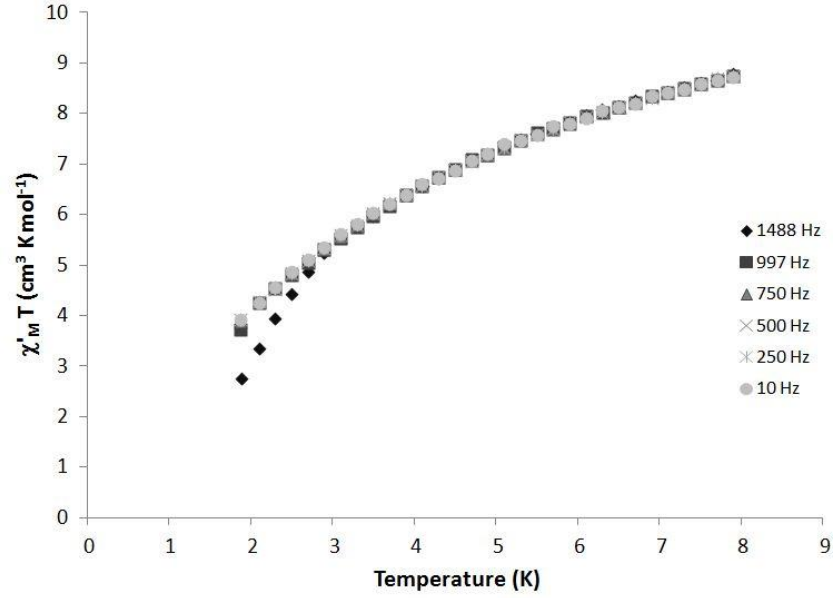

Figure 5.24. The in-phase variable temperature susceptibility of **$HoZn_{16}$** was collected with an applied dc field of 500 G and an ac drive field of 2.7 G from 8 K to 2 K at the indicated frequencies.

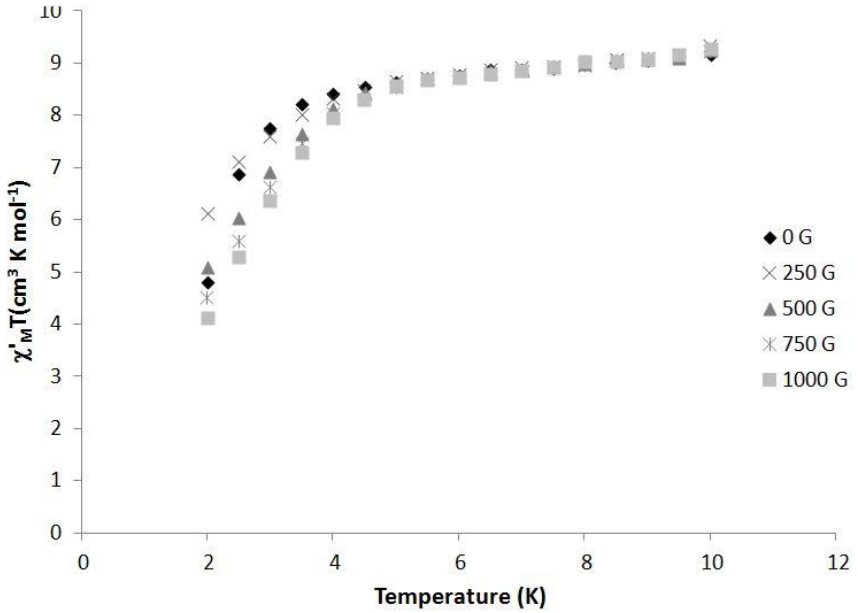

Figure 5.25. The in-phase variable temperature susceptibility of **$ErZn_{16}$** was collected with applied dc fields ranging from 1000 G to 0 G, an ac drive field of 2.7 G, and at a frequency of 997 Hz from 10 K to 2 K. The applied dc fields are indicated in the legend.

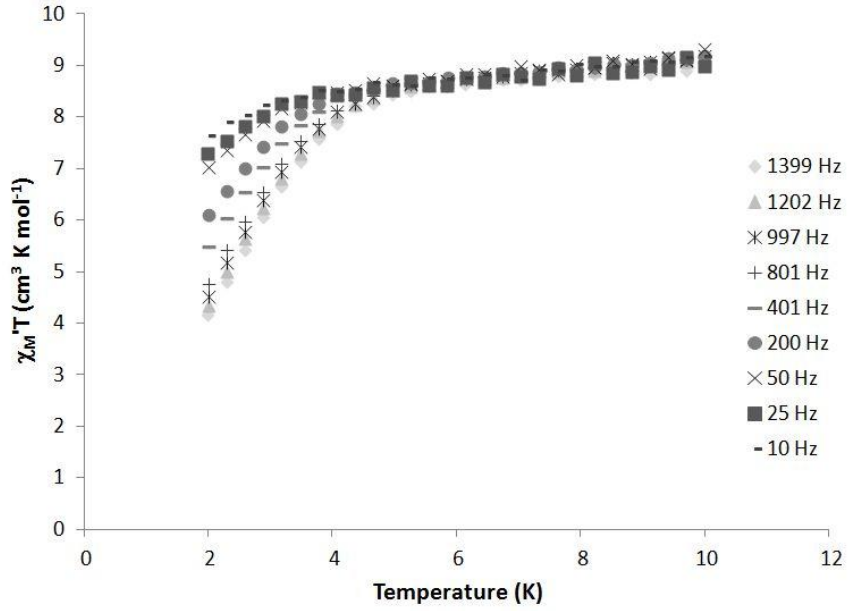

Figure 5.26. The in-phase variable temperature susceptibility of **$ErZn_{16}$** was collected with an ac drive field of 2.7 G, an applied dc field of 750 G, and at the indicated frequencies from 10 K to 2 K.

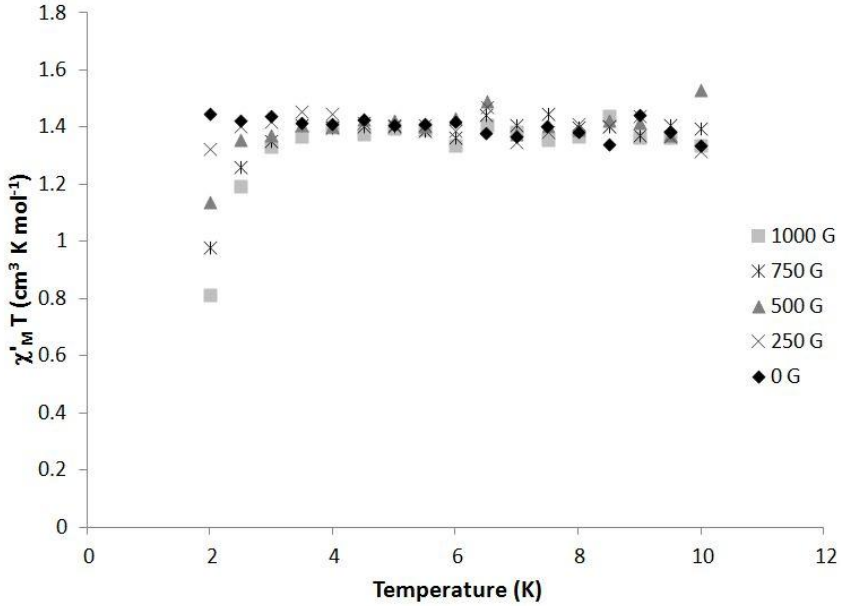

Figure 5.27. The in-phase variable temperature susceptibility of **$YbZn_{16}$** was collected with an ac drive field of 2.7 G, a frequency of 997 Hz, and at the indicated applied dc fields from 10 K to 2 K.

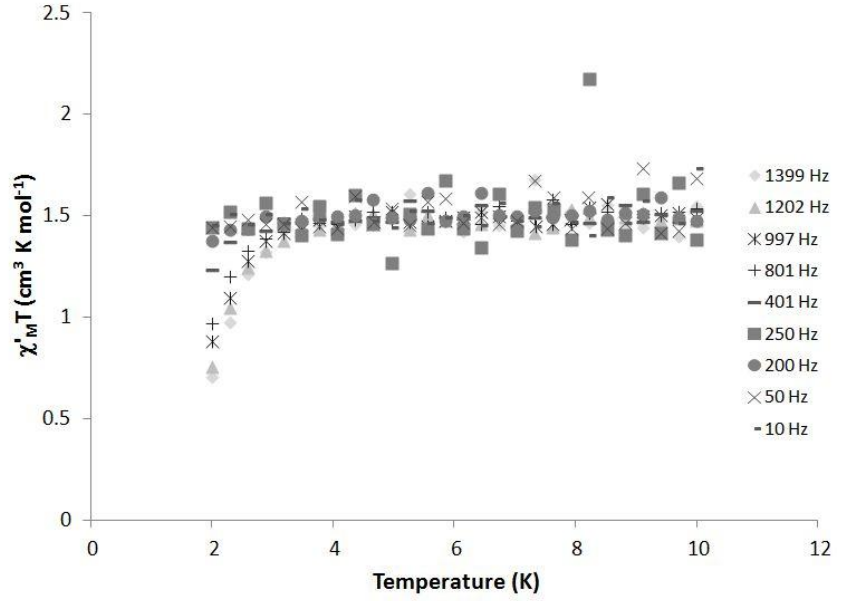

Figure 5.28. The in-phase variable temperature susceptibility of **$YbZn_{16}$** was collected with an ac drive field of 2.7 G, an applied dc field of 1000 G, and at the indicated frequencies from 10 K to 2 K.

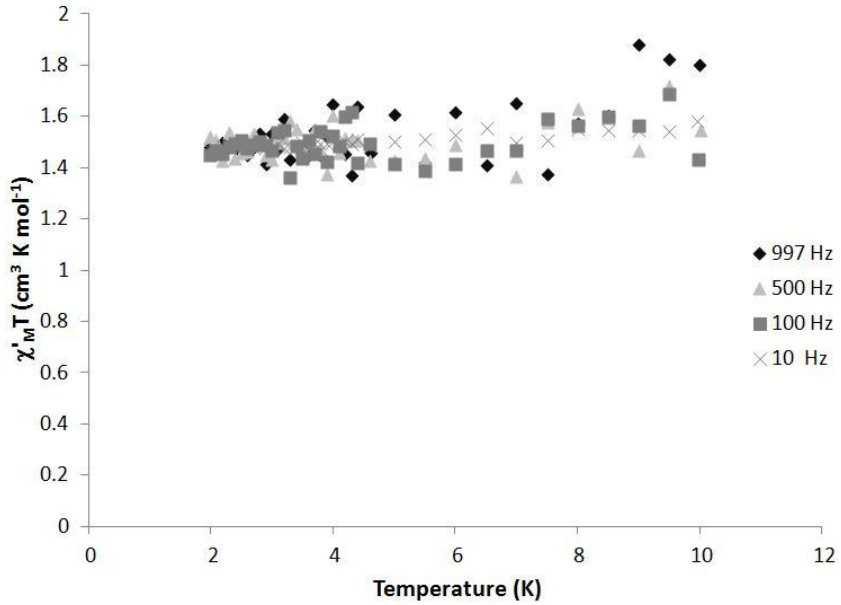

Figure 5.29. The in-phase variable temperature susceptibility of **$YbZn_{16}$** was collected with an ac drive field of 3.5 G, no applied dc field, and at the indicated frequencies from 10 K to 2 K.

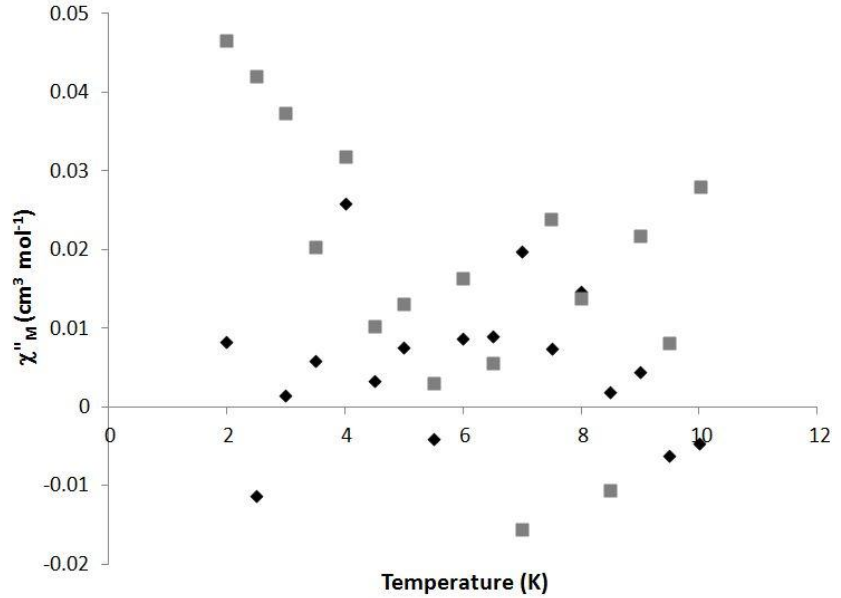

Figure 5.30. The out-of-phase variable temperature susceptibility of **$GdZn_{16}$** was collected with an ac drive field of 2.7 G, a frequency of 700 Hz, and applied dc fields of either 0 G or 500 G between 10 K and 2 K. 0 G dc applied field: ◆ 500 G dc applied field: ■

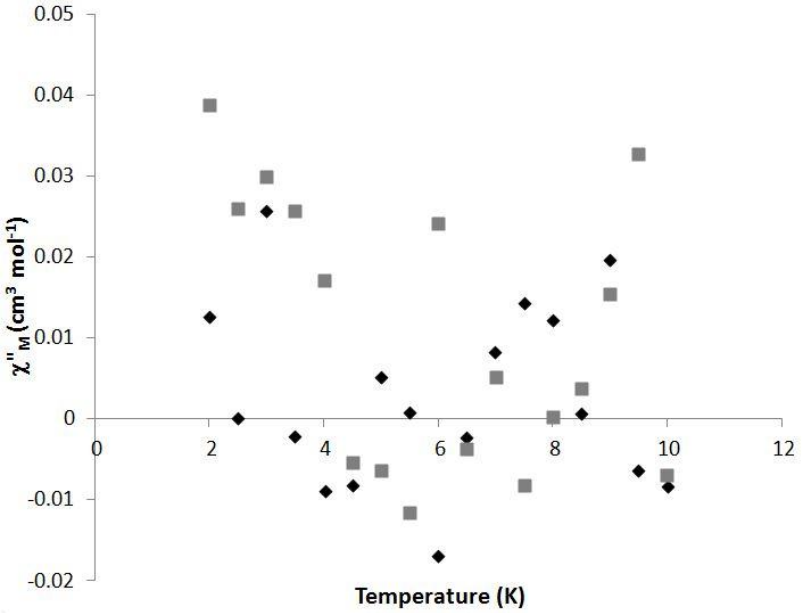

Figure 5.31. The out-of-phase variable temperature susceptibility of **$TbZn_{16}$** was collected with an ac drive field of 2.7 G, a frequency of 700 Hz, and applied dc fields of either 0 G or 500 G between 10 K and 2 K. 0 G dc applied field: ◆ 500 G dc applied field: ■

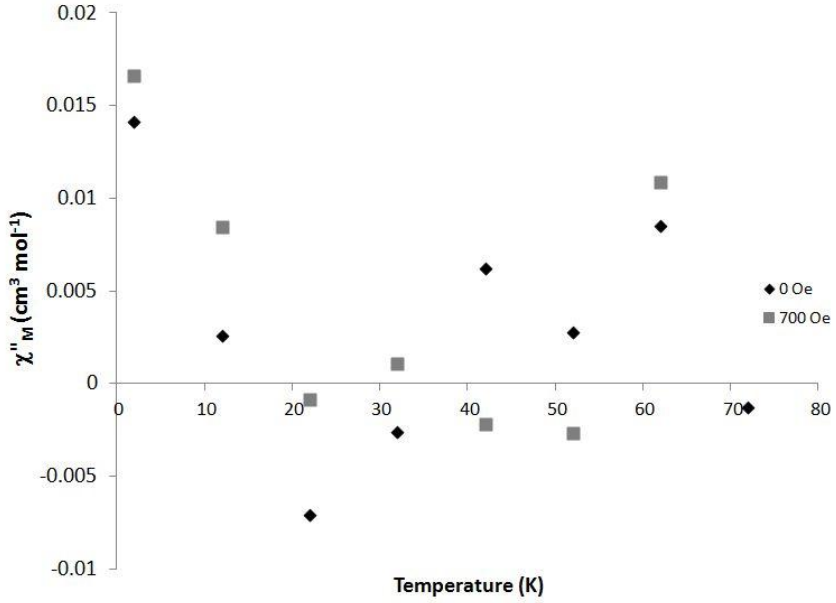

Figure 5.32. The out-of-phase variable temperature susceptibility of **$HoZn_{16}$** was collected with an ac drive field of 2.7 G, a frequency of 700 Hz, and applied dc fields of either 0 G or 700 G between 72 K and 2 K. 0 G dc applied field: ◆ 700 G dc applied field: ■

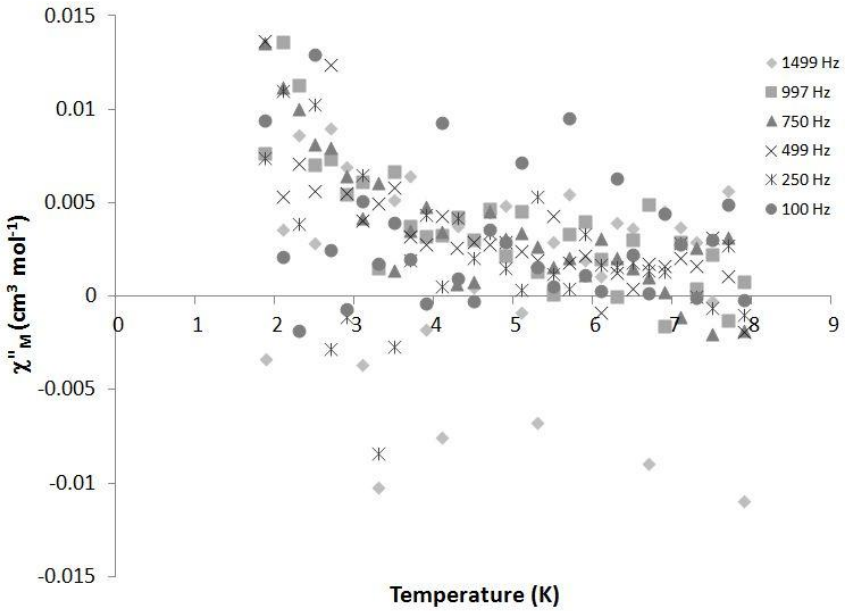

Figure 5.33. The out-of-phase variable temperature susceptibility of **$HoZn_{16}$** was collected with an ac drive field of 2.7 G, an applied dc field of 500 G, and at the indicated frequencies between 8 K and 2 K.

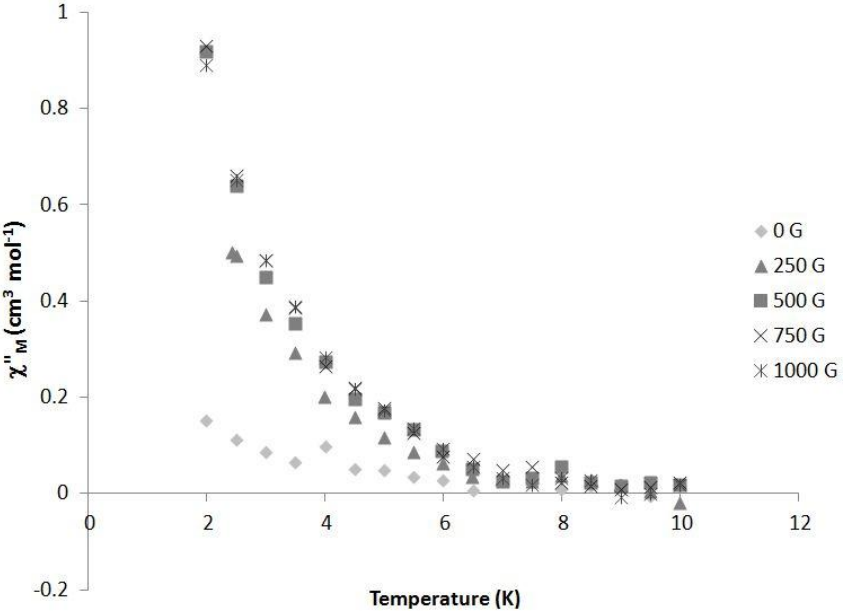

Figure 5.34. The out-of-phase variable temperature susceptibility of **$DyZn_{16}$** was collected with an ac drive field of 2.7 G, at a frequency of 700 Hz, and at the indicated applied dc fields from 10 K to 2 K.

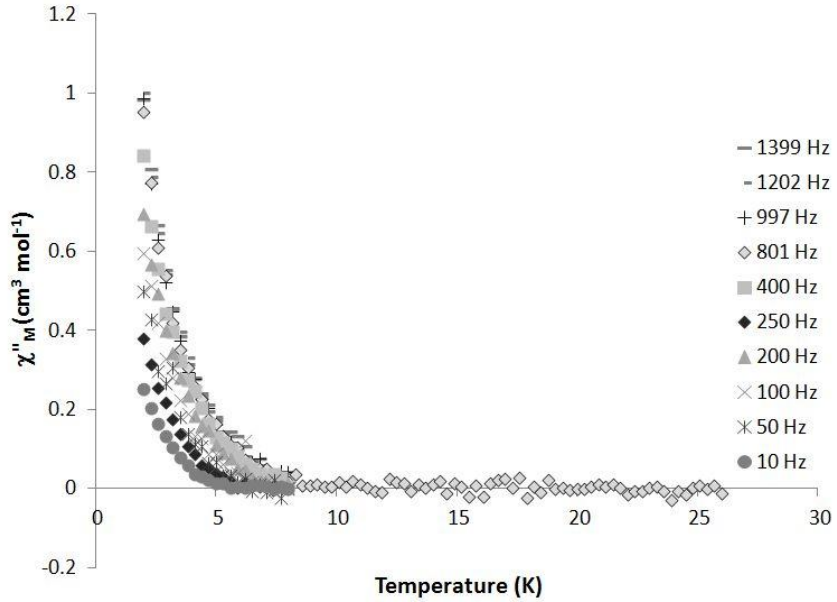

Figure 5.35. The out-of-phase variable temperature susceptibility of **$DyZn_{16}$** was collected with an ac drive field of 2.7 G, an applied dc field of 500 G, and at the indicated frequencies from 2 K to 26 K.

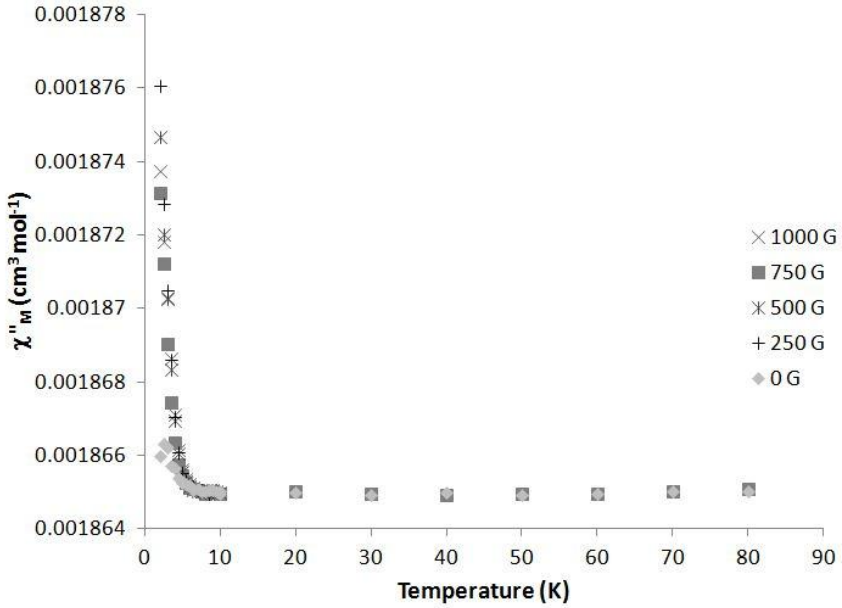

Figure 5.36. The out-of-phase variable temperature susceptibility of **$ErZn_{16}$** was collected with an ac drive field of 2.7 G, at a frequency of 997 Hz, and at the indicated applied dc fields from 80 K to 2 K.

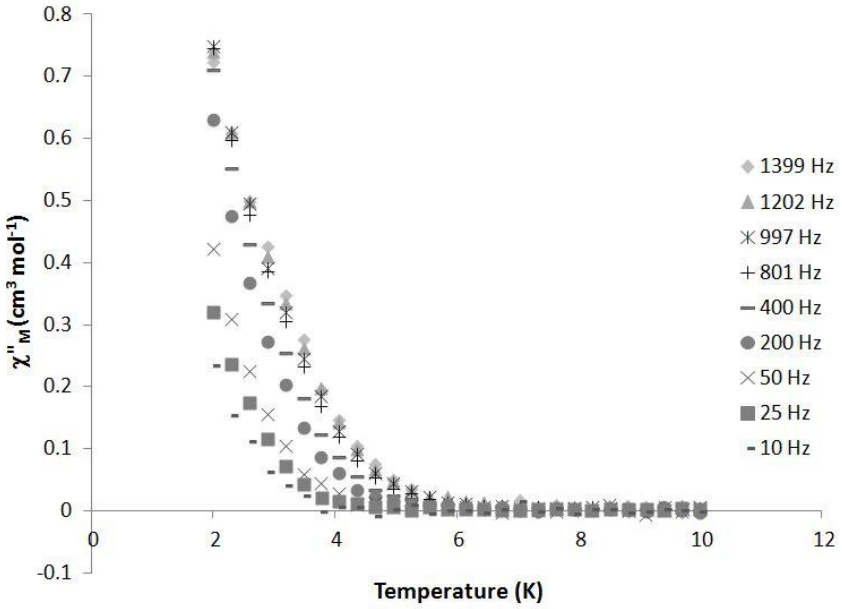

Figure 5.37. The out-of-phase variable temperature susceptibility of **$ErZn_{16}$** was collected with an ac drive field of 2.7 G, at an applied field of 750 G, and at the indicated frequencies from 10 K to 2 K.

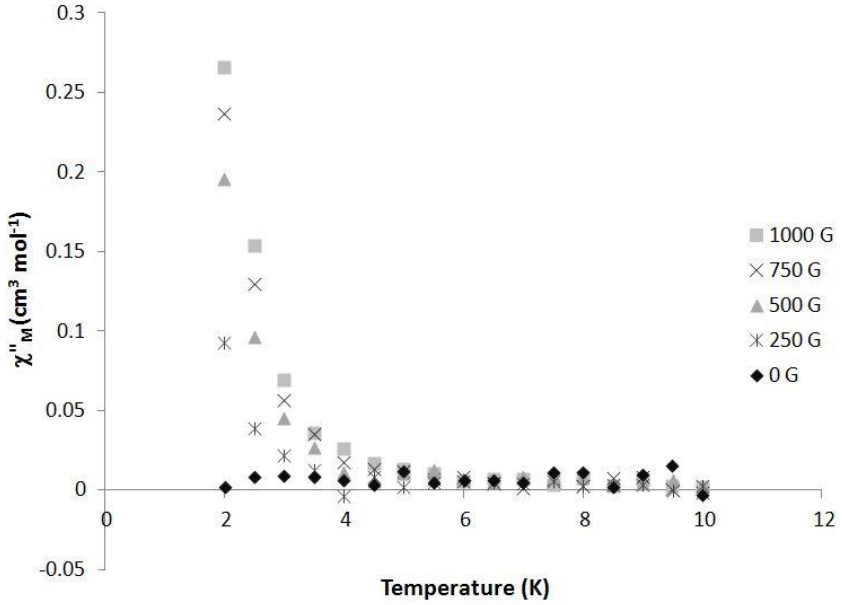

Figure 5.38. The out-of-phase variable temperature susceptibility of **$YbZn_{16}$** was collected with an ac drive field of 2.7 G, at a frequency of 997 Hz, and at the indicated applied dc fields from 10 K to 2 K.

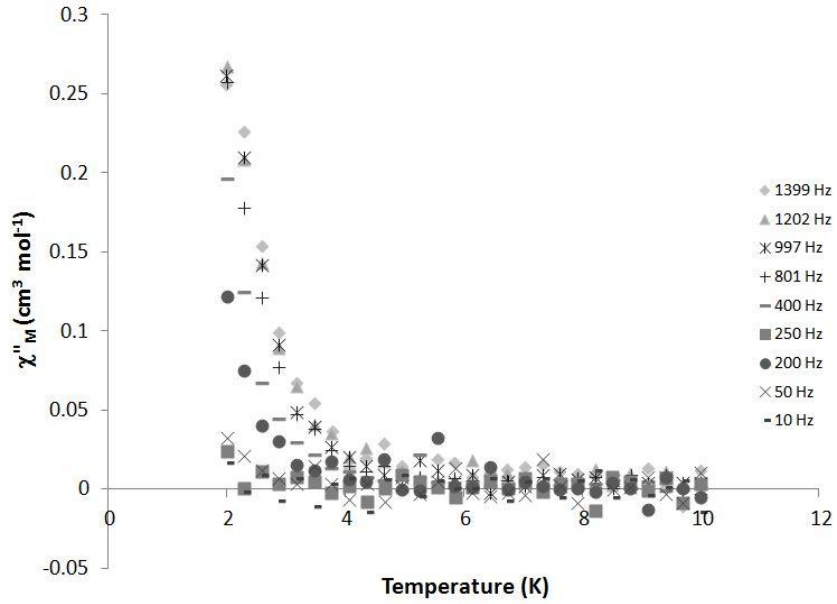

Figure 5.39. The out-of-phase variable temperature susceptibility of **$YbZn_{16}$** was collected with an ac drive field of 2.7 G, an applied dc field of 1000 G, and at the indicated frequencies from 10 K to 2 K.

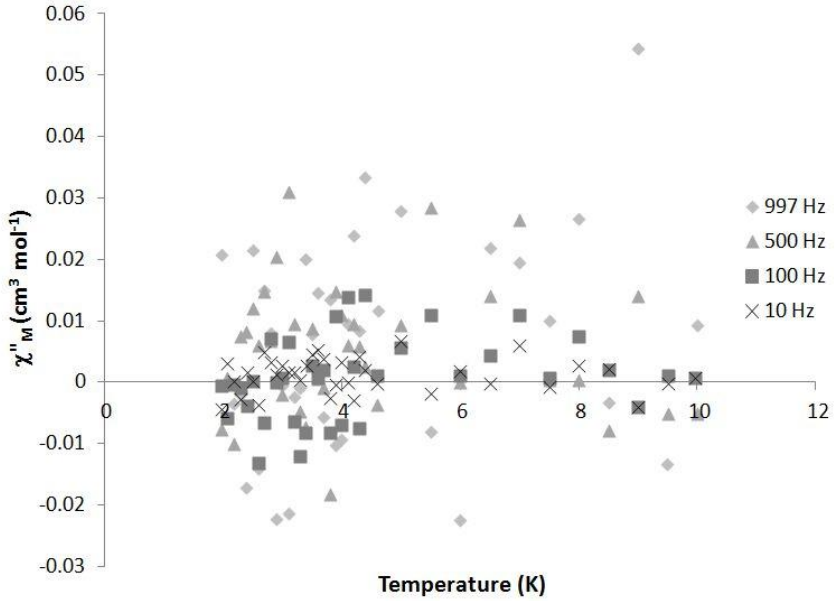

Figure 5.40. The out-of-phase variable temperature susceptibility of **$YbZn_{16}$** was collected with an ac drive field of 3.5 G, no applied dc field, and at the indicated frequencies from 10 K to 2 K.

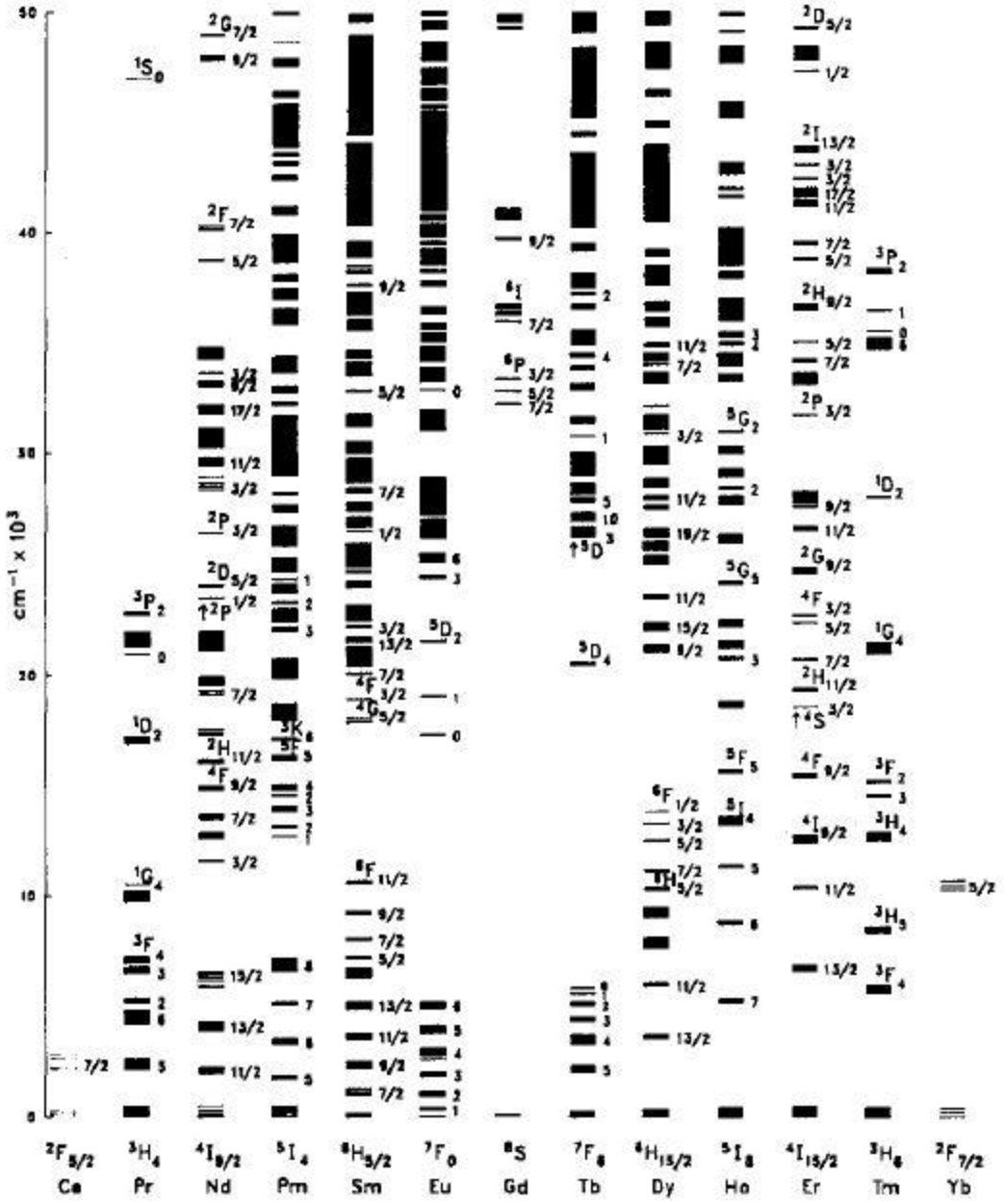

Figure 5.41. The energy level diagram of LnF_3 is shown. Taken from: Carnall, W. T.; Goodman, G. L.; Rajnak, K.; Rana, R. S. *J. Chem. Phys*. **1989**, *90*, 3443. Figure 7.

References

1 Benelli, C. & Gatteschi, D. *Chem. Rev*. **2002**, *102*, 2369.

2 Osa, S.; Kido, T.' Matsumoto, N.; Re, N.; Pochaba, A.; Mrozinski, J. *J. Am. Chem. Soc*. **2004**, *126*, 420.

3 Zaleski, C. M.; Depperman, E. C.; Kampf, J. W.; Kirk, M. L.; Pecoraro, V. L. *Angew. Chem. Int. Ed*. **2004**, *43*, 3912.

4 Zaleski, C. M.; Kampf, J. W.; Mallah, T.; Kirk, M. L.; Pecoraro, V. L. *Inorg. Chem*. **2007**, *46*, 1954.

5 Mereacre, V. M.; Ako, A. M.; Clérac, R.; Wernsdorfer, W.; Filoti, G.; Bartolomé, J.; Anson, C. E.; Powell, A. K. *J. Am. Chem. Soc*. **2007**, *129*, 9248.

6 Mereacre, V.; Lan, Y.; Clérac, R.; Ako, A. M.; Wernsdorfer, W.; Buth, G.; Anson, C. E.; Powell, A. K. *Inorg. Chem.* **2011**, *50* 12001.

7 Mereacre, V.; Ako, A. M.; Clérac, R.; Wernsdorfer, W.; Hewitt, I. J.; Anson, C. E.; Powell, A. K. *Chem. Eur. J*. **2008**, *14*, 3577.

8 Ako, A. M.; Mereacre, V.; Clérac, R.; Wernsdorfer, W.; Hewitt, I. J.; Anson, C. E.; Powell, A. K. *Chem. Commun*. **2009**, 544.

9 Mereacre, V.; Akhtar, M. N.; Lan, Y.; Ako, A. M.; Clérac, R.; Anson, C. E.; Powell, A. K. *Dalton Trans*. **2010**, *39*, 4918.

10 Li, M.; Lan, Y.; Ako, A. M.; Wernsdorfer, W.; Anson, C. E. Buth, G.; Powell, A. K.; Wang, Z.; Gao, S. *Inorg. Chem.* **2010**, *49*, 11587.

11 Koike, N.; Uekusa, H.; Ohashi, Y.; Harnoode, C.; Kitamua, F.; Ohsaka, T.; Tokuda, K. *Inorg. Chem*. **1995**, *35*, 5798.

12 Ishikawa, N.; Sugita, M.; Ishikawa, T.; Koshihara, S.-y. Kaizu, Y. *J. Am. Chem. Soc*. **2003**, *125*, 8694.

13 Branzoli, F.; Carretta, P.; Filibian, M.; Zoppellaro, G.; Graf, M. J.; Galan-Mascaros, J. R.; Fuhr, O.; Brink, S.; Ruben, M. *J. Am. Chem. Soc*. **2009**, *131*, 4387.

14 AlDamen, M. A.; Clemente-Juan, J. M.; Coronado, E.; Martí-Gastaldo, C.; Gaita-Ariño, A. *J. Am. Chem. Soc*. **2008**, *130*, 8874.

15 AlDamen, M.A.; Cardona-Serra, S.; Clemente-Juan, J. M.; Coronado, E.; Gaita-Ariñ0, A.; Martí-Gastaldo,C.;Luis, F.; Montero, O. *Inorg. Chem*. **2009**, *48*, 3467.

16 Takamatsu, S.; Ishikawa, T.; Koshihara, S.-Y.; Ishikawa, N. *Inorg. Chem*. **2007**, *46*, 7250.

17 Rinehart, J. D. & Long, J. R. *Chem. Sci*. **2011**, *2*, 2078.

18 Jankolovits, J.; Andolina, C. M.; Kampf, J. W.; Raymond, K. N.; Pecoraro, V. L. *Angew. Chem. Int. Ed*. **2011**, *50*, 9660.

19 Jankolovits, J. Ph.D. Thesis, TBA, The University of Michigan, 2012.

20 Kahn, O. *Molecular Magnetism*; VCH Publishers, New York, 1993.

21 Shannon, R. D.; *Acta Cryst*. **1976**, *A32*, 751.

22 Ishikawa, N. *Polyhedron*, **2007**, *26*, 2147.

23 Ostendorp, G.; Werner, J.-P.; Homborg, H. *Acta Cryst*. **1995**, *C51*, 1125.

24 Carnall, W. T., Goodman, G. L.; Rajnak, K.; Rana, R. S. *J. Chem. Phys*. **1989**, *90*, 3443.

25 Jiang, S. D.; Liu, S.-S.; Zhou, L. N. Wang, B.-W.; Wang, Z. M.; Gao, S. *Inorg. Chem*. **2012**, *51*, 3079.

26 Ishikawa, N.; Sugita, M.; Okubo, T.; Tanaka, N.; Iino, T.; Kaizu, Y. *Inorg. Chem*. **2003**, *42*, 2440.
27 Abragam, A.; Bleaney, B. *Electron Paramagnetic Resonance*; Clarendon Press: Oxford, 1970.
28 Stevens, K. W. H. *Proc. Phys. Soc., London, Sect*. *A* **1952**, *65*, 209.

Chapter VI

Conclusion and Future Directions

Strategies in the single-molecule magnetism field have rapidly advanced in the past five years. Initial work in the area focused on creating large spin complexes in the hopes of increasing the blocking temperatures of SMMs. To accomplish this goal, large multinuclear systems were created, such as **Mn_{30}**,[1] **Mn_{25}**,[2] and **Mn_{19}** complexes.[3] While groups found success creating large spin complexes, unfortunately the complexes often did not possess large amounts of anisotropy, leading to low observed blocking temperatures. The reason for the small amount of observed anisotropy was often that as the molecules became larger, the individual anisotropy vectors began to overlap and cancel each other out.[4]

The field's focus shifted from large, transition metal only complexes, like the prototypical **Mn_{12}(OAc)**, to mixed *3d*/*4f* complexes, as Ln^{III} ions possess large amounts of intrinsic anisotropy as well as large amounts of spin. The first reported mixed *3d*/*4f* complex was a **Cu_2Tb_2** complex that had an energy barrier of 21 K.[5] While this barrier was not larger than **Mn_{12}(OAc)**,[6] it opened the door to mixed *3d*/*4f* complexes. Following shortly thereafter, Zaleski and co-workers reported a large **$Ln^{III}_6Mn^{III}_4Mn^{IV}_2$** complex, the first mixed Mn/Ln SMM.[7] These two complexes led to a massive research effort to create mixed *3d*/*4f* complexes, of varying degrees of success.[8,9,10,11,12,13,14]

At the same time, a new approach utilizing only a single paramagnetic ion, called single-ion magnets (SIMs) developed. Researchers found that utilizing a single Ln^{III} ion in a square anti-prismatic geometry led to record high blocking temperatures.[15,16] Further work on Ln only SMMs led to the current record in blocking temperature.[17] Against this rapidly evolving field, the current work of this thesis stands.

From the outset of this project, one of the primary goals has been optimizing anisotropy. Initial attempts utilized large mixed Mn/Ln complexes, the $\mathbf{Ln^{III}_6Mn^{III}_2Mn^{IV}_2}$ and $\mathbf{Ln^{III}_4Mn^{III}_4}$ families. The goal was that including intrinsically anisotropic Ln^{III} ions would increase overall molecular anisotropy. While these complexes had large magnetization values, they had very complicated spin states that, in turn, led to complicated magnetic behavior. Even with several Ln^{III} ions, these complexes did not yield significant improvements in blocking temperature compared to existing structures. This led to three major conclusions. One is that with multiple metals, the likelihood of unfavorable antiferromagnetic interactions increase. This decreases the overall spin value of the complex. A second is that as the molecule becomes larger, they tend to become more symmetrical. As a result, individual magnetoanisotropy vectors cancel each other out or point away from the molecular z-axis, ultimately decreasing molecular magnetoanisotropy. The third conclusion was that as a consequence of having large mixed metal complexes, the ground spin states of the complexes were no longer well isolated from the excited states. This led to more of a "band" of spin states within a few wavenumbers of each other.

This "band of spin states" is most likely the source of the low blocking temperatures of the mixed $\mathbf{Ln_6Mn_4}$ and $\mathbf{Ln_4Mn_4}$ complexes described in Chapter II. Comparing $\mathbf{Ln_6Mn_4}$ to Zaleski's $\mathbf{Ln_6Mn_6}$,[7] only two Mn^{III} ions were lost, however, the magnetic behavior of the two complexes were dramatically different, a difference that could not be explained only by the loss of two Mn^{III} ions. Examining the structures of the two mixed $\mathbf{Ln_6Mn_x}$ complexes, the magnetic interactions between the Mn ions were different, but the Ln interactions remained the same. Thus, different coupling between the Mn ions and between the Mn ions and the Ln ions were expected and subsequently observed. However, different interactions alone did not explain the magnetic behavior. The most likely explanation was that multiple spin states were populated and that a ground spin state was not isolated from the other states. Comparing $\mathbf{Ln_4Mn_4}$ to $\mathbf{Ln_6Mn_4}$,[8] the two complexes showed different magnetic susceptibility and magnetization values. However, both showed similar out-of-phase behavior, again indicating complicated magnetic

behavior. To better understand the magnetic behavior, moving away from serendipitous, large, mixed metal complexes to more controlled complexes was necessary and ideal. The ideal construct would allow for rational structures that could be systematically modified to study the impact of metal choice, magnetic interactions, and metal ratio. The construct would also allow for a certain degree of geometric control to prevent accidental cancelling of individual magnetoanisotropy vectors.

The logical choice was a family of metallamacrocycles, known as metallacrowns, because they possess all the desired properties described above.[18] Metallacrowns usually form predictable structures, and under the appropriate conditions, form planar structures that align the anisotropy vectors of the Mn^{III} ions.[19] Planarity would avoid the problem of accidental symmetry found in the larger Mn complexes discussed above. Metallacrowns can easily accommodate structural or constituent modifications, such as introducing or changing Ln^{III} ions and modifying bridging ligands, without dramatically changing the complexes geometry or overall metal stoichiometry. This allowed for direct investigation of the magnetic impact of each individual lanthanide. Only a few other research groups have successfully prepared series of isostructural complexes in order to examine the magnetic impact of the different lanthanide ions present.[20,21,22,23,10]

The **Ln^{III} 14-$MC_{Mn^{III}Ln^{III}(\mu\text{-O})(\mu\text{-OH})N(shi)}$-5** ($Ln^{III}$ = Y^{III}, Gd^{III}, Tb^{III}, Dy^{III}, Ho^{III}, Er^{III}) structure type was isolated and the magnetic properties were studied. The **Dy14MC5** became the first planar SMM and had the third largest U_{eff} (16.7 K) for mixed Mn/Ln SMMs.[24] The largest U_{eff} (38.6 K) at the time had a Ln_5Mn_4 stoichiometry, using a random self-assembly motif.[11] In **Ln14MC5**, the metallacrown ring oriented the four Mn^{III} ions in a plane, with their Jahn-Teller axes aligned parallel to each other and perpendicular to that plane. The two Ln^{III} ions could be systematically changed, while the connectivity and general shape of the molecule was maintained across the *4f* series. This allowed for identification of the source of the observed SMM behavior: the **Y14MC5** complex did not show SMM behavior, indicating that the four Mn^{III} ions in the metallacrown ring alone were not causing SMM behavior; the **Gd14MC5** complex, likewise, did not show SMM behavior, indicating that the additional spin from two Gd^{III}

ions and the anisotropy from the Mn^{III} ions in the metallacrown ring were not sufficient for inducing SMM behavior. Single-molecule magnetic behavior was observed for the other Ln^{III} ions, leading to the conclusion that SMM behavior ultimately derived from the combination of anisotropy and spin from the Ln^{III} ions present as well as the properties originating from the Mn^{III} ring ions. The behavior varied according to the Ln^{III} cation utilized: the Dy^{III} analog showed the best SMM behavior; the Tb^{III}, Ho^{III}, and Er^{III} complexes also showed frequency dependence, but no maxima in χ_M" vs. T plots were observed. Interestingly, this could indicate that Kramers' doublet systems, such as Dy^{III} were ideal for SMM behavior because they have an inherent non-zero ground state. Non-Kramers' doublet ions, such as Tb^{III}, despite having a large amount of anisotropy, can have a ground state of zero, which would not establish the desired energy double well.

It was quite difficult to elucidate the spin states of the **Ln14MC5** series. Most likely, this was due to complex interactions between the Ln^{III} and the ring Mn^{III} ions. Attempting to model the **Y14MC5** magnetic behavior to determine the ground state was not possible due to the unique geometry of the complex: normal Kambe vector coupling could not be used and four different exchange pathways between the Mn^{III} ions existed. Introduction of two additional paramagnetic Ln^{III} ions made it even more difficult to model. Removal of one Ln^{III} ion and using the 12-MC-4 geometry could allow for the isolation of a single ground state while maintaining structural control of the anisotropy vectors.

Motivated by the work on the **$Mn(OAc)_2$ 12-$MC_{Mn^{III}N(shi)}$-4**[19] and **$DyH_3O^+(Hsal)_4$ 12-$MC_{Mn^{III}N(shi)}$-4**,[25] work on other **M 12-$MC_{Mn^{III}N(shi)}$-4** complexes began. Because interesting slow magnetic relaxation of **$Mn(OAc)_2$ 12-MC-4** was observed, namely the presence of a forbidden $S = 1/2$ ground spin state and a highly anisotropic Mn^{II} ion,[19] the more anisotropic **$Ni(OAc)_2$ 12-MC-4** complex was studied. Two different crystal habits were found for the **$Ni(OAc)_2$ 12-MC-4**, dependent on the solvent (methanol or dimethylformamide) used. Structurally, the individual metallacrowns remained remarkably similar, regardless of solvent used. The magnetic properties were studied including micro-SQUID hysteresis measurements. It was found that the **$Ni(OAc)_2$ 12-MC-4 (MeOH)** isolated from methanol showed single-chain magnetism, while the

$Ni(OAc)_2$ 12-MC-4 (DMF) isolated from dimethylformamide showed single-molecule magnetic behavior. The source of this difference in behavior was due to crystal packing and hydrogen bonding between individual metallacrown molecules. The **$Ni(OAc)_2$ 12-MC-4 (MeOH)** had a hydrogen bond network between the rings along the crystallographic *a* and *b* axes, allowing for magnetic exchange between the metallacrowns. The **$Ni(OAc)_2$ 12-MC-4 (DMF)** lacked this hydrogen bond network, resulting in no exchange pathways and only SMM behavior observed. Using hydrogen bond networks could possibly be a fruitful path forward for taking 0-D SMMs and turning them into 1-D SCMs.

Because blocking temperatures above 2 K were not observed for the pure transition metal 12-MC-4 complexes, introducing Ln^{III} ions in the central cavity to increase the blocking temperatures was studied. A series of **DyX_4A 12-$MC_{Mn^{III}N(shi)}$-4** complexes were prepared where A = H_3O^+, Na^+, K^+ and X = salicylate (Hsal), benzoate, or acetate (OAc). Regardless of the counter cation present, the **$Dy(Hsal)_4A$ 12-MC-4** complexes showed frequency dependence. On the other hand, **$Dy(benzoate)_4Na$ 12-MC-4** and **$Dy(OAc)_4K$ 12-MC-4** did not show frequency dependence above 2 K. By studying the series, it was observed that the pK_a of the bridging ligand played a vital role in the out-of-phase magnetic properties. The least basic bridging ligand, salicylate, showed the best out-of-phase behavior. This indicated that electron-withdrawing strength of the ligand could perturb the magnetic behavior. The counter-ion identity seemed to "fine-tune" the observed properties. This finding is important because if SMMs are tethered to surfaces, ideally, that tether, whether through chemical or electrostatic bond, would not impact the magnetic properties.

Interest in controlling the ligand field parameters around the Ln^{III} led to studying the magnetic properties of the **$LnZn_{16}$** complexes. Inspired by Ishikawa's **$[Pc_2Ln^{III}]^-$** complexes[15] and Coronado's Ln^{III} POMs,[16] and their work on studying the ligand field around the Ln^{III}, it seemed appropriate to study the **$LnZn_{16}$** complexes. A crystallographic study of the **$TbZn_{16}$**, **$DyZn_{16}$**, and **$ErZn_{16}$** structures indicated that the Ln^{III} would be in a contracted square anti-prism environment. This environment favored

the smaller Er^{III} ion rather than the larger Ln^{III} ions as the Er^{III} would have lower energy interactions with the ligand field. On the other hand, the ligand field from the Zn metallacrowns sat above and below the Ln^{III} ion, seemingly favoring the Tb^{III} and Dy^{III} complexes due to the direction their occupied *4f* orbitals would point.[26] Utilizing oriented single crystal micro-SQUID magnetometry, it was determined that the **$ErZn_{16}$** complex had easy axis anisotropy and thus was an SMM, while the **$DyZn_{16}$** complex had easy plane anisotropy and was not an SMM. It was concluded that, despite the ligand field being above and below the Er^{III} ion, the contracted ligand field favored the smaller Er^{III} ion. It used to be thought that the ligand field around a Ln^{III} ion played no role on its properties, but it appears that at low temperatures, the ligand field does impact the properties of the Ln^{III}. By knowing the size and shape of the Ln^{III} and the ligand environment, it could be possible to predict future single-ion magnetic properties *a priori*: in more compact environments, smaller prolate lanthanides should be used, while in more axially elongated environments, larger oblate lanthanides are ideal.

Another important result from the **$LnZn_{16}$** complex was that the complex created a ground state that was more isolated than found in the other studied complexes. For these complexes, only the Ln^{III} ion provided magnetic properties. Thus, it was reasonable that these complexes have better isolated states. Because only one paramagnetic ion is present, there are no magnetic interactions, making it easier to obtain a ground state. In the other complexes studied in the thesis, there were numerous magnetic interactions, making it difficult to obtain an isolated ground state.

Outside of the **Dy 14MC5** complexes, none of the complexes studied showed maxima above 2 K for the χ_M" vs. T plots. For the other mixed Mn/Ln complexes, despite having more paramagnetic ions than the **$LnZn_{16}$** complexes, none showed significantly better SMM properties. This strongly indicates that simply making larger mixed metal complexes is not the most prudent strategy for improving SMM behavior. Rather, if one carefully controls the geometry of the complex and the ligand field around the paramagnetic metals, one could create better SMMs.

To accomplish this goal, several design strategies are possible. Rather than using Mn^{III} ions as the ring metals in the 12-MC-4 complexes, one could use diamagnetic Ga^{III} ions while maintaining the central Ln^{III} ions, and then study the magnetism of the resulting complexes. Manganese^{III} and Ga^{III} ions have similar ionic radii[27] and affinities for the salicylhydroxamic acid ligand.[28] Using diamagnetic Ga^{III} ions with a central Ln^{III} would ensure that all magnetic properties originiated from the Ln^{III} ion and eliminate exchange coupling pathways. This should help isolate a single ground state. Using the crystal structure of $\mathbf{Na_2(Na_{0.5}[12\text{-}MC_{Ga^{III}N(shi)}\text{-}4]_2)}$[28] as a guide for a potential $\mathbf{Ln^{III}}$ **[12-**$\mathbf{MC_{Ga^{III}N(shi)}}$**-4]** (Figure 6.1), one can see that the oxygens in the metallacrown plane are separated by 2.677 Å and 2.629 Å, while the analogous oxygen separations in the $\mathbf{Ln^{III}Zn_{16}}$ complexes are approximately 2.9 Å. This difference in cavity radius could affect the displacement of the Ln^{III} ion and thus the ligand field parameters.

If a 12-$MC_{Ga^{III}N(shi)}$-4 dimer was formed, there are two possible locations the Ln^{III} ion could occupy; above the two metallacrown planes or in between the planes. Because the metallacrowns are concaved towards the central cavity and based on observations of previously isolated metallacrowns, the central cavity is the most likely metal binding site (Figure 6.2). The two oxygen mean planes are separated by 3.132 Å, which is much larger than the cavity found in the $\mathbf{LnZn_{16}}$ complexes (approximately 2.1 Å). This would give an axially elongated D_{4h} symmetry if the Ln^{III} ion was bound inside the cavity; recall that the $\mathbf{LnZn_{16}}$ placed the Ln^{III} in axially contracted D_{4d} symmetry. These differences in geometry could greatly affect the ligand field of the Ln^{III}, perturbing the magnetic behavior.

One could also potentially synthesize the Ln^{III} sandwich complex with the 12-$MC_{Mn^{III}N(shi)}$-4 complexes, using the $\mathbf{LnX_4A\ 12\text{-}MC_{Mn^{III}N(shi)}\text{-}4}$ complexes as a guide. Again, two potentially interesting structures are possible; one, where there are two Ln^{III} 12-MC-4 complexes bridged by a large dication at the center, such as Ba^{II} or Pb^{II}; or a second, where the Ln^{III} ion is at the center and the bridging anions are either removed or changed to large bridging anions, such as terephthalate (Figure 6.3).

The first complex type, with Pb^{II} replacing the Na^{I} or K^{I} was attempted, but was not successfully prepared. Attempts with Ba^{II} in dimethylformamide, methanol, and acetonitrile also proved unsuccessful due to insolubility of Ba^{II}. It is unknown why the Pb^{II} synthesis did not work. It is possible that rather than attempt to form the sandwich complex all at once, it may be better to form and isolate the **LnX_4A 12-MC-4** first, then attempt to removed the A^{+} cation, possibly with a crown ether, and then introduce the Pb^{II} ion. In the case of Ba^{II}, multiple solvents were tried, but none could dissolve the Ba^{II} salts. Even using the sonicator did not dissolve the salts. Perhaps a different solvent or a mixed solvent could be used. The second type of metallacrown, with terephthalate, 4,4'-bipyridine, or isonicotinate, were attempted, but were not successful. It is possible that these ligands did not provide enough space between the two metallacrowns, and a longer anion would be appropriate. It is also possible that forming the **LnX_4A 12-MC-4** first, then substituting the anion could be successful.

Both structure types have their merits as well as their own drawbacks. The biggest merit, regardless of structure type is the addition of four anisotropic Mn^{III} ions *if* their anisotropic tensors all align in a parallel fashion. Because it is not possible to determine the direction of the anisotropy tensors *a priori*, the study should be conducted. If the di-Ln^{III} sandwich complex formed, two Ln^{III} ions would increase both the spin and the anisotropy of the complex. The two Ln^{III} ions would far enough apart that there would not be significant coupling between the sites. If the mono-Ln^{III} sandwich complex formed, the bridging anions X found in the **LnX_4A 12-MC-4** complexes would probably need to be removed, thus affecting the magnetic coupling of the Ln^{III} to the ring Mn^{III} ions. This could perturb the magnetic behavior. Some potential drawbacks to these structure types include the possibility of anti-parallel anisotropy tensors as well as complicating the coupling schemes. This last drawback likely impacts the mono-Ln^{III} complex the most. Rather than being exchange coupled with only four Mn^{III} ions, the Ln^{III} ion would now be coupled with eight Mn^{III} ions. If one is trying to get to well isolated ground states, this may not be the best synthetic route. Also, it is quite likely that the exchange coupling between the Mn^{III} ions in the ring would not change significantly in the di-Ln^{III} sandwich complexes, thus little, if any, spin from the ring would be

observed. However, determining Ln^{III} exchange pathways could be interesting, as it is still often erroneously thought that outside of Cu^{II}-Gd^{III}, that the Ln^{III} ions do not exchange couple with *3d* metals.

Another way to create well isolated ground states, as well as test the impact of the ligand field about a Ln^{III} ion, which is currently underway, is to study the rich family of Ln^{III} Zn metallacrowns prepared by Joseph Jankolovits. Joe was able to prepare sandwich **Ln [12-$MC_{Zn^{II}}$-4]$_2$** (Figure 6.4), sandwich **Ln[12-$MC_{Zn^{II}}$-4][12-C-4]** (Figure 6.5), and **Ln [12-$MC_{Zn^{II}}$-4]** complexes (Figure 6.6). Each of these complexes has a different Ln^{III} ligand environment. By studying the series, one could potentially see that elongation of the ligand environment shifts the SMM properties from smaller Er^{III} ions to larger Dy^{III} ions. No other group has the ability, or at the very least, the desire and foresight, to alter such properties in their complexes.

Further insight of the spin structure of **$LnZn_{16}$** complexes could be gained by studying the paramagnetic ^{1}H nuclear magnetic resonance (^{1}H NMR) spectra. Ishikawa showed that the ligand field parameters of triple-decker **PcLnPcLnPc*** complexes, where Pc* is the dianion of 2,3,9,10,16,17,23,24-octabutoxyphthalocyanine, could be determined by multidimensional minimization analyses of the ^{1}H NMR and magnetic susceptibility data.[29,30] Ishikawa utilized this analysis for the simpler **$[Pc_2Ln^{III}]^-$** complex, indentifying the electronic structure of the complex.[15] Coronado then adapted this strategy for his Ln^{III} POM complexes, again determining the ligand field parameters.[31] As the theoretical calculations on the **$LnZn_{16}$** complexes have been performed, and these complexes fit nicely into the parameters already established by Ishikawa and Coronado, it would be very satisfying to see if those predicted spin states are observed experimentally. These calculations could then be carried over to the other **Ln^{III} Zn** metallacrowns, if appropriate.

From the work on these metallacrowns and large mixed Mn/Ln complexes, these general conclusions should help guide future SMM research. From working on the **Ln_6Mn_4** and **Ln_4Mn_4** complexes, it is possible to state that without some degree of geometric control,

it is difficult to produce SMMs with large blocking temperatures. This is due to the fact that as the complexes increase in size, they begin to: 1) become more spherical and accidently decrease anisotropy; 2) have more exchange coupling pathways leading to complicated spin behavior; 3) have uncontrollable ligand field parameters which perturbs ionic spin states. For these large complexes, Dy^{III} ions seem to be the best Ln^{III} to use due to Dy^{III}'s Kramer's doublet ground state and large spin and anisotropy values (S = 5/2, L = 5, J = 15/2). This general trend of Dy^{III} ions creating "good" SMMs was also seen in the **Ln^{III} 14-$MC_{Mn^{III}Ln^{III}(\mu\text{-}O)(\mu\text{-}OH)N(shi)}$-5** complexes. Again, the best performing complex was the **Dy 14MC5** analog. The impact of ligand field around the studied Ln^{III} ions is also important, as determined by the work on the **DyX_4A 12-MC-4** and **$LnZn_{16}$** complexes. For the **DyX_4A 12-MC-4** series, even though the first coordination sphere around the Dy^{III} ion was the same (carboxylate and hydroximate oxygens), frequency dependence was only observed for the salicylate bridged examples and not the benzoate or acetate species. Slight changes in the ligand field, due to the ligand pK_a, did not dramatically affect the dc magnetic properties, but did affect the slow magnetic relaxation properties. The dramatic effect the ligand field had on magnetic properties was observed for the **$LnZn_{16}$** complexes. In this case, the axially contracted ligand environment favored slow magnetic relaxation for the smaller Er^{III} example, while the larger Dy^{III} ion, despite having the ligands geometrically oriented favorably above and below the ion, did not show slow magnetic relaxation. This result corroborates the results and conclusions reported by Coronado.[31] The future studies proposed above will help explore the depth of validity of these conclusions.

The rich chemistry of metallacrowns makes them fascinating complexes to study with regards to single-molecule magnetism. While serendipitous products have their place in the literature,[32] in order to better understand the source of the observed magnetic phenomena, it is better to systematically alter individual parameters of complexes. Metallacrowns present a rare opportunity to structurally control the metal complex product, leading to predictable structures that are available for systematic alterations. There are few other complexes known that permit series of isostructural complexes to be prepared and isolated, allowing for in depth study of the individual contributions of the

metals present. For instance, in the presented series of complexes, it was possible to determine the origin of slow magnetic relaxation in series of mixed Mn/Ln complexes. It was possible to study the impact of metal stoichiometry and ligand pK_a on magnetic properties in structurally similar complexes. It was possible to study the impact of contracted ligand fields on magnetic behaviors of Ln^{III} ions. Few groups have the ability to conduct such a breadth of studies described above. Because of the wide range of sizes of metallacrowns, it is also possible to study the impact of changes to the coordination environment of the metals studied, which as has been demonstrated, can dramatically affect SMM properties. The abilities to control anisotropy, to orient metals closely in space, and to systematically vary metals and ligands give metallacrowns a degree of control not seen in other metal complexes. The future of metallacrowns as SMMs is bright. There are several directions available to the nimble-minded chemist that will hopefully lead to high-performance single-molecule magnets.

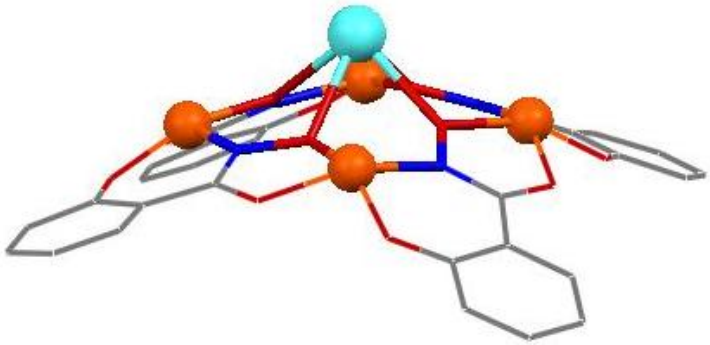

Figure 6.1. The proposed structure of a Ln^{III}[12-$MC_{Ga^{III}N(shi)}$-4] is drawn based on the x-ray crystal structure of **{Na_2(Na[12-$MC_{Ga^{III}N(shi)}$-4]$_2$-(μ-OH)$_4$)}**. Color scheme: aqua sphere: Ln^{III}; orange sphere: Ga^{III}; red tubes: oxygen; blue tubes: nitrogen; gray tubes: carbon.

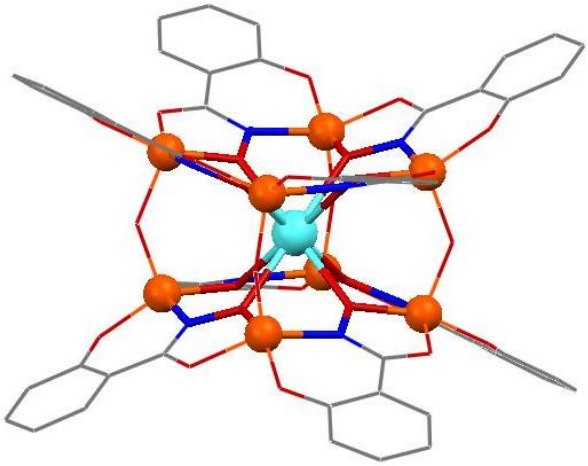

Figure 6.2. The proposed structure of a sandwich Ln^{III}[12-$MC_{Ga^{III}N(shi)}$-4]$_2$(μ-OH)$_4$ is drawn based on the x-ray crystal structure of **{Na_2(Na[12-$MC_{Ga^{III}N(shi)}$-4]$_2$-(μ-OH)$_4$)}**. Color scheme: aqua sphere: Ln^{III}; orange sphere: Ga^{III}; red tubes: oxygen; blue tubes: nitrogen; gray tubes: carbon.

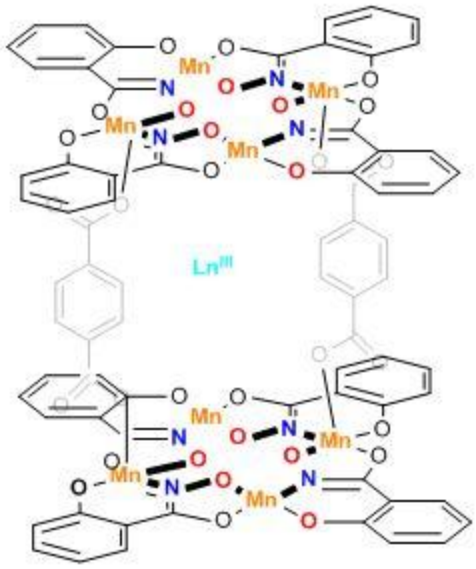

Figure 6.3. The ChemDraw structure of a sandwich Ln^{III} $[12\text{-}MC_{Mn^{III}N(shi)}\text{-}4]_2$ complex bridged by two terephthalate ligands.

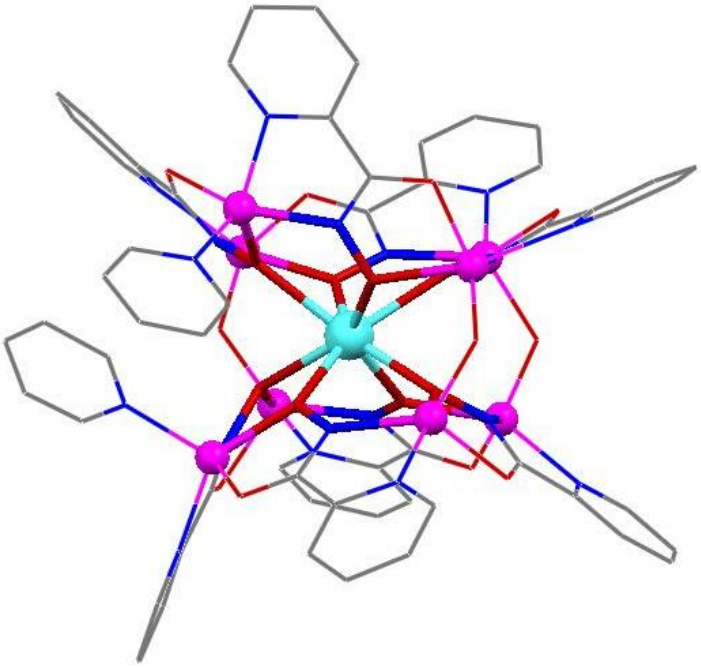

Figure 6.4. The x-ray crystal structure of **Dy^{III} $[12\text{-}MC_{Zn^{II}}\text{-}4]_2$** is shown. Color scheme: aqua sphere: Dy^{III}; pink sphere: Zn^{II}; red tube: oxygen; blue tube: nitrogen; gray tube: carbon.

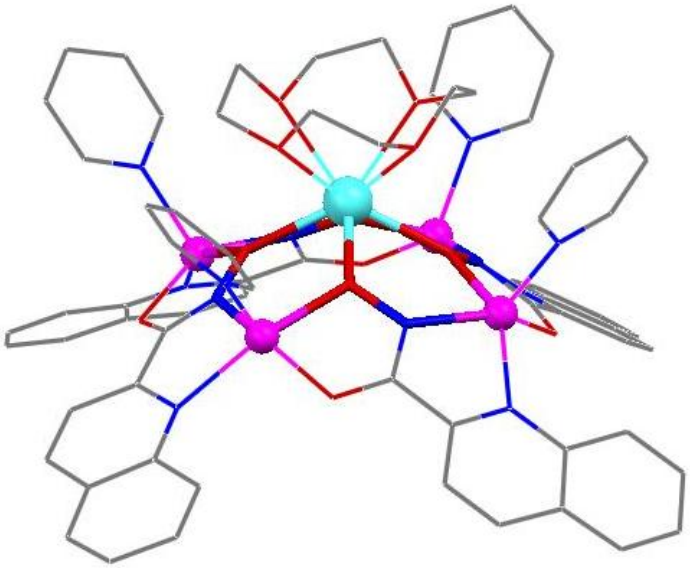

Figure 6.5. The x-ray crystal structure of **Dy^{III}[12-$MC_{Zn^{II}}$-4][12-C-4]** is shown. Color scheme: aqua sphere: Dy^{III}; pink sphere: Zn^{II}; red tube: oxygen; blue tube: nitrogen; gray tube: carbon.

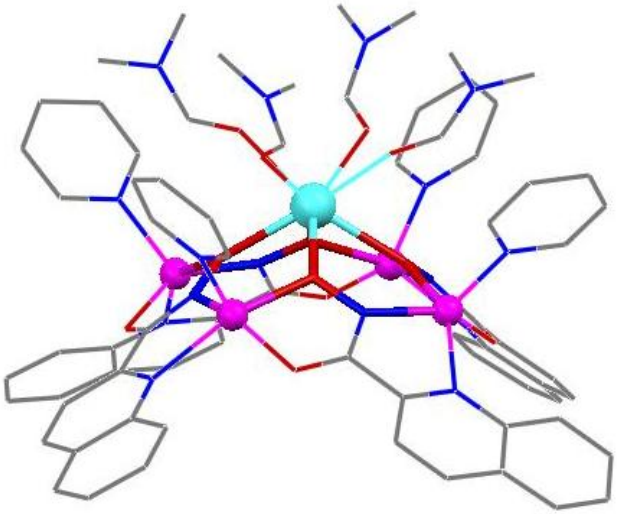

Figure 6.6. The x-ray crystal structure of **Dy^{III}[12-$MC_{Zn^{II}}$-4]** is shown. Color scheme: aqua sphere: Dy^{III}; pink sphere: Zn^{II}; red tube: oxygen; blue tube: nitrogen; gray tube: carbon.

References

1 Soler, M; Wernsdorfer, W.; Folting, K.; Pink, M.; Christou, G. *J. Am. Chem. Soc*. **2004**, *126*, 2156.

2 Murugesu, M.; Habrych, M.; Wernsdorfer, W.; Abboud, K. A.; Christou, G. *J. Am. Chem. Soc*. **2004**, *126*, 4766.

3 Ako, A. M.; Hewitt, I. J.; Mereacre, V.; Clérac, R.; Wernsdorfer, W.; Anson, C. E.; Powell, A. K. *Angew. Chem*. **2006**, *118*, 5048.

4 Waldmann, O.; Ako, A. M.; Güdel, H. U.; Powell, A. K. *Inorg. Chem*. **2008**, *47*, 3486.

5 Osa, S.; Kido, T.; Matsumoto, N.; Re, N.; Pochaba, A.; Mrozinski, J. *J. Am. Chem. Soc*. **2004**, *126*, 420.

6 Hill, S.; Perenboom, J. A. A. J.' Dalal, N. S.; Hathaway, T.; Stalcup, T.; Brooks, J. S. *Phys. Rev. Lett*. **1998**, *80*, 2453.

7 Zaleski, C. M. Depperman, E. C.; Kampf, J. W.; Kirk, M. L.; Pecoraro, V. L. *Angew. Chem. Int. Ed.* **2004**, *43*, 3912.

8 Zaleski, C. M.; Kampf, J. W.; Mallah, T.; Kirk, M. L.; Pecoraro, V. L. *Inorg. Chem*. **2007**, *46*, 1954.

9 Mereacre, V. M.; Ako, A. M.; Clérac, R.; Wernsdorfer, W.; Filoti, G.; Bartolomé, J.; Anson, C. E.; Powell, A. K. *J. Am. Chem. Soc*. **2007**, *129*, 9248.

10 Mereacre, V.; Lan, Y.; Clérac, R.; Ako, A. M.; Wernsdorfer, W.; Buth, G.; Anson, C. E.; Powell, A. K. *Inorg. Chem.* **2011**, *50* 12001.

11 Mereacre, V.; Ako, A. M.; Clérac, R.; Wernsdorfer, W.; Hewitt, I. J.; Anson, C. E.; Powell, A. K. *Chem. Eur. J*. **2008**, *14*, 3577.

12 Ako, A. M.; Mereacre, V.; Clérac, R.; Wernsdorfer, W.; Hewitt, I. J.; Anson, C. E.; Powell, A. K. *Chem. Commun*. **2009**, 544.

13 Mereacre, V.; Akhtar, M. N.; Lan, Y.; Ako, A. M.; Clérac, R.; Anson, C. E.; Powell, A. K. *Dalton Trans*. **2010**, *39*, 4918.

14 Li, M.; Lan, Y.; Ako, A. M.; Wernsdorfer, W.; Anson, C. E. Buth, G.; Powell, A. K.; Wang, Z.; Gao, S. *Inorg. Chem.* **2010**, *49*, 11587.

15 Ishikawa, N.; Sugita, M.; Ishikawa, T.; Koshihara, S.-y. Kaizu, Y. *J. Am. Chem. Soc*. **2003**, *125*, 8694.

16 AlDamen, M. A.; Clemente-Juan, J. M.; Coronado, E.; Martí-Gastaldo, C.; Gaita-Ariño, A. *J. Am. Chem. Soc*. **2008**, *130*, 8874.

17 Blagg, R. J.; Muryn, C. A.; McInnes, E. J. L.; Tuna, F.; Winpenny, R. E. P. *Angew. Chem. Int. Ed*. **2011**, *50*, 6530.

18 Mezei, G.; Zaleski, C. M.; Pecoraro, V. L. *Chem. Rev*. **2007**, *107*, 4933.

19 Zaleski, C. M.; Tricard, S.; Depperman, E. C.; Wernsdorfer, W.; Mallah, T.; Kirk, M. L.; Pecoraro, V. L. *Inorg. Chem*. **2011**, *50*, 11348.

20 Mishra, A.; Wernsdorfer, W.; Abboud, K. A.; Christou, G.; *J. Am. Chem. Soc*. **2004**, *126*, 15648.

21 Mereacre, V.; Ako, A. M.; Clérac, R.; Wernsdorfer, W.; Hewitt, I. J.; Anson, C. E.; Powell, A. K. *Chem. Eur. J*. **2008**, *14*, 3577.

22 Akhtar, M. N.; Lan, Y.; Mereacre, V.; Clérac, R.; Anson, C. E.; Powell, A. K. *Polyhedron*, **2009**, *28*, 1698.

23 Mereacre, V.; Akhtar, M. N.; Lan, Y.; Ako, A. M.; Clérac, R.; Anson, C. E.; Powell, A. K. *Dalton Trans*. **2010**, *39*, 4918.
24 Boron, III, T. T.; Kampf, J. W.; Pecoraro, V. L. *Inorg. Chem*. **2010**, *49*, 9104.
25 Zaleski, C. M. Ph.D. Thesis, Utilizing Metallacrowns to Develop New Single-Molecule Magnets, The University of Michigan, 2005.
26 Rinehart, J. D. & Long, J. R. *Chem. Sci*. **2011**, *2*, 2078.
27 Shannon, R. D. *Acta Cryst*. **1976**, *A32*, 751.
28 Lah, M. S.; Gibney, B. R.; Tierney, D. L.; Penner-Hahn, J. E.; Pecoraro, V. L. *J. Am. Chem. Soc*. **1993**, *115*, 5857.
29 Ishikawa, N.; Iino, T.; Kaizu, Y. *J. Phys. Chem. A*, **2002**, *106*, 9543.
30 Ishikawa, N.; Iino, T.; Kaizu, Y. *J. Am. Chem. Soc*. **2002**, *124*, 11440.
31 AlDamen, M. A.; Cardona-Serra, S.; Clemente-Juan, J. M.; Coronado, E.; Galta-Ariño, A.; Martí-Gastaldo, C.; Luis, F.; Montero, O. *Inorg. Chem*. **2009**, *48*, 3467.
32 Gatteschi, D.; Sessoli, R.; Villain, J. *Molecular Nanomagnets*; Oxford University Press, New York, 2006.